Multidimensional isotropic and anisotropic investigation of the Tajo Basin subsurface

A novel anisotropic inversion approach for subsurface cases with oblique geoelectric strike directions

by

JAN-PHILIPP SCHMOLDT

A thesis submitted to
The Faculty of Science, National University of Ireland, Galway
in fulfilment of the requirements for the degree of

Doctor of Philosophy (PhD)

June 2011

SUPERVISION BY:
Prof. Dr. Alan G. Jones, Dublin Institute for Advanced Studies, Dublin, Ireland
AND
Dr. Colin Brown, National University of Ireland, Galway, Ireland

School of Cosmic Physics,
Geophysics Section,
Dublin Institute for Advanced Studies,
Dublin, Ireland

Faculty of Science,
Department of Earth and Ocean Science,
National University of Ireland,
Galway, Ireland

Contents

List of Figures

List of Tables

List of Acronyms

1D	one-dimensional
2D	two-dimensional
3D	three-dimensional
AMT	audio-magnetotellurics
BBMT	broadband magnetotellurics
CG	conjugate gradient method
CMB	core–mantle boundary
CVP	Calatrava Volcanic Province
DP1	polar magnetic storms with centre of disturbance in the night-time auroral zone
DP2	polar magnetic storms with correlated irregular variations in low latitudes
DS	disturbance local time inequality of smoothed storm-time variations
Dst	storm time-dependent part of smoothed storm-time variations
EEJ	equatorial electrojet
eLAB	electric lithosphere–asthenosphere boundary
EM	electromagnetics
ERC	equatorial ring current in the radiation belt of the magnetosphere
FD	finite difference (method)

FE finite element (method)

FV finite volume (method)

GDS geomagnetic deep sounding

GN Gauss-Newton (method)

GN-CG GN with conjugate gradient (method)

HIMU "high μ" with $\mu = {}^{238}U/{}^{204}Pb$

HFU heat flow unit

IE integral equation (method)

L lunar daily variations

LAB lithosphere–asthenosphere boundary

LEMI long-period electromagnetic instrument

MHD magnetohydrodynamic (waves)

MT magnetotellurics

MTZ mantle transition zone

NLCG nonlinear conjugate gradients (method)

Pc1 – Pc5 regular continuous ultralow frequency waves (pulsations)

Pi1, Pi2 irregular transient ultralow frequency waves (pulsations)

PDE partial differential equation

PEJ polar electrojet in the ionosphere

PICASSO program to investigate the convective Alboran Sea system overturn

QN quasi-Newton (method)

RMS root mean square

SCS Spanish central system

S_D solar daily variation, enhanced on disturbed days

sfe solar flare effect

sLAB	seismic lithosphere–asthenosphere boundary
SNR	signal-to-noise ratio
Sq	solar daily variation on quiet days
ssc	sudden storm commencement
SVD	single value decomposition
TE	transverse electric mode / E-polarisation
TEM	transient (or time-domain) electromagnetic (method)
tLAB	thermal lithosphere–asthenosphere boundary
TM	transverse magnetic mode / B-polarisation
ULF	ultralow frequency (bands / waves)
VLF	very low frequency (bands / waves)
WAL	Weaver, Agarwal, Lilley (method)

List of Symbols

Below is a list of symbols and nomenclature used within this thesis and their meanings as well as their SI units. Vectors are denoted by aan arrow, whereas matrices / tensors are indicated by bold font.

Symbol	SI unit	Denotation
α	·	current channelling number
α_p	·	Caldwell parameter (coordinate dependent)
$\vec{B}$	nT or T = $\frac{Vs}{m^2}$	magnetic field
c	$2.99792458 \cdot 10^8 \frac{m}{s}$	speed of light
$\mathbf{C}$	·	distortion tensor
$c_{xx}, c_{xy}, c_{yx}, c_{yy}$	·	elements of $\mathbf{C}$ in Cartesian coordinates
C_{xy}	·	coherence between elements x and y
$\vec{D}$	$\frac{As}{m^2}$	electric displacement field
$\mathbf{D}_\Phi$	·	distortion of the electric field
D_{perm}	·	deviation from true apparent resistivity due to negligence of the permittivity influence
D_1	Ωm	difference of diagonal elements (of the impedance tensor)
D_2	Ωm	difference of off-diagonal elements / anti-trace (of the impedance tensor)
$\vec{d}$	Ωm or log(Ωm)	observed (magnetotelluric) data
δ_s	m (or km)	skin depth
$\vec{E}$	$\frac{V}{m}$	electric field
E_x, E_y, E_z	$\frac{V}{m}$	elements of $\vec{E}$ in Cartesian coordinates
e_D	·	telluric shear distortion

Continued on Next Page...

Symbol	SI unit	Denotation
ϵ	Ω or log(Ωm)	model misfit, i.e. the difference between model response and measured data
$\varepsilon = \varepsilon_0 \cdot \varepsilon_r$	$\frac{As}{Vm}$	electric permittivity
ε_0	$8.854 \cdot 10^{-12} \frac{As}{Vm}$	electric permittivity of the vacuum
ε_r	·	relative electric permittivity
ε^*	·	breakdown point of an estimator
η	$\frac{C}{m^3}$	electric charge density
η_B	$(\Omega\text{m})^{1/2}$	Bahr parameter: Descriptiveness of MT tensor by superimposed model
f	Hz $= \frac{1}{s}$	frequency
$\mathbf{G}$	·	Transformation matrix between model and observed data
h	m (or km)	height of a body
$\vec{H}$	$\frac{A}{m}$	magnetising field
H_x, H_y, H_z	$\frac{A}{m}$	elements of $\vec{H}$ in Cartesian coordinates
I	A	current
$I_1 - I_2$	$\frac{m}{s^2}$	Weaver tensor invariants
$I_3 - I_7$	·	Weaver tensor invariants
$\vec{J}$	$\frac{A}{m^2}$	electric current density
$\vec{J}_f$	$\frac{A}{m^2}$	electric current density of free charges (Maxwellian term)
$\vec{k}$	$\frac{1}{m}$	horizontal wave number
k	$\frac{1}{m}$	norm of horizontal wave number
κ	·	Swift skew
Λ	m (or km)	adjustment distance / horizontal skin depth
λ_p	m (or km)	ellipticity of Caldwell phase tensor
$L(_i)$	m (or km)	length (of body i)
$M(_i)$	·	induction number (of body i)
$\vec{m}$	Ωm or log(Ωm)	subsurface model data
$\mu = \mu_0 \cdot \mu_r$	$\frac{Vs}{Am}$	magnetic permeability
μ_0	$4\pi \cdot 10^{-7} \frac{Vs}{Am}$	magnetic permeability of the vacuum
μ_r	$\frac{Vs}{Am}$	relative magnetic permeability
μ_B	$(\Omega\text{m})^{-1/2}$	Bahr parameter: Phase difference in the MT tensor
$\mathbf{P}$	·	distortion of the electric field
$P_{xx}, P_{xy}, P_{yx}, P_{yy}$		elements of $\mathbf{P}$ in Cartesian coordinates
ϕ	·	Porosity (of a rock)

Continued on Next Page...

Symbol	SI unit	Denotation
ϕ	·	phase (of the electric impedance)
$\mathbf{\Phi}$	·	Caldwell phase tensor
$\Phi_{11}, \Phi_{12}, \Phi_{21}, \Phi_{22}$		elements of $\mathbf{\Phi}$
$\Phi_1 - \Phi_4$	·	Caldwell parameters (coordinate independent)
π	·	Ludolf's number
ψ	·	error function
$\mathbf{Q}_h$	·	distortion of the horizontal magnetic field
$Q_{xx}, Q_{xy}, Q_{yx}, Q_{yy}$	·	elements of $\mathbf{Q}_h$ in Cartesian coordinates
$\mathbf{Q}_z$	·	distortion of the vertical magnetic field
Q_{zx}, Q_{zy}	·	elements of $\mathbf{Q}_z$ in Cartesian coordinates
R	Ω $(=\frac{1}{\sigma})$	resistance (integrated electric resistivity)
$\mathbf{R}$	·	rotation matrix
R_{dd}	·	error covariance matrix
S_{xy}	·	cross-spectral density
Q_e	$\frac{C}{m^n}$	electric charge density
Q_W	·	Weaver tensor invariant
ρ	Ωm $(=\frac{Vm}{A})$	electric resistivity
ρ_a	Ωm	apparent electric resistivity
S	S $(=\frac{1}{\Omega})$	conductance (integrated electric conductivity)
S_1	Ωm	sum of diagonal elements / trace (of the impedance tensor)
S_2	Ωm	sum of off-diagonal elements (of the impedance tensor)
s_D	·	telluric anisotropic distortion
σ	$\frac{S}{m}$ $(=\frac{1}{\Omega m})$	electric conductivity
Σ_B	·	Bahr parameter: Two-dimensionality
T	s	period
$\vec{T}$	·	geomagnetic transfer function/tipper
T_x, T_y	·	elements of $\vec{T}$ in Cartesian coordinates
t	s	time
τ	$\frac{S}{m^2}$, $\frac{S}{m^3}$, Ω, or $\frac{\Omega}{m}$	Smoothness parameter in inversion, e.g. $\nabla\sigma$, $\nabla^2\sigma$, $\nabla\rho$, $\nabla^2\rho$, or logarithmic values
t_D	·	telluric twist distortion
Θ	$^\circ$ or rad	angle
$\vec{v}$	$\frac{m}{s}$	velocity
ω	$\frac{1}{s}$	angular frequency
x, y, z	m (or km)	Cartesian coordinates (z pos. downwards)

Continued on Next Page...

Symbol	SI unit	Denotation
$\mathbf{Z}$	$\Omega = \frac{V}{A}$	complex impedance tensor
$Z_{xx}, Z_{xy}, Z_{yx}, Z_{yy}$	Ω	elements of $\mathbf{Z}$ in Cartesian coordinates
z	m (or km)	depth
$\hat{e}_x$		unity vector with respect to x-coordinate
$\imath$		complex number
Re		real part of a complex number
Im		imaginary part of a complex number
∂_x		partial derivative with respect to x-coordinate
∂_t		partial derivative with respect to time
∇		Nabla operator
$\Delta = \nabla^2$		Laplace operator
$\mathbf{J}$		Jacobian
$\mathbf{H}$		Hessian
Ξ		linear operator used in the error function
∞		infinite
$\lvert \cdot \rvert$		absolute value
$\lVert \cdot \rVert$		norm
$\langle \cdot \rangle$		estimate
$\vec{x}$		vector x
$\mathbf{X}, \mathbf{X}^T$		matrix X, transpose matrix X
$\mathbf{X}, \mathbf{X}^*$		matrix X, complex conjugated matrix X
$\mathbf{I}$		identity matrix
Cl		Chlorine
Cu		Copper
$CuSO_4$		Copper sulfate
Nd		Neodymium
Pb		Lead (Plumbum)
$PbCl_2$		Lead chloride
Sr		Strontium
U		Uranium

Abstract

The Tajo Basin and Betic Cordillera are the areas investigated by the first phase of the PICASSO (*Program to Investigate the Convective Alboran Sea System Overturn*) project in south-central Spain. The magnetotelluric (MT) component of PICASSO Phase I provides information about the electric conductivity distribution in previously unprobed subsurface regions, as well as enhancing results of prior geological and geophysical investigations, thereby enabling the devise of a petrological subsurface model and a comprehensive understanding about the tectonic setting.

During analysis of the MT data, oblique geoelectric strike directions were determined for the Tajo Basin subsurface, which causes severe artefacts in models from commonly applied isotropic two-dimensional (2D) inversion, or requires computationally expensive three-dimensional (3D) inversion. A novel approach is developed in this thesis, which utilises electric anisotropy in one-dimensional (1D) and 2D inversions to image oblique 2D subsurface structures. Computational expense of this approach is considerably lower and its performance is successfully tested in a synthetic model study and subsequently employed to derive a model of the Tajo Basin subsurface.

In addition to the novel anisotropic approach, isotropic 2D and 3D inversions are used to obtain enhanced insight into Iberian subsurface geology. The most striking features of the model are (i) a distinct vertical interface in the centre of the Tajo Basin that is associated with the "Alpine Spain" – "Variscan Spain" boundary; (ii) a mid- to lower crustal anomaly that is related to remnants of asthenospheric intrusion in connection with Pliocene volcanic events in the Calatrava Volcanic Province; (iii) a low resistivity – low velocity feature in the Tajo Basin lithospheric-mantle, related to the extensive reservoir responsible for volcanic events throughout Europe and Morocco. For the latter two, effects of hydrous phases are inferred that may originate from dehydration processes at the subducting slab beneath Alboran Domain and Betics Cordillera.

Publications

Results of the PICASSO Phase I project, new insights about the Iberian Peninsula subsurface, and development of the novel anisotropic 1D and 2D inversion approaches used to recover a 3D subsurface have been presented to the scientific community as follows:

Conference talks

- Schmoldt, J.-P., A.G. Jones, C. Hogg, and O. Rosell, 2009. PICASSO - Phase I: MT Investigation of Spain from Madrid to the Betics - preliminary results and models. EGU General assembly, Vienna, 19 - 24 April

- Schmoldt, J.-P., A.G. Jones, C. Hogg, and O. Rosell, 2009. PICASSO - Phase I: Magnetotelluric (MT) Investigation of Spain from Madrid to the Betics - preliminary results and models. 52nd Irish Geological Research Meeting (IGRM), Dublin, 20 - 22 February

- Schmoldt, J.-P., A.G. Jones, C. Hogg and O. Rosell, 2008. PICASSO - Phase I: MT Investigation of the Betic-Rif mountain system. Comparison of actual robust processing algorithms. 19th IAGA EM Induction Workshop, Beijing, China, 23 - 29 October

Poster presentations

- Schmoldt, J.-P. and A.G. Jones, 2011. Using anisotropic approaches to realise 2D magnetotelluric inversion of a subsurface with depth-varying geoelectric strike direction - Synthetic model study and application to real data from the PICASSO Phase I project. EGU General Assembly, Vienna, 3 - 8 April

- Schmoldt, J.-P., A.G. Jones, M. Muller, D. Kiyan, C. Hogg, and O. Rosell, 2011. Geometries and structures within the Iberian lithosphere and asthenosphere beneath the Tajo Basin and Betic Cordillera revealed using magnetotellurics - Results of the PICASSO Phase I project. EGU General Assembly 2011, Vienna, 3 - 8 April

- Schmoldt, J.-P., A.G. Jones, J. Fullea, M. Muller, C. Hogg, and O. Rosell, 2011. Magnetotelluric investigation of the lithosphere-asthenosphere boundary beneath the Tajo Basin contrasted with results from seismic and thermal modelling studies - Results of the PICASSO Phase I project in the Iberian Peninsula. EGU General Assembly 2011, Vienna, 3 - 8 April

- Schmoldt, J.-P., A.G. Jones, M. Muller, D. Kiyan, C. Hogg, and O. Rosell, 2010. Realizing 2D magnetotelluric inversion in the case of divergent geoelectric strike directions in the crust and mantle. AGU fall meeting, San Francisco, 13 - 17 December

- Schmoldt, J.-P., A.G. Jones, C. Hogg, and O. Rosell, 2010. Magnetotelluric investigation of the Iberian lithosphere and asthenosphere beneath Tajo Basin and Betic Cordillera (PICASSO Phase I). 20th IAGA EM Induction Workshop, Cairo, 18 - 24, September

- Kiyan, D., J. P. Schmoldt, A.G. Jones, C. Hogg, and O. Rosell, 2009. The PICASSO project: MT Investigation in Southern Spain and Morocco - Results of Phase I and outlook on Phase II. AGU fall meeting, San Francisco, 13 - 17 December

Acknowledgements

In the course of composing a work with the extent of a PhD thesis one cannot avoid to meet lots of great, interesting, and inspiring people during the time it takes to complete it. This Chapter is to express my sincere thanks to all these people and to record their names for everyone to read (personal thanks will also be given to the people in, well, person). Multiple entries are herein explicitly intended. Following the advice of Stephen Benka ("It's the audience, stupid", meaning that content should be presented in the way that best suits the recipient) acknowledgements are given in the people's respective language; at least for those languages that I found myself (more or less) able to communicate in — which effectively means that some of the sentences are in German and here and there a foreign word is interspersed.

In general, acknowledgements follow no specific order —
aber zu allererst moechte ich meiner Familie danken, meinen Grosseltern *Herbert* (der leider das Ende meiner Doktorarbeit nicht mehr erleben konnte) und *Kaethe*, meinen Eltern *Josef* und *Monika*, ihren Partnern *Petra* und *Cora*, sowie meinen Geschwistern *Mareike* und *Johannes*. Vielen Dank dass Ihr all die Zeit zu mir gestanden habt, mich immer wieder aufgebaut habt wenn ich es brauchte und mir die Möglichkeit gegeben habt eine Doktorarbeit anzufangen. Ohne euch hätte ich sie nicht zu Ende gebracht.

I would further like to acknowledge funding of the PICASSO project, and through that my PhD scholarship, by the Science Foundation Ireland (SFI). I wish to acknowledge the SFI/HEA Irish Centre for High-End Computing (ICHEC) for the provision of computational facilities and support. I am thanking *Alan G. Jones* for promoting the PICASSO project, organising the SFI funding, offering me the PhD scholarship, and giving me the opportunity to work with scientists around the work and presenting my work on international meetings. Additional thanks go to *Alan G. Jones* and *Colin Brown* for their role as my supervisors.

Special thanks also go to *Xavi Garcia* for constructive advise, guidance, and great inspiration during the first years of my PhD; and to *Mark R. Muller*, who despite his more than tight schedule always found time for patient and thorough explanations.

Big thanks, grazie, gracias, and Dank go out to the whole PICASSO Phase I fieldwork

Team, namely *Colin Hogg, Clare Horan, Pierpaolo Moretti, Mark Muller, Gerardo Romano, Oriol Rosell, and Sonja Suckro*, who helped me collecting the magnetotelluric data in Spain that was used to conduct this thesis work, and who made the campaign such a great experience.

I want to thank *Maisha Amaru, Jamie Barron, Antonio Villaseñor* for providing me with data, which they extracted from their seismic 3D models, allowing me to contrast my results.

For proof-reading, helpful comments, encouragement, and general help during the writing process, I like to thank *Alan Jones, Andrew Schaeffer, Anna Matheson, Celine Tirel, David Khoza, Jan Vozar, Javier Fullea, Joanne Adam, Mark Muller, Marion Miensopust, Matthew Agius, and Monika Bauch*.

I was fortunate to meet lots of remarkable people during my time as a PhD student with whom I had long and lively discussions — sincere thanks to all of you. In addition to all those great people in DIAS, I particularly want to thank *Al Duba, Javier Fernández-Lozano, Jeff Roberts, and Josef Pek* for inspiring conversations.

There are some people who spend lots of time working on scripts and software which they make available to the scientific community for free. In many cases these codes are not published and their authors are often forgotten despite the great usefulness of their codes. So hats up to *Alan Jones, Anna Martí, Florian Le Pape, Jan Vozar, and Hao Dong*, as well as *Paul Wessel, Donald E. Knuth, Markus Kohm, Sebastian Deorowicz, and Adam Skórczyński*.

Thanks also to DIAS's technical staff *Anna Sewielska, Clare Horan, Colin Hogg, and Louise Collins* and IT crowd *Stephane Dudzinski, Sean O'Sullivan, John Barret* in 5 Merrion Square for keeping all those machines up and running and doing all the supporting work, which allows the scientist to focus on their problems and getting their things done.

I want to give big thanks (or danke, köszönöm, gracias, merci, dziekuje) and hugs to all the people in DIAS (particularly those in 5 Merrion Square), as well as *Ulrike Winkel, Zoltan Lensce, Marta Paternain, Emilio Martín, Louise Heng, Ela Piezcykolan, Viktòria Horwàrth, Tamàs Kovàcs, Michael O'Connor, Àkos Bairo, Veronika Juhàsz, Maria Leonard*, and all the other who made me remember that there is also a life outside the institute. Especially, I would like to thank you for those times when you welcomed me to the strange and foreign city of Dublin, that you provided me with nutrition in various forms, and overall helped me with everyday things so that I could have my mind get lost in the geophysics world.

Mein letzter Dank is reserviert für *Tanja Wielage*, die die viel zu lange Zeit der räumlichen Trennung mit mir erduldet hat und mir die Kraft gegeben hat diese Doktorarbeit zu vollenden. Weiterer Dank wird persönlich überreicht.

For scientists, facts exist, truth is verifiable, interpretations (hypothesis) can be tested, and a definite decision among competing hypothesis can be made, based on weigth of evidence.

– Kenneth L. Verosub

1 Introduction

The Iberian Peninsula is the westernmost extent of the Eurasian Continent, surrounded by the Bay of Biscay to the northwest, the Pyrenees to the northeast, the Atlantic Ocean to the west and southwest, and the Mediterranean Sea to the south and southeast. Surprisingly, especially given its elevation, the central region of the Iberian Peninsula has remained comparatively neglected in terms of deep-probing investigations. Previous studies, particularly of deep-seated structures, have been mostly been focussed on the borders of the peninsula, namely the Pyrenees [e.g. *Ledo et al.*, 2000] and Betic Mountain Chains [*Serrano et al.*, 1998; *Pous et al.*, 1999; *Martí*, 2007; *Martí et al.*, 2009a; *Rosell et al.*, 2010; *Ruiz-Constán et al.*, 2010] as well as on parts of the Iberian Massif in the southwest of Iberia [*Carbonell et al.*, 1998; *Pous et al.*, 2004; *Muñoz et al.*, 2005, 2008]. Deeper structures of central Iberian regions have been determined mainly by large-scale seismic tomography studies [e.g. *Bijwaard and Spakman*, 2000; *Villaseñor et al.*, 2003; *Amaru et al.*, 2008; *Koulakov et al.*, 2009], with models exhibiting a relatively low resolution for the Spanish subsurface.

The magnetotelluric (MT) method uses electromagnetic field variations in order to probe the distribution of electric conductivity at crust and mantle depths; MT has been successfully applied in numerous studies and the interested reader is referred review paper series on *MTNet* (www.mtnet.info) for a comprehensive overview about the methods and its application. In the Iberian Peninsula, MT can enhance knowledge about the geological setting, not only by providing detailed information about local subsurface regions that previously were not well resolved, but also by yielding an additional parameter that can augment other physical (e.g. seismic or thermal) parameters in order to draw conclusions about local petrology. Therein, electric conductivity is highly sensitive to changes in temperature, water, or partial melt in the subsurface, putting strong constraints on the petrological setting and making MT a formidable tool for probing near-surface as well as deep-seated regions. In MT, the depth of investigation is directly dependent on the period of utilised electromagnetic waves, and governing potential functions can be expressed as vector potentials. Thus, MT is superior to other methods like gravity, magnetics, or

thermal modelling, which are inherently non-unique, requiring a range of assumptions regarding values and distribution of related parameters within the Earth. Accordingly, MT is steadily gaining popularity among geoscientist since its development by *Rikitake* [1948], *Tikhonov* [1950] and *Cagniard* [1953] in the middle of the last century and has been used to study various aspects in different regions of the world.

For this investigation, MT data were acquired in the Iberian Peninsula during the first phase of the multinational, multi-disciplinary PICASSO (acronym for *Program to Investigate the Convective Alboran Sea System Overturn*) program, which studies tectonic processes and internal structure of the western Mediterranean lithosphere and surrounding regions. In order to derive structures of the Iberian Peninsula subsurface, MT recordings were carried out along the approximately 400 km long, north-south oriented PICASSO Phase I profile situated in the Spanish Tajo Basin and Betic Cordillera regions. In the Tajo Basin, comprising the northern half of the PICASSO Phase I profile, a difference of approximately 70 degrees is determined for the geoelectric strike directions of the crust (≈N41W) and lithospheric-mantle (≈N29E) regions. The different strike directions are most likely related to the different tectonic events forming the approximately NW-SE stretching Pyrenees in the northeast of the peninsula and the approximately NE-SW stretching Betics in the south of the peninsula.

Oblique geoelectric strike directions for different subsurface regions, e.g. at crust and mantle depths, are a known problem in MT investigation [e.g. *Marquis et al.*, 1995; *Eaton et al.*, 2004; *Miensopust et al.*, 2011]. Crustal structures can usually be recovered in a straightforward manner by confining the modelled frequency range to crustal penetration depths; recovery of mantle structures, on the other, hand is more challenging when the structures have a different strike from the overlying crust. Commonly employed 2D inversion approaches are likely to yield models with inversion artefacts due to misrepresentation of the strike direction in at least one of the regions. Therefore, *Miensopust et al.* [2011] conducted separate inversions for regions with different geoelectric strike directions along their profile using datasets adapted to meet the strike characteristics in the respective regions. Ultimately, the authors decomposed their impedance vectors according to a N35E strike direction for most parts of their profile and used a N55E strike direction for a subset. For more oblique geoelectric strike directions, however, inversion artefacts in the mantle model will prevail, owing to effects of the significantly erroneous decomposition of the impedance tensor at crustal depth. Hence, a simple 'stitching' of inversion models from different strike directions does not adequately recover structures in the deeper regions. Three-dimensional (3D) inversion of MT data, capable of dealing with more complex subsurface structures like oblique strike direction, is computationally expensive, which usually permits detailed inversion of a region with the size of the Tajo Basin.

The problem of oblique geoelectric strike directions in two-dimensional (2D) inversion, previously requiring costly 3D inversion, motivated development of a novel 2D inversion approach. This inversion approach uses electric anisotropy to image 2D structures, enabling the investigator to derive a subsurface model with oblique geoelectric strike di-

rections from enhanced one-dimensional (1D) and 2D inversion procedures for which otherwise 3D inversion is required. Relations between effects of electric anisotropy and regional-scale heterogeneities on MT have been discussed, among others, by *Heise and Pous* [2001] and *Pek and Santos* [2006]; previously, however, the focus has only been on how to distinguish between anisotropy and regional-scale heterogeneities. There has been no published report about the use of anisotropic inversion codes for the recovery of oblique strike directions so far, meaning that this study breaks new ground. Performance of this novel approach is examined in this thesis in a synthetic model study and subsequently used to investigate the Tajo Basin subsurface. The synthetic model comprises orthogonal geoelectric strike directions at depths associated with crust and mantle. MT response data are modelled for numerous locations on top of the model, thereby facilitating inversions along various profiles and a comprehensive assessment of results for the different inversion approaches.

In addition to the development of a novel inversion approach, this thesis comprises an investigation of tectonic processes that shaped the Iberian Peninsula. Therein, models of the Tajo Basin subsurface are presented that were obtained with the anisotropic inversion approach developed in this thesis as well as from isotropic 2D and 3D inversions of the PICASSO Phase I dataset. Results of the different inversion schemes are contrasted and petrological implication of model features are discussed. Obtained models provide a remarkable new insight into the local geology of central Spain, permitting conclusions about a reservoir that is responsible for volcanic events throughout Europe as well as about interaction between the Tajo Basin subsurface and subducted lithospheric material beneath the western Mediterranean Sea and Betic Cordillera.

The content of this thesis is divided into five parts, which illustrate the different aspects related to this work.

A thorough discussion of the MT method is given in Part I: *Theoretical background of magnetotellurics*. Therein, sources of the MT method (Chapter 2) and related mathematical relations (Chapter 3) as well as effects of subsurface characteristics (Chapter 4) are illustrated, followed by descriptions of Earth's electric conductivity properties (Chapter 5) and application of the MT methods in order to derive subsurface structures (Chapter 6).

In Part II: *Geology of the study area* the tectonic evolution of the Iberian Peninsula is examined and results of previous geological and geophysical studies in the Betic Cordillera and central Spain are discussed (Chapter 7). In this Part, the two regions along the profile, Betics Cordillera and Tajo Basin, are discussed individually accounting for their very distinct geology.

The novel inversion approach for MT data, motivated by the significantly oblique geoelectric strike directions of the Tajo Basin crust and mantle is presented in Part III: *A novel inversion approach for oblique geoelectric strike directions in crust and mantle*. The approach is first tested in a synthetic model study and results are compared with results of commonly used isotropic 2D inversions (Chapter 8). Satisfactory performance in the

synthetic model study encourages application of the novel approach to the real PICASSO Phase I dataset.

Investigation of the Iberian Peninsula subsurface within the framework of the PICASSO Phase I project is discussed in Part IV: *Magnetotelluric investigation of the southern Iberian subsurface – PICASSO Phase I*. Therein, acquisition of the PICASSO Phase I data is specified (Chapter 9), followed by a description of inversion procedures used to determine the Tajo Basin crust and mantle structures, and a discussion of the inversion results (Chapter 10). Processing of the dataset includes, among others, investigation of geoelectric strike directions for the different regions along the profile as well as the change of geoelectric strike direction with depth, which leads to the development of the novel anisotropic inversion approach. Anisotropic 1D and 2D inversion that use the novel approach, as well as isotropic 2D and 3D inversion is used to derive models of the complex Iberian Subsurface. Results of 1D, 2D, and 3D approaches are compared with each other, and results of previous geophysical studies in the region are used in the interpretation of model features.

Part V: *Summary, Appendix, and Bibliography* comprises a summary of results for the novel inversion approach and conclusions about the Iberian Peninsula subsurface, together with suggestions for future work (Chapter 11). This summary is followed by the Appendix containing auxiliary information that were moved to the end of this thesis, for the sake of clarity in the main body (Chapter A). Sections in this Appendix comprise a detailed study of the Iberian Peninsula evolution (Section A.1), specific aspects of MT inversion related to this thesis work (Section A.2), and a detailed examination of results from the synthetic model study (Section A.3), as well as a comparison of response curves from the PICASSO Phase I stations and from the derived subsurface models. The list of references referred to in this thesis is given at the end of this body of work (Chapter `Bibliography`).

Part I

Theoretical background of magnetotellurics

I have no picture of the electromagnetic field that is in any sense accurate... I see some kind of vague shadowy wiggling lines - here and there is an E and a B written on them somehow, and perhaps some of the lines have arrows on them - an arrow here or there which disappears when I look too closely at it.

– Richard Feynman

2 Sources for magnetotelluric recording

For magnetotelluric (MT) investigations electromagnetic (EM) waves in the period range $10^{-4} - 10^{5}$ s ($10^{4} - 10^{-5}$ Hz) are commonly used. The period range in an investigation is, among others, dependent on the desired depth of investigation, subsurface characteristics, and noise level. An overview about the MT source signals, their generation and characteristics, is given in this Chapter, together with a description of assumptions regarding characteristics of the source signals.

In principal, every EM wave incident on the Earth's surface with known characteristics can be used as a source for MT investigation, as long as its amplitude exceeds the noise level of the instruments. Commonly used MT signal sources can be divided into two main classes, namely *Electric lightning discharge* (Sec. 2.1) and *electric currents in the magnetosphere* (Sec. 2.2). Both types are of natural origin and form the high and low end of the spectrum used for MT investigation (Fig. 2.1), separated by the *MT dead band*. The MT dead band is usually observed in a period range spanning from approximately 0.1 to 8 Hz and is characterised by a poor signal-to-noise ratio (SNR). The low SNR in this period range is due to low signal amplitudes in comparison with the present noise level from, among others, the motion of trees, generating induced signals on the sensors. The used spectra contains EM waves with periods that usually permit negligence of permittivity and permeability effects (cf. Chapters 3.5 and 3.6).

Besides the above-mentioned natural sources, artificial sources have been developed for the audio-magnetotelluric (AMT) period range in order to enhance the SNR, thereby shorting the required recording time. Controlled source AMT (CSAMT) was first applied by *Goldstein and Strangway* [1975] and descriptions of CSAMT applications are given in various publications, e.g. *Pellerin and Hohmann* [1990]; *Zonge and Hughes* [1991]. For the PICASSO Phase I project no controlled source recording is carried out, therefore the focus of this Chapter is on natural sources and their implication on MT measurements.

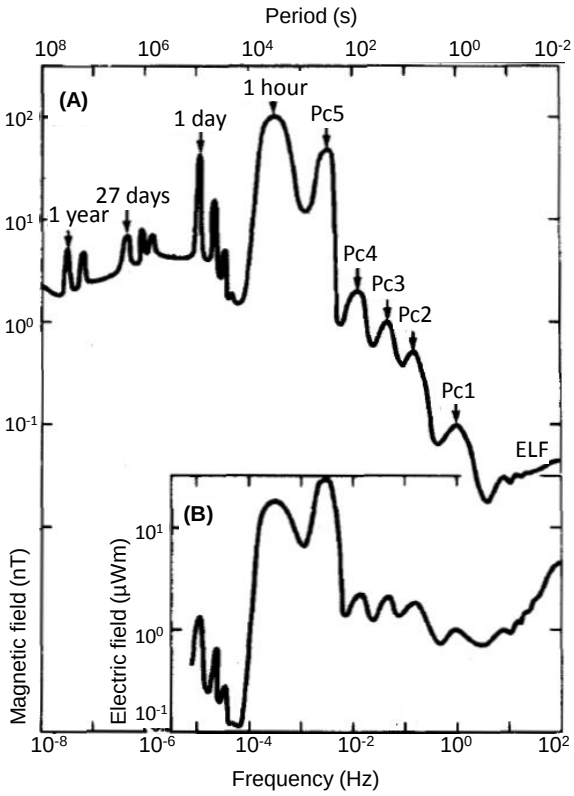

Fig. 2.1.: (A) Amplitude of the natural variations in the horizontal geomagnetic field useful in induction research. (B) Corresponding amplitudes in the geoelectric field, computed for a model Earth of uniform resistivity 20 Ωm; from *Serson* [1973]. See text for details about peaks in the spectrum.

2.1. Electric lightning discharge

Lightning strokes are generated through electric discharges between thunderclouds and either the stratosphere or the Earth's surface with energies primarily occurring in two different frequency bands ranging from 7.8 Hz to 1 kHz and 5 kHz and above, leaving a gap in the amplitude spectrum referred to as the *AMT dead band* [e.g. *Garcia and Jones*, 2002]. The lower limit of the AMT spectrum is given by the fundamental mode of the Schuhmann resonance at 7.8 Hz, related to the maximum wavelength of around 40,000 km that fits into the Earth surface - ionosphere waveguide. Multiples of the fundamental mode produce characteristic peaks in the AMT spectrum in the frequency range >7 Hz [e.g. *Brasse*, 2003].

The global frequency of lightning occurrence is around 100 incidences per second with enhanced occurrence in the tropics (Fig. 2.2), thus providing a reliable source of EM signals. For most regions of the Earth, best results for MT recordings are obtained during the nighttime and during the summer months, due to the attenuation of the absorbing ionospheric D-layer and to the preponderance of thunderstorms during summertime [e.g. *Garcia and Jones*, 2002; *Brasse*, 2003]. Measurements should be carried out in the *far-*

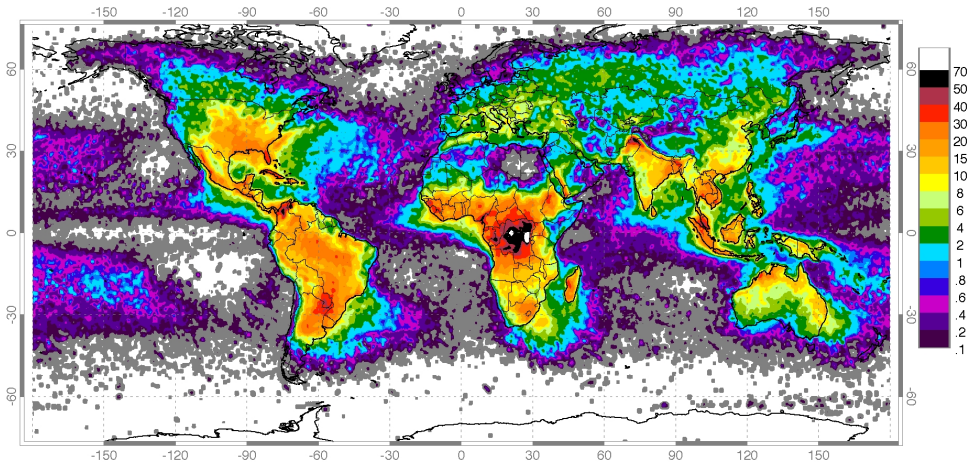

Fig. 2.2.: Annual rate of lightning discharges, indicated by colours; from *Global Hydrology Resource Center* [2010].

field of thunderstorms in order to assure that the plane wave assumption is satisfied (cf. Sec. 2.3).

2.2. Electric currents in the magnetosphere

The Earth's magnetosphere is the region in which behaviour of charged particles is dominated by the Earth's internal magnetic field, with the resulting shape determined by interaction with the electromagnetic components of the solar wind compressing it on the dayside and causing an elongated tail on the night side (Fig. 2.3). The lowermost part of the magnetosphere, extending from around 50 km to 1000 km above Earth's surface, is the relatively conductive ionosphere. The ionosphere consists of plasma and contains mostly oxygen and nitrogen gases, ionised by solar radiation [*Kelley*, 1989; *Vozoff*, 1987; *Andersen and Fuller-Rowell*, 1999] (Fig. 2.4).

Through the interaction of the solar wind, containing charged particles and plasma, with elements of the Earth's magnetosphere, various EM fields are generated, forming the lower end of the MT source spectrum. The strength of generated EM fields are in the range < 0.1 nT, for frequencies in the region of 1 s, and increases with period until it reaches a quasi-steady level of around 3 nT, for periods greater than 10^5 s. Superimposed on this is a multitude of spectral peaks with varying amplitude and sharpness (Fig. 2.1). A list of the contributing signals together with their characteristics and sources is given in Table 2.1 and a detailed description is given in Sections 2.2.1 to 2.2.5.

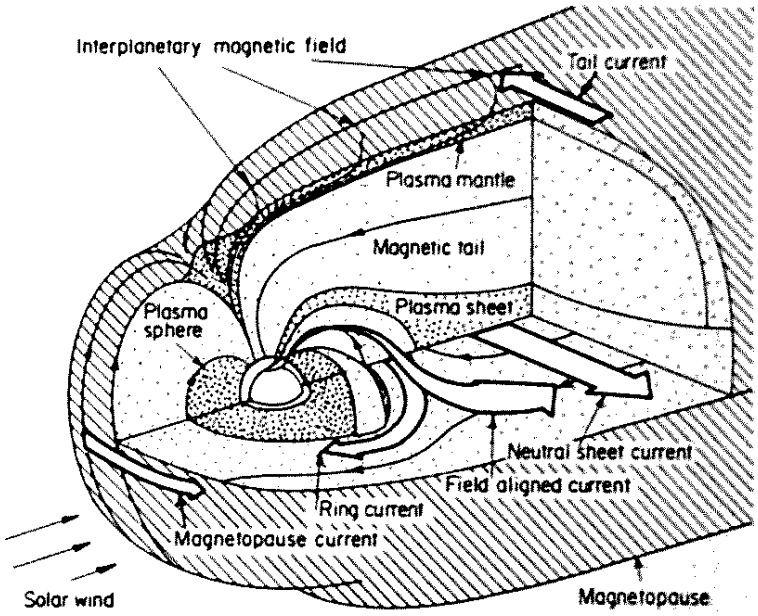

Fig. 2.3.: A schematic view of the magnetosphere; from *Potemra* [1984].

Tab. 2.1.: Classification of geomagnetic variations sorted by their characteristic time τ, after *Schmucker* [1985] with updates for the ULF frequency bands from *McPherron* [2005] and characterisation of the solar daily variation in the equatorial region of the day-side as equatorial electrojet (EEJ). τ: Fundamental period for regular variations, period range for irregular variations. A: Peak-to-peak amplitude or maximum departure from undisturbed level. If a significant dependence on latitudes exists, different values are quoted for auroral zone (a), mid-latitudes (m), low-latitudes (l) and the dip equator region on the day side (dd). ERC: Equatorial ring current in the radiation belt of the magnetosphere.

Type	Symbol	τ	A (nT)	Source
Ultralong periodic variation				
Solar cycle variations		11 years	20	ERC modulation by sunspot cycle
Annual variations		1 year	5	Ionospheric sources
Semi-annual variation		6 month	5	ERC modulation within the Earth's orbit around the sun
Smoothed storm-time variations				
storm time-dependent part	Dst	2 - 27 d	100	
disturbance local time inequality	DS	12 - 24 h	100	
Solar daily variations				
on quiet days	Sq	1 d	30 - 60 (m,l)	Ionospheric current loops on day-side sectors of both hemispheres
equatorial electrojet	EEJ	1 d	60 - 120 (dd)	
enhanced on disturbed days	S_D	1 d	1 - 20	
Lunar daily variations	L	1 lunar day[a]	1 - 3	Dual ionospheric current loops on both hemispheres

Continued on Next Page...

Tab. 2.1 – Continued

Type	Symbol	τ	A (nT)	Source
Polar magnetic storms and short-lived substorms				
centre of disturbance in the night-time auroral zone	DP1	10 m - 2 h	1000 (a) 100 (m,l)	Polar (or auroral) electrojet PEJ in the ionosphere with connecting field-aligned currents to plasma regions of the magnetosphere
with correlated irregular variations in low latitudes	DP2	10 m - 2 h	100 (a) 10 (m,l) 100 (d,d)	
Special effects in connection to polar magnetic storms				
bays (substorms as observed in mid latitudes)	b	30 m -2 h	20 - 100 (a,m) 5 - 25 (l)	see DP1
Sudden storm commencement	ssc	2 - 5 m	10 - 100 m	Impact of intense solar particle stream on magnetopause
Solar flare effect	sfe	10 - 20 m	10	Short-lived enhancement of Sq currents in the ionosphere
Ultralow frequency waves (Pulsations)	ULF (P)	0.2 - 600 s		
regular continuous pulsations	Pc5	150 - 600 s	100 (a) 10 (m)	Standing and propagating hydromagnetic waves in the magnetosphere
	Pc4	45 - 150 s	2	
	Pc3	10 - 45 s	0.5	
	Pc3	5 - 10 s	0.5	
	Pc1	0.2 - 5 s	1	
irregular transient pulsations	Pi2	45 - 150 s	1	
	Pi1	1 - 45 s	1	
Very low frequency emissions, including whistlers	VLF	10^{-5} – 10^{-3} s		

2.2.1. Ultralong periodic variation

In this Section geomagnetic variations with extremely long periods are examined that are not directly related to conventional MT measurements, which are, for logistic reason, usually limited to a duration of a few months or less. Signals of such ultralong variations are more suitable for studies using magnetovariational (MV) datasets, recorded at stationary observatories that provide time series of sufficient length. However, the results of those MV studies can be used to compare findings of MT methods and help to predict structures at greater depth, which in turn can aid interpretation of MT studies.

[a] *Schmucker* [1985] assigns the Lunar daily variations to have a fundamental period of 1 d but as the determining value is the time that it takes the Moon to orbit the Earth this variation has a period of around 24 h 50 m (1 lunar day) instead, e.g. *Merrill and McElhinny* [1983], p.53; *National Oceanic and Atmospheric Administration (NOAA)* [2010].

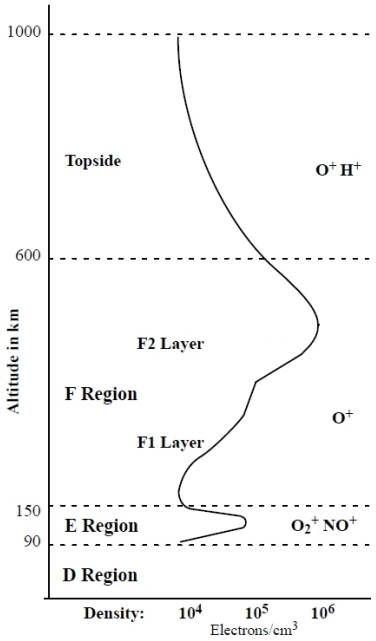

Fig. 2.4.: Layers of the ionosphere with their electron density and predominant ion populations; from *Andersen and Fuller-Rowell* [1999].

Solar cycle variation

Regular solar variations are connected with wave radiation of the Sun with the fundamental period for the solar cycle variations of 11 years [*Schmucker*, 1985], most easily observed by the annual number of sunspots (Fig. 2.5). Even though the cause of the cycle is not yet fully understood, changes in activity can be used to predict the observable signal strength during a fieldwork campaign as the increased magnetic activity intensifies pre-existing current systems used as MT sources [*Mareschal*, 1986]. Presently we are situated in an elongated minimum of the twenty third *11 year cycle* (Fig. 2.6) causing the signal, and hence the signal-to-noise ratio (SNR), to be noticeably lower at mid-latitudes. Moreover, the decreasing maximum field strength of annual sunspots, as observed by *Livingston and Penn* [2009] using measured infrared intensity in the darkest position of the sunspot umbrae, is raising the question of whether we are actually experiencing a new period of severely reduced activity, similar to the Maunder Minimum from 1675 to 1715 AD [*Luterbacher et al.*, 2001]. The present time frame, limited by the emergence of the required instruments, is too short to verify such hypothesis.

(Semi-)Annual variation

Annual and semi-annual variations penetrate into the Earth down to a depth of approximately 1000 km and deeper but are commonly not used for MT investigation due to the required extensive recording time. Furthermore, semi-annual variations exhibit very

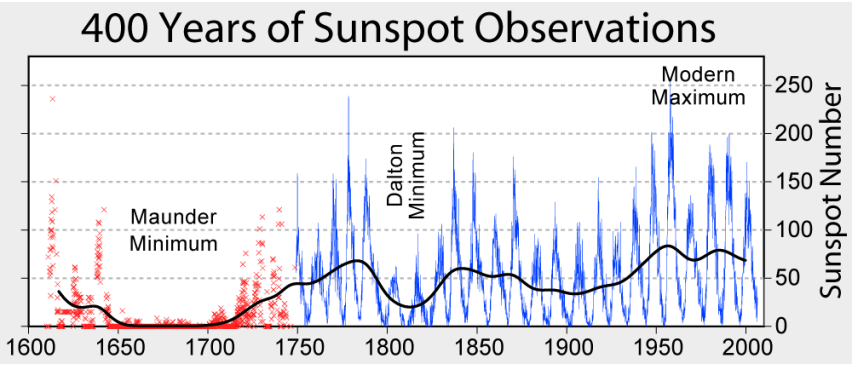

Fig. 2.5.: Monthly average of observed sunspot numbers since 1749 (in blue) and the more sporadic observations prior to 1749 (in red) until 2001, exhibiting a prominent 11 year cycle and periods of altered activity, after *Hoyt and Schatten* [1998a,b].

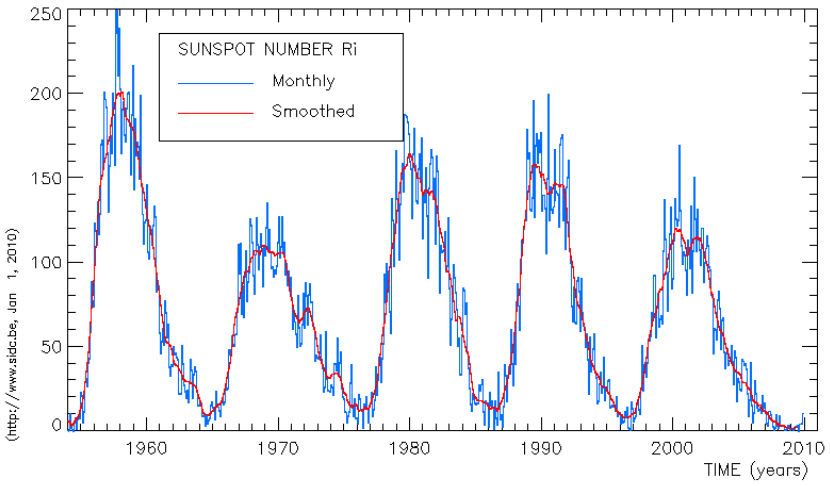

Fig. 2.6.: Monthly (blue) and monthly smoothed (red) sunspot numbers since 1950 until 2010 showing a minimum of solar activity for the time of the fieldwork campaign in 2007, from *Solar Influence Data Analysis Center (SIDC), Royal Observatory of Belgium* [2010]

small amplitudes, which makes the response estimation very difficult given the insufficient baseline stability of electric sensor systems for such a long duration. Special setups are necessary to utilise semi-annual variation signal, e.g. the experiment by *Schultz et al.* [1993] in which electric recording instruments (electrodes) were placed in lakes for thermal and chemical stability.

2.2.2. Regular variations

Regular variations terms effects that occur constantly but are variable in intensity, depending on the present strength of the solar activity and the resulting solar wind.

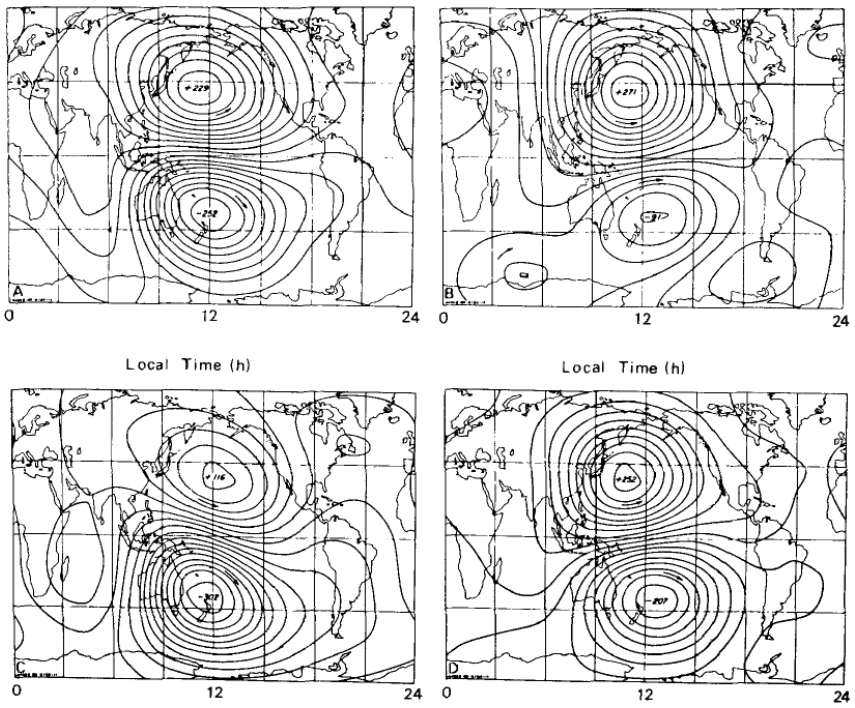

Fig. 2.7.: Equivalent current system representing the S_q field of March equinox, northern summer, September equinox, and southern summer (clockwise, starting on top left) with contour intervals of approximately 25 kA, from *Mareschal* [1986] after *Parkinson* [1983].

Solar daily variation

Thermally and gravitationally induced atmospheric winds generate electric currents in the dayside ionosphere through displacement of entrained charged particles across geomagnetic field lines. The motion of charged particles can be well-represented by an equivalent current system consisting of two approximately circular structures; one structure located on each hemisphere, with their centres at around 45 degrees latitude and nearly the same longitude, situated close to local noon (Fig. 2.7). These two structures displaying the resulting contour intervals of the electric fields exhibit with an opposite sense of rotation and amplitude, i.e. with their eastward component on the equatorial side and a positive amplitude for the northern and negative amplitude for the southern hemisphere. Induced magnetic fields of the *quiet solar* (S_q) variations for peak-to-peak amplitude vary between 30 nT in the winter and 60 nT in the summer for the mid- and low-latitudes, and between 60 nT and 120 nT in the dip equator region on the dayside under the influence of *the equatorial electrojet* (EEJ) [*Schmucker*, 1985; *Mareschal*, 1986].

The EEJ appears as a narrow ribbon of electric current flowing eastward in the day time equatorial region of the Earth's ionosphere causing severe deviations of the plane wave assumption in low latitudes; see Section 2.3 for a discussion of the plane wave assumption and Subsection 2.3.2 for details about MT measurements at low-latitudes. The area of influence for the EEJ is commonly assumed to be limited to approximately

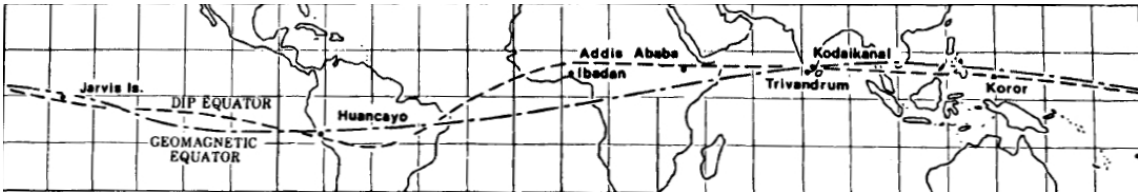

Fig. 2.8.: Projection of the dip equator (dashed) and the geomagnetic equator (dip-pointed) onto the Earth's surface; from *Mareschal* [1986].

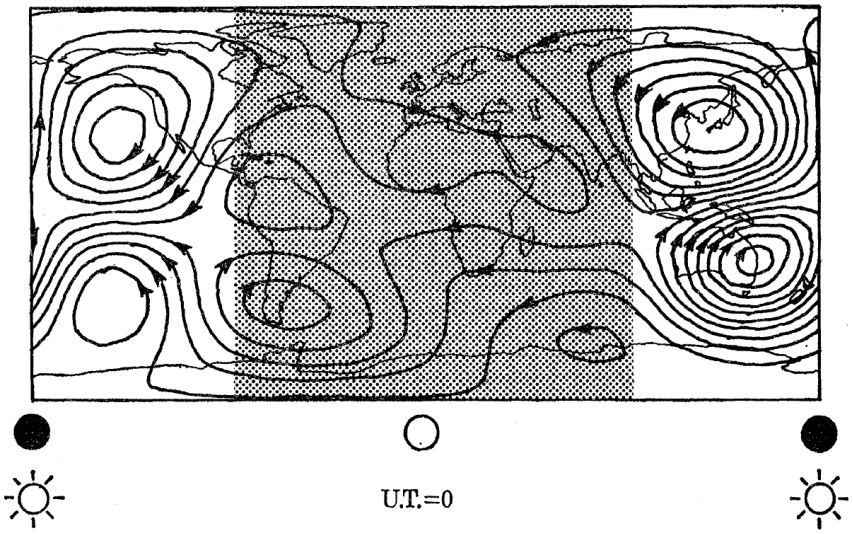

Fig. 2.9.: Equivalent current system for lunar daily variations L exhibiting two separate current loops on the day-lit side of either hemisphere (U.T.: Universal time); from *Malin* [1973]

three degrees around the dip equator [e.g. *Vozoff*, 1987; *Padilha et al.*, 1997; *Padilha*, 1999; *Brasse*, 2003], i.e. the region of horizontal geomagnetic field lines that are usually in close proximity to the Earth's equator (Fig. 2.8). Amplitudes of regular solar daily variations can be enhanced through such irregular variations by up to 20 nT on disturbed days S_D [*Schmucker*, 1985], having serious effects on local MT observations [e.g. *Hesse*, 1982; *Padilha et al.*, 1997; *Padilha*, 1999].

Lunar daily variation

Lunar daily variations are due to tidal effects in the oceans and atmosphere of the Earth originating from the Moon orbiting the Earth, thereby forcing tidal currents to move across field lines inducing effects on the magnetosphere. Such effects can be represented by an equivalent current system exhibiting two characteristic separate current loops on the day-lit side of either hemisphere [*Schmucker*, 1985] (Fig. 2.9). The effect of lunar daily variations is commonly neglected given its minor amplitude in comparison with S_q and the effect of thermal instabilities in the recording of the MT electric components which both occur in a similar frequency range.

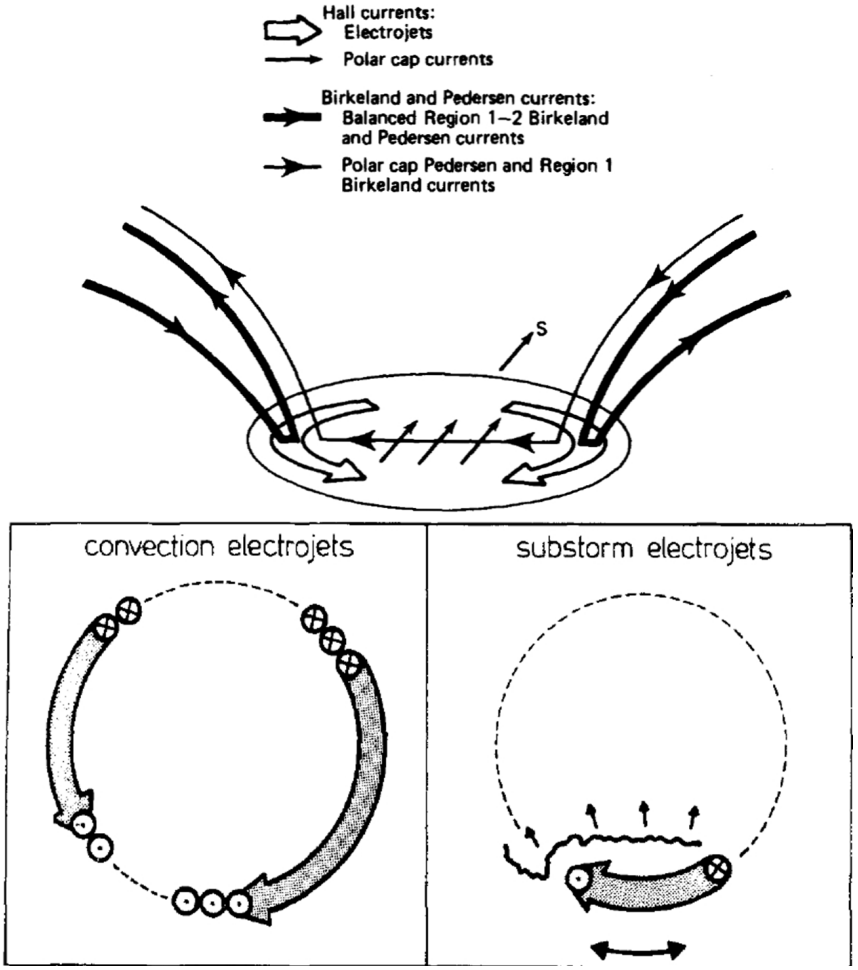

Fig. 2.10.: Top: possible interaction between field-aligned currents with convection electrojets and cross-polar cap current flow the sunlit polar ionosphere; from [*Zanetti et al.*, 1983]. Bottom: Schematic representation of a substorm current system intrusion into the convection electrojets system for a dark ionosphere (left) causing vibrations of the Hall current system (right) ⊗ represents field-aligned currents into the ionosphere, ⊙ out of it; from *Mareschal* [1986].

Polar electrojets

The exact mechanisms of current flow in the Polar Regions are not yet fully understood, but different models have been presented in order to explain certain aspects of the present current system: e.g. Birkeland and Pedersen field align currents generating Hall currents in the polar region that flow towards the Harang discontinuity at local midnight [e.g. *Kisabeth and Rostoker*, 1977; *Rostoker et al.*, 1982; *Baumjohann*, 1983; *Zanetti et al.*, 1983] (Fig. 2.10). As polar electrojets (PEJ) are an important contributor to local polar MT signals, a great deal of effort has been spent on investigating their characteristics in terms of height above the surface, length and the related pulsation structure, e.g. *Walker and Greenwald* [1981]; *Andre and Baumjohann* [1982]; *Baumjohann* [1983]; *Pirjola* [1998]. This led to the conclusion that the PEJ is usually constrained to a height of 100 – 120 km

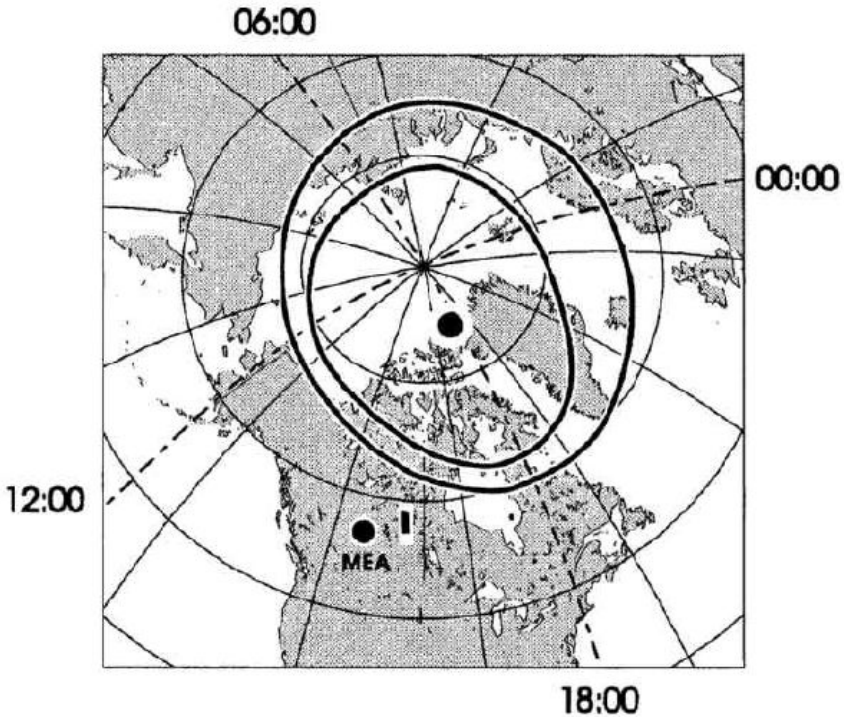

Fig. 2.11.: The shape of the polar electrojet (PEJ) on the northern hemisphere, represented by the thick solid lines is variable in width and lateral extend depending on the relative position of the sun indicated by the four meridians showing the relative magnetic local time; from *Garcia et al.* [1997]. The dots display the location of the geomagnetic North Pole and Meanook Observatory, the line the location of the MT profile used by the authors.

above the Earth's surface and along an oval band with varying width and lateral extension between 58 and 75 degree depending on the relative position of the sun [*Mareschal*, 1986; *Garcia et al.*, 1997] (Fig. 2.11). The PEJ has very strong effects on MT investigations at high-latitudes, producing severe deviations of the plane wave approximation [e.g. *Simpson and Bahr*, 2005] due to its limited dimension (cf. Sec. 2.3) causing serious problems in the local impedance estimation; see Section 2.3.2 for details on processing of MT data collected at high-latitudes.

2.2.3. Storm-time variations

A large portion of MT source signals are generated during magnetic storms and substorms, i.e. times of intensified solar wind and its enhanced coupling with the Earth's magnetic field, whereby the onset of the variations are related to different phases of the storm [*Schmucker*, 1985; *McPherron*, 1991]. Every magnetic storm contains many *substorms*, proposed to be the cause of contemporaneous ULF wave events [*McPherron*, 2005] (Sec. 2.2.5).

Enhanced pre-existing geomagnetic current systems can lead to severe distortion of MT measurements at high-latitudes due to source effects; see Figure 2.12 for an example

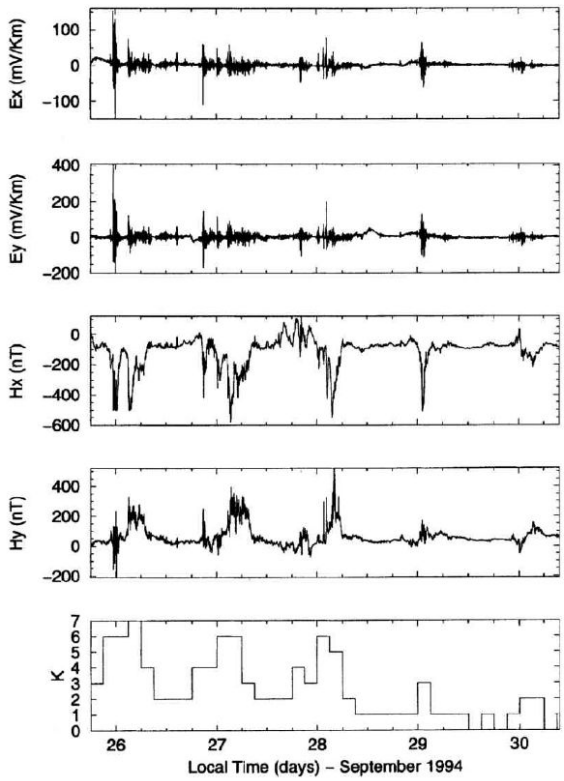

Fig. 2.12.: Effect of storm events on magnetotelluric time series data recorded at high-latitudes, indicated by the correlation of times with high KP index (bottom) and intensified EM fields; from *Garcia et al.* [1997]. The x-axis of MT station is orientated 37 degree against geographic north.

of a MT time series distortion caused by storm events and Section 2.3 for a detailed description of the source effects on MT data. The influence of magnetic storms on the Earth's magnetic field initiates along the bow shock with the impact of the shock wave, formed through interaction of a large amount of erupted plasma, with previously emitted normal solar wind. This causes a sudden eastward displacement of the field lines in the magnetosphere and their subsequent resonance generating *sudden storm commencement* (ssc) variations. This initial phase is followed by the main phase of the storm, indicated by a rapid decrease in the surface field by up to 500 nT (Tab. 2.2), and a subsequent transition from charged particles of the solar wind and the plasma sheet onto trajectories along the Earth magnetic field lines towards the auroral zones of both hemispheres [*Schmucker*, 1985]. The field-aligned magnetospheric currents are connected with the ionosphere of the auroral zone via Hall current systems, thereby intensifying east-west directed PEJ's that are flowing towards the Harang discontinuity at local midnight and form the source of *DP1* variations (Fig. 2.13). Irregular variations at lower latitudes that are correlated with high-latitude activities during substorm times, exhibiting structures similar to the S_q current systems, are referred to as *DP2*. The structures consist of two current loops and a flow direction towards low latitudes in the morning and high latitudes in the evening

Storm strength	Decrease of surface magnetic field
weak	50 nT
moderate	100 nT
strong	150 nT
great	500 nT

Tab. 2.2.: Decrease of the Earth's surface magnetic field during the main phase of a magnetic storm depending on the storm strength; values from *McPherron* [2005].

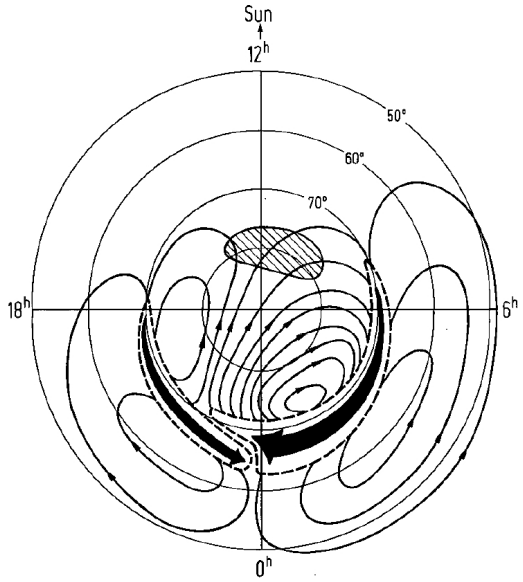

Fig. 2.13.: Equivalent current model representing DP1 by the use of polar electrojets (PEJ) on the night-side as thick black arrows along the 67 degree latitude towards the Harang discontinuity at local midnight; from *Schmucker* [1985].

sectors (Fig. 2.14). The main phase of the storm is followed by the recovery phase, the source of smoothed storm-time variations D, where D_{st} variations are caused by the equatorial ring current (ERC), i.e. the stream of trapped particles encircling the Earth. DS variations on the other hand describe the effect due to ERC that is not completely closed, indicating the local disturbances of the universal-time-dependent D_{st} variations [*Schmucker*, 1985; *McPherron*, 2005].

Polar substorms can also emerge without prior ssc events, generating geomagnetic *bays* which appear as smooth temporary departures of the undisturbed level from early evening to early morning at mid-latitudes with equivalent current systems similar to the ones of DP1 [*Schmucker*, 1985] (Fig. 2.13).

2.2.4. Solar flare effect

The *solar flare effect* (sfe) originates from ionisation of the Earth's ionospheric D and E layers (Fig. 2.4) due to intense solar wave emission, causing an increase of the ionospheric

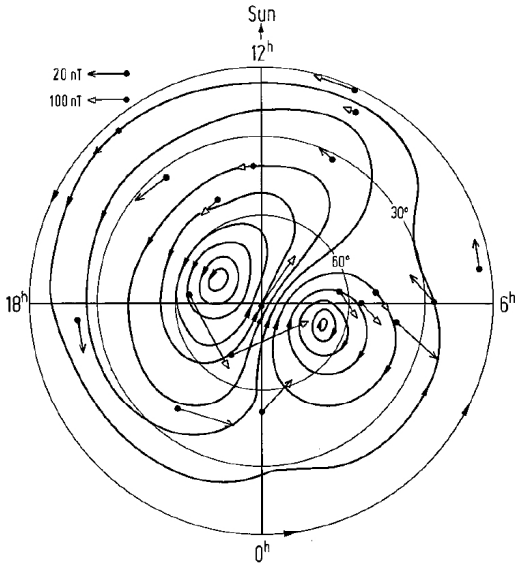

Fig. 2.14.: Equivalent current model representing DP2 with two current loops and flow direction towards low latitudes on the morning and high latitudes on the evening sector respectively. The vectors represent the external part of the horizontal disturbance field, rotated 90 degrees to indicate the direction of overhead currents; from *Schmucker* [1985].

conductivity and intensifying S_q variations (Sec. 2.2.2) on the day-side [*Schmucker*, 1985]. The sfe occurs in geomagnetic observations with a steep onset followed by a slow decay of approximately exponential form with the sign and amplitude of their contribution to the magnetic field components dependent on the location of the recording station relative to the centre of the generated current loop (Fig. 2.15).

2.2.5. Ultra low frequency waves

Ultra low frequency (ULF) waves, or *(micro-)pulsations* as they are referred to in earlier literature, are classified by their waveform and wave period, divided into continuous pulsations (Pc) and irregular pulsations (Pi) that are further subdivided into bands related to specific types of pulsations. ULF waves are part of the period range below the MT dead band of which waves relevant for MT observations have been detected between 0.2 s and 600 s comprising 5 bands for the continuous and 2 for the irregular pulsations (Tab. 2.1). The limits of these bands are not precise, and effects of different pulsation types exhibit overlapping period ranges [*McPherron*, 2005].

Specifics of the circumstances that lead to the observed pulsation characteristics remain elusive, but certain aspects about ULF wave generation and their modification are well known. A comprehensive overview about the sources of ULF waves, and their effect of the Earth's magnetosphere, are given in an excellent review paper by *McPherron* [2005], which is recommended to the inquisitive reader. A complete repetition of this topic is not the aim of this Section and such an in-depth description would go beyond the scope of this Thesis. Summarising in brief, it can be stated that all ULF waves have in common that

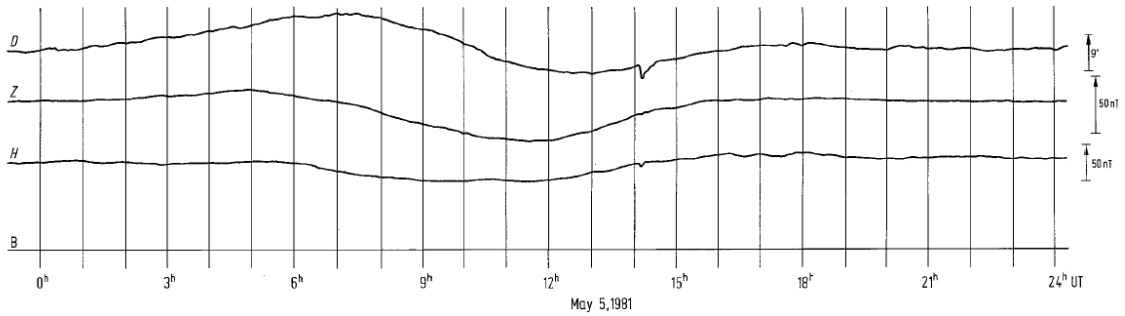

Fig. 2.15.: Geomagnetic field recorded at mid-latitudes showing the effect of a *solar flare effect* (sfe) shortly after 14h with overhead Sq currents toward the equator indicated by a local eastward deflection of the Earth magnetic field (positive deflection of the declination measurements, D); from *Schmucker* [1985].

they are initially generated as magnetohydrodynamic (MHD) waves by processes induced in a plasma under influence of the magnetic field; the plasma is herein part of either solar wind, foreshock, Earth's bow shock, magnetopause, or magnetosphere.

The portion of MHD waves from sources external to the Earth's magnetosphere that reach the Earth's surface interact with each of the regions between the initial source location and the point of detection. Induced effects are known as *field line resonance*, *current induction in the ionosphere*, and *cavity resonance*, determining the actually observed pulsation characteristics. Internal sources of ULF wave include *earthward directed plasma flow* as well as *gyro*, *drift* and *bounce resonances*, responsible for Pi1 and Pi2 signals as well as Pc1, Pc2, and Pc3. An overview about the pulsations and their process of generation as they are understood by today is given in Table 2.3.

2.3. Deviation from plane wave assumption

To simplify mathematic principles of EM induction processes forming the base of the MT method (cf. Sec. 6.2), it is commonly assumed that primary magnetic waves meet the characteristics of a plane wave for the frequency range and study area, i.e. it is assumed that the wave can be considered uniform. A plane wave requires either a uniform source of infinite length or a source at infinite distance, both of which are obviously not physically realisable. Hence, it needs to be examined under which circumstances the deviation of uniformity for a wave can be considered small enough such that the effect of the deviation is negligible for a given resolution.

2.3.1. Mathematical description

Traditionally, the plane wave assumption was considered valid when the recording is made in the *far-field*, i.e. when the distance between source and recording location r is much greater than the wavelength λ (i.e. $r \gg \lambda$). In the review paper by *Mareschal* [1986] on natural MT sources, it is suggested to instead compare the magnitude of the

Wave type	Location of generation external (e) or internal (i)	Process of generation
Continuous pulsations		
Pc5	i	Drift resonance
Pc4	i	Bounce resonance
Pc3	e	During times when the solar wind velocity is high and the solar wind magnetic field is radial
Pc2	i	Generated by electromagnetic ion O(+) cyclotron effects
Pc1	i	Gyro resonance or cyclotron instability
Irregular pulsations		
Pi2	i	Bursty Earthward flows during geomagnetic activity in the plasma sheet on the night-side of the Earth, radiating Alfvén waves that travel to the auroral ionosphere where they are reflected and forced to travel back and interact with the initial flow
Pi1	i	Cavity resonance between the topside of the ionosphere and the auroral acceleration region at ~1 Re altitude that is excited by fluctuating field aligned currents

Tab. 2.3.: Description of the location and process of generation for the different types of ultra low frequency (ULF) waves (also referred to as pulsation) as they are understood by today; after *McPherron* [2005], extended by the information regarding Pc2 using results presented by *Inhester et al.* [1985]; *Sarma et al.* [1974]

horizontal wave number $\|\vec{k}\|$ (i.e. the inverse of the wavelength: $k = \lambda^{-1}$) with the value of $\left(\|\omega + \vec{k} \cdot \vec{v}\|\sigma\mu_0\right)^{1/2}$. Thus, influences of the wave frequency ω, velocity of the source $\vec{v}$ (usually assumed to be zero), and the conductivity of the subsurface σ are taken into account. The approach by *Mareschal* [1986] is based on the solution of the wave equation for electromagnetic fields (cf. Sec. 3.2), i.e.

$$\nabla^2 \vec{F} = \gamma^2 \vec{F} \tag{2.1}$$

where $\vec{F}$ is either the electric or magnetic field and

$$\gamma^2 = k^2 + \imath\omega\mu\sigma + \mu\varepsilon\omega^2 \tag{2.2}$$

(for a non-moving source) with μ: magnetic permeability, ε: permittivity. Assuming that the effect of permittivity is negligible (cf. Sec. 3.5), that $\mu = \mu_0$ (cf. Sec. 3.6), and including the contribution of the moving source yields

$$\hat{\gamma}^2 = k^2 + \imath(\omega + \vec{k}\vec{v})\mu\sigma. \tag{2.3}$$

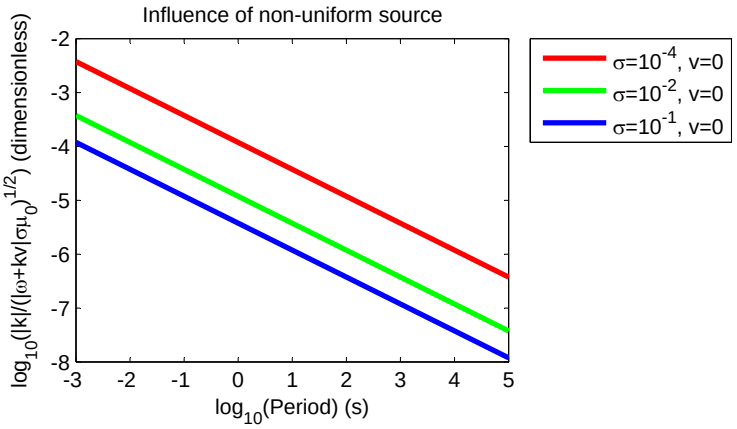

Fig. 2.16.: Estimation of plane wave validity for magnetotelluric (MT) data using the relation given in Equation 2.4 proposed by *Mareschal* [1986]. Validity is therein dependent on period range T, subsurface conductivity σ, and velocity of the source v. Values for source velocities of 10 km/s are plotted as well, but are overlapped by the graph for $v = 0$ because of the small difference.

Validity of the plane wave assumption can then be estimated as the ratio between the different terms:

$$\alpha_{deviation} = \frac{\left|\vec{k}\right|}{\left(\left|\omega + \vec{k} \cdot \vec{v}\right| \mu_0 \sigma\right)^{1/2}}. \tag{2.4}$$

Re-arranging Equation 2.4 using the relations $|k| = f/c$, $\omega = 2\pi f$, and $f = T^{-1}$ with c denoting the speed of light and f and T the frequency and period of the wave respectively, one obtains

$$\alpha_{deviation} = \left(\left[2\pi + \frac{|v|}{c}\right] \mu_0 c^2 \sigma T\right)^{-1/2}. \tag{2.5}$$

From Equation 2.5 it becomes apparent that the motion of the source is negligible for velocities that are small in comparison with the speed of light. Hence, the plane wave validity is dominated by the influence of period range and subsurface conductivity; see Figure 2.16 for an illustration of these relationships.

A more detailed evaluation of the deviation effect is possible when data from co-located stations are available, allowing for a calculation of the wave's spatial change. Mathematically speaking, one looks for situations where the surface from an inclining magnetic wave can be sufficiently described using only the first order terms of the magnetic field, i.e. $\partial_y H_y = 0$, where y refers to the horizontal direction orthogonal to wave propagation. *Dmitriev and Berdichevsky* [1979] and *Berdichevsky et al.* [1981] expressed the magnetotelluric relations for a 1D Earth approximation in terms of power series using the kernel definition by *Schmucker* [1970, 1980]. The authors show that for MT, the effect of non-plane waves can be represented through additional terms appended to the traditional MT

relationship containing even space derivatives for the inclined magnetic wave, viz.

$$E_x(\omega, y) = \sum_{m=0} \frac{I_{2m}}{(2m)!} \frac{d^{2m}}{d^{2m}y} H_y(\omega, y) \tag{2.6}$$

for a 2D source, and

$$E_x(\omega, x, y) = \sum_{m=0} \frac{I_{2m}}{(2m)!} \nabla_h^{2m} H_y(\omega, x, y) \tag{2.7}$$

when considering a 3D source. Therein the spatial variables 'x','y' refer to the two horizontal directions parallel and orthogonal to wave propagation respectively. ∇_h is the horizontal Nabla-operator comprising partial derivatives in the x and y direction, and

$$I_n = \int_{-\infty}^{+\infty} N(u) u^n d(u)$$

with

$$N(\omega, y) = (1/\pi) \int_0^{+\infty} Z(\omega, k) \cos(ky) dk,$$

where $k = 2\pi\lambda$ represents the wave number; therefore $I_0 = Z(\omega, 0)$.

Neglecting the terms with derivatives of order three and higher provides an estimate for the influence of the source effect of a known wave through comparing the amplitudes of the first and second term in the source type related equation, i.e.

$$Deviation \equiv \frac{I_2}{2 \cdot I_0} \frac{d_y^2(H_y)}{H_y}, \tag{2.8}$$

$$Deviation \equiv \frac{I_2}{2 \cdot I_0} \frac{\nabla_h^2(H_y)}{H_y} \tag{2.9}$$

for the case of the two or three dimensional source, respectively. With the approximations that $\partial_x H_x + \partial_y H_y = H_z/Z(\omega, 0)$ and $I_2 = Z(\omega, 0)^3$ over a layered 1D Earth [*Mareschal*, 1986], this leads to the conclusion that significance of the deviation can be estimated by assessing the magnitude of horizontal change in the vertical magnetic field, i.e. $\partial_i H_z$ with $i \epsilon [x, y]$. The change is therein calculated for one of the horizontal directions with the inclining magnetic field orthogonal to the propagation direction in consideration of the present impedance values, i.e.

$$Significance\ of\ Deviation \equiv \frac{Z(\omega, 0)^3}{2 \cdot Z(\omega, 0)} \frac{\partial_i H_z / Z(\omega, 0)}{H_y} = \frac{Z(\omega, 0) \cdot \partial_i H_z}{2 \cdot H_y}. \tag{2.10}$$

This estimation of the source effect by calculating the horizontal change of the vertical magnetic field requires that the change is constant throughout the FFT window (see the studies by *Jones* [1980] in Scandinavia for an example of implementation of the criteria

above).

From Equation 2.10 it becomes apparent that the observed source effect is dependent on the period range and the subsurface conductivity (cf. Sec. 3), as well as the distance between source and receiver, and extent of the study area; see, for example, the study by *Varentsov et al.* [2003a] for a detailed investigation of source effects in data from an extensive MT and GDS station array at high latitudes. Distance between source and receiver as well as the extent of the study area may significantly affect the measured wave gradient at the recording stations and the distance over which the wave must fit the plane wave assumption. It was concluded by *Dmitriev and Berdichevsky* [1979] that, as a guideline, the diameter of the region surrounding one station over which the field constraints must be respected are 100 km to 200 km for a relative resistive sediment cover with thickness up to three km. The region's diameter increases to 300 – 500 km for investigations of relatively conductive formations such as the asthenosphere (usually ≥ 100 km depth), using periods up to 10^4 s [*Mareschal*, 1986]. The diameter may increased even further in case of multiple stations, i.e. extended by the respective inter-stations distance.

2.3.2. Location of recording

Source regions of MT signals, described in Sections 2.1 and 2.2, exhibit different spatial extents that are affecting the character of generated waves, hence the non-uniqueness of waves recorded in the proximity of these sources (cf. Sec. 2.3.1). Whereas, for example, S_q variations with their centre at mid-latitudes are of a more global character, the source signal of equatorial electrojets (EEJ) and polar electrojets (PEJ) are rather limited in their spatial and temporal extension [*Mareschal*, 1986]. Based on measurements in the past, the Earth has been separated into three regions due to existing deviation of the source from the plane wave assumption:

- the high-latitude zone above 50 degrees geomagnetic latitude with a high degree of deviation generated by various current flows in this region,
- the low-latitude zone confined to three degrees geomagnetic latitude above and below the dip equator where deviations are due to the EEJ,
- the mid-latitude zone in-between the two regions mentioned above with a low degree of deviation.

Non-uniformity of signals produced by electric lightning discharges are a relatively minor issue given their comparatively small curvature even for intermediate distances from the source region, due to the high frequency of lightning discharge signals. Moreover, the large number of lightning strikes occurring around the world at all times (Sec. 2.1), in combination with the short window length for the related FFT, leads to high number of degrees of freedom for a recorded time series. When a substantial amount of signals from distant lightning strikes is recorded, segments affected by signal not in agreement with

the plane wave assumptions are down-weighted on a statistical basis; see Section 6.2 for details on data processing schemes.

Mid-latitude zone

As previously noted (Sec. 2.2.2), S_q variations generated at mid-latitudes are of a global nature and do not exhibit strong non-uniformity; source regions of other MT signals are usually sufficiently far away for recordings carried out between 3 and 50 degree geomagnetic latitude on either hemisphere. For datasets collected in these areas, no strong constraints have to be applied to correct for source effects. Processing of such data usually involves weighting of impedance estimates with the vertical field partial coherence [*Beamish*, 1979], and rejection of events that exhibit low coherence with horizontal magnetic fields [*Gough and de Beer*, 1980].

Low-latitude zone

Source effects at low latitudes are mainly caused by the EEJ, initiated by S_q variations, appearing on the day-side of the Earth as an eastward flowing ribbon of electric current most prominent in the region within three degrees on both sides of the dip equator (Sec. 2.2.2). Much work has been done on defining the origin and morphology of the EEJ [e.g. *Untiedt*, 1967; *Hutton*, 1972; *Richmond*, 1973a,b; *Fambitakoye and Mayaud*, 1976a,b,c; *Mayaud*, 1977; *Marriott et al.*, 1979; *Onwumechili and Agu*, 1982] and its effect on MT measurements [e.g. *Forbes*, 1981; *Padilha et al.*, 1997; *Carrasquilla and Rijo*, 1998; *Padilha*, 1999], leading to the conclusion that the effects of the EEJ source are essential during the daytime and can be eliminated by separate investigation of daytime and nighttime records or down-weighting estimates made during the occurrence of EEJ's (analogue to the methods described for mid-latitudes).

High-latitude zone

The regions around the Earth's poles (above 50 degrees geomagnetic latitude) are considered to be the most complicated areas in terms of source effects on MT recordings, given the variety of signals mapping via field lines into these domains. See Table 2.1 for a list of MT sources and their occurrence at different latitudes and Section 2.2.2 for a description of the PEJ dominating the electric current flow in the ionosphere at high-latitudes. The PEJ varies between the different sectors of the Earth in intensity, width, and lateral extent, which, in particular, leads to a different degree of non-uniformity of the MT source signal generated in either the daytime or the nighttime sectors [*Garcia et al.*, 1997]. Source effects are much more prominent during nighttime intervals, exhibiting strong negative excursions of the northern magnetic field and increased activity in the electric fields (Fig. 2.12) which can cause severe distortion of MT recordings.

Effects of non-uniform waves at high-latitudes are addressed through the application of robust processing algorithms [e.g. *Egbert and Booker*, 1986; *Chave et al.*, 1987; *Chave and Thomson*, 1989; *Larsen*, 1989; *Larsen et al.*, 1996; *Garcia et al.*, 1997; *Chave and Thomson*, 2003; *Varentsov et al.*, 2003b] (Sec. 6.2.3), in addition to those attempts used at mid-latitudes (Sec. 2.3.2) with the aim to identify outliers in the magnetic and electric fields. During periods of increased solar activity the majority of nighttime, and a good share of daytime, data can be affected by source effects. This can lead to situations where more than 50 percent of the impedance estimates for the full dataset are biased, causing even the most robust estimators to fail. In such cases it can be beneficial to separate the recorded data into daytime and nighttime intervals in order to assure successful robust processing. Daytime data are concluded to contain fewer effects of non-unique signals, given the usually lower intensity of PEJ during this time and the broadening effect of the solar ionisation on the PEJ. Thus, daytime estimates are more likely to meet the requirements of robust processing estimation. A comparison with separately obtained estimates of the nighttime and the full dataset can then be used for an examination of the amount of source effects in the recorded data [*Garcia et al.*, 1997].

2.3.3. Distance to source region

Degree and manifestation of source effects on MT data is strongly dependent on the horizontal distance between source region and recording site as shown by model studies, e.g. *Hutton* [1969]; *Hermance and Peltier* [1970]; *Peltier and Hermance* [1971]; *Hutton* [1972]; *Hutton and Leggeat* [1972]; *Oni and Alabi* [1972]; *Hughes and Wait* [1975]; *Osipova* [1983]; *Kao* [1984]. Whereas measurements under an electrojet result in an underestimation of the imaginary part of the electric impedance (underestimated apparent resistivity and overestimated phase), the effect is reversed for stations past the edges of the electrojet and slowly decreasing with farther distance [*Peltier and Hermance*, 1971; *Kao*, 1984; *Mareschal*, 1986; *Garcia et al.*, 1997] (Fig. 2.17).

2.3.4. Used period range and subsurface conductivity

Model studies investigating the influence of the studied period range and resistivity of the subsurface on observed source effects show a positive correlation of measured non-uniformity with subsurface conductivity and longest period [*Peltier and Hermance*, 1971; *Hutton*, 1972; *Kao*, 1984; *Garcia et al.*, 1997] (Fig. 2.18). This correlation implies that deviations are more prominent in regions with high inductive skindepth (Sec. 3.3), e.g. continental shields regions, which exhibit low conductivities down to great depth. In contrast, source effects are smaller in regions with relatively high electric conductivity such as tectonically active regions, in which, however, the penetration depth of MT investigation is accordingly smaller.

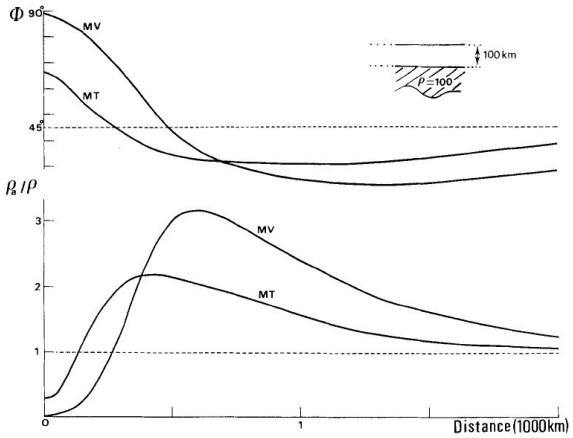

Fig. 2.17.: Deviation of phase ϕ and apparent resistivity ρ_a curves from true values for magnetotelluric (MT) and magnetovariational (MV) data, calculated for the model shown in the inset. The responses are given in terms of the position of the recording point with respect to the line electrojet, showing the underestimation of ρ_a and overestimation of Φ (overestimation of the impedance Z) close to the source region and the opposite case for distances greater than the extend of the electrojet, from *Kao* [1984].

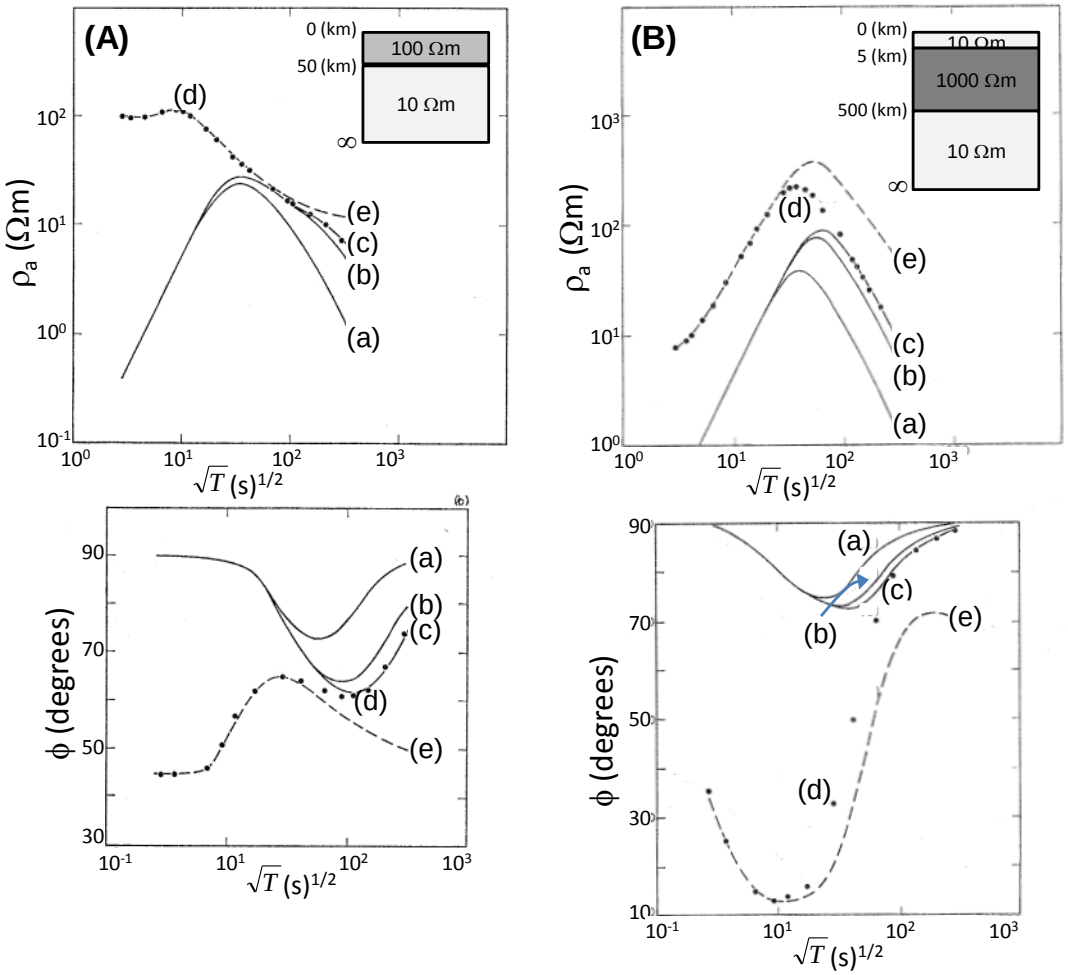

Fig. 2.18.: Apparent resistivity ρ_a and phase ϕ variation curves obtained over an Earth model as defined in inserts (A) and (B) for electrojets of finite length (a, b, c). Half-widths for the finite-length electrojets are assumed to be (a) 400 km, (b) 800 km, and (c) 1000 km. The dotted curve (d) corresponds to the electrojet by *Peltier and Hermance* [1971], whereas the dashed line (e) depicts the traditional MT response (MKS units); modified from *Hutton* [1972].

3

Mathematical description of electromagnetic relations

In principle, all that is needed for a description of electromagnetic (EM) processes relevant for the magnetotelluric (MT) method are the four fundamental Maxwell Equations, Gauss's Law, and boundary conditions, i.e. how the EM fields behave on conductivity interfaces. Respective relations and their application to the MT methods are discussed in this Chapter, together with an examination of commonly used assumptions about properties of subsurface materials; additional assumptions regarding the nature of source fields are illustrated in Chapter 2.

3.1. Basic equations

3.1.1. Maxwell's Equations

The four Maxwell Equations are mostly phenomenological descriptions of relationship between EM fields in a uniform medium, which were experimentally derived and published prior to Maxwell by others authors and are related to them by name:
Gauss's Law

$$\nabla \cdot \vec{D} = Q_e \tag{3.1}$$

Faraday's Law of electromagnetic induction

$$\nabla \times \vec{E} = -\partial_t \vec{B}, \tag{3.2}$$

Gauss's Law for magnetism

$$\nabla \cdot \vec{B} = 0, \tag{3.3}$$

Ampère's circuital Law (with Maxwell's extension)

$$\nabla \times \vec{H} = \partial_t \vec{D} + \vec{J}_f, \tag{3.4}$$

with ∇: Nabla operator, $\vec{D}$: electric displacement field, Q_e: electric charge density, $\vec{E}$: electric field, ∂_t: partial derivative with respect to time, $\vec{B}$: magnetic field, $\vec{H}$: magnetising field, and $\vec{J_f}$: electric current density of free charges. Maxwell found the four original laws to be inconsistent and added the so-called *Maxwellian term* ($\partial_t \vec{D}$) to Ampère's Law in order to provide a complete mathematical description of the physical relationship.

3.1.2. Ohm's Law

Ohm's Law describes the relationship between electric current $\vec{J}$ and electric field $\vec{E}$ for the case of an ohmic conductor with conductivity σ, viz.

$$\vec{J} = \sigma \vec{E}. \tag{3.5}$$

3.1.3. Vector calculus

Stokes theorem relates the rotation of a vector field $\vec{F}$ on a surface A to the flux of the vector field through the boundary s of the volume

$$\int_A (\nabla \times \vec{F}) \cdot \vec{n}\, dA = \int_s \vec{F} \cdot \vec{\tau}\, ds, \tag{3.6}$$

with $\vec{n}$ and $\vec{\tau}$ denoting the unit normal field and the unit tangential field of the surface, respectively.

Gauss's theorem (also referred to *divergence theorem*) relates the change of a vector field $\vec{F}$ inside a volume V to the flux of the vector field through the surface A of the volume

$$\int_V (\nabla \cdot \vec{F})\, dV = \int_A \vec{F} \cdot \vec{n}\, dA, \tag{3.7}$$

with $\vec{n}$ denoting the outward pointing unit normal field of the volume.

3.2. Deriving magnetotelluric parameters

The relation between electric response of a subsurface to an incident magnetic field is the key element of MT, as electric conductivity (or its inverse the electric resistivity) can be derived from the amplitude quotient and phase difference of the EM fields, using basic equations (Sec. 3.1). Rewriting Equation 3.4 and using Ohm's Law (Eq. 3.5) for the case of a homogeneous, isotropic halfspace with use of the constitutive equations

$$\vec{H} = \frac{\vec{B}}{\mu}, \tag{3.8}$$

$$\vec{D} = \varepsilon \vec{E}, \tag{3.9}$$

yields

$$\nabla \times \vec{B} = \mu\varepsilon\partial_t\vec{E} + \mu\sigma\vec{E}, \tag{3.10}$$

with μ: magnetic permeability, and ε: electric permittivity. When considering the rotational component, utilising vector identities and Equations 3.2 and 3.3, this results in

$$\begin{aligned} \nabla \times (\nabla \times \vec{B}) &= \nabla \times (\mu\varepsilon\partial_t\vec{E} + \mu\sigma\vec{E}) && (3.11)\\ \Leftrightarrow \nabla(\underbrace{\nabla \cdot \vec{B}}_{=0}) - \nabla^2\vec{B} &= \mu\varepsilon\partial_t \underbrace{\nabla \times \vec{E}}_{=-\partial_t\vec{B}} + \mu\sigma \underbrace{\nabla \times \vec{E}}_{=-\partial_t\vec{B}} && (3.12)\\ \Leftrightarrow \nabla^2\vec{B} &= \mu\varepsilon\partial_t^2\vec{B} + \mu\sigma\partial_t\vec{B}. && (3.13) \end{aligned}$$

In a similar manner an equivalent equation can be derived for the electric field, starting from Faraday's Law (Eq. 3.2) and resulting in

$$\nabla^2\vec{E} = \mu\varepsilon\partial_t^2\vec{E} + \mu\sigma\partial_t\vec{E}. \tag{3.14}$$

Hence, the relationships for the electric and magnetic fields can be given in the form of a wave equation

$$\nabla^2\vec{F} = \underbrace{\mu\varepsilon\partial_t^2\vec{F}}_{\text{wave propagation}} + \underbrace{\mu\sigma\partial_t\vec{F}}_{\text{wave diffusion}} \tag{3.15}$$

with $\vec{F}$ representing either the electric or magnetic fields. For fields of the form

$$\vec{F} \propto e^{\imath\omega t} \text{ (time dependence)} \tag{3.16}$$

and

$$\vec{F} \propto cos(\vec{k}\vec{x}) \text{ (spatial dependence)},$$

with $\imath$: complex number, ω: angular frequency, t: time, $\vec{x}$: coordinates, $\vec{k}$: wave vector, one obtains for Equation 3.15 that

$$\partial_z^2\vec{F} = \left(\mu\varepsilon\omega^2 + \imath\mu\sigma\omega - \partial_x^2 - \partial_y^2\right)\vec{F}. \tag{3.17}$$

Due to the fact that in MT the spatial variance of the EM fields is considered negligible (cf. Sec. 2.3), Equation 3.17 is reduced to

$$\partial_z^2\vec{F} = \left(-\mu\varepsilon\omega^2 + \imath\mu\sigma\omega\right)\vec{F}, \tag{3.18}$$

and for cases where the influence of permittivity is negligible, as discussed in Section 3.5, this is further reduced to

$$\partial_z^2\vec{F} = \imath\mu\sigma\omega\vec{F}. \tag{3.19}$$

The general solution for Equation 3.19 is

$$\vec{F}(z) = \left(\vec{F}_0 e^{-kz} + \vec{F}_1 e^{+kz}\right) \cdot e^{\imath\omega t} \tag{3.20}$$

with the (positive) wave number

$$k = \sqrt{\imath\omega\mu\sigma} = (1+\imath)\sqrt{\frac{\omega\mu\sigma}{2}}. \tag{3.21}$$

However, since $\vec{F}_1 e^{+kz}$ is unreasonable as it becomes infinitive for large values of z, i.e. $\lim_{z\to\infty} \vec{F}_1 e^{+kz} = \infty$, the fields to be considered here are of the form

$$\vec{F}(z) = \vec{F}_0 e^{-kz-\imath\omega t}. \tag{3.22}$$

Applying the time dependence of magnetic field described by Equation 3.16 to Faraday's Law (Eq. 3.2) yields

$$\nabla \times \vec{E} = -\partial_t \vec{B} = -\imath\omega\vec{B}. \tag{3.23}$$

From this, two decoupled relationships between the horizontal electric fields and the respective orthogonal horizontal magnetic field can be derived as shown in the following paragraphs. In MT, the two cases are commonly referred to as transverse electric (TE) and transverse magnetic (TM) modes, corresponding to the field's orientation relative to a lateral conductivity interface (described in more detail in Chapter 4).

For a setting with a complex 3D subsurface, both modes can be correlated, resulting in further complication of the fundamental MT relationships. For the purpose of illustration, only the case of a layered subsurface (or a situation where the only horizontal conductivity interface is aligned with the coordinate system) is considered here, yielding simple relationships for the EM fields. First, the case of an electric field in x-direction and a magnetic field in y-direction is examined; therein no assumptions are made which one is aligned with the conductivity interface. Considering only the terms of Equation 3.23 that have an $\hat{e}_y$ component, and, again presuming that the waves are uniform, yields

$$\partial_z E_x = -\imath\omega B_y \tag{3.24}$$

$$\overset{Eq.3.22}{\Longleftrightarrow} kE_{x_0}\cancel{e^{-kz-\imath\omega t}} = \imath\omega B_{y_0}\cancel{e^{-kz-\imath\omega t}} e^{-\imath\phi_{xy}}, \tag{3.25}$$

with the index of the phase indicating the relation to the phase difference between E_x and H_y fields. The relationship between the electric and magnetic field can therefore be written as

$$\frac{E_{x_0}}{B_{y_0}} = \frac{\imath\omega e^{-\imath\phi_{xy}}}{\sqrt{\imath\omega\mu\sigma_{xy}}} = \sqrt{\frac{\imath\omega}{\mu\sigma_{xy}}} \cdot e^{-\imath\phi_{xy}}, \tag{3.26}$$

and the resistivity ρ can be calculated from the norm of the EM field ratio, i.e.

$$\Leftrightarrow \left|\frac{E_{x_0}}{B_{y_0}}\right|^2 = \left|\sqrt{\frac{\imath\omega}{\mu\sigma_{xy}}}e^{-\imath\phi_{xy}}\right|^2 = \frac{\omega}{\mu}\rho_{xy} \tag{3.27}$$

$$\Leftrightarrow \rho_{xy} = \frac{\mu}{\omega}\left|\frac{E_{x_0}}{B_{y_0}}\right|^2. \tag{3.28}$$

Equivalently, the resistivity can be expressed using the magnetising field $\vec{H}$ instead of the magnetic field $\vec{B}$, related via the magnetic permeability as described in Equation 3.8, yielding

$$\rho_{xy} = \frac{1}{\mu\omega}\left|\frac{E_{x_0}}{H_{y_0}}\right|^2. \tag{3.29}$$

The resistivity for the orthogonal case ρ_{yx} can be solved in the same manner, using the terms of Equation 3.23 that have an $\hat{e}_x$ component, resulting in

$$\rho_{yx} = \frac{\mu}{\omega}\left|\frac{E_{y_0}}{B_{x_0}}\right|^2 \tag{3.30}$$

and

$$\rho_{yx} = \frac{1}{\mu\omega}\left|\frac{E_{y_0}}{H_{x_0}}\right|^2. \tag{3.31}$$

Phase relationships between orthogonal horizontal electric and magnetic fields can be derived from Equation 3.26, i.e.

$$\phi_{xy} = \arctan\left(\frac{\mathrm{Im}\left(E_x/H_y\right)}{\mathrm{Re}\left(E_x/H_y\right)}\right), \tag{3.32}$$

and, for the orthogonal case,

$$\phi_{yx} = \arctan\left(\frac{\mathrm{Im}\left(E_y/H_x\right)}{\mathrm{Re}\left(E_y/H_x\right)}\right). \tag{3.33}$$

3.2.1. Common notation for magnetotelluric relations

It is common practise to describe the relationship between all horizontal electric and magnetic fields relevant for MT by using the electric impedance $\mathbf{Z}$, which can be written in compact form as

$$\begin{pmatrix} E_x \\ E_y \end{pmatrix} = \begin{pmatrix} Z_{xx} & Z_{xy} \\ Z_{yx} & Z_{yy} \end{pmatrix}\begin{pmatrix} H_x \\ H_y \end{pmatrix}. \tag{3.34}$$

Apparent resistivity and impedance phase are therefore related to electric impedance via

$$\rho_{a_{ij}} = \frac{1}{\mu\omega} \left|Z_{ij}\right|^2 \tag{3.35}$$

where Z_{ij} represents the integrated impedance of the (heterogeneous) subsurface, and

$$\phi_{ij} = \arctan\left(\frac{\mathrm{Im}(Z_{ij})}{\mathrm{Re}(Z_{ij})}\right) \tag{3.36}$$

respectively, with $i, j \in [x, y]$.

3.2.2. Relationships for simple subsurface cases

1D case

For situations where the subsurface exhibits solely vertical conductivity changes, naturally no alignment of any coordinate system axis with lateral interfaces can be made, making the choice of the coordinate system direction completely arbitrary. In such cases, diagonal elements of the impedance tensor (Eq. 3.34) are zero since electric fields are independent of parallel magnetic fields:

$$\begin{pmatrix} E_x \\ E_y \end{pmatrix} = \begin{pmatrix} 0 & Z_{xy} \\ -Z_{xy} & 0 \end{pmatrix} \begin{pmatrix} H_x \\ H_y \end{pmatrix}. \tag{3.37}$$

The off-diagonal elements are of the same amplitude, but with an inverted sign due to the change from a right-handed into a left-handed coordinate system when dealing with the yx-component

2D case

When the subsurface possesses lateral conductivity interfaces in only one direction (with an arbitrary number of vertical conductivity changes), the original coordinate system used for the recording can be rotated to the interface directions using a transformation matrix

$$\mathbf{R} = \begin{pmatrix} \cos(\Theta) & \sin(\Theta) \\ -\sin(\Theta) & \cos(\Theta) \end{pmatrix}. \tag{3.38}$$

For the case of perfect adjustment the impedance matrix reduces to

$$\begin{pmatrix} E_x \\ E_y \end{pmatrix} = \begin{pmatrix} 0 & Z_{xy} \\ Z_{yx} & 0 \end{pmatrix} \begin{pmatrix} H_x \\ H_y \end{pmatrix}. \tag{3.39}$$

Induction arrows	Magnitude	Direction	
		Wiese	Parkinson
Real arrow	$\|\|\mathrm{Re}(T_x) + \mathrm{Re}(T_y)\|\|$	$\arctan\left(\frac{\mathrm{Re}(T_y)}{\mathrm{Re}(T_x)}\right)$	$\arctan\left(-\frac{\mathrm{Re}(T_y)}{\mathrm{Re}(T_x)}\right)$
Imaginary arrow	$\|\|\mathrm{Im}(T_x) + \mathrm{Im}(T_y)\|\|$	$\arctan\left(\frac{\mathrm{Im}(T_y)}{\mathrm{Im}(T_x)}\right)$	$\arctan\left(-\frac{\mathrm{Im}(T_y)}{\mathrm{Im}(T_x)}\right)$

Tab. 3.1.: Induction arrows derived from the magnetic transfer function ($\vec{T} = (T_x, T_y)$) with two different conventions regarding the direction, pointing towards the resistor (Wiese [*Wiese*, 1962]) and the conductor (Parkinson [*Parkinson*, 1959]), respectively.

3.2.3. Vertical magnetic transfer function

The vertical magnetic transfer function ($\vec{T} = (T_x, T_y)$), also referred to as *Tipper*, relates the vertical magnetic field (H_z) to the horizontal magnetic fields ($\vec{H}_h = (H_x, H_y)$)

$$H_z(f) = \vec{T}(f)\vec{H}_h(f). \tag{3.40}$$

For the case of a 2D subsurface and adequate rotation of the coordinate system Equation 3.40 reduces to

$$H_z(f) = T_y(f)H_y(f) \tag{3.41}$$

with the y-axis parallel to the conductivity interface [e.g. *Vozoff*, 1987]. The magnetic transfer function can be displayed using the induction arrows defined in Table 3.1, with arrows pointing towards either resistive regions (Wiese convention [*Wiese*, 1962]) or conductive regions (Parkinson convention [*Parkinson*, 1959]). For the undisturbed 2D case the phases of T_x and T_y are equal, thus the magnitude of the imaginary induction arrow equals zero, and the direction of the real induction arrow is orthogonal to the geoelectric strike direction.

3.3. Magnetotelluric induction area

In MT, the depth of investigation is directly dependent on period range and subsurface conductivity, as the intensity of a penetrating magnetic wave is proportional to each of these. As a measure of the MT method's sensitivity, the distance to the Earth's surface at which the amplitude of the penetrating wave is reduced by $1/e$ is commonly used, i.e.

$$F(\delta_s) = \frac{1}{e}F_0 = F_0 e^{-1} = F_0 e^{-\mathrm{Re}(k)\delta_s}. \tag{3.42}$$

Therein, δ_s is referred to as *skin depth* (or *induction depth*). Using the expression for the magnetic field in Equation 3.22, the wave number as defined in Equation 3.21, and

$$\mathrm{Re}(k) = \sqrt{\omega\mu\sigma/2}, \tag{3.43}$$

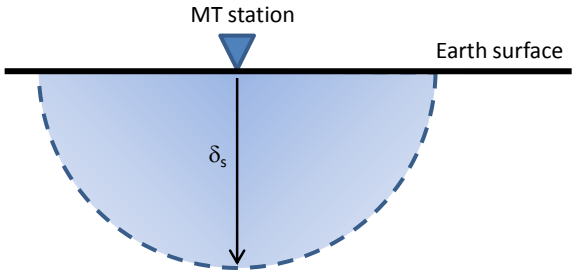

Fig. 3.1.: Induction depth δ_s for an MT station over a conductive half-space.

yields for the skin depth:

$$\delta_s = \sqrt{\frac{2}{\omega\mu\sigma}}. \tag{3.44}$$

When applying $\omega = 2\pi/T$, $\sigma = 1/\rho$, and the assumption that $\mu = \mu_0 = 4\pi 10^{-7}$ Vs/Am, one derives an estimate for the skin depth that depends on period and subsurface resistivity, i.e.

$$\delta_s \approx 0.5\sqrt{\rho T} \qquad \text{[km]}. \tag{3.45}$$

This approximation, however, is only valid for the case of a subsurface with homogeneous electric resistivity, as attenuation will change accordingly, when the penetrating wave enters an area with different electric parameters (Sec. 3.4).

For the halfspace case the lateral extent of the MT study region is roughly equivalent to its vertical counterpart [*Jones*, 1983a]. The surface of a body, describing the area sensed by an MT station for a wave of a certain period, can be approximated by a hemisphere with its flat face coinciding with the Earth's surface (Fig. 3.1). This circumstance enables the investigator to plan the positioning of MT recording stations in a fieldwork campaign by calculating the overlap of station sensitivity areas to be expected at a certain depth and the necessary station spacing required to ensure the desired redundancy of measurements obtained (cf. Sec. 6.1.2).

In case of a heterogeneous subsurface, δ_s can be approximated using the apparent resistivity ρ_a (Eq. 3.60):

$$\delta_s \approx 0.5\sqrt{\rho_a T} \qquad \text{[km]}. \tag{3.46}$$

For the case of a layered subsurface, the skin depth is controlled by subsequent absorption of all layers relevant for a given period. If the energy of the penetrating wave is reduced to $1/e$ of the original value within the n-th layer of a known subsurface model, the respective skin depth can be calculated as the sum of depth to the bottom of the layer *n-1*, i.e. d_{n-1}, and the skin depth in the layer n, i.e. t'_n, (cf. Fig. 3.2):

$$\delta_s = d_{n-1} + t'_n. \tag{3.47}$$

Whereas d_{n-1} is *a priori* known for a given model, t'_n can be calculated using Equation

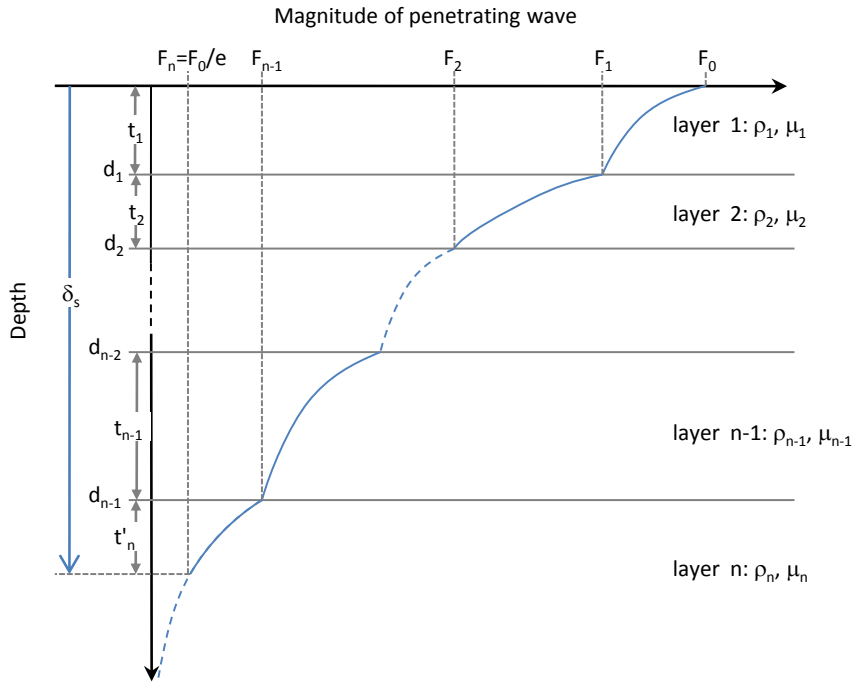

Fig. 3.2.: Change of wave magnitude with depth for the case of a 1D subsurface with n-layers; with F_i Magnitude of the wave at the bottom of the i-th layer, d_i depth to the bottom of the i-th layer, t_i thickness of the i-th layer, ρ_i electric resistivity of the i-th layer, μ_i magnetic permeability of the i-th layer, and δ_s the skin depth.

3.42 for the layer n:

$$F(\delta_s) = \frac{1}{e}F_0 = F_0 e^{-1} = F_{n-1}e^{-\mathrm{Re}(k_n)t'_n} \tag{3.48}$$

where F_{n-1} is the amplitude of the penetrating wave at the bottom of the layer *n-1*. The only unknown in Equation 3.48, i.e. F_{n-1}, can be represented using the wave amplitude at the bottom of the layer *n-2* (F_{n-2}) as well as absorption k_{n-1} and thickness t_{n-1} of the layer *n-1*:

$$F_0 e^{-1} = \underbrace{F_{n-2}e^{-\mathrm{Re}(k_{n-1})t_{n-1}}}_{F_{n-1}} e^{-\mathrm{Re}(k_n)t'_n}. \tag{3.49}$$

In turn, F_{n-2} can be represented using the wave amplitude at the bottom of the layer *n-3* (F_{n-3}) and absorption k_{n-2} and thickness t_{n-2} of the layer *n-2*:

$$F_0 e^{-1} = F_{n-2}\underbrace{e^{-\mathrm{Re}(k_{n-1})t_{n-1}}}_{F_{n-2}} e^{-\mathrm{Re}(k_{n-1})t_{n-1}} e^{-\mathrm{Re}(k_n)t'_n}. \tag{3.50}$$

This process can be repeated up to the Earth surface where the initial amplitude of the wave F_0 is used, yielding the modified form of Equation 3.48:

$$\begin{aligned} F_0 e^{-1} &= F_0 e^{-\mathrm{Re}(k_n)t'_n} \cdot \textstyle\prod_{i=1}^{n-1} e^{-\mathrm{Re}(k_i)t_i} \\ &= F_0 e^{-\mathrm{Re}(k_n)t'_n - \sum_{i=1}^{n-1}\mathrm{Re}(k_i)t_i}. \end{aligned} \tag{3.51}$$

Reducing F_0 in Equation 3.51, applying the natural logarithm to both sides, followed by a multiplication by (-1) yields

$$\begin{aligned} 1 &= \mathrm{Re}(k_n)t'_n + \sum_{i=1}^{n-1} \mathrm{Re}(k_i)t_i \\ \Leftrightarrow t'_n &= \frac{1}{\mathrm{Re}(k_n)} - \frac{1}{\mathrm{Re}(k_n)} \sum_{i=1}^{n-1} \mathrm{Re}(k_i)t_i. \end{aligned} \tag{3.52}$$

With Equation 3.43 this results in

$$t'_n = \sqrt{\frac{\rho_n T}{\pi\mu_n}} - \sum_{i=1}^{n-1} \sqrt{\frac{\mu_i\rho_n}{\mu_n\rho_i}} t_i. \tag{3.53}$$

Hence, the skin depth can be calculated for the case of a known 1D subsurface model with n-layers using

$$\delta_s = \sqrt{\frac{\rho_n T}{\pi\mu_n}} + d_{n-1} - \sum_{i=1}^{n-1} \sqrt{\frac{\mu_i\rho_n}{\mu_n\rho_i}} t_i, \tag{3.54}$$

with d_{n-1} denoting the depth to the bottom of the layer $n-1$, and ρ_i, μ_i, and t_i are the resistivity, permeability, and thickness of the i-th layer, respectively. With the assumptions used for Equation 3.45 this yields:

$$\delta_s \approx 0.5\sqrt{\rho_n T} + d_{n-1} - \sum_{i=1}^{n-1} \sqrt{\frac{\mu_i\rho_n}{\mu_n\rho_i}} t_i \qquad [\mathrm{km}]; \tag{3.55}$$

and with the assumption that $\mu_i = \mu_n = \mu_0$ for all layers (cf. Sec. 3.5) Equation 3.55 further reduces to

$$\delta_s \approx 0.5\sqrt{\rho_n T} + d_{n-1} - \sqrt{\rho_n} \sum_{i=1}^{n-1} \frac{t_i}{\sqrt{\rho_i}} \qquad [\mathrm{km}]. \tag{3.56}$$

3.4. Boundary conditions

The use of the so-called *halfspace case* is purely an idealistic principle and is never obtained in practice for a variety of reasons, such as the long periods used and hence the large area of induction (Sec. 3.3). Usually changes of conductivity, due to variations in composition or condition, are sensed vertically and at minimum in one horizontal direction; at the very least, the air-ground interface is always present in MT data. Furthermore, as MT is often superior to other deep-probing methods, like seismic tomography, in detection of vertical interfaces and therefore in determining the distribution of subsurface

materials and their condition, it is important to examine the effects of such conductivity interfaces on the electric current and EM fields.

From Maxwell's Equations (Eqs. 3.1 - 3.4), with the aid of Stokes' and Gauss' theorems (Eqs. 3.6 and 3.7), it becomes immediately evident that the relationship for EM fields and electric currents on conductivity interfaces are such as given in Table 3.2. In

Continuity on conductivity interface

Field	Component	
	Normal	Transverse
$\vec{B}$	✓	✓
$\vec{H}$	✓	✓
$\vec{E}$	✗	✓
$\vec{D}$	✗	✓
El. current	Normal	Transverse
$\vec{J}$	✓	✗

Tab. 3.2.: Behaviour of electromagnetic fields and electric current on conductivity interfaces with their components in regards to the orientation of the interface.

summary, the magnetic fields $\vec{B}$ and hence the magnetic field strength $\vec{H}$ are constant on conductivity interfaces (presuming no magnetic permeability variation along with the conductivity change). The electric current $\vec{J}$ exhibits a continuous normal and a discontinuous transverse component, and since the electric field $\vec{E}$ is related to the current via the local conductivity as described by Ohm's Law (Eq. 3.5) its behaviour is exactly opposite (and so is the electric displacement fields $\vec{D}$, presuming constant permittivity). The relation between the electric components of two areas can be given in a form similar to Snell's Law, i.e.

$$\frac{J_{1T}}{J_{2T}} = \frac{\sigma_1 E_T}{\sigma_2 E_T} = \frac{\sigma_1}{\sigma_2} = \frac{\rho_2}{\rho_1} = \frac{\tan(\alpha_1)}{\tan(\alpha_2)}, \tag{3.57}$$

and

$$\frac{E_{1N}}{E_{2N}} = \frac{\sigma_2 J_N}{\sigma_1 J_N} = \frac{\sigma_2}{\sigma_1} = \frac{\rho_1}{\rho_2} = \frac{\tan(\alpha_2)}{\tan(\alpha_1)}, \tag{3.58}$$

with α_i representing the angles between the flow lines of electric current and a vector normal to the conductivity interface.

3.4.1. Horizontal interfaces

To illustrate the effect of horizontal interfaces on MT observations consider a layered subsurface with Q layers, hence Q interfaces (including the air-surface interface at depth $z = 0$). In each of the first Q-1 layers the general form of the EM fields as described in Equation 3.20 is valid, including the upward term $\vec{F}_1$, whereas in the bottom half-space

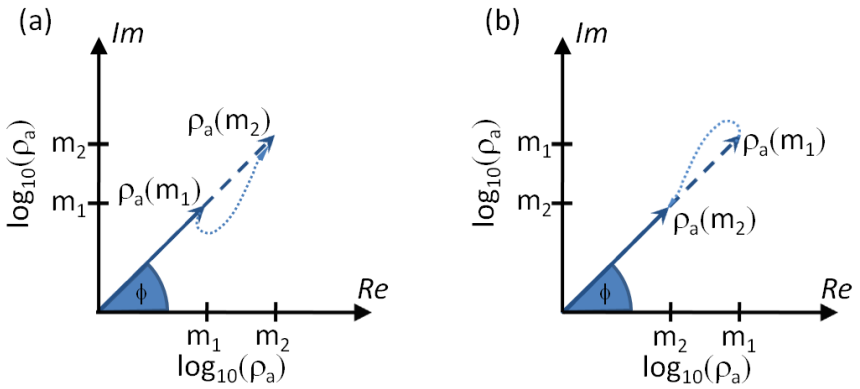

Fig. 3.3.: Illustration of apparent resistivity ρ_a and phase ϕ behaviour in the complex plane using the relevant period range for the case of (a) a resistive medium underlying a more conductive layer, and (b) a conductive medium underlying a more resistive layer. $\rho_a(m_1)$ and $\rho_a(m_2)$ refer to the values of the upper and lower layer respectively, observed for periods that are unaffected by the resistivity interface.

only the downward term $\vec{F}_0$ exists. The impedance Z in every layer m can be derived from wave number k, and thickness t of the layer, and impedance of the layer $m+1$ below using a modified version of Wait's *recursion formula* [*Wait*, 1954], i.e.

$$Z_m = \frac{\Gamma_m \left(k_m Z_{m+1} + \Gamma_{m+1} \tanh(k_m t_m)\right)}{\Gamma_{m+1} + k_m Z_{m+1} \tanh(k_m t_m)}, \tag{3.59}$$

with $\Gamma_m = \imath\omega\mu_m$. The resistivity measured at the surface for a certain frequency is therefore not related to the resistivity of a single layer but can be pictured as the weighted integral over the electric parameters of all layers, usually referred to as *apparent resistivity*

$$\rho_a(T) = \frac{1}{\mu\omega}|Z_{z=0}(T)|^2. \tag{3.60}$$

From Equations 3.32, 3.59, and 3.60 it can be deduced that for the case of a resistive medium underlying a more conductive layer, for the period range sensitive to the transition zone, the apparent resistivity increases with period, whereas the phase decreases. For longer periods, the phase will then re-establish its original value of 45 degrees, presuming that no other effects exert influence on the present EM fields. For the opposite case of a conductive medium underlying a more resistive layer, the effect is reversed, exhibiting a decrease of apparent resistivity and an increase of phase. In both cases, the phase effect is usually observable at shorter periods than the resistivity change (cf. Sec. 4.2.1); however, this is simply due to the greater relative response of the phase at shorter periods. The different behaviour of apparent resistivity and phase at an interface becomes obvious when displayed in terms of real and imaginary values of resistivity; respective curves in the complex *rho*-plane for two layered 1D models are shown in Figure 3.3.

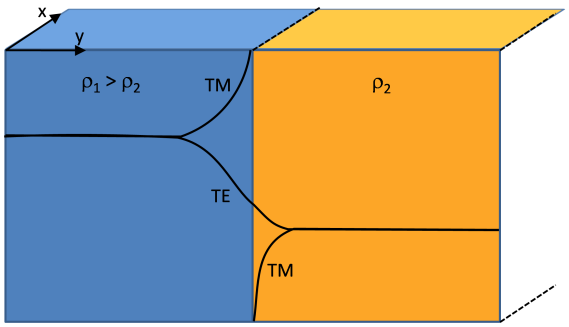

Fig. 3.4.: Behaviour of TE and TM mode for the same period in the presence of a conductivity contact zone, displaying a smoothly varying continuous TE mode and a jump in the TM mode at the interface with the adjustment distance depends on the local resistivity values.

3.4.2. Lateral interfaces

The behaviour of electric currents, and hence of electric and magnetic fields, in the presence of lateral conductivity interfaces can be derived from Maxwell's Equations (Sec. 3.1.1) and is summarised in Table 3.2; a comprehensive overview about lateral boundary effects is given in Chapter 4 and here only the basic principles are illustrated. For MT it is useful to consider EM fields in terms of their contribution to the TM and TE modes, i.e. the combination of normal electric field E_N and transverse magnetic field H_T forming the TM mode, and transverse electric E_T and normal magnetic field H_N forming the TE mode.

For the sake of demonstration, two homogeneous quarter-spaces are considered here, exhibiting different values of resistivity and are connected along an interface parallel to the x-axis. In order to investigate the behaviour of the two modes, it is assumed that MT data have been continuously collected along a profile parallel to the y-axis, crossing the conductivity interface from the relatively conductive to the resistive side (Fig. 3.4). Far away from the contact zone, in an inductive distance sense, both modes will simply represent the conductivity of each quarter-space. For the TE mode the transition between the two regions will be smooth since only E_N is discontinuous on conductivity interfaces. The TM mode, on the other hand, exhibits a jump at the interface caused by the deviation of electric currents towards the interface on the resistive side and parallel to the interface on the conductive side, making TM the favourable mode to detect lateral conductivity changes. The *adjustment distance*, i.e. the distance from the interface where the effect of the conductivity contact is comparably small, is dependent on period range and resistivity for each quarter-space analogue to the vertical skin depth (Sec. 3.3).

3.5. The influence of electric permittivity

In MT, it is commonly assumed that the influence of electric permittivity is small in comparison with the effect of electric conductivity, which is dominating the relationship be-

tween electric and magnetic fields. However, it is worthwhile to examine under what circumstances this assumption is valid.

The relationship between electric and magnetic fields under consideration of the permittivity is

$$\hat{e}_x : H_x = \frac{1}{k}\left[\imath\varepsilon\omega + \sigma_{yx}\right] E_y \tag{3.61}$$

and

$$\hat{e}_y : H_y = -\frac{1}{k}\left[\imath\varepsilon\omega + \sigma_{xy}\right] E_x \tag{3.62}$$

for the two orthogonal horizontal directions. Impedance and apparent resistivity are derived from

$$Z_{ij} = \frac{E_i}{H_j} \tag{3.63}$$

and

$$\rho_{a_{ij}} = \frac{1}{\mu\omega}\left|Z_{ij}\right|^2, \tag{3.64}$$

respectively, with $i, j \in [x, y]$ (cf. Sec. 3.2). To investigate the effect of permittivity, absolute values of the impedance derived with (ρ_{with}) and without ($\rho_{without}$) the first term in Equations 3.61 and 3.62 are compared

$$\frac{\rho_{without}}{\rho_{with}} = \frac{|Z_{without}|^2}{|Z_{with}|^2} = \frac{\left|\frac{1}{k}\left(i\varepsilon\omega + \sigma\right)\right|^2}{\left|\frac{1}{k}\sigma\right|^2} = 1 + \left(\frac{\varepsilon\omega}{\sigma}\right)^2; \tag{3.65}$$

for the sake of convenience indices of resistivity and impedance are dropped in here. Using $\omega = 2\pi f$ and $\sigma = \rho^{-1}$ this can be rewritten as

$$\frac{\rho_{without}}{\rho_{with}} = 1 + (2\pi\varepsilon\rho f)^2, \tag{3.66}$$

showing that the effect of neglecting the permittivity term is given by the second term in the right hand side of Equation 3.66, i.e.

$$D_{perm} := 2\pi\varepsilon\rho f. \tag{3.67}$$

Thus, the deviation is positive proportional to permittivity, resistivity, and frequency, suggesting an assessment in respect to the range of contributing parameters. Permittivity is the product of the permittivity of free air $\varepsilon_0 = 8.89 \cdot 10^{-12}$ As/Vm and the permittivity of the material ε_r with typical values of ε_r for Earth's material lying between 3 (ice) and 81 As/Vm (water), and an average value of 20 As/Vm for dry rocks [*Telford et al.*, 1990]. Common resistivity values for Earth's materials derived by laboratory studies range from 10^{-7} for graphite to 10^7 Ωm for dry igneous rocks (cf. Figs. 3.5 and 3.6, Chap. 5).

Since ε and ρ are both positive, deviation increases with increasing frequencies as

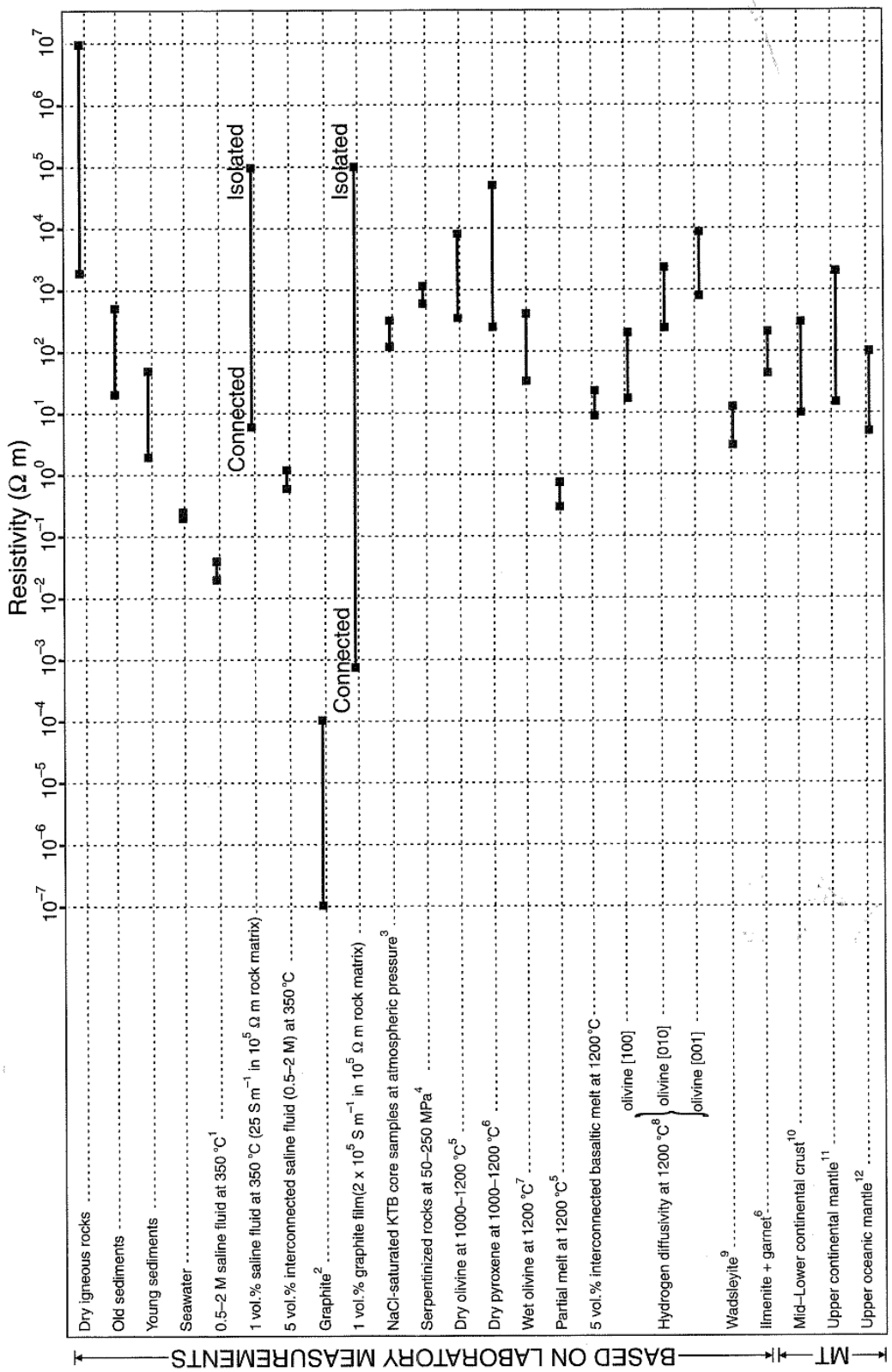

Fig. 3.5.: Electric resistivities of rocks and other common Earth materials. The labels 'connected' and 'isolated' refer to the more conductive component of a two phase medium, and the values are calculated from *Hashin and Shtrikman* [1962] upper and lower bounds assuming a rock matrix with a resistivity of 10^{5} Ωm. Resistivity values are taken from 1: *Nesbitt* [1993], 2: *Duba and Shankland* [1982], 3: *Duba et al.* [1994], 4: *Stesky and Brace* [1973], 5: *Duba et al.* [1974], *Hirsch et al.* [1993], and *Xu et al.* [1998a], 6: *Xu and Shankland* [1999] (and references therein), 7: *Lizarralde et al.* [1995] (and references therein), 8: *Karato* [1990], 9: *Xu et al.* [1998a], 10: *Haak and Hutton* [1986], and *Jones* [1992], 11: *Heinson and Lilley* [1993], and *Lizarralde et al.* [1995], 12: *Schultz et al.* [1993], and *Simpson* [2002a]; Figure from *Bahr and Simpson* [2002].

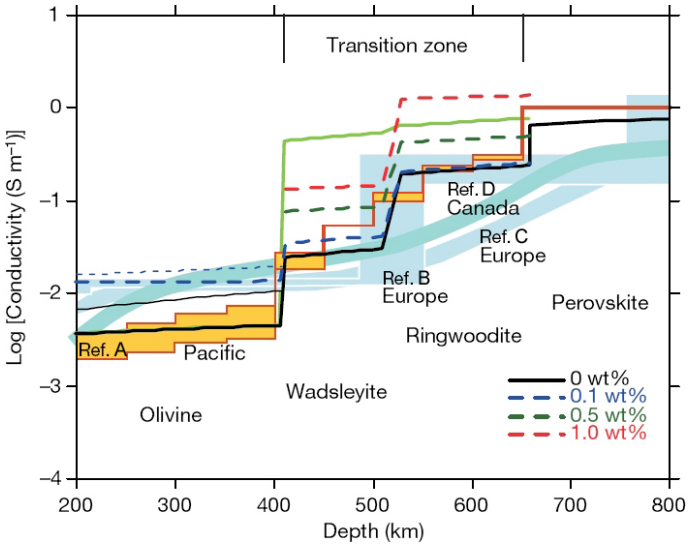

Fig. 3.6.: Electric conductivity profile of the deep Earth; from *Yoshino et al.* [2008]. The orange and bluish areas represent geophysical observed conductivity profiles in the Pacific from ref. A: [*Kuvshinov et al.*, 2005] and the continental mantle from refs B: [*Olsen*, 1998], C: [*Tarits et al.*, 2004] and D: [*Neal et al.*, 2000], respectively. The thick solid line represents the electric conductivity of olivine, wadsleyite, and ringwoodite without water. Dashed lines indicate the electric conductivity of hydrous olivine, wadsleyite and ringwoodite as a function of water content (red: 1.0 wt%; green: 0.5 wt%; blue: 0.1 wt%). Light green solid line denotes the previous experimental result of *Xu et al.* [1998a].

shown in Figure 3.7 for fixed values of ε and ρ, demonstrating that the impedance is generally underestimated by the factor $1 + D^2_{perm}$ when the effect of permittivity is neglected. According to Equation 3.66, for average values of conductivity (100 Ωm) and permittivity (20 As/Vm), the deviation falls below 1 % for frequencies lower than 100 kHz (i.e. periods longer than 10^{-5} s), indicating that neglecting the influence of permittivity is justified for the period range of MT.

Analogue to the expression for the effect of electric permittivity on apparent resistivity given in the previous paragraphs, the effect on the impedance phase can be assessed. When the effect of electric permittivity is negligible and estimates are considerably far away from conductivity interfaces the off-diagonal impedance tensor elements exhibit a phase of 45 degrees (or -45 degrees when changing from a right-handed into a left-handed coordinate system, see Section 3.2.2). Thus, for the impedance phase without a contribution of electric permittivity

$$\tan(\phi_{without}) = \frac{\mathrm{Im}(Z_{without})}{\mathrm{Re}(Z_{without})} = \pm 1 \tag{3.68}$$

with the real and imaginary parts of the impedance tensor elements possessing the same absolute value. Hence, the relation between the impedance phase with (ϕ_{with}) and without ($\phi_{without}$) consideration of electric permittivity reduces to an assessment of the ϕ_{with} term:

$$\frac{\tan(\phi_{without})}{\tan(\phi_{with})} = \frac{1}{\tan(\phi_{with})} \quad \longrightarrow \quad \tan(\phi_{with}) = \frac{\mathrm{Im}(Z_{with})}{\mathrm{Re}(Z_{with})}, \tag{3.69}$$

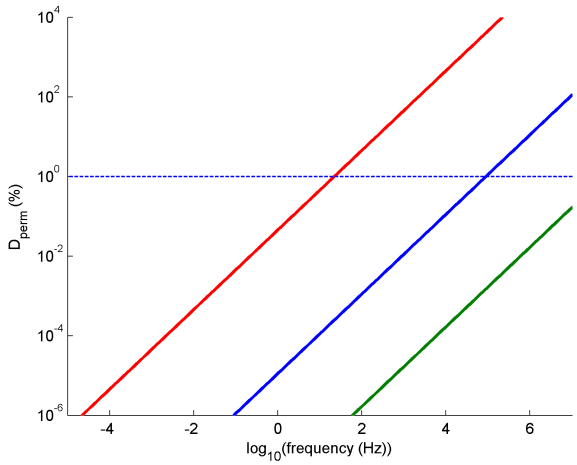

Fig. 3.7.: Difference between the impedance calculated with and without neglecting the permittivity term for different frequencies. The blue line denotes the difference for average values of ρ and ε_r ($\rho = 100\,\Omega$m, $\varepsilon_r = 20$ As/Vm; the red and green lines indicate the upper and lower bounds for Earth's material with $\rho = 1\,\Omega$m, $\varepsilon_r = 3$ As/Vm, and $\rho = 10^5\,\Omega$m, $\varepsilon_r = 81$ As/Vm respectively. The dashed line denotes a deviation of 1 %.

i.e. the relation between imaginary and real parts of the impedance tensor incorporating the electric permittivity effect in the wave propagation term. Wave diffusion and wave propagation terms comprise real and imaginary characteristics in the wave equation, respectively (cf. Eqs. 3.15 and 3.18). In a first order approximation, the effect of neglecting the electric permittivity when estimating the impedance phase, i.e. on the real and imaginary parts of the impedance tensor under consideration of the electric permittivity, can therefore be given as the ratio of the wave propagation and wave diffusion terms

$$1/\tan(\phi_{with}) \propto \frac{\mu\varepsilon\omega^2}{\mu\sigma\omega} = \frac{\varepsilon\omega}{\sigma}. \tag{3.70}$$

Thus, the effect of the wave propagation term can be considered negligible when

$$\varepsilon\omega/\sigma << 1. \tag{3.71}$$

This is equivalent with the expression for the electric permittivity effect on apparent resistivity ($2\pi\varepsilon\rho f << 1$, Equation 3.67) using $\omega = 2\pi f$ and $\sigma = 1/\rho$. Hence, for common MT investigations that use long-period data to investigate the subsurface the effect of electric permittivity is negligible.

For a more detailed analysis of neglecting the electric permittivity effect during impedance data estimation, particular in high-frequency radiomagnetotelluric investigations, the interested reader is referred to the work by, for example, *Hohmann* [1987], *Ward and Hohmann* [1987], and *Kalscheuer et al.* [2008].

3.6. The influence of magnetic permeability

In MT, magnetic permeability is usually assumed equal to the permeability of free space $\mu_0 = 4\pi 10^{-7}$ Vs/Am, rather than the product of μ_0 and the permeability of a specific medium (i.e. the *relative permeability*) μ_r. Neglecting the effect of the relative permeability during the calculation of the electric resistivity results in a frequency independent deviation from the correct value of factor μ_r (cf. Eqs. 3.29 and 3.30). The approximation that $\mu = \mu_0$ is valid for most MT cases, since μ_r is almost always close to 1, except for some uncommon minerals like Magnetite ($\mu_r = 5$) and Phyrrhotite ($\mu_r = 2.55$) [*Telford et al.*, 1990].

4 Distortion of magnetotelluric data

Over time, various definitions for distortion of magnetotelluric (MT) data have been given, wherein in the very most cases the used definition is tailored to the current topic. Distortion is commonly attributed to an effect that impedes or prevents an interpretation of the obtained MT data. These effects include, amongst others, deviation of the source field from the plane wave assumption (Sec. 2.3), and generation of secondary electromagnetic (EM) fields due to regions of different electric conductivity in the area under investigation. Since modern MT processing is capable of dealing with most cases of 1D and 2D subsurface structures, the latter usually refers to situations where responses from regional structures are disturbed by small-scale or 3D features [e.g. *Berdichevsky et al.*, 1973]. In here, a more general definition is chosen, attributing distortion to effects that cause a deviation of the electric currents from a straight-lined behaviour within the region of interest, i.e.

$$\vec{J} = \vec{J}_p + \vec{J}_a, \tag{4.1}$$

with $\vec{J}_p$: undistorted component of the electric current from primary EM fields and $\vec{J}_a$: anomalous current due to distortion.

In this Section different types of distortion are presented, their frequency dependence and the effects of dimensionality of the distorting body are investigated, mathematical formulations of the distortion effects are shown, and an overview about approaches used to remove the effects of distortion are given. Alterations of electric current behaviour due to deviation of MT source fields from the uniform case are examined separately in Section 2. Comprehensive overviews about distortion of MT data are given for example in the review papers by *Jiracek* [1990] and *Ledo* [2005], as well as in the publications by *Berdichevsky et al.* [1989], *Vozoff* [1987], *Groom and Bahr* [1992], and *Simpson and Bahr* [2005]. In addition, various papers have been published regarding specific aspects of distortion and attempts for their removal; these will be referred to in the following sections when the respective topic is addressed.

4.1. Types of distortion

As a first approach, distortion of MT can be separated into two groups according to the electromagnetic (EM) processes involved, i.e. cases where electric charges are accumulated along boundaries of regions with different electric resistivities (referred to as *galvanic distortion*), and cases where an anomalous EM fields is induced within a body of different conductivity (referred to as *inductive distortion*) [*Berdichevsky et al.*, 1989]. Using the Born approximation [*Born*, 1933], measured electric fields E can be expressed as a combination of primary field and superimposed galvanic and inductive distortion [*Habashy et al.*, 1993; *Chave and Smith*, 1994], i.e.

$$\begin{aligned} E(\vec{r}) &= E_p(\vec{r}) && \text{: primary field} \\ &- \iota\omega\mu_0 \sum_j \int_{V_j} g(\vec{r},\vec{r'})\Delta\sigma_j(\vec{r'})E(\vec{r'})d\vec{r'} && \text{: inductive distortion} \\ &+ \frac{1}{k_h^2}\nabla^2 \sum_j \int_{V_j} g(\vec{r},\vec{r'})\Delta\sigma_j(\vec{r'})E(\vec{r'})d\vec{r'} && \text{: galvanic distortion} \end{aligned} \tag{4.2}$$

with $g(\vec{r},\vec{r'}) = \frac{\exp(\iota k|\vec{r}-\vec{r'}|)}{4\pi|\vec{r}-\vec{r'}|}$: the Green's function, $k_h^2 = \iota\omega\mu_0\sigma_h + \omega\mu_0\varepsilon_b$: wave number of the host medium, ω: angular frequency, μ_0: magnetic permeability of free space, ε_b: electric permittivity of the host medium, σ_h and σ_j: conductivity of the host medium and the j-th distorting body respectively, $\Delta\sigma(\vec{r'}) = \sigma_j(\vec{r'}) - \sigma_h(\vec{r'})$, and $\int_{V_j} d\vec{r'}$: volume integral over the j-th body. In Equation 4.2 the contribution of the anomalous current J_a, caused by the distorting body, is directly apparent using Ohm's Law (Eq. 3.5), i.e. $J_a = \Delta\sigma E$.

An equivalent expression for the magnetic field can be derived by applying Faraday's Law (Eq. 3.2) on Equation 4.2, yielding

$$\begin{aligned} B(\vec{r}) &= B_p(\vec{r}) && \text{: primary field} \\ &+ \mu_0\nabla\times \sum_j \int_{V_j} g(\vec{r},\vec{r'})\Delta\sigma_j(\vec{r'})E(\vec{r'})d\vec{r'} && \text{: inductive distortion} \end{aligned} \tag{4.3}$$

Equation 4.3 does not contain a contribution of the galvanic distortion as $\nabla\times\nabla\psi = 0$ for an arbitrary scalar function ψ [*Utada and Munekane*, 2000], which suggests that the magnetic field is not affected by galvanic distortion. However, Equation 4.2 is only valid for cases in which the distorting body can be considered small in comparison to the EM wavelength (implied in the Born approximation [*Habashy et al.*, 1993]). The effect of magnetic galvanic distortion is observable for a frequency range that is sensitive to the distorting body; however, its contribution deteriorates quickly for lower frequencies [e.g. *Garcia and Jones*, 2001]. For deep-probing MT studies, it is therefore often assumed that the effect of magnetic galvanic distortion is negligible in comparison to the electric galvanic distortion effect. Unlike magnetic galvanic distortion, and inductive distortion,

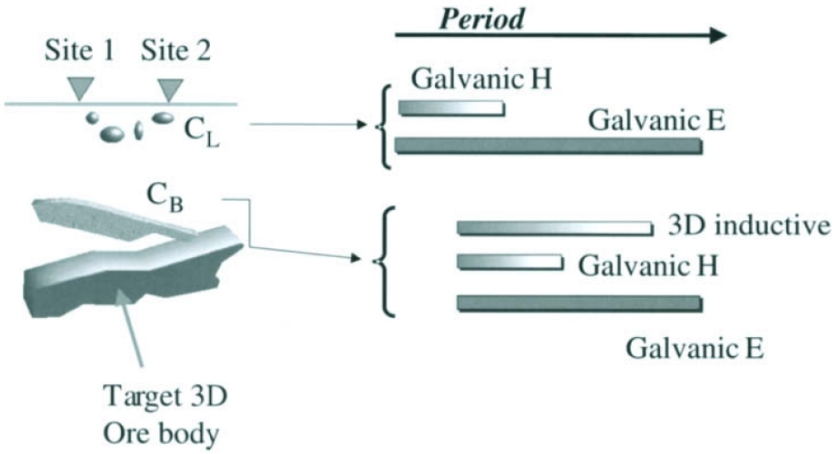

Fig. 4.1.: Model of the potential galvanic and inductive effects in a magnetotelluric (MT) survey; from *Garcia and Jones* [2001].

electric galvanic distortion affects MT data, below a distorter-depth dependent frequency, to a similar extent [*Habashy et al.*, 1993; *Garcia and Jones*, 2001; *Ledo*, 2005; *Simpson and Bahr*, 2005] (Fig. 4.1). The frequency dependence of the inductive distortion is directly evident from the related term in Equation 4.2; note that the galvanic term contains an additional inverse relation to frequency via the wave number k.

Unlike galvanic distortion, inductive distortion effects cause a phase shift of secondary EM fields (cf. complex nature of induction term in Equation 4.2). The phases of the secondary fields are in the range 0 to $\pi/2$, relative to the primary fields, dependent on the degree of the inductive distortion [e.g. *Ward*, 1967; *Ward and Hohmann*, 1987]. A secondary field phase of $\pi/2$ denotes the "resistive limit" case [*Jiracek*, 1990] in which the contribution of the inductive distortion is negligible, whereas the opposite case (phase approximately zero) indicates that inductive distortion effects prevail.

The degree of galvanic and inductive distortion effects onto the response of TE and TM modes is not only dependent on characteristics of the EM wave and conductivity of the distorting body (cf. Eqs. 4.2, 4.3), but also on the shape of the distorting body. *Ledo* [2005] uses a synthetic model containing an elongated 3D body in the proximity of a regional 2D structure, to investigate distortion effect on the responses of both modes in relation to the angle between 3D body orientation and regional strike (see Fig. 4.2). The author finds that for the case of an orthogonal orientation the TE mode is affected mainly by galvanic effects, whereas the TM mode is affected by both, galvanic and inductive effects. On the contrary, when the 3D body is parallel to the regional 2D strike, the TE mode is affected by galvanic and inductive effects, and the TM mode is affected mainly by galvanic effects.

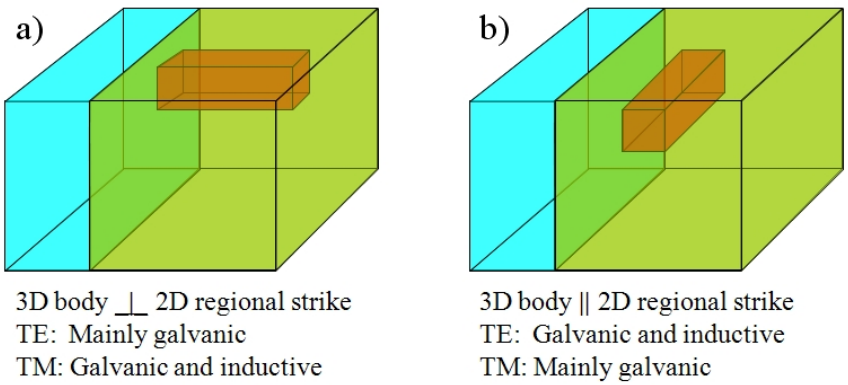

Fig. 4.2.: The effects of a small-scale 3D body onto the modes of the magnetotelluric (MT) measurement depend on the orientation of the 3D body with respect to the 2D regional structure. (a) 3D structure normal to regional structure: TE mode is affected mainly by galvanic effect, TM mode is affected by galvanic and inductive effects. (b) 3D structure parallel to regional structure: TE mode is affected by galvanic and inductive effects, TM mode is affected mainly by galvanic effect; after [*Ledo*, 2005].

4.1.1. Galvanic distortion

The principle of galvanic distortion can be illustrated using a subsurface model with lateral change of electric conductivity, e.g. two quarter-spaces with different conductivity along a vertical interface (cf. Fig. 3.4). Applying an electric field with a component orthogonal to the conductivity interface yields a charge build-up on either side of the interface (with different signs). The charge build-up affects electric current and electric field in the related region, whereas the magnetic field remains comparatively undistorted (cf. Eqs. 4.2, 4.3) [*Price*, 1973; *Kaufman*, 1985, e.g.].

Distortion of the EM field by a small-scale body in an otherwise homogeneous region is dependent on the resistivity difference between the body and the surrounding region. A body which is more conductive than the background acts as an attractor for electric currents, causing the electric field lines to curve towards the inclusion, whereas a more resistive body forces the field lines to bend away from its position (cf. Figure 4.3). This behaviour can be adequately described by the concept of vectorial addition of primary fields with secondary fields generated by the charges at the boundaries, providing traditional terminology like *current channelling*, *flow around effect*, etc. with mathematical framework [*Jiracek*, 1990]. From Figure 4.3 and Equation 4.2, it is apparent that the total electric field is enhanced above a resistive body and reduced over a conductive one. Therefore, the respective TM mode of MT curves is shifted upwards when the electric field is measured right on top of a surficial resistive body and downwards over a conductive body [*Jiracek*, 1990], presuming that the points used for the voltage difference measurement are not crossing the boundaries of the distorter. A quantitative analysis about the relationship between the amplitude of static shift and the location of the current electrodes with respect to the distorter is given by *Pellerin and Hohmann* [1990] and *Spitzer* [2006].

Berdichevsky and Dmitriev [1976a] and *Ranganayaki and Madden* [1990] introduce the concept of *adjustment distance* Λ (also referred to as *horizontal skin depth*) in order to

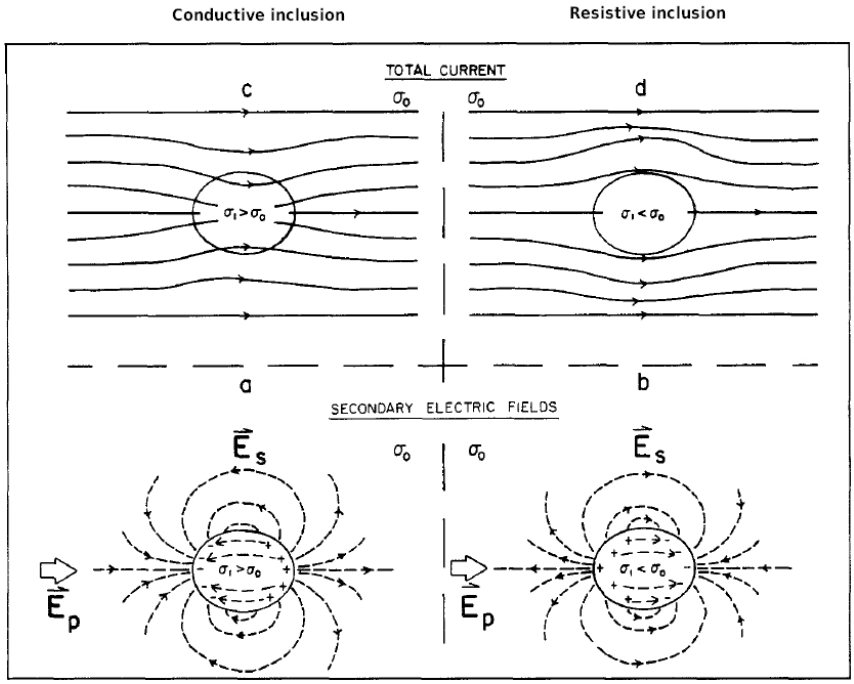

Fig. 4.3.: The galvanic distortion effect is due to electric charge build up on the boundaries between zones of different electric resistivity when an electric field with a component in the direction of the face of the contact area is applied. Such boundary charges on the surface of a (a) conductive inclusion and (b) resistive inclusion generate secondary electric fields $\vec{E_s}$ (dashed). A vectorial addition of primary electric field $\vec{E_p}$ and secondary fields $\vec{E_s}$ result in a curved total electric fields $\vec{E}$ that are traditionally described by the terms of *current channelling* for (c) a relatively conductive inclusion and *current deflection* for (d) a relatively resistive inclusion (modified after [*Jiracek*, 1990]).

provide an approximation of the lateral distance at which the galvanic distortion effect of a surficial conductor can be considered negligible. The approach concerns vertical current distortion due to galvanic distortion, which is significantly related to the coupling between the conductive regions of the surficial body and the mantle through the resistive lower crust [*Ranganayaki and Madden*, 1990]. The authors examine the case of a conducting 2D dyke, relating its area of influence to its conductance S and the resistance of the host medium R, i.e.

$$\begin{aligned} \Lambda &= (S \cdot R)^{1/2} \\ &= \left(\sum_i \sigma_i h_i^d \cdot \sum_j \rho_j h_j^h \right)^{1/2}, \end{aligned} \tag{4.4}$$

with σ: conductivity, ρ: resistivity, h^d and h^h: thickness of the distorting layers and host layers respectively. Therein the generalised thin sheet analysis approximation is applied, which is valid when the incident field wavelength is long in comparison to the adjustment distance [e.g. *Price*, 1949; *Bullard and Parker*, 1970; *Ranganayaki and Madden*, 1990]. For 2D cases in which the lateral extent of the distorter's finite side is smaller than Λ, the

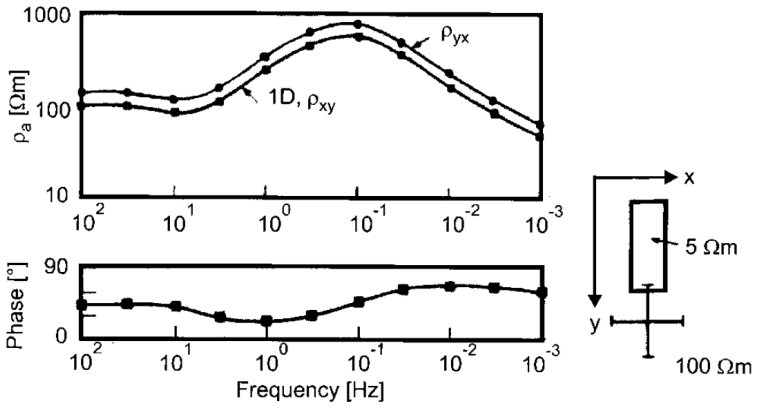

Fig. 4.4.: Magnetotelluric (MT) responses under the influence of *static shift* (electric galvanic distortion). The curve is subject to a constant shift for the whole frequency range of the mode with the electric component in direction of the distorting body (ρ_{yx}) compared to the orthogonal mode ρ_{xy} and the undistorted 1D response $1D$; from *Pellerin and Hohmann* [1990].

lateral concentration of excess current concentration is dominant, whereas in the opposite case, when Λ is greater than the distorter's horizontal extension, the vertical current gathering effect prevails [*Jiracek*, 1990]. For the case of a 3D distorting body the deviation of the electric current, hence the distortion characteristics, is dependent on the body's extent in both lateral directions. Accordingly, a wide range of models exhibiting different geometry can be devised which yield similar adjustment distances, meaning that the problem is highly non-unique.

In order to investigate the issue of galvanic distortion in more detail it is useful to subdivide it into its electric and magnetic components, since these affect the EM to a different degree (cf. Sec. 4.1). The *current channelling* effect, comprising a special case of galvanic distortion is discussed separately.

Electric galvanic distortion

Once periods are long in comparison to the depth extend of the distorting body, the effect of electric galvanic distortion is frequency independent, resulting in a constant shift of the apparent resistivity response curve at longer periods (Fig. 4.4). Accordingly, the effect of electric galvanic distortion on MT data is commonly referred to as *static shift* or *S-effect* (in Soviet literature) [e.g. *Jones*, 1988; *Pellerin and Hohmann*, 1990; *Jiracek*, 1990; *Spitzer*, 2006]. Electric galvanic distortion is often the prevalent effect in MT data, since inductive and magnetic galvanic distortion (Secs. 4.1.1, 4.1.2) are, in most cases, confined to a small frequency range, owing to their decreasing effect for longer frequency. Consequently numerous attempts to correct for electric galvanic distortion have been presented by various authors, concluding that MT data can be corrected for the effect of electric galvanic distortion when

- magnitude and phase of the regional response are known for at least one frequency [e.g. *Berdichevsky et al.*, 1989; *Chave and Smith*, 1994],

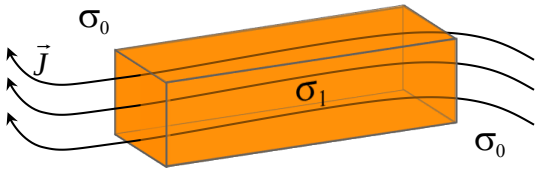

Fig. 4.5.: The principle of *current channelling*, denoting a deflection of the Electric current $\vec{J}$ by a highly conductive anomaly σ_1 in a more resistive surrounding medium σ_0; cf. Figure 4.3.

- information about the resistivity structure of the subsurface is known from other methods like transient or time domain EM (TEM) [e.g. *Andrieux and Wightman*, 1984; *Sternberg et al.*, 1988; *Pellerin and Hohmann*, 1990] or Geomagnetic Deep Sounding (GDS) [e.g. *Wolfgram and Scharberth*, 1986],
- statistical approaches are used [e.g. *Jones*, 1988, and references within], or
- distorting bodies are incorporated in the inversion process.

Magnetic galvanic distortion

The magnetic galvanic distortion effect is frequency dependent, and the decay of its magnitude is approximately proportional to $\sqrt{T}$ [*Chave and Smith*, 1994]. The magnetic galvanic distortion effect of a surficial body can therefore be considered negligible if the period is long compared to the depth extend of the distorting body [e.g. *Groom and Bailey*, 1989]. However, further magnetic galvanic effects can be caused by additional distorting bodies in the subsurface, affecting the frequency range that is related to the body's location. Naturally, the magnetic galvanic effect of such bodies deteriorates in a similar way and becomes negligible again for periods that are comparatively long relatively to the dimension of these bodies [e.g. *Garcia and Jones*, 2001]. Multiple subsurface distorters at different depth ranges will therefore result in several magnetic galvanic distortion effects that are mostly confined to data of the period range related to the location of each distorter.

Current channelling

A special case of galvanic distortion is the channelling of electric currents into a 3D body of higher conductivity, following the orientation of the body, which provides the path of least resistance (Fig. 4.5). Even though this situation can be adequately described by electric and magnetic galvanic distortion, it is addressed in a separate paragraph owing to its distinct emergence in MT recordings. A thorough overview about the problem of current channelling was given by *Jones* [1983a].

Current channelling due to an elongated 3D distorter deflects parts of the electric current into a direction parallel to the orientation of the conductor, thus causing a deviation from the orthogonality of magnetic and electric field. Therefore, off-diagonal elements of the impedance tensor (Eq. 3.34), related to TE and TM mode, are decreased, whereas

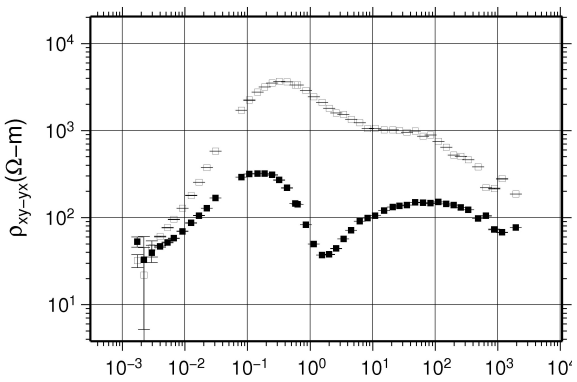

Fig. 4.6.: Distortion of magnetotelluric (MT) responses due to a highly conductive feature at depth, causing resistivities of the TM mode (solid squares) at periods greater than 0.2 s to decrease rapidly, followed by an adjustment to the values of the TE mode (open squares) for longer periods. The drop is caused by a deviation of electric currents into direction of the conductor, decreasing the electric field of the respective mode. This particular form of distortion is occasionally referred to as *birdy*, owing to the distorted mode's similarity in shape with an infantile drawing of a flying bird.

diagonal elements are increased accordingly. The degree of distortion on each mode, caused by the current channelling effect, is therefore dependent on the orientation of the distorter relative to the regional geoelectric strike direction. When the orientation of the conducting distorter is close to the direction of one coordinate-system axis, i.e. either in strike direction or orthogonal to it, the apparent resistivity of the respective mode will exhibit a rapid drop in resistivity. For longer periods, the distorted mode will then, due to mode mixing, approach the apparent resistivity level of the orthogonal mode. This behaviour results in a very peculiar shape of the related mode, occasionally referred to as a *birdy* owing to its similarity in shape with an infantile drawing of a flying bird (cf. solid symbols in Figure 4.6).

In order to provide a quantitative description of the current channelling phenomenon *Edwards and Nabighian* [1981] considered the ratio of current flowing through a conducting dyke J_d to the total available current J_t, using the equation

$$\frac{J_d}{J_t} = \frac{\alpha}{1+\alpha}, \tag{4.5}$$

where α is the *current channelling number*. The authors examine the case of a dyke with vertical extent h, infinitive lateral extent, and conductivity σ_d in a resistive host medium with conductivity σ_h. For controlled source measurements α can be calculated in dependence of the angular frequency ω and the distance down strike of the source L when $\omega h << L^2$ (see Fig. 4.7), via

$$\alpha = \frac{2\omega h}{\pi L^2} \cdot \left(\frac{\sigma_h}{\sigma_d}\right). \tag{4.6}$$

That concept was later extended by *Jones* [1983a] onto natural source techniques, using the skin depth in the host medium δ_h to introduce *current channelling numbers* for a 2D

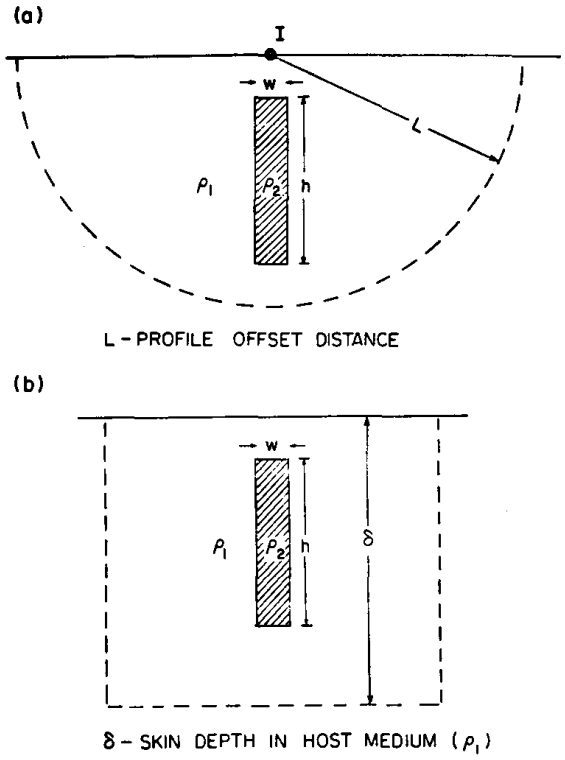

Fig. 4.7.: The effective area of influence of a dyke (a) for a controlled source survey, and (b) for a natural source survey, from [*Jones*, 1983a] (see text for description of variables)

dyke of infinite lateral extension (Fig. 4.7), i.e.

$$\alpha_2 = \frac{\omega h}{\delta_h^2} \cdot \left(\frac{\sigma_h}{\sigma_d}\right) \tag{4.7}$$

and for a 3D structure of horizontal extensions h and L_h

$$\alpha_3 = \frac{\omega h L_h}{\delta_h^3} \cdot \left(\frac{\sigma_h}{\sigma_d}\right), \tag{4.8}$$

showing that the ratio of lateral extension to skin depth is of major influence for the proportion of electric current channelled into the dyke.

4.1.2. Inductive distortion

According to Faraday's Law (Eq. 3.2), a changing magnetic field induces an orthogonal circular electric current in a conducting body, which in turn generates a secondary magnetic field (cf. Eq. 4.2 and Fig. 4.8). The contribution of inductive distortion caused by small heterogeneities is very much dependent on the frequency range (cf. Eqs. 4.2, 4.3),

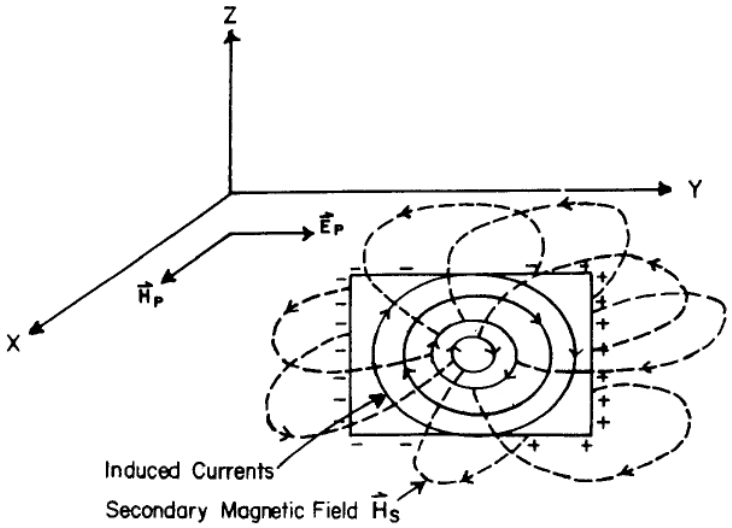

Fig. 4.8.: Sketch of the inductive effect in a vertical sheet conductor; from *Jiracek* [1990] after *Wright* [1988]. A primary magnetic field H_p induces orthogonal electric fields in a body of different electric conductivity, which in turn generate secondary magnetic fields H_s. Note that the charges, placed along the sides of the conducting sheet, are due to the galvanic effect and that the skin effect for the fields within the sheet is neglected in order to simplify the sketch.

and EM measurements are only significantly affected by inductive distortion in cases where the EM wavelength is small compared to the dimension of the distorting body [*Garcia and Jones*, 2001; *Ledo*, 2005]. A quantitative description of the distortion by a small-scale body j can be given by use of the dimensionless *induction number*

$$M_j = \frac{L_j}{\Lambda_j}, \tag{4.9}$$

describing the ratio of the body's physical length L_j and its inductive scale length $\Lambda_j = 1/|\mathrm{Re}(k_j)|$, with $k_j = \sqrt{i\omega\mu_0\Delta\sigma_j}$ and $\Delta\sigma_j = \sigma_j - \sigma_h$ the difference between conductivity of the distorting body σ_j and the host medium σ_h [*Utada and Munekane*, 2000]. Association of the parameter L_j is dependent on the shape of the distorter, i.e. for an elongated body it refers to the body's lateral extent whereas for a sphere it represents the radius; cf. [*Ward*, 1967]. For cases where M_j is significantly smaller than unity the influence of induction onto the recorded response may be considered negligible in regards to the galvanic distortion [*Chave and Smith*, 1994]. This implies that the inductive term in Equation 4.2 is insignificant in comparison to the galvanic contribution, i.e. for periods that are long in comparison to the dimensions of the distorting body and small conductivity differences between distorted and host medium. However, the induction number remains an approximation of the ratio between galvanic and inductive distortion, since only the length of the distorter is considered. Certainly, the body's width and thickness as well as its dip are influencing its distortion characteristics, as indicated by the volume integral in equations 4.2 and 4.3.

Scale	Type	Terminology	Example
Atomic	Intrinsic	Lattice preferred orientation (LPO)	Point defects in the atomic lattice
Micro (crystal)	Fabric	Crystal preferred orientation (CPO)	Alignment of minerals with conductivity dependent on crystal axis, e.g. olivine
Macro	Structural	Shape preferred orientation (SPO)	Dyke swarms or fluid- or graphite-filled micro-cracks system

Tab. 4.1.: Types of electric anisotropy divided according by size; see text for details.

4.1.3. Anisotropy

Electric anisotropy denotes directional dependent conductivity of the subsurface due to small-scale features, imbedded in a host medium of different resistivity. If one of the feature's dimensions is smaller than the sampling wave field it cannot be adequately resolved by the MT method and is commonly attributed as distortion. Anisotropy can be divided according to size, distinguishing between atomic, microscopic (or crystal), and macroscopic cases. The first two refer to intrinsic and fabric anisotropy [e.g. *Shankland and Duba*, 1990; *Poe et al.*, 2010], whereas the latter is related to structural anisotropy [e.g. *Bahr*, 1997; *Jones et al.*, 1997; *Wannamaker*, 2005; *Jones*, 2006]; see Table 4.1 for a summary of anisotropy types and examples.

In principle, many materials are anisotropic to a certain degree, i.e. exhibiting different electric characteristics for different directions, in which adequate current density description requires the general form of Ohm's Law (eq. 3.5)

$$\begin{pmatrix} j_x \\ j_y \\ j_z \end{pmatrix} = \begin{pmatrix} \sigma_{xx} & \sigma_{xy} & \sigma_{xz} \\ \sigma_{yx} & \sigma_{yy} & \sigma_{yz} \\ \sigma_{zx} & \sigma_{zy} & \sigma_{zz} \end{pmatrix} \begin{pmatrix} E_x \\ E_y \\ E_z \end{pmatrix}. \tag{4.10}$$

When investigating the anisotropy of a material, the issue is usually reduced to considering the material's conductivity in three orthogonal spatial directions, with axis defined by the direction of maximal and minimal resistivity (ρ_x, ρ_y, ρ_z); i.e. the inverse of conductivity. These spatial directions are not necessarily aligned with regional geoelectric strike (cf. Sec. 4.3).

Anisotropy can be caused by different geological features, associated with conductive sheets or tubes (Fig. 4.9) dependent on the relation between the resistivity in the three spatial directions (ρ_x, ρ_y, ρ_z). To distinguish between the two cases is often difficult as ρ_z cannot be resolved by MT [e.g. *Heise and Pous*, 2001]; for the same reason a correct determination of anisotropy dip and slant (Fig. 4.10) is usually not achieved. An examination of anisotropic distortion in MT is therefore commonly reduced to the effect on the horizontal EM-field components, i.e. on the elements of the impedance tensor $\mathbf{Z}$. Following the notation by *Groom and Bailey* [1989] and *Garcia and Jones* [2001], introduced in Section 4.3, the impedance tensor in the case of a 2D subsurface with solely anisotropic

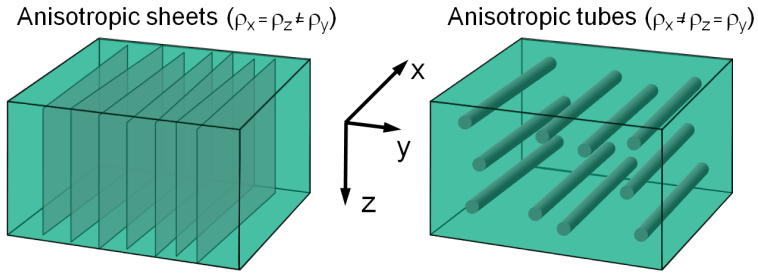

Fig. 4.9.: The two types of electric anisotropy $\rho_x = \rho_z \neq \rho_y$ and $\rho_x \neq \rho_z = \rho_y$ refer to two different geological settings, i.e. anisotropic sheets (e.g. dyke swarms) and anisotropic tubes (e.g. ore veins).

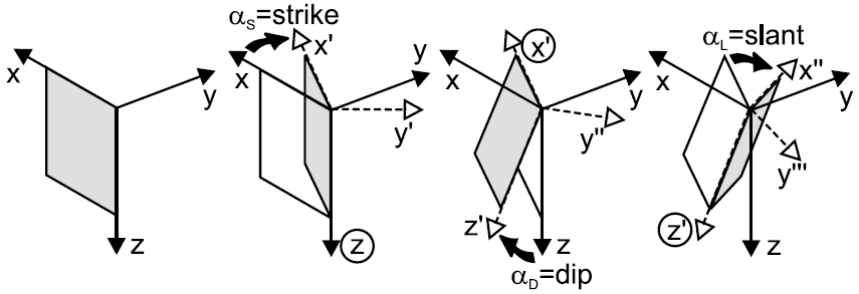

Fig. 4.10.: Illustration of basic anisotropy parameters; from *Pek and Santos* [2002]

distortion ($\mathbf{Z}_{2D}^{ani}$) can be written as product of the undisturbed 2D impedance tensor ($\mathbf{Z}_{2D}$) and a tensor containing the anisotropic contribution ($\mathbf{A}$)

$$\mathbf{Z}_{2D}^{ani} = \mathbf{A} \cdot \mathbf{Z}_{2D} = (1 + S_D^2)^{-1/2} \begin{pmatrix} 1+S_D & 0 \\ 0 & 1-S_D \end{pmatrix} \begin{pmatrix} 0 & Z_{xy} \\ Z_{yx} & 0 \end{pmatrix}. \tag{4.11}$$

Thus, the off-diagonal elements of ($\mathbf{Z}_{2D}^{ani}$)

$$Z_{xy}^{ani} = Z_{xy} \frac{1 + S_D}{\sqrt{1 + S_D}} > Z_{xy}, \tag{4.12}$$

and

$$Z_{yx}^{ani} = Z_{yx} \frac{1 - S_D}{\sqrt{1 + S_D}} < Z_{yx}, \tag{4.13}$$

are always greater for Z_{xy} and smaller for Z_{yx} since S_D is a positive, real number (cf. Sec. 4.3).

Given a sufficiently large array of MT recording station it is possible to investigate whether the subsurface comprises either regional 2D structures or a 1D subsurface with anisotropic structures. Whereas for the 2D case TE and TM modes exhibit significant variation for stations at different distances to the location of the conductivity interface (cf. Fig. 3.4), the horizontal transfer function and the phase split are constant over a large horizontal region in case of a anisotropic 1D subsurface. Moreover, it is in principle possible to distinguish between a 2D subsurface and a 1D subsurface with anisotropy by

the use of vertical magnetic field data. In the 1D anisotropic case no vertical magnetic field should be prominent, whereas for the case of a 2D subsurface a vertical magnetic field, related to the horizontal magnetic field parallel to the conductivity interface, is observable [*Kurtz et al.*, 1993; *Kellett et al.*, 1992; *Bahr et al.*, 2000; *Heise and Pous*, 2001]. However, the presence of noise or deviation of the source from the plane wave assumption (cf. Sec. 2.3) result in a vertical magnetic field, making impeding the separation of 2D and anisotropic 1D cases. For the 2D case, the deviation of the induction arrows from the expected 2D behaviour can be used as an indicator for potential presence of anisotropic conductivity structures in the subsurface. The induction vectors in such cases are no longer perpendicular to the strike direction, but they cannot be directly related to the anisotropy direction either [*Heise and Pous*, 2001].

In many cases, determination of electric anisotropy can be aided by geological observations, e.g through knowledge about dyke swarms in the study area or from the tectonic history. Possible reasons for electric anisotropy in the upper mantle are directional variation in connectivity of highly conducting mineral phases [*Jones*, 1992; *Mareschal et al.*, 1995] or hydrogen diffusion induced conductivity increase along olivine a-axes [*Bahr and Simpson*, 2002]. One recently proposed cause of electric anisotropy in the transition zone between lithosphere and asthenosphere is lattice preferred orientation of the present minerals [e.g. *Simpson*, 2001; *Bahr and Simpson*, 2002; *Hamilton et al.*, 2006]. The maximal anisotropy for this latter case is controlled by the difference between highest and lowest conducting direction of the present minerals, viz. 2.3 for dry olivine [*Shankland and Duba*, 1990]. For wet (or hydrous) olivine the relation between conductivities of the three axes is much more complex due to their H_2O - dependent conductivity characteristics. *Poe et al.* [2010] showed that the activation energy of intrinsic and extrinsic semiconduction for olivine is H_2O - dependent and that P-T - changes result in different σ - variation for the three axes of wet olivine. As a result of this study, σ - ratios of the three wet olivine axes are assumed to be P,T, and H_2O - dependent, but further studies are needed to determine reliable quantitative relations.

Anisotropy at the LAB is further proposed to originate from relative motion between lithosphere and asthenosphere, "dragging along" and aligning material at the LAB. Anisotropy direction in that case should coincide with relative plate motion direction. Identifying features at such depth and relatively small thickness, however, is highly challenging given the associated low resolution. Links between electric anisotropy at the LAB and seismic anisotropy derived for the same depth [e.g. *Vinnik et al.*, 1995; *Silver et al.*, 2001; *Simpson*, 2002b; *Eaton et al.*, 2004; *Debayle et al.*, 2005; *Deschamps et al.*, 2008; *Darbyshire and Lebedev*, 2009] are likely, since both parameters are presumably related to the same tectonic mechanisms (cf. Chapter 5). Details about the relationship between seismic and MT observations are presently still under debate, though [e.g. *Ji et al.*, 1996; *Hamilton et al.*, 2006; *Eaton et al.*, 2009; *Roux et al.*, 2009]

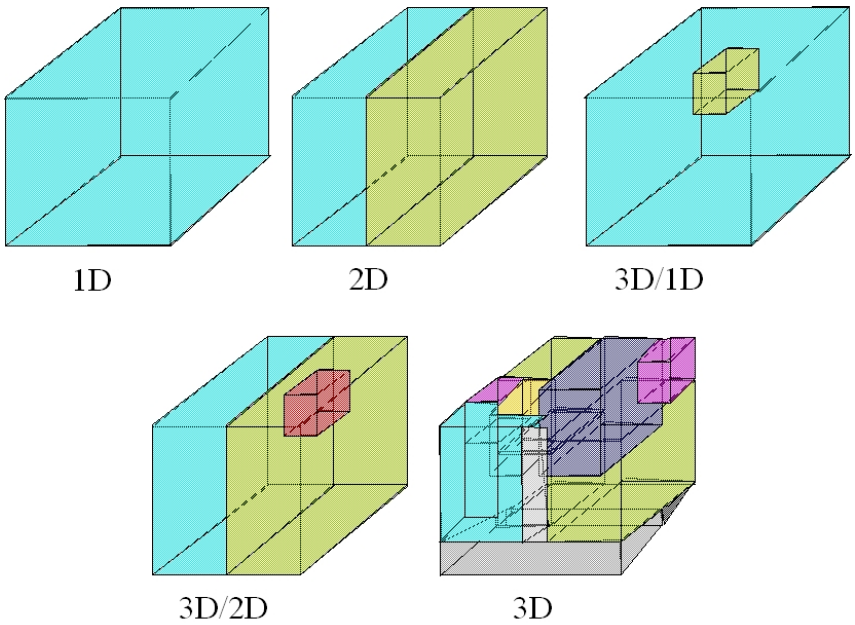

Fig. 4.11.: Simple models of (isotropic) subsurface dimensionality, representing typical cases observed in MT measurements. Coloured blocks denote regions of different electric resistivity (the region representing the conductivity of free air on top each model is implied but not shown here). Models in the top row, left to right: 1D (electric resistivity varies only with depth), 2D (lateral change of resistivity along a vertical interface), 3D/1D (small-scale body imbedded in an otherwise homogeneous 1D body). Models in the bottom row, left to right are 3D/2D (small-scale body in area of regional 2D structure), 3D (3D bodies dominate the responses and no regional structure of lower dimensionality can be found).

4.2. Dimensionality

In MT, dimensionality of a body is usually defined by the number of directions in which boundaries of the body are sensed. The simplest models, comprising only vertical variations of electric resistivity, are referred to as 1D. Such models contain at least one horizontal boundary, located at the air-ground interface for cases where the Earth is modelled as a homogeneous halfspace, an no lateral changes of electric resistivity. Other 1D model contain a multitude of parallel layers with different resistivities, in American literature occasionally referred to as *layer cake model*. 2D models comprise resistivity changes in vertical as well as in one horizontal direction, for which the x-axis of the coordinate system is usually aligned with the lateral interfaces. The simplest 2D model contains two blocks of different resistivity, with the contact zone parallel to one of the axis of the coordinate systems (Fig. 3.4). In the 3D case, boundaries are detected vertically and in both horizontal directions, resulting in a much more complicated structure of the MT response (Fig. 4.2). Presently the interpretation of 3D MT data is intricate and simplification of the 3D situation are often strived for in order to ease the interpretation. For certain cases, measured data can be described by a superposition of bodies with different dimensionality, e.g. a small-scale 3D body imbedded in a regionally 1D (3D/1D) or 2D (3D/2D) host medium (see Figure 4.11 for an illustration of models with different dimensionality).

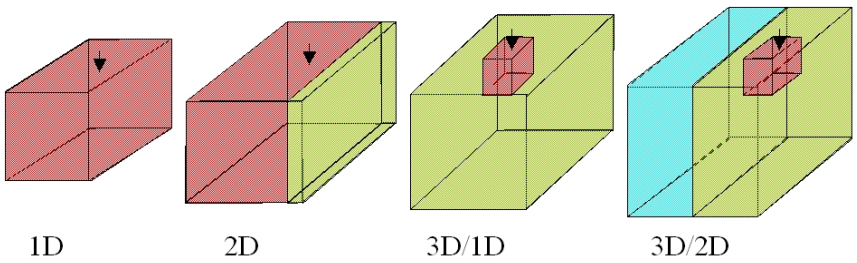

Fig. 4.12.: The four figures represent the induction area for different period ranges at the same station (indicated by the inverted black triangle); the longest period is increased from left to right. The subsurface model is the same for all figures (two quarter-spaces, one with an imbedded small-scale 3D body), only the observed dimensionality varies with period range.

4.2.1. Frequency-dependent dimensionality

To illustrate the phenomenon of frequency dependent dimensionality, the model of a small-scale surficial 3D body, imbedded in one half of a regional 2D structure is considered. The regional structure contains two homogeneous quarter-spaces (except for the small 3D body) with different electric resistivity (cf. rightmost model in Figure 4.12). The response from a MT station, located on top of the 3D body (inverted black triangle in Figure 4.12), is examined first theoretically and later by studying a synthetic model (Sec. 4.2.1).

For short periods, the station is sensitive to the boundaries of the 3D body and the response curve simply represents the resistivity of the body, exhibiting 1D behaviour. Once longer periods are included, effects of the boundaries between the 3D body and the surrounding material are observed, indicated by a change in the shape of the response curve. Assuming that responses are only affected by the lateral boundary of the 3D body and not by its bottom, the data are 2D in nature. Further increasing the period range yields data that are also sensitive to bottom and the other lateral interfaces of the 3D body, resulting in the so-called 3D/1D case (it is assumed here that the distance between the 3D body and the contact zone of the two quarter-spaces is sufficient large). Data at the longest periods contain effects of the 3D body, superimposed on the regional 2D structure response, which is referred to as 3D/2D case. When the coordinate system is aligned to the 2D regional strike direction, the 3D body will only cause a frequency independent shift in the long-period apparent resistivity response curves. This *static shift* is due electric galvanic distortion, i.e. electric charge build up on the faces of the 3D body.

Synthetic model

A synthetic model study is conducted to illustrate the effect of a local 3D distorter embedded in a regional 2D structure on the response for a MT stations located on top of the distorting body. The 3D/2D model ('3D body' in Fig. 4.13) was created using the `WinGLink` software package [*WinGLink*, 2005] wherein the `MT3DFWD` forward algorithm [*Mackie et al.*, 1994] was used to calculated the response data. A second model is gen-

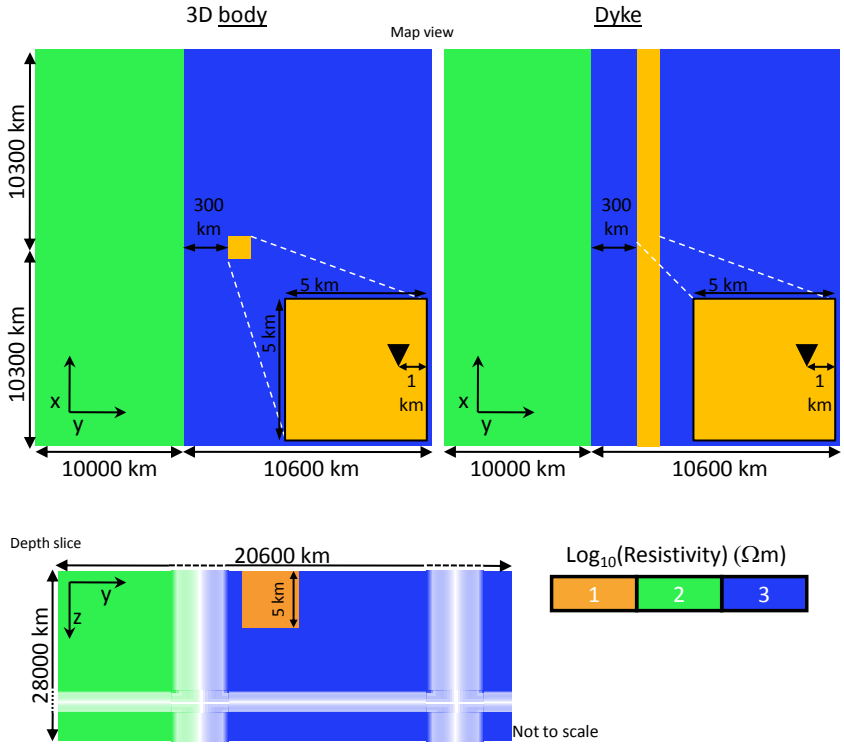

Fig. 4.13.: Two subsurface models used to illustrate the effect of frequency-dependent dimensionality, each containing two halfspaces of 100 and 1000 Ωm and a conductive distorter, i.e. a small-scale body (left-hand side) and a dyke structure (right-hand side). The two models are identical in the *y*-*z* plane shown at the bottom of this figure. Responses for MT stations on top of the conductors (denoted by inverted black triangle) are calculated to illustrate frequency-dependence of distortion; see text for details.

erated in the same manner, in order to compare the results of the 3D/2D model ('Dyke' in Fig. 4.13). The lateral extent of the local distorter is therein increased to the limits of the model (>20000 km) in direction of the regional strike direction, making the body virtually 2D. The models are certainly not an accurate representation of the true Earth, in particularly their depth extends, but they are a useful tool to illustrate the connection between observed dimensionality and frequency range.

The response for the MT station on top of the 3D/2D model (left-hand side in Fig. 4.13) contains four different regimes, which can be related to different dimensional settings (cf. Fig. 4.14). Going from short to long periods (left to right in Figure 4.14), the first regime, comprising periods up to approximately 10^{-2} s, is purely 1D. Responses in this period range do not contain boundary effects and simply reflect the 10 Ωm conductivity of the small-scale body. At longer periods, response curves exhibit a split, first in the phase data followed by the apparent resistivity, indicating a 2D regime. The split in the period range 0.01 – 5 s is due to the lateral interface between the small-scale body and the host medium, accordingly referred to as 'local 2D', as opposed to the 'regional 2D' for the interface between the two quarter-spaces. For the period range 5 – 100 s, responses exhibit a static

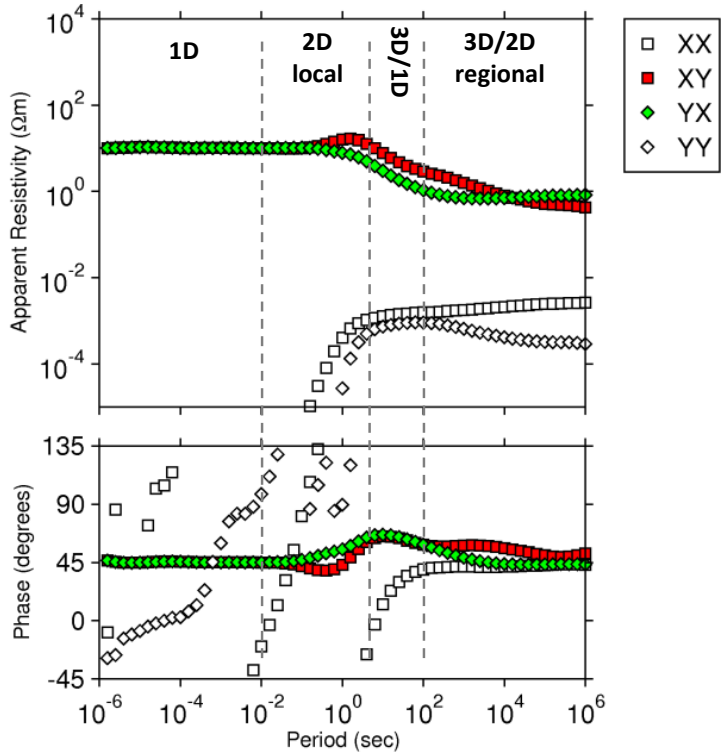

Fig. 4.14.: Responses for the magnetotelluric (MT) station on top of the 3D/2D model (left-hand side in Figure 4.13). Response curves comprises four regimes of different dimensionality for different period ranges. For the shortest periods (located on the left-hand side) the regime exhibits 1D characteristics, changing to 2D, 3D/1D, and 3D/2D for longer periods, when additional boundaries are sensed. A detailed description of the different regimes and related processes are given in the text.

shift of the apparent resistivity curves and similar phase values for the two modes. The shift is due to galvanic distortion at the boundaries of the local distorter (cf. Sec. 4.1.1); this is herein referred to as 3D/1D regime. Due to the distorting nature of the small-scale body, curves do not adjust to the resistivity of the host mediums (1000 Ωm) but instead exhibits a decreased conductivity, owing to the additive secondary currents over the distorter. For comparison, the same station over the conductive dyke in the reference model (right-hand side in Fig. 4.13) shows the similar distortion for the TM mode but an adjustment to the host resistivity by the TE mode (cf. Fig. 4.15). This behaviour is related to the electric component of the TE mode that is parallel to the orientation of the conductor, thus unaffected by charge build-up on its boundaries (cf. Sec. 3.4.2). For the longest periods, greater than 10^2 s, responses exhibit another split of the phase data and a deviation from the parallel nature of the apparent resistivity curves. This response curve behaviour is due to a superposition of effects from the small-scale body and the regional 2D structure, referred to as 3D/2D regime.

An additional observable feature here is the different trends of TE and TM mode at the longest periods. Whereas the TM mode approaches the apparent resistivity value of the host medium and phase values of 45 degrees, the TE mode exhibits a further decrease of

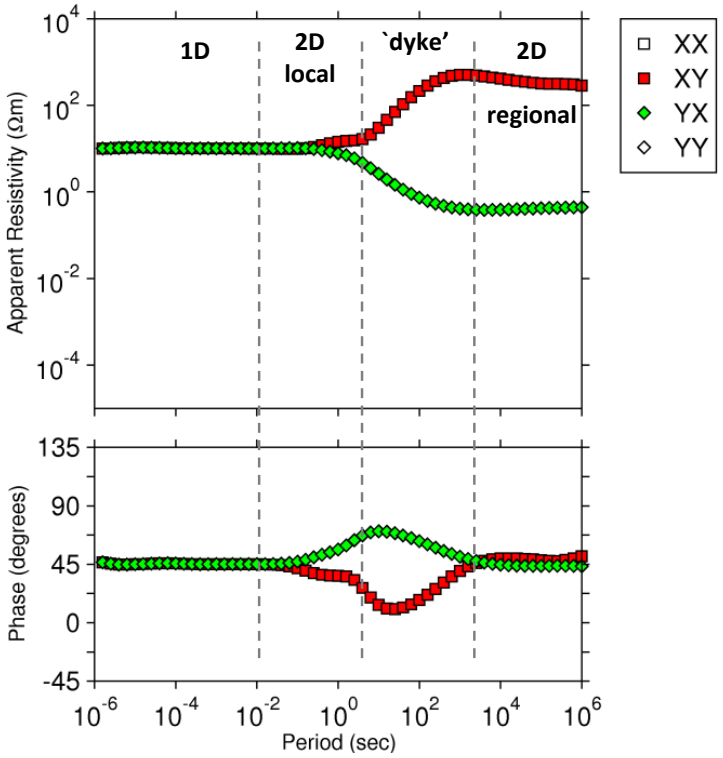

Fig. 4.15.: Responses for the magnetotelluric (MT) station over the 2D/2D regional model (right-hand side in Fig. 4.13) used as a reference for the 3D/2D model response (Fig. 4.14). The 2D/2D model exhibits four different regimes of dimensionality, i.e. 1D for the shortest periods on the left, local 2D (between the small-scale conductor and the host medium), dyke with finite vertical extend, and regional 2D (between the two quarter-spaces).Apparent resistivity values of the diagonal impedance tensor elements are smaller than 10^{-9} Ωm throughout the whole period range, thus outside the plot range.

apparent resistivity and an increased of the phase. This behaviour is due to the 100 Ωm quarter-space to the left of the model, sensed at shorter periods by the TE mode. The circumstance that the apparent resistivity curve of the TE mode decreases even below the level of the left quarter-space is due to the distortion of the small-scale body and the resulting difference in induction depth for the two modes (cf. Sec. 3.3). For comparison, consider the response for the 2D/2D model (Fig. 4.15), comprising a conducting bar instead of the cubic small-scale distorter. It is apparent that the TE mode response exhibits therein a decrease of apparent resistivity and an increase of phase data for the longest periods as well. For this model, the apparent resistivity of the TE mode is close to the resistivity of host medium in the right quarter-space and adjusts to the lower values of the left quarter-spaces at the longest periods. The extremely low resistivity values of the TE mode for the 3D/2D are therefore due to a shift of the curve at shorter periods, caused by the galvanic distortion of the small-scale body.

The last aspect illustrates the problem with MT processing of data at the same period. The induction area of TM and TE mode at one period is dependent on the conductivity distribution above, affecting shorter periods, and responses of the TE and TM mode at the considered period are not necessarily related to the same depth, i.e not to the same

feature. Therefore, when analysing values of TM and TE mode apparent resistivities, e.g. in order to determine the geoelectric strike direction (Sec. 4.4), it is advisable to use data that are related to a similar depth range instead [e.g. *Jones*, 2006]. In MT processing, depth estimates are often obtain through analytical direct transformations (Sec. 6.3.1).

4.3. General mathematical representation

Before examining attempts for the removal of distortion effects, it is useful to have a closer look at the mathematical representation of distortion effects in MT measurements. The most general form of the relation between distorted and undistorted EM fields can be given as

$$\vec{E}_h^D = \vec{E}_h \mathbf{P}, \tag{4.14}$$
$$\vec{H}_h^D = \vec{E}_h \mathbf{Q}_h = \mathbf{I} + \mathbf{Q}_h \mathbf{Z}, \tag{4.15}$$
$$H_z^D = [(T_x, T_y) + \mathbf{Q}_z \mathbf{Z}] \vec{H}_h; \tag{4.16}$$
$$\tag{4.17}$$

following the formulation used, among other, by *Garcia and Jones* [2001] and originally introduced by *Zhang et al.* [1987] with superscript D indicating the distorted version of electric ($\vec{E}$) and magnetic ($\vec{H}$) fields and the impedance matrix ($\mathbf{Z}$), the subscripts h and z indicating the horizontal and vertical components, respectively. Therein, the distortion matrices are denoted by

$$\mathbf{P} = \begin{pmatrix} P_{xx} & P_{xy} \\ P_{yx} & P_{yy} \end{pmatrix}, \ \mathbf{Q}_h = \begin{pmatrix} Q_{xx} & Q_{xy} \\ Q_{yx} & Q_{yy} \end{pmatrix}, \text{ and } \mathbf{Q}_z = \begin{pmatrix} Q_{zx}, & Q_{zy} \end{pmatrix}, \tag{4.18}$$

and $\mathbf{I}$ and (T_x, T_y) are the identity matrix and the vertical magnetic transfer function (sometimes referred to as tipper), respectively. Then the effect of distortion onto vertical magnetic transfer function and impedance, commonly used for interpretation of MT data, can be written as

$$(T_x, T_y)^D = [(T_x, T_y) + \mathbf{Q}_z \mathbf{Z}](\mathbf{I} + \mathbf{Q}_h \mathbf{Z})^{-1}, \tag{4.19}$$
$$\mathbf{Z}^D = (\mathbf{I} + \mathbf{P})\, \mathbf{Z}\, (\mathbf{I} + \mathbf{Q}_h \mathbf{Z})^{-1}. \tag{4.20}$$

Traditionally all effects of distortion are combined in the so-called distortion tensor $\mathbf{C}$, relating the undistorted MT impedance tensor $\mathbf{Z}$ with the measured distorted impedance $\mathbf{Z}^D$, i.e.

$$\mathbf{Z}^D = \mathbf{C} \cdot \mathbf{Z} = \begin{pmatrix} c_{xx} Z_{xx} + c_{xy} Z_{yx} & c_{xx} Z_{xy} + c_{xy} Z_{yy} \\ c_{yx} Z_{xx} + c_{yy} Z_{yx} & c_{yx} Z_{xy} + c_{yy} Z_{yy} \end{pmatrix}, \tag{4.21}$$

indicating that the each component of the impedance obtained in the disturbed case is a superposition of two regional impedance components related to the corresponding mag-

netic field. In case of a regional 2D structure Equations 4.21 simplifies to

$$\mathbf{Z}^D = \begin{pmatrix} c_{xy}Z_{yx} & c_{xx}Z_{xy} \\ c_{yy}Z_{yx} & c_{yx}Z_{xy} \end{pmatrix}, \tag{4.22}$$

and for the regional 1D case to

$$\mathbf{Z}^D = \begin{pmatrix} -c_{xy}Z_{xy} & c_{xx}Z_{xy} \\ -c_{yy}Z_{xy} & c_{yx}Z_{xy} \end{pmatrix} = Z_{xy} \begin{pmatrix} -c_{xy} & c_{xx} \\ -c_{yy} & c_{yx} \end{pmatrix}. \tag{4.23}$$

For measurements with a coordinate system not aligned with the strike angle of the regional structure, the Cartesian rotation matrix R and its transpose R^T can be applied onto the measured impedance Z' to take this into account:

$$\mathbf{Z}^D(\theta) = \mathbf{R}(\theta)\,\mathbf{C}\,\mathbf{Z}\,\mathbf{R}^T(\theta). \tag{4.24}$$

4.4. Removal of distortion effects

Over time, various attempts have been published addressing distortion effects on MT responses and aim to provide the researcher with a superior set of data that solely exhibits the parameters of interest for a given study area. These methods are intended to remove, for example, the effect of small-scale features, like the previously mentioned 3D body, and provide a dataset that is easier to interpret. In this Chapter the overview is limited to commonly used methods, i.e. Swift angle (Sec. 4.4.1), Bahr's invariant parameter (Sec. 4.4.2), and the extension of Bahr's method by Weaver et al. (Sec. 4.4.3), as well as the Groom and Bailey decomposition method (Sec. 4.4.4), and the Caldwell phase tensor approach (Sec. 4.4.5); followed by a short conclusion and comparison of the methods.

4.4.1. Swift angle

The Swift angle, introduced by *Swift* [1967], was developed to determine the strike direction in a 2D environment. Therein, the measured MT impedance tensor is rotated in such way that the off-diagonal elements are maximised and the diagonal elements are minimised, i.e.

$$\left|Z'_{xy}(\Theta)\right|^2 + \left|Z'_{yx}(\Theta)\right|^2 = max, \tag{4.25}$$

$$\left|Z'_{xx}(\Theta)\right|^2 + \left|Z'_{yy}(\Theta)\right|^2 = min. \tag{4.26}$$

In a perfect 2D environment, diagonal elements would be exactly zero when the coordinated is aligned with the strike direction, but for situations where the subsurface is slightly different from a 2D set-up or in the presence of noise, diagonal elements are non-zero.

Therefore, the strike direction is determined using the Swift angle instead, viz.

$$\tan(4\Theta) = \frac{2 \cdot \mathrm{Re}\left[(Z_{xx} - Z_{yy}) \cdot (Z_{xy} + Z_{yx})\right]}{\left|Z_{xx} - Z_{yy}\right|^2 - \left|Z_{xy} + Z_{yx}\right|^2}. \tag{4.27}$$

Applicability of the Swift angle is calculated with the rotational invariant Swift skew κ, relating the trace of the impedance ($S_1 = Z_{xx} + Z_{yy}$) and difference of the off-diagonal elements ($D_1 = Z_{xy} - Z_{yx}$),

$$\kappa = \frac{|S_1|}{|D_1|}. \tag{4.28}$$

For small values of κ the environment is assumed to be sufficient 2D to permit the application of the Swift angle.

In the presence of local frequency-independent distortion, however, the Swift angle is incapable of revealing the correct regional geoelectric strike direction. As an example, consider the 1D case, possessing no regional direction and therefore an undefined strike angle for the undisturbed case. Data affected by local distortion as described in Equation 4.22, yield a distorted Swift angle Θ_c and Swift skew κ_c (the subscript c indicates the distorted case), i.e.

$$\tan(4\Theta_c) = \frac{2 \cdot \mathrm{Re}\left[(c_{xx} - c_{yy}) \cdot (c_{xy} + c_{yx})\right]}{\left|c_{xx} - c_{yy}\right|^2 - \left|c_{xy} + c_{yx}\right|^2}. \tag{4.29}$$

and

$$\kappa_c = \frac{\left|c_{xy} - c_{yx}\right|}{\left|c_{xx} + c_{yy}\right|}, \tag{4.30}$$

dominated by the local distortion effect. This could cause the investigator to draw incorrect assumptions about the regional geoelectric strike.

For the case of a 2D regional geoelectric strike, affected by local distortion, distorted Swift angle and skew are a superposition of the two configurations, thus will not recover the true regional strike, i.e. the angle obtained via the Swift method will be

$$\Theta_c = \Theta_{regional} + \frac{1}{2} \arctan\left(\frac{t_D D_1 + e_D S_1}{D_1 + e_D t_D S_1}\right) \tag{4.31}$$

[*McNeice and Jones*, 2001], using the notation of *Groom and Bailey* [1989] (Sec. 4.4.4) with t_D and e_D are the descriptors of telluric distortion twist and shear respectively.

4.4.2. Bahr parameter

In order to overcome the limitations of the Swift method in identifying the regional geoelectric strike in the presence of local distortion (Sec. 4.4.1), *Bahr* [1988] suggested to

use the phase information of the impedance tensor elements. The approach aims to recover the regional geoelectric strike direction by determining a rotation angle, that, when applied to the impedance tensor, causing the two elements belonging to the same telluric vector $\vec{e}_i$ ($i \in [x, y]$) to have the same phase. Accordingly

$$\mathrm{Im}(Z_{xi}/Z_{yi}) = 0, \tag{4.32}$$

which is equally to $\mathrm{Re}(Z_{xi}/Z_{yi}) = 0$ [*Bahr*, 1985]. Furthermore, the author introduces the phase information of the impedance tensor elements to distinguish between local telluric distortion and regional induction. For that reason, he introduces the complex variables

$$\begin{aligned}
S_1 &= Z_{xx} + Z_{yy} && : \text{sum of diag. elements } (\textit{trace}) && (4.33)\\
S_2 &= Z_{xy} + Z_{yx} && : \text{sum of off-diag. elements} && (4.34)\\
D_1 &= Z_{xx} - Z_{yy} && : \text{difference of diag. elements} && (4.35)\\
D_2 &= Z_{xy} - Z_{yx} && : \text{difference of off-diag. elements } (\textit{anti-trace}) && (4.36)
\end{aligned}$$

with S_1 and D_2 are invariant under rotation of the coordinate system around its vertical axis. From these variables, the *commutators* [*Bahr*, 1988] are calculated:

$$[\Psi_1, \Upsilon_2] = \mathrm{Im}(\Psi_1 \cdot \Upsilon_2^*) \tag{4.37}$$

with Ψ and $\Upsilon \in [S, D]$, and $*$ denoting complex conjugate. The *commutators* are used to define the parameters

$$\begin{aligned}
A &= [S_1, D_1] + [S_2, D_2],\\
B &= [S_1, S_2] - [D_1, D_2],\\
C &= [D_1, S_2] - [S_1, D_2],
\end{aligned}$$

allowing to rewrite Equation 4.32 as

$$-A\, sin(2\alpha) + B\, \cos(2\alpha) + C = 0 \tag{4.38}$$

where α is the angle that rotates the distorted impedance tensor into direction of the regional strike.

As a measure of subsurface dimensionality the parameters given in table 4.2 were introduced by *Bahr* [1988], and the strike direction can be calculated by finding the angle Θ that forces one the phases ϕ_{e_i} to be 0 and the other one to be π

$$\phi_{e_i}(\Theta) = \arctan\left[\frac{(\mathrm{Im}[Z_{xi}(\Theta)])^2 + (\mathrm{Im}[Z_{yi}(\Theta)])^2}{(\mathrm{Re}[Z_{xi}(\Theta)])^2 + (\mathrm{Re}[Z_{yi}(\Theta)])^2}\right]^{1/2} \tag{4.39}$$

with i representing the direction of the telluric vectors e_x and e_y.

Parameter	Geoelectrical application
$\eta_B = \sqrt{C}/\lvert D_2\rvert$	Descriptiveness of MT tensor by superimposed model
$\mu_B = ([D_1, S_2] + [S_1, D_2])^{1/2} / \lvert D_2\rvert$	Phase difference in the MT tensor
$\Sigma_B = (D_1^2 + S_2^2)/D_2^2$	Two-dimensionality

Tab. 4.2.: Parameters defined by *Bahr* [1988] (with modifications by *Prácser and Szarka* [1999]) to describe distortion of the MT impedance tensor; see text for details about parameters.

This concept was later advanced by *Jones and Groom* [1993], who suggest decomposing for an impedance tensor rotated 45 degrees against the strike direction instead of an impedance tensor orientated parallel to strike. The authors' modification is based on the fact that in the case of no distortion, or symmetric distortion, the angles ϕ_{e_x} and ϕ_{e_y} are undefined, because the off-diagonal elements of the distortion matrix c_{xy} and c_{yx} (Eq. 4.21) are zero. Incorporating this modification in Equation 4.39 yields

$$\phi_1(\Theta) = \arctan\left(\frac{\mathrm{Im}[(Z_{xx}(\Theta) + Z_{xy}(\Theta))/(Z_{yx}(\Theta) + Z_{yy}(\Theta))]}{\mathrm{Re}[(Z_{xx}(\Theta) + Z_{xy}(\Theta))/(Z_{yx}(\Theta) + Z_{yy}(\Theta))]}\right), \tag{4.40}$$

$$\phi_2(\Theta) = \arctan\left(\frac{\mathrm{Im}[(Z_{xx}(\Theta) - Z_{xy}(\Theta))/(Z_{yx}(\Theta) - Z_{yy}(\Theta))]}{\mathrm{Re}[(Z_{xx}(\Theta) - Z_{xy}(\Theta))/(Z_{yx}(\Theta) - Z_{yy}(\Theta))]}\right). \tag{4.41}$$

4.4.3. Weaver-Agarwal-Lilley tensor invariants

Weaver et al. [2000] use seven independent plus one dependent parameter that are invariant under horizontal rotation of the coordinate system plus an angle Θ to describe the MT impedance tensor $\mathbf{Z}$, the dimensionality of the subsurface, and the distortion type (Tab. 4.3). Θ defines therein the angle between the x-axis of the coordinate system used for the processing and a fixed direction (e.g. magnetic north). The methods of *Weaver et al.* [2000] is an extension of the work by [*Bahr*, 1988] (Sec. 4.4.2), with the last three Weaver-Agarwal-Lilley's (WAL) independent parameter (Tab. 4.3, i.e. parameters I_5, I_6, I_7) are retraces of Bahr's parameters (Tab. 4.2).

Weaver et al. [2000] define their parameters through the variables ξ, η, and d_{ij} representing real and imaginary parts of the impedance tensor:

$$(2\mu_0)^{-1}[Z_{xx} + Z_{yy}] = \xi_1 + \imath\eta_1 \tag{4.42}$$

$$(2\mu_0)^{-1}[Z_{xy} + Z_{yx}] = \xi_2 + \imath\eta_2 \tag{4.43}$$

$$(2\mu_0)^{-1}[Z_{xx} - Z_{yy}] = \xi_3 + \imath\eta_3 \tag{4.44}$$

$$(2\mu_0)^{-1}[Z_{xy} - Z_{yx}] = \xi_4 + \imath\eta_4 \tag{4.45}$$

$$\frac{\xi_i\eta_j - \xi_j\eta_i}{I_1 I_2} = d_{ij} \tag{4.46}$$

with μ_0 the permeability of free space. A visual representation of the parameters can be

Parameter	Geoelectrical application
$I_1 = (\xi_4^2 + \xi_1^2)^{1/2}$	1D magnitude and phase of the geoelectric resistivity (Eq. 4.47 and 4.48)
$I_2 = (\eta_4^2 + \eta_1^2)^{1/2}$	
$I_3 = (\xi_2^2 + \xi_3^2)^{1/2}/I_1$	} 2D anisotropy
$I_4 = (\eta_2^2 + \eta_3^2)^{1/2}/I_2$	
$I_5 = (\xi_4\eta_1 + \xi_1\eta_4)/(I_1 I_2)$	} Galvanic distortion
$I_6 = (\xi_4\eta_1 - \xi_1\eta_4)/(I_1 I_2)$	
$I_7 = (d_{41} - d_{23})/Q$	
$Q_W = [(d_{12} - d_{34})^2 + (d_{13} + d_{24})^2]^{1/2}$	

Tab. 4.3.: The seven independent (I_1 - I_7) plus one dependent parameter (Q) defined by *Weaver et al.* [2000] to describe the magnetotelluric (MT) impedance tensor and its distortion. Each of the parameters is associated with a certain geological setup, and subsurface characteristics in terms of dimensionality and distortion can be derived from the values of these parameters; see Table 4.4 for details about the relation between parameter values and subsurface dimensionality. Relation of ξ, η, and d with the MT impedance tensor are given in Equations 4.42 – 4.46

Values	Dimensionality
$I_3 = I_4 = I_5 = I_6 = 0$; $I_7 = 0$ or $Q_W = 0$	1D
$I_3 \neq 0$ or $I_4 \neq 0$; $I_7 = 0$ or $Q_W = 0$	2D
$I_3 \neq 0$ or $I_4 \neq 0$; $I_5 \neq 0$, $I_7 = 0$	3D/2Dtwist (only twist)
$I_3 \neq 0$ or $I_4 \neq 0$; $I_5 \neq 0$, I_7 : undefined	3D/2D1D (non-recoverable strike direction)
	galvanic distortion over a 1D or 2D structure
$I_6 \neq 0$	3D/2D
	general case of galvanic distortion over a 2D structure
$I_7 \neq 0$	3D (affected or not by galvanic distortion)

Tab. 4.4.: The dimensionality of the subsurface derived from the parameters defined by *Weaver et al.* [2000], after [*Martí et al.*, 2005] and [*Martí*, 2007].

given via a Mohr circle diagram with the rotated impedance tensor elements Z_{xx} and Z_{xy} forming the x and y-axis (Fig. 4.16).

Assumptions about the subsurface dimensionality can be made with the values WAL parameters (Tab. 4.4). Due to noise in a real data set, the parameters will not exhibit values of exactly zero and threshold values need to be introduced. Certainly, threshold values have significant influence onto the derived dimensionality and have to be chosen carefully. In their publication, *Weaver et al.* [2000] propose a value of 0.1 as tolerance level for all parameters, whereas *Martí et al.* [2009b] use default threshold values of 0.15 for the independent parameters and 0.1 for Q_W in their program *WALDIM*, the latter being an implementation of the theory by *Weaver et al.* [2000].

Information about the apparent resistivity and phase of the related 1D subsurface can be obtained from invariants I_1 and I_2 giving an approximate idea about the conductivity

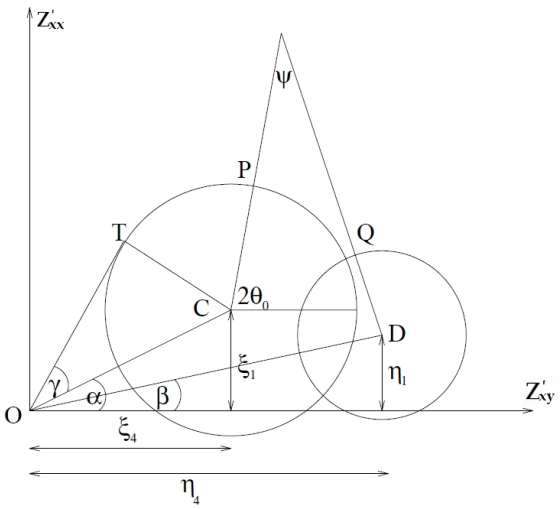

Fig. 4.16.: Visual representation of the parameters used in the tensor analysis after *Weaver et al.* [2000]. This is a schematic diagram of real and imaginary Mohr circles, with centres C and D respectively, depicting the 2x2 matrix associated with an MT tensor. Θ_0 is the angle through which the original coordinate axes must be rotated in order to maximise Re[Z'_{12}] [*Weaver et al.*, 2000].

distribution of the subsurface

$$\rho_{1D} = \frac{\mu_0}{\omega}(I_1^2 + I_2^2) \tag{4.47}$$

$$\varphi_{1D} = \arctan\left(\frac{I_2}{I_1}\right). \tag{4.48}$$

Resistivity and phase values for the more complex regions cannot be calculated with this method.

4.4.4. Groom and Bailey decomposition

A formulation that is widely used in the MT community was given in the classical paper by *Groom and Bailey* [1989] in which the authors present a method to divide the distortion matrix **C** (Eq. 4.21), describing the relationship between distorted impedance $\mathbf{Z}^D$ and regional impedance **Z**, into four parameters representing different aspects of distortion, i.e.

$$\mathbf{Z}^D = \mathbf{CZ} = g\mathbf{TSAZ}. \tag{4.49}$$

The factors used to describe the distortion are

$$g \;:\; \text{scalar} \qquad \textit{gain} \tag{4.50}$$

$$\mathbf{T} = (1 + t_D^2)^{-1/2} \begin{pmatrix} 1 & -t_D \\ t_D & 1 \end{pmatrix} \qquad \textit{twist tensor} \tag{4.51}$$

$$\mathbf{S} = (1 + e_D^2)^{-1/2} \begin{pmatrix} 1 & e_D \\ e & 1 \end{pmatrix} \qquad \textit{shear tensor} \tag{4.52}$$

$$\mathbf{A} = (1 + s_D^2)^{-1/2} \begin{pmatrix} 1+s_D & 0 \\ 0 & 1-s_D \end{pmatrix} \qquad \textit{anisotropy tensor} \tag{4.53}$$

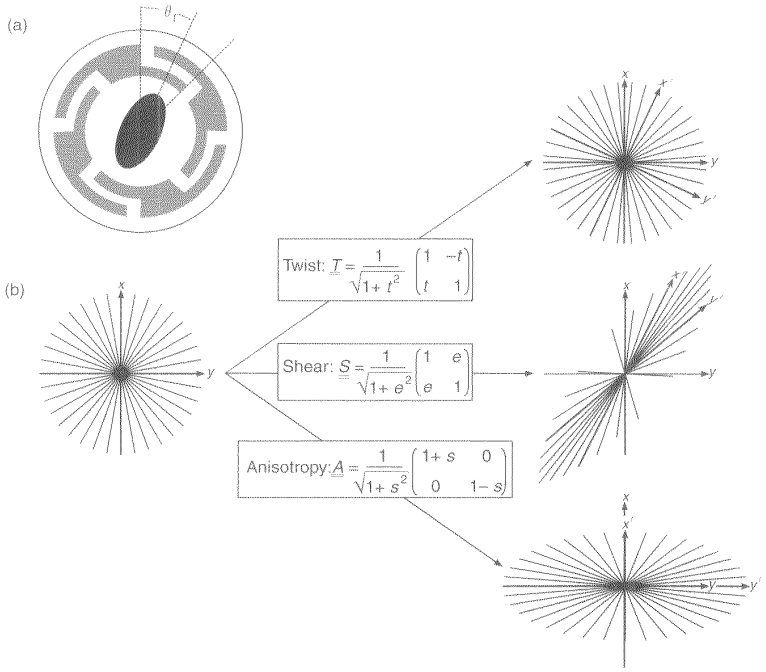

Fig. 4.17.: Visual representation of the Groom and Bailey concept for decomposition of the magnetotelluric (MT) distortion tensor. (a) A contrived scenario in which MT data are collected at the centre of a conductive swamp (black) that is encompassed by a moderately conductive region (gray), and an insulator (white). θ_t denotes the local strike of the swamp, which 'twists' the telluric currents. The anomalous environment also imposes shear and anisotropy effects on the data. (b) Distortion of a set of unit vectors by twist **T**, shear **S**, and anisotropy **A**, operators, which are parameterised in terms of the real values t_D, e_D, and s_D, respectively, from [*Simpson and Bahr*, 2005] (redrawn from [*Groom and Bailey*, 1989])

with t_D, e_D, and s_D are real values. A visualisation of the different distortion effects described by *twist*, *shear*, and *anisotropy* onto the MT impedance tensor is given in Figure 4.17. The gain g at a station simply scales the regional electric field without causing any directional change to the electric field, whereas the anisotropy tensor **A** scales the electric field on the two axes coinciding with the regional electric strike by a different factor, both indistinguishable from the regional structure without independent information. The shear tensor **S** affects both amplitude and phase of the impedance, rotating a vector clockwise on the x-axis of a coordinate system, not coinciding with the regional principle axis system, whereas a vector on the y-axis is rotated anticlockwise, each by an angle $\arctan(e_D)$. The twist tensor **T** affects both amplitude and phase of the impedance as well, rotating the regional electric field clockwise by an angle of $\arctan(t_D)$, but does not introduce any anisotropy to the system [*McNeice and Jones*, 2001]. The advantage of this approach is that the authors separate between the effects of gain and anisotropy, which cannot be determined independently from **Z** [*Groom and Bailey*, 1989], and those that can be derived from the measured impedance, viz. shear and twist.

4.4.5. Caldwell-Bibby-Brown phase tensor

In the previous approaches aiming to recover the regional geoelectric strike direction in a MT dataset it was assumed that the regional conductivity structure is either 1D or 2D, allowing for a representation of the regional EM field by an impedance tensor with only two non-zero components (cf. Secs. 4.4.1 - 4.4.4). In order to deal with situations where both, local and regional conductivity structures are 3D, *Caldwell et al.* [2004] introduced the *magnetotelluric phase tensor* (often simply referred to as *phase tensor*), utilising the circumstance that the phase relationship between (horizontal) magnetic and electric field vectors is unaffected by galvanic distortion; see Section 4.1 for more information on distortion types.

Since horizontal magnetic field components are usually not significantly affected by distortion and respective effects are almost entirely confined to the electric field, horizontal components of the observed magnetic field are assumed to represent the undisturbed regional magnetic field [*Caldwell et al.*, 2004]. With the assumptions that the distortion is only of galvanic nature and that the regional electric field does not vary significantly over the lateral extent of the conductivity heterogeneity, the observed horizontal electric field $\vec{E}_h^D$ can be represented as the product of a distortion matrix $\mathbf{D}_\Phi$ and the regional electric field $\vec{E}_h$, i.e.

$$\vec{E}^D = \mathbf{D}_\Phi \vec{E}_h, \tag{4.54}$$

in which the distortion matrix is a second rank, real, 2D tensor

$$\mathbf{D}_\Phi = \begin{pmatrix} d_{11} & d_{12} \\ d_{21} & d_{22} \end{pmatrix}. \tag{4.55}$$

This assumption implies that the observed field is a linear superposition of the regional electric field and a secondary field, caused by the interaction of the regional field with a local heterogeneity that is in-phase with the regional field.

With the additional assumption that only galvanic distortion is present in the data, the relationship between the distorted impedance $\mathbf{Z}^D$ and the regional impedance $\mathbf{Z}$ can be written as

$$\mathbf{Z}^D = \mathbf{D}_\Phi \mathbf{Z}. \tag{4.56}$$

Separating the impedance tensors into their real ($\mathbf{X}$) and imaginary ($\mathbf{Y}$) parts, i.e.

$$\mathbf{Z}^D = \mathbf{X}^D + \imath \mathbf{Y}^D \tag{4.57}$$

and

$$\mathbf{Z} = \mathbf{X} + \imath \mathbf{Y}, \tag{4.58}$$

yields individual relations for the real and imaginary parts of the distorted and regional matrix, i.e.

$$\mathbf{X}^D = \mathbf{D}_\Phi \mathbf{X} \tag{4.59}$$

and

$$\mathbf{Y}^D = \mathbf{D}_\Phi \mathbf{Y}. \tag{4.60}$$

Without additional information, $\mathbf{Z}$ cannot be recovered from $\mathbf{Z}^D$ for an unknown $\mathbf{D}_\Phi$, but, since $\mathbf{D}_\Phi$ contains only real values, the phase relationship between the horizontal components of the regional electric magnetic and electric fields must be unaffected by distortion [*Caldwell et al.*, 2004].

For the purpose of exemplification, assume the phase tensor

$$\mathbf{\Phi} = \begin{pmatrix} \Phi_{11} & \Phi_{12} \\ \Phi_{21} & \Phi_{22} \end{pmatrix}. \tag{4.61}$$

By deducing the phase from the ratio of real and imaginary parts of the impedance tensor

$$\mathbf{\Phi} = \mathbf{X}^{-1}\mathbf{Y}, \tag{4.62}$$

with $\mathbf{X}^{-1}$ representing the inverse of the $\mathbf{X}$, the phase tensor for the disturbed case can be written as

$$\begin{aligned} \mathbf{\Phi}^D &= (\mathbf{X}^D)^{-1}\mathbf{Y}^D = (\mathbf{D}_\Phi \mathbf{X})^{-1}(\mathbf{D}_\Phi \mathbf{Y}) && (4.63)\\ &= \mathbf{X}^{-1}\mathbf{D}_\Phi^{-1}\mathbf{D}_\Phi \mathbf{Y} = \mathbf{X}^{-1}\mathbf{Y} && (4.64)\\ &= \mathbf{\Phi}. && (4.65) \end{aligned}$$

The phase tensor is therefore independent of distortion and can be expressed in terms of the undistorted $\mathbf{X}$ and $\mathbf{Y}$ components, i.e.

$$\mathbf{\Phi} = \frac{1}{\det(\mathbf{X})} \begin{pmatrix} X_{22}Y_{11} - X_{12}Y_{21} & X_{22}Y_{12} - X_{12}Y_{22} \\ X_{11}Y_{21} - X_{21}Y_{11} & X_{11}Y_{22} - X_{21}Y_{12} \end{pmatrix}, \tag{4.66}$$

or equivalently in terms for the distorted equivalents X^D and Y^D.

In order to describe the local distortion configuration, *Caldwell et al.* [2004] define three rotational invariant parameter

$$\begin{aligned} \Phi_{min} &= (\Phi_1^2 + \Phi_2^2)^{1/2} - (\Phi_1^2 + \Phi_2^2 - \det(\Phi))^{1/2} && (4.67)\\ \Phi_{max} &= (\Phi_1^2 + \Phi_2^2)^{1/2} + (\Phi_1^2 + \Phi_2^2 - \det(\Phi))^{1/2} && (4.68)\\ \beta_p &= \frac{1}{2}\arctan\left(\frac{\Phi_2}{\Phi_1}\right) && (4.69) \end{aligned}$$

(using the corrected form of *Moorkamp* [2007a]) plus one coordinate dependent parameter

$$\alpha_p = \frac{1}{2}\arctan\left(\frac{\Phi_3}{\Phi_4}\right), \tag{4.70}$$

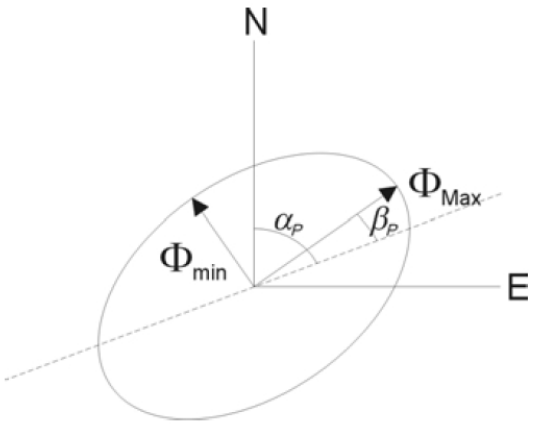

Fig. 4.18.: Graphical representation of the magnetotelluric phase tensor defined by *Caldwell et al.* [2004], with Φ_{max} and Φ_{min} describing the length of the principle axis of the ellipse and $\alpha_p - \beta_p$ the angle between North and the major axis, from *Martí* [2007] after *Caldwell et al.* [2004]

with Φ_1 - Φ_4 defined[1] as

$$\Phi_1 = (\Phi_{11} + \Phi_{22})/2 \tag{4.71}$$
$$\Phi_2 = (\Phi_{12} - \Phi_{21})/2 \tag{4.72}$$
$$\Phi_3 = (\Phi_{12} + \Phi_{21})/2 \tag{4.73}$$
$$\Phi_4 = (\Phi_{11} - \Phi_{22})/2. \tag{4.74}$$

The four parameters Φ_{min}, Φ_{max}, α_p, and β_p defined by *Caldwell et al.* [2004] are minimum and maximum of the ellipse describing $\mathbf{\Phi}$ (i.e. the principle, or singular values of $\mathbf{\Phi}$), skew angle, and a coordinate system orientation dependent angle, respectively. A graphical representation of the four parameters is given in Figure 4.18, illustrating their use in identifying the present distortion. With these four parameters the phase tensor can be represented through a Singular Value Decomposition (SVD) as the product of three matrices

$$\mathbf{\Phi}_D = \mathbf{R}^T(\alpha_p - \beta_p) \begin{bmatrix} \Phi_{max} & 0 \\ 0 & \Phi_{min} \end{bmatrix} \mathbf{R}(\alpha_p + \beta_p) \tag{4.75}$$

where $\mathbf{R}$ is the rotation matrix with the superscript T indicating the transpose of the matrix. In a review of the previous work, *Bibby et al.* [2005] introduced an additional parameter

$$\lambda_p = \frac{(\Phi_3^2 + \Phi_4^2)^{1/2}}{(\Phi_1^2 + \Phi_2^2)^{1/2}}, \tag{4.76}$$

describing the degree of ellipticity and therefore indicating whether the structure is 1D or of higher dimensionality. λ_p supplements α_p and β_p in defining the present subsurface

[1] Parameter Φ_1 used here as defined by *Caldwell et al.* [2004], whereas Φ_2 is replaced by the original Φ_3 owing to the corrections by *Moorkamp* [2007a]; the additional parameter Φ_3, Φ_4 are also included herein for the sake of clearness

	λ_p	β_p	α_p
1D	0	0	undefined
2D	$\neq 0$	0	strike angle
3D	$\neq 0$	$\neq 0$	strike angle

Tab. 4.5.: Values of the parameters defined by *Bibby et al.* [2005] depending of the present dimensionality (note that in practise λ and β are assumed to be zero when they fall below a chosen threshold value λ_c and β_c); see text for further information on the parameters.

configuration, which quantify the validity of a 2D description and provide the geoelectric strike direction (if existing), respectively. Values of λ_p, α_p, and β_p for 1D, 2D, and 3D cases are summarised in Table 4.5. Due to noise in real data, λ_p, and β_p are usually different from zero for all three cases. The ultimate decision about subsurface dimensionality is therefore dependent on the thresholds below which λ_p and β_p are considered close enough to zero. Since modern MT inversion algorithms are capable of coping with 2D situations, whereas the 3D case is still problematic, most workers focus on the verification of the 2D assumption for a given dataset (as opposed to a full 3D treatment). Several authors have investigated the threshold for β_p, proposing a value of three degrees based on results of their synthetic model studies [e.g. *Caldwell et al.*, 2004; *Martí*, 2007; *Ingham et al.*, 2009]. Determination of an optimal λ_p value for the 1D – 2D discrimination, on the other hand, received less attention; however, it was suggested by *Martí* [2007] to use the standard deviation of the error in the determination of α_p (σ_{α_p}) as a threshold for λ_p.

Bibby et al. [2005] point out that the criteria provided by the phase tensor are necessary but not sufficient conditions for determining the dimensionality of the regional conductivity structure. Furthermore, the authors state that the phase tensor at a single period, under suitable conditions of symmetry, can have the characteristics of a lower dimension than that of the regional structure. It is therefore suggested by *Bibby et al.* [2005] to take into account data from neighbouring periods and locations to increase reliability of the phase tensor analysis results.

Whereas the phase tensor method is excellent for determination of the geoelectric strike direction it is limited in terms of recovering regional electric impedance values since the set of equations is underdetermined, i.e. holding a set of four equations in five, six, or eight unknowns for the 1D, 2D, or 3D case, respectively. The problem is therefore clearly non-unique and further constraints need to be applied in order to identify the electric impedance and therefore the apparent resistivity. This could be achieved either by using information of other methods such as TEM soundings, or by introducing mathematical relationships between the parameters similar to the approach by *McNeice and Jones* [2001] for Groom-Bailey decomposition; see *Bibby et al.* [2005] for further examples of possible relationships.

Method	Applicability
Swift angle	2D
Groom and Bailey decomposition	3D/2D
Bahr parameters	3D ⋆
Weaver et al. invariants	3D ⋆
Caldwell et al. phase tensor	3D ⋆

Tab. 4.6.: Comparison of commonly used analysing tools for MT distortion and their applicability depending on the dimensionality of the subsurface. The Swift angle determination [*Swift*, 1967] can only be used in a 2D environment and fails for settings of higher dimensionality while the Groom and Bailey decomposition [*Groom and Bailey*, 1989] is designed to retract the 2D regional structure in the presence of small-scale 3D structures but cannot practical in a fully 3D situation. The methods by *Bahr* [1988], *Weaver et al.* [2000], and *Caldwell et al.* [2004] are able to identify the dimensionality of the MT tensor for 1D, 2D, 3D, and mixed mode settings, but have the drawback that no direct conclusion about the values of resistivity and phase for the regional structures can be drawn.

4.4.6. Conclusion

Today, various attempts have been published that aim to cope with the effects of distortion onto MT data, among which the methods by *Groom and Bailey* [1989], *Weaver et al.* [2000], and *Caldwell et al.* [2004] proofed most applicable (Tab. 4.6). It is not recommended to use the approaches by *Swift* [1967] and *Bahr* [1988] anymore as they fail for certain subsurface characteristics and have been succeeded by the WAL method [*Weaver et al.*, 2000] and the phase tensor method [*Caldwell et al.*, 2004]. The latter two are limited to an analysis of the subsurface dimensionality and solely give resistivity and phase values for an approximated 1D scenario (WAL); hence, these approaches can only be used as an indicator for subsequent methods that provide quantitative results for the different regimes. The technique by *Groom and Bailey* [1989], on the other hand, evaluates the fit for a proposed strike direction and provides quantitative results but fails for cases where the subsurface is highly 3D and no simplification like a 3D/2D scenario (Sec. 4.2) can be identified.

For a typical MT fieldwork, where data are collected along a profile, a combination of the methods by *Weaver et al.* [2000], *Caldwell et al.* [2004], and *Groom and Bailey* [1989] can be most effective. An analysis of the subsurface dimensionality with the WAL and Phase tensor techniques can specify the region suitable for Groom-Bailey decomposition or help to weigh the contribution from stations and frequency ranges during the estimation of Groom-Bailey decomposition.

5

Earth's properties observable with magnetotellurics

Electromagnetic (EM) methods determine the distribution of electric conductivity[1] σ in the subsurface by measuring the relation between time-varying electric and magnetic field components (cf. Sec. 3.2). Electric conductivity is the measure of a material's ability to conduct electric current, specific for a material under given conditions. Thus, EM methods can, in principle, derive the distribution of materials in the subsurface. However, the magnetotelluric (MT) method does not measure the electric conductivity at a certain point in the subsurface, but rather the integrated conductivity of a volume. A volume represented approximately by a hemisphere of radius given by the inductive distance (cf. Sec. 3.3). Therefore, assumptions have to be made about the local conductivity distribution during analysis and interpretation of the obtained data (cf. Secs. 3 and 6).

Electric conductivity of a material depends on a variety of different properties (cf. Sec. 5.3); accordingly, common Earth's materials exhibit a wide range of values from 10^{7} – 10^{-7} S/m (i.e. resistivities in the range $10^{-7} - 10^{7}\Omega$m) (Fig. 3.5). Among the different factors influencing the electric conductivity of materials in the Earth, temperature, water salinity, and interconnectivity of conductors have the most significant effects. These influencing parameters can undergo very localised changes, both in the vertical and the horizontal directions; e.g. a massive ore body or horizontal temperature gradients in mantle convection cells can result in conductivity changes of several orders of magnitude. Therefore, the creation of a global 1D electric reference model possesses a number of challenges when compared to the seismological Preliminary Reference Earth Model (PREM) [*Dziewonski and Anderson*, 1981] (Fig. 5.1). The present spatial coverage with MT measurements is not yet sufficient to take into account the large amount of regional, let alone local conductivity anomalies, to facilitate creation of a global 3D conductivity

[1] There lies a redundancy in terminology when describing the electric properties of materials; in some cases σ is chosen, whereas in other cases electric resistivity ρ is used. As σ and ρ are simply inverses of each other ($\rho = 1/\sigma$ with $[\rho] = \Omega$m and $[\sigma] =$ S/m), the convention used in the remainder of this text is chosen out of convenience; conductivity will be used when the majority of the elements exhibit $\sigma > 1$ ($\rho < 1$) and resistivity in the opposite case.

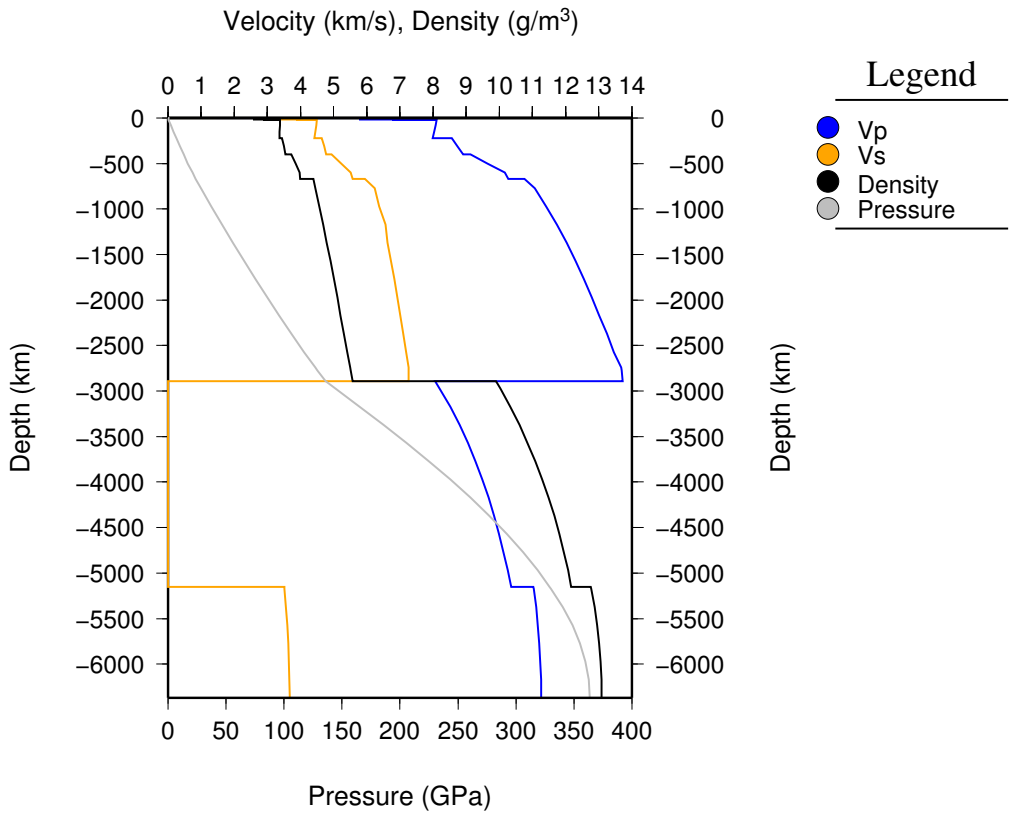

Fig. 5.1.: The Preliminary reference Earth model (PREM); after *Dziewonski and Anderson* [1981]. Note that the same scale is used for seismic velocity and density (with different units).

distribution for the Earth. Fortunately, the Earth's core (Sec. 5.2.3), and with some exceptions the mid and lower mantle (Sec. 5.2.2), can be assumed to exhibit an approximately radial-symmetric conductivity–depth profile. This assumption is based on observed similarity of structures at various depths across a range of areas of the Earth [e.g. *Ichiki et al.*, 2001; *Schultz et al.*, 1993; *Kuvshinov et al.*, 2005; *Neal et al.*, 2000; *Olsen*, 1998; *Tarits et al.*, 2004]. Therefore, these deeper regions of the Earth are commonly described by 1D conductivity models, however, it is important to point out that these finding may be biased due to the decreasing sensitivity of EM methods with depth (Sec. 3.3). Significant lateral conductivity variations at certain depth regions are likely considering the present conditions, e.g. local hot-spot generations at the D"-layer, but are not observable on the surface. Over time, various 1D conductivity–depth profiles have been presented, starting with the fundamental work of *Lahiri and Price* [1939], stratifying the Earth into radial shells with different conductivity properties (Sec. 5.2), where particular sections within the Earth are governed to a certain extent by the different types of electric charge transport. In this Chapter, electric conductivity of the different region within the Earth will be discussed, but first electric charge transport mechanisms are examined.

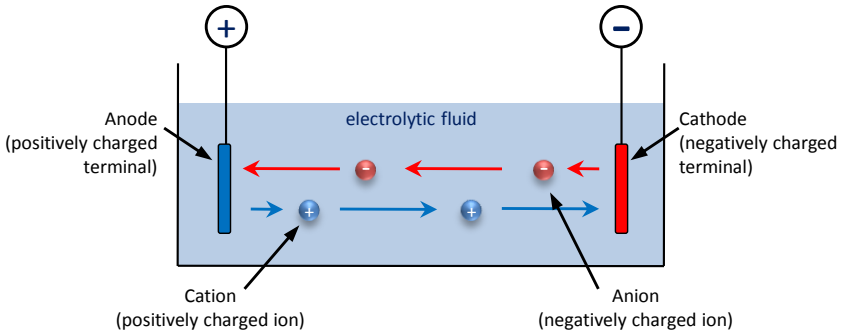

Fig. 5.2.: Illustration of electrolytic conduction.

5.1. Electric charge transport in rocks and minerals

An excellent summary of electrical properties of crustal and mantle rocks and the related conductivity mechanisms are given in the review papers by *Nover* [2005] and *Yoshino* [2010]. The three main contributors to charge transport in rocks and minerals of the Earth are electrolytic conduction, electronic conduction, and semiconduction; however, the effect of the conductive component in a multi-phase medium on MT measurements is highly dependent on interconnection of the conductive component in the host medium. Influence of different charge transport types for a region within the Earth is dependent on type and condition (e.g. temperature, fluid saturation, melt percentage) of the local mineral composition (cf. Sec. 5.3).

5.1.1. Electrolytic conduction

Electrolytic or *ionic conduction* usually refers to charge transport by ion mobilisation in an electrolytic fluid; other ionic conduction, such as hydrogen diffusion, is usually considered separately (cf. Sec.5.3). The electrolytic process can be illustrated using a laboratory setup in which two devices with different electric charge are placed in an ionic fluid (Fig. 5.2). Chemical processes at the positively charged terminal (anode) generate positively charged ions (cations) while the negatively charged terminal (cathode) generates negatively charged ions (anions) through removal or addition of electrons to the neutral ions in the fluid, respectively. The cations then migrate from the anode to the cathode and the anions from the cathode to the anode in order to equalise charge. Responses, recorded during *in situ* EM experiments, which originate from such charge difference within the ionic fluid can therefore result from different causes, such as natural or artificial EM wave signals, or local charge imbalances (e.g. poorly isolated power devices); cf. Sections 2 and 4.

Electrolytic conduction is a very important parameter regarding electric conductivity in the Earth's subsurface, in particular at crustal depth where electrolytic conduction of fluids in porous media is often dominant. For fluid saturated porous rocks an empirical

relationship between observed electric conductivity σ_o, the rocks porosity ϕ, and fluid saturation S_f was derived by *Archie* [1942] and *Dachnov* [1959] (known as *Archie's second law*):

$$\sigma_o = \sigma_f \cdot \phi^m \cdot S_f^n, \tag{5.1}$$

where σ_f: conductivity of the fluid, m: *cementation factor* (exponent of porosity, $m = 1.3$ for unconsolidated sediments [*Dachnov*, 1962, 1975] in *Schoen* [1983]), n: the saturation exponent (range dependent on rock type, often assumed $n = 2$ [e.g. *Archie*, 1942; *Schlumberger*, 1989; *Glover*, 2010]). Equation 5.1 is an extension of the (first) Archie's law:

$$\sigma_o = \sigma_f \cdot \phi^m, \tag{5.2}$$

which is the special case for a fully saturated matrix. The empirical equations 5.1 and 5.2 have been analytical verified for special cases by *Sen et al.* [1981]; *Mendelson and Cohen* [1982]. However, it has to be noted that equations 5.1 and 5.2 do not take into account the contribution of matrix conductivity or surface conductivity (due to conducting phases along grain boundaries), nor do they consider the effect of additional (fluid-)phases. For a wide range of cases, the contribution of matrix and surface conduction is not negligible and the *bulk conductivity* for porous media σ_{bulk} is a combination of electrolytic σ_f, matrix σ_m, and surface conductivity σ_s, i.e.

$$\sigma_{bulk} = f(\sigma_f) + f(\sigma_m) + f(\sigma_s). \tag{5.3}$$

Attempts to identify the contribution of each of the constituent conductivities were made by various authors, utilising the frequency dependence of the different conductivities [e.g. *Olhoeft*, 1985; *Hördt et al.*, 2007]. The presence of a conductive phase along grain boundaries, such as carbon, sulphite, or oxides, is therefore the most likely cause of high conductivity in the crust (and probably in the lithospheric-mantle) [Duba 2010, pers. communication], and studies about their effect have been carried out, among others, by *Duba* [1977, 1983]; *Duba and Shankland* [1982]; *Duba et al.* [1988]; *Shankland et al.* [1997]; *Mathez et al.* [2008]. An extension of Archie's law that incorporates the effect of surface conduction was presented by *Tiab and Donaldson* [2004] and a general formulation for the bulk conductivity of a n-phase medium was given by *Glover* [2010]:

$$\sigma_{bulk} = \sum_{i=1}^{n} \sigma_i \phi_i^{m_i}, \tag{5.4}$$

with σ_i, ϕ_i, and m_i the conductivity, fractional amount, and exponential factor of the i-th phase, respectively. The exponential factor of one phase can be calculated as a function of fractions and exponential factors of all other phases:

$$m_i = \frac{\log(1 - \sum_{j \neq i} \phi_j^{m_j})}{\log(1 - \sum_{j \neq i} \phi_j)}, \tag{5.5}$$

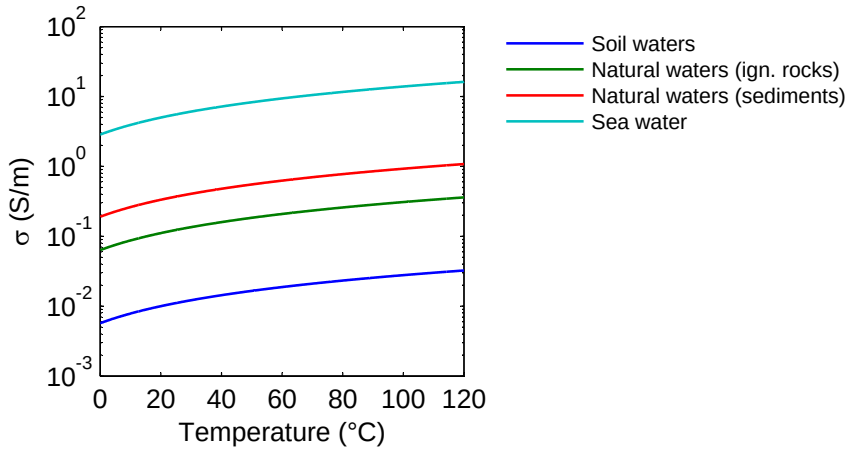

Fig. 5.3.: Temperature-dependent conductivity of fluids, using the formulation by *Dachnov* [1975] (Eq. 5.8) and $\sigma_f(20^OC)$ values of 0.01, 0.11, 0.33, and 5 S/m for soil waters, natural waters in igneous rocks, natural water in sediments, and sea water, respectively [*Telford et al.*, 1990].

and with a first order approximation via

$$m_i = \frac{\sum_{j \neq i} \phi_j^{m_j}}{\sum_{j \neq i} \phi_j} \tag{5.6}$$

[*Glover*, 2010]. The formulation by *Glover* [2010] includes σ-contributions from matrix rocks by considering them as one of the conducting phases.

The electric conductivity of a fluid σ_f can be considered a function of salt concentration, ion charge, and temperature [e.g. *Rein et al.*, 2004]. An equation for this relationship was formulated by *Ruffet et al.* [1995]:

$$\sigma_f = \sum (C_a \cdot v_a \cdot f_a + C_c \cdot v_c \cdot f_c), \tag{5.7}$$

with C: concentration, v: mobility, f: conduction coefficient, and the indices a and c denoting anions and cations, respectively. An empirically derived relation between temperature of a fluid and its conductivity was presented by *Dachnov* [1975]:

$$\sigma_f(T) = \sigma_f(20^OC) \cdot (1 + 2.16 \cdot 10^{-2} \Delta T + 8 \cdot 10^{-6} (\Delta T)^2) \tag{5.8}$$

with ΔT representing a temperature difference from 20°C. (cf. Fig. 5.3). However, due to the temperature dependence of ion mobility this formula is probably only valid for temperatures below 40°C [G. Nover 2009, personal communication]. Thus, the relation by *Dachnov* [1975] can only be applied during near-surface investigations; formulations for higher temperatures, i.e. greater depth, are still to be derived.

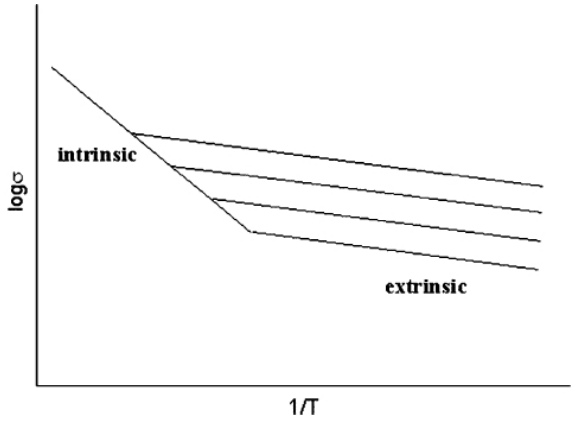

Fig. 5.4.: Arrhenius diagram displaying the relation between log conductivity and reciprocal of the absolute temperature for charge transport by semiconduction. The four lines represent different extrinsic charge transport processes. The variation of the gradient at higher temperatures is due to transition between the two regimes of semiconduction, either dominated by extrinsic or intrinsic charge transport; Figure from *Nover* [2005].

5.1.2. Electronic conduction

In electronic conduction, charge is transported by the movement of free electrons; the conductivity of media, comprised of good conductors in a more resistive host material, can be described using Ohm's Law (Eq. 3.5). The presence of a good conductor (metal, graphite, sulphidic ore body, or oxides with a significant amount of graphite or sulphides) in a medium can increase the electric conductivity by orders of magnitude [e.g. *Nover*, 2005]; again, as in the case of electrolytic conduction, the crucial factor is the interconnection of good conductors.

5.1.3. Semiconduction

When a semiconductor is not in an excited state, i.e. it has energy equal to its ground state, it has a full valence band and acts as an insulator. Since semiconduction needs a certain amount of energy to lift one or more electrons from the valence band into the conduction band (*activation energy*, ΔE), semiconduction is extremely dependent on externally supplied energy that, in the case of Earth's materials, is usually provided by temperature. Accordingly, charge transport by semiconduction is attributed to two different processes, i.e. extrinsic (also referred to as *proton conduction* or *proton hopping*) and intrinsic (also referred to as *small polaron conduction* or *hole hopping*). Extrinsic charge transport is due to H^+ "hopping" between lattice impurities, dominant at low temperatures; whereas intrinsic charge transport is dominantly for high temperatures above the transition point (see Fig. 5.4), when charge is transported through electrons in the conduction band and by "movement of electron holes" in the valence band of exited atoms[2]. For semiconductive

[2]Electron holes do not actually move, but are filled by electrons from neighbouring atoms, which in turn leave behind new electron holes.

Description	Depth (km)	Change of electric resistivity (Ωm) from	to	Type of change
Moho (oceanic)	5-7	$< 10^3$	$10^3 - 10^5$	Material: mafic to ultra-mafic
Moho (continental)	33-50			Material: felsic to ultra-mafic
LAB	50-160	$10^2 - 10^3$	5-25	Rheology: strong to weak*
Opx-cpx	∼300	30-80	100-200	Abundance: ortho- to clinophyroxene
MTZ top	410	100-200	20-30	Phase: olivine to Wadsleyite
MTZ internal	520	20-30	3-6	Phase: wadsleyite to Ringwoodite
MTZ bottom	660-670	3-6	1-3	Phase: ringwoodite to Perovskite

Tab. 5.1.: Step like changes in the Earth's conductivity-depth profile for the depth range potentially observable with magnetotelluric (MT) and geomagnetic deep-sounding (GDS) measurements. Moho: Mohorovičić discontinuity (Crust-mantle boundary), LAB: Lithosphere-Asthenosphere boundary, MTZ: Mantle transition zone. Values from *Heinson* [1999], *Jones* [1999], *Xu et al.* [2000a], *Yoshino et al.* [2008], and *Eaton et al.* [2009]. See Figures 5.5, and 5.6 for further details about the electric conductivity values of the different regions. *: note that electric conductivity properties of the LAB are controversial; see Section 5.2.2 for a discussion of this issue.

charge transport processes, an Arrhenius-like description of the conductivity–temperature relation has be found, i.e.

$$\sigma = \sigma_1 \exp\left(-\Delta H_1/k_B T\right) + \sigma_2 \exp\left(-\Delta H_2/k_B T\right), \tag{5.9}$$

with σ_i: pre-exponential factor, k_B: Boltzmann's constant, T: Temperature in Kelvin, and the activation enthalpy

$$\Delta H_i = \Delta E_i + P \cdot \Delta V_i, \tag{5.10}$$

with ΔE_i: activation energy, P: pressure, ΔV_i: activation volume, and the index $i \in [1, 2]$ referring to intrinsic and extrinsic charge transport, respectively. In laboratory experiments, values of pre-exponential factors, activation energies, and activation volumes of a sample can be derived by determining slopes and axis intercepts of the two regimes in the Arrhenius diagram (Fig. 5.4). Given that (the intrinsic part of) semiconduction appears to dominate conductivity of mantle materials at local $P - T$ conditions, numerous studies were carried out in order to determine these parameters for the relevant materials [*Duba and Shankland*, 1982; *Duba et al.*, 1994; *Karato*, 1990; *Constable et al.*, 1992; *Xu et al.*, 1998a; *Xu and Shankland*, 1999; *Yoshino et al.*, 2008, e.g.]; see Section 5.3 for a detailed discussion of semiconduction at mantle conditions.

5.2. Variation of electric conductivity with depth

The Earth is commonly divided into crust, mantle, and core; however, due to enhanced measurements and modern techniques, these three layers can be subdivided into smaller regions (Tab. 5.1). Despite the afore-mentioned difficulties to create 1D models for the

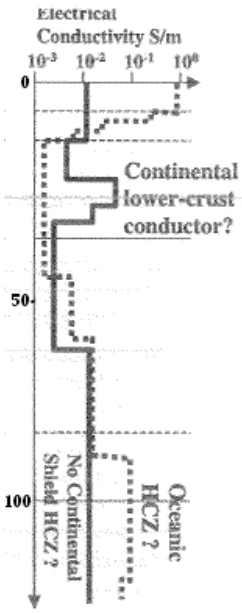

Fig. 5.5.: Typical electric conductivity structures below a continental shield (solid line) and oceanic lithosphere (dashed line); from *Heinson* [1999]

Earth's conductivity structures, different models have been proposed (e.g. Figs. 5.5 and 5.6). The different models are based on (long-term) Earth bound MT and GDS measurements [e.g. *Bahr et al.*, 1993; *Schultz et al.*, 1993; *Olsen*, 1998; *Heinson*, 1999; *Neal et al.*, 2000; *Utada et al.*, 2003; *Tarits et al.*, 2004; *Kuvshinov et al.*, 2005], satellite supported geomagnetic experiments [e.g. *Kuvshinov and Olsen*, 2006, 2008], laboratory studies on Earth's materials [e.g. *Xu et al.*, 1998a, 2000a; *Nover*, 2005; *Yoshino et al.*, 2008], and theoretical considerations [e.g. *Ledo and Jones*, 2005; *Jones et al.*, 2009].

More recent models, incorporating step like changes of conductivity, are favourable over previous smooth models as they have been proven to demonstrate better agreement with assumed phase changes within the Earth. Phase changes of Earth materials are a consequence of moving across boundaries in the P-T space. Lab studies (Sec. 5.3) aim to derive the conditions at which these phase changes occur for certain materials and their results can be used to guide interpretations of magnetotelluric and seismic investigations. The depth of the different step changes for certain regions of the Earth is strongly dependent on the geological history of the region; today it is commonly assumed that interfaces of the mantle transition zone (MTZ) and below are comparatively flat, whereas shallower interfaces are thought to exhibit a more pronounced topography. This conclusion, however, is certainly biased by the reduced resolution of deep-seated features.

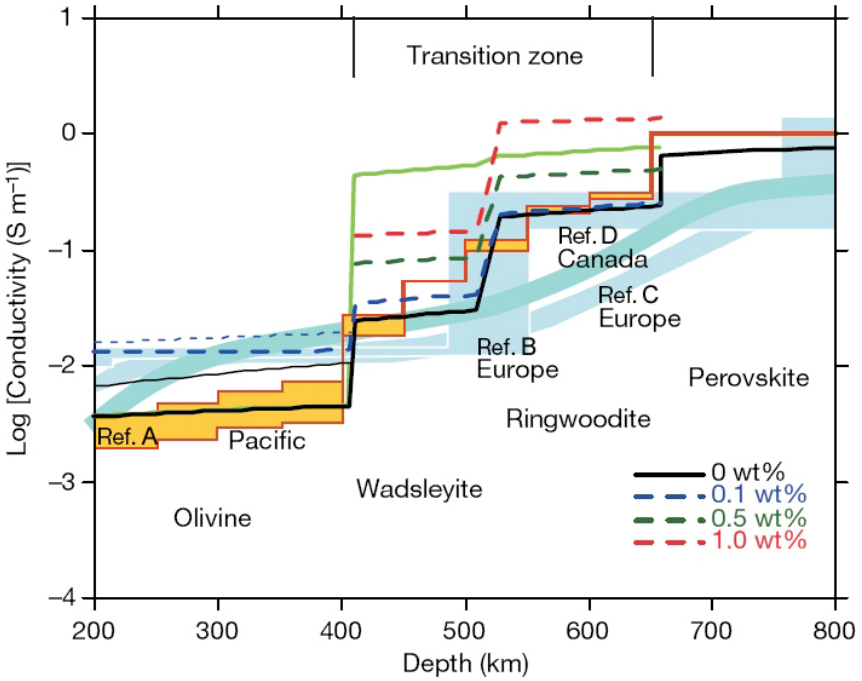

Fig. 5.6.: Collection of electric conductivity-depth profiles; from *Yoshino et al.* [2008]. Orange and blue regions represent geophysically observed conductivity profiles in the Pacific (Ref. A) [*Kuvshinov et al.*, 2005], and the continental mantle (Ref. B) [*Olsen*, 1998], (Ref. C) [*Tarits et al.*, 2004], and (Ref D.) [*Neal et al.*, 2000], respectively. The thick solid line represents the electric conductivity of olivine, wadsleyite and ringwoodite without water, whereas dashed lines indicate the electric conductivity of hydrous olivine, wadsleyite and ringwoodite as a function of water content (red: 1.0 wt%; green: 0.5 wt%; blue: 0.1 wt%), all derived through lab experiments by *Yoshino et al.* [2008]. The light green solid line denotes the results of previous experimental studies by *Xu et al.* [1998a].

5.2.1. The Earth's crust

The Earth's crust is petrological defined as the area above the peridotitic mantle usually exhibiting a thickness of 5 – 7 km (oceanic crust) or 30 – 50 km (continental crust). In regions with basaltic or non-existing underplating the crust–mantle boundary coincides with the Mohorovičić discontinuity (commonly referred to as *Moho*). The Moho was first identified by *Mohorovičić* [1910] using refracted waves from the 1909 shallow-focus earthquake near Zagreb to determine the existence of a medium with higher velocity at depth. Today, the Moho is seismologically defined by a significant increase in velocity, with values changing usually from approximately 6 km/s to 8 km/s (P-waves) and from approximately 3.5 km/s to 4.5 km/s (S-waves); however, velocity values may vary for certain regions of the Earth. Chemically the Moho is defined by a change from felsic (continental crust) or mafic (oceanic crust) to ultra-mafic materials. For Archean regions with komatiitic (ultramafic) underplating the Moho can be sensed at significantly shallower depth than the petrologically defined crust–mantle boundary. The Moho usually coincides with a change in density from around 2.7 g/cm^3 (continental crust) or 2.9 g/cm^3 (oceanic crust) to around 3.2 g/cm^3. An identification of the Moho using electric methods is more difficult, since the changes from felsic or mafic material to ultra-mafic material

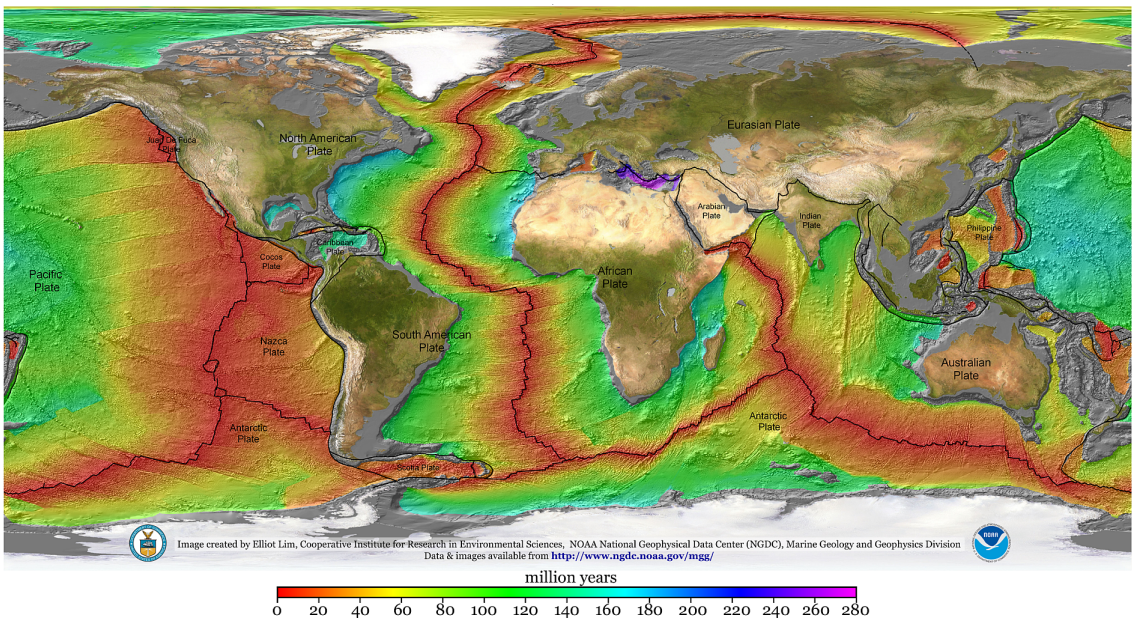

Fig. 5.7.: Age of the oceanic plates, from 0 (red) to 280 Ma (violet); from *Mueller et al.* [2008].

exhibits a relatively small response in comparison with other factors, e.g. water content (cf. Sec. 5.1).

The crust is commonly subdivided into continental and oceanic crust, accounting for the difference in composition (examined in the next paragraphs). Continental crust is usually thicker and older than oceanic crust, because oceanic crust is constantly recycled between mid-ocean-ridges (MOR) and subduction zones and rarely gets older than 280 million years (cf. Fig. 5.7).

The composition of the crust

The Earth's continental crust contains a high amount of silica and aluminium and possesses a more felsic (or granitic) composition, in contrast to the more mafic (or basaltic) oceanic crust possessing a higher proportion of magnesium and calcium [*Rudnick and Gao*, 2003] (cf. Tab. 5.2). Close to the surface, both types of crust comprise a high amount of porous rocks, for which the measured electric conductivity is a combination of host matrix and contained fluid content (cf. Sec. 5.1.1). *In situ* EM investigation, barring marine experiments, that deal with structures at crustal depth are in most cases dominated by electrolytic conduction of fluids in a porous medium. Furthermore, fluids not only affect the bulk conductivity of a region through its inherent electrolytic conduction, but also by facilitating enhanced heat transport, e.g. through circulation of fluids along fault planes *Pous et al.* [1999].

Besides electrolytic conduction of fluids, electronic conduction in ore bodies and graphite or sulphide bearing oxides (Sec. 5.1.2) is of major importance for the conductivity at

Compound	Formula	Whole crust (A)	Oceanic (B)	(C)	Continental (D)	(E)	(F)
Silica	SiO_2	59.71	47.8	63.3	58.0	57.3	60.6
Alumina	Al_2O_3	15.41	12.1	16.0	18.0	15.9	15.9
Lime	CaO	4.90	11.2	4.1	7.5	7.4	6.4
Magnesia	MgO	4.36	17.8	2.2	3.5	5.3	4.7
Sodium oxide	Na_20	3.55	1.31	3.5	3.7	3.1	3.1
Iron(II) oxide	FeO	3.52	9.0	7.5	3.5	9.1	6.7
Potassium oxide	K_2O	2.80	0.03	1.5	2.9	1.1	1.8
Iron(III) oxide	Fe_2O_3	2.63	-	-	1.5	-	-
Water	H_2O	1.52	1.0	-	0.9	-	-
Titanium dioxide	TiO_2	0.60	0.59	0.8	0.6	0.9	0.7
Phosphorus pentoxide	P_2O_5	0.22	-	-	-	-	0.1
Manganese oxide	MnO	-	-	0.14	-	-	-

Tab. 5.2.: Models of the Earth's crust bulk composition, in weight-percent (major elements >0.01%). A: [*Clarke*, 1889]; B: [*Elthon*, 1979], C: [*Condie*, 1982], D: [*Taylor and McLennan*, 1985] (Andesite model), E: [*Taylor and McLennan*, 1985] (Theoretical model) in *Anderson* [2004], F: *Rudnick and Gao* [2003].

crustal depth. Massive ore bodies and interconnected sulphide and graphite phases in shear zones can result in a vast increase of local conductivity at crustal depth, e.g. a conductivity of approximately 2 – 5 S/m is inferred for the North American Central Plains conductivity anomaly (NACP) [*Jones and Craven*, 1990] and conductivities of less then 1 Ωm are inferred by *Korja et al.* [1996] for the Lapland Granulite Belt. As for fluid phases in rock matrices, extension and connectivity of the conducting phase in an ore body is a fundamental factor (cf. Fig. 3.5). The effect of pressure on the conductivity of the Earth's crust, in the absence of temperature changes, is mainly due to resulting changes in connectivity of a good conductor in its host medium, namely (i) closing fractures, (ii) changing the geometry of dry and fluid saturated porous media, or (iii) connecting areas with a high content of water or metal [e.g. *Brace et al.*, 1965; *Duba*, 1976; *Shankland et al.*, 1997; *Wanamaker and Kohlstedt*, 1991]. Such effects are highly dependent on the configuration of the composite structure and therefore extremely non-linear and localised.

5.2.2. The Earth's mantle

The Earth's mantle describes the zone between the Moho and core–mantle boundary (CMB) at approximately 2890 km, which is further divided into upper mantle, mantle transition zone (MTZ), and lower mantle according to their chemical and rheological properties. Moreover, the upper mantle is commonly subdivided by the so-called lithosphere–asthenosphere boundary (LAB) into a lithospheric part (also referred to as *uppermost mantle*) and an asthenospheric part, referring to the rheological strong and weak layers, respectively. Except for extraordinary regions like MOR's, the LAB is situated in

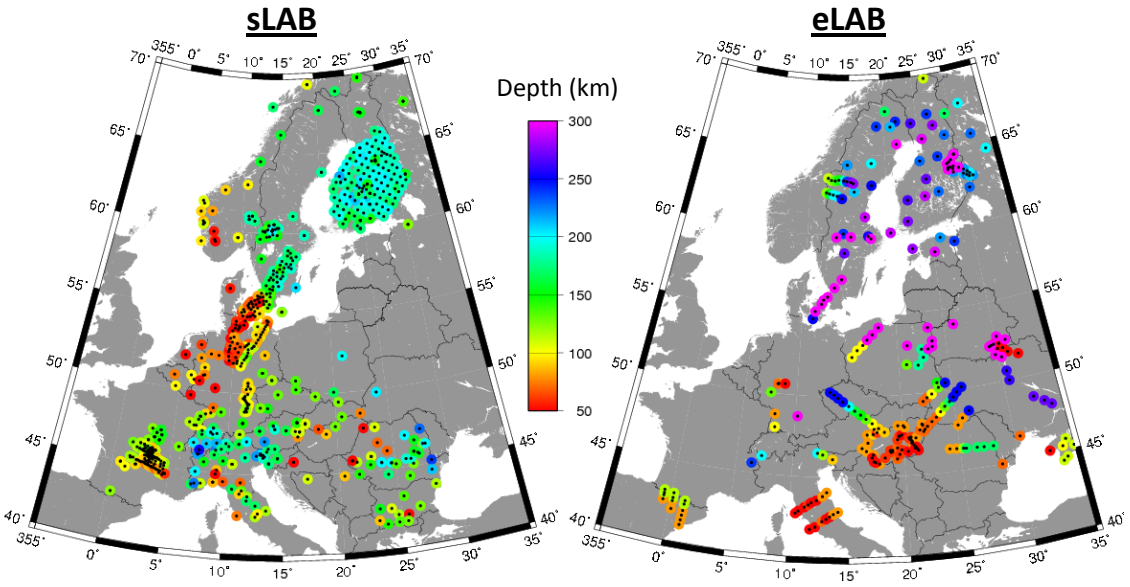

Fig. 5.8.: Depth of the lithosphere-asthenosphere boundary (LAB) beneath Europe, defined in terms of seismic anisotropy observed with teleseismic body waves (sLAB) and in terms of electric conductivity observed with magnetotellurics (eLAB). Figure taken from *Jones* [2009] using seismic data from *Babuska and Plomerová* [2006] and magnetotelluric data from *Korja* [2007].

the upper mantle at depth usually within the range 50 to 160 km; in cratonic regions the LAB can reach significantly greater depth, as much as 250 km [*Eaton et al.*, 2009]. Depth estimates of the LAB for the same region may vary between different geophysical methods. Different LAB depths have been reported for example for Europe by *Babuska and Plomerová* [2006] using teleseismic body waves and by *Korja* [2007] using magnetotellurics (Fig. 5.8). This discrepancy might originate from different definitions of the LAB in terms of the related property, i.e. changes in mechanical properties, electric conductivity, seismic velocity, temperature gradient, or anisotropy (seismic and electromagnetic) [e.g. *Eaton et al.*, 2009, and references therein] (Fig. 5.9). The discussion about the LAB thickness evoke the question of whether the LAB is indeed a sharp boundary or rather a smooth transition zone with considerable vertical extent [e.g. *Cavaliere and Jones*, 1984; *Praus et al.*, 1990; *Jones*, 1999; *Artemieva*, 2009; *Eaton et al.*, 2009; *Jones*, 2009; *Meier et al.*, 2009]. Discrepancies between the depth estimates of the LAB from different methods might therefore result from their varying sensitivity to different properties, which are located at the top, bottom, or within the LAB. In EM induction studies (presuming that the data possess an adequate period range) the LAB can be identified as a significant reduction in resistivity, i.e. from values between $10^3 - 10^4\,\Omega$m to values as low as $5 - 25\,\Omega$m [*Eaton et al.*, 2009]. However, such low resistivity values are not in agreement with predictions by integrated petrophysical modelling [e.g. *Fullea et al.*, 2011], which propose a relatively smooth transition from lithospheric mantle values ($10^3 - 10^4\,\Omega$m) to values around 100 Ωm that are related to the asthenosphere (Fig. 5.10). Three groups of explanations for the discrepancy between EM induction studies and laboratory studies, which

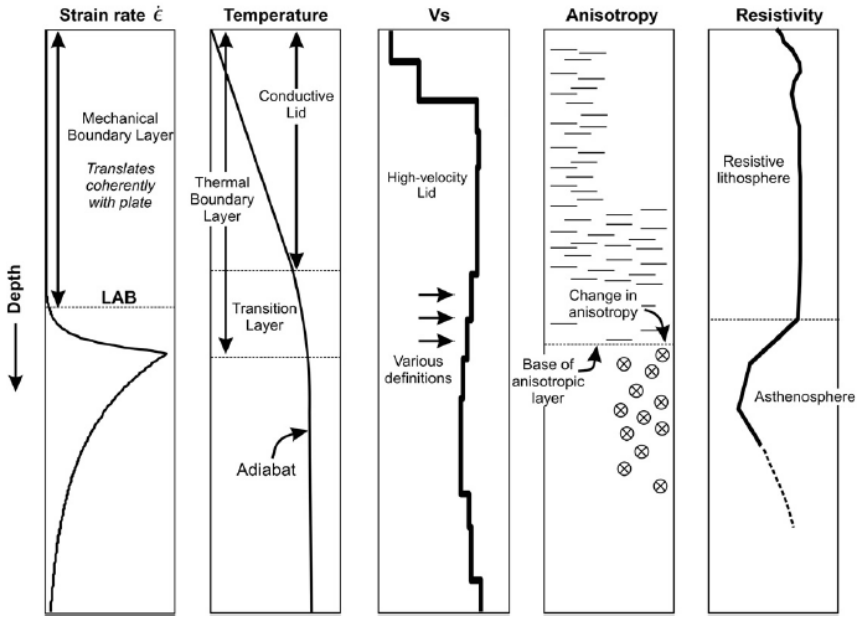

Fig. 5.9.: Definition of the lithosphere and common proxies used to estimate its thickness, i.e. the depth of the lithosphere–asthenosphere boundary (LAB); from *Eaton et al.* [2009]. The lithosphere forms, in the classical meaning, a mechanical boundary layer with the LAB defined as the top of a zone of decoupling between the lithosphere and asthenosphere, marked by an increased strain rate. The thermal boundary layer (TBL), containing a conductive lid and a transition layer, represents a near-surface region where temperature deviates from adiabatic behaviour. A zone of low seismic shear-wave velocity (V_s) is sometimes detected beneath a high velocity lid whereby various definitions have been used to correlate this zone with the LAB. The LAB may also correlate with a downward extinction of seismic anisotropy or a change in the direction of anisotropy. A significant reduction in electric resistivity at the electrical LAB is inferred from EM induction studies [*Eaton et al.*, 2009].

are the base for the integrated petrophysical modelling, can be conceived:

hypotheses A: results of EM induction studies are erroneous,

hypotheses B: results of laboratory studies are erroneous,

hypotheses C: results of EM induction as well as laboratory studies are correct; the discrepancy is due special characteristics of a layer in the uppermost asthenosphere.

A description of causes for each of the three hypotheses is given in the paragraphs below.

Hypotheses A: the asthenosphere exhibits a high degree of electric anisotropy due to relative motion between lithosphere and asthenosphere, “dragging along” and aligning material at the LAB (cf. Sec. 4.1.3). The electric anisotropy causes a misinterpretation of responses from EM induction studies that did not adequately consider its effects.

Hypotheses B: laboratory studies, base of the petrophysical modelling, are carried out in the very most cases on single crystal samples. The contribution of surface conduction along grain boundaries may increase the bulk conductivity for the respective regions,

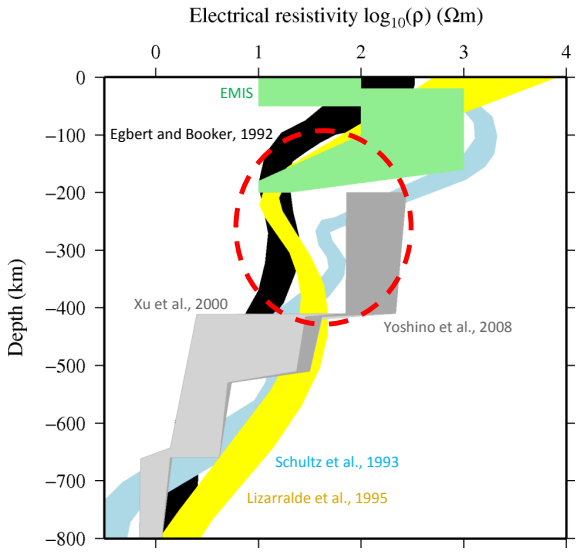

Fig. 5.10.: Compilation of resistivity–depth profiles derived by deep-probing electromagnetic (EM) induction studies (MT, GDS) and laboratory experiments on mantle minerals. The dashed red oval indicates the region related to the upper mantle, for which significant difference between EM induction studies and laboratory experiments is observable. light-green shaded area: common resistivity range for deep-reaching EM induction studies in (not tectonically active) regions, cf. e.g. *Eaton et al.* [2009]; black shaded area: thin lithosphere and partial melt-bearing mantle region beneath the western US [*Egbert and Booker*, 1992]; yellow shaded area: stable Archean craton region in the south-central part of the Canadian Shield (Superior Province) [*Schultz et al.*, 1993]; light-blue shaded area: oceanic setting in the Northeastern Pacific region [*Lizarralde et al.*, 1995]; light-grey shaded area: range of laboratory results with most conductive values derived by *Xu et al.* [2000a] and most resistive values derived by *Yoshino et al.* [2008] for a relatively dry mantle (water content $\leq$ 0.1 wt.%).

resulting in a shift of theoretical curves towards more conductive values. *ten Grotenhuis et al.* [2004] derived an inverse relation between bulk conductivity and grain size of a region, proposing that upper mantle shear zones can exhibit a conductivity increase of 1.5 – 2 orders of magnitude in respect to less deformed lithospheric regions. The relative motion between lithosphere and sublithospheric-mantle can potentially yield a similar fine grained region, which facilitates a local conductivity increase.

Hypotheses C: the increased conductivity of the uppermost asthenosphere region is due to special properties of the layer that are not considered by laboratory studies. If those special properties are restricted to the related depth range and reduction of conductivity occurs below the asthenosphere, EM induction studies would meet the results of laboratory studies for subjacent regions. Potential properties (presuming a significant amount) that can facilitate high conductivity values at that depth: (i) partial melt (small fractions of, particularly carbonotite, melts can significantly reduce the resistivity [e.g. *Gaillard et al.*, 2008; *Yoshino et al.*, 2010]), originating from shear processes along the LAB, (ii) hydrogen, originating from dehydration of subducting slabs, (iii) a refertilised mantle. Certainly, such anomalous properties require special settings of related processes and a global extend is therefore unlikely. Additional long-term EM induction studies are required to investigate existence of the electric asthenosphere in different regions of the

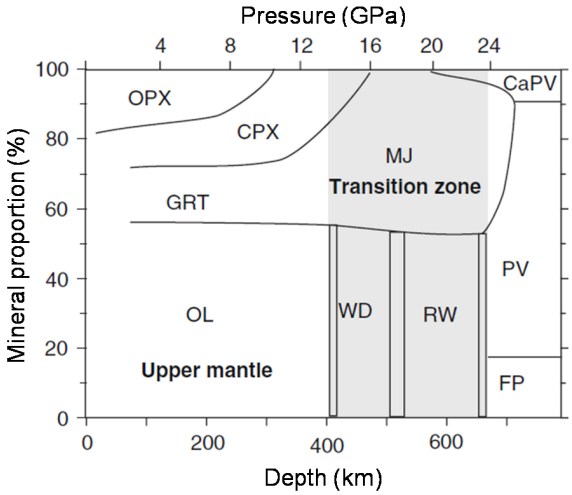

Fig. 5.11.: Mineral proportions and phase transitions in the Earth's mantle assuming pyrolitic composition, with the shaded areas indicating the mantle transition zone between the 410 and 660 km discontinuities; from *Yoshino* [2010]. PX: pyroxene, OPX: orthopyroxene, CPX: clinopyroxene, GRT: garnet, MJ: majorite garnet, OL: olivine, WD: wadsleyite, RW: ringwoodite, FP: ferro-periclase (magnesiowüstite), PV: silicate perovskite, Ca-PV: Ca-perovskite.

world. Such studies would enable investigators to evaluate the hypotheses of a laterally confined anomalous region by comparing the EM induction results with findings from other methods, and in the long run to aid the merging of data from induction and laboratory studies in the depth range of the LAB. Until then, exact electrical properties of the upper asthenosphere will remain controversial.

Below the LAB, *Xu et al.* [2000a] infer an increase in resistivity at around 300 km depth, coinciding with the disappearance of orthopyroxene (opx) in favour of clinopyroxene (cpx) proposed for a pyrolitic bulk composition [*Ringwood*, 1975; *Irifune and Ringwood*, 1987] (cf. Fig. 5.11), due to the relatively higher resistivity of cpx derived in laboratory experiments [*Xu and Shankland*, 1999]. However, in global seismic models no discontinuity is inferred for this depth, raising the question about sharpness of this boundary, and its lateral extent. This finding supports the idea that the replacement of opx by cpx takes place within a broader zone, and potentially, regionally at different depth ranges.

The MTZ is located in the depth region between approximately 410 km and 670 km with its boundaries electromagnetically defined by increases of conductivity, commonly attributed to phase changes of olivine to its high-pressure polymorph wadsleyite, and from ringwoodite to perovskite. Today, the existence of an additional phase change from wadsleyite to ringwoodite is widely accepted and considered to occur at a depth of around 510 km. Exact composition of the MTZ and nature of its boundaries are still the subject of ongoing debate (cf. Secs. 5.2.2 and 5.3).

MTZ conditions are of particular interest for geophysical studies as the MTZ plays an important role in Earth convection models. The MTZ can provide a restraint and aggre-

gation zone for rising hot mantle material (plumes) originating at the CMB, as well as for descending crustal material subducted from the Earth's surface. Subducting slabs, for instance, may be horizontally deflected in the MTZ and become dehydrated before continuing to sink into the lower mantle [*Richard and Bercovici*, 2009]. This implies reduced water content in the lower mantle, affecting local composition, density, and temperature conditions. Permeability of the MTZ, hence characteristics of its interaction with such vertical transport mechanisms, is highly dependent on its conditions [e.g. *Davies*, 1995; *Karato et al.*, 1995; *Jin et al.*, August, 2001; *Karato et al.*, 2001].

The composition of the Earth's mantle

Two classic models exist for the composition of the mantle: pyrolytic (transformation of the compounds caused by heat) and piclogitic (*pic*ritic ec*logite*). In pyrolytic mantle models, the chemical difference between the upper and lower mantle is assumed negligible and differences within the mantle are attributed to mineral phase changes, whereas in piclogitic mantle models a more silica-(and iron-)rich lower mantle is proposed. Pyrolytic models are in good agreement with measured data and are favoured by the majority of authors [e.g. *Ringwood*, 1975; *Poirier*, 2000; *Xu et al.*, 2000a]. Recent support for the pyrolytic model was provided, for example, by the results of *Matas et al.* [2007] proposing that the Earth's mantle is most likely relatively homogeneous. The authors state that the lower mantle must have an average Mg–Si ratio lower than 1.3 in order to satisfactorily fit 1D seismic profiles. Moreover, *Matas et al.* [2007] claim that when a low value for the pressure derivative of the shear modulus for perovskite is adopted ($\mu_0^{'} \approx 1.6\,\mathrm{GPa/km}$), consistent with the most recent experimental results, the Mg–Si ratio of the bottom part of the lower mantle reduces to a value close to 1.18, thus denoting a more homogeneous mantle composition.

The composition of the Earth's mantle can either be derived directly from rock samples transported from the lithospheric-mantle to the surface as kimberlitic or volcanic xenoliths, or indirectly through interpretation of geophysical measurements. As a result of those measurements it is inferred that olivine, clinopyroxene, orthopyroxene, garnet, and perovskite are the most common minerals in the Earth's mantle (cf. Fig. 5.11, and Tabs. 5.3 and 5.4). Olivine and its high-pressure polymorphs (wadsleyite, ringwoodite) form the most abundant minerals by volume (50 – 60 %) in the upper mantle, thus dominating its bulk electric conductivity, whereas perovskite and magnesiowüstite account for the majority of the lower mantle minerals [e.g. *Ringwood*, 1975; *Xu et al.*, 2000a].

In the absence of areas with well-connected networks of fluids, ion conductors, or partial melt, the electric conductivity of the mantle is dominated by semiconduction (Sec. 5.1.3), therefore the conductivity of the mantle is mostly controlled by temperature (Eq. 5.9, Sec.5.3). Exact values of conductivity are dependent on specific parameters of the related materials and their fraction of the local composition. Conductivity of mantle minerals is primarily controlled by proton (H^+) and small polaron conduction (electron holes "hopping" between Fe^{2+} and Fe^{3+}) [*Xu et al.*, 1998a; *Yoshino et al.*, 2008; *Yoshino*, 2010]

Species	Whole-mantle models (1)	(2)	(3)	Upper mantle (4)
Olivine	47.2	36.5	37.8	51.4
Orthopyroxene	28.3	33.7	33.2	25.6
Clinopyroxene	22.5	16.8	13.6	11.65
Garnet	1.53	11.6	14.2	9.6
Ilmenite	0.2	0.5	0.24	0.57
Chromite	-	1.6	0.94	0.44

Tab. 5.3.: Earlier models of mantle mineralogy, 1: Equilibrium condensation [*BVP-Project*, 1981], 2: Cosmochemical model [*Ganapathy and Anders*, 1974], 3: Cosmochemical model [*Morgan and Anders*, 1980], 4: Pyrolite [*Ringwood*, 1977]; in *Anderson* [2004]. Polymorph phases of olivine and lower mantle minerals (perovskite and magnesiowüstite) are not considered in these earlier mantle models (cf. Fig. 5.11 and Tab. 5.5).

Name	Formula
Olivine	$(Mg,Fe)_2SiO_4$
Orthopyroxene	$(Mg,Fe)_2Si_2O_6$
Clinopyroxene	$(Ca,Na)(Mg,Fe,Al,Ti)(Si,Al)_2O_6$
Garnet	$(Ca,Al,Mg)_3(Al,Fe_{3+},Cr)_2(SiO_4)_3$
Ilmenite	$FeTiO_3$
Chromite	$FeCr_2O_4$
Perovskite	$CaTiO_3$
Magnesiowüstite	(Mg,Fe)O

Tab. 5.4.: Typical mantle rocks and there chemical formula; polymorph phases of olivine are wadsleyite and ringwoodite.

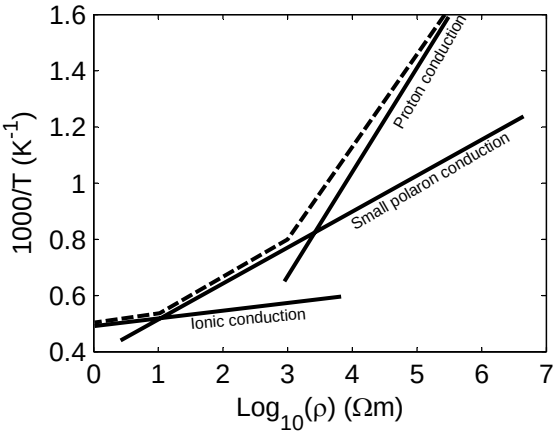

Fig. 5.12.: Conductivity of hydrogen-iron bearing mantle silicate minerals; redrawn from *Yoshino* [2010]

Mineral	σ_{0_H} (S/m)	H_H (eV)	σ_{0_P} (S/m)	H_P^0 (eV)	α
Wadsleyite	399(311)	1.49(10)	7.74(4.08)	0.68(3)	0.02(2)
Ringwoodite	838(442)	1.36(5)	27.7(9.6)	1.12(3)	0.67(3)

Tab. 5.5.: Parameter values for wadsleyite and ringwoodite derived in lab studies by *Yoshino et al.* [2008]. Numbers in parentheses denote the errors determined through nonlinear least squares fitting (1 σ standard deviation).

(Fig. 5.12). One of the most recent formulation for the relationship between mantle mineral semiconduction and its controlling parameters was given by *Yoshino et al.* [2008]. The authors extended earlier formulations by taking into account the influence of both the intrinsic and the extrinsic conductivity, as well as the effect of water onto the extrinsic term:

$$\sigma = \sigma_{0_H} \exp\left(-\frac{\Delta H_H}{k_B T}\right) + \sigma_{0_P} C_w \exp\left(-\frac{\Delta H_P^0 - \alpha C_W^{1/3}}{k_B T}\right) \tag{5.11}$$

with C_W: water content in wt%, α: fitting factor, and subscripts H and P denoting small polaron (hopping) conduction and proton conduction, respectively. Parameter values for the olivine high-pressure polymorphs wadsleyite and ringwoodite, derived by the authors by fitting measured laboratory data to Equation 5.11, are given in Table 5.5. Conductivity of the individual mantle materials, their specific parameters, and relation to pressure, temperature, and fluid content are examined in more detail in Section 5.3.

5.2.3. The Earth's core

The Earth's core is situated beneath the CMB at around 2890 km depth, down to the centre of the Earth, approximately 6378 km from the Earth's surface. The core is subdivided into a liquid outer core and a solid inner core. The existence of a solid inner core was first proposed by Inge Lehmann in 1936, using the observations of seismic waves caused

Element	Formula	Composition
Iron	Fe	88.8
Nickel	Ni	5.8
Sulphur	S	4.8

Tab. 5.6.: Composition of the Earth's Core; from *Morgan and Anders* [1980].

by the large earthquake near New Zealand in 1929. This hypothesis was subsequently supported by various authors [e.g. *Gutenberg and Richter*, 1938; *Jeffreys*, 1939; *Birch*, 1952; *Jacobs*, 1953] before it became widely accepted in 1971 when *Dziewonski and Gilbert* published the results of their studies on normal mode vibrations of the Earth due to large earthquakes.

The composition of the core

The Earth's core consists mainly of iron with a smaller amount of nickel and sulphur, and is most likely a Fe-FeS alloy [*Morgan and Anders*, 1980; *Sherman*, 1995]. Lab studies, intended to determine the composition of the Earth's core, suffer from the requirement to reproduce the P-T conditions; i.e. 140 – 360 GPa and 4000 – 7000 K [*Dubrovinsky and Lin*, 2009]. Therefore, type and proportion of minor constituents are still under debate; the presence of silicon, oxygen and sulphur is suggested by mineral physics studies [*Badro et al.*, 2003] (cf. Tab. 5.6). Due to the high amount of metallic components, the conductivity of the Earth's core is dominated by electronic conduction. Electric properties of the Earth's core cannot be investigated with the MT or GDS method due to its enormous distance from the Earth's surface where measurements are made [e.g. *Xu et al.*, 2000a]. Despite its high content of conductive material, recording times of several decades are needed to identify signals of the Earth's core in MT data [*Rikitake*, 1952]. Furthermore, any data with sufficiently long periods to detect the boundary of the core would suffer from the very short induction depth caused by the high conductivity of the materials within, making investigations of the core's internal structure virtually impossible (cf. Section 3.3 for details on induction depth). Therefore, investigations of the Earth's core are usually limited to Geodynamic modelling [e.g. *Glatzmaier and Roberts*, 1995; *Glatzmaier*, 2002; *Turcotte and Schubert*, 2002].

5.3. Parameters controlling the conductivity of the Earth's mantle

Conductivity variations in the Earth's mantle (Sec. 5.2.2) are, besides changes in composition, mainly due to changes in pressure, water content, and especially temperature. Modern estimates of temperature–depth and pressure–depth profiles are considered rea-

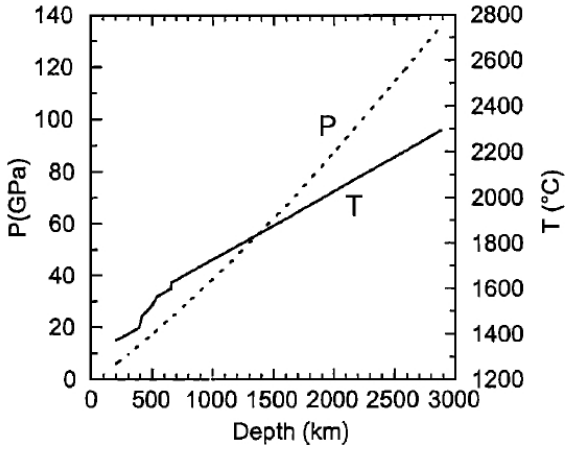

Fig. 5.13.: Pressure and temperature profiles in the depth range 200 – 2800 km; from *Xu et al.* [2000a].

sonably accurate (cf. Figs. 5.1, 5.11, 5.13), thus these two parameters are commonly used as depth proxies during studies investigating the electric conductivity of materials within the Earth. Effects of pressure, temperature, and water content on the electric conductivity of materials within the Earth are often coupled, e.g. in cases of material phase changes, taking place once a certain point in the pressure-temperature (P-T) space is reached. Local water content affects the P-T conditions required for the phase change, and in turn are altered during the phase change due to hydration or dehydration (e.g. partial melting, graphitisation, or serpentinisation).

Various lab studies have been carried out in the past in order to derive electric conductivity and its dependence on different parameters, such as temperature, pressure, and water content (see *Yoshino* [2010] for a review about relevant studies). However, in 1976, *Duba* showed that failing to control oxygen fugacity (f_{O_2}) and to assure that samples reach equilibrium can mask the effects of temperature and pressure. In the Earth, time and f_{O_2} are not as important, since time is usually sufficient for most chemical reactions to attain equilibrium and f_{O_2} is controlled within narrow limits by the phases present. In lab studies, on the other hand, most experiment are performed in a time-frame of hours therefore time and f_{O_2} effects need to be considered. Not taking into account time-dependent effects, such as the order-disorder phenomenon in silicates, can seriously bias obtained results [*Duba*, 1976]. For example, it was shown through experiments by *Piwinskii and Duba* [1974] that the conductivity of albite, the sodic end member of plagioclase, increases with time and becomes equal to the conductivity of molten albite. In addition to silicates, some minerals exhibit time-dependent changes once they reach a certain P-T ratio, e.g. pyroxene undergoes large irreversible time-dependent conductivity changes outside its P-T stability field [*Duba et al.*, 1973, 1976]. Moreover, some indications of variation with time were found for olivine at temperatures above 1500 °C [*Duba et al.*, 1974]. Failing to control the effect of oxygen fugacity, on the other hand, can lead to differences in results for olivine conductivity by four orders of magnitude [*Duba*, 1976, and references within].

Sample	Pressure (GPa)	Temperature (°C)	Conductivity (S/m) $\log(\sigma_0)$	σ_0	Activation enthalpy (eV)	Activation volume (cm^3/mol)
ol	4-10	1000-1400	2.69±0.12	490	1.62±0.04[b]	0.68±0.14
opx	5	1000-1400	3.72±0.10	5248	1.80±0.02	
cpx	13	1000-1400	3.25±0.11	1778	1.87±0.02	
il + gt	21	1200-1500	3.35±0.18	2239	1.66±0.03	
Al /pv	25	1400-1600	1.12±0.12	11	0.62±0.04	-0.1[c]
Al + pv	25	1400-1600	1.87±0.11	74	0.70±0.04	-0.1[c]
mw	10	1000-1400	2.69±0.10	490	0.85±0.03	-0.26[c]

Tab. 5.7.: Activation enthalpies and pre-exponential factors for typical mantle materials (assuming the contribution of extrinsic semiconduction to be negligible); after *Xu et al.* [2000a]. Values for wadsleyite and ringwoodite have been removed from the original table, because *Huang et al.* [2005] identified a significant amount of water in samples used by *Xu et al.* [1998a] which was not taken into account for in the original publication. Revised values for wadsleyite and ringwoodite are given in Table 5.5. References for the different materials are taken from: *Xu et al.* [2000b] olivine (ol); *Xu and Shankland* [1999] orthopyroxene (opx), clinopyroxene (cpx), and ilmenite phase plus garnet (il + gt); *Xu et al.* [1998b] Aluminium-free and Aluminium-bearing silicate perovskite (al + pv, al /pv); *Xu et al.* [2000a] magnesiowüstite (mw). [b]: This value refers to the activation energy instead, [c]: Values from *Shankland et al.* [1993]. Graphs for the different minerals are shown in Figure 5.14.

Since these findings by *Duba* [1976], many laboratory studies use a special furnace in which the f_{O_2} is controlled through passing a mix of CO and CO_2 at atmospheric pressure across the sample and by the use of molybdenum shields and electrodes [e.g. *Constable et al.*, 1992, and references within]. In addition, pyroxene is added to olivine sample tests to buffer silica activity [*Xu et al.*, 1998a, 2000a]. Despite these improvements, laboratory σ-temperature studies still suffer from instrumental limitations as high temperature conductivity measurements are difficult to carry out on polycrystalline materials. Therefore, most reliable measurements above 1100,°C are made on single-crystal specimens [*Constable et al.*, 1992].

Recently, a lot of effort is spend on determining activation energy, temperature and water dependence of mantle materials using single-crystal samples to draw conclusions about their distribution in the mantle; a thorough overview about methodology and results of these lab studies is given in the review paper by *Yoshino* [2010]. In his review on electric properties of crustal and mantle rocks, *Nover* [2005] provides a range for the activation energy, namely 1 – 1.5 eV, referring to experiments by different authors (see references therein). Not included by *Nover* [2005] are the findings by *Xu et al.* [1998a], which determine an activation energy of 1.62 eV and an activation volume of 0.68 cm^3/mol for a San Carlos olivine sample, which is consistent with earlier results of *Constable et al.* [1992]. An overview about typical mantle materials and their values of activation energy, activation volume and pre-exponential factors are given in Table 5.7. *Yoshino et al.* [2008] revise earlier results by *Xu et al.* [2000a] and *Huang et al.* [2005], claiming these earlier results to be biased because of unconsidered contamination of the samples with water (*Xu et al.* [2000a]) and "serious methodological problems" (*Huang et al.* [2005]). *Yoshino et al.* [2008] formulate an equation for the conductivity that takes into account the effect of proton (H^+) and small polaron hopping (Fe^{+3}–Fe^{+2}) conductivity as well as

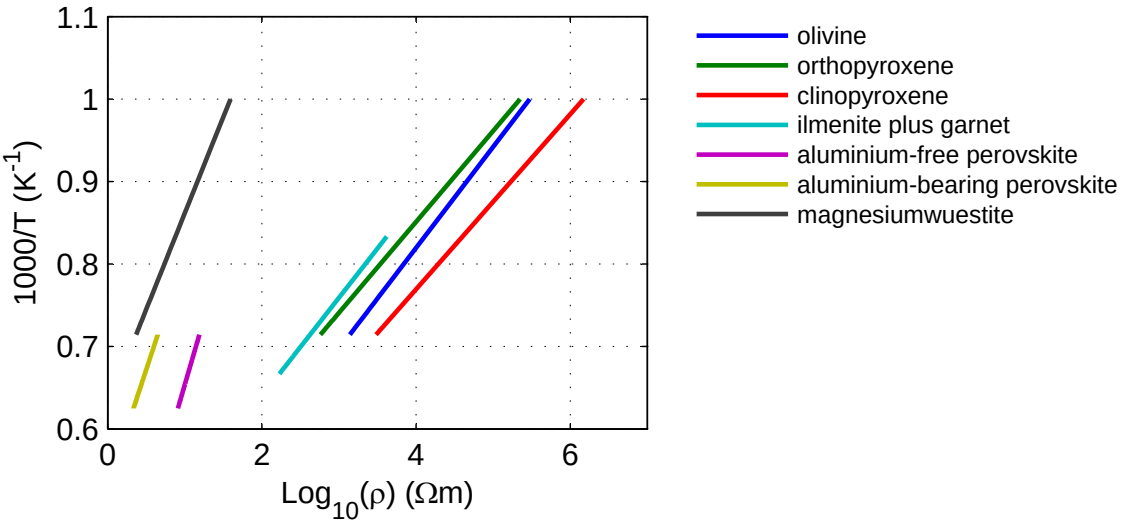

Fig. 5.14.: Conductivity – temperature profiles for typical mantle minerals using an Arrhenius-like relationship (Eq. 5.9 with the assumption that contribution of proton conduction is negligible); see Table 5.7 for references regarding mineral parameters.

the effect of water onto the small polaron conductivity (Eq. 5.11, Fig. 5.15). Through their experiment *Yoshino et al.* [2008] could show that the mantle transition zone (MTZ, Sec. 5.2.2) has to be essentially dry and that changes of conductivity in the MTZ can be adequately described by transformation of olivine into its high-pressure polymorphs wadsleyite and ringwoodite. However, they admit that the MTZ cannot be proven to be entirely dry, since water content of less than 0.1 wt% cannot be adequately resolved for the normal geotherm. This is due to fact that at MTZ temperatures the contribution of proton conduction is masked by small polaron conduction owing to the higher activation enthalpy of the latter [*Yoshino et al.*, 2008]. Whereas exact parameters of pre-exponential factors and activation energies are still under debate, wide agreement exists regarding general relations between mantle material conductivity and the dominant controlling parameters, temperature, pressure, and water content. A short summary about the relations is given in the following paragraphs.

Temperature Temperature is the dominating factor of electric conductivity within the Earth's mantle due to the exponential relationship between semiconduction and temperature (Eq. 5.9 and 5.11). The σ–T relation is dependent on the temperature, which determines whether the intrinsic or extrinsic component of semiconduction is the dominant mechanism in charge transport (cf. Fig. 5.4). The transition from extrinsic to intrinsic transport is material specific, e.g. for wadsleyite it is derived to takes place at approximately 1500 °C [*Yoshino et al.*, 2008], whereas for olivine it does not occur before 1400 °C [*Constable et al.*, 1992].

Pressure The effect of pressure on the electric conductivity of the most abundant mantle materials is smaller than the effects of temperature or fluid content; the σ-dependence on pressure is small for olivine, its effect over an 800 MPa range is less than a temperature change of 5 °C at temperatures between 1270 and 1440 °C [*Shankland*, 1975]. The conductivity of the MTZ minerals wadsleyite and ringwoodite appears to be virtually independent of pressure [*Xu et al.*, 2000a]. This finding may be biased, because these minerals are only stable over a narrow pressure interval, i.e. in the thin layer between top and bottom of the MTZ. As a first order approximation, used in PREM (Fig. 5.1), pressure increases in the mantle by around 47.5 MPa/km, yielding an approximate pressure difference for the MTZ of only 12 GPa. However, this model certainly does not take into account local pressure changes due to material composition or phase changes within the mantle.

Water content *Yoshino et al.* [2008] formulated an equation for the relation of Earth's mantle electric conductivity onto different parameters that included the effect of water content C_w in minerals (Eq. 5.11). The formulation proposes a linear as well as an exponential dependence of σ on C_W for the semiconduction in olivine and its high-pressure polymorphs wadsleyite and ringwoodite. However, due to instrumental limitations, precise laboratory studies are very difficult at present and results are still under debate [*Yoshino*, 2010].

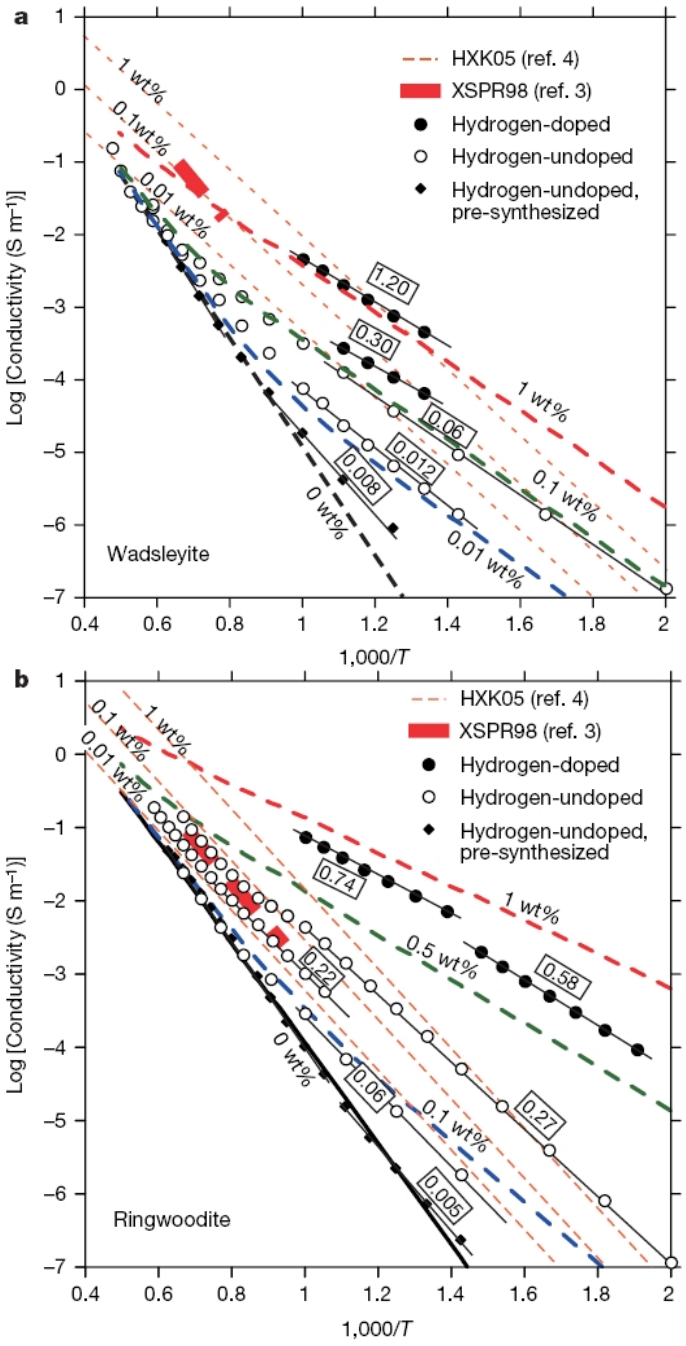

Fig. 5.15.: Electric conductivity of wadsleyite and ringwoodite as a function of reciprocal temperatures in the range 500 – 2500 °C. a: Wadsleyite; b: ringwoodite. The symbols indicate raw data for each sample with different water contents. Results from *Xu et al.* [1998a] and *Huang et al.* [2005] are shown as a function of water content. Coloured thick dashed lines indicate the electric conductivity calculated by data fitting based on equation 5.11 as a function of water content. Numbered boxes denote the estimated water content (in weight percent) by Fourier-transform infrared analysis. Errors for the estimated water content become larger with decreasing water content and range from ±20 (≈1 wt%) to ±50% (<0.01 wt%); from *Yoshino et al.* [2008].

6 Using magnetotellurics to gain information about the Earth

In order to investigate the Earth's subsurface with magnetotellurics (MT), time-series data of the natural electromagnetic (EM) variations, described in Section 2, are recorded at the surface above the area of interest. Advanced instrumentation and installation procedures are used in order to enhance quality of recorded data, which in turn determine the grade of all subsequent steps.

Processing of the recorded electric and magnetic field data involves transformation from the time domain into the frequency domain and deduction of electric impedance. During the impedance deduction, different processing schemes, such as remote reference and robust processing, are used to enhance impedance estimate quality.

In MT investigations, impedance estimates (or the related apparent resistivity and phase) allow for derivation of a subsurface structure distribution, using forward modelling and inversion algorithms. Application of forward modelling and inversion algorithms is computationally very expensive and various schemes have been proposed to lower computational load and to speed up the process. Commonly used schemes hold advantages and disadvantages, and the choice of a scheme usually depends on computational facilities, the characteristics of the problem, and the personal preference of the investigator.

6.1. Recording of magnetotelluric signals

6.1.1. Instrumentation

Since the beginning of MT investigation in the early 1950's [*Tikhonov*, 1950; *Cagniard*, 1953] multiple advances have been made to the initial systems and today a variety of instruments are available. During the PICASSO Phase I fieldwork campaign in Spain, two different types of instruments were used: The Phoenix broadband MTU-5 recording system [*Phoenix Geophysics*, 2005] with 1.41 m long MTC-50 induction coils and the

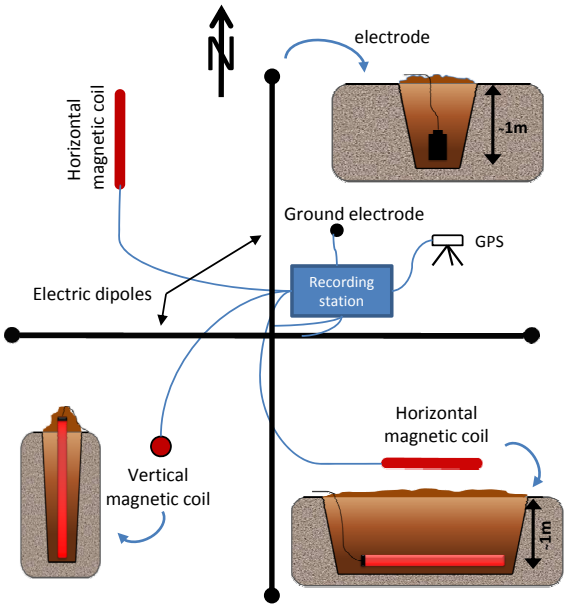

Fig. 6.1.: Schematic layout of the broadband magnetotelluric (MT) recording system used during the PICASSO Phase I fieldwork campaign; see Section 6.1.2 for details.

Lviv long-period LEMI-417M recording system [*Lviv Centre of Institute for Space Research*, 2009]. For the measurement of the electric field, Phoenix Geophysics and WOLF Pb-$PbCl_2$, as well as Lviv Cu-$CuSO_4$ non-polarising sensors (commonly referred to as *electrodes*) are used with both recording systems. To avoid polarisation effects only electrode pairs of the same material are used during a recording. Time-series data of electric and magnetic fields are stored internally by the two systems and can be transferred onto a computer via a removable solid state disc.

The two different systems are employed to investigate both crustal and mantle structures; the limiting factor of a recording system, regarding depth of investigation, is usually the magnetic sensor. The MTC-50 induction coils are able to record data in the period range $10^{-3} - 5 \cdot 10^{4}$ s whereas the fluxgate magnetometer, used with the Lviv system, is designed to record data with a period length of 30 s and above. The maximum usable period for a MT station is then dependent on recording duration and noise level.

6.1.2. Station setup

A typical layout for a Phoenix broadband MTU-5 recording system and Lviv long-period LEMI-417M recording system is shown in Figure 6.1 and 6.2, respectively. The station setup starts by assigning the location of the electric field measurements. Two pairs of electrodes, each forming an electric dipole, are aligned to geomagnetic north-south and east-west respectively, using a compass. A dipole length of 90 m is usually chosen, however, the length may vary depending on the local environment. In addition, a fifth electrode is installed, acting as protective ground for the main recording unit; in the case

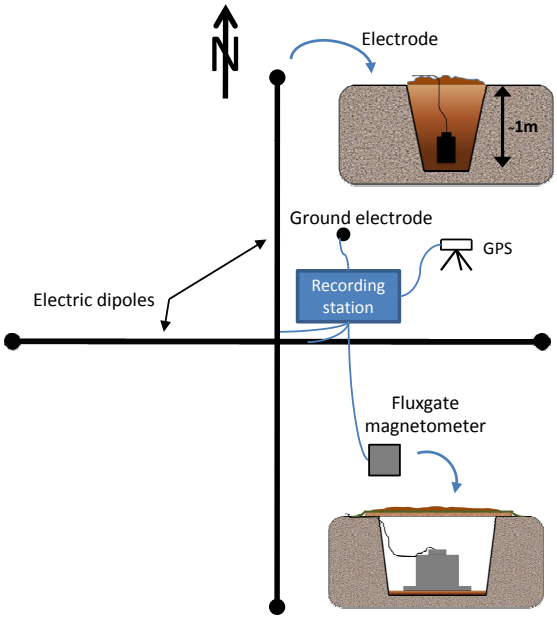

Fig. 6.2.: Schematic layout of the long-period magnetotelluric (MT) recording system used during the PICASSO Phase I fieldwork campaign; see Section 6.1.2 for details.

of the new LEMI-417 design, the fifth electrode can be used as an additional source of information (see Sec. 9.3), requiring it to be located in the centre of the two dipoles. The above-described configuration may vary in certain situations, e.g. when topographic circumstances would force a significant shortening of a dipole in one geomagnetic direction. In such cases, the orientation of the electric dipoles can be rotated; however, the two electric dipoles must remain orthogonal. The electric field can then be derived for an arbitrary horizontal orientation through a simple coordinate transformation (cf. Sec. 4.3).

To prevent polarisation effects due to electric charge build-up along the electrode-ground interface, the metallic electrodes are placed in an electrolytic mud, i.e. Cu-electrodes in a $CuSo_4$ solution and Pb-electrodes in saltwater brine (since exposure to $PbCl_2$ may cause lead poisoning). Electrodes are buried in the ground to protect them from drying-out, human or animal interference, and effects of temperature variation. The ultimate depth is usually limited by ground condition and logistic considerations; a depth of an extended arm-length (approx. 1 m) is considered as a good compromise.

The main difference between the systems, regarding their setup, is the installation of the magnetic sensors, i.e in case of the MTU-5 system, two (three, if the vertical magnetic field is recorded as well) magnetic coil-sensors are installed; whereas, in case of the LEMI-417 system, only one fluxgate magnetometer, recording all three magnetic components simultaneously, needs to be installed. For the MTU-5 system, the two (horizontal) coils are buried in the ground, with the depth controlled by the same factors as the electrode depth and 1 m again assumed an acceptable compromise. The two horizontal coils have to be accurately levelled and aligned to geomagnetic north–south and east–west. As

for the electric dipoles, orthogonality of the sensors is the key property, since the magnetic field can then be derived for an arbitrary orientation through mathematical rotation of the coordinate system. Because the coil-sensors measure only the magnetic flux parallel to the coil's normal orientation, a precise alignment is required.

For the MT method, only the measurements of the horizontal EM fields are required (cf. Sec. 3.2), but an additional vertical magnetic coil is often installed if logistic and ground circumstances permit. Resulting data allow for further investigation of the conductivity distribution using the relation between horizontal and vertical magnetic fields, i.e. the *vertical magnetic transfer function* (also referred to as *tipper*); cf. Sec. 3.2.3. A vertical electric dipole on the other hand is not installed during MT fieldwork, due to the complexity in accomplishing a suitable dipole length (effectively implying to dig a hole of logistically unreasonable depth) and the circumstance that the vertical electric field at the earth-air interface is zero by definition (cf. Sec. 3.4.1). The LEMI-417, unlike the MTU-5, is equipped with a fluxgate magnetometer, which measures the magnetic field in all three directions. Therefore, only one magnetic sensor has to be installed, as opposed to the three of the MTU-5. For the fluxgate sensor, usually only a small hole is required, just big enough to fit the sensor and a base plate. The sensor is then levelled and aligned, and the hole sealed by a firm cover (e.g. a hardboard) and an impermeable layer, to protect it from disturbances by living beings and weather conditions.

Magnetic and electric sensors are connected to the main recording unit of the system, which stores the recorded time-series data and saves it on either an internal drive (MTU-5) or a removable solid-state drive (LEMI-417). The instruments are equipped with internal batteries, but in order to provide sufficient energy for a long recording-duration, external batteries such as car batteries or marine deep cycle batteries are used. A GPS antenna is connected to the main recording unit to determine the location of the recording site and, most importantly, to provide accurate timing information.

As a final step, all cables are buried, to protect them from interference and prevent the generation of EM noise through motion of electric dipoles. Finally, the main unit is covered by a tarpaulin to shield it from rainfall. In practise the layout of both systems can be combined in a *piggyback* sense when recorded at the same location, i.e. electric dipoles are used by both systems, saving time and effort since only one set of electrodes has to be installed.

6.2. Processing of magnetotelluric data

Fundamentally, magnetotelluric (MT) processing involves a transformation of electric and magnetic field time-series data into the frequency domain and deriving the electric impedance of the subsurface as the quotient of the transformed values (cf. Sec. 3). Frequency dependence of the EM wave's induction depth is utilised to gain information about the distribution of electric properties in the subsurface (cf. Sec. 3.3). In principle, the initial impedance estimates could be used for subsequent inversion processes (Sec. 6.3), but

in nearly all cases, it is profitable to apply some type of processing to time-series data in order to enhance the estimate quality. The individual steps along with the different methods of data processing are presented in the following sections.

For the MT method, variation of the magnetic field and the related electric response of the subsurface are used, which are obtained through measurements at the Earth's surface as described in Section 6.1. It should be noted that the electric field is derived from potential difference measurements along an electric dipole of finite length:

$$e(t) = dV(t)/L \tag{6.1}$$

with e: electric field in the time domain (indicated by the character t), dV: potential difference, and L: length of the electric dipole. The circumstance that the electric field is obtained from a potential difference between a finite distance, rather than from a point measurement, can result in a bias of the derived valued (cf. Sec. 4), but measuring along finite distance is inevitable for logistic reasons.

6.2.1. Pre-processing of the time-series data

Initially, the time-series of electric and magnetic fields are corrected for mistakes such as layout errors and bad records within the datasets. The former usually involves only simple mathematical modifications or re-assignment of the dataset vectors:

- For the case of reverse connection of an electric dipole, e.g. connecting the southern electrode to the channel for the northern electrode and vice versa, the correction can be accomplished by simply inverting the sign for all entries in the related dataset.

- Accidentally swapping two dipoles or swapping the coil sensors during the connection of the recording channels, can be taken into account for by re-arranging the dataset vectors.

- The reverse installation of a magnetic coil sensor or a misalignment of the fluxgate sensor by an exact multiple of 90 degrees can be corrected for by swapping the datasets and altering the nominal layout accordingly. E.g. for the case of a reverse coil sensor measuring the magnetic field in the north-south direction (H_x) the correction involves interchanging the datasets for two horizontal magnetic fields and an increase of the angle between magnetic north and the H_x orientation by 90 degrees.

An elementary visualisation of the re-assignment can be found, for example, in the user manual by *Phoenix Geophysics* [2005].

Even though such layout errors are supposed to be avoided, they do occasionally happen (apparently often enough for Phoenix Geophysics to implement an automatic layout-error correction in their processing software), but for the cases described above correction

is straightforward. However, certain cases of layout errors cause severe loss of data, e.g. accidentally swapping two electrodes from different dipoles during connection with the recording channels. Such a mistake results in measuring two parallel electric dipoles, which prohibits any subsequent rotation of the data because orthogonality of the dipoles is no longer fulfilled. In principle, all layout errors for which the electric and/or magnetic field are not measured in two orthogonal directions are severe and must be avoided.

The correction for bad records in the magnetic (outliers) and electric (leverage points) time-series, such as spikes, null-records, or obvious disturbances, usually involves removal of the corrupted segments and interpolation where required. In many cases these effects are automatically removed during the processing since related segments usually exhibit low coherence with relevant segments of the other time-series and are accordingly down-weighted (see Sec. 6.2.3). However, when the number of good records is sparse, pre-processing of the time-series can be beneficial as initially corrupted segments might be usable for subsequent processing and hence enhance the quality of the obtained information.

6.2.2. Transformation into the frequency domain

Commonly, time-series data are transformed into the frequency domain using the Fourier-Transformation (FT); numerically implemented as the Fast-Fourier-Transformation process [e.g. *Press et al.*, 2007, p.608–616], often simply referred to as *FFT*. FT's are performed for subsets (so called *windows*) of the full record, related to different intervals along the time-series and commonly tapered in order to reduce *spectral leakages* (or *side-lobes*), which occur for FT's on time-series of finite length [e.g. *Gubbins*, 2004, Ch. 3]. Over time, various window functions (or 'tapering functions') have been developed, and their performance has been studied for the different applications [e.g. *Nuttall*, 1981]. Commonly used window functions for MT processing are cosine, Hamming, Hann, and Tukey (cf. references in Sec. 6.2.3). For each of the windows the FT provides an estimate of the E or H field for the respective duration of the recording. The available frequency (f_F) range for which estimates can be made, is bounded by the Nyquist-frequency (f_{Ny}) on the high end and the time-length of the window (T_w) on the low end:

$$f_{Ny} = 2/\Delta t \leq f_F \leq 1/T_w, \tag{6.2}$$

with Δt: time-step interval of the record and the index F indicating either an electric or magnetic field estimate. The time-step interval, and therefore the minimal window length, is usually determined by the sampling rate (sr) of the recording ($\Delta t = 1/sr$). The maximal window length, on the other hand, is in principle only limited by the duration of the recording. For a typical broadband sounding, with a recording time of 2 – 3 days, theoretically the longest observable period (the inverse of the shortest frequency) is in the order of 10^5 s. For real recordings the maximum windows length is usually shorter, due to noise in the recorded data, sensor characteristic, and the requirement of additional

estimates in order to evaluate the confidence level of an estimate. The effective maximal period for broadband recording is usually of some 10^3 s and for long-period recording with duration of 7-9 days at around 10^5 s.

During processing, the window length is usually chosen to be as short as possible for a given frequency in order to increase the number of estimates. Increasing the window length increases reliability of each estimate but yields a smaller number of estimates. For an undisturbed dataset, the final estimates and their confidence intervals are independent of the window length (once a minimum number of windows is reached). This circumstance already offers an approach to inspect the dataset for disturbances as demonstrated by *Jones* [1980]. Overlapping windows increase the number of estimates, but for the cost that the respective estimates are interdependent; the chosen overlap is therefore usually a compromise, which is also dependent on the shape of the tapering-window. To lower computational costs and decrease the time-requirement for the FT, different schemes of window handling have been exploited, e.g. *cascade decimation* [*Wight and Bostick*, 1980], which facilitates considerably fast transformation for datasets of typical size on commercially available computers. Alternatively, MT time-series can be transformed into the frequency domain using wavelet-transformation as performed, for example, by *Garcia and Jones* [2008], which comes at the cost of a higher computational time but offers additional information about the temporal component of the estimate.

6.2.3. Robust remote reference processing

In order to enhance the quality of impedance estimates for MT datasets, which contain erroneous records of non-Gaussian distribution in the electric and magnetic time-series, various processing methods have been developed. Today, common processing schemes comprise two steps: *Remote Reference* analysis to weight the estimates by the coherence of the respective time-series with contemporaneous time-series at distant stations, and *Robust Processing* to cull out a superior subset of estimates that are less biased by erroneous estimates. *Jones et al.* [1989] evaluate and compare the performances of different robust processing methods with each other and traditional least square estimator (LS) methods. In their study the authors show that remote reference analysis provides superior results and that robust processing methods usually outperform LS methods. As stated by *Jones et al.* [1989], remote reference methods will therefore yield larger statistical errors than LS methods for a given length data set. An overview about remote reference analysis and common robust processing methods is given in the following paragraphs.

Remote reference analysis

Remote reference analysis, introduced to MT processing by *Gamble et al.* [1979], uses the coherence between time-series data of the particular site with data from one or more distant stations that are recorded at the same time. The coherence (C_{xy}) between two time-series x(t) and y(t) can therein be evaluated as the square root of the related normalised

mean cross-spectral density (S_{xy}), which in turn is the product of the respective FT's $X(f)$ and $Y(f)$, i.e.

$$C^2_{xy}(f) = \frac{\left|\langle S_{xy}(f)\rangle\right|^2}{\langle S_{xx}(f)\rangle\langle S_{yy}(f)\rangle} = \frac{|\langle X^*(f)Y(f)\rangle|^2}{\langle X^*(f)X(f)\rangle\langle Y^*(f)Y(f)\rangle} \tag{6.3}$$

where the asterisk denotes the complex conjugate of the function. Coherence weighting is implicitly applied during the impedance estimation using the remote reference method, in which modern processing schemes also consider partial and multiple coherence as indicators for the quality of an impedance estimate.

To illustrate the application of this procedure to an MT dataset consider the explicit form of Equation 3.34 for the electric field component in x-direction (E_x), i.e.

$$E_x = Z_{xx}H_x + Z_{xy}H_y \tag{6.4}$$

where both, the electric and magnetic channels E_x and H_y are assumed here to contain noise. Multiplication of this Equation with the complex conjugate of either the electric or magnetic field component in x-direction (R^*_x) or in y-direction (R^*_y) yields

$$\langle E_x R^*_x\rangle = Z_{xx}\langle H_x R^*_x\rangle + Z_{xy}\langle H_y R^*_x\rangle \tag{6.5}$$

and

$$\langle E_x R^*_y\rangle = Z_{xx}\langle H_x R^*_y\rangle + Z_{xy}\langle H_y R^*_y\rangle, \tag{6.6}$$

respectively. Combining these two equations results in an estimate of the Z_{xy} component

$$Z_{xy} = \frac{\langle E_x R^*_y\rangle\langle H_x R^*_x\rangle - \langle E_x R^*_x\rangle\langle H_x R^*_y\rangle}{\langle H_x R^*_x\rangle\langle H_y R^*_y\rangle - \langle H_x R^*_y\rangle\langle H_y R^*_x\rangle}. \tag{6.7}$$

Expressions for all components of the impedance tensor can be derived in a similar manner, therefore the general form can be stated as

$$Z_{ij} = \frac{\langle E_i R^*_j\rangle\langle H_k R^*_k\rangle - \langle E_i R^*_k\rangle\langle H_k R^*_j\rangle}{\mathsf{DET}}, \tag{6.8}$$

with $\mathsf{DET} = \langle H_x R^*_x\rangle\langle H_y R^*_y\rangle - \langle H_x R^*_y\rangle\langle H_y R^*_x\rangle$, and $i, j, k \in [x, y]$, with $k \neq j$. Whether processing with the electric or the magnetic component as reference provides superior results depends on the type of noise and its effect on each channel. The magnetic component is commonly assumed to be less contaminated by noise and usually chosen as remote, however the choice is often a rather subjective one. To use a combination of remote references from different components or stations can often be useful.

For the case of a perfectly 2D subsurface and according rotation of the magnetic field

data, H_x and H_y are uncorrelated and Equation 6.8 reduces to

$$Z_{ij} = \frac{\langle E_i H_j^* \rangle}{\langle H_j H_j^* \rangle}, \tag{6.9}$$

in situations where the magnetic field is used as remote reference. Separating the electric and magnetic components into a term containing the noise (N_{E_i} and N_{H_j}) and a noise free term (E_{i_f} and H_{j_f}) yields

$$Z_{ij} = \frac{\langle E_{i_f} H_j^* \rangle + \langle N_{E_i} H_j^* \rangle}{\langle H_{j_f} H_j^* \rangle + \langle N_{H_j} H_j^* \rangle}. \tag{6.10}$$

In Equation 6.10 it is shown that the effect of noise on the impedance estimate depends on the correlation between the noise in either the electric or magnetic channel and the chosen remote reference channel. For dominant correlation between the noise in the electric channel and the remote reference, the term $\langle N_{E_i} H_j^* \rangle$ will cause an overestimation of the impedance, whereas, in the opposite case where $\langle N_{H_j} H_j^* \rangle$ dominates, the impedance will be underestimated.

Estimates of the magnetic transfer function in the presence of disturbances are derived accordingly, i.e.

$$\langle H_z R^* \rangle = T_x \langle H_x R^* \rangle + T_y \langle H_y R^* \rangle \tag{6.11}$$

with R^* denoting the respective remote reference. Therefore transfer function components are estimated as

$$T_i = \frac{\langle H_z R_i^* \rangle \langle H_j R_j^* \rangle - \langle H_z R_j^* \rangle \langle H_i R_i^* \rangle}{\mathsf{DET}}, \tag{6.12}$$

with DET as defined for Equation 6.8, and $i, j \in [x, y]$ with $j \neq i$.

Robust processing methods

A processing method is considered robust when it is relatively insensitive to the presence of a moderate amount of bad data [*Jones et al.*, 1989], and thus able to cull out a superior set of estimates from a contaminated data set. Robust processing methods have been adapted for MT processing and their application was discussed, among others, by *Egbert and Booker* [1986]; *Chave et al.* [1987]; *Chave and Thomson* [1989]; *Larsen et al.* [1996]; *Smirnov* [2003]. Common applications of robust processing in MT include bounded influence estimator, M-estimator [*Huber*, 1981], or Jack-knife processing and iterative rejection of estimates to either increase the coherence of the estimates or decrease the variance (or standard deviation) of the resulting impedance estimate. Errors of the resulting estimates are then calculated on a statistical basis using Bootstrap analysis.

The crucial point of a processing algorithm, i.e. its robustness, is the *breakdown point* ε^*, which describes the maximal fraction of erroneous data that can be handled by the algorithm [*Hampel et al.*, 1986]. Certainly the optimal breakdown point is 50 %, common robust algorithms, using the M-estimator and linear regression, approach 30 %; LS

estimators exhibit a breakdown point of zero, meaning that the smallest amount of erroneous data may seriously bias the final estimate [*Smirnov*, 2003]. An approach with a considerable higher breakdown point ($\varepsilon^* = 50\,\%$) was presented by *Siegel* [1982] using a repeated median algorithm, and an application for MT processing has been developed by *Smirnov* [2003]. Therein, the author uses a reduced M-estimator to supplement the initial Siegel estimator approximation in order to enhance the performance for short time-series.

6.3. Deriving subsurface structure using magnetotelluric data

Deriving the distribution of Earth properties and thereby enhancing knowledge about geological processes is the aim of most geophysical investigations. In MT, the electric properties of the Earth are studied, which are usually derived through an inversion of the dataset (cf. Sec. 6.3.3). Overviews about general principles of inversion processes and related theory are given, among others, by *Aster et al.* [2005]; *Tarantola* [2005]; their application for MT problems was reviewed by *Avdeev* [2005]; *Börner* [2010]; *Siripunvaraporn* [2010]. Here a condensed description of the parts relevant for MT inversion is given; namely a characterisation of common forward modelling methods, followed by an illustration of the basic inversion approach, and lastly an examination of the non-uniqueness problem of MT inversion. Thereafter, different solvers for the MT inversion problem are discussed and common inversion codes are presented. At first, however, the principles of traditional analytical transformations are illustrated.

6.3.1. Analytical direct transformation

Analytical approaches aim to find mathematical relationships between MT response data and the resistivity-depth distribution of the subsurface. The three most commonly used relations for 1D MT transformation were derived by *Niblett and Sayn-Wittgenstein* [1960], *Bostick* [1977], and *Weidelt et al.* [1980]. All approaches calculate the resistivity at the so-called Niblett-Bostick depth δ_{NB} from a given apparent resistivity ρ_a and the magnetic permeability μ_0 at the related period, i.e.

$$\delta_{NB} = \sqrt{\frac{\rho_a(T)T}{2\pi\mu_0}}. \tag{6.13}$$

The Niblett-Bostick depth is related to the skin depth δ_s as $\delta_s = \sqrt{2}\delta_{NB}$ (cf. Sec. 3.3), hence referring to a depth at which the amplitude of the wave F_0 is reduced by a factor $e^{-\frac{1}{\sqrt{2}}}$ (approximately $F_0/2$):

$$F(\delta_{NB}) = F_0 e^{-\sqrt{\frac{\pi\mu_0}{\rho_a T}}\delta_{NB}} = F_0 e^{-\frac{1}{\sqrt{2}}}. \tag{6.14}$$

Analytical direct transformations can provide a first insight to the subsurface structures and their results can be used to create a starting model for subsequent inversion. Moreover, depth estimations from analytical transformations are also commonly used during processing of MT data, e.g. strike estimation (Sec. 9.6.1).

Niblett-Bostick transformation

The so-called *Niblett-Bostick* transformation refers to the two independently-developed formulations by *Niblett and Sayn-Wittgenstein* [1960], and *Bostick* [1977]. Both equations use apparent resistivity values ρ_a (or its inverse apparent conductivity σ_a) and its depth-derivative to derive a 1D resistivity-depth (or conductivity-depth) profile, i.e. *Niblett and Sayn-Wittgenstein* [1960]:

$$\sigma_{NB}(\delta_{NB}) = \sigma_a(T) + \delta_{NB}\frac{\partial\sigma_a(T)}{\partial\delta_{NB}}, \tag{6.15}$$

and *Bostick* [1977]:

$$\rho_{NB}(\delta_{NB}) = \rho_a(T)\frac{1+m(T)}{1-m(T)} \tag{6.16}$$

with

$$m(T) = \frac{\partial\log(\rho_a(T))}{\partial\log(T)} = \frac{T}{\rho_a(T)}\frac{\partial\rho_a(T)}{\partial T}, \tag{6.17}$$

in where δ_{NB} is given in Equation 6.13. It was shown by *Jones* [1983b] that the transformation by *Niblett and Sayn-Wittgenstein* and *Bostick* are equivalent. *Jones* [1983b] further points out that an alternative expression of the Bostick resistivity at depth δ_{NB} can be used, i.e.

$$\rho_W(\delta_{NB}) = \rho_a(T)\left(\frac{\pi}{2\phi(T)} - 1\right). \tag{6.18}$$

This formulation is related to the 'appproximate phase' [*Weidelt et al.*, 1980] (next paragraph) and uses phase $\phi(T)$ and apparent resistivity $\rho_a(T)$ information at one period to estimate the resistivity. The resistivity is derived directly without the extra step of calculating the apparent resistivity gradient, which speeds up the calculation process; however, the two formulations yield different resistivity estimates (i.e. $\rho_W \neq \rho_{NB}$).

Schmucker and Weidelt transformation

Like the formulation in Equation 6.18, and unlike the approaches by *Niblett and Sayn-Wittgenstein* and *Bostick* (Eqs. 6.15-6.16), the $\rho^* - z^*$ *transform* [*Schmucker*, 1987] uses phase information $\phi(T)$ and does not require prior calculation of the derivative. The transformation calculates the resistivity for a depth z^* which is equivalent to the skindepth δ_s

(Sec. 3.3):

$$\rho_{SW}(\delta_s) = \begin{cases} 2\rho_a(T)\cos^2\phi(T), & \text{for } \phi > 45^o \\ \frac{\rho_a(T)}{2\sin^2\phi(T)}, & \text{for } \phi < 45^o. \end{cases} \tag{6.19}$$

The $\rho^* - z^*$ transform is based on earlier approaches by [*Schmucker*, 1970; *Weidelt*, 1972; *Schmucker*, 1973; *Weidelt et al.*, 1980] using similar formulations.

$\rho_{SW}(\delta_{NB})$ and $\rho_{NB}(\delta_{NB})$ will not exhibit the same resistivity depth profile, except for the case of a homogeneous halfspace. In this case $m(T) = 0$ and $\phi(T) = 45°$, thus $\rho_{SW}(\delta_s) = \rho_{NB}(\delta_{NB}) = \rho\ \forall z$, where ρ is the resistivity of the halfspace and z is the depth.

6.3.2. Forward modelling

In contrast to analytical approaches (Sec. 6.3.1), which attempt to find a direct mathematical relation between the measured data and subsurface characteristics, forward modelling (and the related inversion processes) aim to find a set of model parameters $\vec{m}$ that reproduce the measured data $\vec{d}$ through a functional f:

$$\vec{d} = f(\vec{m}). \tag{6.20}$$

In MT, the model parameters $\vec{m}$ are usually logarithmic resistivity $\log(\rho)$ or logarithmic conductivity $\log(\sigma)$ of the subsurface, wherein the logarithmic expression is chosen to fit with the range of electric conductivity within the Earth as sensed by the MT method (cf. Sec. 5). The data vector $\vec{d}$ is usually given in terms of the electric impedance $\mathbf{Z}$ or the apparent resistivity ρ_a and phase ϕ for each station (cf. Sec. 3.2). In the following it is assumed that the vectors $\vec{m}$ and $\vec{d}$ are of length M and N, respectively. When vertical magnetic field data are available, the elements of the magnetic transfer function $\vec{T}$ can also be derived, adding further information about the subsurface. Alternatively, the (rotational invariant) determinant of the impedance matrix $\det(\mathbf{Z})$ can be used instead of ρ and ϕ to evaluate the model, having the advantage of being unaffected by certain types of distortion (cf. Sec. 4). However, due to the reduction of the number of degrees of freedom (eight[1] for the complex impedance vector, two for its determinant), certain information about the subsurface is omitted when using the determinant to evaluate the model; thus the determinant evaluation is inferior and should not be used on its own.

In MT, the functional f, which relates the model and data vectors, is usually an approximation of Maxwell's Equations (Sec. 3.1.1) and is commonly carried out by *forward modelling* methods: *finite difference* (FD), *finite element* (FE), or *integral equation* (IE) [e.g. *Avdeev*, 2005; *Press et al.*, 2007]. All methods approximate Maxwell's Equations, or deduced equations, by reducing the differential terms therein to a system of linear equations

$$\mathbf{A} \cdot \vec{x} = \vec{b} \tag{6.21}$$

[1] four in the case of a 2D subsurface

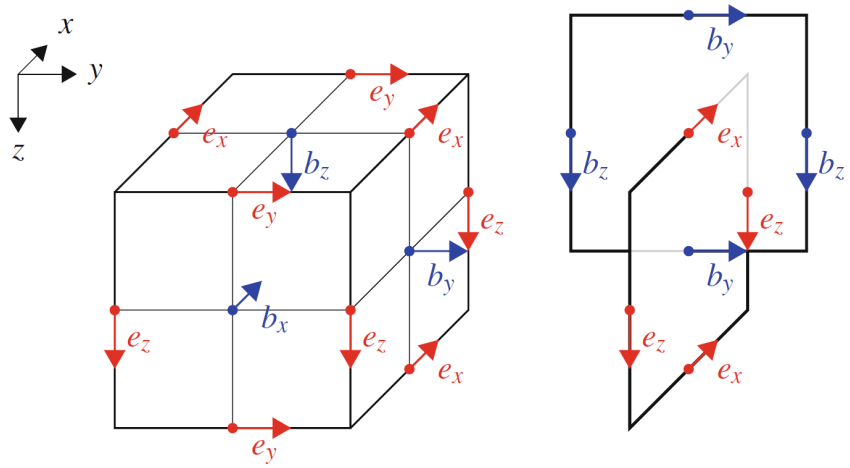

Fig. 6.3.: Part of the staggered grid by *Yee* [1966], where the electric and magnetic field components are sampled on edges and faces of the box, respectively; from *Börner* [2010].

solved on a *staggered-grid* (Fig. 6.3) [*Avdeev*, 2005]. The forms of $\mathbf{A}$, $\vec{x}$, and $\vec{b}$ in Equation 6.21 are dependent on the forward modelling type. In general, a partial derivative equation (PDE) is derived from the laws by Faraday, Ampere, and Ohm (Eqs. 3.4, 3.2, and 3.5) in the quasi-static regime. An expression for the electric field can be found by starting from Faraday's Law:

$$\nabla \times \vec{E} = \imath\omega\mu\vec{H} \xrightarrow{curl} \nabla \times \nabla \times \vec{E} = \imath\omega\mu\nabla \times \vec{H} \xrightarrow[Law]{Ampere's} \nabla \times \nabla \times \vec{E} = \imath\omega\mu\sigma\vec{E}. \tag{6.22}$$

Equivalently an expression can be found for the magnetic field by starting from Ampere's Law:

$$\nabla \times \vec{H} = \sigma\vec{E} \xrightarrow{curl} \nabla \times \nabla \times \vec{H} = \sigma\nabla \times \vec{E} \xrightarrow[Law]{Faraday's} \nabla \times \nabla \times \vec{H} = \imath\omega\mu\sigma\vec{H}. \tag{6.23}$$

Hence, for both components the equation takes on the form of a second order PDE:

$$\nabla \times \nabla \times \vec{F} = \imath\omega\mu\sigma\vec{F}. \tag{6.24}$$

Note that during MT forward modelling and inversion, $\log(\sigma)$ is usually used instead of σ as it offers a more linearised solution and positive constraints on the model. An excellent summary of commonly used forward modelling methods in MT is given in the review paper by *Avdeev* [2005], and the content of the following paragraphs is related to this reference unless stated otherwise.

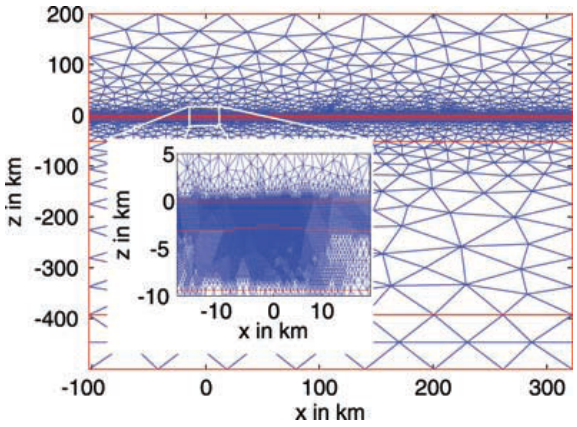

Fig. 6.4.: Finite element (FE) mesh parameterising the model of a mid-oceanic ridge; from *Franke et al.* [2007]

Finite difference methods

The FD method is probably the most commonly applied approach [e.g. *Yee*, 1966; *Jones and Pascoe*, 1972; *Madden and Mackie*, 1989; *Smith and Booker*, 1991; *Mackie et al.*, 1994; *Newman and Alumbaugh*, 1995; *Weaver et al.*, 1999; *Newman and Alumbaugh*, 2002], approximating the differential equations by their finite difference counterparts. The difference is calculated between grid nodes, resulting in a linear equation $\mathbf{A}_{FD} \cdot \vec{v_n} = \vec{c_{sb}}$. Therein $\mathbf{A}_{FD}$ is a complex, large, sparse, and symmetric matrix; $\vec{v_n}$ and $\vec{c_{sb}}$ are the values on grid nodes and the boundary conditions, respectively. Due to simplicity of its approach the FD method is comparatively easy to implement and therefore widely used.

Finite element methods

The FE method uses an explicit representation of the approximate EM field (or its potentials), and a system of equations is constructed by multiplying differential equations, source and boundary conditions by a set of weighting functions. This linear system of equations defines the conditions on the nodes or edges of the grid[2] and is non-symmetric, sparse, and complex. The FE method has the advantage that the shape of the grid can be adapted to the problem, i.e. having a dense mesh in the main areas of interest and sparse mesh elsewhere[3] (Fig. 6.4). FE methods are commonly used [e.g. *Reddy et al.*, 1977; *Pridmore et al.*, 1981; *Livelybrooks*, 1993; *Haber*, 1999; *Zyserman and Santos*, 2000; *Mitsuhata and Uchida*, 2004], but not as popular as FD methods due to the more complex construction of the system of equations.

[2] A variation of the FE method is the *finite volume* (FV) method in which the basis functions are solved within the cells of the grid, instead of on its nodes.

[3] FE methods with adaptive meshes are available, e.g. *Franke et al.* [2007], but are not commonly used due to the even greater complexity of their implementation.

Integral equation methods

The IE method is most applicable for problems in which the subsurface comprises a relatively simple background model (e.g. a halfspace) in which an anomalous layer is embedded. The problem is then reduced to separately solving Maxwell's equations for the background model and the response of the anomalous layer. The latter is commonly referred to as 'scattered' or 'secondary' field and is deduced using the Green's function G. The PDE in IE methods is then reduced to a second-kind Friedholm's integral equation:

$$\vec{E}(\vec{r}) = \vec{E_{bg}}(\vec{r}) + \int_{V_a} G(\vec{r}, \vec{r'})(\sigma - \sigma_{bg})\vec{E}(\vec{r})d\vec{r} \tag{6.25}$$

in case of the electric field, where the index 'bg' refers to the parameters of the background medium [*Raiche*, 1974; *Hohmann*, 1975; *Weidelt*, 1975]. A discretisation of the *Scattering Equation* 6.25 yields a system of linear equations ($\mathbf{A}_{IE} \cdot \vec{x} = \vec{b}$); the advantage of the IE method is that it only requires an integration over the volume V_a where $\sigma \neq \sigma_{bg}$. Therefore, all entries of the matrix $\mathbf{A}_{IE}$ are filled, and $\mathbf{A}_{IE}$ is more compact than the related matrices for the FD and FE methods. The IE method has been implemented by range of authors [e.g. *Wannamaker et al.*, 1984; *Hohmann*, 1987; *Newman and Hohmann*, 1988; *Wannamaker*, 1991; *Avdeev et al.*, 2002; *Avdeev and Avdeeva*, 2009], but due to the challenging task of computing $\mathbf{A}_{IE}$ it has not gain the same popularity as the FD and FE methods.

6.3.3. Inversion

Inversion methods can be subdivided into categories according to their approach; namely direct methods, iterative methods, and stochastic methods. Direct inversion methods (e.g. the *Gauss-algorithm* [*Press et al.*, 2007]) attempt to invert the function f in order to derive the model parameters from the observed data, i.e.

$$\vec{m} = f^{-1}(\vec{d}). \tag{6.26}$$

In the linear approach it is assumed that the relation between measured data and model parameters (Eq. 6.20) can be adequately approximated by a linearised analogue, viz.

$$\vec{d} = \mathbf{G}\vec{m}, \tag{6.27}$$

where $\mathbf{G}$ is a $N \times M$ matrix. In that case Equation 6.26 can be rewritten as

$$\vec{m} = \mathbf{G}^{-1}\vec{d}, \tag{6.28}$$

where $\mathbf{G}^{-1}$ is the inverse of $\mathbf{G}$. As $\mathbf{G}$ is usually ill-conditioned, it is often difficult or computationally expensive (or even impossible) to invert $\mathbf{G}$ directly, an iterative or stochastic approach to the inversion process is usually superior.

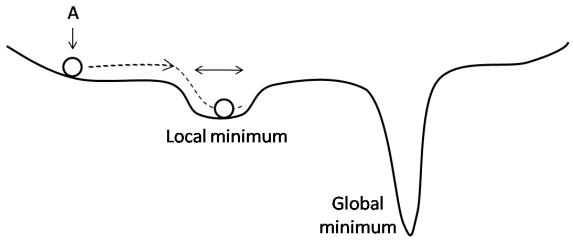

Fig. 6.5.: Types of minima types, illustrated using of a ball's behaviour on a curved surface under the effect of gravity; redrawn from *Bahr and Simpson* [2002]. A ball released at a point 'A' will be trapped in the local minimum instead of the global minimum unless a sufficient force is applied to push it over the ridge between the minima.

Iterative and stochastic inversion is similar to a 'trial and error' process wherein one or more starting models $\vec{m}_0$ are created and their responses $\vec{d}'$ are calculated using a forward modelling process (Sec. 6.3.2). The misfit of each model, i.e. the difference between model response and measured data, is given in terms of the error function ϵ, viz.

$$\epsilon = \|\vec{d}' - \vec{d}\|. \tag{6.29}$$

A common choice of the error function is the L_2 norm:

$$\epsilon = \|\vec{d}' - \vec{d}\|_2 = \sum_i \left(\vec{d}' - \vec{d}\right)^2, \tag{6.30}$$

i.e. the root mean square (RMS) misfit. Model parameters are subsequently adapted during the inversion process in order to minimise ϵ. The crucial part of an inversion approach is to optimise the adaption process in a way that it exhibits a high convergence rate but also adequately samples the model parameter space. The latter is to ensure that a global minimum of the error function is obtained, as opposed to a local one (Fig. 6.5).

Non-uniqueness of MT inversion models

Except for the idealistic case of 1D subsurface and noise-free data for the complete frequency range, MT inversion is non-unique, i.e. a range of models fit the measured data equally well. The non-uniqueness for the general case of inversion with differential equations was proven by *Langer* [1933] and for the MT problem by *Tikhonov* [1965], *Bailey* [1970], and *Weidelt* [1972] (Fig. 6.6); see also *Parker* [1983]; *Constable et al.* [1987]; *Vozoff* [1987] for illustration of the non-uniqueness problem in MT inversion. Rough models are superior in terms of data misfit, but often contain resistivity distributions that are not in agreement with physical laws, e.g. conductivities of a few hundreds of Siemens per meter. Therefore, more elaborate criteria are required to evaluate a model, incorporating additional (*a priori* known) constraints about the characteristics of the model, such as a limited parameter range or the so-called smoothness of the model. The smoothness is usually described in terms of first or second order spatial derivatives of the model param-

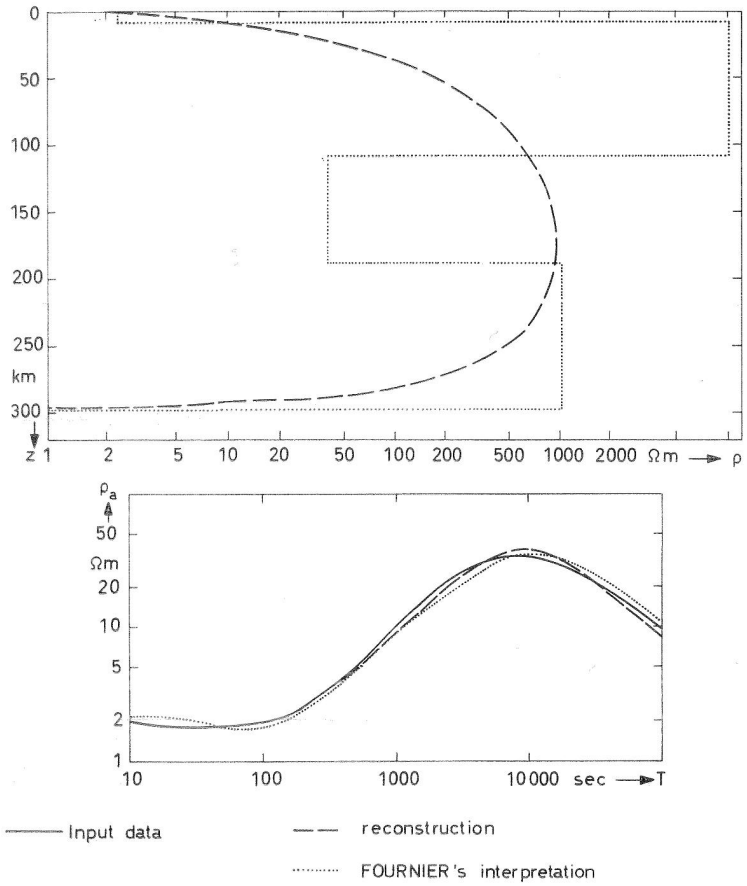

Fig. 6.6.: The non-uniqueness problem of magnetotelluric (MT) inversion illustrated using of two very different inversion models (top). Both models reproduce the input data reasonably well (bottom), but describe very different subsurface behaviour. Figure and (dashed) inversion model taken from *Weidelt* [1972]; MT sounding data from *Wiese* [1965]; (doted) inversion model used for comparison by *Fournier* [1968].

eters $\vec{m}$, which, in the case of MT application, is calculated using $\nabla \log(\sigma)$ and $\nabla^2 \log(\sigma)$ (or $\nabla\sigma$ and $\nabla^2\sigma$) [e.g. *Constable et al.*, 1987; *Smith and Booker*, 1988; *de Groot-Hedlin and Constable*, 1990; *Smith and Booker*, 1991]. Functionals $\psi(\vec{m})$, which consider data misfit as well as model smoothness, have the form

$$\psi(\vec{m}) = \epsilon(\vec{m}) + \tau \cdot \xi(\vec{m}), \tag{6.31}$$

where $\epsilon(\vec{m})$ is some measure of the data misfit, $\xi(\vec{m})$ is some measure of the model smoothness, and τ is a weighting parameter (often referred to as *smoothing parameter*). The related inversion processes attempt to find a *regularised solution* of the inverse problem, i.e. models which yield a minimum of $\psi(\vec{m})$. A higher degree of smoothing is generally desirable as it usually yields models with less structure, meaning that the persisting structures are more reliable. However, due to the additional constraints on the model parameters a trade-off between smoothness of the model and data misfit is commonly observed (e.g.

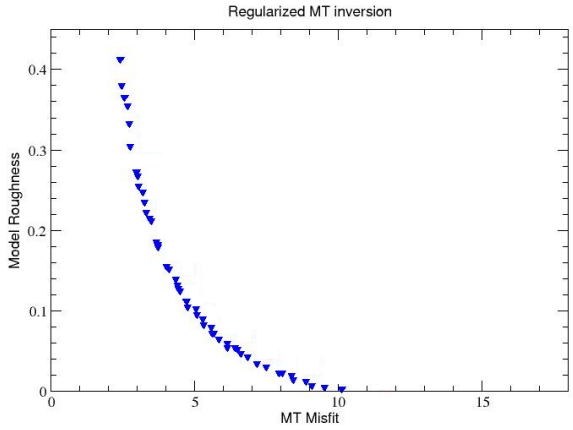

Fig. 6.7.: Plot of magnetotelluric (MT) data misfit versus Model Roughness (inverse of Model Smoothness) for a range of subsurface models; modified after *Moorkamp* [2007b]. The distribution of the model-values in the diagram follows a trend that is referred to as *L-curve* [e.g. *Hansen*, 1998], indicating that the final model has to be a compromise between sought low misfit and high smoothness (i.e. low roughness) values.

Fig. 6.7). The applied error functional differs between inversion algorithm, but most of them belong to one of two forms; namely the unconstrained functional:

$$\psi_u(\vec{m}) = \left[(\vec{d} - f(\vec{m}))^T \mathbf{R}_{dd}^{-1}(\vec{d} - f(\vec{m})) - \Upsilon^2\right] + \tau \cdot \Xi(\vec{m} - \vec{m_0}), \tag{6.32}$$

or the constrained functional (also referred to as *objective functional*) [*Tikhonov and Arsenin*, 1977]:

$$\psi_c(\vec{m}) = (\vec{d} - f(\vec{m}))^T \mathbf{R}_{dd}^{-1}(\vec{d} - f(\vec{m})) + \tau \cdot \Xi(\vec{m} - \vec{m_0}), \tag{6.33}$$

with $\mathbf{R}_{dd}$: error covariance matrix, Υ: desired level of misfit, Ξ: operator that provides a value of the model smoothness (usually the gradient ∇ or the laplacian Δ), $\vec{m_0}$: an *a priori* model[4] [*Siripunvaraporn*, 2010]. The unconstrained functional is used mostly in Occam's inversion, whereas the constrained functional is used, for example, in *nonlinear conjugate gradient* (NLCG), *Gauss-Newton* (GN), *quasi-Newton* (QN), and GN with conjugate gradient (GN-CG). A detailed comparison of the methods and a list of references regarding their implementation in different inversion algorithms is given later in this Section.

For 2D or 3D inversion processes, additional smoothness parameters can be applied to separately control the smoothness in horizontal and vertical direction. In the `WinGLink` 2D inversion program [*WinGLink*, 2005], based on the algorithm by *Rodi and Mackie* [2001], horizontal and vertical smoothness are controlled by the factors α and β, respectively. α is a multiplier of the horizontal derivatives in Equations 6.32 and 6.33 enforcing an increase of horizontal smoothness, whereas β controls weighting of the cell size dependent influence of the smoothness operator Ξ. Different values for the smoothing parameters have been proposed, e.g. *Mackie* [2002]: $\alpha = 1$ (unless reasons for a higher

[4] In this formulation of the functional an inversion model that is similar to the *a priori* model is sought; if the inversion model is supposed to be independent of an *a priori* model, the term $\vec{m_0}$ in Equation 6.33 is omitted.

Regularisation operator	Regularisation order	Proposed value for β
Standard grid	$\left(\nabla^2 m\right)^2$	3.0
	$\|\|\nabla m\|\|^2$	1.0
Uniform grid	$\left(\nabla^2 m\right)^2$	1.0
	$\|\|\nabla m\|\|^2$	0.3

Tab. 6.1.: Proposed values for the factor β by *Mackie* [2002].

degree of horizontal smoothness are found), $\beta \in [0.3, 3]$ (dependent on regularisation, see Tab. 6.1), and $\tau \in [3, 300]$. However, the optimal set of values is certainly dependent on the local subsurface and the mesh used during the inversion; it is therefore strongly advised to test a range of values in order to identify their effect on the final model.

Stochastic methods

Stochastic methods have the advantage that they randomly search the model space and are therefore unlikely to be trapped in a local minimum [e.g. *Aster et al.*, 2005; *Tarantola*, 2005] (Fig. 6.5). Common stochastic methods are *Monte Carlo* [*Metropolis and Ulam*, 1949; *Press*, 1968] (and subsequent techniques, e.g. *Markov chain Monte Carlo* [*Hastings*, 1970] algorithms) and *Genetic Algorithm* [*Goldberg*, 1989]. Stochastic inversion methods have been applied to MT problems by different authors, e.g. *Jones and Hutton* [1979]; *Agarwal and Weaver* [1993]; *Pérez-Flores and Schultz* [2002]; *Moorkamp et al.* [2007]; *Roux et al.* [2009], and *Moorkamp et al.* [2010]. However, due to the significantly higher computational cost of stochastic methods, owing to the larger number of models involved, the application of stochastic methods is usually limited to grids with a small number of nodes. Accordingly, stochastic methods are usually only used for 1D inversion (or 2D inversions with a sparse grid).

Iterative MT inversion algorithms

Commonly used iterative inversion algorithms for MT applications, are presented in Table 6.2. In this Section, differences of the approaches are examined and their advantages and disadvantages are compared. In general, iterative inversion seeks a minimum of the error function (Eq. 6.31), which can be found as an extremal of its derivative with respect to the model parameters

$$\min(\psi(\vec{m})) \rightarrow \frac{\partial \psi(\vec{m})}{\partial \vec{m}} = 0 \Longrightarrow \frac{\partial \epsilon(\vec{m})}{\partial \vec{m}} + \tau \cdot \frac{\partial \xi(\vec{m})}{\partial \vec{m}} = 0. \tag{6.34}$$

Iterative approaches can be divided into two main groups according to the implemented error functional: the unconstrained functional (Eq. 6.33) is mostly used in Occam's inver-

sion, whereas the objective functional (Eq. 6.32) is used by most of the other approaches.

The *Gauss-Newton* (GN) method is based on Newton's method, which uses

$$\vec{m}_{k+1} = \vec{m}_k - \mathbf{H}_k^{-1} \nabla^T \vec{m}_k, \tag{6.35}$$

with the Hessian $\mathbf{H} = \partial^2 W / \partial \vec{m}^2$ and the gradient $\nabla^T \vec{m}$ to derive the model for the (k+1)-th iteration step. In contrast to Newton's method the GN method keeps only the first derivative of $\mathbf{H}$ and uses the first order Taylor's series expansion to linearise the forward response in the forward model approach $f(m_k)$ (cf. Eq. 6.20). The forward response of the (k+1)-th iteration step can then be expressed in terms of $f(m)$ at the previous step, the $N \times M$ Jacobian $\mathbf{J}_k = \partial f / \partial \vec{m}_k$, and the difference between the models of the two steps:

$$f(\vec{m}_{k+1}) = f(\vec{m}_k) + \mathbf{J}_k \cdot (\vec{m}_{k+1} - \vec{m}_k). \tag{6.36}$$

Using Equation 6.34 with the objective functional (Eq. 6.33) yields the iteration scheme

$$\vec{m}_{k+1} - \vec{m}_k = \left[\tau \mathbf{R}_{mm}^{-1} + \mathbf{J}_k^T \mathbf{R}_{dd}^{-1} \mathbf{J}_k + \lambda_k \mathbf{I}\right]^{-1} \left[\mathbf{J}_k^T \mathbf{R}_{dd}^{-1} (\vec{d} - f(\vec{m}_k)) + \tau \mathbf{R}_{mm}^{-1} (\vec{m}_k - \vec{m}_0)\right], \tag{6.37}$$

where $\mathbf{I}$ is the identity matrix and λ_k is a damping factor introduced for numerical stability [*Marquardt*, 1963]. Accordingly, GN methods need to invert the $M \times M$ matrix $\left[\tau \mathbf{R}_{mm}^{-1} + \mathbf{J}_k^T \mathbf{R}_{dd}^{-1} \mathbf{J}_k + \lambda_k \mathbf{I}\right]$ to calculate the $N \times M$ Jacobian $\mathbf{J}_k$, making it computational very expensive.

Occam's inversion [e.g. *Siripunvaraporn*, 2010] is a variation of the classical GN method and can be divided into two phases: first the RMS misfit is reduced to the specified level of misfit Υ^2 through varying the smoothing parameter τ, thereafter τ is minimised as much as possible without increasing the RMS misfit. In the first phase, the first term on the right hand side in Equation 6.33 is reduced to a minimum specified by Υ, followed by minimising the second term on the right hand side, which then defines the value of the error function (together with the covariance matrix $\mathbf{R}_{dd}$). Derivation of the optimal τ can be carried out through simple search schemes, e.g. bisection search [*Siripunvaraporn and Egbert*, 2000; *Press et al.*, 2007]. A common choice of Υ^2 is 1 RMS, but the value may vary for certain problems [*Siripunvaraporn*, 2010]. Occam's inversion can be further subdivided into data and model space inversion. The model space algorithm, like the GN method, uses the first order Taylor's series expansion to linearise the forward response (cf. Eq. 6.36). In that case the solution to Equation 6.34 with the error function as defined in Equation 6.33 yields the iterative sequence

$$\vec{m}_{k+1} - \vec{m}_0 = \left[\tau \mathbf{R}_{mm}^{-1} + \mathbf{J}_k^T \mathbf{R}_{dd}^{-1} \mathbf{J}_k\right]^{-1} \mathbf{J}_k \mathbf{R}_{dd}^{-1} \vec{d'}_k, \tag{6.38}$$

where $\vec{d'}_k = \vec{d} - f(\vec{m}_k) + \mathbf{J}_k \cdot (\vec{m}_{k+1} - \vec{m}_0)$. Equation 6.38 can be solved for a number of different τ at each iteration step, and the model with the smallest misfit and norm at the target level (determined in phase I and phase II, respectively) is kept for the next iteration

[*Siripunvaraporn and Egbert*, 2000; *Siripunvaraporn*, 2010]. The advantages of the code are that it converges in a small number of iterations, and that it searches for a minimum structure model [*Constable et al.*, 1987; *Siripunvaraporn and Egbert*, 2000]. The latter means that all structures in a model are more reliable as they are required by the data and not unconstrained artefacts of the inversion [*Siripunvaraporn*, 2010]. The disadvantage of the code is its large computational cost, similar to the GN methods, i.e. inverting the $M \times M$ matrix $\left[\tau \mathbf{R}_{mm}^{-1} + \mathbf{J}_k^T \mathbf{R}_{dd}^{-1} \mathbf{J}_k\right]$ and computing the $N \times M$ Jacobian.

The issue of large computational cost can be mitigated by transforming the computational space from the model space into the data space, rearranging Equation 6.38 as

$$\vec{m} - \vec{m_0} = \mathbf{R}_{mm} \mathbf{J}^T \vec{\beta}, \tag{6.39}$$

where $\vec{\beta}$ is a unknown coefficient vector of length N [*Parker*, 1994; *Siripunvaraporn and Egbert*, 2000; *Siripunvaraporn et al.*, 2005a]. Inserting Equation 6.39 into Equation 6.32 and differentiating the resulting function with respect to $\vec{\beta}$ yields the iterative sequence of approximate solutions

$$\vec{m}_{k+1} - \vec{m_0} = \mathbf{R}_{mm} \mathbf{J}_k^T \mathbf{R}_{dd}^{-1/2} \left[\tau \mathbf{I} + \mathbf{R}_{dd}^{-1/2} \mathbf{J}_k \mathbf{R}_{mm} \mathbf{J}_k^T \mathbf{R}_{dd}^{-1/2}\right]^{-1} \mathbf{R}_{dd}^{-1/2} \vec{d'}_k, \tag{6.40}$$

where $\mathbf{I}$ is the identity matrix. Therefore, only a $N \times N$ matrix $\left[\tau \mathbf{I} + \mathbf{R}_{dd}^{-1/2} \mathbf{J}_k \mathbf{R}_{mm} \mathbf{J}_k^T \mathbf{R}_{dd}^{-1/2}\right]$ (instead of the $M \times M$ matrix in the model space) needs to be inverted, which significantly reduces CPU time and memory usage [*Siripunvaraporn and Egbert*, 2000; *Siripunvaraporn et al.*, 2005a]. However, the algorithm still requires the costly computation of the Jacobian.

In the data space Occam's inversion and in the GN approach, inversion of the matrices (Eqs. 6.38 and 6.37, respectively) is usually computational the most expensive part of the process. In the *quasi-Newton* (QN) method the inverse matrix is therefore approximated through a recursive process, in which $\mathbf{H}^{-1}$ is replaced by a successively adapted matrix [*Fletcher and Powell*, 1963; *Shanno*, 1970]. As a result the main computation for each QN iteration is reduced to computing $\nabla^T \vec{m}$ and performing the line search, meaning that the memory requirement of the QN method is insignificant in comparison with the GN method [*Siripunvaraporn*, 2010]. Because of the QN method's slow convergence rate [*Haber*, 2005] modifications are made to permit large datasets; e.g. approximating only the part of $\mathbf{H}$ that is related to the data misfit, rather than the full $\mathbf{H}$ [*Haber*, 2005]; or introducing additional regularisations [*Avdeev and Avdeeva*, 2009].

Like the QN method, the *Gauss-Newton with Conjugate Gradient* (GN-CG) method is set up to reduce the computational load of inverting the large matrices in Equations 6.37, 6.38, and 6.40. The method is referred to as model space GN-CG or data space GN-CG, respectively, dependent on whether it is set up to solve Equation 6.38 or 6.40. The advantage of the method is that instead of $\mathbf{J}$ only the product of $\mathbf{J}$ and $\mathbf{J}^T$ with an arbitrary vector $\vec{V}$ is required, i.e. $\mathbf{J}\vec{V_a}$ and $\mathbf{J}^T\vec{V_b}$. $\vec{V_b}$ and $\vec{V_b}$ can be computed by solving one forward problem [*Mackie and Madden*, 1993; *Newman and Alumbaugh*, 2000; *Rodi*

and Mackie, 2001; *Siripunvaraporn and Egbert*, 2007]. The different computation results in a significant reduction of the computational cost [e.g. *Siripunvaraporn*, 2010]. GN-CG inversion is divided into two loops: the outer inversion loop, and the inner CG loop replacing the direct solver (e.g. LU-factorisation [*Smith and Booker*, 1991]). The efficiency of the GN-CG method is controlled by the number of CG iterations (N_{CG}) [*Avdeev*, 2005; *Siripunvaraporn and Egbert*, 2007; *Siripunvaraporn and Sarakorn*, 2010], which in turn is anti-proportional to the smoothing parameter τ [*Siripunvaraporn and Egbert*, 2007; *Siripunvaraporn and Sarakorn*, 2010]. A pre-conditioner, such as the QN method, can be included to reduce the inversion time by speeding up the CG solver [*Haber et al.*, 2005].

In the *nonlinear conjugate gradient inversion* (NLCG) method the computation of **H** is replaced by a line search determining the step length parameter in the CG approach. The direction for the CG iteration step is usually derived using either the Fletcher-Reeves [*Fletcher and Reeves*, 1964] or the Polyak-Ribiere [*Polyak and Ribiere*, 1969] methods. Computational requirements of the NLCG method are similar to the QN method and are dominated by the computation of $\nabla^T \vec{m}$ and the line search [*Newman and Alumbaugh*, 2000; *Rodi and Mackie*, 2001]. The efficiency of the NLCG method is controlled by the number of NLCG iterations and the line search step, the former can be significantly reduced using a pre-conditioner [*Newman and Alumbaugh*, 2000; *Rodi and Mackie*, 2001; *Newman and Boggs*, 2004]. The overall CPU time is in the order of the model space GN-CG method [*Rodi and Mackie*, 2001].

Inversion programs for MT data

A list of commonly-used, freely-available inversion programs for MT data is given in Table 6.3, with most of the programs being accessible via the MTNet website. Whereas a range of 1D and 2D inversion programs is today easily obtainable, only one non-commercial 3D inversion code (`WSINV3DMT`) is available at present. Even though the `WSINV3DMT` program is based on model space Occam's inversion (cf. Sec. 6.3.3) it is computationally still very expensive, making inversion of larger datasets with a high resolution virtually impossible. Full 3D investigations of the subsurface with MT data are therefore presently limited to forward modelling processes. Further 3D inversion programs are under development, e.g. `MCMT3DID` [*Miensopust*, 2010], which will hopefully allow 3D inversion to become a common tool of MT investigation in the future. The `MCMT3DID` program has the advantage that it is set up to include the effects of distortion; however, because the algorithm uses a FE forward solver and the Gauss-Newton method for inversion it is computational very expensive. Therefore, faster and more powerful computing machines are required to facilitate detailed 3D inversion of MT data. One solution to the problem of required computational power might be parallelisation of the algorithms and intensive employment of cluster computers, carried out, among others, by *Ritter et al.* [1998]; *Newman and Alumbaugh* [2000]; *Newman et al.* [2003].

In principle, inversion programs can also be applied to cases of lower dimensionality investigation, such as 3D inversion of 2D MT profile data [e.g. *Siripunvaraporn et al.*,

2005b]). Those inversions are able to cope with distortion effects by small-scale bodies (cf. Sec. 4), but they might exhibit an inferior performance (in terms of speed or resolution) due to a set-up that is adjusted to the respective dimensionality. It is therefore advised to first determine the dimensionality for the dataset (cf. Sec. 4.2) and then apply the adequate inversion tool. Using an inversion program for a case of higher dimensionality, e.g. 2D inversion of 3D structures, could significantly reduce computation time, therefore allowing for higher resolution. However, such inversion can result in serious misinterpretations of the subsurface when the effects of 3D structures are not adequately accounted for [e.g. *Jones*, 1983a; *Wannamaker et al.*, 1984; *Garcia et al.*, 1999; *Ledo et al.*, 2002; *Ledo*, 2005] (cf. Sec. 4). Recent inversion programs (`1Dai`, in Tab. 6.3; `MT2Dinv v6.7` [*Baba et al.*, 2006]) also consider effects of anisotropic structures on MT responses. These inversion programs account for advances in instrumentation and the resulting enhanced resolution, as well as revised theoretical concepts. However, such inversion processes have to be carried out with caution in order to prevent mixing up dimensionality and anisotropy; e.g. anisotropic 1D instead of isotropic 2D, or anisotropic 2D instead of isotropic 3D (cf. Sec. 4.1.3).

For all types of MT inversion, it has to be kept in mind that the resulting model is only a fit to the response data and is highly non-unique. Therefore, additional information from other geological and geophysical studies should be used wherever possible and careful considerations should be given to the physical implications of the model.

Inversion algorithm	Advantages	Disadvantages	Applications
Model space Occam's inversion	Small number of iterations to converge; Robust; Smoothness parameter is obtained automatically; obtain minimum model norm	Long CPU time and large memory usage; It is often impractical to apply	*Constable et al.* [1987]; *de Groot-Hedlin and Constable* [1990]; *Pek and Santos* [2002]
Data space Occam's inversion	Same as the model space Occam's inversion but faster and uses significantly less memory	May still require large memory for large problems	*Siripunvaraporn and Egbert* [2000]; *Siripunvaraporn et al.* [2005a]
GN method	Small number of iterations to converge	Same as the model space Occam's inversion; convergence depends on smoothness parameter; requires several runs with different smoothness parameter	*Haber et al.* [2000]; *Rodi and Mackie* [2001]
GN-CG method	Same as GN method but small amount of memory usage	Convergence depends on smoothness parameter; can fail to converge for some smoothness parameters; can be slower than GN method	*Mackie and Madden* [1993]; *Newman and Alumbaugh* [1997]; *Siripunvaraporn and Egbert* [2007]
QN method	Small amount of memory usage	Convergence rate is slower than others	*Avdeev and Avdeeva* [2009]
NCLG method	Small amount of memory usage; convergence rate is comparable to GN	Convergence depends on smoothness parameter; requires several runs with different smoothness parameter; can fail to converge for some smoothness parameters	*Rodi and Mackie* [2001]; *Baba et al.* [2006]

Tab. 6.2.: Comparison of inversion algorithms; after *Siripunvaraporn* [2010].

Dimensionality	Name	Reference
1D and 2D	OCCAM	*Constable et al.* [1987]
2D	inv2D[1]	*Smith and Booker* [1991]
2D	REBOCC	*Siripunvaraporn and Egbert* [2000]
2D	RLM2DI[2]	*Rodi and Mackie* [2001]
3D	WSINV3DMT	*Siripunvaraporn et al.* [2005a]
anisotropic-1D	1Dai	*Pek and Santos* [2006]

Tab. 6.3.: List of commonly-used, freely-available inversion programs for MT data; 1: The program inv2D is commonly referred to as RRI (Rapid Relaxation Inversion), 2: An updated inversion of the RLM2DI program is included in the commercial *WinGLink* [2005] software package. A multitude of 1D inversion programs for MT data is today easily available and individual versions are therefore not included here.

Part II

Geology of the study area

It is rock science, not rocket science.

– JPS

7 Geology of the Iberian Peninsula

7.1. Overview

The Iberian Peninsula is the westernmost extent of the Eurasian Continent, bordered by the Bay of Biscay to the north, the Atlantic Ocean to the west, the Mediterranean Sea to the south and southeast, and connected to the test of the Eurasian plate in the northeast (Fig. 7.1). Its most prominent topographic features are the Cantabrian Mountain Chain in the northwest, the Pyrenees in the northeast, the Betic Mountain Chain in the south, as well as the intraplate ranges Spanish Central System and Iberian Ranges. Thorough descriptions of the Iberian Peninsula geology are given for example in *Gibbons and Moreno* [2002b, and references within] and *Moratti and Chalouan* [2006, and references within]. A detailed overview about the geological evolution as well as past and present-day stress fields of the Iberian Peninsula are given in *Andeweg* [2002]; a compilation of figures therein, related to the PICASSO Phase I investigation, is given in Section A.1 in the appendix. A general summary of the events most relevant for the PICASSO Phase I investigation is given in the following paragraphs, focussing on the regions in the vicinity of the PICASSO Phase I profile. Therefore, this Chapter deals mostly with the tectonic settings of the Betic Cordillera and the Tajo Basin, including its subbasins and surrounding regions. But at first a general overview is given in the following paragraphs describing the main tectonic features of the Iberian Peninsula.

Due to the distinct geological contrast between the eastern and western Iberian Peninsula these two parts are commonly referred to as *Alpine Spain* and *Variscan Spain* (sometimes also referred to as *Hercynian Spain*), respectively. The former is dominated by Mesozoic and Cenozoic sediments and young belts, whereas the latter comprises Precambrian and Palaeozoic rocks with minimal overprint by Alpine deformation [e.g. *Gibbons and Moreno*, 2002a]. The Variscan belt results from oblique collision and interaction between the Palaeozoic supercontinents Gondwana, Laurentia, and Baltica and a number of continental microplates taken place during Neoproterozoic through Palaeozoic times [*Abalos et al.*, 2002]. The Iberian Massif, accounting for the majority of the Variscan

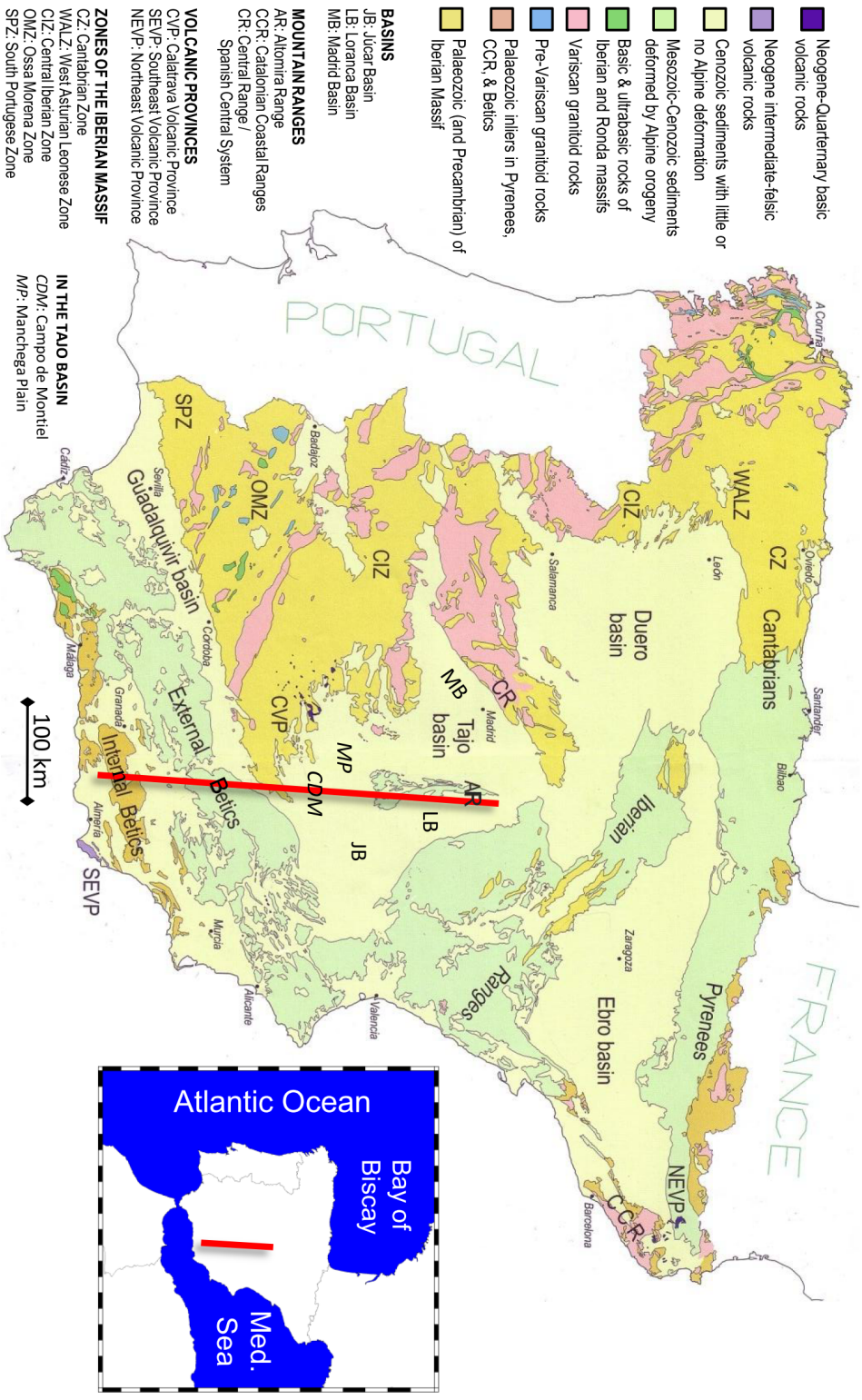

Fig. 7.1.: Geology of the Iberian Peninsula displaying the main tectonic features and geological units of Spain; modified after *Gibbons and Moreno* [2002a]. The location of the PICASSO Phase I profile is indicated by the red line.

part, represents a thick Palaeozoic shelf sequence of sediments, including Silurian graptolitic black shale [*Garcia-Alcalde et al.*, 2002] and Devonian carbonates [*Colmenero et al.*, 2002], both materials possessing the potential to form good electric conductors (see Section 5 for details about electric conductivities), and extension-related volcanic rocks, with a Proterozoic basement [*Gibbons and Moreno*, 2002a]. The Iberian Massif also contains the Ossa-Morena Zone (OMZ in Fig. 7.1), located in the south-west of Spain, which originates from the Cadomian orogeny and is therefore pre-Variscan [*Gibbons and Moreno*, 2002a].

The Cantabrian Mountains were initially formed during Variscan orogeny and underwent post-orogenic deformations during subsequent tectonic processes, whereas the Betics and Pyrenees are due to Alpine orogeny, the result of successive collision of the Iberian continental plate with Eurasia and Africa in Late Mesozoic – Cenozoic times [e.g. *Dewey et al.*, 1989; *DeMets et al.*, 2006; *Muñoz*, 1992; *Abalos et al.*, 2002; *Azanon et al.*, 2002; *Capote et al.*, 2002; *Gibbons and Moreno*, 2002a; *de Vicente and Vegas*, 2009]. The intraplate ranges are compressional mountain belts from Alpine orogeny (Spanish Central System, CR in Fig. 7.1) and Tertiary orogeny (Iberian Ranges), separating the three major Iberian basins, namely Duero, Ebro, and Tajo. Details about geologic settings of these intraplate ranges and the Tajo Basin are given in Section 7.3, describing the regions around the PICASSO Phase I study area more closely.

For the central Iberian Peninsula, a lithospheric thickness of around 110 km (±5 km) has been inferred (cf. Sec. 7.3), diminishing towards the boundaries of the peninsula to depths as shallow as 60 km at the Valencia Trough. The crust beneath the stable interior has a typical continental structure with a thickness of 31 – 32 km and increased thickness under the Alpine ranges [e.g. *Capote et al.*, 2002]. Deep structures beneath the peninsula are not well resolved since deep probing seismic studies are complicated due to Iberia's location on the edge of Europe. Seismic studies in this region, which, besides MT, have the best potential to reveal deep-seated features, are challenged by the need to install and maintain long-term stations in the Atlantic Ocean [e.g. *Cloetingh et al.*, 2009] (cf. Sec. 7.3.2).

7.2. Betic Mountain Chain

The Betic Mountain Chain (also *Betic Cordillera* or *Betics*) is part of the arc-shaped alpine Betic-Rif Cordilleras, stretching from the southeastern edge of the Iberian Peninsula through the strait of Gibraltar down to the east of Morocco. The Betic-Rif Cordilleras surround the Alboran Basin (also referred to as *Alboran Domain* and *Alboran Microplate*), located beneath the western Mediterranean Sea. The Rif and Betic mountains are thrust belts characterised by south-, west-, and north-vergent low angle thrust systems with tectonic transportation directed away from the Alboran Basin [*Seber et al.*, 1996]. The tectonic setting of the Betic Cordillera is reasonably well known, and it is widely accepted that the mountain chain was formed due to the collision of the African and Iberian plates

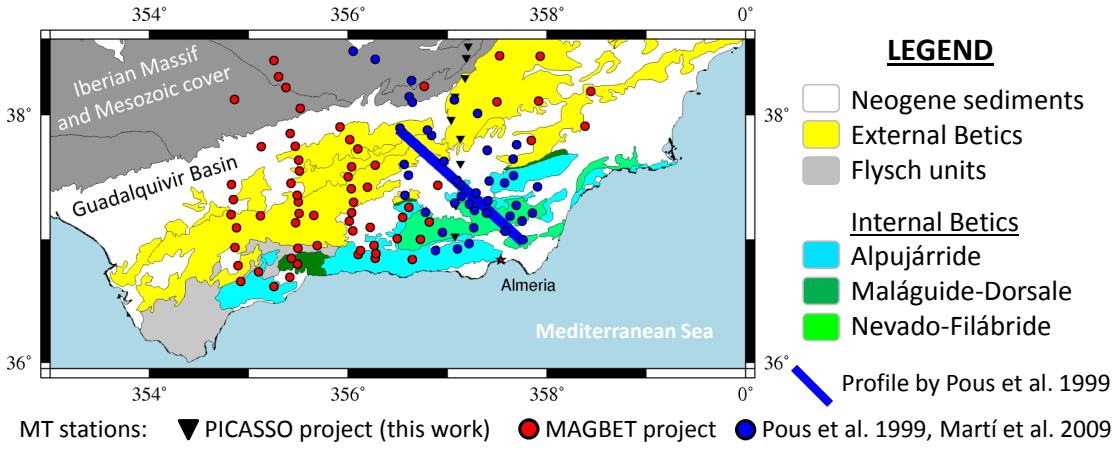

Fig. 7.2.: Location of magnetotelluric (MT) recording sites in the Betic Cordillera denoted by dots, with colours indicating the affiliation with the respective projects. Studies by *Martí et al.* [2009a] and *Rosell et al.* [2010] include data from preceding projects; the blue line refers to the 2D profile location of *Pous et al.* [1999].

since the Late Cretaceous. The Betic Cordillera exhibits two geological very distinct regions referred to as the *Internal part* and the *External part* (Fig. 7.1). The two parts are separated by the *Flysch units*, deformed deep-water sediments of Cretaceous to Miocene age, supposedly a former sedimentary cover at the palaeomargins of the westernmost part of the Tethys Ocean [e.g. *Platt and Vissers*, 1989; *ILIHA DSS Group*, 1993; *Gibbons and Moreno*, 2002a; *Tejero and Ruiz*, 2002; *Chalouan et al.*, 2006; *Pedrera et al.*, 2006; *Martí*, 2007]. The Internal Betics region is composed of graphite-rich, metamorphic Palaeozoic, and locally Triassic, rocks that initially were part of the Alboran Domain. These rocks were stacked over southern Iberia in latest Palaeogene – Neogene times due to the opening of the Alboran Basin and propagated further into the Iberian margin during the Miocene epoch. The related Oligocene – Miocene faults cut and alter the previous strata of the Internal Betics, originally containing stacked thrust sheets emplaced in pre-Mesozoic times, resulting in a highly complex subsurface structure [e.g. *Platzman*, 1992; *Pous et al.*, 1999; *Gibbons and Moreno*, 2002a; *Chalouan et al.*, 2006; *Martí et al.*, 2009a]. The External Betics region, on the other hand, comprises the allochthonous cover of the former Mesozoic south-Iberian continental margin and overlying foreland sediments, consisting of a deformed wedge of Mesozoic to Lower Miocene carbonates and marls, overthrusting the Neogene Guadalquivir Basin [e.g. *Pous et al.*, 1999; *Martí et al.*, 2009a].

7.2.1. Previous geophysical studies in the region

Magnetotelluric investigation in the central region of the Betic Chain has previously been carried out by *Pous et al.* [1999] and *Martí et al.* [2009a] and has recently been advanced by the MAGBET project [*Rosell et al.*, 2010] (see Fig. 7.2 for the location of the MT recordings). During the project by *Pous et al.* [1999], broadband MT data were inverted along an approximately NW-SE aligned profile, crossing the mountain chain roughly per-

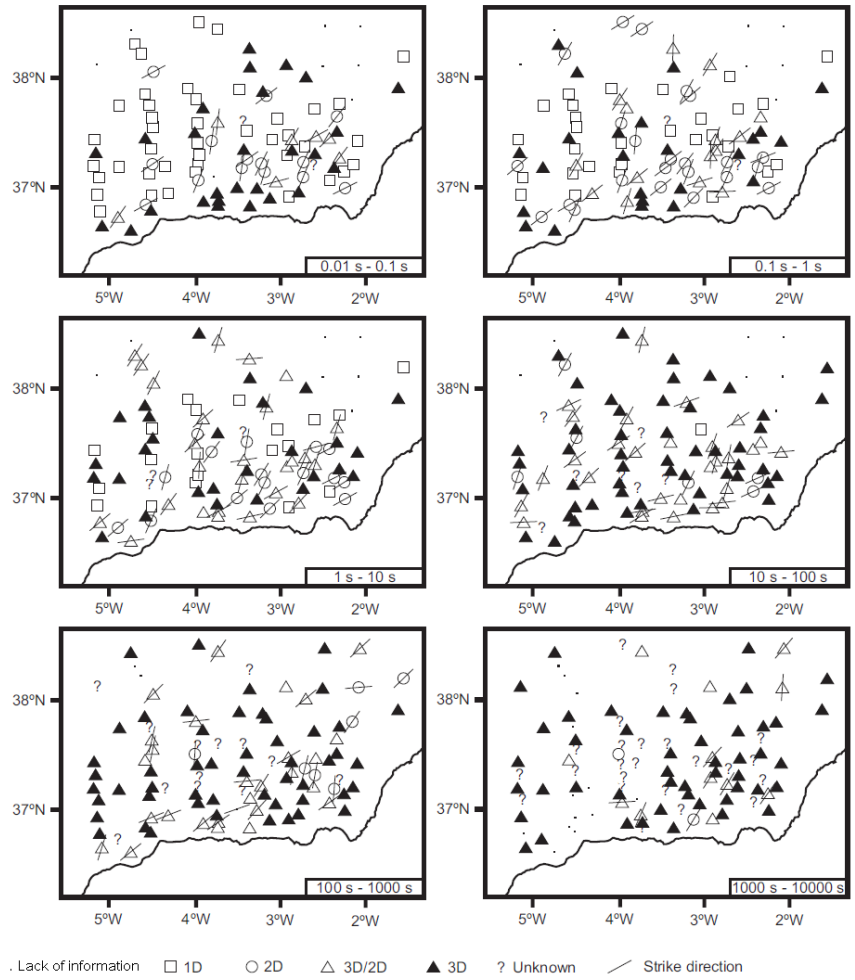

Fig. 7.3.: Dimensionality analysis results for magnetotelluric data from the Betic Cordillera using the WALDIM approach (Sec. 4.4.3); from *Rosell et al.* [2010].

pendicular; whereas *Martí et al.* [2009a] and *Rosell et al.* [2010], accounting for the complex regime of the Betics, deployed stations in a 2D array in order to facilitate 3D. The presence of 3D structures affecting the MT data was determined by *Martí et al.* [2009a] and *Rosell et al.* [2010] using the WALDIM algorithm *Martí et al.* [2009b] (Fig. 7.3; see Sec. 4.4.3 for details about the WALDIM method). Results by *Rosell et al.* [2010] confirm earlier findings by *Martí et al.* [2009a], showing that 3D geoelectric behaviour prevails for periods longer than 10 s, therefore emphasising the need to thoroughly consider such effects during the inversion process. The concept of a highly complex 3D Betics structure is supported by other recent studies carried out in this region, utilising different geophysical methods to investigate orogeny, tectonic setting, and internal structure of the Betics [e.g. *Carbonell et al.*, 1998; *Serrano et al.*, 1998; *Banda et al.*, 1993; *Zeyen et al.*, 2005; *Pedrera et al.*, 2006; *de Vicente and Vegas*, 2009; *Fullea et al.*, 2009].In the following, the three MT studies (*Pous et al.* [1999], *Martí et al.* [2009a], and *Rosell et al.* [2010]) are

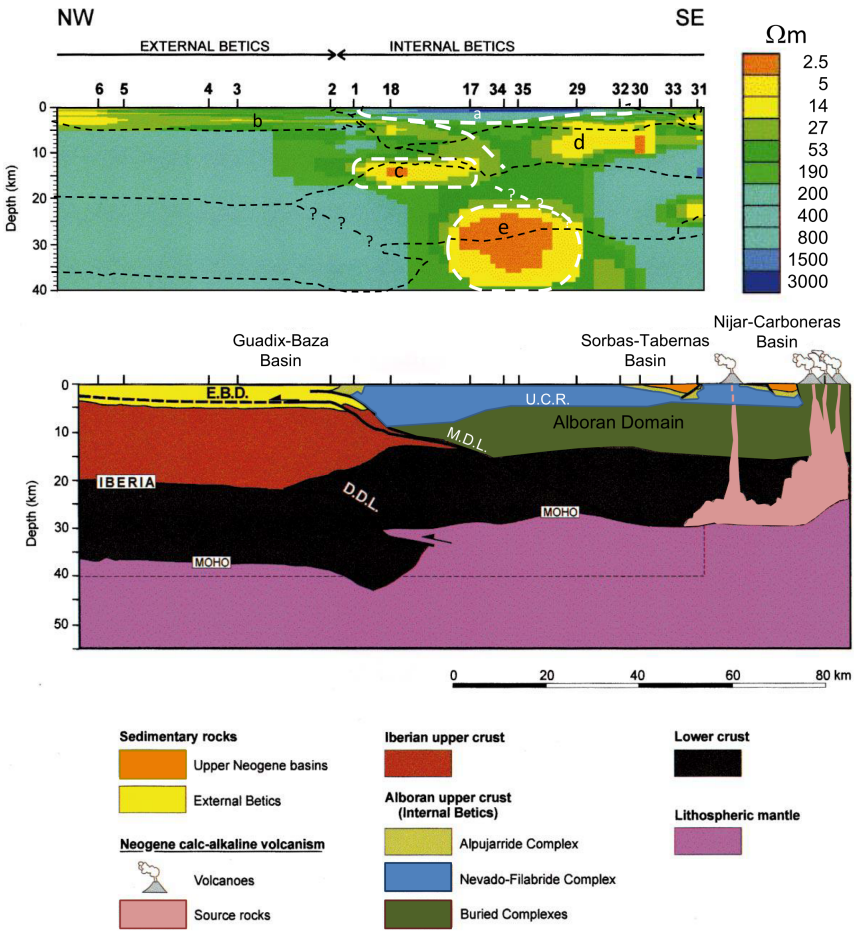

Fig. 7.4.: Subsurface model of the electric conductivity distribution beneath the Betic Cordillera by *Pous et al.* [1999] (upper panel); see Figure 7.2 for location of the profile. Letters refer to major features of the model (see text for details), whereas black, dashed lines denote the location of different geological regions (colour-coded in lower panel), inferred from structural and reflection seismic data. Question marks indicate that the interface is solely deduced on the base of geometrical considerations. Dashed lines in the lower panel denote the location of the electric conductivity model and acronyms EBD, UCR, MDL, and DDL refer to the main seismic reflectors.

inspected in more detail, their results are contrasted and used to understand the setting of the Betic Cordillera.

Pous et al. [1999] combined results from their 2D MT profile inversion with findings from geological and seismic studies (see references in *Pous et al.* [1999]) in order to aid their interpretation (Fig. 7.4). The shallow subsurface distribution is derived from surface structural data, whereas deeper features are constrained by seismic reflection profiles. The interface DDL is geometrically inferred, proposed in order to explain the duplication of the lower crust and a jump in the Moho. The interpretations for the features in their 2D MT subsurface model given by *Pous et al.* [1999] are summarised in Table 7.1. As a result of their observations, the authors provide two subsurface models that are in agreement with their data and the other geophysical and geological studies (Fig. 7.5). The two models are particularly different in terms of the Internal Betics Lower Crustal origin; the region may

Feature	Interpretation
(a)	Outcrops of the Nevado-Filábride Complex, containing graphite-rich rocks. The low conductivity indicates a low connectivity of the conducting phases in this region.
(b)	Sedimentary layer of the Guadalquivir Basin with high conductivity due to fluid intrusion in the porous medium.
(c) and (d)	Increased conductivity due to fluid circulation along faults
(e)	Increased conductivity due to partial melting of the Iberian lower crust in this region.

Tab. 7.1.: Interpretation of the features in their Betic Cordillera subsurface model by *Pous et al.* [1999]; the location of the profile is shown in Figure 7.2.

either be part of Iberian plate or the Alboran Domain. The two models imply different locations of the plate boundaries, thus different tectonic histories. No preference for either of the models is given by *Pous et al.* [1999], noting that additional data is required for a ratification.

Among the features in the model by *Pous et al.* [1999], the authors' interpretation that the lower crustal conductor ('e' in Figure 7.4) is due to partial melting of the subducted Iberian lower crust is certainly the most controversial. Their interpretation is supported by observed low P-wave velocity in this region [*Carbonell et al.*, 1998], but all conclusions drawn from a 2D inversion are associated with a higher degree of uncertainty when conducted in a highly 3D region like the Betic Cordillera (cf. Fig. 7.3). In order to determine whether 2D inversion for the profile by *Pous et al.* [1999] is valid, *Martí* [2007] conducted a dimensionality analysis using the WALDIM approach (Sec. 4.4.3). *Martí* [2007] assesses the dimensionality for different areas of the profile by projecting the dimensionality analysis results for each station on the inversion model by *Pous et al.* [1999], using a Niblett-Bostick depth-transformation (Sec. 6.3.1). The results indicate that most regions of the lower crust, in particular in the area of the good conductor, are three-dimensional (Fig. 7.6). Accordingly *Martí et al.* [2009a] use a 3D inversion of the dense broadband MT station array (see Fig. 7.2 for station location) obtaining a small scale, high conductive feature that is confined to crustal depth, instead of an extensive lower crustal conductor (see Fig. 7.7). *Martí et al.* [2009a] interpret the small scale feature as body of basic or ultra-basic rocks (ophiolites or peridotites) due to results of other geophysical studies; i.e. low seismic activity, relatively high P-wave velocity in the crust [*Dañobeitia et al.*, 1998], normal heat flow [*Fernandez et al.*, 1998], uncorrelated topography and gravity data, and a magnetic anomaly (-40 to +30 nT) [*Galindo-Zaldívar et al.*, 1997]. The hypothesis of a basic or ultra-basic body is supported by observations of similar materials in the region [*Reuber et al.*, 1982; *Tubía et al.*, 1997; *López Sánchez-Vizcaíno et al.*, 2001; *Crespo et al.*, 2006] and the presence of a differentiated lithologic unit in the core of the main Nevado-Filábride antiform [*Azanon et al.*, 2002].

Martí et al. [2009a] present three models for the origin of the conductive body, varying

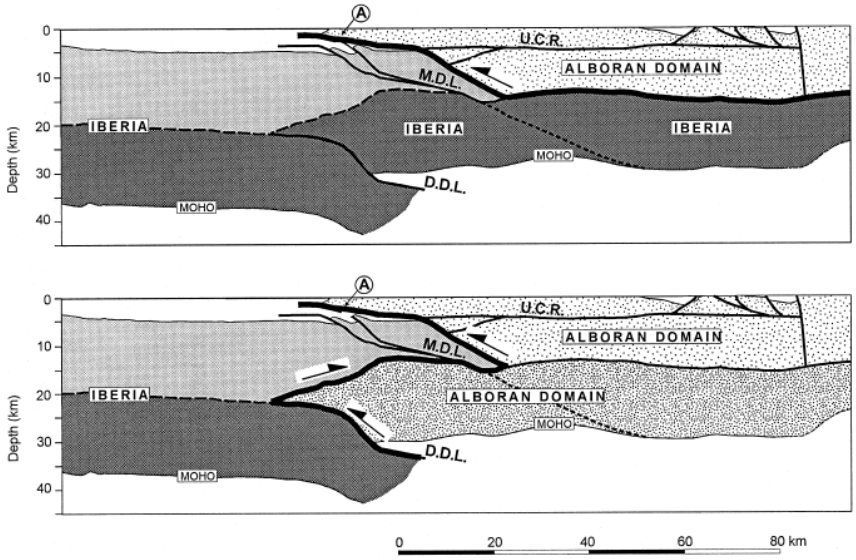

Fig. 7.5.: Two regional models of the Betic Cordillera with different affiliation of the lower crust beneath the Internal Betics, and cause for the subduction of the Iberian Plate beneath the boundary of Internal and External Betics as observable at the surface; from *Pous et al.* [1999]. Upper panel: Lower crust beneath the Internal Betics belongs to the Iberian Plate and the subduction of the Iberian lower crust is an intraplate structure. Lower panel: Lower crust beneath the Internal Betics belongs to the Alboran Domain and the Iberian lower crust is the subducted beneath the Alboran Domain lower crust. *A* denotes the contact between Iberian and Alboran Domain.

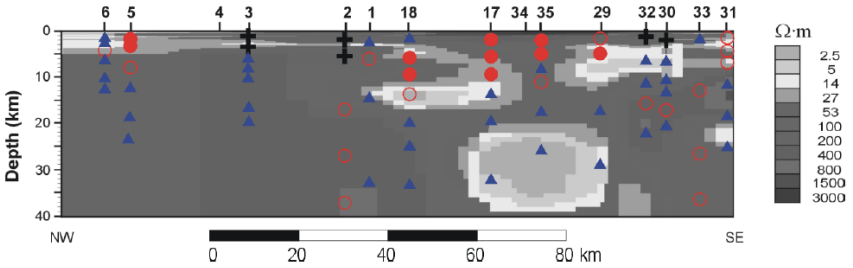

Fig. 7.6.: Dimensionality of the subsurface along the magnetotelluric (MT) profile by *Pous et al.* [1999] using the WALDIM approach (Sec. 4.4.3), with Niblett-Bostick depth-transformation (Sec. 6.3.1) and static shift corrections (Sec. 4.1.1); from *Martí* [2007]. +: 1D, ○: 2D or 3D/2D, ●: 3D/2D, ▲: 3D.

in terms of initial geological setting and occurring trust kinematics (Fig. 7.8). Among these, the authors favour the models containing two well-differentiated oceanic lithospheric blocks (A1, A2 in Fig. 7.8) due to their better consistency with models based on other geophysical data [e.g. *Tubía et al.*, 1993; *Platt et al.*, 2006]. However, results from further studies are needed to verify the hypotheses regarding the origin of the conductive body.

Rosell et al. [2010] extended the work by *Martí et al.* [2009a] by re-recording previous sites with long-period MT instruments as well as collecting data at additional sites, located mostly to the northeast and to the southwest of previous recordings (Fig. 7.2). This enables the authors to carry out a 3D inversion for a larger area of the Betic Cordillera, as well as for greater depth extent. At crustal depth, the inversion model by *Rosell et al.*

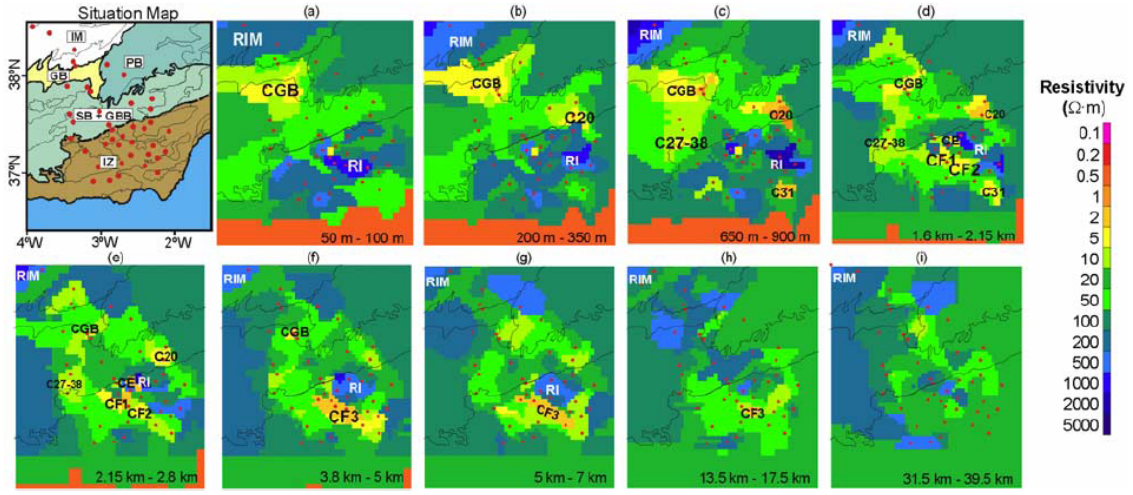

Fig. 7.7.: Situation map and horizontal cross sections of the 3D model by *Martí et al.* [2009a]; red dots denote the location of MT recording stations. Main geological zones in situation map: IM (Iberian Massif), GB (Guadalquivir Basin), PB (Prebetics), SB + GBB (Subbetics + Granada and Guadix-Baza Basin), and IZ (Internal Zone). Cross sections: Narrow lines mark the geological divisions; the depth range of each layer is indicated in the bottom right. Main conductive and resistive features are indicated by alphanumeric acronyms with *C* and *R* referring to a conductor and resistor respectively. The conductor related to the feature (e) in the model by *Pous et al.* [1999] (Fig. 7.4) is labelled *CF3*.

[2010] is in general agreement with the previous model by *Martí et al.* [2009a] for the respective regions; new insights are gained in particular about deeper-seated structures, located in the Earth's mantle (cf. Fig. 7.9). The authors use the transition from high conductivities ($\geq 500\,\Omega$m) to values around $10\,\Omega$m as a proxy for the lithosphere–asthenosphere boundary (LAB), yielding a LAB depth of approximately 110 km for the eastern region of their model, increasing to 160 km for the western region. An elongated conductive region ($5 - 10\,\Omega$m) with an approximately north–south orientation, observed at depth greater than 35 km (labelled 'CB2' in Figure 7.2) is considered by *Rosell et al.* [2010] as most striking feature (Fig. 7.10). The authors interpret the feature as asthenospheric intrusion into the lithosphere, due to its increases conductivity and the absence of earthquake events within the area attributed to the feature. *Rosell et al.* [2010] relate the asthenospheric intrusion to a break-off phase and detachment of lithospheric material in the eastwards subducting slab beneath Alboran Domain and Betic Cordillera [e.g. *Gutscher et al.*, 2002; *Spakman and Wortel*, 2004; *Amaru*, 2007] (Fig. 7.11). For the gap in the slab to be located at the position proposed by *Rosell et al.* [2010], the break-off event needs to be relatively recent, since otherwise the gap is likely to have migrated away. Alternatively, a conductivity anomaly in the lithosphere could originate from corner flow around the subducting slab [e.g. *Arcay et al.*, 2005]. Note that the low resistivity region in the lithosphere in the model by *Rosell et al.* [2010] is not strongly constrained, due to the screening effect of the highly conductive feature above; the authors do not exclude such a screening effect in their paper. Investigating the focal mechanisms of the earthquake events in the proximity of the conductivity anomaly could enhance knowledge about the local stress regime and

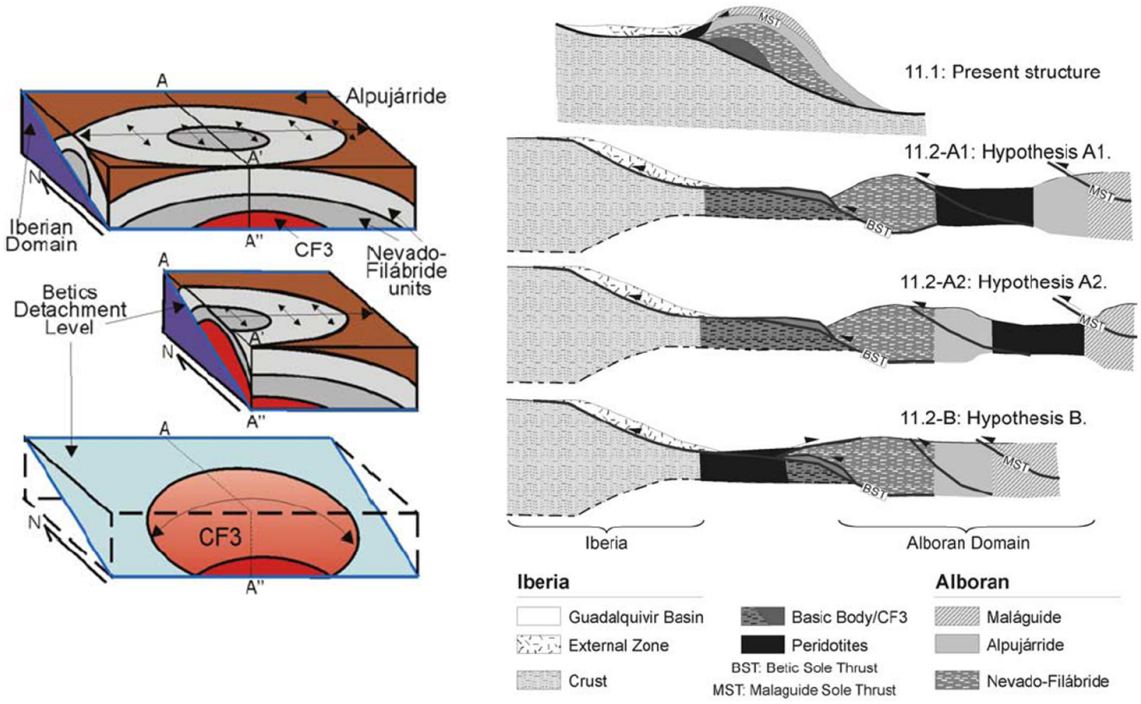

Fig. 7.8.: Schematic representation of the conductive feature in the Betic Cordillera (left-hand side, labelled CF3 in Fig. 7.7) and models regarding the tectonic history of the Betics that led to the formation of the feature; from *Martí et al.* [2009b]

therefore about the likelihood of a slab detachment in this region. Other causes of conductive anomalies, often observed to occur in conjunction with the subduction of a slab, are hydration, partial melt, and serpentinisation processes [e.g. *Stesky and Brace*, 1973; *Peacock*, 1990; *Jones*, 1992; *Karato et al.*, 2001; *Xie et al.*, 2002; *van Keken*, 2003; *Arcay et al.*, 2005; *Evans et al.*, 2010; *Pommier and Le-Trong*, 2011; *Reynard et al.*, 2011]. However, details about mechanisms related to these conductive features and the resulting responses in electric conductivity are presently still under debate. Determination of the true cause of this anomaly beneath the Betic Cordillera is therefore challenging, and additional data are required to enhance knowledge about this feature.

It is shown by these previous magnetotelluric investigations of the Betic Cordillera, that the complex tectonic history of the region is reflected by the electric conductivity distribution. The Betics subsurface is highly 3D, requiring adequate inversion of MT array data and careful interpretation of the results. Additional data, in particular in the Alboran Sea, are necessary to study the nature of the present lithospheric subduction and its interaction with the Betic Cordillera subsurface.

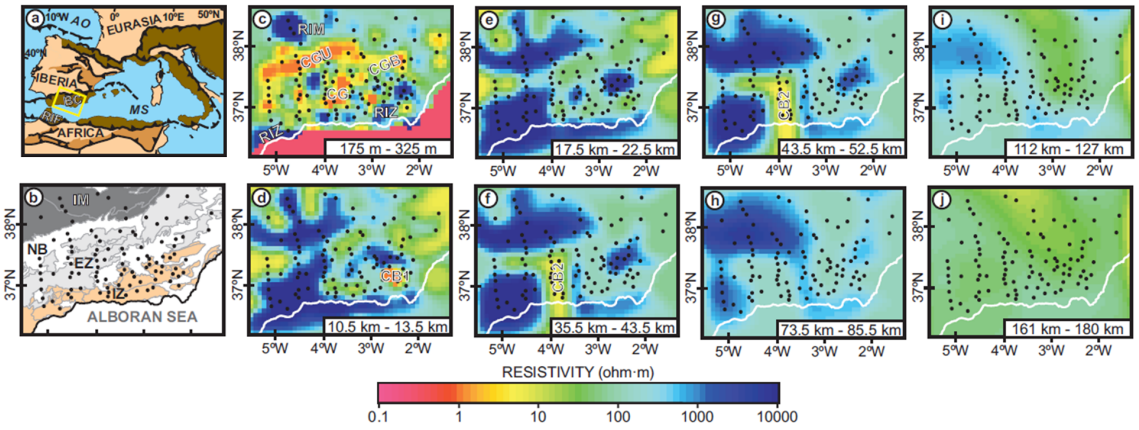

Fig. 7.9.: a) Regional tectonic map of the Western Mediterranean with the yellow rectangle denoting the study area; AO: Atlantic Ocean, BC: Betic Cordillera, MS: Mediterranean Sea. b) Simplified structural map of the study area with distinguished main tectonic units, i.e. IM: Iberian Massif (dark grey), NB: Neogene Basins (white), EZ: External Zone (light grey), IZ: Internal Zone (orange). c-j) Top view slices selected from the 3D resistivity model with the main resistive and conductive features identified, i.e. RIM: Resistive Iberian Massif, RIZ: Resistive Internal Zones, CGU: Conductive Guadalquivir Basin, CG: Conductive Granada Basin, CGB: Conductive Guadix-Baza Basin, CB1: Conductive Body 1, CB2: Conductive Body 2. Black dots in b-j) denote magnetotelluric recording locations. From *Rosell et al.* [2010].

7.3. Tajo Basin and central Spain

The central region of Spain, comprising the Tajo Basin and its surrounding units, is described here in more detail because parts of the PICASSO Phase I profile are located in, and the focus of this study is on, this region. Thorough descriptions of evolution and properties of the Tajo Basin are given, for example, in the work by *Alonso-Zarza et al.* [2002] and in the respective chapters of the collection by *Gibbons and Moreno* [2002b]. In the following paragraphs, the relevant content of these references is summarised and extended by findings of different authors covering certain aspects of the Tajo Basin geology; furthermore, the results of geophysical investigations from a range of methods is used to enhance knowledge about the geological setting.

7.3.1. Tectonic evolution and characteristics

The Tajo Basin (English: *Tagus Basin*) is bordered to the west by the Iberian Massif, to the north by the Spanish Central System, to the east the Iberian Range, and in the south by the Betics Chain and the Campo de Montiel (cf. Figs. 7.1, 7.12) all described in more detail in the following paragraphs. The basin was formed during the Anisian age (Middle Triassic) and subsequently widened until the Norian age (Late Triassic) due to propagation of the Tethys Sea (which later became the Tethys Ocean) over the eastern margin of the Iberian plate [*Lopez-Gomez et al.*, 2002] (Fig. 7.13). Arising shallow marine carbonates drowned the NW-SE trending Palaeozoic high that originally separated the Tajo Basin from the Iberian Basin in the NW, resulting in a basin that is bounded to the NW by the Iberian Massif, opened eastwards to the Tethys, and linked with the Betic basin

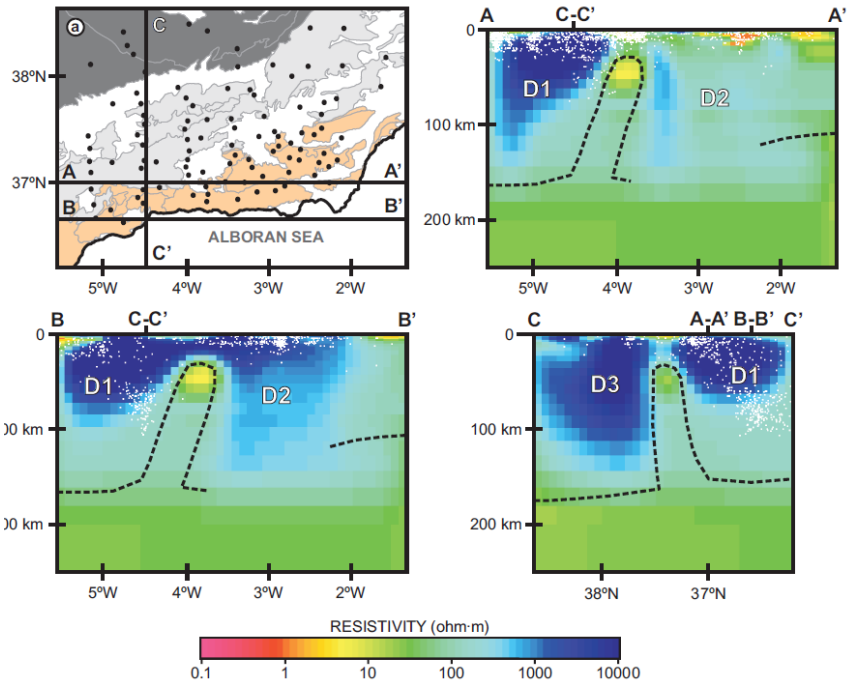

Fig. 7.10.: a) Structural map of the Betic Cordillera with black dots denoting the location of MT recording sites and black lines indicating the location of transects shown in this figure. A-A', B-B', C-C') vertical slices of the 3D model crossing the CB2 body. Therein, white dots show hypocentre locations within a 8 km margin of the respective profile, recorded since 1900. Dashed lines indicate the lithosphere–asthenosphere boundary (LAB) inferred from the resistivity distribution, and labels D1, D2, and D3 refer to features in the 3D model. From *Rosell et al.* [2010].

to the south [*Lopez-Gomez et al.*, 2002] (Fig. 7.14). The basin was again separated from the northern regions of the Iberian Basin (forming the Ebro and Duero Basins) during Palaeogene Alpine convergence between Europe and Africa due to the resulting uplift of the Iberian and Catalonian Coastal Ranges [*Aurell et al.*, 2002; *Lopez-Gomez et al.*, 2002; *Martin-Chivelet et al.*, 2002]. Thereafter, the Tajo Basin became the locus of Tertiary sedimentation, establishing it as an intracratonic depocentre [*Alonso-Zarza et al.*, 2002; *Gutierrez-Elorza et al.*, 2002]. It underwent little or no alpine deformation, but later became subdivided due to the Pliocene uplift of the Altomira Range (*Sierra de Altomira* in Spanish literature), a branch of the Iberian Range. The resulting subbasins are the Madrid Basin and the much smaller Loranca Basin (also referred to as *Intermediate Depression* or *western sector of the Júcar Basin*) to the north, and the Manchega Plain to the south [*de Vicente et al.*, 1996; *Alonso-Zarza et al.*, 2002; *Andeweg*, 2002; *Gibbons and Moreno*, 2002a; *Gutierrez-Elorza et al.*, 2002] (Fig. 7.12).

The *Loranca Basin* has been characterised as foreland basin produced by a westward-moving Iberian fold–thrust belt, possessing a 1 – 1.4 km thick layer of Eocene to Quaternary sediments containing primarily sandstone, gravel, mudstones, limestone, gypsum, and lacustrine carbonates [*Gomez et al.*, 1996; *Torres et al.*, 1997; *Andeweg*, 2002]. The basin experienced a folding phase during the early Miocene, presumably due to the on-

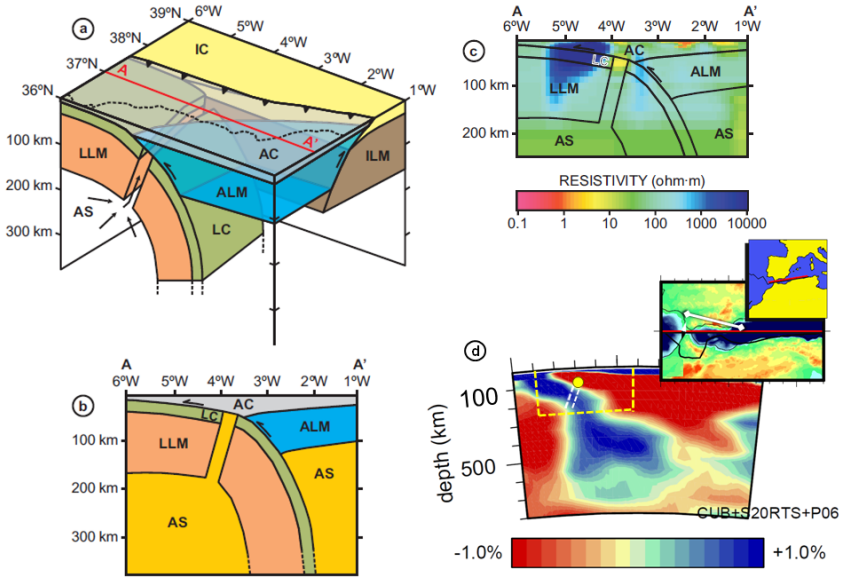

Fig. 7.11.: a–b) geodynamic scheme and cross-section of the subsurface beneath Betic Cordillera and Alboran Domain proposed by *Rosell et al.* [2010], wherein the dashed line denotes the coast line and the red line A-A' indicates the location of the transects b) and c). c) shows a projection of the model onto the collocated transect of the 3D inversion model by *Rosell et al.* [2010]. d) Seismic velocity distribution of the same region inferred from a 3D seismic tomography study by *Amaru* [2007], with the location of the seismic velocity–depth profile and the transects c) and d) shown in the inset as red and white line respectively. The dashed yellow line shows the approximate location of b) and c) whereas the yellow dot and the dashed white line indicate the location of the conductivity anomaly and the area of asthenospheric intrusion proposed by *Rosell et al.* [2010]. IC: Iberian Crust, AC: Alboran Crust (Internal Betics and Alboran Sea), LC: Ligurian Crust, ILM: Iberian Lithospheric-Mantle, ALM: Alboran Lithospheric-Mantle, LLM: Ligurian Lithospheric-Mantle, AS: Asthenosphere. Projection of the results by *Rosell et al.* [2010] onto a velocity–depth transect shows that anomaly is located on top of the region with relatively high velocity associated with the slab.

set of the Betics–Iberian collision [*Andeweg*, 2002]. To its south the *Manchega Plain*, representing the southern region of the Tajo Basin, comprises Quaternary aeolian sediments covering a substratum made up of the terraces of the alluvial systems of the Guadiana and the Júcar rivers [*Rebollal and Pérez-González*, 2008]. Further south, outside the Tajo Basin, the Campo de Montiel, a region of low-lying hills of Mesozoic carbonates, formed during Jurassic – Triassic times may constitute the southernmost part of the Iberian Ranges adjacent to the Betic Cordillera (Sec. 7.2) [*Aurell et al.*, 2002; *Gutierrez-Elorza et al.*, 2002]. Hence, the Jurassic strata of Iberian Range and Campo de Montiel are potentially connected below the Manchega Plain forming the base of the overlying younger layers [*Aurell et al.*, 2002, Fig. 11.7, p. 225].

The *Iberian Range* (also referred to as *Iberian Chain* in English and *Sistema Ibérico* or *Cordillera Ibérico* in Spanish literature) is a NW-SE orientated intraplate mountain range formed as consequence of pre-Alpine sedimentary Basin inversion [*Tejero and Ruiz*, 2002] due to the *Pyrenean Orogeny* [*de Vicente and Vegas*, 2009]. The Range was one of the few regions of the eastern Iberian Peninsula rising above sea level in pre-Cenozoic times [*Andeweg*, 2002]. After very limited deformation during the Late Oligocene, the

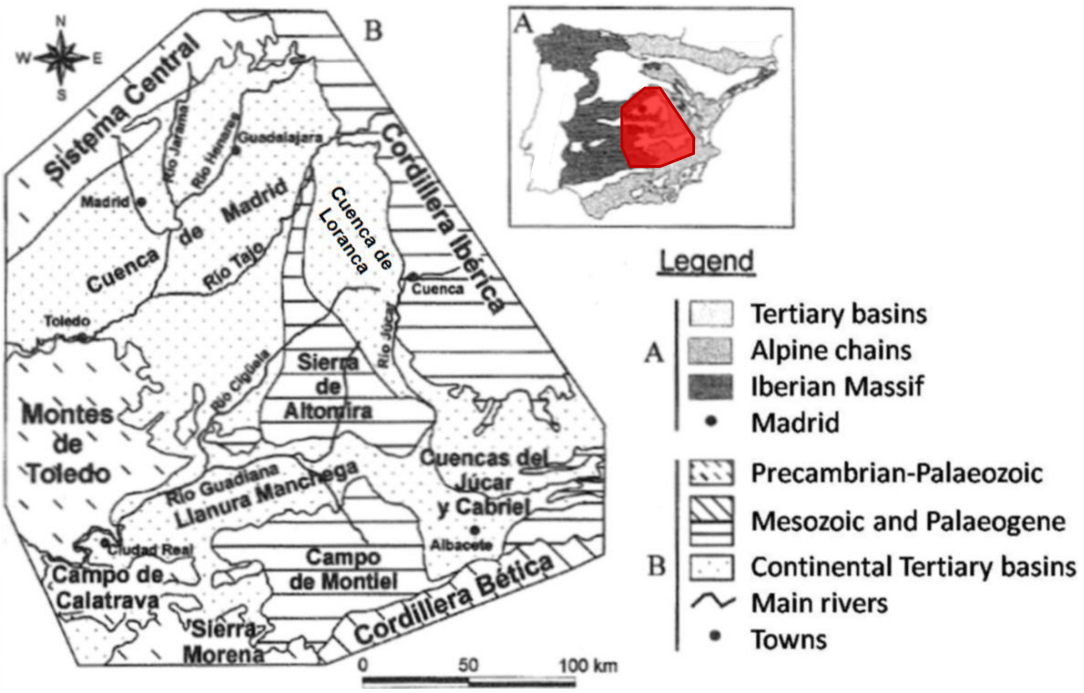

Fig. 7.12.: Main morphostructural units of the south submeseta and their location in the Iberian Peninsula; modified after *Gutierrez-Elorza et al.* [2002] (note: Cuenca = Basin, Montes = Mountains, Sierra = Mountain range, Llanura = Plain, Rio = River); the location of map B is indicated by the red area in map A in the top-right of this figure.

Iberian Range experienced intense deformation during the Middle Miocene, initiated by the Iberian – Internal Betics collision [e.g. *Andeweg*, 2002].

To the west of the Iberian Range, bordering the Tajo Basin to the northwest, the Spanish Central System (SCS; also referred to as *Central Range* or in Spanish as *Sistema Central*) forms a NE-SW trending mountain range branch. Outcrops of Variscan basement, associated with the Iberian Massif, contain mainly metamorphic and igneous rocks with granitic rocks dominating in the west and metamorphic rocks in the east [*Tejero and Ruiz*, 2002]. Details of the SCS formation process are not known at present, but several models have been proposed, describing the SCS as pop-up structure [*Warburton and Alvarez*, 1989; *de Vicente et al.*, 1996; *Tejero et al.*, 1996; *Andeweg*, 2002; *Alonso-Zarza et al.*, 2002; *Tejero and Ruiz*, 2002, and references within], or as a flower structure [*Portero and Aznar*, 1984; *Tejero et al.*, 1996] and attributing it to simultaneous strike-slip faulting and block rotation [*Vegas et al.*, 1990]. The start of the SCS configuration is dated at the Eocene – Oligocene boundary, with sedimentation in the Loranca and Madrid Basin (*Cuenca de Loranca* and *Cuenca de Madrid* in Fig. 7.12) as well as in the Iberian Range evidencing that at least the northeastern region of the SCS was constructed at that time [*Andeweg*, 2002]. The Moho deepens beneath the SCS, reaching a depth of 34 km, primarily due to thickening of the lower crust [*ILIHA DSS Group*, 1993], which was attributed by *Surinach and Vegas* [1998] to Cretaceous – Miocene shear zone activity of the SCS comprising rotation of brittle upper crust segments, together with ductile deformation and thickening of

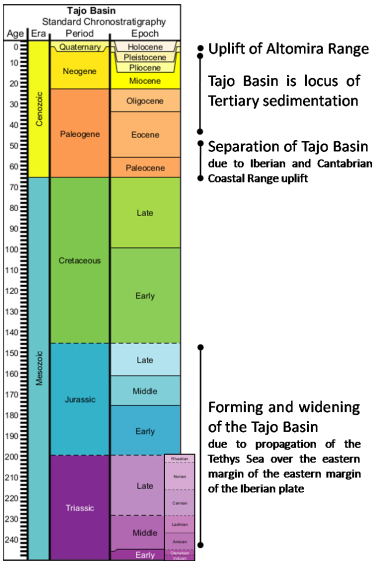

Fig. 7.13.: Geologic timescale with most relevant geologic events of the Tajo Basin

the deeper crust, resulting in elevated topography. The contact between the SCS and the sediments of the Tajo Basin to the south is a NE-SW trending reverse fault with a throw of more than 2 km, active from Palaeogene into Middle Miocene times [*Alonso-Zarza et al.*, 2002].

To the west of the Tajo Basin, accounting for the majority of the western region of the Iberian Peninsula, the *Iberian Massif* crops out, constituting the oldest part of the European Variscan orogeny formed during the Middle Devonian – Early Permian times as consequence of the collision between Laurentia and Gondwana [e.g *Colmenero et al.*, 2002; *Gibbons and Moreno*, 2002a]. The Iberian Massif was above sea level during pre-Cenozoic times and had a planar and low relief [*Stapel*, 1999], but was subsequently deformed by various Cenozoic tectonic events resulting in an arcuate geometry [e.g. *Andeweg*, 2002; *Colmenero et al.*, 2002; *Gibbons and Moreno*, 2002a, and references within]. The Iberian Massif consists mainly of igneous and metamorphic rocks and has commonly been divided into six zones or domains with the Precambrian outcrops of the *Central-Iberian zone* bordering the Tajo Basin to the west and south-west as well as to the north-west as part of the SCS [*Colmenero et al.*, 2002; *Tejero and Ruiz*, 2002; *Valladares et al.*, 2002] (Fig. 7.1).

Location and shape of the interface between the Jurassic – Triassic rocks forming the Iberian Range and the Variscan rocks of the Iberian Massif below the Tajo is presently unclear, but since the Altomira Range is part of the Iberian Range the interface is most likely to be found to its west, below the Madrid Basin. Hence, crustal materials beneath the northern part of the PICASSO Phase I profile, located in the Loranca Basin and the Manchega Plain are presumably of Mesozoic times.

Investigations of neotectonic stress tensors in the SCS and Madrid Basin [*de Vicente*

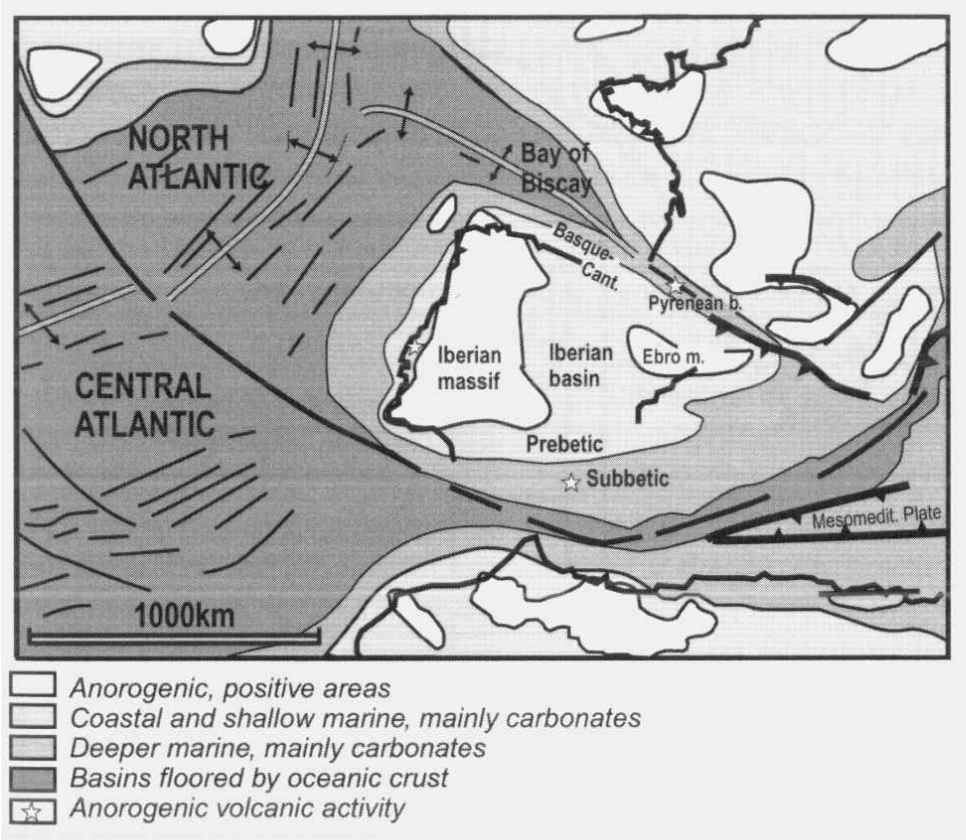

Fig. 7.14.: Palaeotectonic-palaeographic map of Iberia and surrounding areas during Cretaceous (Santonian), showing the main tectonosedimentary domains for that time; from *Martin-Chivelet et al.* [2002].

et al., 1996] indicate average directions between N130E and N155E for the different geological times from Middle Miocene to the present day. A number of faults, identified in the study by *de Vicente et al.* [1996], intersect the PICASSO Phase I profile, exhibiting a strike direction of approximately N45E (Fig. 7.15). Even though the precise depth of these faults is presently unknown, they could provide a good approximation of the dominant geoelectric strike direction to be expected in the Tajo Basin crust. The points of intersect between the three relevant faults and the PICASSO Phase I profile are located in the proximity of stations pic005, pic009, and pic013, hence an enhanced 2D nature of the upper crustal responses for these three stations is likely.

Volcanism in the Tajo Basin

Four main provinces of Cenozoic volcanism can be located in Iberian, mostly confined to the SE region of the peninsula [e.g. *López-Ruiz et al.*, 2002] (cf. Figs. 7.1, 7.16, 7.17). One of these provinces, the Calatrava Volcanic Province (CVP), is situated in the southwestern region of the Tajo Basin around the city of Ciudad Real, located approximately 100 km to the west of the PICASSO Phase I profile. For the CVP rocks

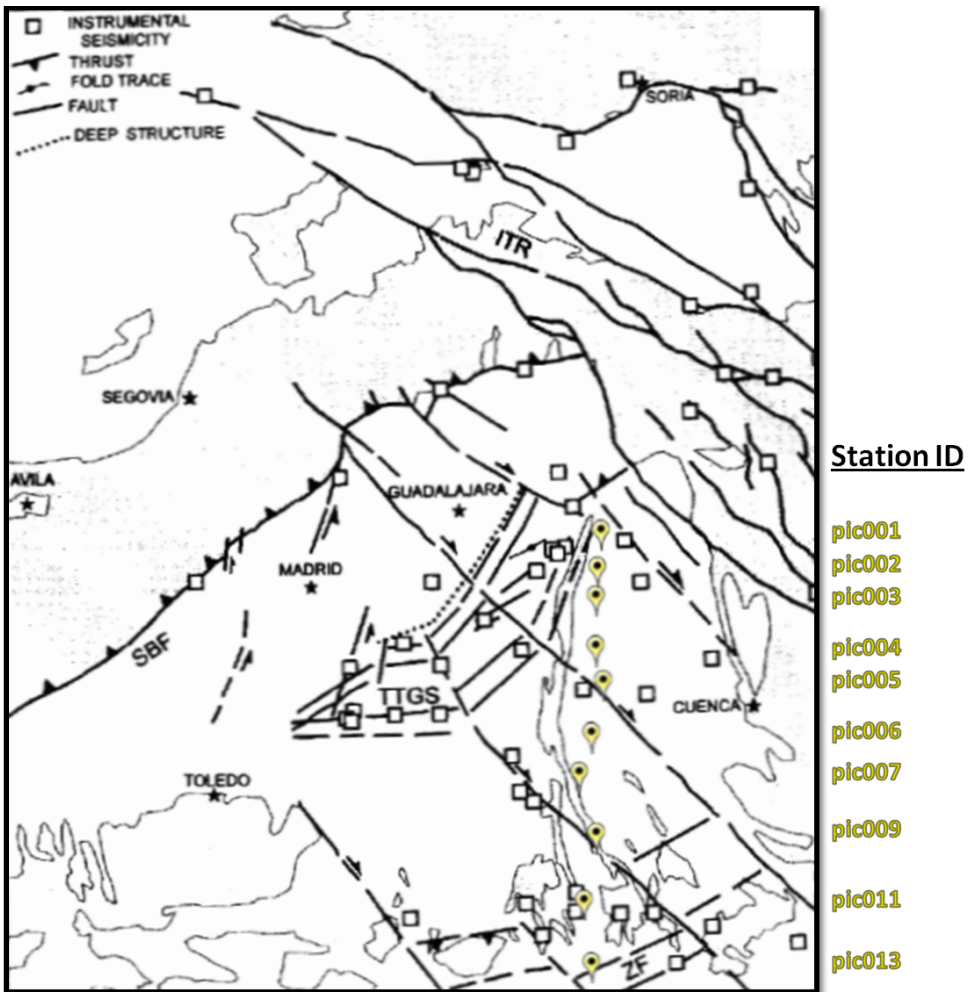

Fig. 7.15.: Structural outline of active present-day faults in the Tajo Basin and surrounding regions (from *de Vicente et al.* [1996]), overlain by the location of PICASSO MT recording sites. ITR: Iberian Transpressive Range, SBF: Southern Border Fault (of the Spanish Central System), TTGS: Tajo-Tajuña Graben System, ZF: Záncara River Fault.

two different sources have been determined by *López-Ruiz et al.* [1993], *Cebriá and López-Ruiz* [1995], and *Cebriá and López-Ruiz* [1996] based on geochemical composition; namely a ^{87}Sr-enriched and ^{143}Nd-depleted continental lithospheric-mantle as well as a ^{87}Sr-depleted and ^{143}Nd-enriched sublithosphere source relative to a primitive mantle. The authors relate the former to potassic volcanism during Miocene times (6.4 – 7.3 Ma) with olivine leucitites, whereas the latter is concluded to have formed the alkali basalts during Pliocene times (≈1.5 – 5 Ma). Age determination of the two volcanic intervals were therein based on K-Ar ratio analysis by *Ancochea et al.* [1979] and *Bonadonna and Villa* [1986]. For the basaltic suite *Cebriá and López-Ruiz* [1995] and *Cebriá and López-Ruiz* [1996] determine a degree of melting between 5% and 17% using quantitative trace element modelling, whereas for the olivine leucitites a relatively low degree of melting (≈4%) was inferred.

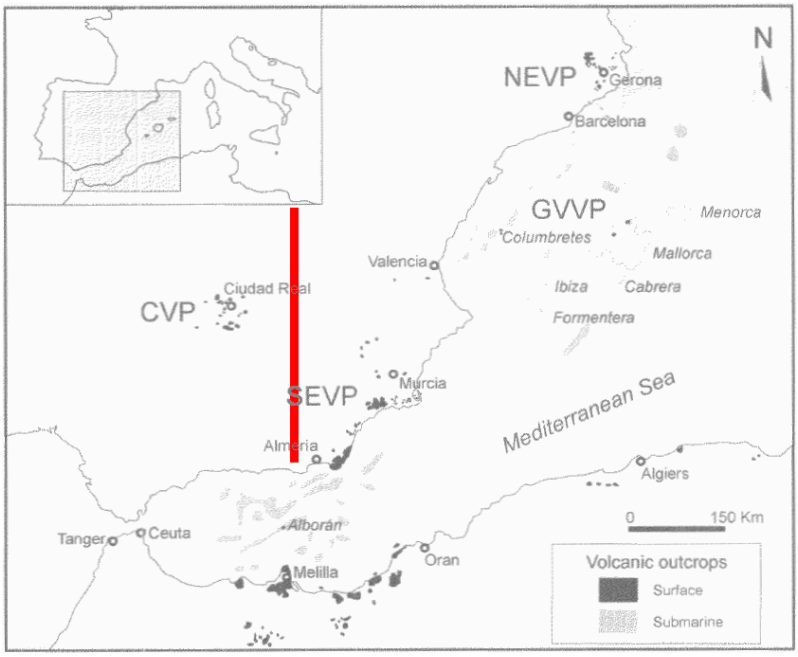

Fig. 7.16.: Cenozoic volcanic provinces in the SE Iberian Peninsula and NW Africa; from *López-Ruiz et al.* [2002] with the red line indicating the location of the PICASSO Phase I profile. NEVP: Northeastern Volcanic Province, GVVP: Gulf of Valencia Volcanic Province, CVP: Calatrava Volcanic Province, SEVP: Southeastern Volcanic Province (cf. Figs. 7.1 and 7.17).

Based on lava composition and geological characteristics of the related regions a two-stage process has been proposed by *López-Ruiz et al.* [1993] (later corroborated by *Cebriá and López-Ruiz* [1995] and *López-Ruiz et al.* [2002]): the first (Mesozoic) stage comprises melting of the lithospheric-mantle by a mantle-diapir resulting in the olivine leucitite volcanism and causing a general weakening of the crust; during the second (Pliocene) stage tectonic indentation in the eastern Betics (SE border of the Iberian Peninsula) [*Doblas et al.*, 1991] led to feeding of asthenospheric material in a NWN direction causing the basaltic volcanism in the CVP. CVP lavas of the secondary process may have been transported through the lithospheric fault network that was formed by extensional tectonics during late Miocene times [*López-Ruiz et al.*, 1993, 2002]; a hypotheses that is supported by predominant NW-SE trends of emission vents in the CVP [*Ancochea and Brändle*, 1982]. Connection between CVP and eastern Betics region is inferred by *Cebriá and López-Ruiz* [1995] and *López-Ruiz et al.* [2002] based on similarity of the basalt composition of the CVP rocks with the extensive trans-Moroccan, western Mediterranean, European (TMWME) reservoir that is the cause of volcanic events all across Europe and the eastern Atlantic [*Wilson and Downes*, 1991; *Cebriá and Wilson*, 1995; *Hoernle et al.*, 1995] (cf. Figs. 7.16, 7.17). The indentation event in the eastern Betics, which is thought to have initiated the second CVP event, is in agreement with the convex-to-the-NW arc-shaped geometry of the Prebetics and the Aguilas coastal region (SE edge of the Iberian Peninsula), as well as the uplift in the Campo de Montiel region (*Ruidera uplift*) [*López-Ruiz et al.*, 1993].

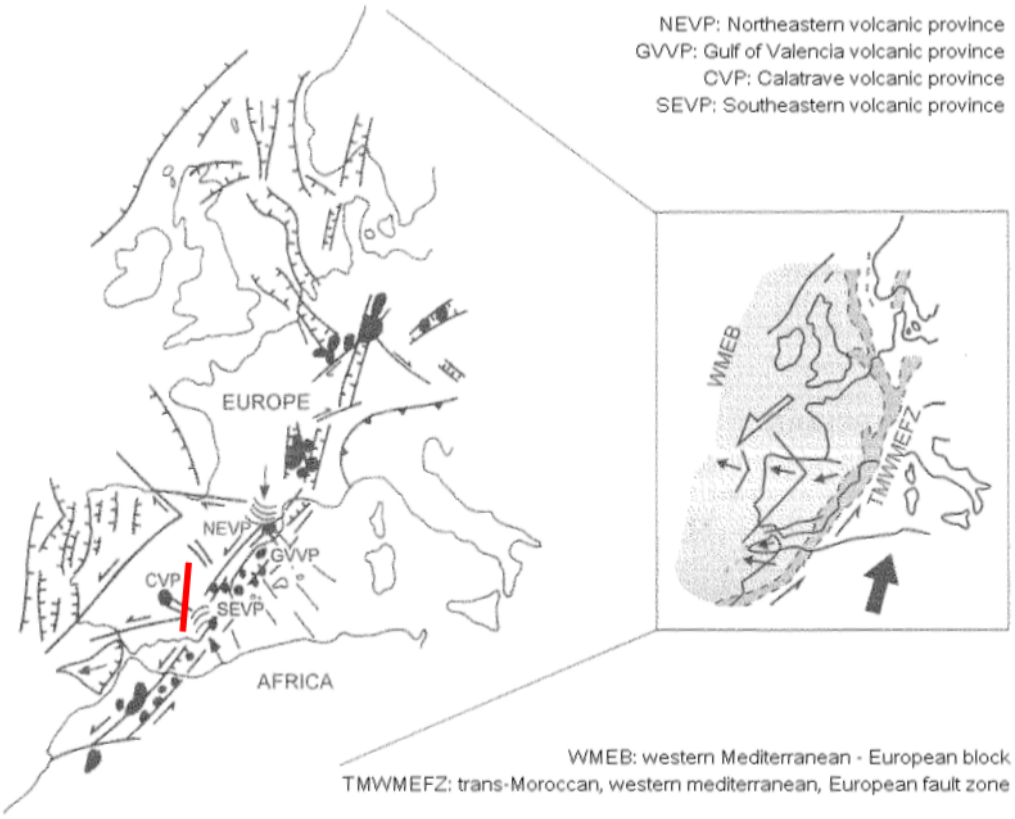

Fig. 7.17.: Tectonomagmatic scenario for the latest Miocene to present alkaline basaltic volcanism in western Europe; modified after *López-Ruiz et al.* [2002]. The tectonomagmatic scenario involves a NW-SE connection between the trans-Moroccan, western Mediterranean European (TMWME) fault zone and the Calatrava volcanic province (CVP) intersecting the PICASSO Phase I profile (indicated by the red line) in the area of the Campo de Montiel region. (cf. Figs. 7.1 and 7.16)

Alternatively to the indentation scheme, *López-Ruiz et al.* [1993] propose a mantle diapir as source for the second stage of volcanism in the CVP. A mantle diapir source could explain the horizontally small-scale (< 100 km) lithospheric thinning from approximately 100 km to 80 km thickness beneath the CVP proposed by *Bergamín and Carbó* [1986] based on an observed negative Bouguer anomaly in the region [*López-Ruiz et al.*, 1993; *Cebriá and López-Ruiz*, 1995].

The PICASSO Phase I investigation may provide additional information about the nature of the second stage since, in case of the Betics indentation source proposed by *Cebriá and López-Ruiz* [1995] and *López-Ruiz et al.* [2002], the course of the lava transport would intersect the PICASSO Phase I profile in the area of the Campo de Montiel region. Hence, indentation processes are likely to cause significant decrease of electric resistivity in station data at the related region along the PICASSO Phase I profile, presuming a sufficient amount of partial melt or remanent asthenospheric material in a region in close proximity to the profile.

Layer	Depth of lower boundary (km)	Velocity (km/s) P-wave	S-wave	Interpretation
Sediments	3.0	3.3	2.50	Tertiary and Mesozoic sediments
Crystalline basement	5 - 9	5.9 - 6.1	3.48	Low grade Palaeozoic metamorphic rocks (mostly shale and quartzite)
Intermediate crust	23 - 25	6.2 - 6.3	3.58	Igneous and metamorphic rocks (Migmatites, quartz-monozite, and granodiorite)
Lower crust	30 - 33	6.7 - 6.8	3.90	Igneous and metamorphic rocks (granodiorite, diorite, and granulites)
Uppermost mantle	...	8.0 - 8.2	4.4 - 4.5	Ultramafic rocks

Tab. 7.2.: Crustal layer thickness and seismic velocity below the Tajo Basin in proximity of the Iberian Massif, according to *Banda et al.* [1981]. Values for shear wave velocity and sedimentary layer are taken from *Díaz and Gallart* [2009]. Data were observed using seismic reflection and wide-angle profile, interpreted with reflectivity and ray-tracing methods (depth of uppermost mantle not resolved in this work).

7.3.2. Previous geophysical studies in the region

Previous geophysical studies, in particular MT, have been focussed on the area of the Pyrenees and the Betics Chain with their alpine orogeny (see Sec. 7.2); see *Korja* [2007] for a summary of MT investigations in Europe. Central Spain has been mainly the subject of near-surface research and has remained comparatively neglected in terms of deep-probing investigations, meaning that our study breaks new ground. An extensive literature search, however, did yield a number of studies providing information that are used to construct initial subsurface models and to contrast results of the PICASSO Phase I investigation (cf. Chap. 10). Results from this body of work are briefly presented here divided into groups of methods, followed by a summary of key aspects most relevant for the PICASSO Phase I project.

Seismic reflection

The crust–mantle interface beneath the Iberian Peninsula was investigated by *Banda et al.* [1981] and, recently, by *Díaz and Gallart* [2009] using a compilation of seismic sounding profiles. The authors derive a Moho depth between 30 km and 33 km, which deepens towards the SE and NE corners, coinciding with the locations of the Betic mountain chain and the Pyrenees – Iberian Chain respectively (Fig. 7.18). Additionally, wide-angle profiles interpreted with reflectivity and ray-tracing methods reveal two first-order discontinuities in the crust below the Tajo Basin region [*Díaz and Gallart*, 2009](Fig. 7.20). Accordingly, the authors divide the crust into three layers, i.e. upper crust (including sedimentary layer and crystalline basement), intermediate crust, and lower crust (associated with the Variscan basement of the Iberian Massif); respective values of seismic velocities

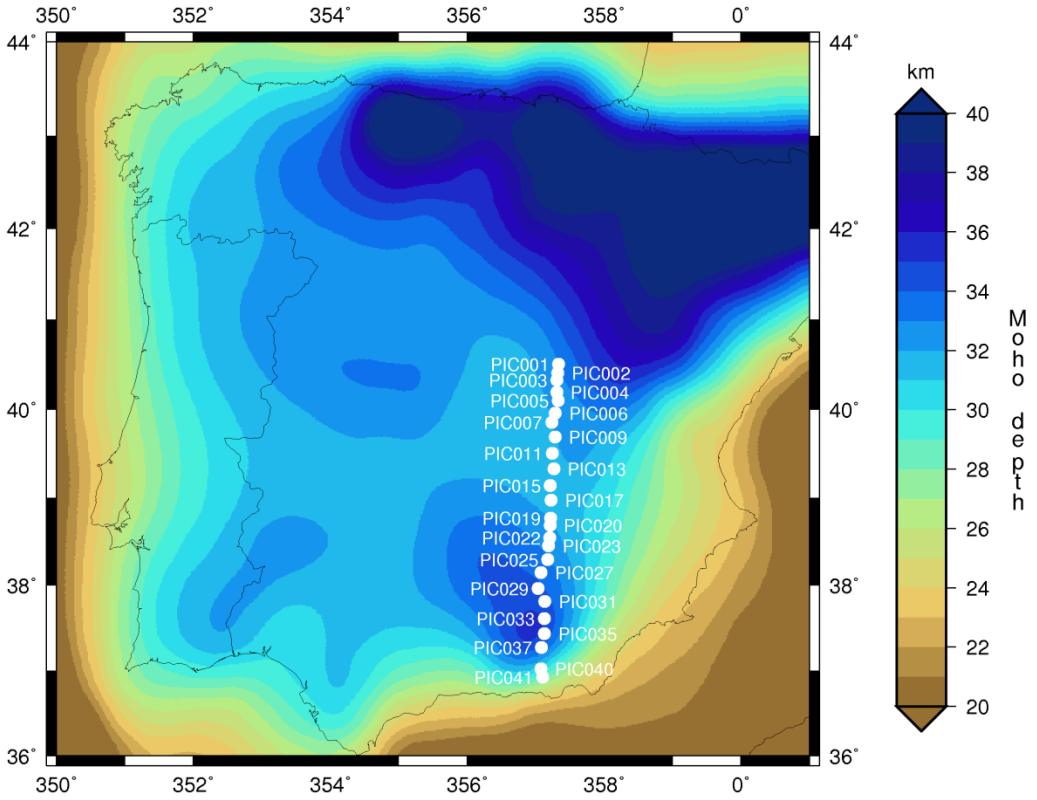

Fig. 7.18.: Depth of the Moho beneath the Iberian Peninsula and surrounding regions. Gridded data from seismic sounding results by *Díaz and Gallart* [2009] with dots denoting the location of MT recordings carried out during the PICASSO Phase I fieldwork campaign. Location of refraction and reflection profiles used by the authors to derive the Moho depth are given in Figure 7.19.

and crustal layer thicknesses are summarised in Table 7.2. Some authors propose an additional low velocity layer (V_p = 5.60 km/s, V_s = 3.18 km/s) at the bottom of the upper crust [*Banda et al.*, 1981]. However, this has not been confirmed by recent high-resolution experiments [*Palomeras et al.*, 2009].

Seismic refraction

Results of seismic refraction experiments are in agreement with findings by seismic reflection studies, indicating a three-layer crust with thicknesses of around 14 km (upper crust), 9 km (middle crust), and 8 km (lower crust); however, details about the layer properties vary slightly between different authors. Beneath the central Iberian region, the Moho occurs at an average depth of 31 km with no significant lateral variation except under the SCS where the crust exhibits an increased thickness of up to 34 km [*Banda et al.*, 1981; *Surinach and Vegas*, 1998; *ILIHA DSS Group*, 1993; *Gallart et al.*, 1995; *Pulgar et al.*, 1996].

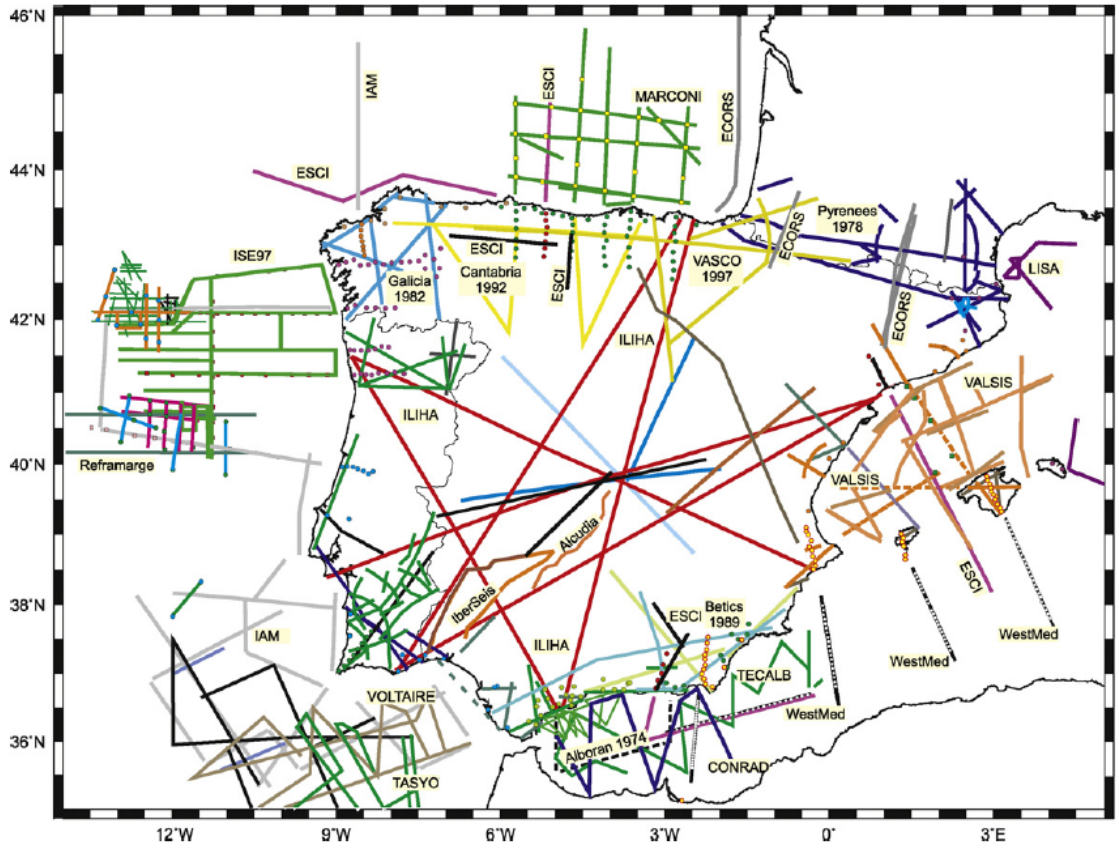

Fig. 7.19.: Location of refraction and reflection profiles used by *Díaz and Gallart* [2009] to derive the Moho depth with colours accounting for the different experiments (see *Díaz and Gallart* [2009] for respective references). Therein circles depict the location of Ocean Bottom Seismometers (OBS) and land stations of onshore-offshore profiles.

Seismic tomography

Seismic tomography allows, similar to magnetotellurics, investigation of deep-seated structures, thus having the potential to identify features in the region of the lithosphere–asthenosphere boundary (LAB). However, the seismically defined LAB does not necessarily always coincides with the one obtained by MT since the methods are sensitive to different material properties, namely seismic velocity and electric conductivity (cf. Sec. 5.2.2). Therefore, it is advised to refer to them as seismic LAB (sLAB) and electric LAB (eLAB) instead. Since the changes in velocity and conductivity are often due to changes of the material which are reflected in both properties, one may be used a good indicator of the other, justifying the consideration of seismic tomography as auxiliary material here.

Villaseñor et al. [2007] utilised four months of recorded waveforms for an ambient noise surface wave tomography study in which Rayleigh waves at periods from 8 s to 25 s are used to map group velocity across the Iberian Peninsula shallow subsurface. Obtained Rayleigh wave group velocity maps at 10 s and 20 s (representing average shear velocities in the upper 10 km and between 15 km and 30 km, respectively) reveal a SE-NW striking

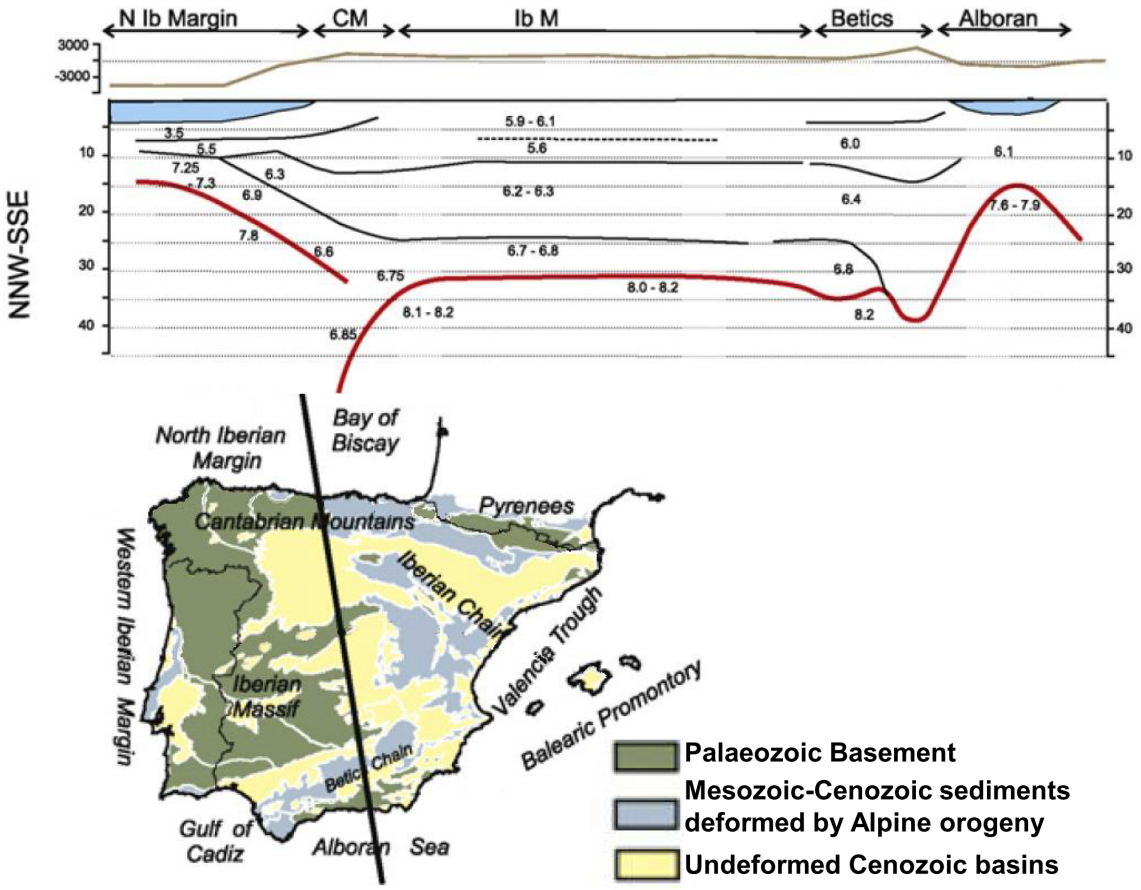

Fig. 7.20.: Velocity–depth distribution along a profile through the Iberian Peninsula (location of the profile is shown in the right hand side); modified after *Díaz and Gallart* [2009]. Results of the study are summarised in Table 7.2. '`N Ib Margin`': North Iberian margin; `CM`: Cantabrian Mountains; '`Ib M`': Iberian Massif.

high-velocity anomaly for the central Spain region (Fig. 7.21). The authors associated this feature with Palaeozoic basement rocks of the central region within the Iberian Range, in contrast to the lower velocities of Mesozoic sediments in the surrounding Tertiary basins, i.e. Ebro, Duero, and Tajo Basin. The high velocity is diminished in the 20 s map, interpreted by the authors as an indicator for the presence of an igneous and/or metamorphic core and a deep crustal root in the Iberian Range. This results in relatively low velocities in comparison with the surrounding material, in particular the high velocities in the Iberian Massif to the south and west. This lateral change in seismic velocity, indicating a lateral change in geology for this region, is likely to be reflected in MT data as well. It is supposedly emerging as a geoelectric strike with an approximate SE-NW direction for data at the northern end of the PICASSO profile, related to crustal depths of 30 km and above; see Section 9.6.1 for details on the geoelectric strike estimation.

Ambient noise tomography can only adequately resolve crustal structures given the small amplitude of the long period signals. Body wave and surface wave tomography studies, on the other hand, use signals generated by earthquakes, and are therefore able

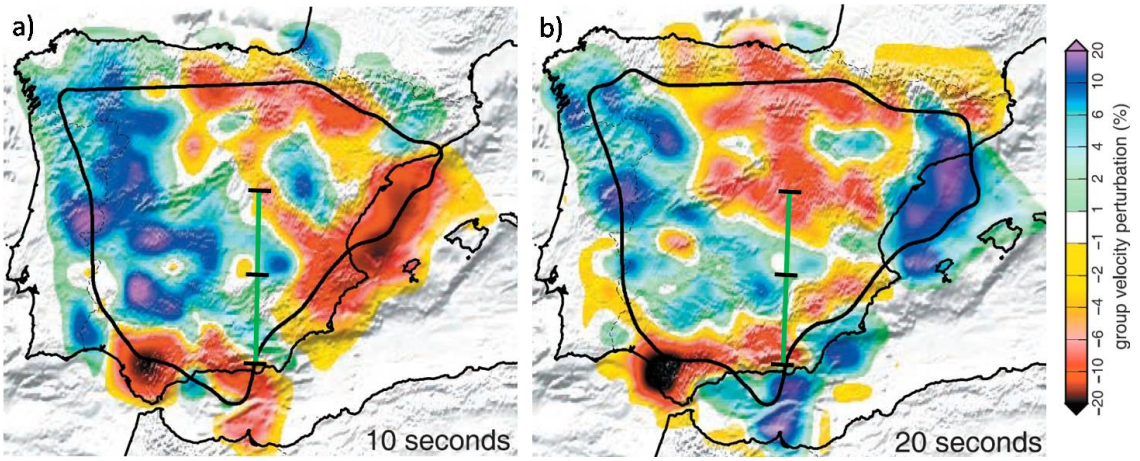

Fig. 7.21.: Group velocity maps of the Iberian Peninsula subsurface, obtained from ambient noise tomography using Rayleigh waves at periods of (a) 10 s and (b) 20 s, related to structures of the upper 10 km and between 15 km and 30 km, respectively. Thick contour lines indicate the region in which features with a lateral extend greater than 100 km are well resolved; from *Villaseñor et al.* [2007]. The green line denotes the location of the PICASSO Phase I profile, with black ticks indicating the limits of the profile and the boundary between Tajo Basin (to the north) and Betic Cordillera (to the south).

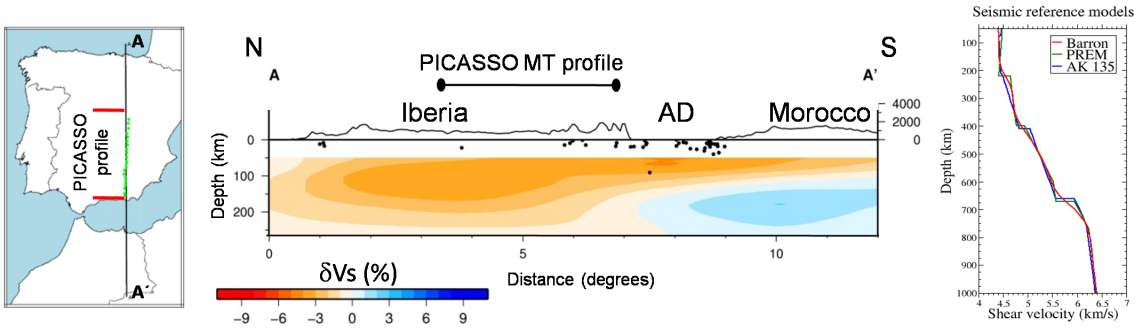

Fig. 7.22.: Shear velocity relative to a smoothed PREM-like model (shown on the right hand side) beneath a transect coinciding with the PICASSO Phase I profile, acquired from an European scale model by *Barron* [2010] using a horizontal correlation length of 250 km (AD: Alboran Domain). Also shown by black dots in the central graph are earthquake events, which occurred within a 150 km margin of the profile.

to investigate much deeper regions. Investigations related to the deep Spanish subsurface were conducted, among others, by *Barron* [2010], using surface wave tomography as part of his PhD study. The constructed surface-wave shear velocity model is based on the inversion of fundamental and higher-mode Rayleigh waveforms and has a footprint of 2 x 2 degree in the region of Spain, from which the author provided a 1200 km transect coinciding with the PICASSO Phase I MT profile. *Barron* [2010] used a horizontal correlation length of 250 km in order to construct the model (Fig. 7.22); however, these results are certainly preliminary. The displayed perturbation is relative to a smoothed PREM-like model and is assumed reliable down to a depth of 250 km. The top of the model is removed since only periods in the range 50 – 160 s are used. The transect displays a slight relative increase of velocity beneath the region of the PICASSO Phase I profile but mainly illustrates the above-mentioned difficulties of deep-probing seismic investigation due to

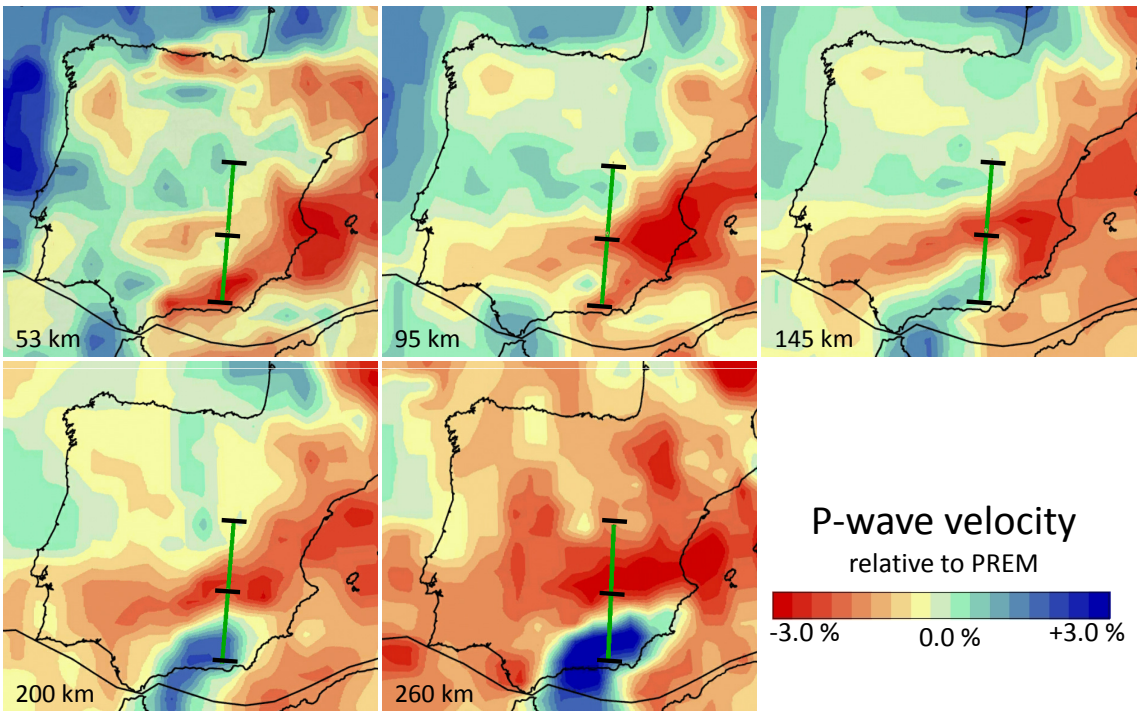

Fig. 7.23.: Body wave tomography of the Iberian Peninsula and surrounding regions shows a generally low relative P-wave velocity beneath the peninsula. Deep reaching roots of the Pyrenees and Betic Chain are indicated by even lower velocity, whereas a region of high velocity is observed beneath the Alboran Domain; from *Villaseñor et al.* [2003]. The green line denotes the location of the PICASSO Phase I profile, with black ticks indicating the limits of the profile as well as the boundary between Tajo Basin (to the north) and Betic Cordillera (to the south).

the location of the Iberian Peninsula.

Further information about the seismic velocity of the Iberian Peninsula deep interior is provided by *Villaseñor et al.* [2003] using body wave tomography to derive P-wave velocity, enhancing the resolution of earlier work by *Bijwaard et al.* [1998] and elucidating structures between 50 km and 260 km depth (Fig. 7.23). The upper mantle beneath Iberia appears to contain predominantly low velocity materials, except for the region below the Alboran Domain exhibiting relatively high velocities, in particular for the deeper regions. The most striking features of this model are regions of exceedingly low velocities associated with the Pyrenees and Betics Chain, the latter indicating a material change along an approximately NE-SW striking interface down to a depth of at least 200 km. Given that the feature, which is causing the obtained change in seismic velocity, is likely to also have a prevailing effect on the electric conductivity structure, points towards a roughly NE-SW orientated geoelectric strike direction for the deep regions beneath southern Iberia.

A distinct indication of features beneath the PICASSO Phase I profile cannot be derived from the model by *Villaseñor et al.* [2003], but further seismic tomography studies in this region were carried out by *Amaru* [2007] and *Amaru et al.* [2008] as part of a global subsurface investigation using P-wave travel time. A vertical transect, co-located with the PICASSO Phase I profile, was extracted from the 3D model, displaying the seismic

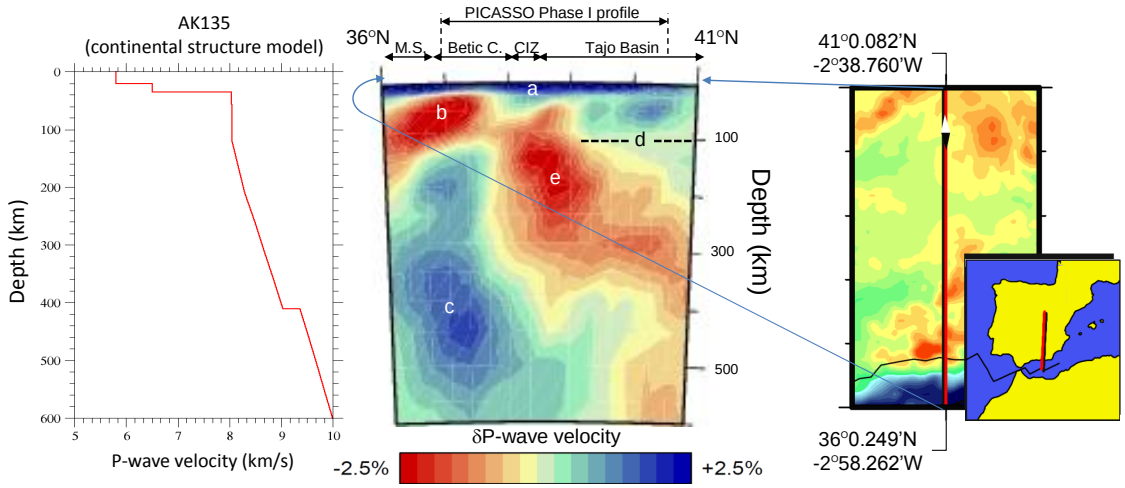

Fig. 7.24.: Anomalies of P-wave velocity in respect to the AK135 reference model (left hand side) [*Kennett et al.*, 1995] for a transect coinciding with the PICASSO Phase I profile, extracted from a global travel time tomography model [*Amaru*, 2007]; Betic C.: Betic Cordillera, CIZ: Central Iberian Zones, M.S.: Mediterranean Sea; see text for details.

P-wave travel time variation relative to the AK135 reference model [*Kennett et al.*, 1995] (Fig. 7.24). Synthetic tests show that anomalies up to 0.5×0.5 degree in the original 3D model can be reconstructed in the best-sampled regions of the uppermost mantle for the European–Mediterranean region, with resolution decreasing with depth. Based on results of spike-tests and hit count map inspection, most features of the vertical transect are found to be reliable [Amaru 2010, pers. communication], with the region of least sensitivity (less than 500 rays/cell) located in the northern extend of the crust beneath the Tajo Basin. The cell size increasing with depth, from 10 km in the crust to 50 km at a depth of 660 km, implies a corresponding sensitivity decrease with depth. Moreover, the vertical extend of features at greater depth is accordingly less constraint than those of crustal structures.

Key elements of the model are: (a) relatively high velocity of the crust; (b) the low velocity lithosphere beneath Betic Cordillera and Mediterranean Sea; (c) the high velocity region at sublithospheric depth beneath the Betic Cordillera; (d) the vertical change of velocity beneath the northern Tajo Basin; as well as (e) the low velocity zone beneath the Tajo Basin, observed at mantle depth with a northward dip and a small branch reaching north- and upwards in the lithospheric-mantle. No interpretation for features of this particular transect are published by the authors at this stage, meaning that all conclusions presented here provide new insights about processes taking place in the Iberian Peninsula. Therefore, these features are examined here in more detail, together with a brief interpretation of possible mechanisms.

(a) The relatively fast crust is most likely due to an inaccurate representation of the local conditions by the AK135 model used as reference during the study. (b) The relatively low velocity region beneath Betic Cordillera and Alboran Sea, at depth between 30 km and

approximately 110 km, on the other hand, most likely represents a real geological feature. The anomaly is potentially due to subduction or delamination of lithospheric material, being replaced by warmer, and therefore less dense, mantle material [e.g. *Torres-Roldan et al.*, 1986; *Platt and Vissers*, 1989; *Seber et al.*, 1996; *Calvert et al.*, 2000; *Gutscher et al.*, 2002; *Amaru*, 2007]. The descending lithospheric material is most likely represented by (c) the observed relatively high velocity region in the asthenosphere beneath Alboran Sea and Betic Cordillera. A slab subducting beneath Alboran Sea and Betics Cordillera has been modelled, for example, in seismic tomography studies by *Bijwaard et al.* [1998]; *Spakman and Wortel* [2004]; *Amaru* [2007]. (d) Below the Tajo Basin the seismic LAB (sLAB) may be located at a depth between 90 and 120 km depth, as indicated by the change from relatively high velocity to low values with respect to the AK135 reference model[1]. However, due to the inherent spatial smoothing of seismic tomography no solid conclusions can be drawn about the LAB from this method. The feature in the seismic tomography model most interesting for the PICASSO Phase I investigation is certainly (e) the northward-dipping, low velocity region beneath the Tajo Basin, extending closest to the surface beneath the southern boundary of the Tajo Basin. This deep-seated anomaly is in agreement with previous work by *Hoernle et al.* [1995] and results by *Villaseñor et al.* [2003] deriving a structure of similar location and depth extent with an ENE-WSW orientation (Fig. 7.23). According to its location, this anomaly could potentially be a related to the Betic Cordillera – Iberian Peninsula collision in Miocene times (Sec. 7.2) or to the subducting lithosphere beneath Alboran Sea and Betic Cordillera (feature 'c' in Figure 7.24); however, its vast depth extent is somehow puzzling.

Potential candidates for the lowered velocity of feature 'e' are increased temperature, different chemistry (e.g. a more iron-rich, fertile mantle), and presence of fluids (partial melt or water). The latter could originate from dehydration of sinking lithospheric materials beneath the Alboran Sea, in particular, if the material stems from a slab of oceanic crust as indicated by seismic tomography models of *Bijwaard et al.* [1998], *Spakman and Wortel* [2004], and *Amaru* [2007, p. 111]. Sensitivity of seismic velocity to various parameters are calculated by *Goes et al.* [2000] for depths of 50 km and 200 km beneath Europe, deducing that a 2% decrease of compressional wave velocity at this depth would require a minimum temperature increase of 100°C or a melt fraction of up to 4%. The authors also state that a minimum of 2% melt is required before an effect on seismic velocity is observable; cf. *Sato et al.* [1989]. The effective velocity effect of fluids is therein strongly dependent on the geometry of the melt distribution and interconnection of the melt pockets, i.e.

$$\text{attenuation(films)} > \text{attenuation(tubes)} > \text{attenuation(spheres)}$$

[1] The AK135 contains only a marginal jump in velocity at 80 km and a smooth transition from continuous to increasing velocity at 120 km in the depth range that is usually associated with the LAB (cf. left-hand side plot in Figure 7.24)

Station	Moho depth (km)
NE17	32.0 ±2.5
PAB	31.0 ±1.0
NE13	30.0 ±1.0

Tab. 7.3.: Depth of the Moho derived from Receiver Function analysis by *Julià and Mejía* [2004] for three stations on top of the Iberian Massif to the west of the Tajo Basin (see Figure 7.25 for station locations).

and

velocity reduction(films) < velocity reduction(tubes) < velocity reduction(spheres)

[*Mavko*, 1980]. *Goes et al.* [2000] further argue that changes of composition and magnesium number (Mg#) have no significant direct effect on seismic velocity, but rather through related density changes; see also *Jones et al.* [2009] for details on this aspect. The actual effect of Mg# change is dependent on the local mineral composition, e.g. compressional velocity increases with increasing Mg# for olivine [*Chen et al.*, 1996; *James et al.*, 2004] and decreases for spinel and garnet peridotites [*Kopylova et al.*, 2004]. However, the observed low velocity region may be due to a combination of the above-described parameters, wherein temperature is commonly assumed to account for the bulk of the velocity variation. More light on this aspect will be shed by results of the PICASSO Phase I investigation, providing additional information about the present material distribution and their condition in terms of electric conductivity.

Receiver Function

Receiver Function studies, the seismic method generally most capable of detecting the LAB, have been carried out in Spain by *Julià et al.* [1998] and *Julià and Mejía* [2004]. The authors use data from stations installed in the area of Ebro Basin, Betic Cordillera, and in the SW of the Iberian Peninsula of which four stations are located in proximity of the PICASSO Phase I profile (Fig. 7.25). Three of those stations are installed in the region of the southeastern Iberian Massif, whereas the forth station is located in the Betic Cordillera, all within approximately 1 degree to the west of the PICASSO Phase I profile. For the Tajo Basin the authors derive a Moho depth of around 31 km, slightly deepening towards the north (see Tab. 7.3 for details), using direct P teleseismic wave reverberation [*Julià et al.*, 1998] and P-to-S converted waves (also referred to as *P-wave receiver function* (PRF)) [*Julià and Mejía*, 2004]. No details about deeper-seated features like the LAB are presented by *Julià et al.* [1998] or *Julià and Mejía* [2004], owing to the lack of sufficient data. The lack of good quality data is due to the masking effect of P-wave reverberations on PRF data and the general difficulty to obtain S-to-P converted waves (also referred to as *S-wave receiver function* (SRF)).

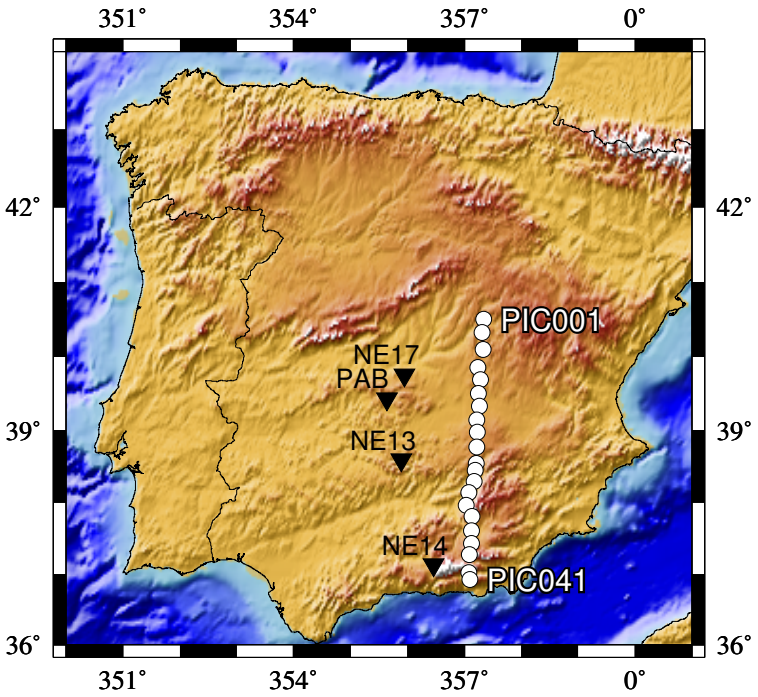

Fig. 7.25.: Locations of four Receiver Function stations used by *Julià and Mejía* [2004] to derive the Moho depth beneath the Iberian Peninsula (inverted triangles) and the MT stations deployed during the PICASSO Phase I fieldwork campaign (dots).

Thermal and rheological models

The difference of materials in terms of their ability to conduct heat from the Earth's interior to the surface as well as their different degree of radiogenic activity enables scientist to draw conclusions about the material distribution within the crust and the depth of the thermal lithosphere–asthenosphere boundary (tLAB). The latter is due to the fact that in the asthenosphere heat is transported by convection, hence an adiabatic temperature gradient prevails, whereas the temperature gradient of the lithosphere is due to heat conduction and therefore accordingly lower. This allows for an estimation of the tLAB depth coinciding with the depth of change in the heat transport mechanism, which is a good indicator of the mechanical LAB [e.g. *Pollack and Chapman*, 1977]. However, the transport-process change occurs within a transition zone rather than at a sharp boundary, and the tLAB has been proposed to coincide with temperatures of 1200, 1333, or 1350°C. Ambiguity regarding depth and temperature of the tLAB is aggravated due to the fact that location of the tLAB within the transition zone (i.e. its top, middle, or bottom) varies between authors.

A summary of heat flow values for the Iberian Peninsula and its margins was published by *Fernandez et al.* [1998] using data from exploration wells and sea floor measurements. The Tajo Basin exhibits some degree of spatial variation of heat flow values from approximately 62 mW/m^2 in the north of the basin to approximately 70 mW/m^2 for the Campo de Montiel region in its south (Fig. 7.26) Higher heat flow values are indicative of a shal-

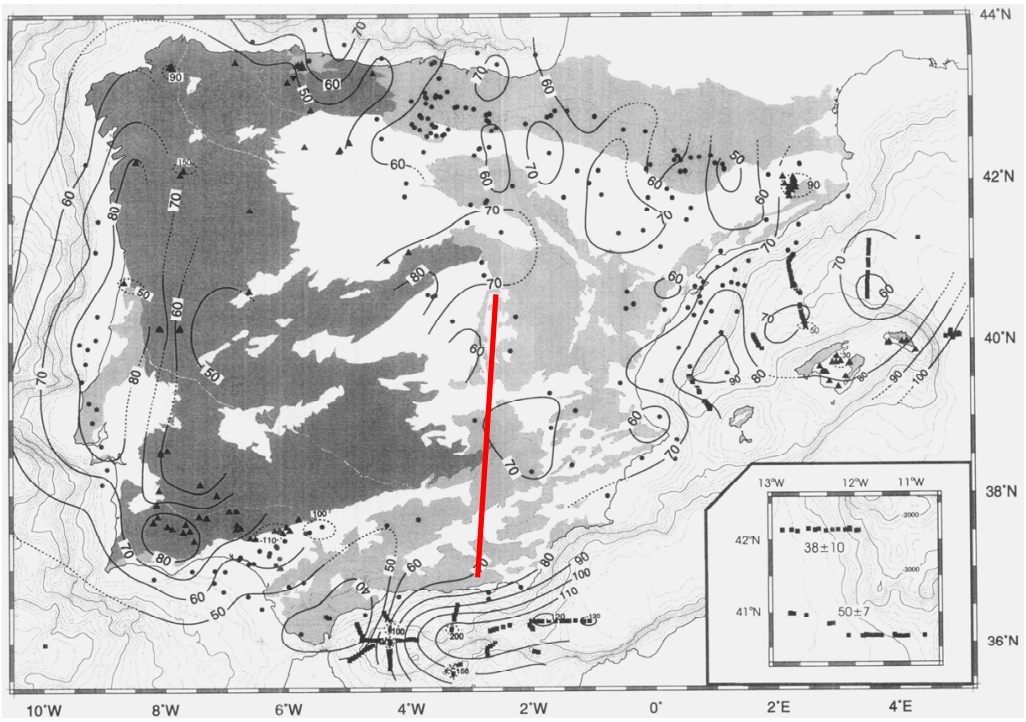

Fig. 7.26.: Filtered heat flow map of the Iberian Peninsula; from *Fernandez et al.* [1998]. Squares, dots, and triangles denote the location of sea floor heat-flow measurements, measurements in oil wells, and measurements in water or mining exploration wells, respectively. The approximate location of the PICASSO Phase I profile is indicated by the red line. The bathymetry is indicated every 200 m.

lower tLAB, a region of enhanced thermal conductivity, or increased radiogenic activity beneath these southern regions.

Tejero and Ruiz [2002] created 1D thermal models for the Tajo Basin based on surface heat flow data by *Fernandez et al.* [1998] and using seismic data of *Banda et al.* [1981]; *Surinach and Vegas* [1998]; *ILIHA DSS Group* [1993]; *Gallart et al.* [1995]; *Pulgar et al.* [1996] for constraints of the lithosphere layer thickness. The authors use heat flow values of 65 and 70 mW/m^2 for southern and northern Tajo Basin regions, respectively; as well as a lithosphere consisting of five layers (sediments, upper crust, middle crust, lower crust, uppermost mantle) with a Moho temperature of 650°C , tLAB temperature of 1350°C , and a tLAB depth of 110 km. Details about the layer properties used for the calculation of the thermal model are summarised in Table 7.4. The tLAB depth derived by *Tejero and Ruiz* [2002] is in agreement with results by *Artemieva* [2006] inferring depths between 100 km and 125 km for the tLAB beneath central Spain using a 1300°C isotherm and statistical analysis to determine the global lithosphere model TC1; therein, data coverage was low for the central Spain region though.

From their results, *Tejero and Ruiz* [2002] derive the geotherms for the Tajo Basin shown in Figure 7.27, inferring that in this region the Moho does not represent a strong mechanical discontinuity and that the upper and middle crust are competent layers, with

Layer	Density	Thermal conductivity	Thickness		Heat production	
			North	South	North	South
	($kg\,m^{-3}$)	($W\,m^{-1}K^{-1}$)	(km)		($\mu W\,m^{-3}$)	
Sediment layer	2400	2.5	2	1	2.5	2.5
Upper crust	2700	2.5	12	13	3.3	2.5
Middle crust	2850	2.5	9			
Lower crust	2900	2.1	8		0.8	

Tab. 7.4.: Parameters of the thermal model for the Tajo Basin, assuming the thermal conductivity of the lithospheric-mantle to be $3.4\,Wm^{-1}K^{-1}$; after *Tejero and Ruiz* [2002].

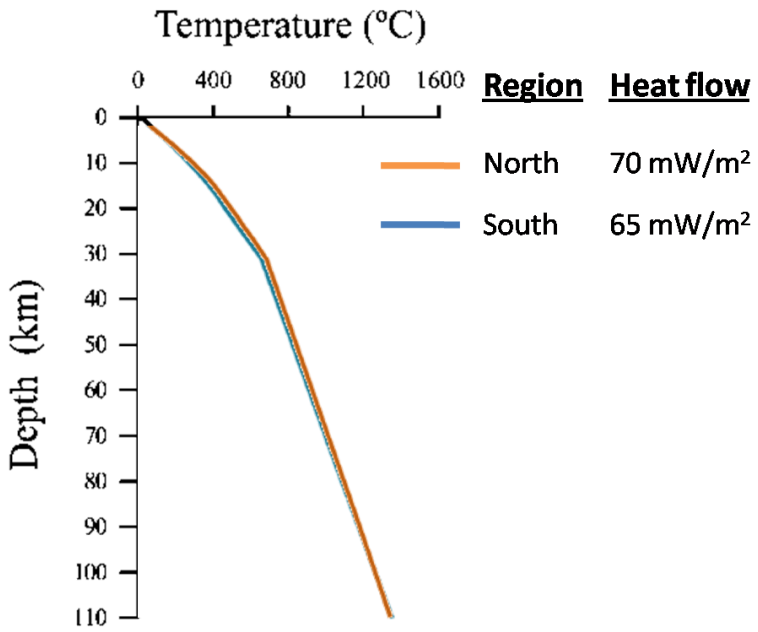

Fig. 7.27.: Geotherms of the Tajo Basin calculated for the parameters given in Table 7.4; modified from *Tejero and Ruiz* [2002].

the lower crust acting as an incompetent layer (Fig. 7.28). The concept of a weak lower crust, as proposed by *Tejero and Ruiz* [2002], is in agreement with the observed seismicity in this region, exhibiting no events in the lower crust of central Spain [*Instituto Geografico Nacional*, 2010] (cf. earthquake locations depict in Figure 7.22). The seismic–aseismic boundary is accordingly related to the brittle–ductile boundary of the crust; observed events are assumed to be transmitted through inherit fault zones and flexural bounding stresses from regional compression [*Tejero and Ruiz*, 2002]. However, the assumption of an exponential decay of heat production with depth used by the authors for the calculation of their model is questionable (cf. *Vilà et al.* [2010]), and the obtained thermal structure could be significantly different for the case of a constant heat production within each layer.

Recently European scale models of the lithosphere's thermal and rheological proper-

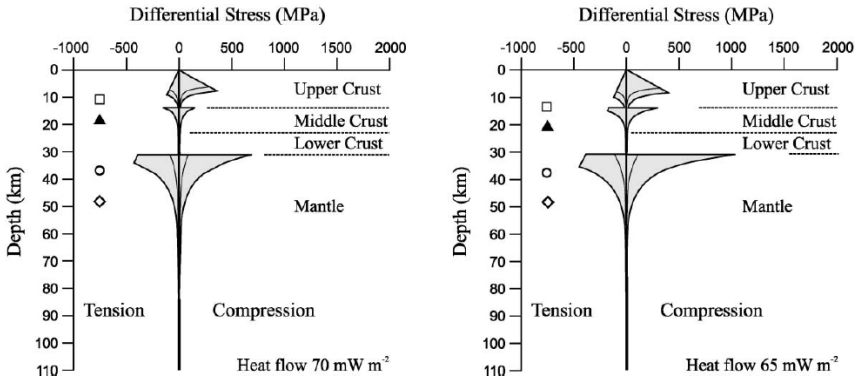

Fig. 7.28.: Rheological profiles of the Tajo Basin (northern part on the left-hand and southern part on the right-hand side) in terms of tension and compression at a strain rate of 10^{-15} s^{-1} for rheological parameters given in Table 7.4. Outer black lines bind differential stress estimated for dry rock composition; inner black lines denote stress for wet rock composition of the upper crust (quartzite or granite) and lithospheric-mantle (peridotite). Geometric symbols mark the base of competent layers for the upper, middle, and lower crust as well as the lithospheric-mantle, i.e. □: wet quartzite, ▲: quartzdiorite, ○: wet peridotite, ⋄: dry peridotite; note that only wet rock data shown for the upper crust, from *Tejero and Ruiz* [2002].

Rheological property	Thickness (km)	
	Central Spain	Central Betic Cordillera
Elastic thickness T_e	20 - 25	15 - 20
Mechanical strong upper crust (MSUC)	~18	~15
Mechanical strong lower crust (MSLC)	6 - 10	~11
Mechanical strong upper mantle (MSL)	8 - 12	~6

Tab. 7.5.: Rheological properties of the regions relevant for the PICASSO Phase I investigation of the Iberian subsurface; the values are visually derived from the thermal and rheological European lithosphere model by *Tesauro et al.* [2009a, Figs. 3, 4].

ties, with characteristic values of the radiogenic heat production for each crustal layer are presented by *Tesauro et al.* [2009a] and *Tesauro et al.* [2009b]. The authors use the seismic tomography model by *Koulakov et al.* [2009], which incorporates teleseismic events as well as travel time data, with a correction of the travel times based on the EuCrust-07 model [*Tesauro et al.*, 2008]. For the region coinciding with the PICASSO Phase I profile, the authors derive a depth between 120 km and 130 km for the 1200°C isotherm, indicating the lithosphere–asthenosphere transition. In their model, *Tesauro et al.* [2009a] and *Tesauro et al.* [2009b] further infer temperatures of approximately 880 – 980°C and 1120°C at 60 km and 100 km depth, respectively. From their thermal model, in combination with the EuCrust-07 model [*Tesauro et al.*, 2008], the authors derive rheological settings for the European lithosphere with properties of the region most relevant for the PICASSO Phase I investigation summarised in Table 7.5. However, results by *Tesauro et al.* [2009a] and *Tesauro et al.* [2009b] are associated with a higher degree of uncertainty since they are based on seismic data, which have lower resolution in Iberia; aggravated by the fact that the model is of European scale, hence down-weighting local effects. The lower resolution in Iberia is therein due to its location on the edge of the European continent as

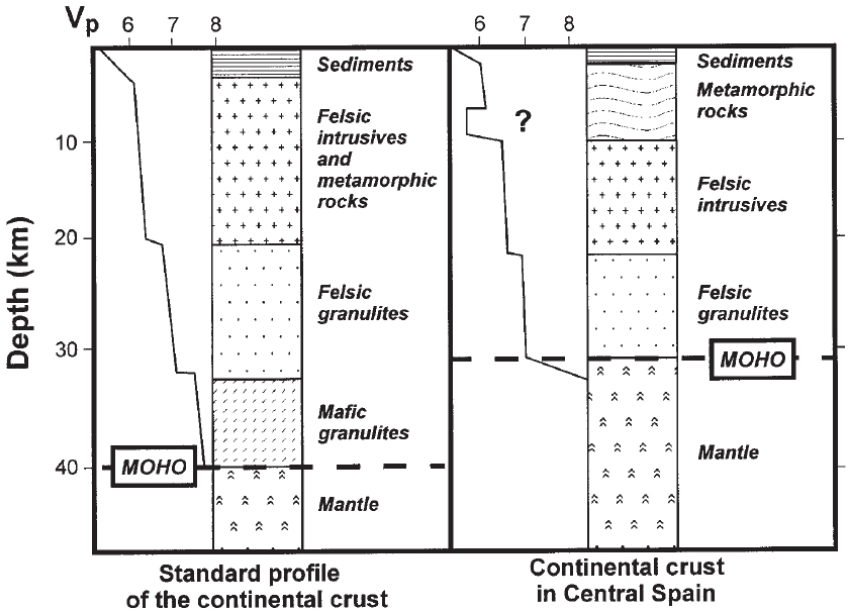

Fig. 7.29.: Comparison of estimates for the continental crust in the Spanish Central System (Central Spain) by *Villaseca et al.* [1999] (using seismic data by *Banda et al.* [1981]) with the standard profile for the European continental crust derived by *Wedepohl* [1995] from an integrated 3000 km long geotraverse (seismic velocities in km/s), from *Villaseca et al.* [1999].

well as the low station coverage on the peninsula.

Xenoliths studies

Villaseca et al. [1999] studied xenolith-bearing alkaline dykes, intruded into the Variscan basement of the SCS in early Mesozoic times, and conclude that these xenoliths represent lower continental crust material as indicated by thermobarometric calculations based on mineral paragenesis. From their results, revealing a felsic granulite composition of the lower continental crust in Spain in contrast to the more mafic lower-crustal composition estimated in other European Variscan areas, the authors deduce that the crust in this region is not underplated (Fig. 7.29). A non-underplated crust implies the absent of mafic and ultramafic materials in the lithospheric-mantle, which would in turn imply relative low seismic velocity and increased electric resistivity in this region.

7.3.3. Summary and conclusions

From previous geophysical studies it can be inferred that the subsurface below the Tajo Basin contains sedimentary cover with a thickness of 3 km on top of three crustal layers, reaching down to depths of 8 – 12 km, 23 – 25 km, and 30 – 33 km, respectively. It has been further proposed, based on results of thermal modelling studies and transformation of seismic tomography data, that the tLAB is located at a depth between 110 km and 130 km beneath the Tajo Basin. The upper crustal layer is thought to be formed from

crystalline rocks, whereas seismic and xenolith studies indicate that the middle and lower crust consist of felsic intrusives and granulites, respectively. Since no seismic activity was recorded below the middle crust, it is likely that the lower crust, is an incompetent, ductile layer between the mantle and the other crustal layers.

Faults with an approximately N45W direction intersect the PICASSO Phase I profile in the proximity of stations pic005, pic009, and pic013, potentially yielding a respective geoelectric strike direction in MT data of shorter periods. Material interfaces at crustal depth below the Tajo Basin, as interred from seismic studies, coincide with the borders of the Betic Cordillera and the Iberian Range. The respective ENE-WSW and NW-SE orientation of the interfaces indicate different geoelectric strike directions for the northern and southern parts of the PICASSO Phase I profile (cf. Sec. 9.6.1). Furthermore, since the low velocity feature, occurring slightly north of the Betic Cordillera, reaches down to at least 200 km, whereas the anomaly associated with the Iberian Range cannot be observed at depths greater than 53 km, it is likely that the geoelectric strike direction in the Tajo Basin below the PICASSO Phase I profile will also change with depth.

Seismic tomography studies further derive low velocity structures at crustal depth beneath Betic Cordillera and Alboran Sea, in the mid- and lower crust beneath in the Campo de Montiel region, and an extensive low velocity region located approximately 50 km to 350 km beneath the Tajo Basin. Different settings could explain such decreases of velocity, e.g. increased temperature, different chemistry, and the presence of partial melt or fluids. Investigation of the electric conductivity distribution in this region will add further constraints on this issue and might help to better understand the geological setting and the related tectonic evolution.

In addition, results of the PICASSO Phase I investigation can help to reassess the stratigraphy of Tajo Basin and Betic Cordillera as deduced from seismic reflection and refraction studies. Formation of proposed Miocene folding and the depth extend of faults in the Tajo Basin may also be evaluated using results of this study. Further, the currently unknown eastward extent of the Iberian Massif beneath the Tajo Basin, in the region of the Manchega Plain, can be investigated given the significantly higher resistivity of the Iberian Massif.

At deeper regions, it can be tested whether an uppermost electric asthenosphere layer with values of approximately 10 Ωm (proposed for the Betics region) is observable beneath central Iberia, or whether a more resistive upper mantle (as suggested by laboratory studies) satisfies the responses. If the location of the eLAB can be derived for the study area, its relative position in respect to the estimates for sLAB and tLAB in the region can be used to enhance knowledge about the local geological processes. Furthermore, by contrasting results of MT, seismic, and thermal studies conclusions can be drawn about composition and condition of the south-central Iberian Peninsula subsurface.

Part III

A novel inversion approach for oblique geoelectric strike directions in crust and mantle

The most exciting phrase to hear in science, the one that heralds new discoveries, is not "Eureka!" (I found it!) but "That's funny"

– Isaac Asimov

8

Recovering a synthetic 3D subsurface model using lower-dimensional inversion schemes

8.1. Motivation

Two-dimensional (2D) inversion of magnetotelluric (MT) data is at present far more commonly used than three-dimensional (3D) inversion since 2D inversion significantly outperforms 3D inversion in terms of speed, thus allowing for much better resolution of the subsurface through a larger feasible number of grid cells (cf. Sec. 6.3). Moreover, due to the shorter computation time of 2D inversion, investigators can study various aspects of subsurface regions through hypothesis testing, e.g. by using different *a priori* models or by removing features of an inversion model and examining whether they are re-introduced in subsequent inversion steps. Models of 3D inversion are often a "like it or lump it", because computational cost prohibit calculation of additional inversion steps. However, validity of 2D inversion needs to be tested for cases where the electric resistivity structure of the subsurface is potentially 3D to some extent. Not taking into account the effects of 3D structures can severely corrupt resulting models; see Chapter 4 for a detailed discussion of distortion and dimensionality aspects of MT investigation.

Different 2D inversion approaches have been applied to 3D subsurface cases before, but respective models have to be regarded with suspicion. For example, during their approach, using interpolation of Z_{yx}-only 2D inversions[1] to image 3D structures of the Pannonian Basin (Hungary), *Tournerie and Chouteau* [2005] note that responses from 3D forward modelling of their interpolated model are significantly different for Z_{xy} periods related to deeper regions (> 20 s). The authors relate the discrepancy to unaccounted for anisotropic structures in the subsurface. However, Z_{xy} data, with the electric component orthogonal to the profile (i.e. TE in 2D MT inversion), is commonly assumed to be more affected by

[1] For a 3D subsurface no alignment of Z_{xy} and Z_{yx} data with a 2D electric resistivity interface can be made in the classical sense. Thus, TE and TM mode only denote 'transverse' in terms of 'transverse to the profile direction' and are not necessarily related to the orientation of a resistivity interface. With the profile along the y-axis, Z_{yx} is associated with the TM mode.

small scale 3D bodies due to charge build up on the off-profile boundaries of these small scale bodies [e.g. *Jones*, 1983a; *Wannamaker et al.*, 1984; *Berdichevsky et al.*, 1998; *Ledo et al.*, 2002; *Ledo*, 2005; *Siripunvaraporn et al.*, 2005b]. Hence, 3D inversion appears to be required for the Pannonian Basin region.

The circumstance that MT data are usually acquired along a profile (as opposed to an array of recording stations) does not prohibit 3D inversion. *Siripunvaraporn et al.* [2005b] illustrate that 3D inversion of profile data can account for off-profile features and as a result yields an improved model of structures beneath the profile. However, longer computational time and higher computational costs are associated with 3D inversion and it would be desirable to find a 2D inversion approach that can cope with certain types of 3D subsurface without these drawbacks of 3D inversion.

One particular 3D subsurface case consists of lateral changes in electric conductivity along regional-scale interfaces with varying orientations of the interfaces at depth, e.g. at crustal and mantle depths. Such a case might emerge, for instance, where crustal faulting, originating from present day tectonics, is situated above a mantle where structures are dominated by earlier or current plate tectonic processes, e.g. continental collision from an oblique direction. Cases of oblique geoelectric strike directions for different subsurface regions are a known problem in MT investigation and have previously been reported, among others, by *Eaton et al.* [2004], and *Miensopust et al.* [2011]. Whereas recovery of crustal structures can usually be achieved in a straightforward manner by confining the modelled frequency range to crustal penetration depths, deriving mantle structures is more challenging. Presently, no silver bullet solution is known to the problem of recovering mantle structures for cases of significantly oblique strike directions.

Miensopust et al. [2011] inferred varying strike directions for their profile in north-eastern Botswana and used separate focussed inversions with a different geoelectric strike directions to enhance their model. Therein, the authors used a strike direction of 55 degrees clockwise from North (N55E) for a subset of their model, whereas a strike direction of N35E was used for the rest of the model. However, an extension of the approach by *Miensopust et al.* [2011] to a case with more oblique geoelectric strike directions is not straightforward. In such a case, TE and TM mode estimates for the deeper region will be related to incorrect depths because of the significantly erroneous decomposition of the impedance tensor in at least one of the regions. A simple 'stitching' of inversion models from different strike directions is therefore highly likely to yield a model in which structures of the deeper region are misrepresented.

In the PICASSO Phase I investigation, varying geologic strike direction with depth and along the profile is deduced for the region of the Tajo Basin (cf. Sec. 9). Geoelectric strike direction in the Tajo Basin crust is approximately NW-SE, coinciding with the direction of the Iberian Range and Neogene faults, whereas at mantle depths a dominant NNE-SSW direction is observed (Figs. 8.1). The defined change in strike direction is supported by results from seismic tomography studies (cf. Sec. 7.3.2) inferring a NW-SE directed interface at crustal depth and a NE-SW direction for deeper regions (cf. Fig. 8.2). Based on their orientation, a correlation with alpine orogenies that formed the approximately

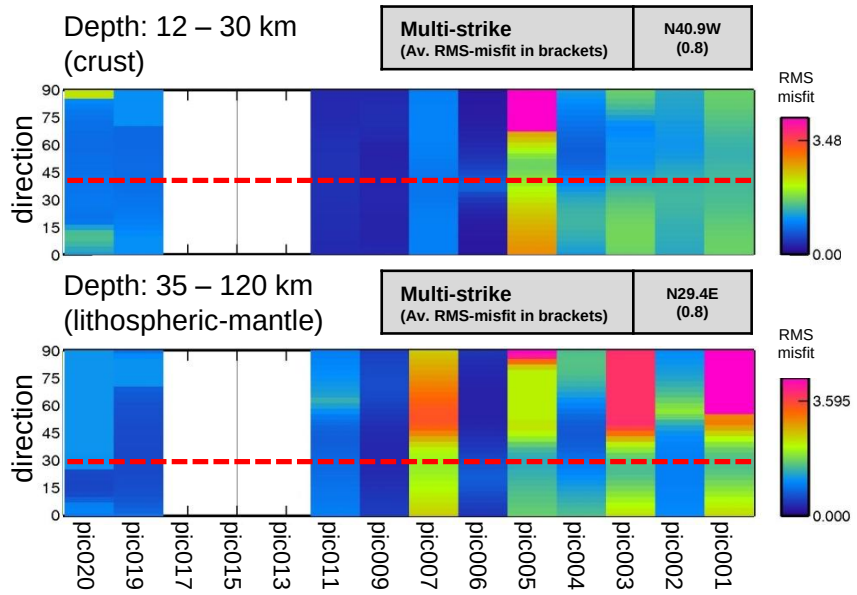

Fig. 8.1.: RMS misfit for different geoelectric strike directions applied to data from magnetotelluric (MT) stations in the Tajo Basin recorded during PICASSO Phase I, using data in the Niblett-Bostick depth (cf. Sec. 6.3.1) ranges 12 - 30 km and 35 - 300 km. Empty spaces are due to lack of sufficient data for this depth range at the respective station. Also shown in the top right corner is the optimal common geoelectric strike direction calculated using the program `strike` by *McNeice and Jones* [2001].

NW-SE stretching Pyrenees and the NE-SW stretching Betics during Late Mesozoic – Cenozoic times (cf. Sec. 7) seems likely.

Computational cost of 3D inversion is high, usually permitting detailed inversion of a region with the size of the Tajo Basin. 2D inversion, on the other hand, requires the investigator to commit to one strike direction to be used for the inversion process, hence to invert data of at least one region with an erroneous strike direction assumption. This problem motivated construction and investigation of a synthetic model case that contrasts results of different inversion schemes and parameter settings for the case of oblique strike directions at crust and mantle depths. In particular, advances of novel algorithms that incorporate effects of anisotropic structures in the subsurface are utilised to recover structures at mantle depth. The use of anisotropic inversion codes for the recovery of oblique strike directions has not been reported before, meaning that this study breaks new ground.

8.2. Generating synthetic 3D model data

8.2.1. Generating the synthetic 3D model

According to published velocity distribution (Sec. 7.3.2) and derived distribution of electric resistivity for the Tajo Basin subsurface and surrounding regions (Chap. 9), a synthetic 3D model (Fig. 8.3) is created using the 3D forward modelling program of the WinGLink software package [*WinGLink*, 2005], based on the algorithm by *Rodi and Mackie* [2001].

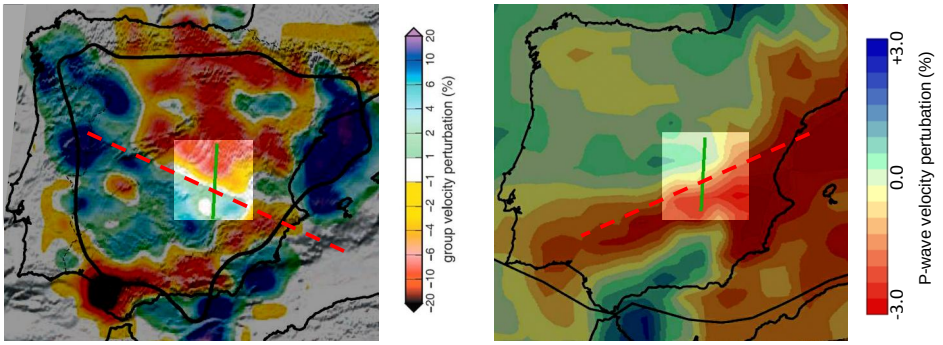

Fig. 8.2.: Left: group velocity map of the Iberian Peninsula subsurface, obtained from ambient noise tomography using Rayleigh waves at periods of 20 s, related to structures between 15 km and 30 km (cf. Sec. 7.3.2), with the thick black contour line indicating the region in which features with a lateral extend greater than 100 km are well resolved; modified after *Villaseñor et al.* [2007]. Right: body wave tomography map of the Iberian Peninsula and surrounding regions; modified after *Villaseñor et al.* [2003]. In both figures dashed red lines denote the approximated course of lateral changes in the Tajo Basin at the respective depth, green lines denote the location of the PICASSO Phase I profile, and the highlighted area indicates the region associated with the synthetic 3D model used in this study (Fig. 8.3).

Mesh dimensions		Forward response generation	
Number of cells (x,y,z):	61, 58, 49	Min. error:	10^{-5}
Number of air layers:	10	Relaxations:	75
Dimension (x,y,z) (km): (rounded)	100, 100, 10^5	Number of airlayers:	10
		Convergence factor:	5
		Period range (s):	10^{-3}–10^5

Tab. 8.1.: Left: parameters of the 3D model used to investigate the optimal inversion setting for the case of two very different geoelectric strike directions in crust and mantle. Right: settings used to generate the forward response of the model; for details about the forward response generation see *WinGLink* [2005].

The model features four blocks of different electric resistivity, with geoelectric strike directions of N45E (+45°) for the top 30 km and N45W (-45°) for the region below; further details about the model and the generation of the forward response are given in Table 8.1 and Section A.2.1. The model is rotated clockwise by 45 degrees to accommodate straight mesh lines at an angle +45° and -45°, thereby avoiding edge effects of the rectangular mesh used for the finite difference (FD) modelling (cf. Sec. 6.3.2). MT responses are modelled for stations arranged in a grid on top of the synthetic model as well as for 13 additional sites, which are a projection of the PICASSO Phase I stations (cf. Fig. 8.4). Arranging the stations in a grid facilitates evaluation of inversion results along a range of 2D profiles; the course of a selection of profiles is indicated in Figure 8.5.

8.2.2. Data preparation and analysis

Data obtained through forward modelling responses for stations on top of the 3D subsurface (cf. Fig. 8.4) are modified in order to meet requirements of the different inversion programs used in this investigation. First, a minuscule uncertainty level is assigned to the

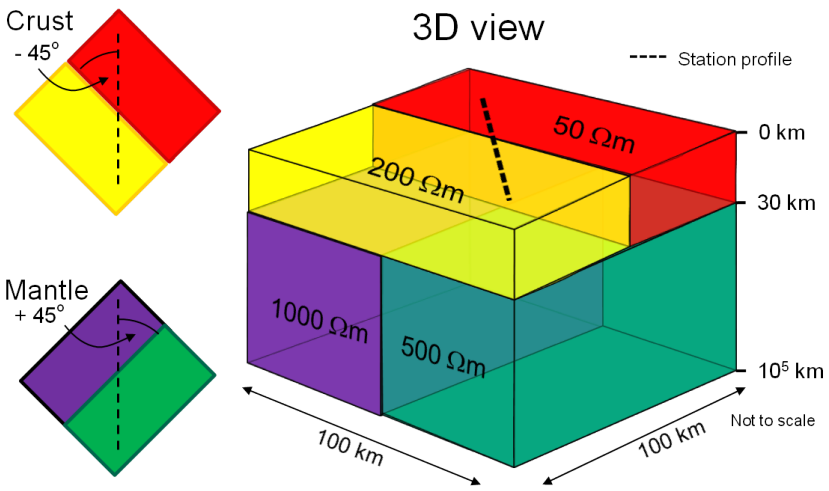

Fig. 8.3.: Subsurface model with orthogonal geoelectric strike directions at crust and mantle depths. Constructed to derive an optimised 1D or 2D inversion approach that provides an optimal recovery of the resistivity distribution at mantle depth for such a case of oblique strike directions in crust and mantle. The approximate location of the projected PICASSO Phase I profile is indicated by the dashed line.

impedance values of each station, i.e. a variance of 10^{-21}. This step is required to permit subsequent calculations, which otherwise would fail due to attempted divisions by zero. Performance of the different approaches for datasets with higher noise levels is studied at a later stage of this investigation. From those files with minuscule uncertainty levels two different types of datasets are created, i.e 'rotated' and 'decomposed', which are used for anisotropic and isotropic inversion processes, respectively (see Sec. 8.3).

Creation of the first dataset type simply involves rotating of data from all stations to N45W and N45E using a script by Xavier Garcia (personal communication, 2008). Note that N45W and N45E represent the respective strike directions of crust and mantle, and that TE and TM modes are swapped for datasets with a difference of rotation by 90 degrees. For these rotated datasets, diagonal elements of the impedance tensor are in general non-zero and are used for the novel anisotropic inversion approach.

The second type of data (decomposed) is created using the program `strike` by *McNeice and Jones* [2001], based on the theory by *Groom and Bailey* [1989] (Sec. 4.4.4), commonly used to provide datasets suitable for isotropic 2D inversion. Therein, two datasets are generated that are adequate for the strike directions at either crustal or mantle depth, i.e. N45E and N45W, respectively. For these decomposed datasets, the diagonal elements of the impedance tensor (Z_{xx} and Z_{yy}) are considered insignificant and are not used during isotropic 2D inversion.

Prior to inversion of forward responses from the synthetic 3D model, data are analysed to identify characteristics of the responses which help to understand applicability of the different inversion approaches. First the response data are visualised using maps of four different periods (periods are used as a depths proxy, cf. Section 6.3.1), in which North is located towards the top left (Fig. 8.6); figures are rotated anticlockwise by 45 degrees

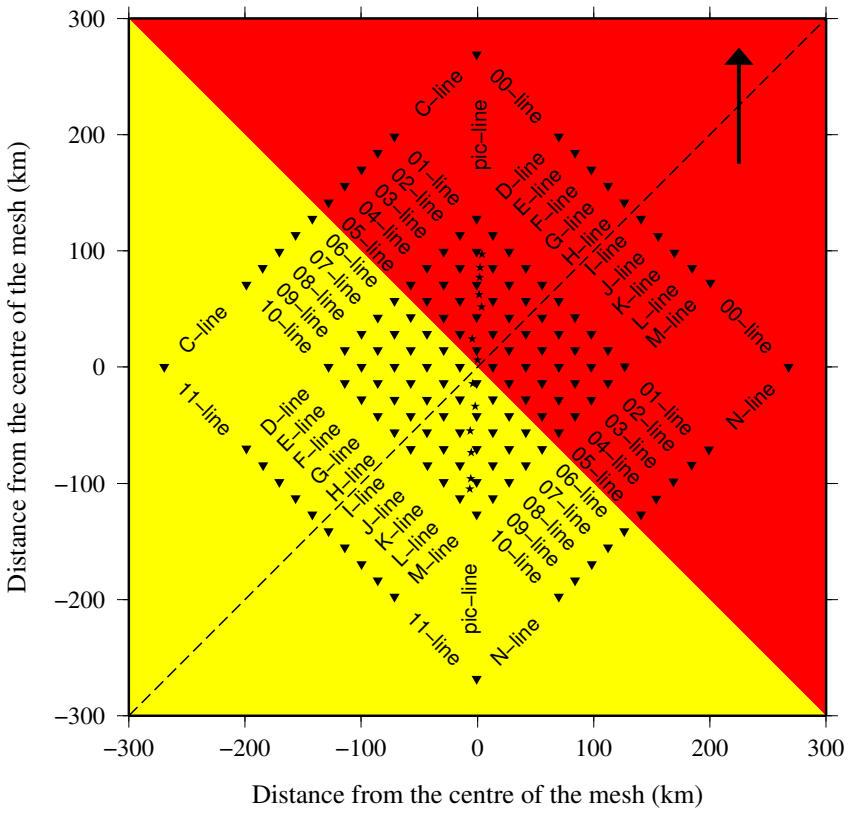

Fig. 8.4.: Location of magnetotelluric (MT) recording sites on top of the synthetic 3D subsurface model; North is located to the top of the figure. Displayed are 144 station arranged in a grid (inverted triangles), as well as 13 additional sites, which are a projection of the PICASSO Phase I stations. Locations of these 13 additional stations (pic001 – pic020, situated along the 'pic-line' in this figure) are a translation of the PICASSO Phase I stations with the respective indices (cf. Chapter 9) onto the synthetic 3D model with pic001 and pic020 located in the North and South, respectively. Nomenclature for the other stations follows the grid system, i.e the name of a station is the combination of the two lines intersecting at the respective location, e.g. the centre-top station is named 'C00'. Background colours indicate the relatively conductive (red) and resistive (yellow) regions of the crust; the location of the resistivity interface at mantle depth is indicated by the dashed line (cf. Fig. 8.3). Profiles 3D-crust and 3D-mantle (not displayed) coincide with the conductivity interfaces at mantle and crust depth, respectively.

(in respect to Figures 8.4 and 8.5) to accommodate plotting of multiple maps side by side. Using Niblett-Bostick depth estimation (Sec. 6.3.1) yields that on the resistive side periods greater than 18 s (appr. 1.26 in log-scale) penetrate into the mantle, whereas on the conductive side penetration into the mantle is first achieved by periods of 72 s (appr. 1.86 in log-scale). In Figure 8.6 'XY data' refers to the TE mode and 'YX data' refers to TM mode for the dataset adjusted to the crustal strike direction (N45W), whereas the 'XY data' refers to the TM mode and 'YX data' refers to TE mode for the dataset adjusted to the mantle strike direction (N45E). The similarity of crustal TE and mantle TM data (and vice versa) is due to the 90 degrees difference between the two strike directions, resulting in swapping of the two modes. Different colour scales are used to display values in maps of different modes and periods (rather than using uniform colour scale values) to highlight structures at the respective period. Note that, in order to enable plotting of all phase data in the first quadrant (0 - 90 degrees), 180 degrees are added to the respective YX phase

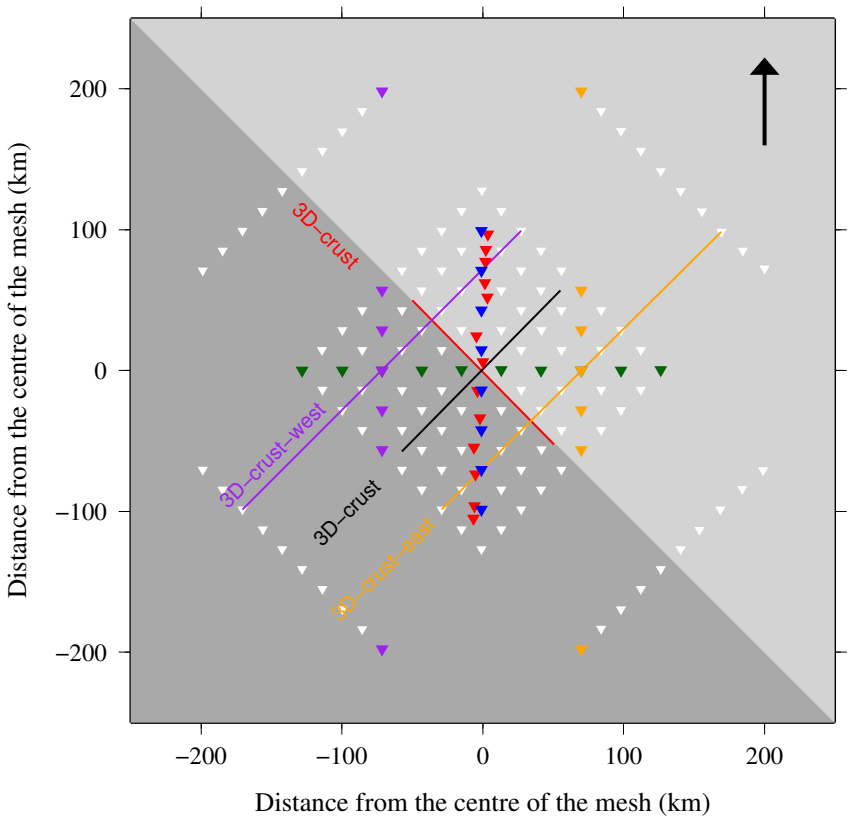

Fig. 8.5.: Location of profiles on top of the synthetic 3D model (cf. Figs. 8.3 8.4); North is located to the top of the figure. Stations are associated with profiles of the same colour; for the profile labelled '3D-crust' three different sets of stations are used: red (3D-crust, using stations representing the PICASSO Phase I recording sites), blue (3D-crust-NS), and green (3D-crust-EW). Every profile contains at least one station on top of each of the four electric conductivity regions (two at crustal depth, two at mantle depth), to assure that data of every profile is affected by the oblique strike directions. Profiles are constructed orthogonal to the geoelectric strike direction of either crust or mantle and station locations are projected onto the profile. Background colours indicate the conductivity distribution at crustal depth (cf. Fig. 8.4).

data.

At shorter periods (0.01 s, top-left figures), responses are dominated by characteristics of crustal structures, therefore values for the two modes are alike and $\rho_a = \rho$; hence $\rho_a = 50\,\Omega$m (appr. 1.7 in log-scale) in the northeastern half and $\rho_a = 200\,\Omega$m (appr. 2.3 in log-scale) in the southwestern half. For longer periods (100 s, top-right figures) mantle structures start to add observable contributions to the response data. Values of ρ_a at 100 s are similar to values of ρ_a at 0.01 s (note the different colour scale), but ϕ differs significantly. In general, $\phi(100\,s) < \phi(0.01\,s) \approx 45$ degrees owing to the more resistive nature of mantle regions in respect to the crust. At 100 s periods, skin depth (cf. Sec. 3.3) for stations on the resistive side of the crustal fault is appr. 70 km, whereas on the conductive side it is appr. 35 km. Thus, at 100 s periods all sites are sensitive to electric properties of the mantle. Phase anomalies at 100 s exhibit a point symmetry in regards to the centre of the station array, i.e. where crust and mantle interfaces intersect. Phase anomalies are a superposition of effects from crustal and mantle structures with

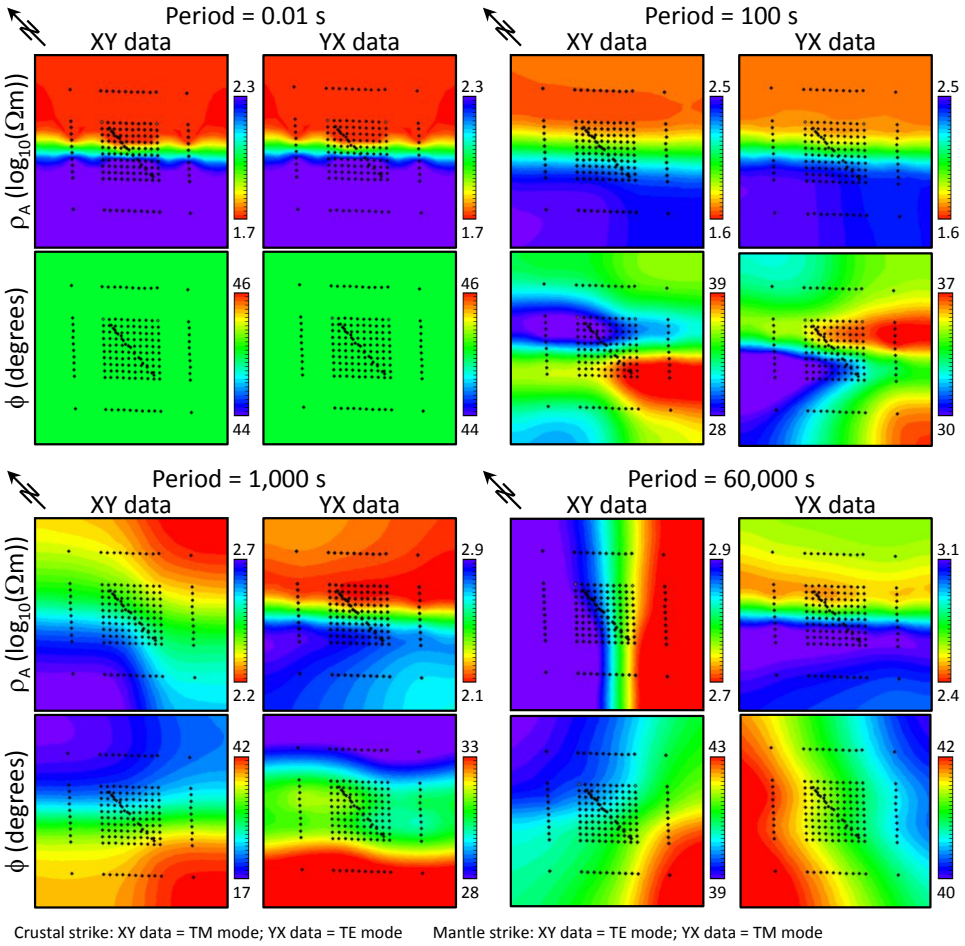

Fig. 8.6.: Maps of apparent resistivity (ρ_a) and impedance phase (ϕ) of the 3D synthetic model (Fig. 8.3) at four periods representing different regimes; see text for details. Note that different colour scales are used to highlight structures of each plot. Plots are rotated anticlockwise by 45 degrees in respect to Figures 8.4 and 8.5 in order to accommodate plotting of multiple figures side-by-side; as a result North is located towards the top-left.

the anomaly magnitude (i.e. the absolute difference of ϕ values from 45 degrees) being controlled by the resistivity difference between crust and mantle (highest in the northern quadrant: 50 to 1000 Ωm) and the induction depth (greater in the southwestern half).

Response data for periods around 1000 s (bottom left figures) also exhibit point symmetry with the strongest phase anomalies (lowest ϕ values) located in the northern quadrant. In the southwestern half, phase values are closer to 45 degrees and apparent resistivity values are closer to values of the synthetic model mantle owing to the higher resistivity of local crustal structures and the resulting greater induction depth.

Responses for the longest periods of the dataset ($6 * 10^4$ s, bottom-right figures), are still affected by distortion of crustal structures. Phase data, for both modes, differ between the four quadrants (N, S, E, W), thus indicating effects from different induction depths and resistivity contrasts of the regions. ρ_{xy} data are similar to mantle values of the synthetic

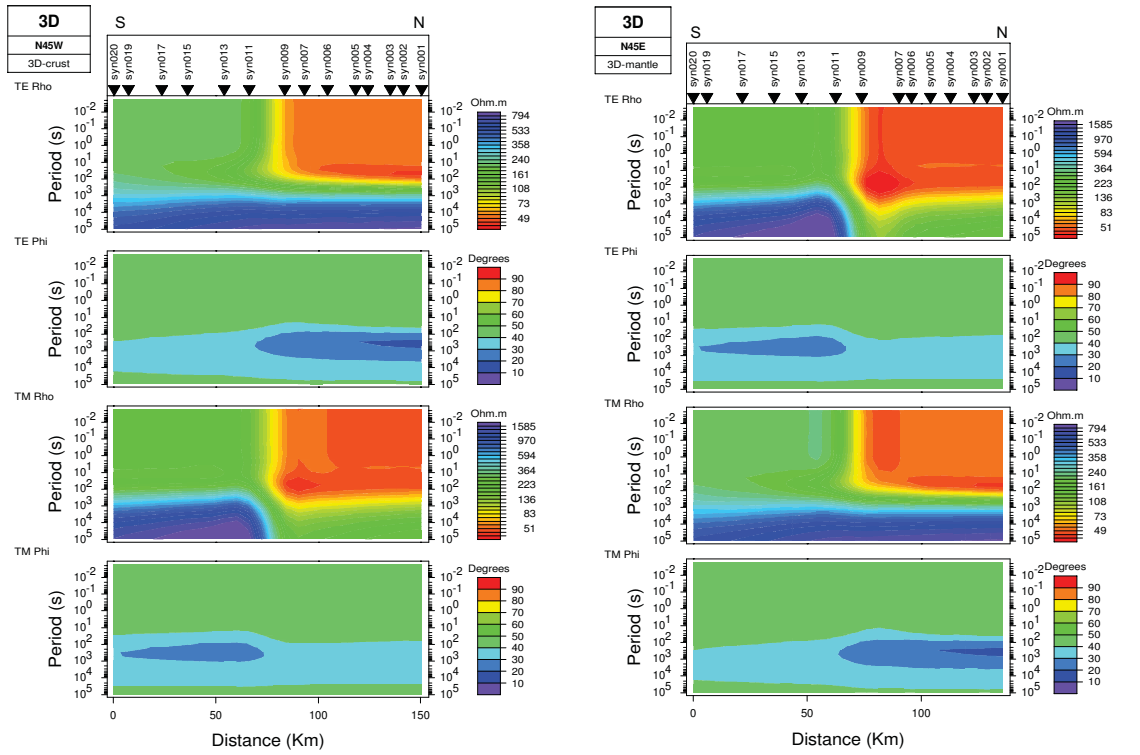

Fig. 8.7.: Pseudosections of the profiles 3D-crust (left-hand side) and 3D-mantle (right-hand side) with stations representing the MT recording sites of the PICASSO Phase I investigation; see Figures 8.4 and 8.5 for the location of stations and profiles. The northern end of the profile (NE for 3D-crust profile, and NW for 3D-mantle profile) is shown to the right.

model (1000 Ωm in the northwestern half, and 500 Ωm in the southeastern half), however, ρ_{yx} values are significantly different. YX data at long periods exhibit significant distortion effects, originating from crustal structures and the oblique strike directions between the two depth regions. Among other, ρ_{yx} data of the southern quadrant are higher than for the northern quadrant resulting in an issue concerning, in particular, profiles using the pic-stations (pic001 - pic020, denoted by stars in Figure 8.4). The circumstance that YX responses of the southern mantle region are significantly more resistive than responses in the northern mantle region is reflected in TM mode data of the crustal strike direction and TE data of the mantle strike direction (see also Figure 8.7).

Forward response data can be displayed using so-called *pseudosections*, i.e. gridded resistivity–period values beneath the profile, in which period is used as a depth proxy. The pseudosection for the pic-line (stations syn001 – syn020 in Figure 8.7) is displayed here because these stations form the most challenging combination by containing stations from each resistivity region of the synthetic 3D model, and, moreover, because the station locations are representations of the PICASSO Phase I recording sites (cf. Sec. 9.1). Due to the characteristics of the 3D model, two profiles are created with data arranged according to the geoelectric strike directions at crustal depth (N45W, left-hand side plot in Figure 8.7) and mantle depth (N45E, right-hand side plot in Figure 8.7); see Figure

8.5 for the location of the profiles. Data from the crustal strike TE mode are similar to mantle strike TM mode data and vice versa because of the 90 degrees difference between the two strike directions. Small variations in the two pseudosections are due to the fact that the pic-stations are not located equidistant along a line and the resulting variation in projection of stations onto the profile. For both profiles and both modes, crustal range periods ($T \leq 10^2$) exhibit a phase of approximately 45 degrees and resistivities that are close to values of the synthetic 3D model for regions beneath the respective pic-site locations. Furthermore, the resistivity interface at crustal depth between stations pic009 and pic011 is clearly marked.

In the period range related to the mantle, values of the two modes differ significantly. In the following, nomenclature of the modes is according to the mantle strike assignment (i.e. 'XY data' refer to the TM mode and 'YX data' refer to the TE mode, cf. left-hand side plot in Figure 8.7), and the note that mode nomenclature is opposite for the crustal strike direction is omitted. At mantle depth, variation of apparent resistivity for the TE mode (E parallel to mantle strike) exceed the TM mode variation: values for the TE mode range from 200 Ωm (northern end) to 1500 Ωm (southern end), whereas the TM mode values are mostly confined to a range 300 – 700 Ωm. It should be noted that the relative distribution of the TE mode apparent resistivities is opposite to the true model, which exhibits higher resistivity values in the northern mantle region than in the southern mantle region (cf. Fig. 8.3). Apparent resistivity values of the TM mode are higher in the northern mantle region than in the southern region, thus it is more similar to the synthetic model.

A noteworthy issue of the TM mode data, however, is the apparent greater inductive depth of the southern mantle region (best observable in the phase data) even though the resistivity of the respective crustal region is higher than its northern counterpart. For an ordinary 2D subsurface, the higher resistivity of the southern crustal region would result in a greater induction depth of the related data. Accordingly, the interface between crust and mantle would be sensed at shorter periods in the south than in the north. The discrepancy must therefore originate from the oblique geoelectric strike direction of the synthetic model at crust and mantle depth, making it a challenging model for 1D and 2D inversion and thus a good test for the novel inversion approaches.

8.3. Inversion of 3D model data

Today, recovery of subsurface structures using MT data usually consists of isotropic 2D inversion along a profile during which effects of 3D bodies in the subsurface are regarded as distortion and are removed where possible, e.g. *Brasse et al.* [2002]; *Pous et al.* [2004]; *Tournerie and Chouteau* [2005]; *Wannamaker et al.* [2009]; *Garcia and Jones* [2010]. Thorough descriptions of distortion effects in MT data and processes used to remove such effects are given in Section 4.4 and Chapter 6, respectively. In here, responses for the 3D subsurface model (cf. Sec. 8.2) are inverted with a range of isotropic 2D inversion

schemes in order to evaluate the limitations of the method and to identify an optimal isotropic inversion scheme for the case of oblique geoelectric strike directions at crustal and mantle depth (Sec. 8.3.1).

Owing to the inadequacies of isotropic 2D inversions for the case of oblique geoelectric strike directions, anisotropic inversion approaches are developed in this work to obtain superior subsurface models. Mathematical considerations of the anisotropic inversion approaches and their application to 1D and 2D inversion are illustrated in Sections 8.3.2 and 8.3.3, respectively.

8.3.1. Isotropic 2D inversion of 3D model data

Inversion approach

Oblique strike directions at crustal and mantle depths of the synthetic 3D model pose severe problems for isotropic 2D inversion of the response data. In isotropic 2D inversion, impedance tensor data are decomposed in respect to the geoelectric strike direction of the subsurface and stations are projected onto a profile that is orthogonal to the strike direction. Due to characteristics of the 3D model used in this study, every profile will be parallel to the strike direction of one depth region when it is oriented according to the strike direction of the other. For example, a profile intersecting the N45W oriented crustal interface at a right angle has a direction of N45E and is therefore parallel to the mantle strike direction. Thus, off-diagonal elements of the decomposed impedance tensor, i.e. TE and TM mode, will always be erroneously assigned for one of the depth regions; for this 3D model with orthogonal strike directions the modes will be interchanged. As a result, artefacts will be introduced during the inversion of the respective depth region. Recovery of the crustal region can be achieved using a dataset and profile that fit the geoelectric strike direction and limiting the period range to periods sensing only the crust, but inversion for mantle structures will suffer from the misrepresentation of either crustal or mantle structures since long-period responses that sense the mantle region are also affected by crustal structures.

In isotropic 2D inversion, various attempts can be conceived in order to recover the mantle structures: common tools are *fixing* of the crustal structures, *tear zone* application, *static shift* correction, and the use of *smoothing parameters*. Fixing of structures at crustal depth is generally reasonable as thereby the inversion is focussed onto the mantle region. For the same reason, the application of two tear zones (separating inversion for crustal and mantle structures) appears to be worthwhile; however, its practicability will be tested here since resulting effects are not clearly predictable. An inevitable misrepresentation of structures at crustal depth related to short period data and consequent effects on data at longer periods suggest the application of static shift correction. The correct choice of smoothing parameters is a general issue in MT investigation and is dependent on characteristics of the subsurface.

The optimal choice and weighting of parameters in inversions for the mantle structures

will certainly be very much dependent on the initial choice whether to represent the crust by a homogeneous layer or by *locally true* resistivity values (i.e. values of the crust, but with an oblique crustal strike direction). The problematic of approximating the crust by a homogeneous layer is evident: long-period data for all stations are affected by overlying structures and will be related to wrong depth regions when short periods are different from the approximation, e.g. in cases where the crustal conductivity structure varies laterally. Wrong depth relation is therein related to the erroneous induction depth for data of affected stations (cf. Fig. 8.7 and Sec. 3.3). A detailed discussion of the induction depth problem in case of the true crustal representation in conjunction with orthogonal strike directions is given in Section A.2.2.

Inversion process

To deduce the optimal combination of parameters, isotropic 2D inversion is carried out using the `WinGLink` 2D inversion software [*WinGLink*, 2005], based on the algorithm by *Rodi and Mackie* [2001], as well as the updated version (i.e. v 6.11 [*Baba et al.*, 2006]) with an isotropic setting (τ_{iso} = 999999). Inversions are conducted applying the Jones Catechism (Sec. A.2.3) with a range of smoothing parameter values, with and without fixing of the crustal range, tear zone application, and static shift correction in order to determine an optimal set of inversion parameters for subsurfaces similar to the synthetic 3D model.

Testing the effect of smoothing parameters is conducted by carrying out inversions with three different sets of parameter values: (i) the increased values ($\alpha = 3, \beta = 1, \tau = 6$) derived during inversion of the crust with real data from the PICASSO Phase dataset I (Sec. 10.1.1); (ii) minimum values ($\alpha = 1, \beta = 1, \tau = 1$), which are likely to introduce a rougher model with more defined interfaces; and (iii) intermediate values ($\alpha = 1, \beta = 1, \tau = 6$) with low constraints on the horizontal and increased constraints on the global smoothness, thus promoting vertical interfaces (cf. Sec. 6.3).

Inversion results

To keep this Chapter to a manageable length, only results for the *3D-mantle* profile using stations syn001 – syn020 (cf. Figs. 8.4 and 8.5) are shown here; results for further profiles are presented in the Appendix (Sec. A.3). The location of stations syn001 – syn020 are a translation of the PICASSO Phase I stations with the same numbers (cf. Sec. 9.1) onto the synthetic 3D model with syn001 and syn020 located in the North and South, respectively. The 3D-mantle profile is chosen as it is a good illustration of the associated relations and issues. In particular, it gives an idea about issues to be expected for the PICASSO Phase I profile inversion, because the synthetic model is constructed according to (simplified) predicted characteristics of the Tajo Basin subsurface. Impedance tensors of stations used for the 3D-mantle profile are decomposed in respect to a geoelectric strike direction of N45E, i.e. the strike direction of the synthetic 3D model at mantle depth.

Model variation	RMS misfit
Optimal model	0.64
Higher horizontal smoothing	2.09
Lower global smoothing	0.40
With "true crust"	4.53
Using tear zones	0.43
No static shift correction	2.43

Tab. 8.2.: RMS misfit for selected inversion models of the synthetic 3D model shown in Figure 8.3 using a 5% error floor for phases and a 10% error floor for apparent resistivities. Related inversion models are shown in Figure 8.8.

A number of inversion models with different subsurface characteristics fit the response data reasonably well RMS misfit < 3, cf. Table 8.2 for misfits of a selection of models), thereby demonstrating the known non-uniqueness problem of MT inversion (cf. Sec. 6.3.3). In here, the optimal inversion model is selected through comparison with the true subsurface model; see central plot in Figure 8.8 (other models shown in Figure 8.8 are selected for illustration purposes). A selection of inversion models is shown here to illustrate effects of the different parameters that can be chosen to enhance the inversion model for the mantle region.

Through comparison of the models it becomes evident that a higher horizontal smoothing ($\alpha \geq 3$) increases the misfit and, moreover, yields models with a diagonal resistor, extending from 30 km at the northernmost stations of the profile down to a depth of approximately 200 km in the south. A low global smoothing ($\tau = 1$) decreases the misfit, but results in models with a more pronounced second resistor in the south of the profile at depth greater than 60 km. The lateral extent of the resistor depends on the choice of other inversion settings like static shift correction or the resistivity of the crust.

In comparison with effects of different smoothing parameters, the influence of the remaining parameters is relatively small. Using a "true crust", i.e. the local crustal resistivity distribution of the synthetic model for the region beneath the stations (cf. bottom right plot in Figure 8.8), increases the misfit significantly, and introduces an additional resistive body in the left-hand side of the model. Increased misfit and additional resistor are most likely a result of the incorrectly modelled crustal strike direction: during the inversion, a N45W strike direction of is assumed for the crust (like for the rest of the model), whereas the synthetic 3D model contains a N45E strike direction at crustal depth instead. Omitting a static shift correction causes in general a higher RMS misfit, for the case of a homogeneous crust as well as for the case of the true crust. It is further confirmed that keeping crustal structures fixed is beneficial as this focuses the inversion onto the deeper regions. On the other hand, using two tear zones to enforce separate inversion for crust and mantle of the model does not have a significant effect on the resulting model; this is presumably due to the fixing of the crust, which already enforces separate inversions.

It has been proposed that TM mode data are less effected by 3D anomalies [e.g. *Tournerie and Chouteau*, 2005] and that isotropic 2D inversion of data from only the TM mode

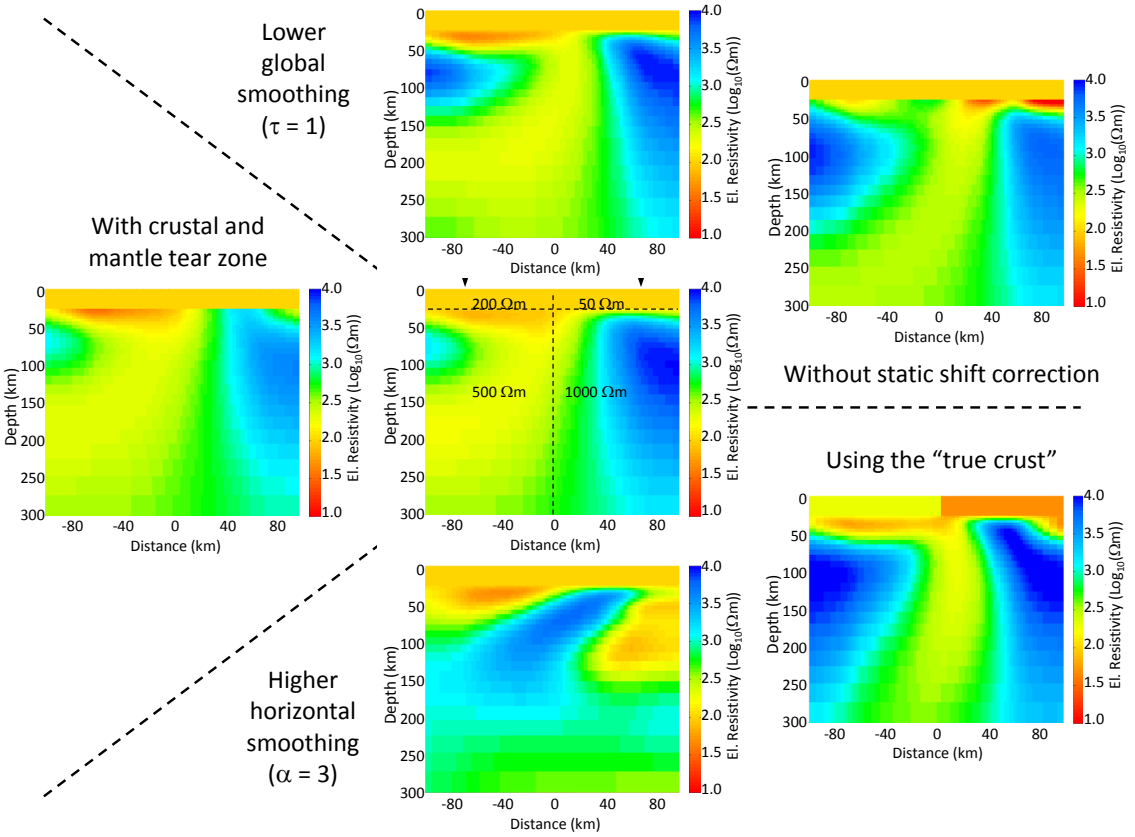

Fig. 8.8.: Selection of isotropic 2D inversion models for a synthetic 3D model with orthogonal strike direction at crust and mantle depth using the profile 3D-mantle and the stations syn001 – syn020 (cf. Figs. 8.3 and 8.4). The true resistivity distribution beneath the profile is indicated on the central model together with the northern and southern ends of the profile, denoted by the inverted triangles. See text for details about the inversion settings.

("TM-only inversion") may therefore yield superior results. This hypotheses is tested here with the synthetic 3D model using datasets decomposed according to the crustal strike direction (N45W, profile: 3D-crust) as well as the mantle strike direction (N45E, profile: 3D-mantle) for the whole period range ($10^{-3} - 10^{5}$ s) with the same smoothing parameters determined for the isotropic 2D inversion with both modes (Tab. 8.3). Results of the TM-only inversion indicate that this approach is not appropriate for the subsurface model used in this study since respective models (Figs. 8.9 and 8.10) differ significantly from the electric resistivity distribution of the true model (Fig. 8.3).

In conclusion, it has been found that approximating the crust by a 30 km layer and applying static shift correction during isotropic 2D inversion yields models that are closest to the synthetic 3D model (cf. central graphic in Figure 8.8). The preferential combination of parameters used for an isotropic 2D inversion of the 3D subsurface model with oblique geoelectric strike directions at crust and mantle depths is given in Table 8.3. However, even the model with the relatively best agreement with the true subsurface distribution suffers from a lateral shift of the resistivity interface towards the North (i.e. to the right

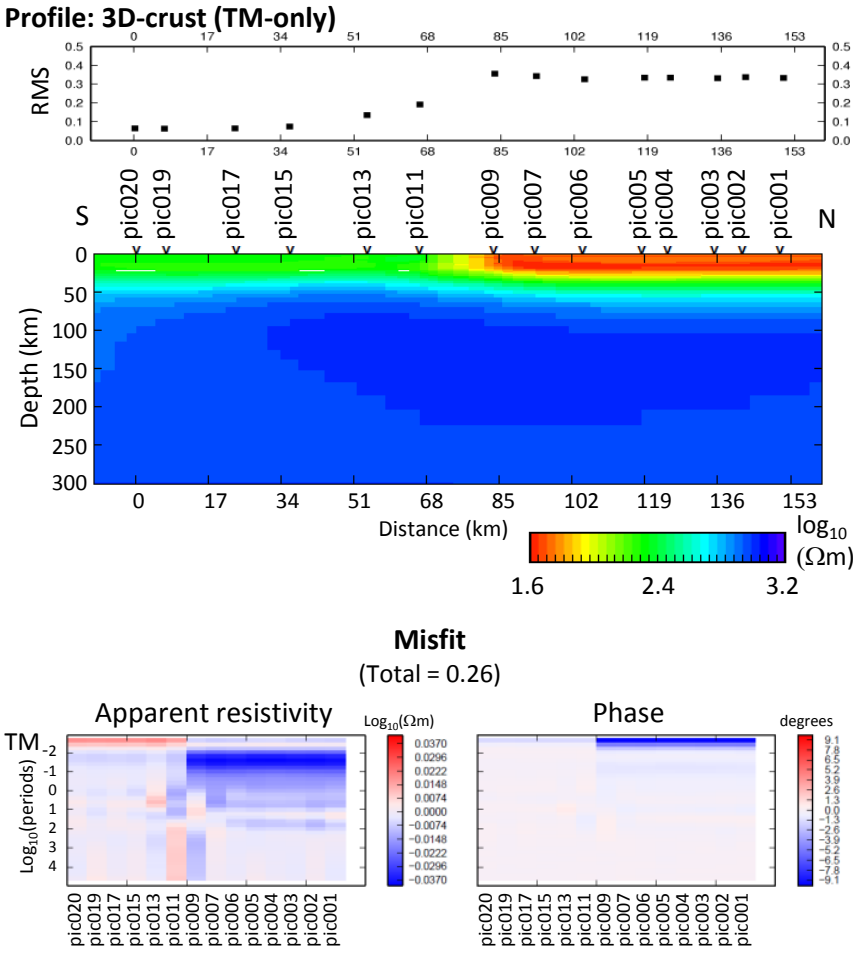

Fig. 8.9.: Result of isotropic 2D inversion for the 3D-crust profile (cf. Fig. 8.5) using only data from the TM mode ("TM-only") of stations pic001 – pic020, decomposed according to the geoelectric strike direction of the crust (N45W). Misfit values for this model are of lesser significance since error and scatter levels of the data are not realistic.

in Figure 8.8) and the introduction of a resistive body in the South of the model. Introduction of such artefacts needs to be kept in mind when interpreting results of isotropic 2D inversions for similar subsurface cases. Using only data from the TM mode for the inversion did not result in a better agreement of inversion models with the synthetic 3D model, hence the TM-only inversion approach is found not appropriate for this special case of electric resistivity distribution with oblique strike directions.

Furthermore, the decision about the best subsurface model, hence the optimal combination of inversion parameters, is achieved through comparison with the true model. Selecting the best model for a case in which the subsurface is not *a priori* known will be more challenging and the doubt of ambiguity regarding the chosen model will remain, due to the non-uniqueness of MT inversion.

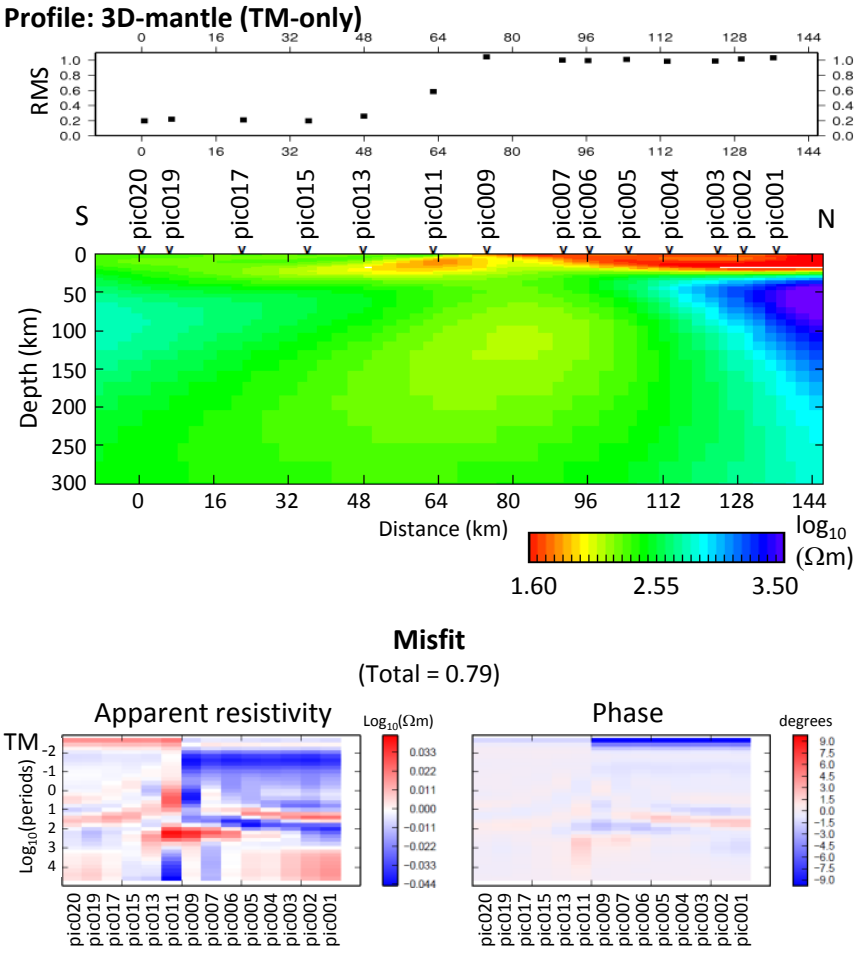

Fig. 8.10.: Result of isotropic 2D inversion for the 3D-mantle profile (cf. Fig. 8.5) using only data from the TM mode ("TM-only") of stations pic001 – pic020, decomposed according to the geoelectric strike direction of the mantle (N45E). Misfit values for this model are of lesser significance since error and scatter levels of the data are not realistic.

8.3.2. Anisotropic 1D inversion of 3D model data

Inversion approach

The use of anisotropic inversion to recover the 3D model is motivated by the fact that 2D structures can be imaged by an anisotropic 1D region and vice versa [e.g. *Heise and Pous*, 2001; *Pek and Santos*, 2006]. The principle of using anisotropy to image macro-scale 2D structures can be best illustrated using the basic MT relations and distortion formulations introduced in Chapters 3 and 4, which are recapped here briefly. In MT, characteristics of the subsurface, usually given in terms of apparent resistivity ρ_a and phase ϕ, can also be described using the magnetotelluric impedance tensor, viz.

$$\mathbf{Z} = \begin{pmatrix} Z_{xx} & Z_{xy} \\ Z_{yx} & Z_{yy} \end{pmatrix}. \tag{8.1}$$

Parameter	Value
Fixing structures at crustal depth:	yes
Setting crustal structures to:	homogeneous layer (rather than "true values")
Static shift correction:	yes
Tear zone to separate crust and mantle:	optional
Horizontal smoothing:	low ($\alpha = 1$)
Global smoothing:	increased ($\tau = 6$)

Tab. 8.3.: Preferential combination of isotropic 2D inversion setting for the case of the synthetic 3D model used in this study, featuring two very different strike directions for crust and mantle depth.

The tensor is calculated from the relation between horizontal components of electric field $\vec{E_h} = (E_x, E_y)$ and magnetic field $\vec{H_h} = (H_x, H_y)$ at one frequency f:

$$\vec{E_h}(f) = \mathbf{Z}(f) * \vec{H_h}(f). \tag{8.2}$$

Penetration depth of electromagnetic waves is frequency-dependent; therefore, information about different depths can be obtained by using $\mathbf{Z}$ at different frequencies. For the case of a 1D subsurface, diagonal elements of $\mathbf{Z}$ are equal zero and off-diagonal elements exhibit the same amplitude but different signs[2] [e.g. *Vozoff*, 1987], i.e.

$$\mathbf{Z}_{1D} = \begin{pmatrix} 0 & Z_{xy} \\ -Z_{xy} & 0 \end{pmatrix}. \tag{8.3}$$

In case of a regional 2D subsurface (i.e. a vertical interface separating two homogeneous quarter-spaces with different electric resistivity) and if the coordinate system is aligned with the orientation of the interface the off-diagonal elements are again non-zero, but in general different:

$$\mathbf{Z}_{2D} = \begin{pmatrix} 0 & Z_{xy} \\ Z_{yx} & 0 \end{pmatrix}. \tag{8.4}$$

Commonly, in MT investigation the y-axis is associated with the direction of the profile, which is oriented orthogonal to the regional electric resistivity interfaces. Therefore, elements Z_{xy} and Z_{yx} comprise data of the electric component parallel and the magnetic component orthogonal to the resistivity interface and vice versa. Accordingly, Z_{xy} and Z_{yx} are commonly referred to as transverse electric (TE) and transverse magnetic (TM) mode response data, respectively.

A significant degree of anisotropy can cause a decoupling of the off-diagonal impedance tensor elements (Eq. 8.3) that is similar to the 2D subsurface case presuming respective directions of the electrical anisotropy axes. In such a case, the TE and TM modes of the

[2]Different signs of 1D off-diagonal impedance tensor elements are due to the use of right-hand and left-hand coordinate systems for Z_{xy} and Z_{yx} elements, respectively [e.g. *Vozoff*, 1987]

Parameter	Value
Inverting for	Apparent resistivity and impedance phase
Standard deviation	2.5 Ωm (Resistivity), 3 degrees (Phase)
Diagonal elements	Included
Depth range (km)	0.05 - 4000
Increment of layer thickness	1.2
Regularisation	
- Max. and min. resistivity, direction	First derivative (weighting = 50)
- Anisotropy	Penalty in L2 norm (weighting = 20)

Tab. 8.4.: Parameter values used during the 1D anisotropic inversion; for details about the parameters see *Pek and Santos* [2006].

2D subsurface case can be imaged by the relatively conductive and resistive anisotropy direction:

$$\mathbf{Z}_{2D} = \begin{pmatrix} 0 & Z_{xy} \\ Z_{yx} & 0 \end{pmatrix} \Leftrightarrow \begin{pmatrix} 0 & Z_{xy}^{ani} \\ Z_{yx}^{ani} & 0 \end{pmatrix} = \mathbf{Z}_{1D}^{ani}, \tag{8.5}$$

where Z_{xy}^{ani} and Z_{yx}^{ani} are special forms of the 1D impedance tensor elements given in Equation (Eq. 8.3). Certainly, values of the two 2D subsurface modes, TE and TM, differ between conductive and resistive side of the interface and vary with (inductive) distance from the interface (cf. Fig. 3.4). It will be shown in this Section that such behaviour at a vertical interface can be accounted for through the corresponding selection of electric anisotropy direction and a changing magnitude of anisotropy for the respective stations and periods.

Inversion process

In this study, anisotropic 1D inversion is carried out using the `ai1d` algorithm by *Pek and Santos* [2006] with parameters given in Table 8.4. The `ai1d` algorithm yields impedance values in terms of minimum resistivity ρ_{min}, maximum resistivity ρ_{max}, and *anisotropic direction* for different depths at each station. Anisotropic direction denotes the angle between ρ_{min} (σ_{max}) and the x-axis; for this anisotropic 1D study, the latter is oriented towards true North.

Inversion results

Results of the anisotropic 1D inversion are plotted side by side to yield pseudo-2D subsurface models for ρ_{min} and ρ_{max}, thereby facilitating comparison of results from different inversion approaches. Crustal-range values of ρ_{min} and ρ_{max} (depths ≤ 30 km in left-hand and right-hand plots of Figure 8.11) are similar to each other (hence isotropic) and to the true subsurface model (uppermost plot in Figure 8.11), whereas mantle structures are significantly different. Whilst the left (or south) mantle region of the ρ_{min} model is similar to the true model, the mantle region to the right (or north) is clearly different. For the ρ_{max}

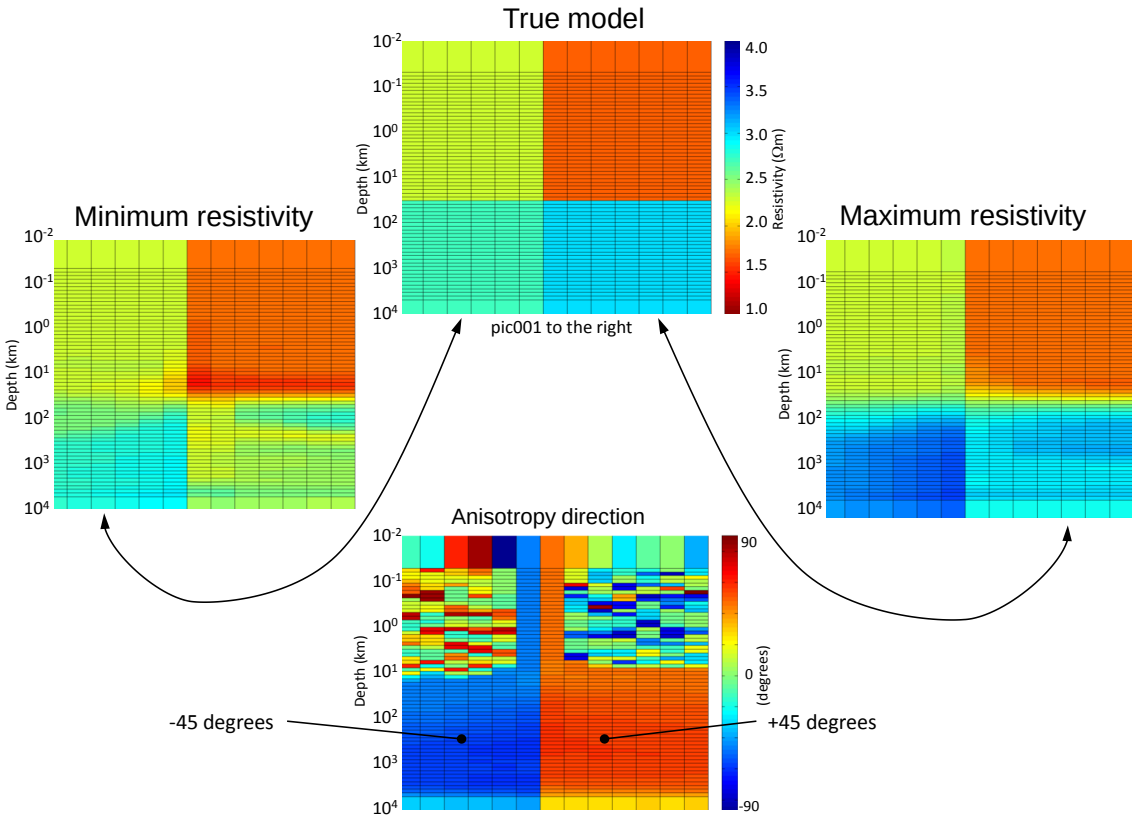

Fig. 8.11.: 1D anisotropic inversion of a 3D subsurface model (Fig. 8.3) using the `ai1d` algorithm by *Pek and Santos* [2006] showing that the true model can be reproduced from a combination of derived minimum and maximum inversion models. The strike direction of the true model is -45 degrees (N45W) at crustal and +45 degrees (N45E) at mantle depth. Note that the strike direction for the crust are insignificant since the degree of anisotropy is negligible (cf. Fig. 8.12).

model the opposite case occurs: the mantle region to the right is similar to the true model, whereas the mantle region to the left is significantly different (indicated by arrows in Figure 8.11). The magnitude of anisotropy is given in terms of the difference between ρ_{min} and ρ_{max} at crustal and mantle depths (Fig. 8.12). Whereas at crustal depth the $\rho_{max} - \rho_{min}$ quotient is approximately one, values between three and eight are observable for the mantle region. The region of maximum anisotropy magnitude is located at a depth between 100 km and 500 km in the resistive region of the mantle (in the right-hand side of plot (b) in Figure 8.12).

Analysis of the anisotropic strike direction shown at the bottom of Figure 8.11 reveals that for the region to the right the anisotropic strike is parallel to the geoelectric 2D strike at mantle depth, i.e. +45° or N45E, whereas for the region to left the anisotropic strike direction is orthogonal to it. Sorting the resistivity values of the models according to their orientation yields models of resistivity parallel to the 2D strike of the synthetic model at mantle depth ($\rho_{\parallel}$) and orthogonal to it ($\rho_{\perp}$). Comparison with the true models shows that the $\rho_{\perp}$ model exhibits an electric resistivity distribution similar to the true model, whereas

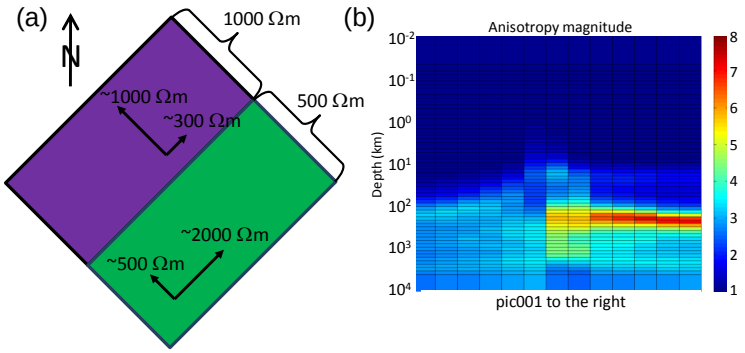

Fig. 8.12.: (a) Values and direction of minimum and maximum resistivity obtained through 1D anisotropic inversion of the 3D model, and (b) magnitude of anisotropy for the 1D inversion calculated from the $\rho_{max} - \rho_{min}$ quotient exhibiting a rather isotropic crust and a mantle with an anisotropic magnitude between 1 and 8.

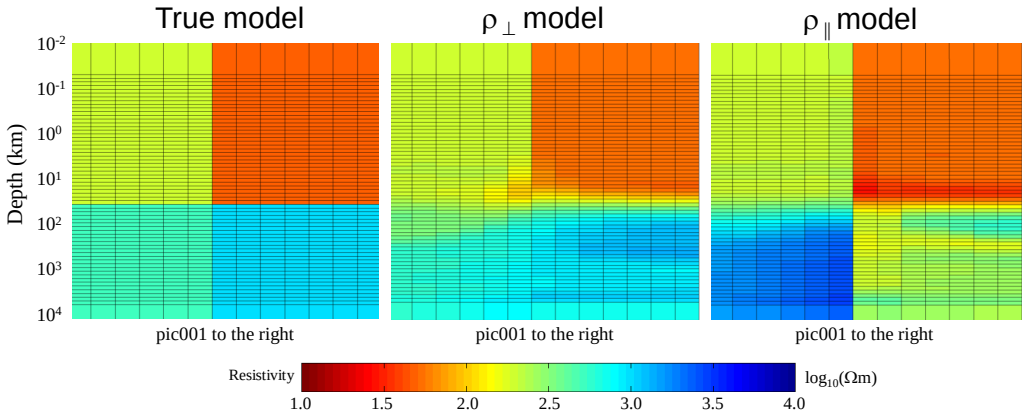

Fig. 8.13.: Comparison of $\rho_\perp$ and $\rho_\parallel$ model with the true model, demonstrating good agreement of the $\rho_\perp$ model.

the $\rho_\parallel$ model underestimates the resistivity in the relatively resistive region and underestimates the resistivity on the relatively conductive side (cf. Fig. 8.13). Using the maximum and minimum anisotropic resistivity for the northern and southern region respectively, resembles the 1D approach for cases of a local surficial conductor embedded in a resistive host region in which the TE mode is used on the conductive region and the TM mode is used on the resistive region [e.g. *Berdichevsky and Dmitriev*, 1976a; *Jiracek*, 1990; *Agarwal et al.*, 1993]. The difference between $\rho_\perp$ and the true model is mostly confined to a small area at the crust–mantle boundary to the northern end of the profile, i.e. of the region on the right-hand side in Figure 8.14. The misfit coincides with the transition from 50 Ωm to 1000 Ωm in the true model and it is concluded that the discrepancy originates from smoothing regularisations of the inversion process, meaning that the 1D anisotropic inversion yields an adequate reproduction of the synthetic model for the major part of the mantle. However, the 3D subsurface model used in this study comprises a considerably simple electric conductivity structure, and 1D anisotropic inversion is likely to fail for more complex models, e.g. a model containing dipping structures. Therefore, results of

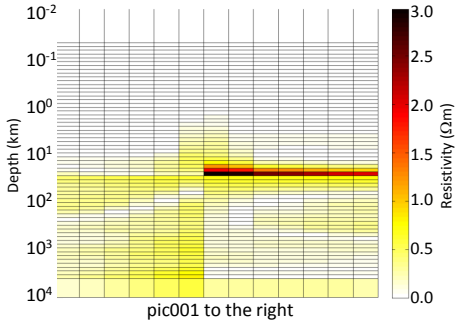

Fig. 8.14.: Relative difference between the model with resistivity values perpendicular to the 2D strike direction at mantle depth ($\rho_\perp$) and the true model.

the `ai1d` algorithm may instead be used as a first approach to the subsurface structures and to construct an elaborate starting model for subsequent 2D inversions.

8.3.3. Anisotropic 2D inversion of 3D model data

Inversion approach

After successfully applying anisotropic 1D inversion to recover the synthetic 3D model by imaging 2D structures with a 1D anisotropic region (Sec. 8.3.2), principles are extended to 2D inversions which do not suffer from the limitations of 1D inversion, i.e. handling more complex structures in the subsurface. In general, the coordinate system related to the 2D regional structure and the coordinate system related to the anisotropy direction are not required to be identical. Therefore, anisotropic 2D models have the potential to image effects of oblique strike directions in different subsurface regions by incorporating variable orientations of regional and anisotropy coordinate systems for the respective regions; this concept will be illustrated in the next paragraph.

Two contrary approaches can be conceived for anisotropic 2D inversion of the 3D model with oblique geoelectric strike directions in crust and mantle (Fig. 8.3): (1) isotropic 2D representation of the crust and anisotropic imaging of the mantle, or, the opposite case, (2) anisotropic imaging of the crust and 2D isotropic representation of the mantle (cf. Fig. 8.15). The approaches differ in terms of required rotation of the datasets as well as in terms of period range assigned to the isotropic and anisotropic part of the model. The latter determines whether the crust is isotropic and the mantle anisotropic (approach 1) or vice versa (approach 2). The dataset has to be rotated to fit the requirements of the isotropic model part; i.e. for the 3D model used here, to N45W for the first approach and to N45E for the second.

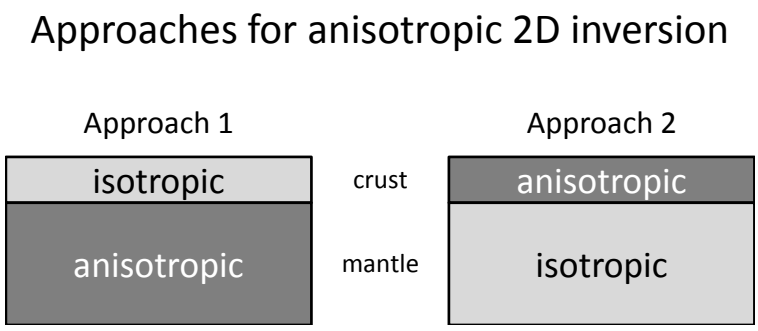

Fig. 8.15.: Approaches for anisotropic 2D inversion of the 3D subsurface model; see text for details.

Inversion process

In this study, the algorithm `MT2Dinv` [*Baba et al.*, 2006], an augmented version of the algorithm by *Rodi and Mackie* [2001], is used for the anisotropic inversion. The `MT2Dinv` algorithm requires that the anisotropy coordinate system is correlate with the coordinate system chosen for the 2D inversion, i.e. the anisotropic conductivities $\sigma_{xx}, \sigma_{yy}, \sigma_{zz}$ (cf. Sec. 4.1.3) denote conductivities parallel to the axes of the 2D coordinate system. This limitation does not impair the anisotropic inversion approach for the 3D subsurface model used in this study as the two different geoelectric strike directions in crust and mantle are orthogonal to each other. Alignment of the two strike directions with one of the two horizontal axes of the model can be achieved through either a clockwise or an anticlockwise rotation of the dataset by 45 degrees, i.e. to N45E or N45W. Sense of the dataset rotation, hence alignment of x-axis or y-axis with either strike direction at crust or mantle depth depends on the inversion approach.

Unfortunately, the current version of the `MT2Dinv` algorithm does not permit the assignment of 'anisotropy zones' to the subsurface model, i.e. it is not possible to separate the model into isotropic and anisotropic parts. Instead, the program only permits a global definition of an isotropy paramater τ_{iso}, which controls the anisotropy constraint in the objective function (see Sec. 6.3). Suggestions regarding incorporation of anisotropy zones have been made to the authors of the `MT2Dinv` algorithm, but these are not yet implemented. Therefore, anisotropic 2D inversion has to be carried in two sequences: first isotropic 2D inversion of shorter periods, followed by anisotropic 2D inversion for the mantle range (approach 1) or isotropic inversion of long period data followed by inversion of crustal-range periods (approach 2). The region inverted for in the first sequence is kept fixed during the second sequence (Fig. 8.16) and inversions in both sequences follow the Jones Catechism (Sec. A.2.3). In approach 1, the first inversion sequence is carried out with a 100 Ωm halfspace starting model, whereas the second sequence uses a starting model with crustal values derived in the first sequence and mantle values set to 1000 Ωm. In approach 2, the first inversion sequence is carried out with a 1000 Ωm halfspace starting model and the second sequence uses a starting model with mantle values derived in the first sequence and crustal values set to 100 Ωm.

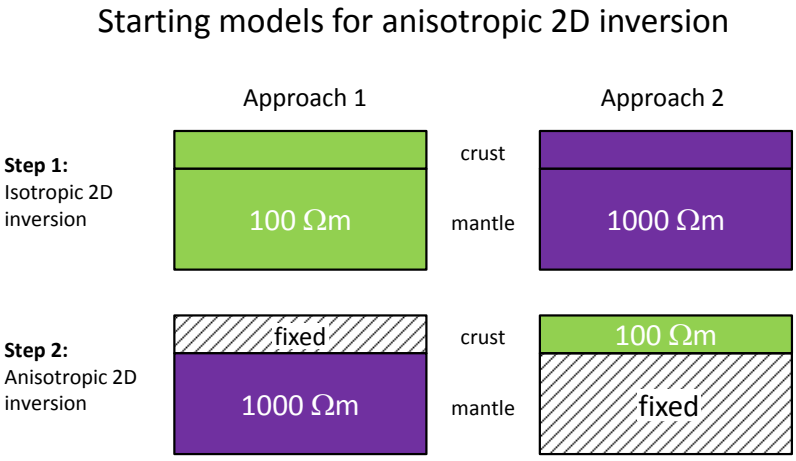

Fig. 8.16.: Starting models used for anisotropic 2D inversion; see text for details about the two inversion approaches.

Parameter	Value
Period range for inversion	10^{-2} – –10^{5} s
Mesh resistivity value	1000 Ωm
Horizontal block width increase factor	1.2
Horizontal block target width	1.2 of a skin depth
Vertical block width increase factor	1.1

Tab. 8.5.: Parameters used to generate the mesh for the anisotropic 2D inversion

In this section, the focus is on the advances of anisotropic 2D inversion in contrast to an isotropic approach. The effect of different inversion parameters (smoothing, static shift correction, tear zone application) was the focus of the previous Section 8.3.1 and in the following the therein identified optimal smoothing parameter values are used, i.e. $\alpha = 1$, $\beta = 1$, $\tau = 6$. Because the aim of this anisotropic inversion approach is to use anisotropic "distortion" to recover the 3D subsurface structures, no static shift corrections or tear zones are applied and the crust is neither fixed as a homogeneous layer nor with its "true values" (cf. Sec. 8.3.1). Instead, crustal values are determined by the inversion process. Parameters used to generate the mesh for the anisotropic 2D inversion are summarised in Table 8.5.

Inversion results

As for the cases of isotropic 2D and anisotropic 1D inversion (Secs. 8.3.1 and 8.3.2), evaluation of anisotropic 2D inversion results in this Chapter is limited to stations related to the PICASSO Phase I recording sites (stations pic001 – pic020 in Figure 8.4). Results for other profiles are used to illustrate certain issues of the anisotropic 2D inversion approach and are presented in more detail in the Appendix (Sec. A.3.2). In general, anisotropic 2D

inversion is reasonable fast; for most profiles, inversions of one sequence is carried out in under four hours using one processor of an Intel Xeon CPU X5680 dual core machine with 3.33 GHz for a mesh with 108×146 cells and 1600 data points (product of number of stations, number of period estimates, and impedance tensor elements).

The `ai2D` inversion algorithm [*Baba et al.*, 2006] yields electrical resistivity models for the direction parallel and orthogonal to the profile, i.e. ρ_{xx} and ρ_{yy}. Thus, no rearrangement of data vectors for the different cells of the model (like in the case of anisotropic 1D inversion) is required. The ρ_{xx} model can be used to recover the resistivity distribution of the region that is not in agreement with the assumption of isotropic strike direction; i.e. the mantle in approach 1 and the crust in approach 2 (cf. Fig. 8.15). Results of the ρ_{yy} model are therein shown for comparison.

The second approach currently suffers unfortunately from a systematic problem. Long-period data, sensing the mantle region, are affected by the resistivity distribution of regions above. Hence, results obtained in step one are biased and, even though crustal structures can be recovered to some degree using anisotropic inversion during step 2, mantle structures remain erroneous (cf. Fig. A.11). Subsequent isotropic inversion of the mantle (in a third inversion sequence) destroys the anisotropic crustal structures due to the inherent isotropy constraints. An anisotropic inversion in the second sequence, on the other hand, contradicts the anisotropic inversion approach by introducing anisotropic features to the mantle region. For a successful application of the second anisotropic inversion approach 'anisotropy zone' assignment would be required, but this is not yet implemented as already noted in the previous section. As a result, realisation of approach 2 has to be postponed for the time being. This is unfortunate, since approach 2 is likely to yield superior inversion results for the mantle given its isotropic (instead of anisotropic) inversion of mantle range using the true mantle strike direction. It is therefore strongly recommended that performance of the second approach is thoroughly investigated, once anisotropy-zones are implemented in the inversion code

Approach 1 does not suffer from the lack of anisotropy-zones, because the isotropic inversion of shorter periods is conducted prior to the anisotropic inversion of long-period data. Fixing the crustal structures at their isotropic values does not impede anisotropic inversion in the secondary sequence and approach 1 yields ρ_{xx} inversion models that exhibit resistivity distributions similar to the true model (cf. Fig. 8.17). Crustal structures are recovered reasonable well for both anisotropy directions (ρ_{xx} and ρ_{yy}) and in the ρ_{xx} model the resistivity interface at mantle depth is considerably well resolved. The ρ_{xx} model exhibits a distinct lateral change from intermediate resistivity values in the south of the profile to high resistivity values in the north, whereas the ρ_{yy} model contains a less distinct lateral change. The change of electric resistivity is facilitated through a changing degree of anisotropy magnitude (ρ_{AA} plot in Figure 8.17).

Exceedingly high values of the northern mantle region as well as smooth variation in anisotropy magnitude, hence the less distinct lateral interface in the ρ_{xx} model, are due to smoothness constraints of the inversion process (cf. Sec. 6.3). The agreement of ρ_{xx} inversion models with the synthetic 3D model can be enhanced by choosing a lower smoothing

parameter τ and a resistivity gradient regularisation (instead of a laplacian regularisation) for the objective function of the inversion process (cf. Fig. 8.18). The misfit for the inversion models, obtained through inversion with different smoothing parameters, is generally low (RMS misfit $\leq$ 2 for phases with a 5% error floor and apparent resistivities with a 10% error floor) and its distribution within the TE and TM mode responses varies between inversion models with different parameters; cf. plots of apparent resistivity and phase misfit in Figure 8.17 and in the respective figures in Section A.3.2.

For the 3D-crust profile with stations that represent the PICASSO Phase I recording sites generally a good agreement with the true subsurface is achieved and the results can be reproduced for other profiles and datasets from different stations (cf. Fig. 8.19). However, the selection of inversion parameters is tailored to the characteristics of the 3D model and its very localised changes of electric resistivity (e.g. from 50 Ωm to 1000 Ωm in the northern region of the model). Thus, for the case of real subsurface, with unknown distribution of electric resistivity, using a higher degree of smoothing may proof more appropriate.

In order to test robustness of the anisotropic 2D inversion approach, inversion of the 3D-crust profile is repeated for data with low, medium, and high amount of noise. For that purpose 1%, 3%, and 10% random noise is added to the dataset and inversion is carried out according to the second approach, with resistivity gradient regularisation and low smoothing (τ = 6). Inversion results for the three noise levels indicate that synthetic model structures can be resolved for low and medium amount of noise, whereas for higher amount of noise the vertical resistivity interface at mantle is not well reproduced (cf. Fig. 8.20). For subsurface cases that are more complex than the synthetic model used in this study responses will be affected by noise as well as by additional geological features (e.g. small-scale bodies). Therefore, a smaller amount of noise may already result in a significant corruption of the data.

Anisotropic 2D inversion is capable of recovering the electric resistivity distribution for a profile over a 3D subsurface to a certain degree. Lateral changes of resistivity in the model are reproduced at crustal and mantle depth, however, sharpness and apparent lateral location of the interface at mantle depth are subject to the choice of smoothing parameters. Moreover, values of the resistive mantle region are less constrained and may significantly exceed values of the synthetic model without adequate inversion constraints. For the 3D model and parameter range used in this study, a combination of low smoothing parameter (τ = 1) and resistivity gradient regularisation yields an optimal model. As the synthetic model is a (simplified) representation of predicted Tajo Basin subsurface characteristics, anisotropic 2D inversion has the potential to yield a model of the local electric resistivity distribution that is superior to the results of isotropic 2D inversion without the need for costly 3D inversion (presuming low or medium amount of noise in the data); cf. Section A.2.4 for a comparison of computational time for the different inversion approaches.

8.4. Summary and conclusions

Oblique geoelectric strike directions in the crust and mantle are a common issue in MT investigation, particularly causing problems during 2D inversion due to the requirement of defining a common strike direction. Different approaches can be conceived, of which constrained isotropic 2D inversion, anisotropic 1D inversion, and anisotropic 2D inversion attempts were studied in this Chapter. After illustrating general applicability of anisotropic inversion approaches using basic mathematical relations for anisotropy effects on MT data, the different approaches were applied to data from a synthetic 3D model with orthogonal strike direction in crust and mantle (Fig. 8.3) and results for different profiles over the 3D model were analysed. In particular, inversion models for a profile containing a set of stations that represent MT recording sites of the PICASSO Phase I investigation were evaluated and results of the different approaches were contrasted.

For isotropic 2D inversion, a set of inversion parameters was identified which yields a subsurface model closest to the original model (for this inversion approach). Whereas crustal structures were reconstructed reasonable well, the electric resistivity distribution of the mantle was not particularly well recovered (Fig. 8.8). Even the optimal isotropic 2D model contained significant inversion artefacts, in particular a resistive body at mantle depth. Using only TM mode data for the isotropic 2D inversion process did not result in a more adequate reproduction of mantle structures. Results of isotropic 2D inversion for subsurface cases similar to the 3D model used in this study are therefore to be used with caution and its applicability to the Tajo Basin subsurface is questionable.

Anisotropic 1D inversion yielded models that are close to the 3D subsurface model, thereby indicating the potential of anisotropic inversion for the case of complex subsurface structures. In the anisotropic 1D inversion approach the crust was approximated by a quasi - isotropic 1D layer and the mantle was imaged by an anisotropic 1D structure. Crustal structures of the synthetic 3D model were in general adequately reproduces by the anisotropic 1D inversion; the vertical electric resistivity interface at crustal depth were imaged by a step-like change of resistivity between stations at the respective location (Fig. 8.11). Mantle structures were recovered reasonably well using resistivity values for the anisotropy direction perpendicular to the mantle strike direction. This finding demonstrates practicality of anisotropic inversions in resolving certain types of 3D subsurface models. However, due to inherent limitations of 1D inversion (e.g. less likely to adequately recover a model containing more complex structures) its results may not be used as a final model, but rather to aid subsequent 2D inversion.

In anisotropic 2D inversion, anisotropic structures can be introduced for certain regions of the model in order to account for effects of oblique geoelectric strike directions in different depth regions, e.g. crust and mantle. Those effects originate from the inevitable erroneous assignment of TE and TM mode in either crustal or mantle region during the 2D inversion. For the case of two oblique strike directions at different depth regions the coordinate system used for the inversion was aligned with one of the strike directions, thereby facilitating isotropic 2D inversion of the respective region. The electric resistivity distri-

bution of the other region can be recovered by models with anisotropy direction parallel to the strike direction at the respective depth. Due to limitations of anisotropic inversion algorithms, it is currently required that the isotropic region is located above the anisotropic region. The alternative approach, containing anisotropic inversion of the crustal range and isotropic inversion of the mantle range, has the potential to yield optimal inversion results given the inherent isotropic inversion of the mantle using the mantle strike direction. Is is strongly recommended that investigation of the alternative approach is accomplished once respective suggestions have been implemented in inversion algorithms. The current approach, consisting of isotropic 2D inversion for the crust and subsequent anisotropic inversion for the mantle, wherein initially obtained crustal structures are kept fixed, yielded electric resistivity distributions that are similar to the 3D model. Details about location of the electric conductivity interface and values at mantle depth are subject of smoothing parameters used in the inversion, but generally inversion models provided useful information about the subsurface structures. It can therefore be concluded that anisotropic 2D inversion is a reasonable approach for investigations of subsurface regions with oblique geoelectric strike directions that does not require computational expensive and time-consuming inversion in the order of 3D inversion. Given the similarity of the synthetic 3D model and the assumed characteristics of the Tajo Basin subsurface, application of this anisotropic 2D inversion approach to data from the PICASSO Phase I investigation is likely to provide useful insight into the local geology.

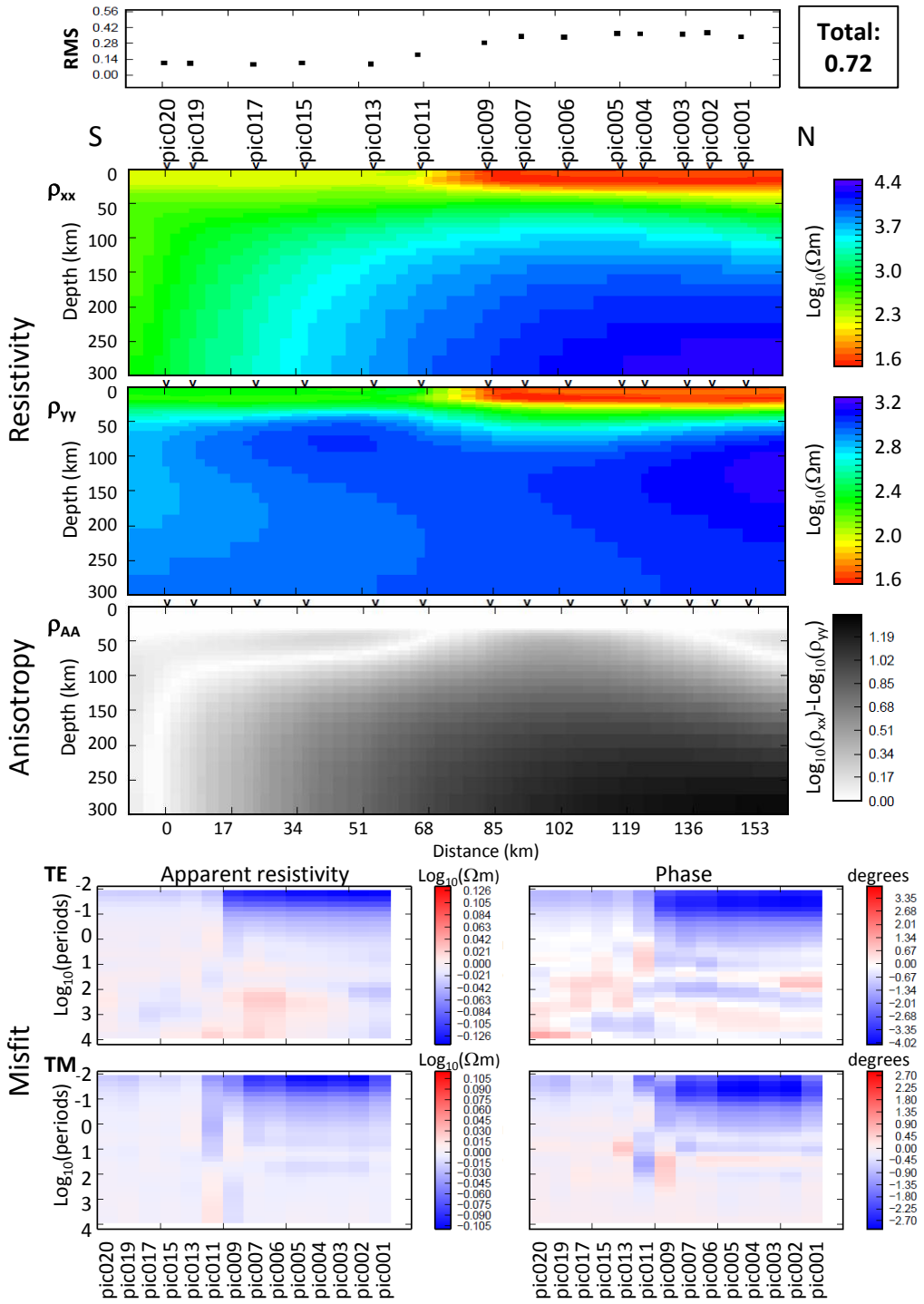

Fig. 8.17.: Anisotropic 2D inversion results for the 3D-crust profile over the synthetic 3D body, using data from the stations pic001 – pic020 (cf. Figs. 8.3, 8.5 and 8.4), related to the PICASSO Phase I recording sites (Sec. 9.1). A horizontal electric resistivity interfaces is located at a depth of 30 km and vertical interfaces are located between stations pic009 and pic011 (at crustal as well as at mantle depth). ρ_{xx} and ρ_{yy} denote subsurface models of electric resistivity orthogonal and parallel to the profile, respectively; the ρ_{AA} model displays the anisotropy magnitude. See text for further details about models and inversion approach.

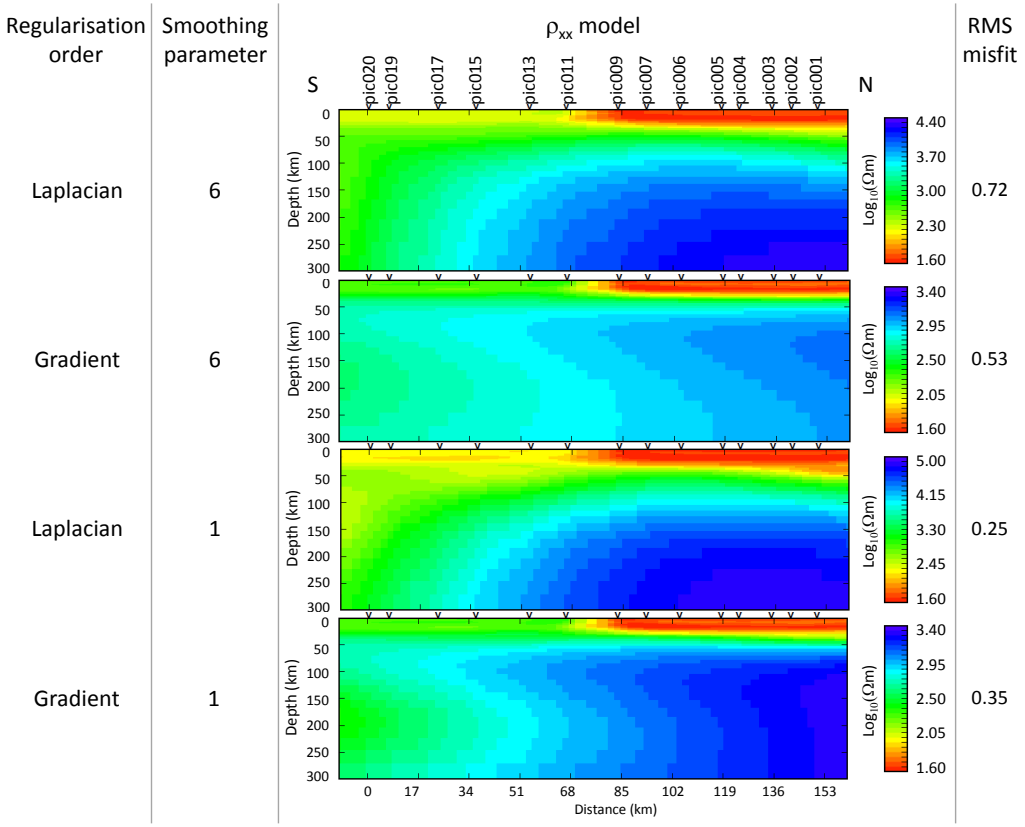

Fig. 8.18.: Comparison of ρ_{xx} inversion models for the profile 3D-crust and stations pic001 – pic020 using different smoothing parameters (note the different colour scales used for the models); see Figures 8.5 and 8.4 for location of profile and stations. Results for the opposite direction (ρ_{yy}) as well as anisotropy magnitude and misfit distribution of the inversion models obtained with different smoothing parameters are shown in Figure 8.17 and the Section A.3.2 in the Appendix (Figs. A.12 – A.14).

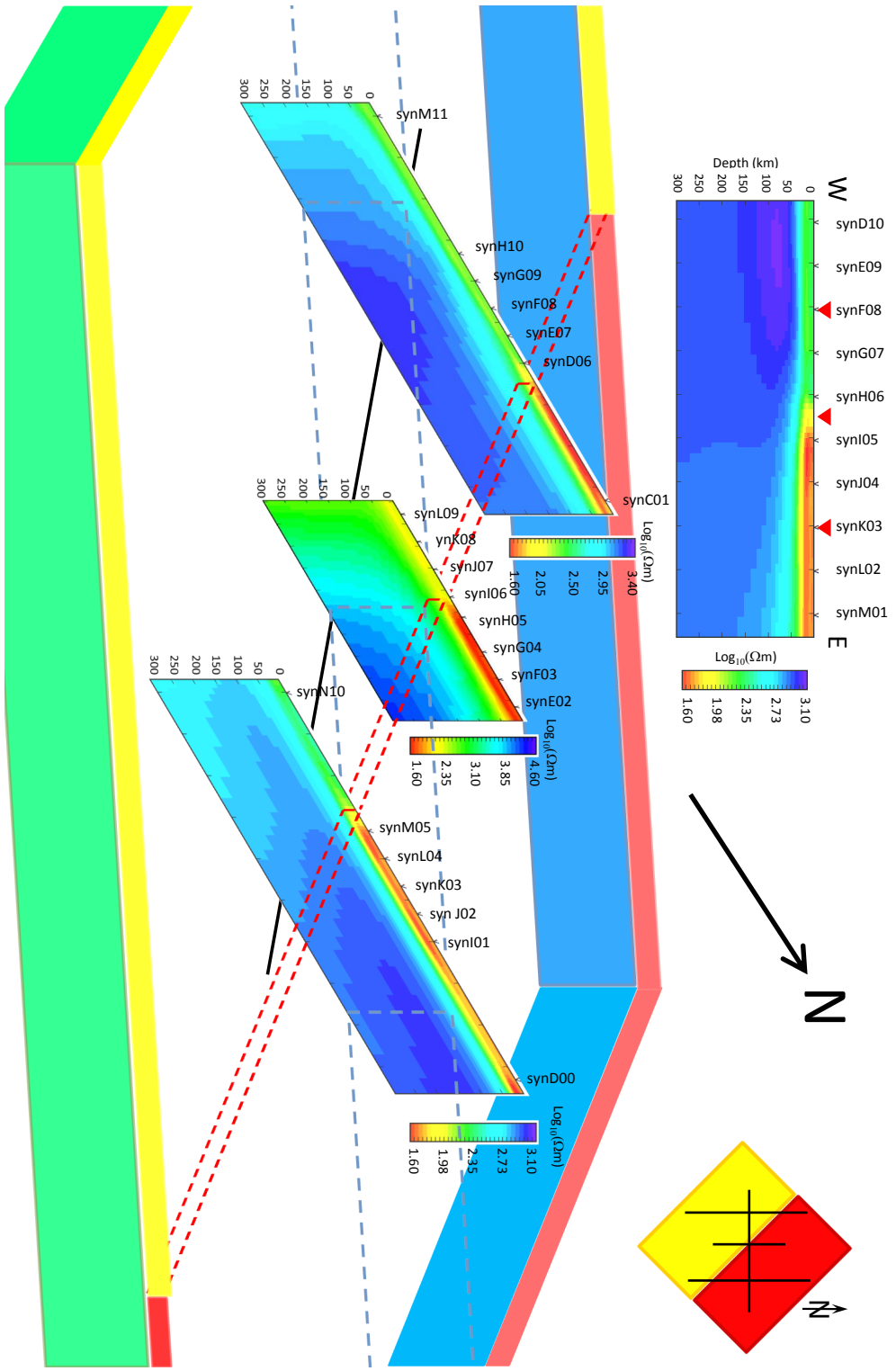

Fig. 8.19.: Results of anisotropic 2D inversion of the synthetic 3D model for a selection of profiles, from left to right: 3D-crust-west with stations synM11 – synC01, 3D-crust-NS with stations synE02 – synL09, and 3D-crust-east with stations synN10 – synD00, as well as 3D-crust-EW profile with stations synD10 – synM01 (upper most plot); see Figures 8.4 and 8.5 for location of stations and profiles. Results are plotted in respect to the station locations; see black lines in the inset on the top-right of the figure. The solid black line in the main plot indicates the projected location of the 3D-crust-EW profile result (model shown on the top of this Figure), and red inverted triangles on the 3D-crust-EW profile denote location of intersection by the other profiles. Dashed lines indicate resistivity interfaces of the synthetic 3D model at crust (red) and mantle (blue) depth (cf. Fig. 8.3). For orientation, side panels are shown, which indicate regions of the synthetic 3D model by colour, following the colouring of the synthetic model. More detailed inversion results for the four profiles are given in Section A.3.2 (Figs. A.15 - A.18).

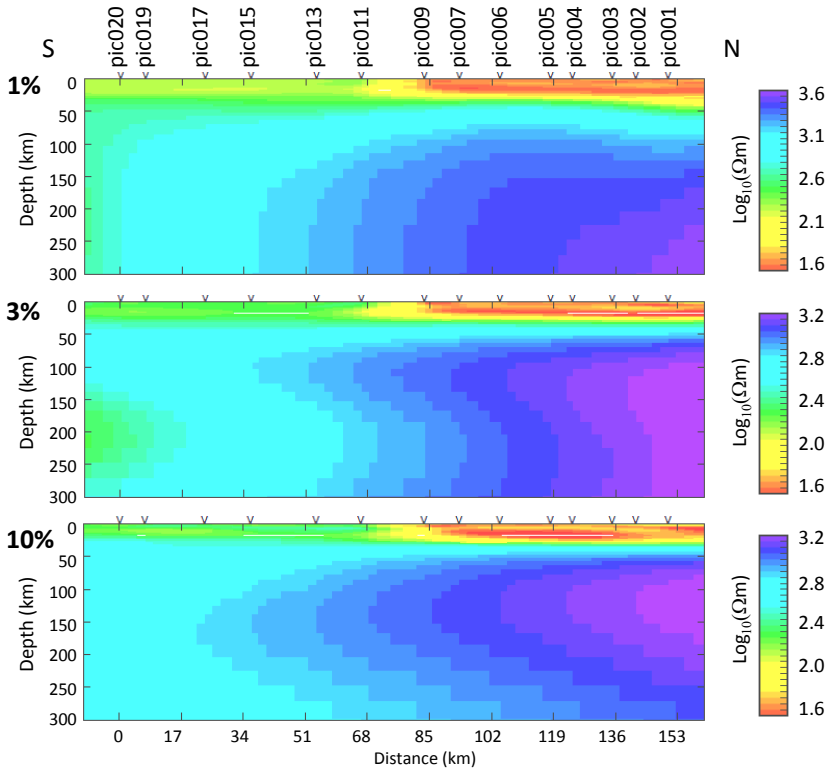

Fig. 8.20.: Results of anisotropic 2D inversion for the 3D-crust profile over the synthetic 3D body, using data from the stations pic001 – pic020 (see Figures 8.3, 8.5 and 8.4 for synthetic model, profile locations, and station locations), with 1%, 3%, and 10% random noise added to the data.

Part IV

Magnetotelluric investigation of the southern Iberian subsurface - PICASSO Phase I

I will paint my picture
Paint myself in blue and red and black and gray
All of the beautiful colors are very very meaningful
Gray is my favorite color
I felt so symbolic yesterday
If I knew Picasso
I would buy myself a gray guitar and play.

– from the song ‘Mr. Jones’ by Counting Crows

9 Data collection and processing

9.1. Profile location

In October and November 2007 magnetotelluric (MT) data are acquired along an approximately 400 km long, north-south oriented profile from a region around 100 km east of Madrid to the city of Almeria near the Mediterranean Sea, crossing the Tajo Basin and the Betic Cordillera (cf. Figs. 7.1 and 9.1). North-south orientation of the profile is chosen in order to intersect the main geological feature, i.e. the Betic Cordillera, as close to perpendicular as possible and to allow for continuation of the profile on the southern side of the Mediterranean Sea. Subsequent fieldwork campaigns in Morocco are executed as part of the PICASSO Phase II and TopoMed projects, as well as a marine survey in the Alboran Domain by the AMELIE project. As well as being informative in their own right about the nature of the lithosphere of the central Iberian Peninsula, data from the PICASSO Phase I project can support investigations of these subsequent projects regarding nature of the putative anomaly beneath the Alboran Domain [e.g. *Platt and Vissers*, 1989; *Seber et al.*, 1996; *Calvert et al.*, 2000] and the complex plate tectonic processes involved in the continental collision between Africa and Europe.

The location of the PICASSO Phase I profile is chosen to avoid sources of electromagnetic (EM) noise, like highly populated areas and the electric train network, as much as possible. Along the profile, data are successfully recorded at 20 locations using Phoenix Geophysics broadband MTU-5 stations and Lviv long-period LEMI-417 stations, with a station spacing close to 20 km where possible. A description of recording systems and their installation in the field is given in Chapter 6. Additional broadband recordings are conducted at four locations along certain parts of the profile, reducing the station spacing to 10 km in order to increase the resolution in these regions. A complete list of all stations installed during the PICASSO Phase I fieldwork campaign together with their location and duration of recording is given in Table 9.1 and in the timeline plot (Fig. 9.2). The profile can be divided into sections according to the different geological setting (Figs. 7.1, 9.1) as summarised in Table 9.2; see Section 7 for details about local geological settings.

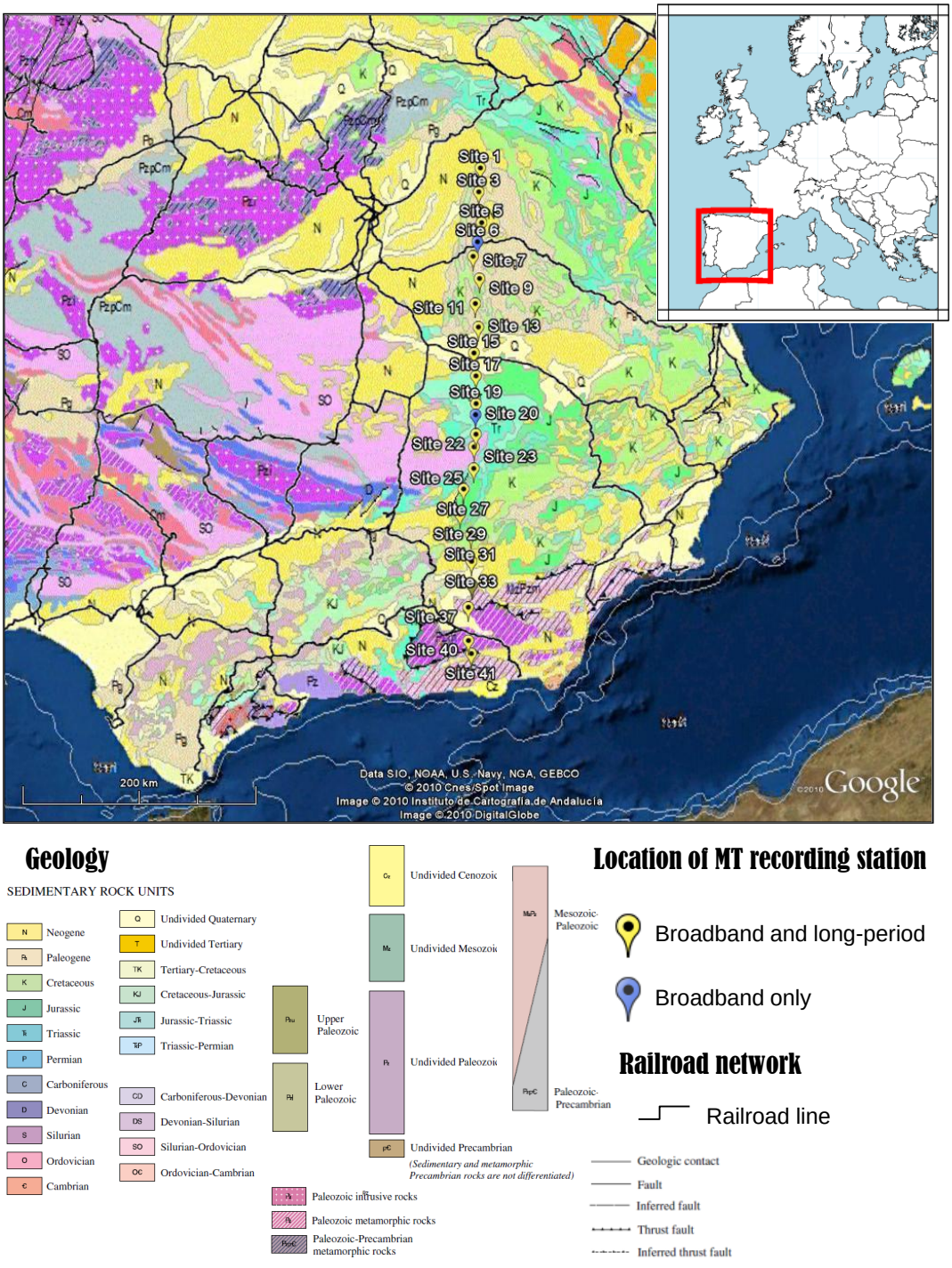

Fig. 9.1.: Location of PICASSO Phase I recording stations, together with the Spanish DC railroad network in the study area (black lines) on top of the surface geological map of Spain from the EnVision map of the *USGS Energy Resources Program* [2010]. Pins indicate the location of magnetotelluric recordings, with colours denoting sites where only broadband systems (blue pins) and both broadband and long-period systems (yellow pins) are used.

Station	Location (degrees)		Recording period (year = 2007)	
	Latitude	Longitude	Long period system (Lemi417)	Broadband system (Phoenix MTU5)
pic001	40.5079	-2.6643	Oct,15 14:29:00.000 – Oct,24 10:51:09.000	Oct,15 17:59:59 – Oct,20 15:57:59
pic002	40.4086	-2.6800		Oct,20 18:59:59 – Oct,23 08:43:36
pic003	40.3309	-2.6881	Oct,16 13:37:00.000 – Oct,24 12:42:23.750	Oct,16 17:59:59 – Oct,23 11:44:26
pic004	40.1954	-2.6933		Oct,23 17:59:59 – Oct,26 08:09:18
pic005	40.1015	-2.6706	Oct,17 10:52:00.000 – Oct,26 09:48:59.750	Oct,17 17:59:59 – Oct,20 09:33:57
pic007	39.8547	-2.7641	Oct,17 16:47:43.750 – Oct,27 08:26:41.500	Oct,17 17:59:59 – Oct,20 09:25:23
pic009	39.6889	-2.7178	Oct,26 16:41:00.000 – Nov,03 09:52:43.750	Oct,26 17:59:59 – Oct,28 08:53:40
pic011	39.5061	-2.7577	Oct,19 14:38:00.000 – Oct,28 10:26:17.750	Oct,19 17:59:59 – Oct,22 09:03:12
pic013	39.3324	-2.7359	Oct,21 11:57:00.000 – Oct,29 15:25:20.750	Oct,23 17:59:59 – Oct,25 08:10:26
pic015	39.1420	-2.7862	Oct,22 13:52:00.000 – Oct,30 16:29:45.750	Oct,22 17:59:59 – Oct,25 10:36:41
pic017	38.9727	-2.7746	Oct,25 16:25:47.000 – Nov,03 08:13:43.750	Oct,25 17:59:59 – Oct,30 00:47:23
pic019	38.7690	-2.7821	Oct,26 14:02:00.000 – Nov,05 12:17:39.750	Oct,26 17:59:59 – Oct,29 09:03:02
pic020	38.6884	-2.7903		Oct,15 17:59:59 – Nov,19 21:20:23
pic022	38.5443	-2.7926	Oct,30 16:21:00.000 – Nov,08 14:03:51.750	Oct,31 15:59:59 – Nov,02 12:17:48
pic023	38.4524	-2.8141	Oct,28 18:08:00.000 – Nov,08 15:35:31.750	Oct,28 18:59:59 – Nov,01 23:21:23
pic025	38.2934	-2.8241	Nov,08 11:53:00.000 – Nov,17 11:05:17.750	Nov,10 17:59:59 – Nov,12 08:08:30
pic027	38.1450	-2.9245	Nov,07 14:58:00.000 – Nov,15 17:11:43.750	Nov,07 17:59:59 – Nov,10 14:37:12
pic029	37.9612	-2.9646	Nov,10 15:14:00.000 – Nov,21 10:20:35.750	Nov,10 17:59:59 – Nov,12 12:18:22
pic031	37.8095	-2.8696	Nov,11 13:42:26.000 – Nov,21 13:37:05.750	Nov,11 17:59:59 – Nov,13 11:50:47
pic033	37.6100	-2.8727	Nov,13 10:29:00.000 – Nov,21 14:50:51.750	Nov,17 17:59:59 – Nov,19 10:20:40
pic035	37.4344	-2.8741	Nov,14 14:00:00.000 – Nov,24 09:49:41.750	Nov,14 17:59:59 – Nov,16 17:21:40
pic037	37.2731	-2.9159	Nov,15 13:50:00.000 – Nov,24 08:03:17.750	Nov,15 17:59:59 – Nov,19 12:25:33
pic040	37.0247	-2.9244	Nov,18 14:50:00.000 – Nov,25 10:58:37.750	Nov,20 17:59:59 – Nov,22 08:45:27
pic041	36.9266	-2.9019	Nov,16 12:42:56.250 – Nov,25 09:37:46.000	Nov,16 17:59:59 – Nov,20 09:26:36

Tab. 9.1.: Location of magnetotelluric (MT) stations and recording duration of long-period (LEMI417 [*Lviv Centre of Institute for Space Research*, 2009]) and broadband (MTU5 [*Phoenix Geophysics*, 2005]) recording systems used for the PICASSO Phase I processing.

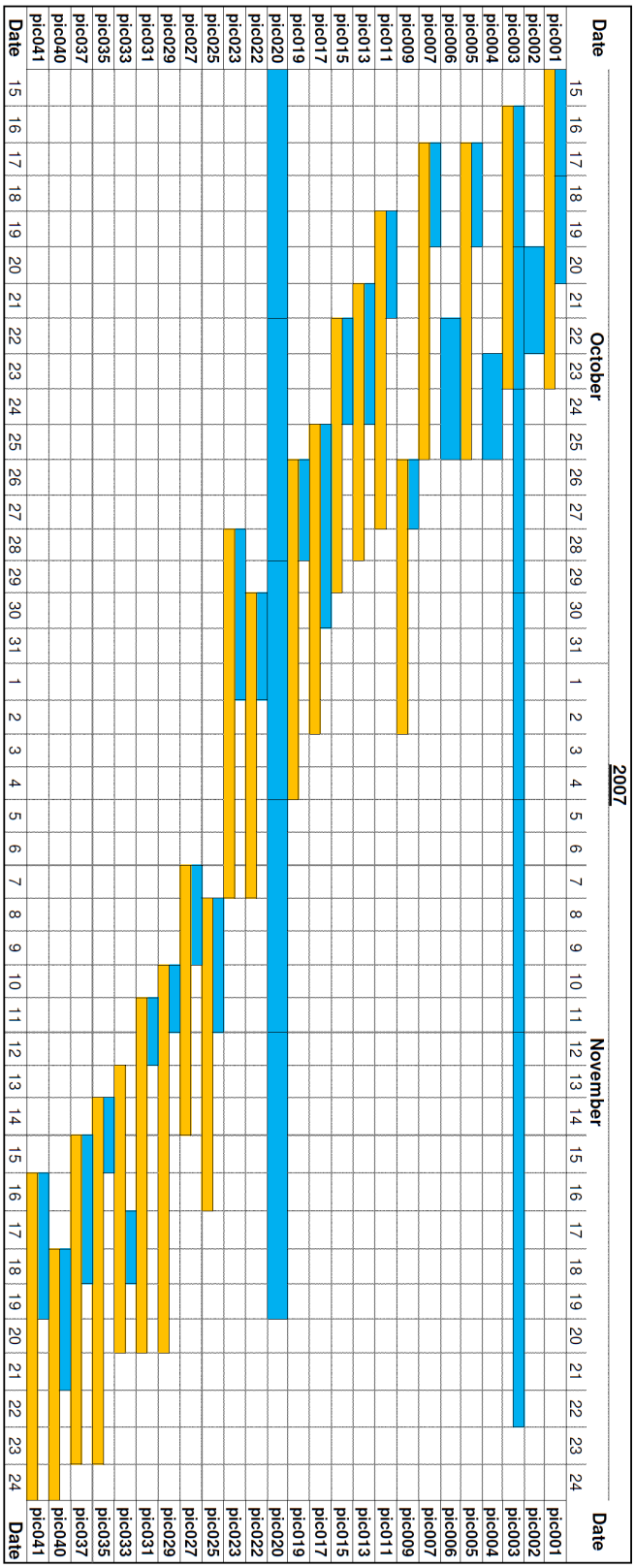

Fig. 9.2.: Timeline plot of the broadband (blue) and long-period (orange) MT recording systems used during the PICASSO Phase I fieldwork campaign. At two sites (pic003, pic020) broadband systems are re-installed to provide continuous data for remote reference processing (cf. Sec. 6.2.3).

Geological region	Stations	Geological region
Tajo Basin	pic001 - pic011 pic013 pic015 - pic020	Loranca Basin Manchega Plain Campo de Montiel
Central Iberian Zone	pic022 + pic023	Central Iberian Zone
Betic Cordillera	pic025 - pic033 pic035 - pic041	External Betics Internal Betics

Tab. 9.2.: Separation of the PICASSO Phase I profile into different regions according to the geological setting (cf. Figs. 7.1, 9.1).

9.2. Analysis of collected data

After field layout correction and standard pre-processing, as described in Section 6.2.1, data are processed using different remote reference robust processing algorithms (see Section 6.2.3 for an overview about the respective principles). Applied algorithm are the `SSMT2000` software [*Phoenix Geophysics*, 2005] (based on a scheme by *Jones and Jödicke* [1984]) and the `EMTF` algorithm [*Egbert*, 1997] for broadband systems, and the `BIRRP` [*Chave and Thomson*, 2003] and `tscascade` [*Jones et al.*, 1989] algorithms as well as a program developed by *Smirnov* [2003] for long-period systems. Among these, the algorithms by *Egbert* [1997] and *Smirnov* [2003] yield superior results in terms of the usable period range and scattering of the impedance estimates, and are therefore used for further processing. The list of stations used for remote reference processing of the PICASSO Phase I data is given in Table 9.3.

9.3. Correction of faulty records in electric channels of long-period instruments

Due to a novel design of the Lviv instruments (Sec. 6.1.1), equipped with four separate electric input channels allowing for a simultaneous recording of the voltage difference between four electrode pairs, it is possible to identify faulty records in the time-series data of an electrode pair and correct for this using information from other channels. During the PICASSO Phase I fieldwork campaign the four channels record the voltage difference between one central electrode (c) and four distal electrodes located to the north (n), south (s), east (e), and west (w) (in a geomagnetic coordinate system) (see Fig. 9.3). This yields two separate measurements for the north-south direction (n-c and c-s) and for the east-west direction (e-c and c-w). Moreover, since the voltage differences are measured end-to-end a third voltage difference can be deduced for each direction using the sum of the two aligned pairs, i.e. n-c+c-s (n-s) and e-c+c-w (e-w).

This layout is superior to previous setups, as erroneous records in one of the channels

Station	Reference station(s) used for processing of	
	Broadband	Long-period data
pic001	pic020	pic001, pic003, pic005, pic007, pic011, pic013, pic015
pic002	pic003	-
pic003	pic037	pic001, pic003, pic005, pic007, pic011, pic013, pic015
pic004	pic004	-
pic005	pic007	pic001, pic003, pic005, pic007, pic011, pic013, pic015, pic017
pic006	pic003	-
pic007	pic005	pic001, pic003, pic005, pic007, pic011, pic013, pic015, pic017
pic009	pic003	pic009, pic011, pic013, pic015, pic017, pic019, pic022, pic023
pic011	pic020	pic001, pic003, pic005, pic007, pic011, pic013, pic015, pic017, pic019
pic013	pic020	pic001, pic003, pic005, pic007, pic009, pic011, pic013, pic015, pic017, pic019, pic023
pic015	pic003	pic001, pic003, pic005, pic007, pic009, pic011, pic013, pic015, pic017, pic019, pic023
pic017	pic003	pic005, pic007, pic009, pic011, pic013, pic015, pic017, pic019, pic022, pic023
pic019	pic003	pic009, pic011, pic013, pic015, pic017, pic019, pic022, pic023
pic020	pic037	-
pic022	pic003	pic009, pic017, pic019, pic022, pic023, pic027
pic023	pic003	pic009, pic013, pic015, pic017, pic019, pic022, pic023, pic027
pic025	pic003	pic025, pic027, pic029, pic031, pic033, pic035, pic037, pic041
pic027	pic003	pic022, pic023, pic025, pic027, pic029, pic031, pic033, pic035
pic029	pic003	pic025, pic027, pic029, pic031, pic033, pic035, pic037, pic040, pic041
pic031	pic031	pic025, pic027, pic029, pic031, pic033, pic035, pic037, pic040, pic041
pic033	pic033	pic025, pic027, pic029, pic031, pic033, pic035, pic037, pic040, pic041
pic035	pic035	pic025, pic027, pic029, pic031, pic033, pic035, pic037, pic040, pic041
pic037	pic003	pic025, pic029, pic031, pic033, pic035, pic037, pic040, pic041
pic040	pic003	pic029, pic031, pic033, pic035, pic037, pic040, pic041
pic041	pic003	pic025, pic029, pic031, pic033, pic035, pic037, pic040, pic041

Tab. 9.3.: Station pairs for remote reference processing of PICASSO Phase I data. For processing of broadband stations remote (or local) reference sites are chosen based on the quality of resulting response estimates; for long-period processing all stations with overlapping recording times are used (*multi-site remote referencing*). See Table 9.1 Figure 9.2 for location and recording times of all stations.

can be detected by comparing the three E-field estimates with each other. The optimal channel (with respect to data quality), or a time-segment of a channel, can then be determined for usage in further processing steps. Erroneous records can be due to either damaged electric cables connecting the electrode pair, or disturbance of one of the electrodes (e.g. polarisation effects or very localised small-scale features). Figure 9.4 illustrates one case in which the centre-south (South) electrode pair underwent severe disturbance during the 21st of October whereas the north-centre (North) pair suffers from the effect of slow saturation of the northern electrode at the beginning of the recording time. Both circumstances affect the combined north-south electrode pair data (Average). Furthermore, the two electrode pairs provide different base levels for the estimated electric field. From these three time-series datasets an optimal subset is culled based on the coherence with the related orthogonal magnetic field measurements (see Section 6.2 for details on coherence estimation in MT data processing). Among others, this is to ensure that the obtained change in electric field behaviour, measured by the centre-south dipole (South), is indeed due to disturbance and does not originate from natural sources. The effect related to the

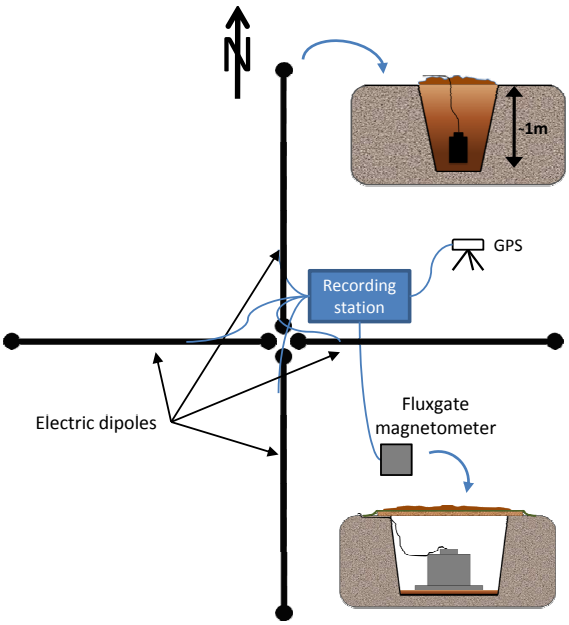

Fig. 9.3.: Modified station layout for the Lviv LEMI-417 recording system, featuring four electric dipoles, in order to utilise the new design of the recording system, possessing four separate input channels for the electric fields; for logistic reasons the same centre-electrode is used for all dipoles and as ground electrode.

disturbance of the centre-south dipole is more severe, requiring the respective data to be omitted, whereas the slow saturation of the northern electrode has only a minor effect. As a result of this analysis, data from the north-centre dipole are selected to be used in subsequent processing steps.

9.4. Segregation of data acquired with the long-period systems according to phase values

PICASSO Phase I stations with long-period recordings, processed with the algorithm of *Smirnov* [2003], can be divided into three groups according to their phases values (cf. Fig. 9.5):

- **a** stations that contain only phase estimates of more than 25 degrees for the whole period range,
- **b** stations that exhibit phase estimates around 0 degrees for most of the periods,
- **c** stations that exhibit phase estimates around 0 degrees for shorter periods only.

Two stations that are part of group **b**, i.e. pic013 and pic015, are located in the proximity of a DC railway line (see Fig. 9.1), hence abnormal phase characteristics of these stations are most likely caused by contamination of the respective datasets by EM noise emitted by the railway line (see Section 4 for details about noise in EM data). Neighbouring

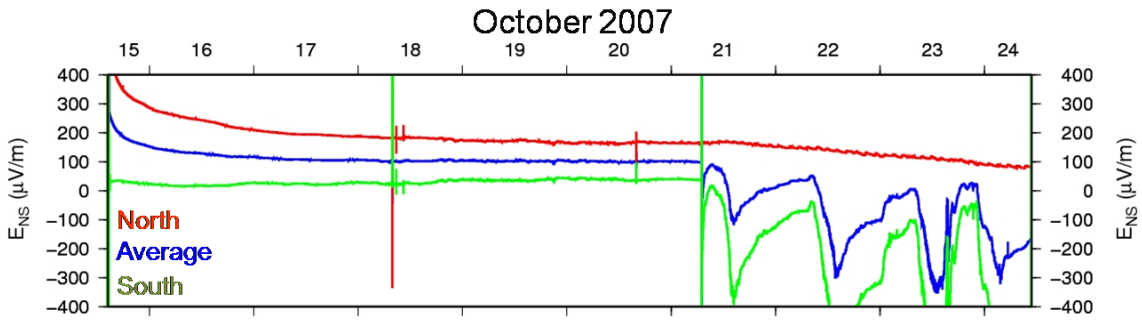

Fig. 9.4.: Time-series data of the electric field measured by the north-centre (North) and the centre-south (South) electrode pair of an Lviv long-period instrument at the same location during the PICASSO fieldwork campaign. Also displayed are time-series data of the averaged north-centre and centre-south dipole (Average). A change of behaviour in the centre-south data during the 21st of October is apparent as well as the effect of slow saturation of the northern electrode at the beginning of the recording; note that the disturbance in all channels during the 18th of October was due to a retrieval of the collocated MTU-5 recording system. Due to separate recording of the two channels, a superior subset of the data can be identified and segregated for further processing.

sites (pic009, pic011, pic017) are part of group **c** and most likely affected by the same noise source; the smaller effect seen by these stations is presumably due to their greater distance to the source location. Among the stations of group **c**, pic011 also exhibits a deviant behaviour for the Z_{yx} phase response, showing an additional interval of decreased phase for longer periods (right-hand plot in Figure 9.5).

No known source of EM noise is located near pic022, also part of group **c**, which can explain the small phase values at this station throughout its entire long-period recording. Hence, the disturbance has to be due to either its geological setting, causing an enhanced conduction of the train line noise towards station pic022, or another, unknown, noise source in the proximity of the station.

Electric noise of the railway line, intersecting the PICASSO Phase I profile between station pic013 and pic015 (Fig. 9.1), has a devastating influence on the derived responses, indicated by phase values of approximately 0 degrees. The effect of this electric noise requires complete rejection of long-period data from station pic013 and pic015, and a truncation of the responses for station pic011, pic017, and pic019 at 1500 s on the base of a D^+-like consistency test [*Parker*, 1980; *Parker and Whaler*, 1981; *Parker*, 1982]. Furthermore, long-period data of station pic022 are rejected and responses of stations pic023 and pic027 are truncated at 900 s in order to remove data corrupted by electromagnetic noise, indicated by very small phase values. Information about the subsurface in regions where data from long-period systems are rejected is, however, still available from responses of broadband stations.

9.5. Merging broadband and long-period data

Subsequent to separate processing of broadband and long-period data, responses are merged for stations where both types are recorded, using in-house programmes `mtmerge` and `mtoverlap` (written by A.G. Jones). The program `mtoverlap` calculates the optimal

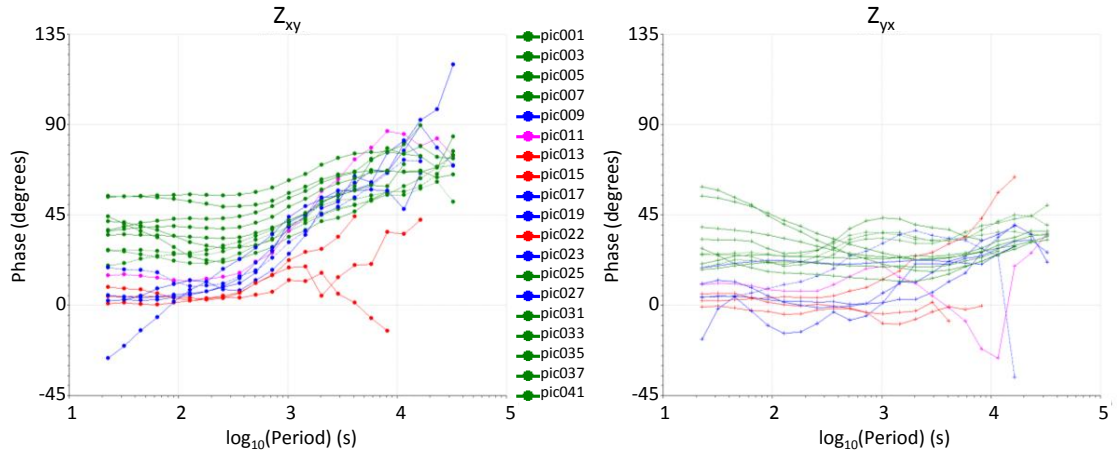

Fig. 9.5.: Phase values for long-period data of the PICASSO Phase I stations (before decomposition), with the Z_{xy} mode on the left-hand side and Z_{yx} on the right-hand side; error bars are omitted for the sake of clarity. The stations are divided into three groups as indicated by colour according to their phase characteristics: (**a**) Only values above 25 degrees (green); (**b**) values around 0 degrees for the majority of the period range (red); and (**c**) values around 0 degrees for shorter periods only (blue). Note that station pic011 (purple) behaves like those of the group **c** for Z_{xy} mode, but also exhibits an interval of decreased values for long periods of the Z_{yx} mode.

shift to be applied to the response curves of one system in order to achieve a smooth transition between curves of the two systems. Results of `mtoverlap` are then used as input for `mtmerge`, conducting the respective adjustment during the merging of the dataset. In principle, for correctly calibrated systems the responses should lie within the error bounds of each other. Shifts between response curves of broadband and long-period data can be due to differences in either sensitivity of the magnetic sensors, coupling of the electric sensors to the ground, or data handling of the instrument types (see Section 6.1.1 for details about the instruments used during the PICASSO Phase I data acquisition).

Along the profile, no consistent relation between shifts of the impedance tensor elements can be observed, indicating that the shift is not due to a systematic difference of one sensor systems. In general, shifts are considerably small and are likely to be caused by marginal inaccuracies during the magnetic sensor installation or due to temporal instability of the electric sensors, i.e. varying electrolytic fluid saturation around the electrodes. Response curves for all PICASSO Phase I stations have been shifted to the level of the broadband data; in most cases the shift, calculated as weighted mean from the difference between impedance values of suitable periods, is considerable low. The choice to shifting towards the broadband data level is reasoned by the fact that electric field estimates of long-period data are more likely to be biased due to drying-out of the electrodes during the longer recording time.

9.6. Compensating for distortion of the impedance tensor

Removing distortion of the data, as described in Section 4, is a crucial, but difficult, step during the analysis for most MT datasets. Moreover, since previous geological and geophysical studies indicate a complex subsurface setting for the region under investigation by the PICASSO Phase I project (cf. Sec. 7), this step is carried out with great diligence.

9.6.1. Geoelectric strike estimation

Determining whether a regional 2D approximation is justified, and (if that is found true) subsequent identification of the geoelectric 2D strike direction are major elements of MT impedance tensor analysis as it affects the decomposition of EM fields into TM and TE mode contribution. The approach used here for the PICASSO Phase I data utilises a script developed by Jan Vozar, displaying the RMS misfit calculated by the `strike` algorithm for different directions at all stations. The `strike` algorithm is based on the impedance tensor decomposition method by *McNeice and Jones* [2001], using the *Groom and Bailey* [1989] technique (Sec. 4.4.4), and is today commonly used my many in the MT community. The RMS misfit is therein calculated for a chosen depth range derived by the Niblett-Bostick depth approximation for the rotational invariant arithmetic average of the off-diagonal elements (also referred to as *Berdichevsky average*) [*Berdichevsky and Dmitriev*, 1976b] (cf. Sec. 6.3.1). A relative impedance error floor of 3.5% is used during the application of the `strike` algorithm, resulting in an error floor of 2.0 degrees for the phase and 7.12% for the apparent resistivity.

The range of directions under investigation is limited to the interval 0 to 90 degrees, owing to the 90 degrees ambiguity of the geoelectric strike estimation. The ambiguity originates from the fact that during the calculation no assumption can be made about the orientation of the two modes, TE and TM, except that they are orthogonal. Hence the true geoelectric strike direction and its orthogonal fit the data equally well. For example, a calculated strike direction of N50E (50 degrees clockwise from North) indicates that the true strike of the geological features has a direction of either N50E or N140E. The decision about the direction has than to be made by considering additional sources of information, such as results of geological studies or the vertical field responses. For the strike analysis of the PICASSO Phase I data an increment of one degree is chosen in order to provide sufficient resolution.

The geoelectric strike analysis using the above-described RMS misfit calculation is supplemented by a multisite, multifrequency (transformed into Niblett-Bostick depth) analysis with the same `strike` program. Therein, optimal strike direction and average RMS misfit are calculated for the chosen depth and stations ranges of; results are from here on referred to as *multi-strike*. These multi-strike directions are calculated separately for the whole profile and its northern region only, reasoned by the observed difference

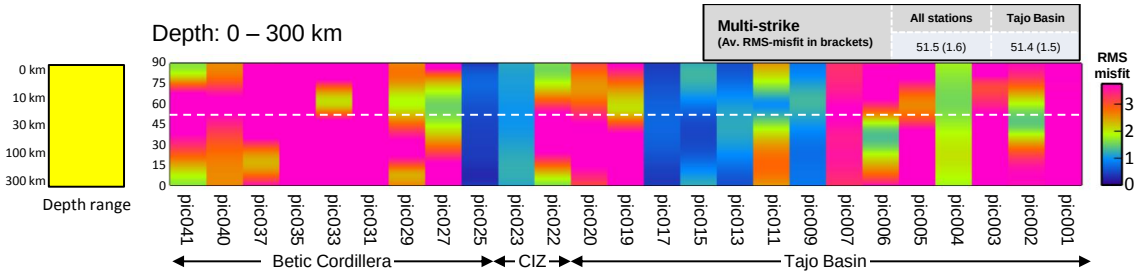

Fig. 9.6.: RMS misfit for different geoelectric strike directions of the stations recorded during PICASSO Phase I, using data in the Niblett-Bostick depth range 0 – 300 km; shown in the inset. Also shown in the top right corner is the optimal common geoelectric strike direction clockwise from North calculated for all stations and for stations in the Tajo Basin only; indicated by the dashed white line in the main plot. Assignment of stations to the different geological regions, displayed on the bottom of the plot, is based on their location in respect to geological units of the USGS EnVision map for Europe (Fig. 9.1), CIZ: Central Iberian Zone, part of the Iberian Massif. See text for further details.

in geoelectric strike characteristics described in the following paragraphs. For a 2D subsurface, satisfactory multi-strike directions should coincide with low RMS misfits for the same direction at a number of adjacent stations, bounded by higher RMS misfits for other directions. Cases where the RMS misfit is low for most directions, on the other hand, indicate a rather 1D nature of the subsurface. In the following paragraphs geoelectric strike direction is determined for different depth ranges in order to investigate whether the best-fitting direction varies for individual regions in crust and mantle.

Complete depth range

Initially, the RMS misfit for different directions is calculated for the whole depth range spanning from 0 to 300 km, revealing an unsystematic distribution of the RMS misfit (cf. Fig. 9.6). Low RMS misfits at stations pic013 – pic017 and pic023 – pic025 are due to the truncation of their long-period data affected by EM noise sources, as described in Section 9.4. The low RMS misfit of station pic009, on the other hand, observed throughout the whole frequency range, is due a higher degree of uncertainty of the responses for this station. Multi-strike analysis yields optimal strike direction and RMS misfit (in brackets) of N51.5E (1.6) and N51.4E (1.5) for the whole profile and the Tajo Basin, respectively; which however, is not significant given the observed unsystematic RMS misfit distribution along the profile.

Crust and mantle depth

As a second step, the depth range is divided into crust and mantle regions spanning from 0 km to 30 km and 35 km to 200 km, respectively (Fig. 9.7); therein, Moho depths of 32 km derived by seismic reflection data (cf. Sec. 7.3.2) are used as crustal-thickness proxy with a small error margin. The crustal depth range exhibits an unsystematic RMS misfit distribution and a multi-strike direction of N58.0E (1.3 av. RMS misfit) and N51.2E (1.5 av. RMS misfit) for the whole profile and the Tajo Basin, respectively.

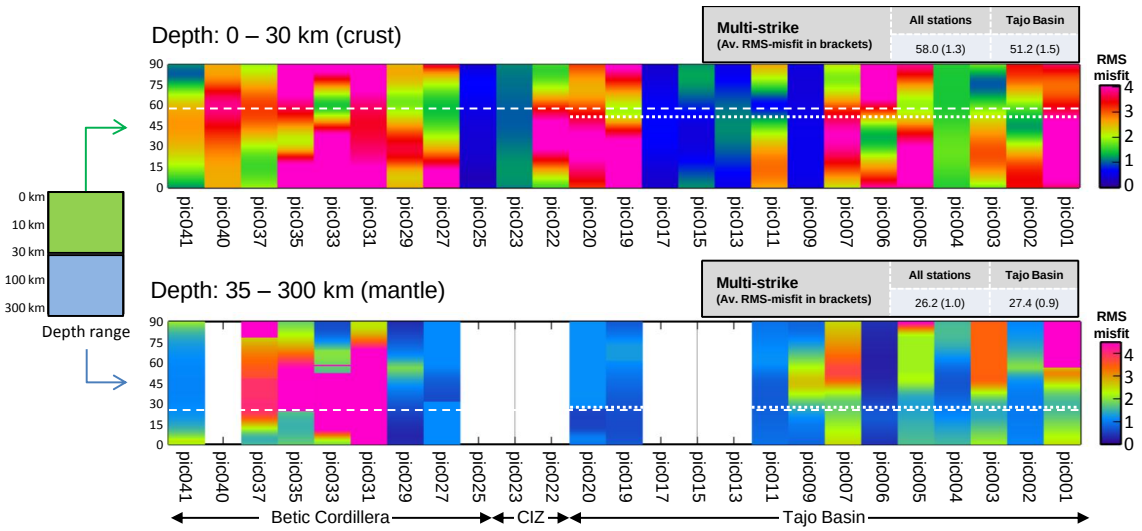

Fig. 9.7.: RMS misfit for different geoelectric strike directions of stations recorded during PICASSO Phase I, using data in the Niblett-Bostick depth ranges 0 – 30 and 35 – 300 km; shown in the inset. Empty spaces are due to lack of data for this depth range at the respective station. Also shown in the top right corner is the optimal common geoelectric strike direction clockwise from North calculated for all stations and for stations in the Tajo Basin only; indicated by dashed and dotted white lines in the main plot, respectively. Assignment of stations to the different geological regions, displayed on the bottom of the plot, is based on their location in respect to geological units of the USGS EnVision map for Europe (Fig. 9.1), CIZ: Central Iberian Zone, part of the Iberian Massif. See text for furhter details.

The mantle exhibits different characteristics for the Betic Cordillera and the Tajo Basin regions. For the Betics no favourable geoelectric strike direction can be identified, the optimal direction varies between stations and the RMS misfit is in general relatively high. A strike direction between N80E and N100E (or N10W and N10E) fits for most of the stations in the Betic Cordillera. However, data from these stations are potentially affected by the presence of the highly conductive Mediterranean Sea to the south of the profile, with a distance of approximately 20 km and 150 km to station pic041 and pic027, respectively. The so called *ocean effect* can severely disturb data of stations in the proximity of the body of water, becoming evident in a deviation of induction vectors towards the conductor (in Parkinson convention) and masking of effects of 2D structure in the local subsurface *Brasse et al.* [e.g. 2002]; *Kuvshinov et al.* [e.g. 2002]; *Muñoz et al.* [e.g. 2008].

The Tajo Basin region, on the other hand, possesses a low RMS misfit for directions around N25E; this observation is supported by the multi-strike analysis yielding a direction of N27.4E (0.9 av. RMS misfit). The multi-strike direction for the whole direction is N26.2E (1.0 av. RMS misfit), most likely dominated by the characteristics of the Tajo Basin.

Intra-crustal depth

In order to determine a reasonable geoelectric strike for the crust, the respective depth range is subdivided into three layers according to the results of seismic studies discussed

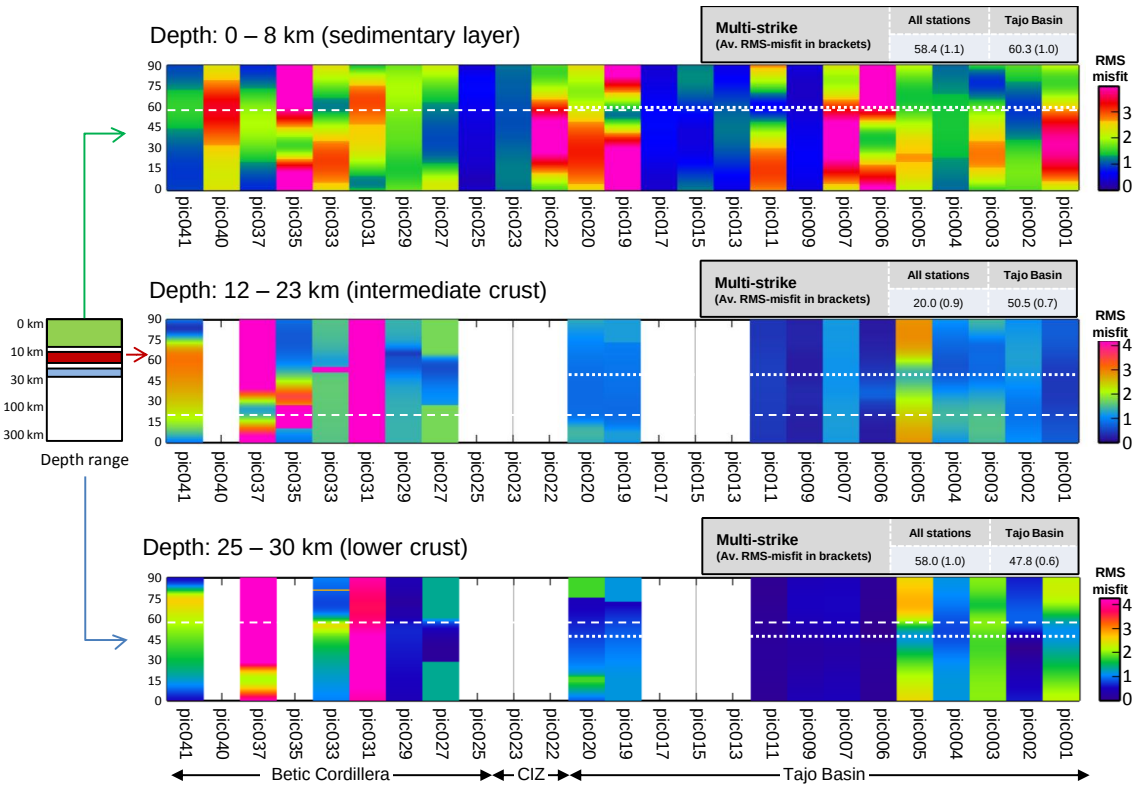

Fig. 9.8.: RMS misfit for different geoelectric strike directions of stations recorded during PICASSO Phase I, using data in the Niblett-Bostick depth ranges 0 – 8 km, 12 – 23 km, and 25 – 30 km; shown in the inset. Empty spaces are due to lack of data for this depth range at the respective station. Also shown in the top right corner is the optimal common geoelectric strike direction clockwise from North calculated for all stations and for stations in the Tajo Basin only; indicated by dashed and dotted white lines in the main plot, respectively. Assignment of stations to the different geological regions, displayed on the bottom of the plot, is based on their location in respect to geological units of the USGS EnVision map for Europe (Fig. 9.1), CIZ: Central Iberian Zone, part of the Iberian Massif. See text for further details.

in Section 7.3.2 identifying an upper crustal layer (≤ 10 km), intermediate crust (10 – 24 km), and lower crust (24 -. 31 km). The upper crust exhibits a rather diverse RMS misfit distribution, probably originating from inhomogeneous features of smaller scale, whereas for intermediate and lower crust of the Tajo Basin a favourable direction is apparent (Fig. 9.8). In general, the RMS misfit for intermediate and lower crust of the Tajo Basin is lower than for the same depth range of Betic Cordillera and the upper crust above. The multi-strike analysis yields N50.5E (0.7 av. RMS misfit) and N47.8E (0.6 av. RMS misfit) as optimal direction for the Tajo Basin intermediate and lower crust, respectively. Calculated values of the Tajo Basin are strongly affected by the characteristics of pic005, exhibiting a pronounced directional variation of the RMS misfit, whereas most other stations are closer to 1D.

These geoelectric strike estimates are in considerably good agreement with results of fault location studies (Sec. 7.3.1) determining three faults that intersect the PICASSO Phase I profile at an angle of approximately N135E in the proximity of stations pic005,

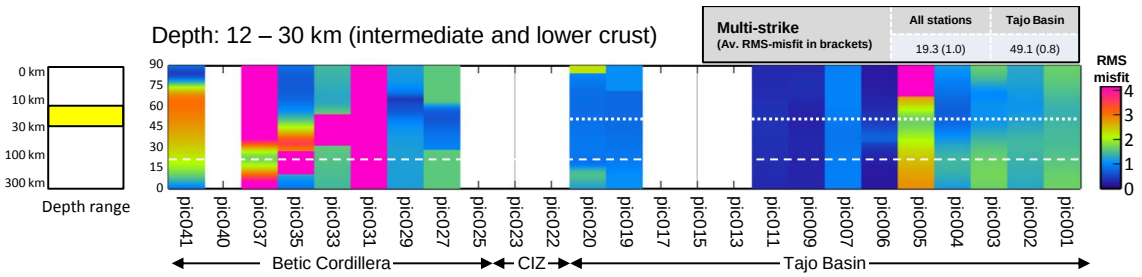

Fig. 9.9.: RMS misfit for different geoelectric strike directions of stations recorded during PICASSO Phase I, using data in the Niblett-Bostick depth range 12 – 30 km; shown in the inset. Empty spaces are due to lack of data for this depth range at the respective station. Also shown in the top right corner is the optimal common geoelectric strike direction clockwise from North calculated for all stations and for stations in the Tajo Basin only; indicated by dashed and dotted white lines in the main plot, respectively. Assignment of stations to the different geological regions, displayed on the bottom of the plot, is based on their location in respect to geological units of the USGS EnVision map for Europe (Fig. 9.1), CIZ: Central Iberian Zone, part of the Iberian Massif. See text for further details.

pic009, and pic013. Note that the geoelectric strike estimate has a 90 degrees ambiguity; therefore calculated values of N50.5E and N47.8E imply that geoelectric strike directions of N140.5E and N137.5E fit the data equally well. However, unlike station pic005, stations pic009 and pic013 do not exhibit a strong 2D behaviour, indicating that the two respective faults do not result in a significant vertical geoelectric interface.

Comparing RMS misfits of the Tajo Basin intermediate and lower crust with the region associated with the Betic Cordillera reveals the different subsurface structures present along the profile, i.e. no distinct strike direction observable for the Betic Cordillera. This circumstance can be explained by the complex 3D structures below the mountain chain originating from its intricate origin (cf. Sec. 7). This difference in dimensionality for Tajo Basin and Betics region of the profile, also observed at mantle depth (shown in the next paragraphs), suggests separate investigation of the two regions. Strike analysis results for other depth ranges, shown in the following figures, support the concept of the complex structure of the southern region.

Combined intermediate and lower crust

Given the similarities in optimal strike direction, as well as overall directional variation of RMS misfit for intermediate and lower crust, strike analysis is conducted for the combined depth range as well. Analysis for the combined depth range yields a directional RMS misfit distribution that is similar to distributions of the individual depth ranges and a multi-strike direction of N49.1E (0.8 av. RMS misfit) for the Tajo Basin region (Fig. 9.9). Northern-most stations (pic001 – 004) agree well with this strike direction, whereas central stations (pic006 - 020) exhibit a considerable 1D structure. Results from seismic studies in the Tajo Basin, indicating a geologic strike direction with an NW-SE orientation (cf. Section 7.3.2), are used to solve the 90 degrees ambiguity. Accordingly, the geoelectric strike direction chosen for this region is N40.9W (or N139.1E). RMS misfits for stations associated with the Betic Cordillera is generally higher and no optimal strike direction is observable.

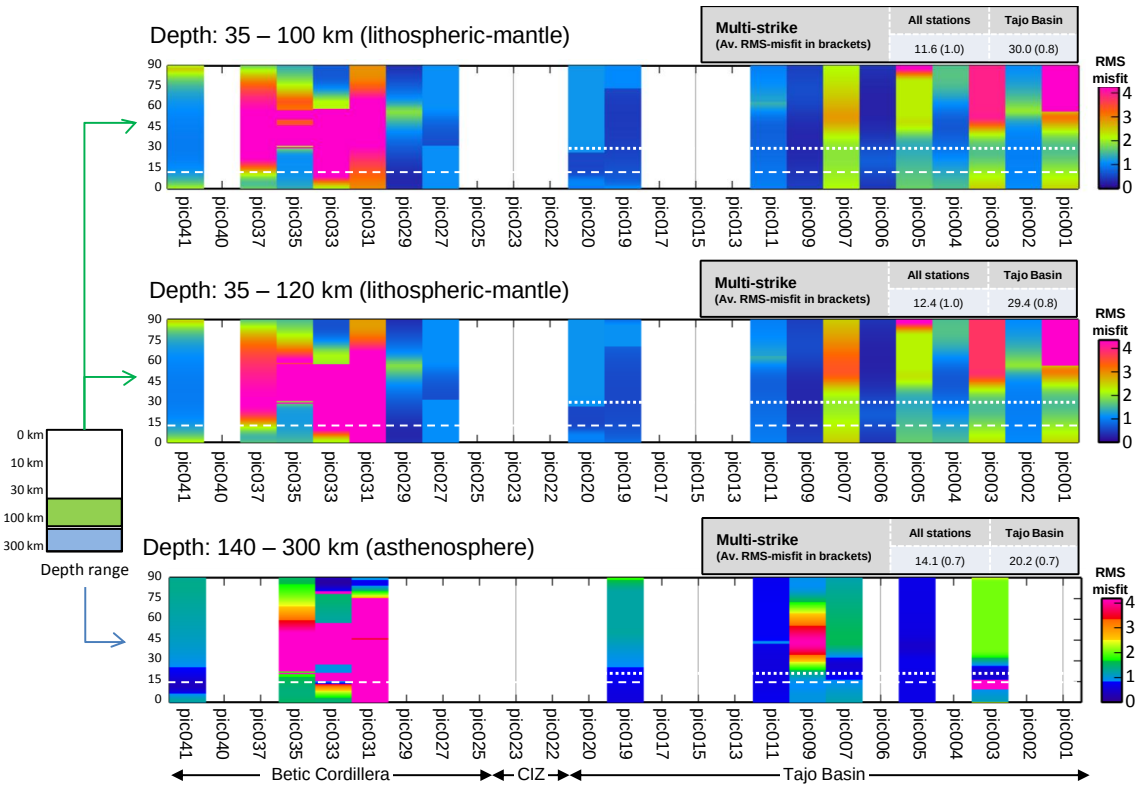

Fig. 9.10.: RMS misfit for different geoelectric strike directions of stations recorded during PICASSO Phase I, using data in the Niblett-Bostick depth ranges 35 – 100, 35 – 120, and 140 – 300 km; shown in the inset. Empty spaces are due to lack of data for this depth range at the respective station. Also shown in the top right corner is the optimal common geoelectric strike direction clockwise from North calculated for all stations and for stations in the Tajo Basin only; indicated by dashed and dotted white lines in the main plot, respectively. Assignment of stations to the different geological regions, displayed on the bottom of the plot, is based on their location in respect to geological units of the USGS EnVision map for Europe (Fig. 9.1), CIZ: Central Iberian Zone, part of the Iberian Massif. See text for further details.

Intra-mantle depth

As for the crust, directional distribution of the RMS misfit is investigated in more detail for regions within the mantle by subdividing the respective depth range into layers related to lithospheric-mantle and asthenosphere. No detailed information is available about the lithosphere–asthenosphere boundary (LAB) depth in this region, but from seismic data it can be inferred, that the LAB is likely to be found within the depth range 110 – 130 km (Sec. 7.3.2). Therefore, one section spanning from 140 km to 300 km, representing the asthenosphere, and two sections related to the lithospheric-mantle, extending down to 100 km and 120 km, are investigated (Fig. 9.10).

Similar to the crust, the Tajo Basin exhibits an overall lower RMS misfit and an apparent optimal direction. Of those stations, the RMS misfit is in general higher for the odd-numbered stations, equipped with broadband and long-period systems, than for the data from even-numbered stations, recorded by broadband systems only. The difference in behaviour is due to the fact that data from sites with broadband stations only are less

constraint at greater depth given their limited period range and larger errors. The multi-strike analysis yields directions of N30.0E and N29.4E (0.8 av. RMS misfit) for the Tajo Basin of the lithospheric-mantle with depth down to 100 km and 120 km, respectively; as well as a direction of N20.2E (0.7 av. RMS misfit) for the asthenosphere.

The significantly different values indicate that the geoelectric strike below the Tajo Basin varies between lithospheric and asthenospheric parts of the mantle, and that the LAB is likely to be found at depth below 120 km. The latter assumption is based on the fact that the observed strike direction is similar for the depth ranges with and without the interval 100 – 120 km, indicating that this interval agrees with structures of the region above. This observation, however, is not well constraint since structures for such a thin layer at this depth are not well resolved. The true strike directions for the lithospheric-mantle can be assumed to possess an orientation between 0 and 90 degrees, rather than the orthogonal direction, considering the results of seismic tomography studies in this regions, indicating a NE-SW geological strike (cf. Section 7.3.2).

Lithospheric depth

Finally, despite indications for different strike directions of crust and mantle by previous analyses and seismic results (cf. Sec. 7.3.2), it is tested whether a reasonable, common strike direction can be found for the depth range spanning from intermediate crust to LAB. The multi-strike analysis yields a direction of N37.2E (1.1 av. RMS misfit) and N35.3E (1.1 av. RMS misfit) for the Tajo Basin lithosphere with an assumed LAB depth of 100 km and 120 km respectively; coincident with a range of low RMS misfit in the main plot of Figure 9.11. For the whole profile a direction of N15.0E is determined, which however does not fit with the RMS distribution of stations in the Betic Cordillera. In principle, a common geoelectric strike direction of intermediate crust, lower crust and lithospheric-mantle can be found: However, certain aspects favour a separate treatment of the two regions, namely the higher average RMS misfit for the combined range indicating an inferior fit of local structures and, more importantly, results of the other geophysical methods that are in favour of two different strike directions at crust and mantle depths (cf. Sec. 7.3.2).

Conclusions

Thorough investigation of the geoelectric strike direction beneath the PICASSO Phase I profile presented in the previous paragraphs results in the following conclusions:

- Strike characteristics differ between the southern region of the profile associated with the Betic Cordillera, and the northern region associated with the Tajo Basin. The Betic Cordillera exhibits complex subsurface structures for the whole depth range for which no distinct geoelectric strike direction can be identified, whereas for the Tajo Basin common geoelectric strike directions can be fitted to the majority of the different depth layers.

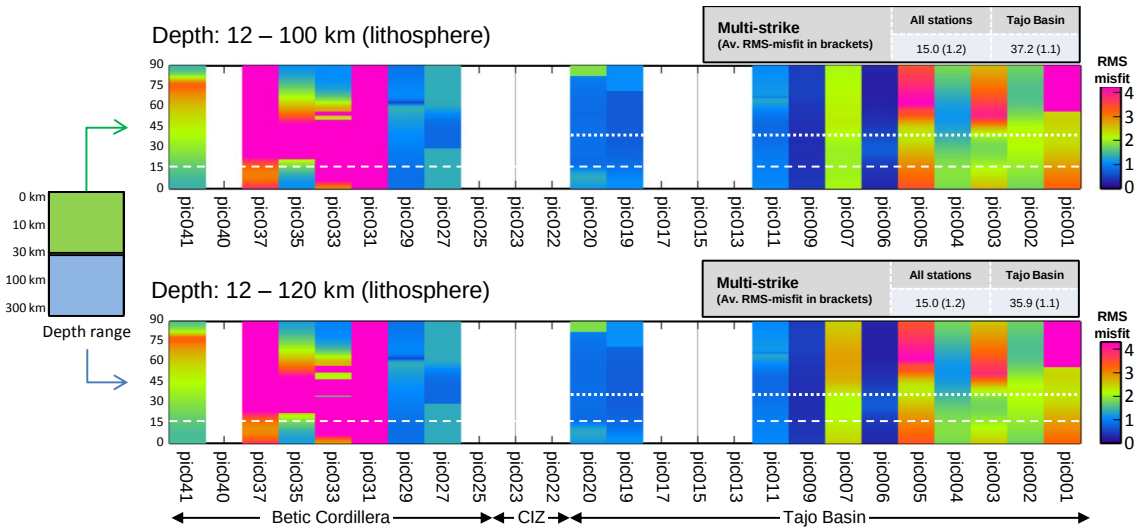

Fig. 9.11.: RMS misfit for different geoelectric strike directions of stations recorded during PICASSO Phase I, using data in the Niblett-Bostick depth ranges 12 – 100 and 12 – 120 km; shown in the inset. Empty spaces are due to lack of data for this depth range at the respective station. Also shown in the top right corner is the optimal common geoelectric strike direction clockwise from North calculated for all stations and for stations in the Tajo Basin only; indicated by dashed and dotted white lines in the main plot, respectively. Assignment of stations to the different geological regions, displayed on the bottom of the plot, is based on their location in respect to geological units of the USGS EnVision map for Europe (Fig. 9.1), CIZ: Central Iberian Zone, part of the Iberian Massif. See text for further details.

- Beneath the Tajo Basin, four groups of layers are derived according to their preferential geoelectric strike direction, namely upper crust (≤ 10 km), combined intermediate and lower crust (12 - 30 km), lithospheric-mantle (35 - 120 km), and asthenosphere (≥ 140 km). Among these, structures in the upper crust are found to be relatively heterogeneous, and structures of the asthenosphere are less constrained due to their greater depth.

- Layers in the Tajo Basin subsurface can be grouped into two bands: crustal layers with a geoelectric strike direction of N40.9W, determined for the structures of the intermediate and lower crust; and mantle layers with a geoelectric strike direction of N29.4E, associated with the lithospheric-mantle. The strike direction of the lithospheric-mantle is similar to the direction of the asthenosphere (N20.2E) and can be expected to provide a suitable estimation for the upper mantle given that constraints on the asthenosphere are weaker due to decreasing resolution of the MT method with depth.

- The determined geoelectric strike direction at mantle depth is not in agreement with derived plate motion of Eurasia (at Long: 3W, Lat: 40N), i.e. N50.6E (2.5 cm/a) [*Argus and Gordon*, 1991] and N50.5E (2.4 cm/a) [*De Mets et al.*, 1994]. It is therefore unlikely that the mantle geoelectric strike direction originates from processes in connection with relative plate motion. Thus, it is unlikely that effects of anisotropic structures, caused by lattice preferred orientation from drag along alignment

Parameter	Value
Intervals per decade	4
Step width along profile	≈ 5.5. km
Interpolation radius	7
Spline weight	7
Smoothing factor	7

Tab. 9.4.: Gridding parameters used to create the pseudo-sections (Figs. 9.12 and 9.13) from the PICASSO Phase I datasets

at the LAB, are mistaken for 2D structural strike (cf. Sec. 4.1.3).

9.6.2. Decomposition of the impedance tensor

The aim of this study is, among others, the investigation of lithospheric-mantle structures. Therefore, two datasets are derived through decomposition of the original dataset: one according to the geoelectric strike of the crust (N40.9W), and a second according to the geoelectric strike direction of the Tajo Basin mantle (N29.4E). No further separation of the mantle is made, e.g. into lithospheric and asthenospheric regions, owing to the lower resolution to structures below the LAB. The two resulting datasets can be used for separate inversion during investigation of crust and mantle structures (Ch. 10).

After geoelectric strike directions for crust and mantle of the Tajo Basin are determined, common distortion parameters for each region are derived for the stations associated with the basin (pic001 – pic020), using the program `strike` by *McNeice and Jones* [2001]. Therein, parameters are derived in the Niblett-Bostick depth range (cf. Sec. 6.3.1) 0.003 m to 30 km and 35 km to 350 km, related to crust and mantle regions, respectively. Resulting parameters are used to decompose the impedance tensor of each station into TE and TM mode contributions, wherein uncertainty levels are determined on a statistical base.

9.7. Analysis of TE and TM mode response data

Data of the TE and TM mode can be visualised by so-called ‘pseudo-sections’. Pseudo-sections are obtained through gridding of MT station period–resistivity (and period–phase) data under consideration of the station locations along the profile. For the PICASSO Phase I profile pseudo-sections are created for TE and TM modes of both, the dataset decomposed for the crustal strike direction (N40.9W, Figure 9.12) and the dataset decomposed for the mantle strike direction (N29.4E, Figure 9.13). Parameters used for the gridding are summarised in Table 9.4. The pseudo-sections from the dataset decomposed in respect to the crustal geoelectric strike direction will in the following be referred-to as ‘crustal strike pseudo-sections’, whereas the opposite case will be referred to as ‘mantle strike pseudo-sections’ (Fig. 9.13).

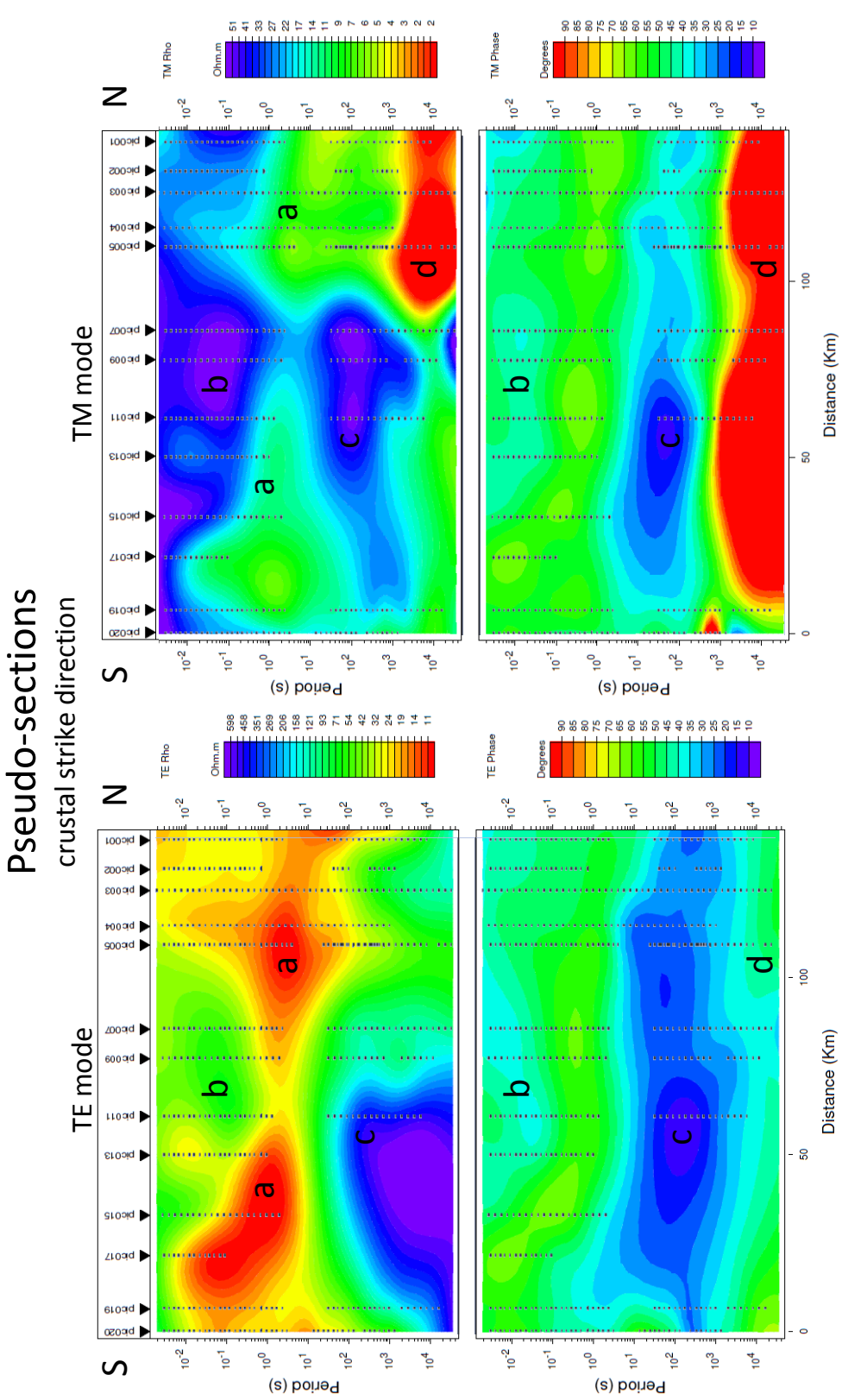

Fig. 9.12.: Pseudo-section of PICASSO Phase I data for a profile with an orientation orthogonal to the crustal geoelectric strike direction (N40.9W) and respective decomposition of the dataset. TE mode data are plotted on the left-hand side, TM mode data on the right-hand side; apparent resistivity is plotted on the top, impedance phase on the bottom. Note that the apparent resistivity colour ranges are set to fit values of the individual mode, thus differ between modes. Black dots indicate at which periods apparent resistivity and phase estimates are used at each station.

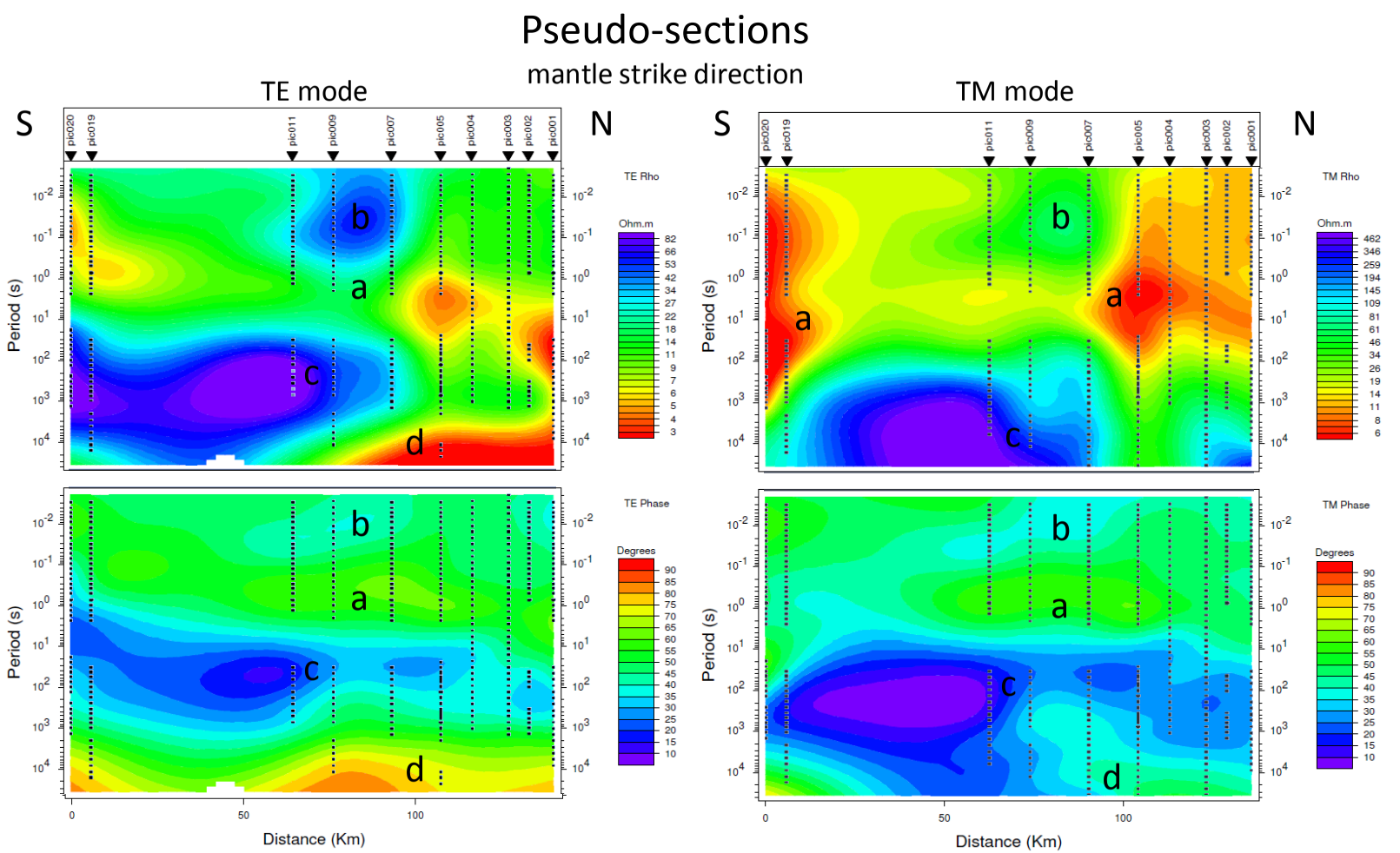

Fig. 9.13.: Pseudo-section of PICASSO Phase I data for profile with an orientation orthogonal to the mantle geoelectric strike direction (N29.4E) and respective decomposition of the dataset. TE mode data are plotted on the left-hand side, TM mode data on the right-hand side; apparent resistivity is plotted on the top, impedance phase on the bottom. Note that the apparent resistivity colour ranges are set to fit values of the individual modes, thus differ between modes. Black dots indicate at which periods apparent resistivity and phase estimates are used at each station. Stations pic013, pic015, and pic017 are omitted owing to lack of data related to mantle depth (cf. Sec. 9.4).

The crustal strike pseudo-section plot (Fig. 9.12) exhibits (a) a region of increased conductivity for periods in the range of 1 second in both modes along the whole profile, extending to shorter periods towards the ends of the profile. The region (b) related to shorter periods in the centre of the profile, between stations pic005 and pic017, appears to be more resistive. For longer periods, pseudo-sections for the two modes exhibit a significantly different behaviour: the TE mode indicates two continuous features at longer periods, whereas the TM mode exhibits four different regions of conductivity at longer periods. This discrepancy can potentially be related to different induction depth of the two modes, owing to the different resistivities sensed [*Jones*, 2006], or the disagreement of longer period data with the crustal strike decomposition. However, common features for longer periods, generally supported by apparent resistivity and phase data of both modes, are (c) a considerably more conductive region in the south of the profile as well as (d) an conductivity increase at the longest periods greater than 10^4 s.

In principle, mantle strike pseudo-sections (Fig. 9.13) support the crustal strike pseudo-section findings: (b) a more resistive region at shorter periods in the centre of the profile, underlain by (a) a conductive feature at approximately 1 second, as well as (c) a resistive feature at longer periods in the south of the profile, and (d) an increase of conductivity at longest periods of the TE mode and the phase data of the TM mode. In these pseudo-section plots, the northern limitation of feature (c) appears to be located beneath stations pic007 in the area where seismic tomography indicates a change from low (to the south) to high (to the north) velocity values (cf. Fig. 7.24); an inversion of the PICASSO Phase I data should enable a more detailed analysis of this circumstance. Feature (d) might indicate the location of the asthenosphere; inversion of the MT data may therefore also permit an evaluation and depth estimate of the LAB in this region.

9.8. Analysis of vertical magnetic transfer function data

Horizontal and vertical H-field data from the LEMI-417 recording systems are used to aid MT investigation of the deeper regions. LEMI-417 systems record long-period data of the magnetic field in two horizontal directions (H_x and H_y) as well as in the vertical direction (H_z) by use of a fluxgate magnetometer (cf. Sec. 6.1.1). Magnetic field data can be used to derive induction arrows, which help to interpret subsurface conductivity distributions by pointing towards or away from a conductive region (dependent on convention, cf. Section 3.2.3). Moreover, vertical magnetic field data can help to identify electric anisotropy in the subsurface; it is possible to distinguish between cases of an anisotropic-1D subsurface and an isotropic-2D subsurface since only the latter will exhibit a significant H_z (cf. Sec. 4.1.3).

Magnetic transfer function data are derived with the algorithm by *Smirnov* [2003] (cf. Sec. 6.2.3) and Figure 9.14 is generated using the *WinGLink* [2005] software. Results

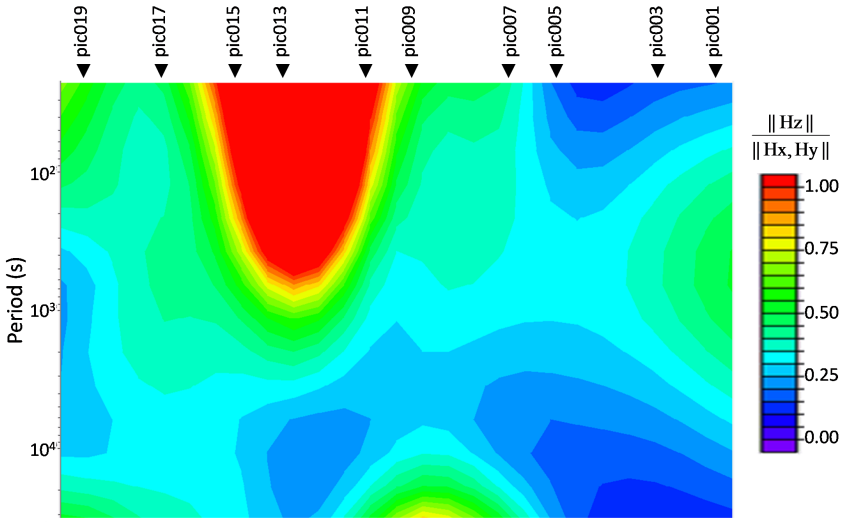

Fig. 9.14.: Magnitude of the magnetic transfer function for the Tajo Basin subsurface; see text for details.

reveal a significant distortion of the area around stations pic011, pic013, and pic015, indicated by a transfer function magnitude greater one. A magnitude greater one is physically implausible as this implies that $\|H_z\| > \|H_x, H_y\|$, meaning that the strength of the secondary field is greater than the strength of the primary field. The interpolated area of distortion has an approximately parabolic shape with its vertex beneath station pic013, at periods of approximately 10^3 s. The area of distortion widens at shorter periods, extending to the regions in-between stations pic009 and pic011 and stations pic015 and pic017 at periods around 10 s. The centre of the anomalous area coincides with the intersection of the PICASSO Phase I profile with a DC railway line at the surface, a known source of EM noise (cf. Fig. 9.1, Sec. 9.4). In contrast to processing results by the EMTESZ working group [e.g. *Kreutzmann et al.*, 2005] for station in proximity of DC railroad lines in Poland, the DC railroad noise in the PICASSO Phase I cannot be removed by current remote robust processing schemes; similar cases of prevailing DC railroad noise has been reported, for example, by *Pádua et al.* [2002] for an MT investigation in Brazil. Accordingly, data from the respective region along the PICASSO Phase I profile are to be interpreted meticulously or even to be rejected. In contrast to these exceptionally high magnitudes, some regions of particularly low magnitude of the magnetic transfer function are observable beneath the profile; namely one region beneath stations pic001 – pic005, and one region beneath most of the profile at periods greater than 10^3 s. The latter could be an indication for a more 1D mantle beneath the Tajo Basin. The increase in magnitude for data of the longest periods beneath station pic009 might suggest a deep-seated 2D feature, but such a feature is not well constraint due to the low resolution at this period range.

Analysis of the real induction vectors reveals a preferred direction between N10W and N40W (Parkinson convection: vectors pointing to conducting anomalies) for most of the

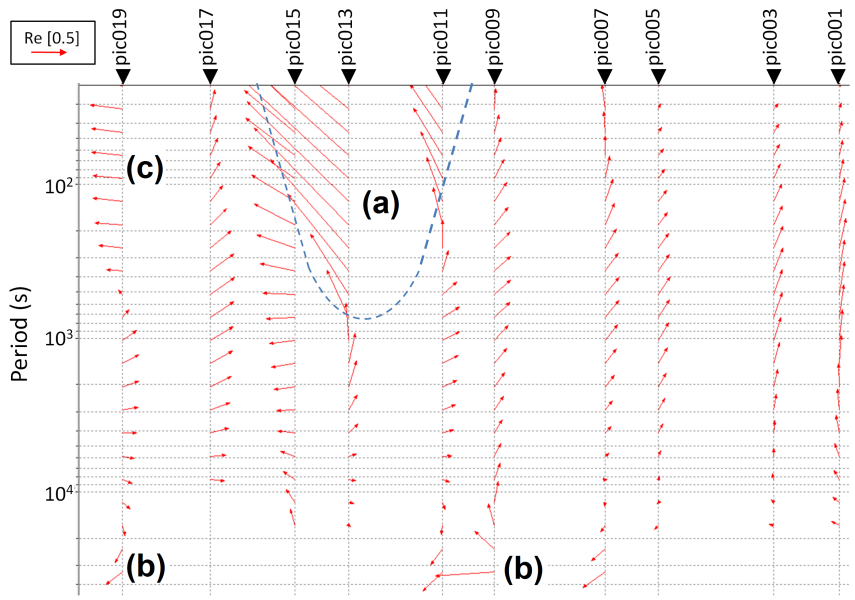

Fig. 9.15.: Real induction vectors (Parkinson convention) for the Tajo Basin subsurface denoted by red arrows; the arrows are plotted for a projection with North located to the top and East located to the right of this figure. The dashed blue lines indicates an area of magnitude greater one (cf. Fig. 9.14), see text for further details.

profile (Fig. 9.15). Since real induction vectors are orthogonal to electric resistivity interfaces, presuming no prevailing disturbance, this relates to a geoelectric strike direction between N100W and N130W. This direction is similar to the results of the strike analysis for the crustal region using the MT impedance tensor (cf. Sec. 9.6.1). Deviations from these directions are observed particularly for **a**) data in the area of disturbance, discussed in the previous paragraph, for **b**) longest-period data of most stations, and for **c**) shorter period data of the southernmost station (pic019). Anomalies **a** and **b** are probably caused by low signal-to-noise ratio, wherein the long-period deviation (**b**) could be due to low resolution and related disturbance of the data by small amount of noise. The deviation in the area of exceedingly high magnitude (**a**) most likely originates from disturbances generated by the nearby DC railway line. The deviation at station pic019 (**c**) is probably related to a conductive region to the west; inversion of the MT data should provide further information about this feature.

10 Data inversion

Details about collection and processing of the PICASSO Phase I dataset were presented in the previous Section 9, and this Chapter is concerned with inversion of the data and evaluation of inversion model features. Due to the profoundly 3D nature of the Betic Cordillera subsurface (cf. Secs. 7.2 and 9.6.1), and that fact that resistivity structures of the Betics are relatively well studied by prior work, the focus of this investigation is on the Tajo Basin region, which has hitherto not been studied using electromagnetic methods. For depth ranges associated with the Tajo Basin crust and mantle, geoelectric strike directions of N40.9W and N29.4E were determined, respectively (cf. Sec. 9.6.1). Derived significant oblique strike directions between the crust and mantle are supported by results of seismic tomography studies for the same region, determining changes of seismic velocity along a NW-SE oriented interface at crustal depth and a NNE-SSW oriented interface at mantle depths (cf. Sec. 7). Decomposing MT data with an incorrect geoelectric strike direction introduces inversion artefacts (cf. Sec. 4); therefore, impedance data were individually decomposed according to the strike direction of the crust and the mantle followed by separate inversions for the two depth ranges. In addition, as shown by *Spratt et al.* [2009] and *Miensopust et al.* [2011], focussed inversion for crustal regions can enhance the quality of inversion models regarding local features. In inversions of data related to a wide depth range, local features can be underfitted due to a global definition of smoothing constraints and model misfit [e.g. *Spratt et al.*, 2009].

Initially, isotropic 2D inversion, the common tool in modern MT investigation, is used for data from the PICASSO Phase I stations located in the Tajo Basin owing to inferred general suitability of the dataset with 2D inversion (cf. Sec. 9.6.1). In addition to isotropic 2D inversion, anisotropic 1D and 2D, as well as isotropic 3D inversions are conducted with the PICASSO Phase I dataset in order to determine detailed information about the subsurface. Application of anisotropic inversion approaches is motivated by their satisfactory performance in a synthetic 3D model (cf. Sec. 8). Isotropic and anisotropic 2D inversions are carried out using the program `MT2Dinv` [*Baba et al.*, 2006], an enhanced version of the algorithm developed by *Rodi and Mackie* [2001], as well as the commercial

WinGLink software [*WinGLink*, 2005], also based on the algorithm by *Rodi and Mackie* [2001]. The `ai1D` code by *Pek and Santos* [2006] is used for anisotropic 1D inversion, and isotropic 3D inversion is carried out using the program `WSINV3DMT` [*Siripunvaraporn et al.*, 2005a].

First, optimal smoothing parameters and enhanced *a priori* models are determined for inversion of crust and mantle ranges. Inversion models for the two modes of MT in 2D (TE and TM) are derived separately to gain better insight about the nature of the subsurface; particularly, in order to infer the extent of 3D effects in each of the modes. In addition, hypotheses from previous studies regarding the Tajo Basin subsurface (see Sec. 7) are tested and an enhanced subsurface model is presented. Furthermore, results of anisotropic 1D, isotropic 2D, anisotropic 2D, and isotropic 3D inversion are contrasted and their applicability for the Tajo Basin subsurface case is evaluated.

10.1. Inversion for crustal structures

10.1.1. Determining smoothing parameters for inversion

As illustrated in Section 6.3, inversion of MT data is non-unique and additional constraints have to be applied to limit the range of acceptable models. The choice of smoothing parameters, reducing spatial variation of electric resistivity in the inversion model, can have significant impacts on the derived inversion model. Therefore, a deliberate parameter study is carried out prior to the final inversion for crustal structures. The 2D inversion program implemented in WinGLink [*WinGLink*, 2005], based on the algorithm by *Rodi and Mackie* [2001], includes three smoothing parameters, controlling different aspects of model constraints (cf. Sec. 6.3), namely

- α: multiplication factor of the horizontal derivatives in the objective function; higher values of alpha drive horizontal smoothness of the inversion model;
- β: exponential factor in the weighting function for uniform grid Laplacian regularisation; higher values increase the penalty on horizontal roughness;
- τ: "global" weighting function, determines the trade-off between data-misfit and model-roughness (cf. Eq. 6.31); higher values are in favour of smoother models.

An increased global model smoothing (i.e. an increased τ) is usually preferable, as it reduces the number of features within a model for most cases; thus, yielding a *minimum structure model* (cf. Sec. 6.3.3). An increased horizontal smoothing (i.e. an increased α) is reasoned for the Tajo Basin subsurface model by results of crustal seismic studies in the region (Sec. 7.3.2), indicating relatively homogeneous intermediate and lower crustal layers with small variations in depth. β is kept at a value of 1, following recommendations by *Mackie* [2002] for the case of isotropic 2D inversion using uniform grids with Laplacian regularisation ($||\Delta(m)||^2$).

Parameter	Value
Invert modes:	TM and TE
min./max. resistivities:	$0.1 - 10^5$ Ωm
period range:	$10^{-3} - 10$ s and $10^{-3} - 100$ s
interpolate data:	5 Freq./decade (use smooth curve if existing)
solving for:	the smoothest model
regularisation operator:	uniform grid Laplacian
regularisation order:	minimising integral of $\|\|\Delta(m)\|\|^2$
smoothing parameters (α):	[1.0, 1.1, 1.3, 1.6, 2.0, 3.0, 5.0]
smoothing parameters (β):	1
smoothing parameters (τ):	[0.01, 0.1, 1.0, 3.0, 6.0, 10.0]
static shift correction:	yes (variance: 20 %, damping: 10000)
fixed parameters:	no
data errors:	ρ_a = 10 %, ϕ = 5 % (use data if existing)
error floor:	ρ_a = 10 %, ϕ = 5 % (use data if existing)

Tab. 10.1.: Settings used to determine the optimal smoothing parameter combination in the inversion for Tajo Basin crustal structures.

A range of α and τ values is sampled in order to identify an optimal parameter combination for inversion of the Tajo Basin subsurface. To assure that all crustal structures are sensed while the influence of mantle structures kept at a minimum, the optimal smoothing parameter combination is determined for two different period ranges, i.e. $10^{-3} - 10$ s and $10^{-3} - 100$ s. For both period ranges, global RMS misfits of 42 models are determined, wherein each model is generated through inversion with different combinations of smoothing parameters and the same set of auxiliary inversion parameters (summarised in Table 10.1). RMS misfits for intermediate smoothing parameter combinations are derived through linear interpolation. Resulting plots for the two frequency ranges exhibit similar *L-curve*-like behaviour (cf. Sec. 6.3), i.e. curves possessing low RMS misfit values for low values of τ and α (Fig. 10.1). Hence, the chosen parameter combination has to be a trade-off between increased values of τ and α, and a low RMS misfit. An RMS misfit of 2, i.e. 95% of the data are fit to within their error bounds, is chosen as the acceptable upper limit and α,τ - combinations of three models are selected, which represent distinct situations for the range of smoothing parameters used in this study, i.e.

- model `a3b1t6` ($\alpha = 3, \beta = 1, \tau = 6$): possessing intermediate values for both variables in the parameter space under consideration;
- model `a5b1t3` ($\alpha = 5, \beta = 1, \tau = 3$): representing the horizontally smooth end-member; and
- model `a2b1t10` ($\alpha = 2, \beta = 1, \tau = 10$): representing the (relatively) horizontally rough end-member.

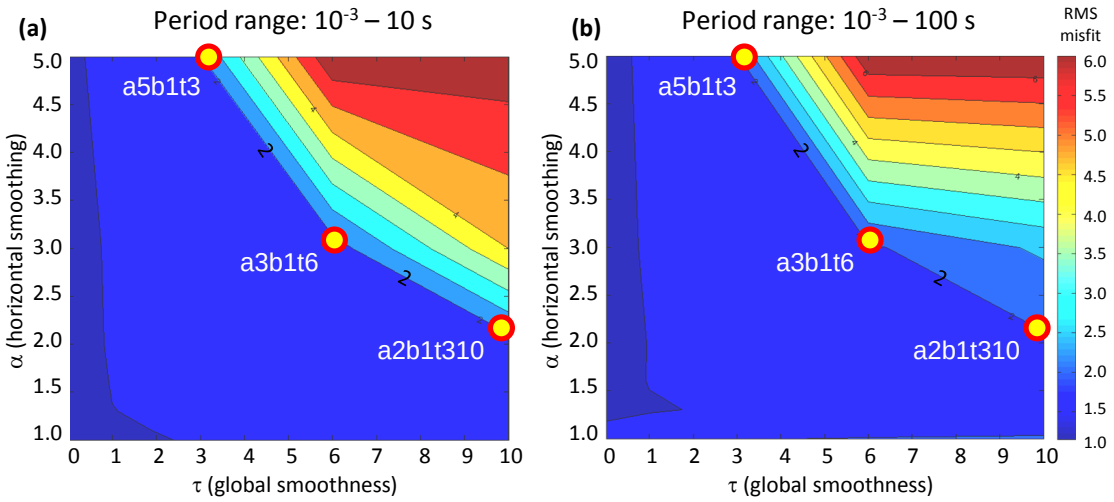

Fig. 10.1.: RMS misfit for models of the Tajo Basin crustal structures with different combinations of global (τ) and horizontal smoothing parameters (α), using (a) a period range of 10^{-3} – – 10 s and (b) of 10^{-3} – – 100 s. Values are obtained through linear interpolation of 42 α,τ-combinations for each frequency range with applied parameters summarised in Table 10.1. Red-yellow markers, together with the respective model name, indicate combinations chosen for further investigations.

These six models (three for each period range) are kept for further investigation in subsequent inversion steps.

10.1.2. Starting model construction

Results of non-stochastic MT inversion are, in general, dependent on the starting model. For an unsuitable starting model the inversion may yield a model related to a local, rather than the global, misfit minimum (cf. Sec. 6.3). A uniform halfspace, often 100 Ωm, is commonly used as a starting model for MT inversion as it is assumed firstly to be less likely to introduce inversion artefacts, and secondly to be relatively close to average resistivity values of the Earth at crustal and upper mantle depths (cf. Sec. 5.2). However, using *a priori* information about the subsurface, e.g. from 1D inversion of MT data or results of other geophysical or geological investigations, an enhanced starting model can (and should be) created that is superior to the halfspace model approach. For the Tajo Basin, supplementary information about the subsurface is available, in particular, from seismic reflection and refraction studies, inferring four layers within the crust and a Moho depth of approximately 31 km (see Table 7.2 for thickness of crustal layers). Presently, there is no reliable relation between seismic velocity and electric resistivity at crustal depth that allows for a straightforward construction of a MT starting model from seismic velocity results. Instead, electric resistivity values for the four crustal layers are inferred from horizontally averaged resistivities of the six models chosen during the smoothing parameter analysis (Sec. 6.3.3) using an in-house script developed by Mark Muller. The script yields mean and standard deviation resistivity values for each row of the model within the specified horizontal region of the profile.

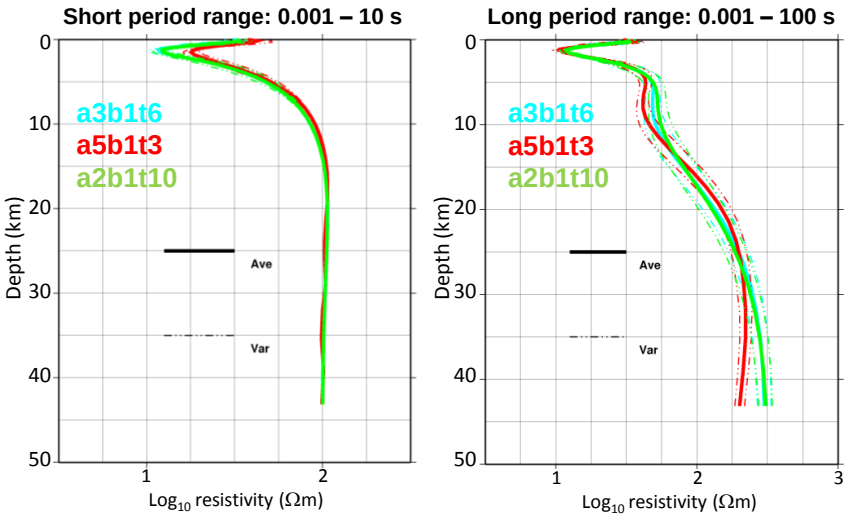

Fig. 10.2.: Resistivity–depth profiles of horizontally averaged models for the Tajo Basin subsurface, obtained through inversion of PICASSO Phase I response data from two different period ranges and three sets of smoothing parameters; see text for details. Different sets of smoothing parameters are indicated by colour, with solid and dashes lines denoting average values and variance of electric resistivity for the different regions, respectively.

Initially, models from different smoothing parameter combinations and both period ranges are examined to identify dominant and robust characteristics of the different regions. For the sedimentary layer (depth range 0 – 2.5 km) all models yield an average resistivity of approximately 30 Ωm decreasing towards the bottom of the layer (cf. Fig. 10.2). Except for the short period range and the model with most horizontal smoothing (`a5b1t3`), the conductive region at the bottom of the sedimentary layer exhibits values of approximately 10 Ωm, most likely originating from saline fluid intrusion into the sedimentary layer. For the top of the upper crustal layer (depth range 2.5 – 5 km) an increase of average resistivity to values of approximately 50 Ωm is determined by all models. The upper region of this layer is not well constrained due to the shielding effect of the conductor above, thus assuming a resistivity of 50 Ωm for the top of the upper crustal layer can be considered reasonable. At the bottom of the upper crustal layer (depth range 5 – 10 km), models are significantly different for the two period ranges, with 'short period range' models exhibiting more resistive structures than the 'long period range' models (left-hand and right-hand side plots in Figure 10.2, respectively). At greater depth (≥ 10 km), the behaviour is reversed: 'short period range' models exhibiting more conductive structures than the 'long period range' models. Since shorter period range models approach average resistivity values of approximately 100 Ωm at a depth of around 10 km, which is the value of the starting model, the discrepancies between the two model groups is likely to originate from a lack of sensitivity to intermediate and lower crust structures for the shorter period range models. Longer period models, on the other hand, appear to be sensitive down to greater depth as they vary from the 100 Ωm starting values down to a depth of 42 km.

Due to the notable degree of lateral variation in the models (indicated by the dashed

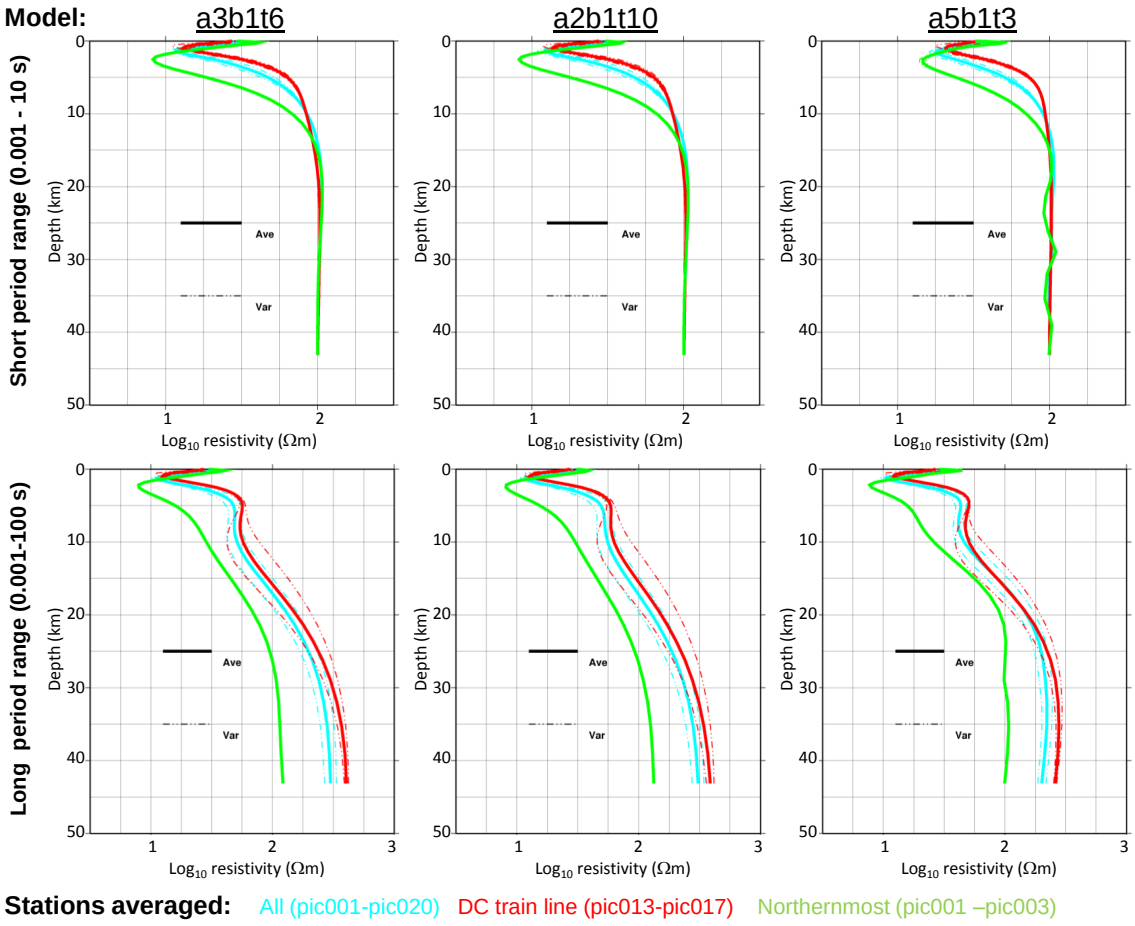

Fig. 10.3.: Resistivity–depth profiles of horizontally averaged models for different regions of the Tajo Basin subsurface, obtained through inversion of PICASSO Phase I response data from two different period ranges and three sets of smoothing parameters; see text for details. Different regions are indicated by colour, with solid and dashes lines denoting average values and variance of electric resistivity for the different regions, respectively. Variance curves for the northernmost stations (dashed green lines) are covered by their average value curves due to the small lateral variation of electric resistivity in the respective regions.

lines in Figure 10.2), the distribution of electric resistivity along the profile is also examined. For that purpose horizontal averages of electric resistivities from two distinct regions are calculated (red and green lines in Figure 10.3, respectively): structures beneath stations pic013 – pic017, located in the proximity of the DC train line with response curves truncated at longer periods (see Section 9.4 for details); and stations pic001 – pic003, located at the northern end of the profile, thus considerably far away from the DC train lines. Average resistivity–depth profiles for these two regions are calculated separately for the different smoothing parameters and period ranges, respective results are compared with each other and the average resistivity for the whole profile. The resulting Figure 10.3 infers noticeable variations in resistivity along the profile, with a more resistive nature of the stations close to the train line. The increased resistivity for the region in close proximity to the train line is likely to originate from data truncation (cf. Sec. 9) and

Depth (km)	Description	Resistivity (Ωm)
0 - 3	Sediments	20
3 - 5	Sediments with fluid intrusion	10
5 - 10	Upper crust	15
10 - 24	Intermediate crust	70
24 - 31	Lower crust	100
≥ 31	Lithospheric-mantle	100

Tab. 10.2.: Layers of the Tajo Basin lithosphere with layer boundaries based on seismic reflection studies and estimates of electric resistivity values inferred from horizontal averaging of inversion models constructed using different sets of smoothing parameters; see text for details. Therein, average resistivity values of the layers contain contributions of the (more resistive) crustal rocks and conductive anomalies such as fluid phases and ore bodies. The lithospheric-mantle resistivity is underestimated, presumably a result of low sensitivity to the mantle region for the used period range ($10^{-3} - 10^{2}$ s), which was chosen to suit investigation of the crust. Note that thicknesses of sedimentary and upper crustal layer are increased to facilitate a minimum thickness of 2 km.

resulting decreased sensitivity at greater depths. The average resistivity determined for the whole length of the PICASSO Phase I profile is certainly affected by the increased resistivities inverted for the subsurface region in proximity of the train line. Therefore, average resistivity values are potentially too high. Even though they only represent part of the profile, average resistivities for the northernmost stations are more reliable given their lower disturbance and untruncated response curves. The starting model for subsequent inversions is therefore created on the base of the average resistivity–depth profile for the longer period range and northernmost stations (green lines in plots at the bottom of Figure 10.3); note that the difference between average resistivity–depth profiles from inversion with different smoothing parameters is negligible. Resulting electric resistivity values for crust and lithospheric-mantle are summarised in Table 10.2.

10.1.3. Investigating characteristics of TE and TM mode response data

The two modes in 2D MT investigation, TE and TM, relate to the off-diagonal elements of the 2D MT impedance tensor (Eq. 3.39) and are affected to different degree by the characteristics of the subsurface; see Section 4 for a detailed discussion of subsurface characteristics and their effect on the two modes. It is therefore usually useful to invert each of the modes separately to identify similarities and differences of the models in order to infer contribution of the modes to the combined-mode inversion model.

The PICASSO Phase I dataset for the Tajo Basin crust is inverted for each of the modes individually ('TE-only' and 'TM-only'), as well as for both modes together. The inversion follows the Jones Catechism (Sec. A.2.3) and uses the optimal smoothing parameter combination determined in the previous Sections 10.1.1 and 10.1.2 with a 100 Ωm halfspace as starting model. Resulting inversion models are displayed in Figure 10.4. The RMS misfit of the three models is above acceptable: 3.01 (TE and TM mode), 3.13 (TE-only), and 2.63 (TM-only); however, the aim of this inversion process step is not to determine

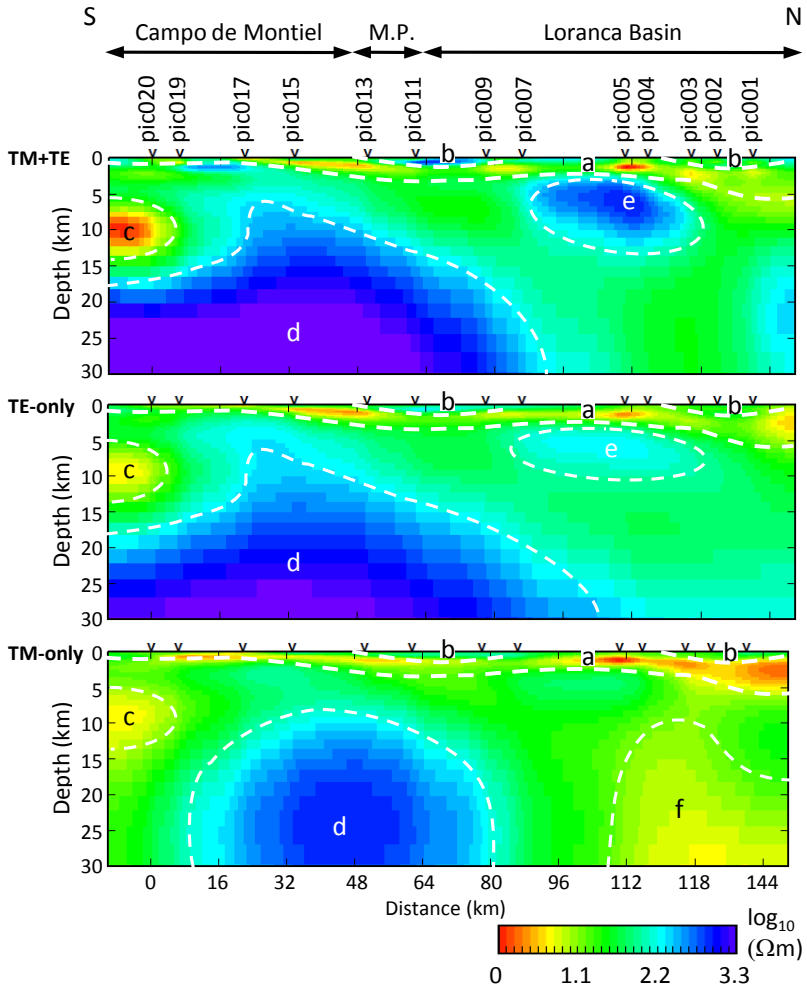

Fig. 10.4.: Comparison of results from isotropic 2D inversion for the Tajo Basin crust using a 100 Ωm halfspace as starting model and data from both MT modes (TM+TE, top plot), only from the TE mode (TE-only, middle plot), and only from the TM mode (TM-only, bottom plot). Location of PICASSO Phase I stations and the geological regions (based on the USGS EnVision map for Europe, Figure 9.1) are shown on the top of this figure; M.P: Manchega Plain

minimum-misfit models, but instead to contrast features of inversion models from the two modes individually and simultaneously.

A common feature in all three inversion models is a near-surface conductive layer, labelled ‘a’ in Figure 10.4. For the majority of the profile, layer ‘a’ is in a depth range associated with the bottom of the sedimentary layer proposed by seismic studies (cf. Sec. 7.3.2). The increase in conductivity is likely to originate either from accumulation of fluid or from an increase in salinity of the fluid at the bottom of the sedimentary layer. All three inversion models indicated a vertical downward displacement of the conductive layer for two regions located at the Manchega Plain – Loranca Basin boundary and at the northern end of the profile (labelled ‘b’ in Figure 10.4).

Another feature evident in each of the three models is the conductive region at the

southern edge of the profile at a depth of approximately 5 – 15 km (labelled 'c' in Figure 10.4). Existence of a conductor in this region is supported by inversions of each of the modes as well as by the fact that a conductive structure is also apparent in the station response data of the TE mode (for an impedance tensor decomposition according to the crustal strike direction) at around 10 s beneath the southernmost stations; cf. Figure 9.12. However, the depth extent of this feature is less well-constrained due to the reduced sensitivity of MT inversion below a conductive region (cf. Sec. 6.3).

The highly resistive region, modelled at the bottom of the southern half of the Tajo Basin crust, (labelled 'd' in Figure 10.4) is present in all three inversion models; however, its lateral extent, as well as its maximum resistivity, differs significantly between the modes. In the TM-only inversion the anomaly is mostly confined to a region below stations pic009 to pic019, whereas inverting data from the TE mode produces a more extensive resistor, extending from beneath station pic007 to the southern edge of the profile. The TE mode is commonly assumed to be more affected by 3D off-profile bodies (cf. Sec. 4); given its location, it is possible that the feature is related to the Iberian Massif (cf. Sec. 7). In that case, the anomaly could originate from charge accumulation along the north-south oriented, thus parallel to the profile located, interface between the lower crust of the Tajo Basin and the easternmost extent of the Iberian Massif. Alternatively, the resistive feature may be related to distortion of MT data by the DC train line (cf. Sec. 4).

The two anomalies 'e' and 'f' are only supported by data of the TE and TM mode, respectively (however, anomaly 'e' is also introduced into the combined mode inversion model). For this initial inversion process, potential explanations of the two features are the presence of a 3D body (anomaly 'e') and difference in induction depth of the two modes, due to the different conductance modelled for the conductive layer 'a' above (anomaly 'f'). Investigation, using refined and more detailed inversion as well as additional constraints, will help to confine the different anomalies, thereby providing better information about their possible causes.

10.1.4. Evaluating proposed layered crustal model

As illustrated in Section 6.3, MT inversion is non-unique, i.e. a range of models fit station response data equally well within the given uncertainty levels. Conversely, a model that can be rejected on the basis of its MT response misfit is definitely not representative of the studied subsurface area. Therefore, MT is a formidable tool in rejecting proposed subsurface structures.

Based on findings of seismic reflection and refraction studies a relatively levelled layer structure has been presented for the Tajo Basin crustal region located slightly to the west of the PICASSO Phase I profile (cf. Sec. 7.2.1). Seismic model were created by projecting results from different studies in the proximity of the region; therefore, layering beneath the PICASSO Phase I profile is potentially different from the seismic model. The hypothesis of a levelled layer structure beneath the PICASSO Phase I profile is tested using sharp-boundary inversion with so-called *conductivity interfaces* (in the following referred

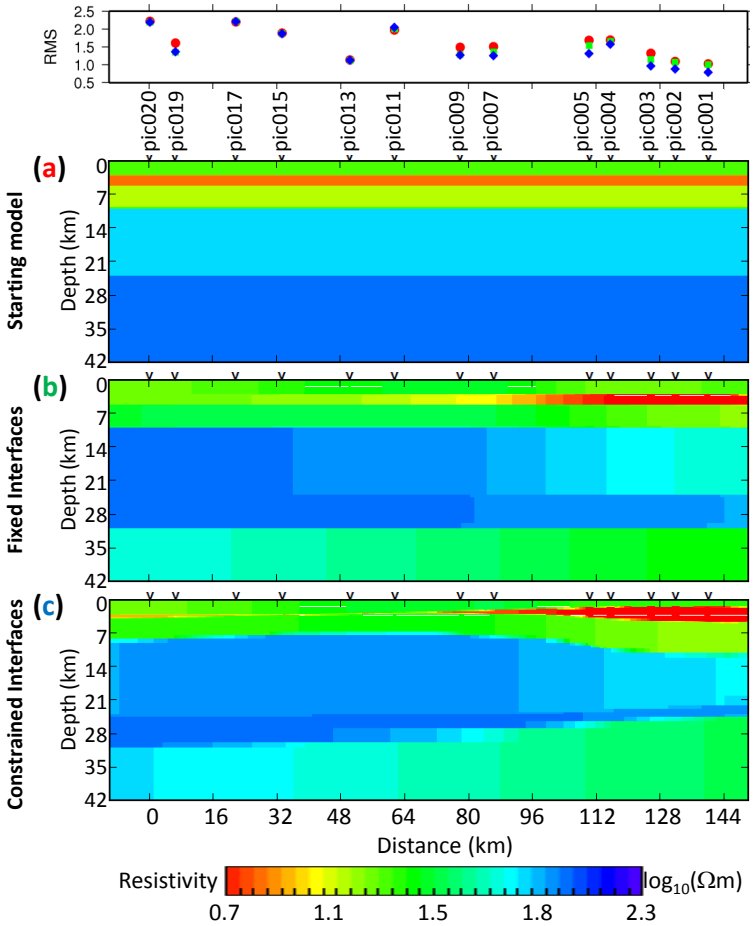

Fig. 10.5.: Results of isotropic 2D sharp-boundary inversion using conductivity interfaces (*CI-inversion*) to evaluate proposed levelled layer structure of the Tajo Basin crust. Uppermost plot: RMS misfit for each station, with coloured symbols indicating the misfit for the models shown below (red circles: model a, green squares: model b, blue diamonds: model c). Model (a) is created with layering according to a compilation of results from seismic reflection studies. Models (b) and (c) are results of sharp-boundary inversion with fixed and constrained conductivity interfaces, respectively; using model (a) as starting model. See text for further details.

to as *CI-inversion*), part of the MT2Dinv inversion software implemented in WinGLink [*WinGLink*, 2005]. In CI-inversion, changes of electric resistivity (or its inverse, electric conductivity) along the conductivity interfaces are not penalised by smoothing regularisation (cf. Sec. 6.3). Therefore, in CI-inversion models, boundaries of regions with different electric resistivity usually coincide with conductivity interfaces, and variations within the different regions are small. The layered subsurface model derived in the previous Section 10.1.2 is used as a starting model for the CI-inversion with conductivity interfaces located at the layer boundaries, coincident with layer depths proposed by seismic studies (upper plot in Figure 10.5). Forward modelling of the starting model yields a RMS misfit of 5.34 (error floor: $\rho_a = 10\%$, $\phi = 5\%$ for the TM mode, and $\rho_a = 20\%$, $\phi = 10\%$ for the TE mode), indicating that the model possesses a minor degree of similarity with the true model.

During the initial inversion sequence interfaces are kept fixed at their location along the layer boundaries, allowing only lateral variation of electric resistivity values within the layers. The RMS misfit is reduced to a value of 4.56 through the lateral variation of electric resistivity within layers; most layers exhibit relatively higher resistivity in the southern region of the model (middle plot in Figure 10.5). Owing to the prevailing increased misfit, additional CI-inversions are conducted in which conductivity interfaces are no longer kept fixed along layer boundaries. Instead, deviation of conductivity interfaces from their initial location along the layer boundaries is only constrained; i.e. changes of their locations are added to the objective function (cf. Sec. 6.3). CI-inversions with constrained interface locations (bottom plot in Figure 10.5) yield inversion models with interfaces that deviate significantly from a levelled layer case. In the northern region of the model, layer boundaries of the CI-inversion model exhibit some agreement with proposed seismic layer locations. However, in the south and centre of the model, location and thickness, particularly, of the intermediate crustal layer are significantly different. The RMS misfit for the constrained CI-inversion model remains unacceptable high (4.67) and reduction of the misfit can only be achieved through further deviation from the levelled layer case. Hence, a perfectly levelled layer structure of the Tajo Basin crust is not in agreement with MT response data of the PICASSO Phase I project. Results of seismic reflection studies are usually accurate and reliable; it is therefore concluded that the layered subsurface model, derived by *Díaz and Gallart* [2009] through their compilation of results from seismic studies in Central Spain, cannot be projected to the region of the Tajo Basin beneath the PICASSO Phase I profile. Alternatively, the seismically derived layers may not exhibit a significant difference in terms of their electric conductivity properties in comparison to lateral changes of electric conductivity beneath the Tajo Basin. Respective prevailing lateral changes in crustal layers may originate, for example, from compositional differences or the presence of a highly conducting phase in subareas of the crustal layers (cf. Sec. 5.2.1). Lateral changes of electric conductivity are indicated by results of initial inversions (Fig. 10.4) and subsequent inversion steps will provide more detailed information about the nature as well as possible interpretations of this lateral discontinuity.

10.1.5. Final model of the Tajo Basin crust

The advanced starting model determined in Section 10.1.2, containing layers inferred from seismic reflection studies (Sec. 7.3.2) and electric resistivity values derived through averaging of inversion results with a range of smoothing parameters, is used to obtain an enhanced model of the crustal structures beneath the Tajo Basin; see Table 10.2 for depth extent and electric resistivity values of the starting model. Inversion for Tajo Basin crustal structures is carried out according to the Jones Catechism (Sec. A.2.3) using a range of adaptive processes during the inversion, which are described below.

- During initial inversion steps four tear zones are applied to maintain separation of

the model into upper (0 – 10 km), intermediate (10 – 24 km), and lower crust (24 – 31.5 km) as well as the mantle (≥ 31 km).

- Features are manually removed or their resistivity values are modified in order to test whether they become re-established in subsequent inversion steps and are therefore likely to be data-supported structures.
- Focussed inversions are carried out for specific regions of the model by individually inverting responses from selected stations[1], namely
  - stations pic013 – pic017, to refine the shape of the resistive body beneath the Manchega plain (labelled 'e' in Figure 10.6); and
  - stations pic004 and pic005, to investigate the lateral extent of the upper crustal conductor in the north of the Tajo Basin (labelled 'c' in Figure 10.6).
- Anisotropic 2D inversion is carried out using a range of isotropy parameters (τ_{iso}) in order to test for potential anisotropic structures with the results that even for relatively low constraints ($\tau_{iso} = 10$) the anisotropy magnitude is overall low and mostly confined to the surficial conductive layer (cf. Fig. 10.7).

Misfit and sensitivity to regions of the Tajo Basin crustal model (Fig. 10.6) are examined in the paragraphs below, followed by a discussion of model features and their geological implication in the next subsection ('Features of the crustal model', Page 239); deep-seated features at mantle depth are examined in the subsequent Section 10.2.

Model misfit and sensitivity

The concluding Tajo Basin crustal model fits observed MT data considerably well; the model exhibits a RMS misfit of 1.47 using error floors of 5% for the phases and 10% and 20% for the apparent resistivities of TM and TE mode, respectively. During the inversion, attention was also paid to the misfit distribution, assuring that the global misfit is not controlled by the misfit of a small number of confined regions. As a result, a relatively even distribution of the misfit is obtained using focussed inversions during the model identification process, which reduce the misfit of respective regions (cf. Fig. 10.8). It should be noted, however, that response data of stations in proximity of the DC train line had to be truncated due to high noise levels; thus, structures in this region are less constrained (indicate by white space in Figure 10.8). For the final crustal model (Fig. 10.6), all stations exhibit a RMS misfit of 2.5 or lower with a relatively uniform distribution of the misfit for all stations and periods. Detailed comparison of recorded data and model response for each stations is given in the Appendix (Section A.4.1).

In order to determine reliability of regions within the inversion model, sensitivity analysis is carried out following the approach by *Schwalenberg et al.* [2002]. Therein, a

[1] alteration of other model regions during that process is restricted by fixing respective regions and setting the parameter '`solving for smoothest variation away from a priori model`'

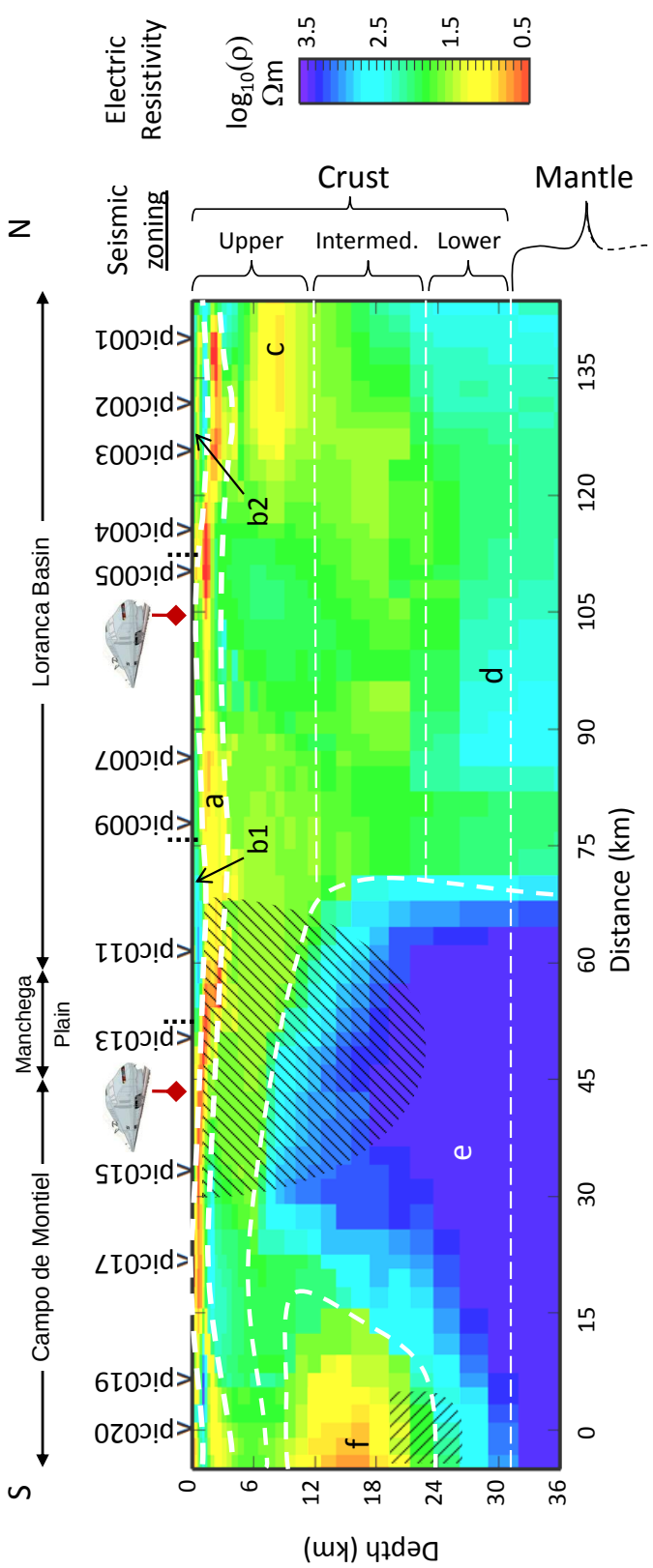

Fig. 10.6.: Final model of the electric resistivity distribution at crustal depth beneath the Tajo Basin, derived through inversions of the magnetotelluric PICASSO Phase I profile data in the period range $10^{-2} - 10^{3}$ s; see Figure 7.1 for the profile location. Also shown are the geological regions of the Tajo Basin (based on the USGS EnVision map for Europe, Figure 9.1), cross-over point locations of faults with the PICASSO Phase I profile (dotted black lines, cf. Sec. 7.3.1), different crustal and mantle layers derived by seismic studies in this region (thin white horizontal dashed lines, cf. Sec. 7.3.2), and regions of low resolution (shaded). A discussion of model features is given in subsection 10.1.5 (page 239)

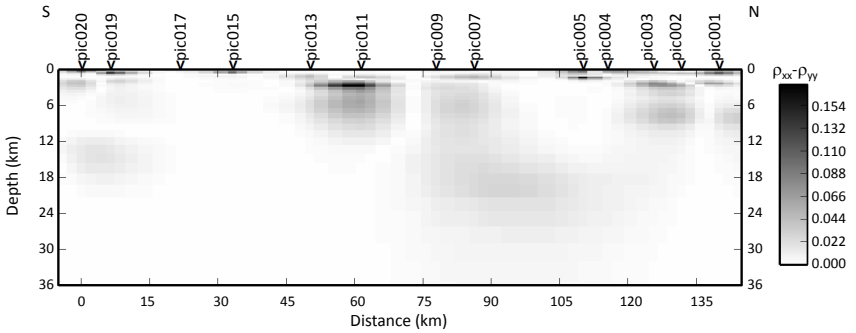

Fig. 10.7.: Potential anisotropy of the Tajo Basin crust, derived by anisotropic 2D inversion with the algorithm `MT2Dinv` [*Baba et al.*, 2006], based on the algorithm by *Rodi and Mackie* [2001], and low isotropic constraints ($\tau_{iso} = 10$).

normalised form of the Jacobian, derived for each cell during the inversion process, is used to calculate the sensitivity distribution (cf. Sec. 6.3). The resulting sensitivity model (Fig. 10.9) indicates firstly an overall decrease of sensitivity with depth and, secondly a particularly low sensitivity to the area of the resistor associated with the Iberian Massif (labelled 'f' in Figure 10.6; see subsection 10.1.5 for a discussion of model features). Whereas the former is due to general attenuation of diffusive EM fields with depth (cf. Sec. 3.3), the latter is a result of response data truncation for stations in the proximity of the DC train line. Lower sensitivity to the region between stations pic005 and pic007 is due to the larger stations spacing in the area.

Most structures in the Tajo Basin crust (above 31 km) are above the 10^{-4} sensitivity isoline calculated from the linear sensitivity analysis; a value used by different authors as threshold above which structures of a model can be adequately resolved [e.g. *Schwalenberg et al.*, 2002; *Brasse et al.*, 2002; *Ledo et al.*, 2004]. However, presently no physical explanation can be found for the choice of this limit; therefore, sensitivity results should rather be considered as a qualitative model evaluation. Furthermore, it was shown by *Ledo et al.* [2004] that this sensitivity analysis with data from a linearised inversion approach is less adequate in determining an accessibility limit in regions with high resistivity, such as the feature 'f'.

In addition to the linearised sensitivity analysis, various forward model calculations were carried out in this study, in which resistivity values of different regions are manually modified in order to examine robustness of the model features in a non-linear trial-and-error exercise. As a result, values of resistive features in the final model were reduced to the minimum values possible without increasing the RMS misfit of the model. Higher values of very resistive features are possible are but not well constraint due to low sensitivity of the MT method to highly resistive regions (cf. Sec. 3.3). In particular, both the extent and resistivity of the massive resistor at lower crustal depth in the south of the model (labelled 'e' in Figure 10.6) are not well resolved by the crustal model. Inversion for mantle structures, using longer period data, will provide more information about this resistive feature and its characteristics (see Sec. 10.2).

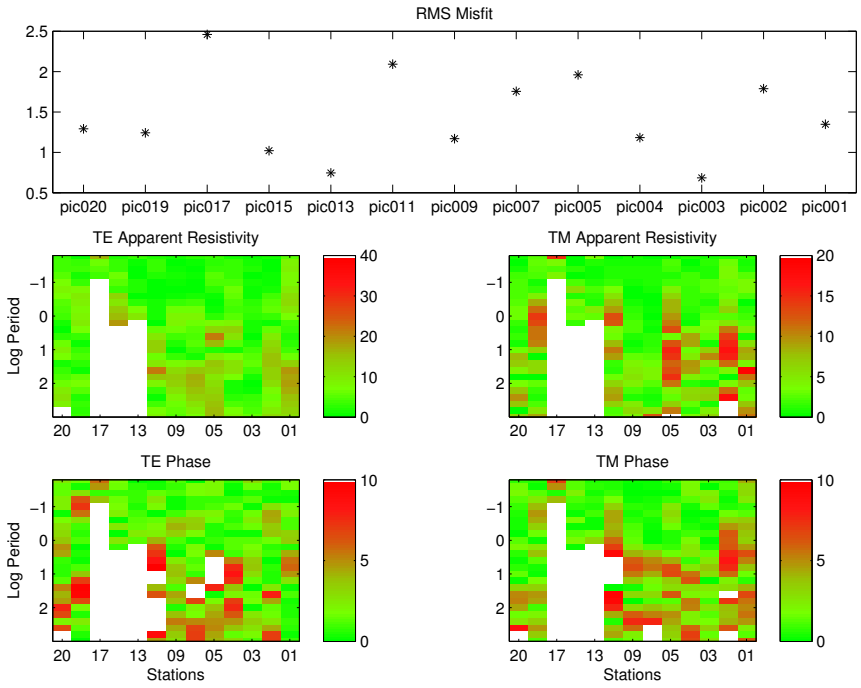

Fig. 10.8.: Misfit of the final Tajo Basin crust model, individually broken down into an average for each station (top), as well as for apparent resistivity and phase of the two modes (bottom); due to space restriction only a selection of station indices is given at the bottom of apparent resistivity and phase plots. The colour scale is set to a range of two times the error floor used in the inversion.

Features of the crustal model

Close to the surface, down to a depth of around 3 km, a highly conductive structure (labelled ‘a’ in Figure 10.6, highlighted by thick dashed white lines) is present throughout the whole length of the profile. This surficial conductor is likely to be caused by accumulation of saline fluid or an increase of fluid salinity at the bottom of the Tertiary and Mesozoic sedimentary layer. Along the profile, the location of this conductor is displaced downwards by two more resistive regions (b1) and (b2). The horizontal limits of region ‘b1’, located in the centre of the profile (around station pic011), coincide with two faults intersecting the PICASSO profile in the proximity of stations pic009 and pic013 (see Figure 7.15 for course and location of the two faults in a map of the Tajo Basin). The northern downwards displacement of conductor ‘a’ (labelled ‘b2’) coincides with the location of a fault between stations pic004 and pic005. An additional fault is located to the north of the PICASSO Phase I and may coincide with the northern limit of the downward displacement ‘b2’; however, since this fault is outside the PICASSO Phase I profile no reliable correlations can be given regarding a correlation between fault and northern extent of feature ‘b2’.

Besides the two conductors ‘a’ and ‘c’, a relatively homogeneous region of around 100 Ωm is observed in the upper and intermediate crust of the northern region of the profile, whereas the southern region exhibits a highly different behaviour. The upper

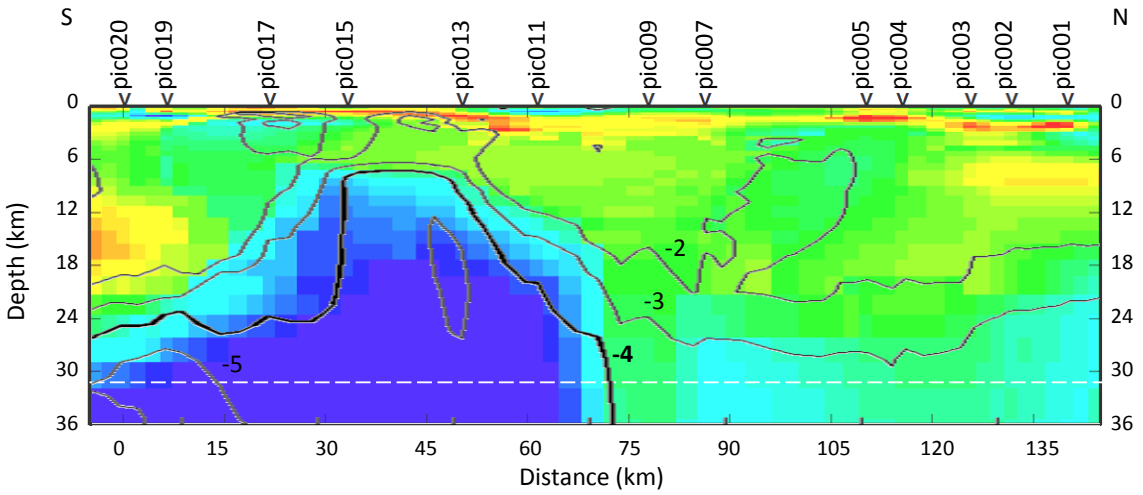

Fig. 10.9.: Inversion model of the Tajo Basin crustal structures overlaid by isolines from linear sensitivity analysis following an approach by *Schwalenberg et al.* [2002] using the Jacobian determined for each cell during the inversion; isoline labels are given in terms of logarithmic sensitivity values. For clarity reasons only a selection of isolines is displayed here, of which the thicker isoline (10^{-4}) indicates the threshold value chosen by different authors as lower limit above which structures of a model are adequately resolved; see text for details on this aspect. The dashed white line denotes the crust–mantle boundary derived by reflection seismology. A discussion of model features is given in subsection 10.1.5 (page 239).

crustal conductor 'c', situated at the northern end of the PICASSO Phase I profile at depths between 6 km and 12 km, is located in proximity of the Iberian Range and potentially represent a feature of its crustal root region. However, mechanisms than can cause such a pronounced anomaly are presently unknown for the Iberian Range region. Respective MT stations, at the northern end of the PICASSO Phase I profile, are located in an area where Altomira Range and Iberian Range are in close proximity; see Figure 7.1 for the local tectonic setting with the PICASSO Phase I profile location indicated by the solid red line. Thus, significant 3D effects could be expected for this area; see Section 10.2.4 for a discussion of 3D inversion results. The lateral extent of conductor 'c' was investigated using a series of forward models with different southward extents of the conducting area. Result of the forward modelling analysis yield a minimum RMS misfit for southward extent of conductor 'c' beneath station pic003 (cf. Fig. 10.10). The bottom of conductor 'c' exhibits some agreement with the bottom of the seismically defined upper crust, but due to the low sensitivity of the MT method to regions below a conductor a correlation between conductor and seismic boundary is debatable.

Below anomaly 'c', the model exhibits two regions with resistivity values of approximately 100 Ωm, and 500 Ωm of which the bottom region (labelled 'd' in Figure 10.6) is likely to depict the more resistive nature of the Iberian Peninsula lower crust (cf. Sec. 7.3.2). Structures in the northern region of the PICASSO Phase I profile exhibit some agreement with the seismically determined layered structure (Sec. 7.3.2). Moreover, layering in the northern region obtained using smooth inversion matches results of CI-inversion in which layering was enforced by inversion constraints (Sec. 10.1.4).

To the south of station pic009, the Tajo Basin crust model exhibits a massive resistive

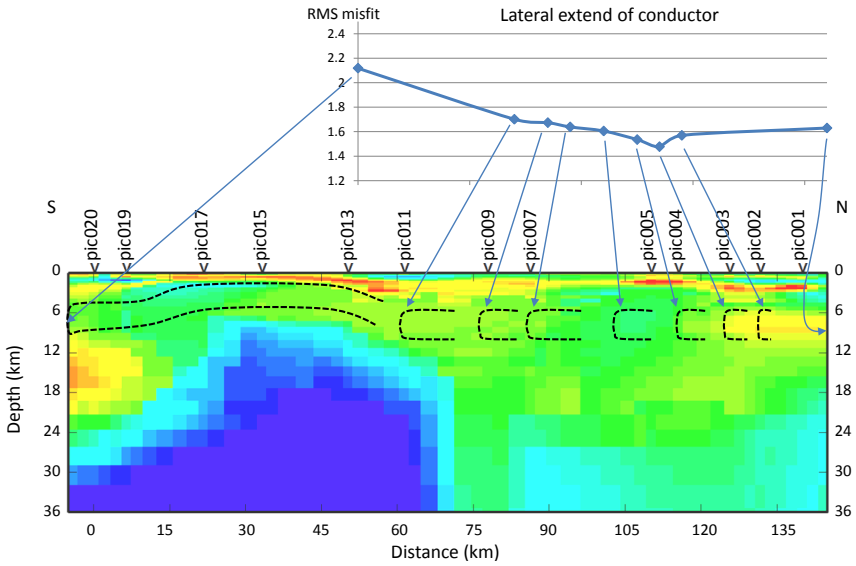

Fig. 10.10.: RMS misfit variation for different lateral extents of the upper crustal conductor labelled 'c' in Figure 10.6; the rightmost misfit value refers to a model in which conductor 'c' is removed.

body (labelled 'e' in Figure 10.6) extending upwards to a depth of approximately 10 km below the Manchega Plain and Campo de Montiel region. Unfortunately, the upper region of resistor 'e' is not well constrained due to distortion of MT responses by DC train line noise in this region and the required truncation of affected stations (cf. Sec. 9.4); the shaded area in Figure 10.6 indicates the region associated with distortion of the magnetic components, inferred from magnetic transfer functions data (cf. Fig. 9.14). In addition, distortion in the electric component may affect longer responses which are related to deeper structures. It is therefore arguable to what degree feature 'e' originates from the distortion caused by the DC train line or a real geological feature. In support of a geological feature as cause of anomaly 'e' is the spatial correlation between the vertical resistivity interface (between stations pic009 and pic011) and the lateral change of velocity inferred by seismic tomography data (cf. Fig. 10.11). It is therefore concluded that resistor 'e' relates to the Variscan Iberian Massif basement, whereas the more conductive region to the north represents the *Alpine Spain* basement (cf. Chap. 7). The interface between the two regions of different velocity shown in Figure 7.21, exhibits a NW-SE orientation, which is in agreement with geoelectric strike direction determined for the Tajo Basin crust (cf. Sec. 9.6.1).

The modelled downward extent of the resistive region is disputable, considering the seismic low velocity of the mantle in this region derived by *Villaseñor et al.* [2003] and *Amaru* [2007] (Figures 7.23 and 7.24, respectively). A region of increased resistivity and low velocity is somehow counter-intuitive, as common causes for low velocities, like fluids, partial melt, and increased temperature, usually exhibit a concomitant decrease of electric resistivity. Only very special geological settings may accommodate a low velocity – high resistivity region, e.g. the presence of isolated fluid pockets in a resistive

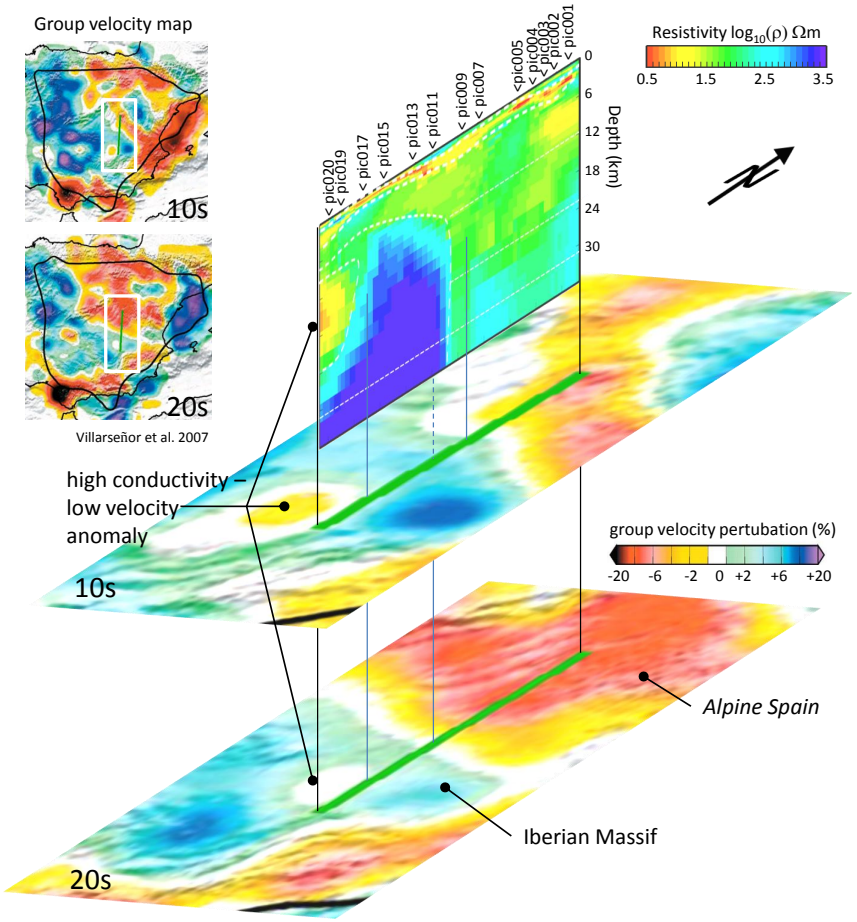

Fig. 10.11.: Comparison of the crustal model for the Tajo Basin derived through inversion of MT data and results of the surface wave tomography study by *Villaseñor et al.* [2007]; group velocity maps at 10 s and 20 s are related to structures of the upper 10 km and between 15 and 30 km, respectively. The location of the PICASSO Phase I profile is indicated by the thick green line. Correlation between seismic and MT results are observable for the lateral change of resistivity and velocity that are related to the Iberian Massif–Alpine Spain boundary beneath the Tajo Basin as well as to a high conductivity – low velocity anomaly at the southern extent of the PICASSO Phase I profile in the Tajo Basin; see text for details.

host medium. Therein, fluid pockets lower the seismic velocity, which is sensitive to the bulk properties, whereas the electric resistivity remains high, owing to the low degree of connectivity; cf. Section 5. As such a geological setting is very uncommon it is more likely that the resistive body is confined to the crustal range and deeper regions are distorted by DC train disturbance, off-profile features, or the oblique strike direction of the mantle (cf. Sec. 9.6.1).

At the southern end of the profile, to the south of station pic017, the model exhibits a region of increased electric conductivity in the depth range 7 – 25 km (labelled ‘f’ in Figure 10.6). The assumption, that anomaly ‘f’ is due to geological a geological feature, rather than an end-of-profile inversion artefact, is supported by results of the initial inversion with only TE or TM data (feature ‘c’ in Figure 10.4), the response data (conductive structure at around 10 s beneath station pic020 in Figure 9.12), as well as to some degree

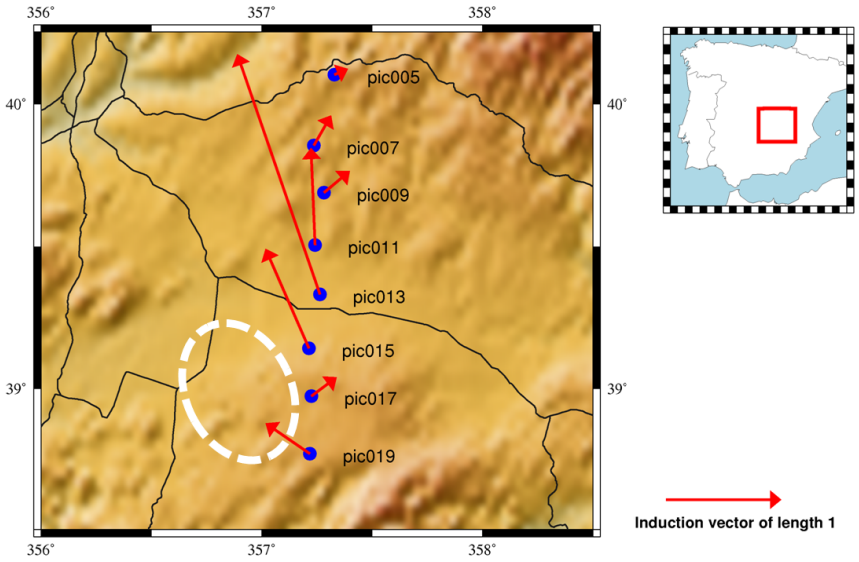

Fig. 10.12.: Real induction vectors (Parkinson convention) for 64 s periods at PICASSO Phase I station in proximity of the high conductivity – low velocity anomaly within the Iberian Massif (labelled 'f' in Figure 10.6, cf. Figure 10.11); location of the region on display shown in the inset. The dashed white ellipse indicates the location of the low velocity anomaly derived by seismic tomography [*Villaseñor et al.*, 2007] (cf. Fig. 7.21). Thin black lines denote the location of DC train lines in the area. Additional insight about this feature are given by the 3D inversion result (Fig. 10.34)

by characteristics of the induction arrows for station pic019 (in Parkinson convention) which point directly towards the anomaly, thus indicating higher conductivity in this area (cf. Fig. 10.12). Stations to the north exhibit different behaviour, pointing in NE (pic017) and NW (pic013, pic015) direction, i.e. not towards the anomaly. However, the DC train line, intersecting the PICASSO Phase I profile in between stations pic013 and pic015, may distort magnetic transfer functions of these nearby stations; see Section 9.8 for an analysis of magnetic transfer functions of PICASSO Phase I stations in the Tajo Basin and their distortion. For station pic017, on the contrary, no straightforward explanation can be devised for the fact that its induction arrows point away from the low velocity anomaly. Thus, induction arrow data do not yield a strong support for a highly conductive region to the west of stations pic017 and pic019 unless future geological or geophysical investigations provide plausible reasons for the diverging induction arrow at station pic017, e.g. an additional conductor to the northeast of station pic017.

Given their similarity in location, anomaly 'f' is most likely related to the low velocity region within the Central Iberian Zone (CIZ) derived in the tomography study by *Villaseñor et al.* [2007]; the anomaly is situated close to the PICASSO Phase I profile at the southern edge of the Tajo Basin (cf. Fig. 10.11). The seismic anomaly comprises a velocity reduction of up to 4% within the relatively faster region associated with the Iberian Massif. Thus, the anomalous region is inferred, based on results of the PICASSO Phase I processing, to possess high conductivity and low velocity characteristic. This rules out most cases of ore bodies as cause of the conductive anomaly, because they exhibit a higher density which would produce an increase in seismic velocity instead. The increased con-

ductivity of this region is therefore unlikely to originate from interconnected graphite-rich materials in the Variscan igneous and metamorphic CIZ rocks as inferred by *Pous et al.* [2004] and *Muñoz et al.* [2005] for features in their profiles to the west of the PICASSO Phase I profile, located in the southwest of the Iberian Peninsula. Potential causes of this anomaly are instead the presence of fluids, partial melting of middle and lower crust or remains of the asthenospheric material intruded into the lithosphere, all facilitating low velocity – high conductivity characteristics.

Partial melt in the lower crust requires heating from below and is likely to have some form of surface expression (e.g. volcanic activity, surface elevation, or surface heat-flow). Seismic tomography results of deeper regions indicate a substantial low velocity feature beneath the anomaly (cf. Figs. 7.23 and 7.24), which may be related to an enhanced heat transport (in support of the partial melt hypothesis) or an upward migration of fluids (in support of the fluid hypothesis). Heat-flow measurements, which could provide additional information about local temperature conditions, are unfortunately very sparse in the respective region of central Spain (cf. Fig. 7.26).

A potential source of partial melt in the Tajo Basin crust are remnants of remnants of asthenospheric material that was intruded into the lithosphere during volcanic events in Pliocene times (cf. Sec. 7.3.1). The asthenospheric material hypothesis is reasoned by observed volcanism in the Calatrova volcanic province (CVP), located to the west of the PICASSO Phase I profile, and the proposed connection with the trans-Morrocan, western-Mediterranean, European (TMWME) megafault system, located to the east of the profile, forming the source region (cf. Figs. 7.16 and 7.17). *López-Ruiz et al.* [1993] (corroborated by *Cebriá and López-Ruiz* [1995] and *López-Ruiz et al.* [2002]) propose a NW-SE directed connection between the CVP and a section of the TMWE beneath the eastern Betics, intersecting the PICASSO Phase I profile in the area of the Campo de Montiel.

An estimation of the minimum melt fraction required to produce the reduced resistivity of feature 'f' can be made using the formulation by *Partzsch et al.* [2000], viz.

$$\sigma_c = \frac{1}{\frac{1-a}{\sigma_{melt}} + \frac{a}{\sigma_{melt}(1-a^2)+\sigma_{solid}a^2}} \tag{10.1}$$

with σ_c conductivity of the composite, σ_{melt} conductivity of the melt, σ_{solid} conductivity of the solid rock, and[2]

$$a = (1 - f_m)^{1/3}, \tag{10.2}$$

with f_m the melt fraction. *Partzsch et al.* [2000] use a modified brick layer model (MBLM) for their formulation, which implies a completely interconnected network of melt along grain surfaces. Hence, melt value estimates derived from Equation 10.1 are close to the Hashin-Shtrikman upper bound [*Hashin and Shtrikman*, 1962]. For a lower degree of

[2]The formulation of Equation 10.2 in *Partzsch et al.* [2000] contains a mistake, i.e. $a = 3 * (1 - f_m)^{1/2}$ instead of $a = (1 - f_m)^{1/3}$; this has been corrected for in this work.

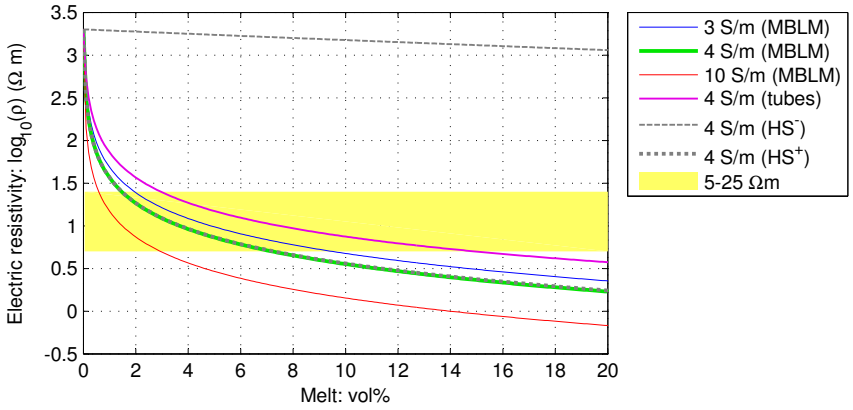

Fig. 10.13.: Electric resistivity of a partially molten rock as function of melt fraction; using the modified brick layer model (MBLM) by *Partzsch et al.* [2000] (Eq. 10.1, $\rho = \sigma^{-1}$) with melt conductivities of 3 S/m (blue line), 4 S/m (green line), and 10 S/m (red line), the equally spaced conducting (4 S/m) tubes model by *Schmeling* [1986] (purple line), as well as Hashin-Shtrikman extremal bounds [*Hashin and Shtrikman*, 1962] with a conductivity of 4 S/m for the melt phase; the conductivity of the sold phase is set to $5 * 10^{-1}$ S/m (2000 Ωm) for all approaches. 4 S/m represents the conductivity of the alkaline olivine basalt [*Partzsch et al.*, 2000, and references therein] determined as composition for the second volcanic event in the Calatrava Volcanic Province (CVP) (cf. Sec. 7.3.1); 3 and 10 S/m are inferred by *Partzsch et al.* [2000] as upper and lower boundary for conductivities of melts with a crustal composition at 1300°C. The shaded region indicates the resistivity range for feature 'f' in Figure 10.6.

interconnection a higher amount of melt is required to yield the same increase in conductivity. Thus, Equation 10.1 yields the minimum melt fraction required to facilitate the conductivity increase.

For the Tajo Basin subsurface, values of $\sigma_{melt} = 4$ S/m (i.e. $\rho_{melt} = 0.25\,\Omega$m) for the alkaline olivine basalt melt conductivity [*Partzsch et al.*, 2000, and references therein], and $\sigma_{solid} = 5 * 10^{-4}$ S/m (i.e. $\rho_{solid} = 2000\,\Omega$m) for the surrounding solid rock (cf. Fig. 10.6) are used. As a result, 1 vol% and 7 vol% are determined as minimum melt fraction for the increased electric conductivity of the feature 'f', related to composite conductivity values of 0.04 S/m and 0.2 S/m (i.e. resistivities of ≈25 Ωm and 5 Ωm), respectively. Corresponding resistivity–melt fraction curves are shown in Figure 10.13.

Also shown in Figure 10.13 are the Hashin-Shtrikman extremal bounds [*Hashin and Shtrikman*, 1962] and the equally spaced conducting tubes model by *Schmeling* [1986] for a melt conductivity of 4 S/m and a solid phase conductivity of $5 * 10^{-4}$ S/m. The Hashin-Shtrikman upper bound, representing an optimal connection of the conducting melt phase, is similar to the values obtained using the modified brick layer model (MBLM) by *Partzsch et al.* [2000] (Eq. 10.1). The Hashin-Shtrikman lower bound, on the other hand, denotes compound conductivity values for the case when the melt phase is contained in isolated spherical pockets, i.e. the lowest degree of connectivity for the melt phase.

For an intermediate degree of connection of the melt phase, the required melt fraction is certainly higher than the values derived for the formulation by *Partzsch et al.* [2000] and the Hashin-Shtrikman upper bounds, cf. values for the conducting tubes model by *Schmeling* [1986] in Figure 10.13. However, *Partzsch et al.* [2000] propose a completion of the interconnected network at a melt fraction of 10 vol% (related to temperatures of 1070°C) for their samples and experimental setup. According to this finding, Hashin-

Shtrikman upper bounds and the MBLM formulation (Equation 10.1) are valid for melt amounts above 10 vol%. If results by *Partzsch et al.* [2000] can be applied to the Tajo Basin subsurface case, partial melt conductivity of 4 S/m, solid phase conductivity of $5 * 10^{-4}$ S/m, and melt fraction between the minimum of 1% and the value of 10% could facilitate the electric conductivity anomaly of feature 'f'.

In the calculation of required melt fraction, discussed in the paragraph above, rocks are assumed dry and a contribution of water to the composite conductivity is not considered. For inferred P-T conditions of the intermediate crustal Tajo Basin subsurface ($\approx$ 0.3 GPa and 400°C [*Tejero and Ruiz*, 2002]) partial melting is implausible [e.g. *Thompson and Connolly*, 1995; *Gaillard*, 2004; *Nover*, 2005]. Water would be required to reduce the solidus of local rocks in order to facilitate partial melting. In addition, water increases ion mobility, hence conductivity, of the melt phase [*Gaillard*, 2004] and, in case of interconnected saline fluids, can further increase conductivity by adding electrolytic conduction effects (cf. Sec. 5.1.1). Therefore, if water is present in the area of the feature 'f', a lower amount of melt is required to produce the electric conductivity anomaly.

Water in the lower and intermediate Tajo Basin crust could originate from a deeper source region, e.g. from dehydration processes in the slab subducting under the Alboran Domain and the Betic Cordillera (cf. Section 7.2, and Figures 7.11 and 7.24). Respective hydrous phases may have migrated upwards into the lithosphere that was weakened by Pliocene indentation events (cf. Sec. 7.3.1), and accumulated at the bottom of an impermeable upper crustal layer. Upward migration of fluids originating from dehydration of a subducting slab was, for example, reported by *Wannamaker et al.* [2009] as cause for an lower crustal conductor in Marlborough, New Zealand. Hence, the increased electric conductivity in the intermediate and lower crust beneath the Campo de Montiel could be due to a combined contribution of water an partial melt.

With the current dataset it is not possible to distinguish between these two potential contributions and it is concluded that a combination of fluid and melting is a likely cause of the crustal electric anomaly 'f' in Figure 10.6 and the low velocity region in Figure 7.21. Inversion results of the PICASSO Phase I dataset for mantle structures will provide further insight about the contribution of water and its possible sources since in case of upward migrations of fluids a corresponding increase in conductivity for mantle regions between the dehydration region of the slab and the conductive feature in the crust is likely (cf. Sec. 10.2).

10.2. Inversion for mantle structures

In the previous Section 10.1 crustal structures of the Tajo Basin were investigated using short period response data from PICASSO Phase I stations. This Section is concerned with structures at mantle depths beneath the Tajo Basin; thus, longer period data are utilised. Separate investigation of crust and mantle structures is motivated by significantly different geoelectric strike directions of the two depth ranges and related issues of 2D

inversion described in Section 9. In order to enhance results of isotropic 2D inversion, novel anisotropic 1D and 2D inversion approaches are used that were successfully applied in a synthetic model study (cf. Sec. 8). In addition, isotropic 3D inversion is conducted that provides further information about the subsurface and yields an advanced subsurface model that can be used to contrast 1D and 2D inversion results.

Investigation of Tajo Basin mantle structures in this Section is started using isotropic 2D inversion. For that purpose impedance tensors of the PICASSO Phase I dataset were decomposed according to a strike direction of N29.4E, which was inferred for the mantle (cf. Sec. 9). Features of TE and TM mode pseudosections were discussed in Section 9.7, identifying, in particular, a resistive feature in the southern region of the profile and a decrease of resistivity at the longest periods (features 'c' and 'd' in Figure 9.13). The latter is potentially related to the more conductive asthenosphere, indicating that PICASSO Phase I data may provide information about the LAB depth beneath the Tajo Basin and existence of the highly conductive electric asthenosphere in this region.

10.2.1. Isotropic 2D inversion

Characteristics of TE and TM mode response data

As for the crustal depth region, in an initial step inversion results for data from each of the two MT modes (TE and TM) are compared with each other and with an inversion model using both modes. Thereby, contribution of the two modes to the combined-mode inversion model can be inferred. The anisotropic `MT2Dinv` program [*Baba et al.*, 2006], based on the algorithm by *Rodi and Mackie* [2001], is used for the inversion, with the isotropy parameter (τ_{iso}) set to a value of 10^7 to preclude anisotropic structures.

In order to focus the inversion onto features in the mantle, only long-period data (≥ 1 s) data are used for this initial isotropic smooth 2D inversion and cells in the crustal depth range (≤ 30 km) are kept fixed at a resistivity of 100 Ωm, thereby minimising the effect of crustal structures with their oblique geoelectric strike direction. This procedure was derived as the optimal approach for isotropic 2D inversion in case of a subsurface with oblique geoelectric strike direction by the synthetic model study presented in Section 8.3.1. Inversion results for the Tajo Basin mantle, in which crustal structures derived during the inversion with shorter periods and crustal strike direction (cf. Sec. 10.1.5) are used, are examined at the end of this section.

Inversion models obtained for the three datasets (TE-only, TM-only, TM+TE) are significantly different, particularly in the northern region where inversion of TE mode data yields a strongly conductive region, whereas inversion of TM mode data yields a resistive region instead (cf. Fig. 10.14). Electric resistivity characteristics at greater depths are not well constrained, especially beneath the highly conductive feature in the northern region of TE-only and combined-mode inversion model (indicated by the dashed areas). The skin effect traps most of the energy at the top of the conductor, thereby shielding deeper features. However, in 2D MT inversion the lateral extent of the conductor at different

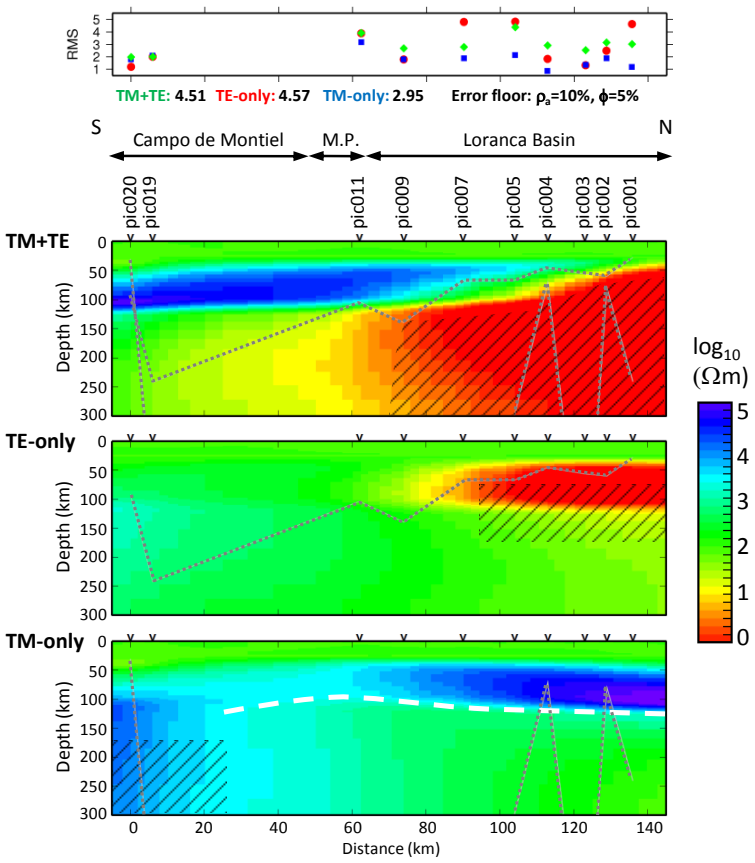

Fig. 10.14.: Results of initial isotropic 2D smooth inversion for the Tajo Basin subsurface; using data from both MT modes ('TM+TE', uppermost plot), only from the TE mode ('TE-only', middle plot), and only from the TM mode ('TM-only', bottom plot). Shaded areas indicate regions with low resolution (see text for details), dotted grey lines denote the Niblett-Bostick depth (Sec. 6.3.1) for the longest period of each mode at the respective MT recording station, and the dashed white line in the TM-only inversion model plot indicates a potential location of the electric lithosphere-asthenosphere boundary (LAB) that would be in agreement with previous estimates of the seismic and thermal LAB depth for the Tajo Basin subsurface (cf. Sec. 7.3.2). Location of stations is indicated on the top of the figure, together with labels denoting regions within the Tajo Basin (M.P.: Manchega Plain). Also shown on the top of this figure is the average RMS misfit of the stations with colours denoting values for each of the three datasets.

depths can be inferred, indicating a depth extent of approximately 100 km and 300 km for the TE-only and combined-mode inversion models, respectively (cf. Fig. 10.14). A vast extent of the conductive feature, as modelled for TE-only and combined-mode data, is unlikely as it would require an extraordinary geological setting. The purpose of this initial inversion sequence is not to provide a final concluding model though, but to identify contributions of the two modes to the combined mode model.

The RMS misfit of the TM-only model is generally lower than the misfit of TE-only and combined-mode models; however, the distribution of the three inversions (TE-only, TM-only, TM+TE) is similar (cf. plot on the top of Figure 10.14). A significant difference between misfits of the three inversion models is observable at stations pic001, pic004, and pic005, for which TE mode data are poorly fit by the best-fitting models derived by the inversion program. The increased misfit, as well as the increased electric conductivity

of the TE mode model, may be a result of galvanic distortion by small-scale off-profile features or crustal structures which remain in the dataset despite decomposition of the impedance tensor and cannot be adequately modelled with 2D inversion. The TE mode is usually more affected by small-scale off-profile features than the TM mode (cf. Sec. 6.3); therefore, the TE mode is often down-weighted in cases where effects of 3D structures are assumed. In this initial inversion procedure, error floors of apparent resistivity and impedance phase for both modes are set to 10 % and 5 %, respectively. Modification of error floors in the combined-mode inversion can later be used to weigh the two modes, through that controlling their influence on the resulting inversion search for the best-fitting model. Such weighting of the modes will be carried out in subsequent inversion sequences of this work.

A remarkable feature of this initial inversion step is the transition from the resistive uppermost mantle ($10^3 - 10^4\,\Omega$m) to the more conductive region below ($\approx 10^2\,\Omega$m). For the northern and central part of the TM-only model and the southern part of the combined-mode model, the transition is modelled at a depth of approximately 100 – 150 km, which is consistent with LAB depth estimates for the Tajo Basin region in proximity of the PICASSO Phase I profile by other investigations (cf. Sec. 7). The upward extension of the more conductive region in the south-central area of the TM-only model coincides to some degree with the location of a low velocity region determined in seismic tomography studies (cf. Fig. 7.24). The vast downward extension of the resistor at the southern edge of the TM-only model (indicated by the dashed areas), on the other hand, does not seem plausible and is most likely an inversion artefact.

Owing to the low validity of the isotropic 2D inversion results when using a homogeneous crust, the investigation is extended by using projected results of the crustal inversion model (cf. Sec. 10.1.5) as starting model in the inversion for mantle structures. The starting model is augmented by assigning resistivity values of 100 Ωm to cells below the crustal model. Inversion is carried out like the previous inversions at the beginning of this Section, following the Jones Catechism (Sec. A.2.3), using data of periods greater 100 s to minimise contribution of crustal structures, and examining results for each of the modes individually and in combination (Fig. 10.15). Therein, structures at crustal depths (above 30 km) are kept fixed. Data for the TE mode can only be fit poorly by the isotropic 2D inversion models; i.e. despite (unduly) high levels for related error floors of 20% (ρ_a) and 10% (ϕ), an unacceptable RMS misfit of 4.01 prevails. Likewise, the misfit for the inversion model using both modes is exceedingly high (RMS misfit = 3.39). Thus, isotropic 2D inversion models are not adequately representing the Tajo Basin subsurface but can only be used to examine characteristics of the models.

As for the inversion with a homogeneous crust (Fig. 10.14), models for the three datasets (only TE mode, only TM mode, both modes) differ significantly. At greater depth (>100 km) the TE mode inversion model exhibits a highly conductive region, whereas TM mode inversion yields a highly resistive region. Different characteristics may in parts be related to the limited depth of induction for the TE mode (indicated by the grey lines in Figure 10.15, denoting Niblett-Bostick depth (Sec. 6.3.1) estimates for the longest period

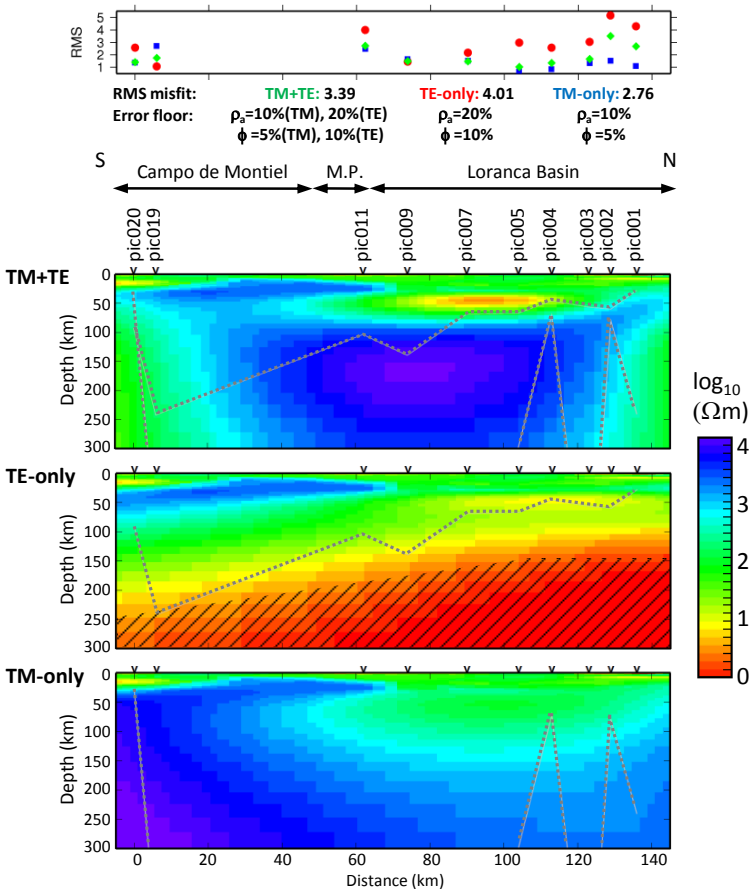

Fig. 10.15.: Results of initial isotropic 2D smooth inversion for the Tajo Basin subsurface, using a starting model that contains crustal structures obtained through inversion with shorter periods and crustal geoelectric strike direction (Fig. 10.6). In the inversion for mantle structures periods greater 100 s are selected, using data from both MT modes ('TM+TE', uppermost plot), only from the TE mode ('TE-only', middle plot), and only from the TM mode ('TM-only', bottom plot). Shaded areas indicate regions with low resolution (see text for details) and dotted grey lines denote Niblett-Bostick depths (Sec. 6.3.1) for the longest period of each mode at the respective MT recording station. Locations of stations are indicated on the top of the figure, together with labels denoting certain regions within the Tajo Basin (M.P.: Manchega Plain). Also shown is the average RMS misfit of the stations with colours denoting values for each of the three datasets.

at each station). However, significant difference in electric resistivity can also be observed for the region in the south of the PICASSO Phase I profile, for which a Niblett-Bostick depth of more than 200 km is calculated for both modes. Moreover, subsurface structures inferred by, particularly the combined and TM-only, models are implausible; i.e. the increase of resistivity at depths that are usually associated with the Earth's asthenosphere. Implausible isotropic 2D inversion models are most likely the result of oblique geoelectric strike direction of the Tajo Basin crust and 3D effects that are not adequately taken into account during decomposition of the impedance tensor (Sec. 4.4). Hence, inversion results for mantle structures of the Tajo Basin confirm result of the synthetic model study inferring shortcomings of isotropic 2D inversions using structures from a crustal model with an oblique geoelectric strike direction (cf. Chap. 8).

Features of the inversion models shown in Figures 10.14 and 10.15 should not be over-interpreted as they are solely the result of an initial inversion sequence in order to examine contributions of the two modes. However, through this initial inversion sequence insights about the characteristics of each modes are already gained. These insights can be used to guide subsequent isotropic 2D combined-mode inversion steps; namely, (a) that TE mode data are potentially distorted by crustal or off-profile features and should be down-weighted, and (b) an enhanced starting model based on the TM mode inversion model suggesting an eLAB in the depth range 100 – 150 km.

Estimation of lithosphere-asthenosphere boundary depth

In its original, rheological, definition the lithosphere–asthenosphere boundary (LAB) denotes the transition from a rigid to a viscously deforming region within the Earth's mantle; i.e. a transition from a mechanical strong to a weak region[3]. The LAB depth is therefore of major importance for understanding tectonic processes in the study area. Moreover, due to the strong temperature-dependence of mantle material viscocity, a correlation of the mechanical lithosphere (or *mechanical boundary layer*, MBL) and the thermal LAB (tLAB, also referred to as *thermal boundary layer*, TBL) has been proposed [e.g. *Artemieva*, 2009]. The tLAB indicates the change from conductive to convective heat transport and its depth is commonly defined using an isotherm; with the isotherm value depending on the choice of the investigator, usually within the range 1200 – 1350°C [e.g. *Tejero and Ruiz*, 2002; *Artemieva*, 2006; *Tesauro et al.*, 2009b]. The thermal estimate of the LAB is derived through thermal modelling using surface heat flow measurements with a range of assumptions regarding heat conduction and production within the lithosphere [e.g. *Tejero and Ruiz*, 2002] or by deducing thermal conditions from results of other methods like seismology [e.g. *Artemieva*, 2006; *Tesauro et al.*, 2009b]. The LAB depth has in most cases a strong impact on the geologic setting of the regions above, as it significantly affects local T-P condition.

Owing to its great depth only few methods are capable of probing the LAB location, namely seismology and magnetotellurics. These methods do not measure rheological properties directly, but yield LAB estimates in terms of their respective properties under investigation. Accordingly, these LAB estimates may be referred to as seismic LAB (sLAB), electric (eLAB). A range of different seismic approaches are used to determine parameters that are used as indicators for the LAB; i.e. change of seismic anisotropy direction or magnitude (sLABa), reduction of surface wave velocity (sLABsw), and signals in receiver functions data (sLABrf). Since these seismic approaches use different parameters as LAB indicator, depth estimates can vary between the approaches [e.g. *Eaton et al.*, 2009, and references within] and may even be refer to features that at not related to the LAB; i.e. variation in magnitude or direction of seismic anisotropy, the top of an older solidified melt layer, the spinel-garnet transition, or presence of water or carbon dioxide

[3] Over time different, and sometimes misguiding, use has been made of the term LAB by different authors and disciplines; see Section 5.2.2 and the reviews by *Eaton et al.* [2009] *Artemieva* [2009] for details.

in the lithospheric-mantle [e.g. *Levin and Park*, 1997; *Stixrude and Lithgow-Bertelloni*, 2005; *Thybo*, 2006; *Abt et al.*, 2010].

Magnetotelluric, on the other hand, yields electric LAB (eLAB) depth estimates using a significant decrease of electric resistivity as proxy for the LAB. Electric conductivity of Earth materials is strongly temperature-dependent (cf. Sec. 5); hence, a relation between eLAB and tLAB, and ultimately with the mechanical LAB, is plausible (cf. Sec. 5.2.2). Depths of the different LAB indicators as well as difference or semblance between LAB estimates for the different parameters can yield valuable information about geological settings of the study area.

For regions of the Iberian Peninsula in proximity of the PICASSO Phase I profile, lithosphere thicknesses between 110 km and 130 km have been inferred by different methods (cf. Sec. 7). In their investigations of the eastern Betic Cordillera *Rosell et al.* [2010] determine an eLAB depth of 110 km using magnetotellurics (the study area of *Rosell et al.* [2010] is shown in Figure 7.11). A 110 km depth of the tLAB beneath the Tajo Basin was derived by *Tejero and Ruiz* [2002] using thermal modelling with heat-flow values from *Fernandez et al.* [1998] and assuming a temperature of 1350°C at the tLAB. *Tesauro et al.* [2009a] and *Tesauro et al.* [2009b], on the other hand, use the seismic tomography model by *Koulakov et al.* [2009] to construct a thermal model of the European lithosphere and derive a tLAB between 120 km and 130 km for the same region using the 1200°C isotherm as indicator for the tLAB. *Fullea et al.* [2010] determined a LAB depth between 110 km and 130 km for the southern Tajo Basin region using integrated geophysical modelling; however, the focus of their work is on regions in close proximity of the Alboran Domain and characteristics of areas to the North, such as the Tajo Basin, are less constrained.

The eLAB is usually associated with a significant change in electric conductivity from values of approximately 1000 Ωm in the lithospheric-mantle to values of 100 Ωm or lower in the asthenosphere (values as low as 5 Ωm have been reported for the upper asthenosphere; see Section 5.2.2 for a discussion about the electric asthenosphere anomaly). Thus, the eLAB should yield a measurable response in MT data of sufficient period length. Reduced electric resistivities and increased impedance phases of the PICASSO Phase I response data shown in Figure 9.13 (feature 'd') may indicate an eLAB response in the data, therefore motivating a detailed investigation of eLAB depth and characteristics beneath the Tajo Basin.

First, the eLAB beneath the Tajo Basin is studied using isotropic 2D sharp-boundary inversion with conductivity interfaces (in the following referred to as 'CI-inversion'), which is part of the `2DMTinv` programme implemented in the WinGLink software package [*WinGLink*, 2005]. For that purpose a starting model is constructed (upper plot in Figure 10.16) that comprises three layers representing a 100 Ωm crust (depth range 0 – 33 km), a 1000 Ωm lithospheric-mantle (depth range 33 – 110 km), and a 100 Ωm asthenosphere (depths ≥ 110 km). Therein, resistivity values are based on the TM-only inversion model obtained in the previous Section 10.2.1. The starting model has a RMS misfit of 6.28 with error floors of $\rho_a = 20\%$ and $\phi = 5\%$ (TM mode) and $\rho_a = 40\%$ and $\phi = 10\%$ (TE mode).

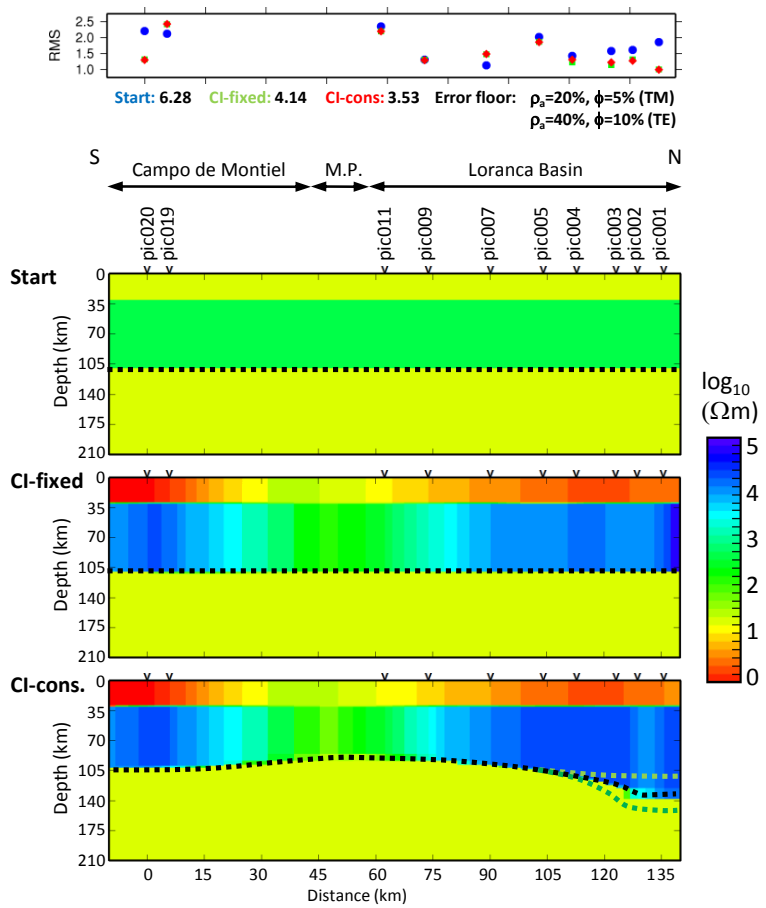

Fig. 10.16.: Isotropic 2D sharp boundary inversion (CI-inversion) models of the Tajo Basin subsurface; top: Starting model, middle: model from CI-inversion with fixed interfaces at 30 and 110 km, bottom: model from CI-inversion with variable interfaces. Error floors used in the inversion are ρ_a = 20% and ϕ = 5% for the TM mode and ρ_a = 40% and ϕ = 10% for the TE mode, taken into account the previously inferred galvanic distortion and its higher effect on the TE mode. Dashed black lines denote the lithosphere-asthenosphere boundary (LAB); the dashed green lines indicate shallower and deeper LABs for the northern region of the profile, inferred from models with similar RMS misfit.

Error floors of TE mode and apparent resistivity data are increased because of galvanic distortion, inferred during the initial inversion sequence (cf. Fig. 10.14), and its different impact on the model parameters; see Chapter 4 for a detailed description regarding distortion of MT data.

As a first approach, it is tested whether a subsurface model of electric conductivity can be found that contains an entirely levelled eLAB at a depth of 110 km. For that reason, locations of conductivity interfaces are fixed during the inversion and the misfit can only be reduced through variation of electric resistivity values within the layers. Changes of electric resistivity values at crustal depth are constrained to avoid inversion artefacts due to the oblique strike direction. The resulting model (middle plot in Figure 10.16) exhibits a relatively lower resistivity in the centre-south region of the profile. However, an unacceptable misfit of the model prevails (RMS = 4.14), indicating that a levelled

isotropic 2D layer model is not in agreement with data collected for the Tajo Basin.

Because of the prevailing increased misfit for the CI-inversion with fixed conductivity interfaces, constrains on the interfaces are lowered in order to permit a laterally changing LAB depth. A variety of intermediate processing steps are conducted and effects of different sequences of apparent resistivity and impedance phase data weighing are examined; the final model is then chosen on the base of the lowest overall misfit. The CI-inversion model with variable interface depths exhibits a RMS misfit of 3.53 indicating that the model is not an acceptable fit; however, the model remains an interesting entity to investigate structures supported by the dataset. The LAB is modelled at depths between 90 km and 140 km with the shallowest region in the south-central region of the profile and greater depths at the edges of the profile. The upwards extension of the eLAB in the south-central region of the profile, together with the relatively lower resistivity of the lithospheric-mantle in this region ($\approx 10^3$ Ωm), was also modelled in the CI-inversion with fixed interfaces (upper plot in Figure 10.16); it is further supported by the seismic tomography model of *Amaru* [2007] (Fig. 7.24). The seismic model exhibits a collocated low velocity region that may be caused by fluids or higher temperature; the latter could be caused by enhanced heat transport in conjunction with a shallower tLAB.

LAB depth of the northernmost region is not strongly constrained since, for the same misfit, models with thinner as well as with thicker lithosphere could be found. Modelled thickening of the lithosphere in the bottom plot of Figure 10.16 is based on geological considerations. The deeper LAB in the north of the profile coincides with the Iberian Range, an intraplate mountain ranges formed by the Mesozoic collision of the Iberian Peninsula with the Eurasian Plate (cf. Sec. 7). The associated compressional stress regime in the Iberian Peninsula, in conjunction with isostatic equilibrium processes, is likely to have caused thickening of crust and lithosphere [e.g. *Airy*, 1855; *Pratt*, 1855; *Surinach and Vegas*, 1998; *Vegas et al.*, 1990; *Turcotte and Schubert*, 2002; *Stacey and Davis*, 2008; *Teixell et al.*, 2009]. The uppermost mantle beneath the Tajo Basin has been inferred as a competent layer [*Cloetingh et al.*, 2002; *Tejero and Ruiz*, 2002; *Fernández-Lozano et al.*, 2011] and is therefore likely to exhibit a vertical displacement as a result of horizontal stress. Cases of thinner lithosphere beneath mountain ranges have been reported for other regions of the Earth, namely the Atlas Mountains in Morocco [*Teixell et al.*, 2005; *Fullea et al.*, 2007] and the southern Sierra Nevada region in California [e.g. *Jones*, 1987; *Zandt and Carrigan*, 1993; *Park et al.*, 1996; *Zandt et al.*, 2004; *Abt et al.*, 2010]. However, lithospheric thinning under mountain ranges can, if at all, only to be found in exceptional geological settings. Keeping the crust–mantle boundary at a fixed depth of 30 km in order to reduce effects of the oblique crustal strike direction, rather than increasing its depth beneath the northern region, may contribute to the uncertainty of the LAB depth below. For the southern region of the profile, the model exhibits an eLAB depth of approximately 110 km, which is in agreement with results by *Rosell et al.* [2010] for the proximate eastern Betics region, as well as with LAB estimates of *Fullea et al.* [2007] and *Fullea et al.* [2010] for the southern Tajo Basin.

Besides the overall increased misfit of the isotropic 2D models, isotropic 2D inversion

can introduce artefacts in the resulting subsurface model, as shown in the synthetic model study (Sec. 8.3.1). Therefore, the investigation of the Tajo Basin subsurface is extended in the following Sections using anisotropic 1D and 2D approaches as well as isotropic 3D inversion.

10.2.2. Anisotropic 1D inversion

Motivated by the successful application of anisotropic 1D inversion for the case of a synthetic 3D model with oblique strike direction (Sec. 8.3.2) the approach is used for the PICASSO Phase I data from the Tajo Basin. For anisotropic inversion, impedance tensor data are not decomposed (cf. Sec. 9.6.2) in order to preserve information in the off-diagonal elements of the impedance tensor. Effects of electric resistivity interfaces are imaged by anisotropic structures with anisotropy directions (directions of maximum and minimum resistivity) aligned with the 2D geoelectric strike direction. For 1D inversion no alignment of the coordinate axes with a specific strike direction is required and the anisotropy direction is determined during the inversion process. During the PICASSO Phase I fieldwork campaign MT recording systems are aligned in respect to magnetic North, which is within a range of 2° of true North for the PICASSO Phase I stations. Hence, a rotation to true North (yielding a common orientation of all recording stations) causes only a minor mixing of errors from different channels. Anisotropic 1D inversion of Tajo Basin data is carried out with the algorithm `ai1D` [*Pek and Santos*, 2006] and the same parameters used during the synthetic 3D model study (Tab. 8.4).

The inversion yields no systematic direction of maximum anisotropy and no straightforward relation with the mantle strike direction (N29.4E) that can be made (cf. top-left plot in Figure 10.17). Therefore, anisotropic resistivity values are assigned to the mantle strike-parallel model ($\rho_{\parallel}$) if they are inside a ±90° range of N29.4E and otherwise assigned to the orthogonal model ($\rho_{\perp}$); i.e. the bottom-right and bottom-left plot in Figure 10.17, respectively. Resulting models exhibit a diverse subsurface structure with the $\rho_{\perp}$ model containing mostly values in the range $10^{2.5} - 10^{4}\,\Omega$m, whereas the $\rho_{\parallel}$ model contains mostly values between 10^{1} and $10^{3}\,\Omega$m (the anomaly below stations pic013 and pic015 is due to rejection of long-period data at these station, cf. Section 9.4). The anomaly beneath stations pic013 and pic015 is also reflected in the anisotropy magnitude (top-right plot in Figure 10.17), exhibiting for the respective region a value of 1 (i.e. no anisotropy). Unlike for the synthetic model (Sec. 8.3.2), the anisotropic inversion 1D model for the Tajo Basin yields anisotropy magnitude values greater than one for the crustal depth range, thereby indicating that the Tajo Basin crust is more complex and cannot approximated by an isotropic 1D structure. Further, in the anisotropic 1D inversion models no change of electric resistivity can be found that could be associated with the LAB.

Since anisotropic 1D inversion of the undecomposed datasets fails to provide a plausible model of the Tajo Basin subsurface, anisotropic 1D inversion is also conducted for a dataset decomposed according to the strike direction of the mantle. Decomposition of

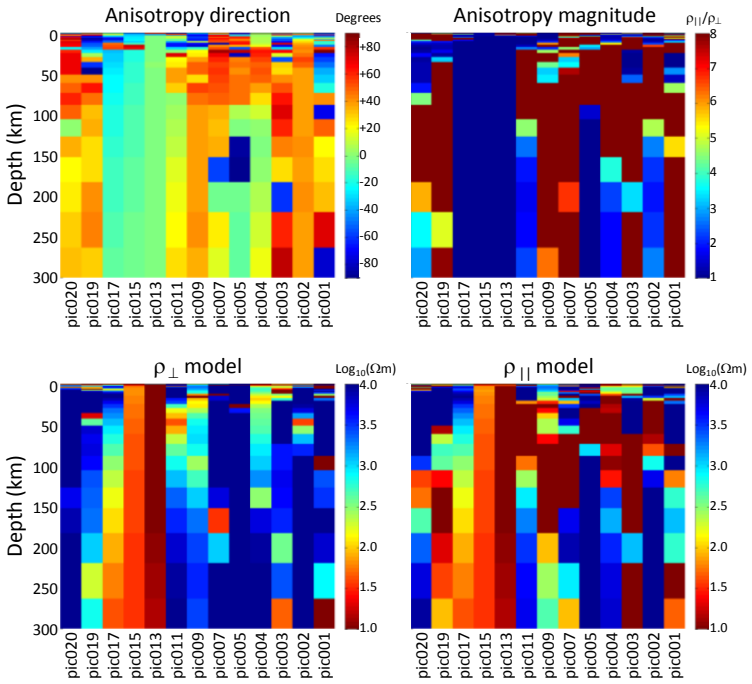

Fig. 10.17.: Results of anisotropic 1D inversion for Tajo Basin subsurface structures using the `ai1D` algorithm by *Pek and Santos* [2002]. Top-left: anisotropic strike direction, i.e. direction of maximum electric resistivity; top-right: magnitude of electric resistivity, i.e. ratio of maximum and minimum electric resistivity; bottom-left and bottom-right: electric resistivities perpendicular $\rho_{\perp}$ and parallel $\rho_{\parallel}$ to the mantle strike direction, respectively; see text for details.

impedance data aims to yield a dataset free from distortion effects that are suitable for 2D inversion; thus, this may provide a dataset more adequate for the anisotropic 1D inversion approach. Decomposition is carried out using the `strike` program by *McNeice and Jones* [2001] and a strike direction of N29.4E; related inversion results are shown in Figure 10.18. Evidently, the anisotropic 1D inversion of the decomposed dataset does not result in a more plausible subsurface model than for the undecomposed dataset. It is therefore concluded that anisotropic 1D inversion is not suitable for recovering complex structures like those observed for the heterogeneous Tajo Basin subsurface, thereby confirming prognoses made during the synthetic 3D model study (Sec. 8.3.2). Anisotropic 2D inversion may yield superior results for these more complex subsurface structures, since therein no inherent 1D assumption for the subsurface are made.

10.2.3. Anisotropic 2D inversion

Due to implausible results of isotropic 2D and anisotropic 1D inversion in recovering the Tajo Basin subsurface, the anisotropic 2D inversion approach is applied, which showed satisfactory results for the synthetic model study (cf. Chap. 8). Due to current limitations of the `MT2Dinv` algorithm [*Baba et al.*, 2006], an enhanced anisotropic version of the algorithm by *Rodi and Mackie* [2001], only the first approach is use. The first ap-

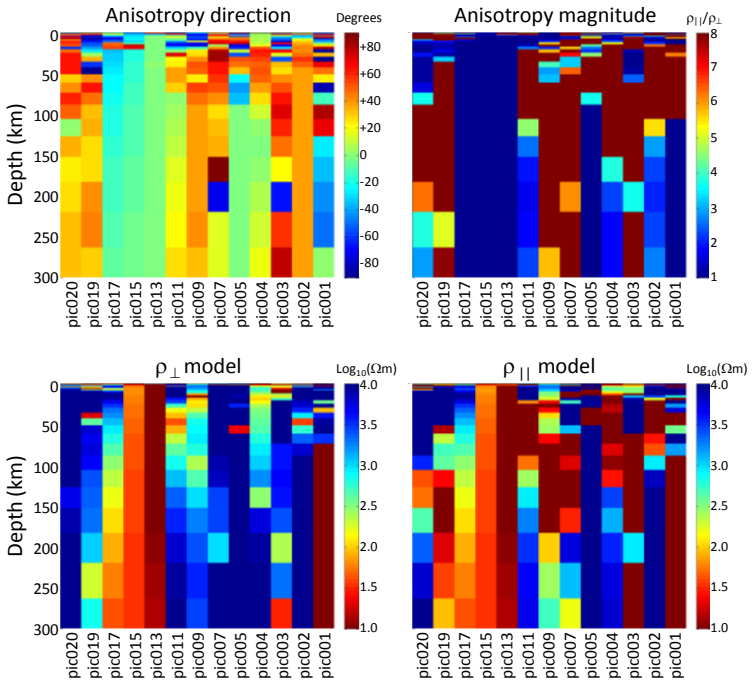

Fig. 10.18.: Results of anisotropic 1D inversion for Tajo Basin subsurface structures using the `ai1D` algorithm by *Pek and Santos* [2002] and a dataset decomposed according to the strike direction of the mantle (N29.4E) using the `strike` program by *McNeice and Jones* [2001]. Top-left: anisotropic strike direction, i.e. direction of maximum electric resistivity; top-right: magnitude of electric resistivity, i.e. ratio of maximum and minimum electric resistivity; bottom-left and bottom-right: electric resistivities perpendicular $\rho_\perp$ and parallel $\rho_\parallel$ to the mantle strike direction, respectively; see text for details.

proach comprises initial isotropic 2D inversion for the crustal structures and subsequent anisotropic 2D representation of the mantle; a thorough description of the approaches is given in Section 8.3.3. Since the first anisotropic 2D inversion approach uses data that are rotated according to the strike direction of the crust (N40.9W), the previously obtained isotropic 2D inversion results for crustal structures (Sec. 10.1.5) can be used for the first sequence. The starting model for the second sequence contains the crustal inversion model shown in Figure 10.6 and a mantle which consists of either a 100 Ωm halfspace or a 100 Ωm lithospheric-mantle and a 10 Ωm asthenosphere (cf. Fig. 10.19). In consideration of isotropic 2D inversion results (Sec. 10.2.1) as well as findings of collocated studies presented in Section 7.3.2, the lower boundary of the resistive lithospheric-mantle region in the second starting model is set to 110 km. Crustal structures are kept fixed and only long-period data are used for the anisotropic 2D inversion in order to focus the inversion onto the mantle region.

Different combinations of smoothing parameters (α, β, and τ) as well as electric resistivity gradient and Laplacian regularisation (cf. Sec. 6.3) are used for the inversion process with an inversion sequence according to the Jones Catechism (Sec. A.2.3). Inversion models exhibit different subsurface structures dependent on the combination of constraints, because improper regularisation can dominate the objective function (cf. Sec.

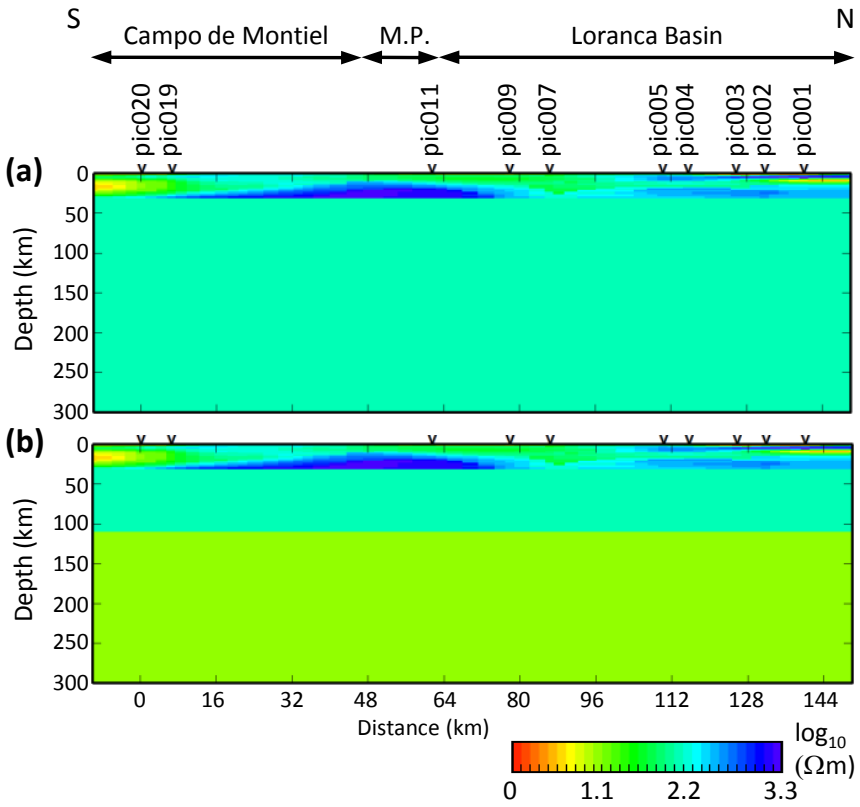

Fig. 10.19.: Models of the Tajo Basin subsurface used as starting model for anisotropic 2D inversion. The models contain crustal structures derived by the isotropic 2D inversion for the Tajo Basin crust and either (a) a homogeneous 100 Ωm halfspace or (b) a 100 Ωm lithospheric-mantle and a 10 Ωm asthenosphere to represent the mantle.

6.3); thereby masking information in the dataset. In particular, data for the longest periods are not well constraint due to their higher uncertainty levels. Accordingly, sensitivity to the asthenospheric region is low and regularisations are chosen to fit the characteristics of this region; i.e. (a) increased horizontal smoothing ($\alpha = 3$) since the eLAB can be assumed to exhibit relatively low vertical variation, (b) intermediate global smoothing ($\tau = 6$) to avoid loosing the electric resistivity decrease at the LAB due to too high smoothing, and (c) electric resistivity gradient regularisation because the asthenosphere is commonly assumed as a region of relatively homogeneous electric resistivity.

Corresponding to findings of the synthetic model study presented in Chapter 8, results of the anisotropic 2D inversion approach are shown using electric resistivity values of the direction orthogonal to the profile (ρ_{XX}). Electric resistivity models for the opposite direction (ρ_{YY}) exhibit implausible low values (cf. Fig. 10.21) and are not considered representative for the Tajo Basin mantle. Inversion models obtained using either a halfspace or two layers to represent the mantle region (top and bottom plot in Figure 10.19, respectively) are virtually identical (cf. Fig. 10.21), thereby indicating robustness of the inversion process. Moreover, both models exhibit electric resistivity values $\geq 100\,\Omega$m for the region associated with the asthenosphere; thus, indicating that an electrically conduc-

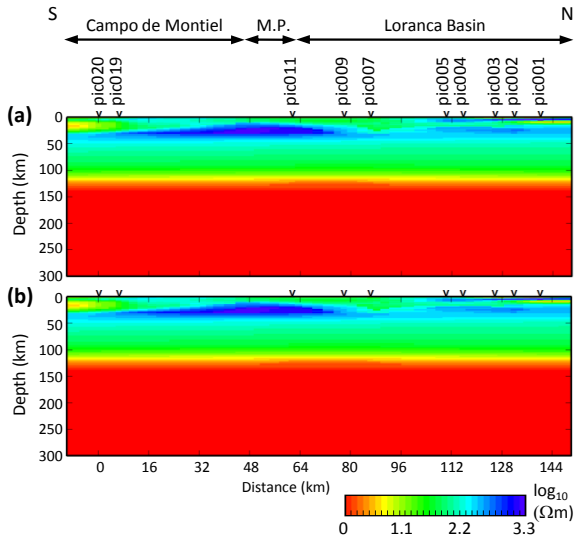

Fig. 10.20.: Results of the ρ_{YY} component from the anisotropic 2D inversion approach for structures of the Tajo Basin subsurface. Models are obtained using the `MT2Dinv` inversion algorithm [*Baba et al.*, 2006] with electric resistivity gradient regularisation, smoothing parameters $\alpha = 3, \beta = 1, \tau = 6$, and starting models shown in Figure 10.19 (with the same letters). Inversion models obtained using either starting model are virtually identical and exhibit implausible high electric conductivity values for mantle regions. As concluded in a synthetic model study (Sec. 8), reliable subsurface structures are to inferred from the ρ_{XX} model (Fig. 10.21) instead; see text for details.

tive asthenosphere anomaly with only a few tens of Ωm's, determined for some regions of the Earth (cf. Sec. 5.2.2), is not strongly demanded by the data. For the lithospheric-mantle, resistivity values between 200 Ωm and 500 Ωm are derived with higher values located to the south, contrary to observations of isotropic 2D inversion[4]. Note that, due to regularisation of the inversion process, models depict the minimum resistivity values supported by the data. This means that higher resistivities are possible, particularly in the lithospheric-mantle region, but are restrained by smoothing constraints in the inversion process.

In order to infer the LAB depth beneath the Tajo Basin from anisotropic 2D inversion, ρ – depth profiles are created by laterally averaging electric resistivity values along the PICASSO Phase I profile. In addition, average ρ – depth profiles are determined for the southern and northern region of the PICASSO Phase I to examine lateral changes of electric resistivity in more detail. Resulting ρ – depth profiles (Fig. 10.22) are compared with each other as well as with reference profiles from *Muller et al.* [2009]. The latter are calculated using laboratory electrical resistivity versus temperature and pressure measurements for dry olivine and pyroxene [*Constable et al.*, 1992; *Xu and Shankland*, 1999; *Xu et al.*, 2000b] with hypothetical mantle geotherms for different lithospheric thicknesses. Note that the reference profiles only consider semiconduction of dry mineral as electric

[4]Horizontal dimensions differ between isotropic and anisotropic inversion models due different projection, as stations are projected onto profiles that are orthogonal to either the mantle strike direction (isotropic inversion) or the crustal strike direction (anisotropic inversion, approach 1; see Section 8.3.3 for details of the approach)

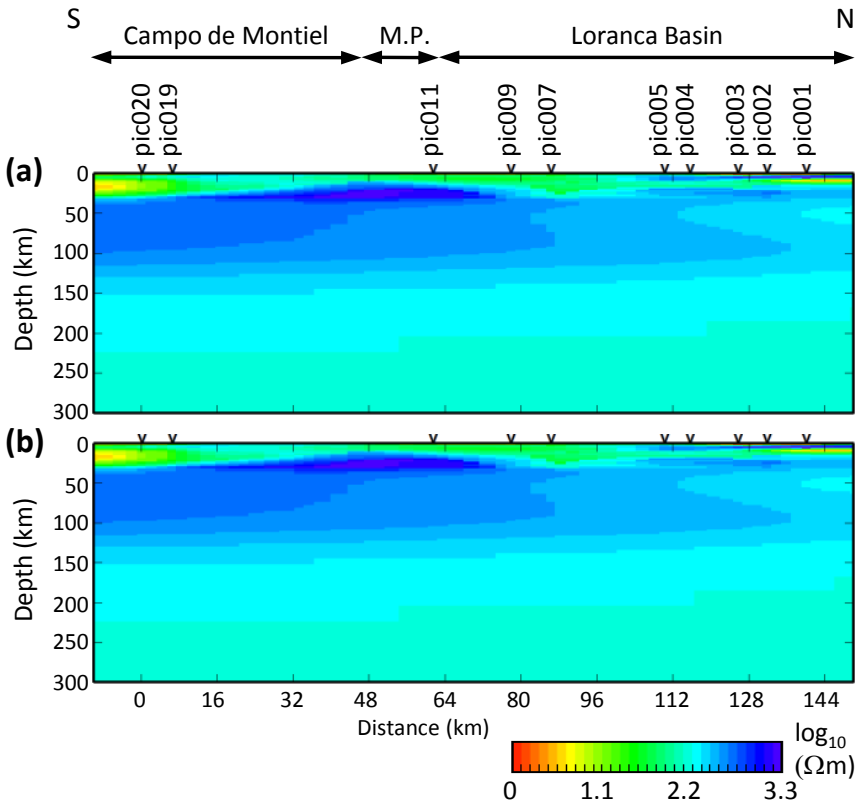

Fig. 10.21.: Models of electric resistivity distribution beneath the Tajo Basin using an anisotropic 2D inversion approach. Models are obtained using the `MT2Dinv` inversion algorithm [*Baba et al.*, 2006] with electric resistivity gradient regularisation, smoothing parameters $\alpha = 3, \beta = 1, \tau = 6$, and starting models shown in Figure 10.19 (with the same letters). Inversion models obtained using either starting model are virtually identical and exhibit a RMS misfit of 3 with error floors of 20% and 10% for ρ_a and ϕ, respectively.

charge transport mechanism and do not take into account contributions of electronic or electrolytic conductivity (cf. Sec. 5.1). Hence, resistivity values in the lithosphere, where other conduction mechanisms are likely to have a significant contribution, may be overestimated by this approach. Moreover, electric resistivity values of the asthenosphere are likely to be higher than denoted by the reference profiles, i.e. in the range of 100 Ωm (or 5 – 25 Ωm for an electrically conductive uppermost asthenosphere; cf. Section 5.2.2).

The eLAB is commonly assumed to coincide with the transition from resistive lithospheric mantle values of ≥1000 Ωm to values of approximately 100 Ωm for a dry asthenosphere[5]. The change of the electric resistivity gradient is associated with the transition from conduction to convection as the dominant heat-transport mechanism at the LAB and the resulting changing slope in the mantle geotherm. Since electric resistivity of Earth materials is profoundly affected by temperature (cf. Sec. 5.1), the LAB is likely to be associated with a similar change in the ρ – depth profile. Despite lateral varying average electric resistivity values, denoted by the differences between ρ – depth profile of the

[5]Water, partial melt, or grain-size variation along the eLAB may cause significant further reduction of resistivity in the uppermost asthenosphere; cf. Section 5.2.2

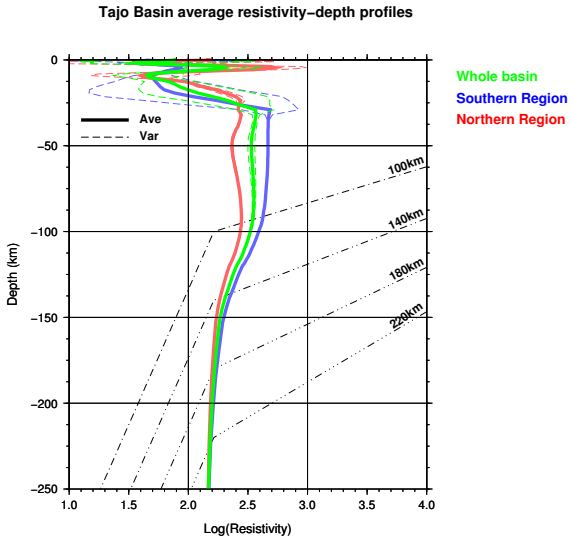

Fig. 10.22.: Average apparent resistivity – depth profile for the Tajo Basin subsurface; obtained through anisotropic 2D inversion of the PICASSO Phase I data. Different colours indicate average resistivity values for different regions of the basin and solid and dashed lines denote average values and variance, respectively. Reference profiles (dotted-dashed lines) are taken from *Muller et al.* [2009], based on results by *Constable et al.* [1992]; *Xu and Shankland* [1999]; *Xu et al.* [2000b].

northern and southern region, a similar depth of the eLAB is indicated by all three profiles through a transition from decreasing resistivities to a relatively homogeneous regime below 140 km. Depending on which part of the changing ρ – depth slope is used as indicator for the eLAB, depths between 110 km and 140 km can be inferred. These LAB depth estimates are in the range of results from the isotropic 2D inversion (Sec. 10.2.1), MT investigation to the southern of the PICASSO Phase I profile by *Rosell et al.* [2010], and results of thermal and integrated geophysical modelling [*Tejero and Ruiz*, 2002; *Tesauro et al.*, 2009b; *Fullea et al.*, 2010].

Results of this novel anisotropic 2D inversion approach, however, may be biased by the fact that the difference in geoelectric strike direction of the Tajo Basin crust and mantle are not 90°, but instead ≈70°. The `MT2Dinv` inversion algorithm [*Baba et al.*, 2006] facilitates only anisotropic directions parallel and perpendicular to the profile. Thus, the program does not permit a 70° difference between anisotropy direction and geoelectric strike direction. Hence, additional investigations of the Tajo Basin subsurface are carried out using isotropic 3D inversion to gain better insights about electric resistivity distribution and tectonic implications.

10.2.4. Isotropic 3D inversion

Owing to limitations of isotropic and anisotropic 1D and 2D inversion approaches employed in previous Sections 10.2.1 – 10.2.3, isotropic 3D inversion is used to enhance knowledge about the Tajo Basin subsurface. Due to significantly higher computational costs of 3D inversion with respect to lower-dimensional inversion approaches, 3D inves-

tigation is usually limited to forward modelling or a small number of inversion steps. This study uses the algorithm `wsinv3d` by *Siripunvaraporn et al.* [2005a], which reduces computational load and time by conducting inversions in the data space and calculating only an approximation of the sensitivity matrix during the forward modelling (cf. Sec. 6.3). The `wsinv3d` algorithm could therefore, in principle, be run on a PC [*Siripunvaraporn et al.*, 2005a]; however, in order to obtain results within a reasonable time, in this study inversions are carried out using a parallel version of the `wsinv3d` algorithm and 30 processors on a cluster of the Irish Centre for High-End Computing (ICHEC).

The 3D modelling program of the WinGLink software package [*WinGLink*, 2005] is used to create the 3D meshes and starting models. The horizontal mesh size of the central area is as small as 2.5 km, with eight cells used for horizontal padding outside the central area increasing in horizontal size by a factor of 1.5. Vertical mesh size is 50 m at the surface, constantly increasing downwards by a factor 1.2. A model with irregularly increasing vertical mesh size was also appraised, containing a particularly small cell size at the depth range 100 – 140 km (assumed eLAB depth), but the resulting inversion model exhibited inversion artefacts at the respective region due to insufficient resolution at this depth range. Thus, smoothly increasing mesh size is employed for deriving models of the Tajo Basin subsurface. The final model has $21 \times 97 \times 48$ cells in E-W, N-S, and z-direction (plus an additional 10 air layers), respectively; resulting in a total mesh size of approximately $380 \times 570 \times 474$ km. The bottom two layers are fixed at values of 1 Ωm (last layer) and 100 Ωm (second last layer), which is not representative of the true Earth but to ensure that boundary conditions on the base of the model are met. Starting models comprise either a (a) homogeneous 100 Ωm halfspace or (b) a layered structure with a 100 Ωm crust (≤30 km), a 1000 Ωm lithospheric-mantle (30 – 110 km), and a 100 Ωm asthenosphere (≥100 km). The whole impedance tensor with eight degrees of freedom (four complex values) per period is used for the computation; therein only 30 periods from the range $10^{-3} - 10^{5}$ s are selected in order to reduce computation time. Following the recommendations by W. Siripunvaraporn [2008, unpublished] 5% of a normalised off-diagonal impedance element magnitude is used as error floor, i.e.

$$\text{Error floor} = 5\% \cdot \sqrt{\|Z_{xy}\| \cdot \|Z_{yx}\|}. \tag{10.3}$$

As 3D inversion is computational expensive, after five initial inversion steps models from the two different starting models are compared in order to infer to what degree they are affected by the starting model and which model to use for further inversion. For each iteration step the `wsinv3d` algorithm yields a range of inversion models (for this initial sequence up to four) with different smoothing parameters[6] (cf. Fig. 10.23). Therefore, inversion results can be investigated for a range of models with different degree of smoothness and model misfit. In Figure 10.23, the typical trade-off between model fit

[6]For sake of consistency with notation in Section 6.3 (Eqs. 6.31 and subsequent forms), in here τ is used as smoothness parameters instead of λ (used by the authors [*Siripunvaraporn et al.*, 2005a,b]).

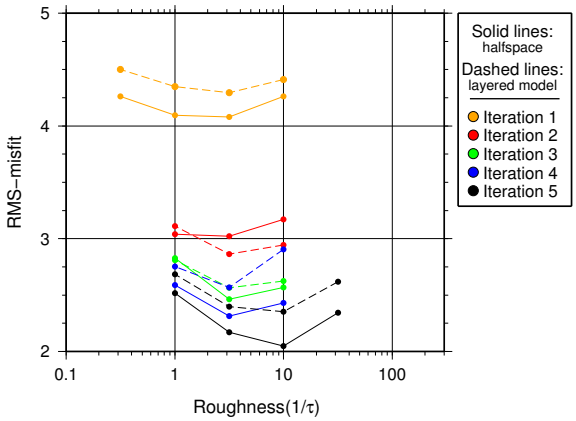

Fig. 10.23.: RMS misfit for isotropic 3D inversion models at different iteration steps (colour-coded) using a 100 Ωm halfspace and a layered arrangement as starting model (solid and dashed lines, respectively); see text for details about the layered starting model. This initial inversion sequence only involves five iteration steps for each starting model. Results are plotted in terms of RMS misfit versus roughness[6] for all models at each iteration step. The `wsinv3d` algorithm [*Siripunvaraporn et al.*, 2005a] yields up to four models at each iteration step and uses the lowest misfit model as starting model for the following inversion step (cf. Sec. 6.3).

and smoothness (i.e. inverse of model roughness) is observable for a higher number of iterations, i.e. iteration 5 (models with higher roughness and misfit represent inferior results). Inversion models of the fifth iteration step exhibit RMS misfits in the range 2.0 – 2.5 (halfspace starting model) and 2.3 – 2.7 (layered starting model); thus, model responses exhibit an intermediate degree of similarity with the observed data. Despite the increased misfit of these models (owing to the limited number of iteration steps), results can be used to examine characteristics of the initial inversion sequence for both starting models.

For sake of clarity and compactness, illustration is limited here to models from the fifth iteration, which yield the respective lowest RMS misfit for both starting models (cf. Fig. 10.23). Herein, results are compared using a series of horizontal and vertical slices for the two models (Fig. 10.24). The most striking difference between models using either a halfspace or a layered starting model (labelled ‘a’ and ‘b’ in Figure 10.24, respectively) is the electric resistivity of the region associated with the lithospheric-mantle beneath the Tajo Basin (at depths between 30 km and 110 km). Inversion models exhibit a strong correlation in the lithospheric-mantle with their respective starting models, i.e. 100 Ωm and 1000 Ωm, respectively. Thus indicating that these deeper regions are not strongly constraint by the data or not well fit by the model at the current inversion step.

Despite the small number of inversion steps, derived isotropic 3D inversion models can be used to infer features of the Tajo Basin subsurface that are supported by data of the PICASSO Phase I project. At crustal depths (≤ 30 km), models exhibit some degree of similarity with each other as well as with the focussed isotropic 2D inversion for crustal structures (cf. Sec. 10.1.5). However, due to increased cell size and small number of iteration, some of the features are not as well established as in the focussed inversion. For example, the extensive near-surface conductor that is modelled in the focussed inversion

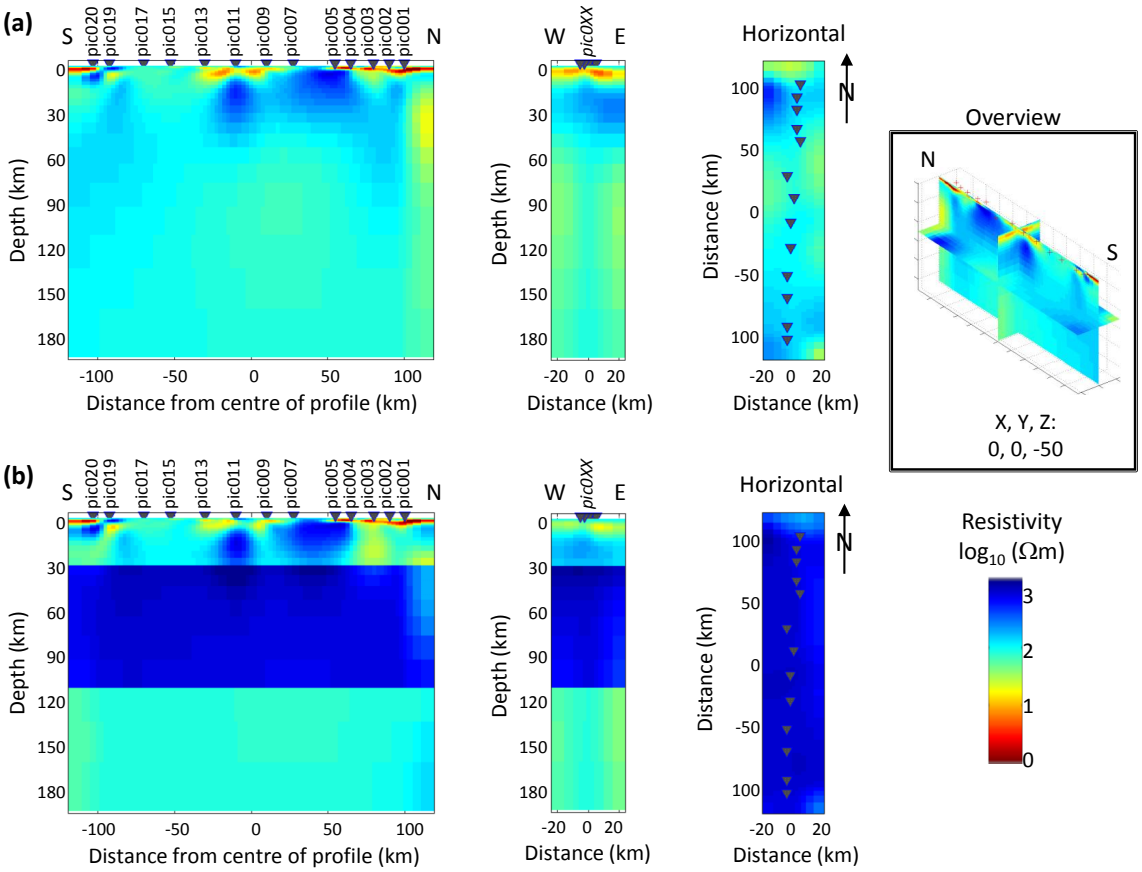

Fig. 10.24.: Results of the initial 3D inversion sequence using (a) a halfspace starting model and (b) a layered starting model. The two inversion models on display possess the minimum RMS misfit for the respective starting model, i.e. 2.05 (a) and 2.35 (b); cf. Fig. 10.23. Models are displayed, from left to right, by a vertical slice parallel to the N-S axis, i.e. approximately parallel to the PICASSO Phase I profile (left-hand plot); a vertical slice through the central area of the profile, parallel to the E-W axis (middle plot); and a horizontal slice through the model at 50 km depth (right-hand plot); relative positions of the slices are indicated in the overview plot at the top-right of this Figure.

along the whole length of the PICASSO Phase I profile (labelled 'a' in Figure 10.6) is discontinuous in the 3D inversion models. Also, the crustal region is more resistive in the isotropic 3D inversion (for both starting models) than in the isotropic 2D inversion; i.e. in the order of a few hundreds to a thousand of Ωm's in contrast to the few tens of Ωm's in the 2D inversion. Model features from this initial inversion sequence, however, are not to be over-interpreted and additional iterations are required to enhance the model.

Based on its overall lowest RMS misfit, the model obtained through inversion with a halfspace starting model and a model roughness of 10 (model 'a' in Figure 10.24) is used as starting model for an additional inversion sequence of ten iterations. After eight inversion steps the RMS misfit is reduce to 1.5 with subsequent inversion steps exhibiting higher misfits; indicating that a misfit minimum is reached (cf. Fig. 10.25). A comparison between observed and calculated responses for the minimum misfit model of the second 3D inversion sequence (labelled 'a' in Figure 10.27) is displayed in Figure 10.26; figures

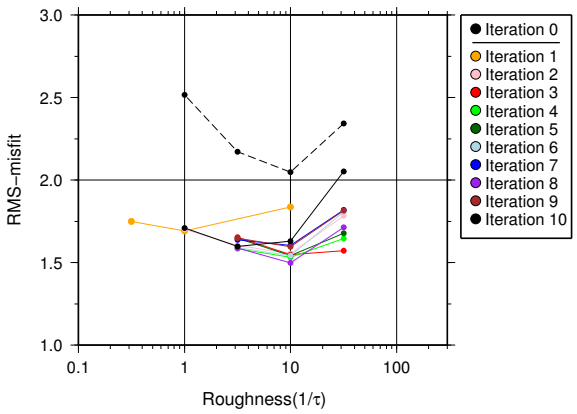

Fig. 10.25.: RMS misfit for isotropic 3D inversion models at different iteration steps of the second inversion sequence using the lowest misfit model of the initial inversion sequence as starting model; i.e. the model obtained from the fifth iteration with a halfspace starting model and a model roughness of 10 (cf. Fig. 10.23). The RMS misfits for the fifth iteration of the initial sequence are indicated by markers connected with the dashed black line. The `wsinv3d` algorithm [*Siripunvaraporn et al.*, 2005a] determined up to four models at each iteration step and uses the lowest misfit model as starting model for the following inversions (cf. Sec. 6.3). The overall lowest RMS misfit is obtained during the second inversion sequence after eight iterations (purple markers). Results are plotted in terms of RMS misfit versus roughness[6] for all models at each iteration step.

displaying individual misfits for each station are moved to the Appendix (Sec. A.4.2). It is possible that the model of the eighth iteration step represents a local, rather than the global, minimum (cf. Sec. 6.3), but owing to the considerably low misfit of this model the second inversion sequence is terminated after ten iterations (resulting in a total of 15 iteration steps).

Results of the second 3D inversion sequence are presented in terms of the lowest misfit model with the highest model roughness (RMS = 1.50, $1/\tau = 10$), the model with the lowest misfit for a slightly lower roughness (RMS = 1.59, $1/\tau = 3.16$), and the lowest roughness model (RMS = 1.75, $1/\tau = 0.32$); labelled 'a', 'b', and 'c' in Figure 10.27, respectively. The three models exhibit a strong mutual similarity, i.e. all models comprise a relatively conductive region $\leq$100 Ωm in the centre of the PICASSO Phase I profile at a depth range associated with the lithospheric-mantle beneath the Tajo Basin (i.e. 30 – 110 km). For the Earth's lithospheric-mantle usually electric resistivities in the range of 1000 Ωm or greater are determined (cf. Sec. 5.2.2). A reduction in the order of one magnitude in electric resistivity implies an unusual geological setting of the lithospheric-mantle, e.g. significantly increased temperatures or well-connected networks of conducting constituents (cf. Sec. 5.1).

Ten additional iterations are carried out to ensure that the relatively low electric resistivity of the lithospheric-mantle in the centre of the profile is not the result of smoothing constraints used during the inversion process in combination with low sensitivity of the PICASSO Phase I dataset to the lithospheric-mantle. Therein, a layered *a priori* model containing a 100 Ωm crust ($\leq$31 km), a 1000 Ωm lithospheric-mantle (31 – 110 km), and 100 Ωm sublithospheric mantle is used, which enforces a more resistive lithospheric-mantle. Inversion models obtained using the layered *a priori* model exhibit a more re-

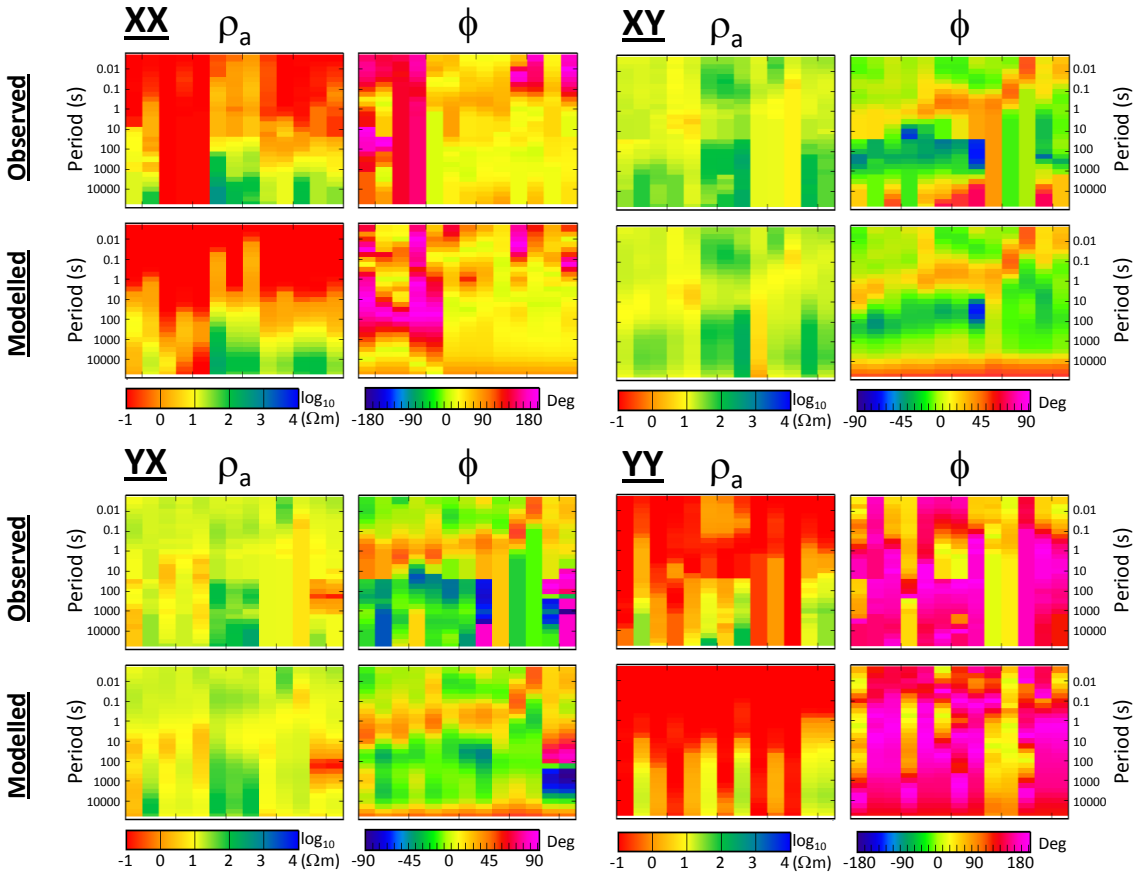

Fig. 10.26.: Comparison of observed and modelled response data for the 3D inversion model labelled 'a' in Figure 10.27 in terms of apparent resistivity (ρ_a) and impedance phase (ϕ) for all periods and stations. Due to space restrictions station labels are omitted; in each plot stations are ordered by their latitude from South (left, station pic020) to North (right, station pic001). Individual plots for each station are given in Section A.4.2.

sistive lithospheric-mantle (Fig. 10.28); however, RMS misfits are in generally higher than for the previously obtained model with a more conductive lithospheric-mantle (cf. Fig. 10.29)

To examine feasibility of a more resistive lithospheric-mantle region as well as the possibility of a highly conductive layer in the uppermost asthenosphere, a series of forward models are generated. Models are created by using the crustal structure of the minimum misfit model obtained during the second 3D inversion sequence (labelled 'a' in Figure 10.27) and introducing an exponential decrease of electric resistivity with depth in the lithospheric mantle. The exponential decrease is controlled by the electric resistivity at the top of the lithospheric-mantle and the depth of the LAB, which is associated with a resistivity of 100 Ωm (or 10 Ωm in case of a conductive asthenosphere anomaly); sub-lithospheric regions are modelled using a 100 Ωm halfspace. In all models an electric resistivity of 710 Ωm is assigned to the top of the lithospheric-mantle, according to values obtained for the outer regions of the PICASSO Phase I profile (cf. Fig. 10.27). The LAB

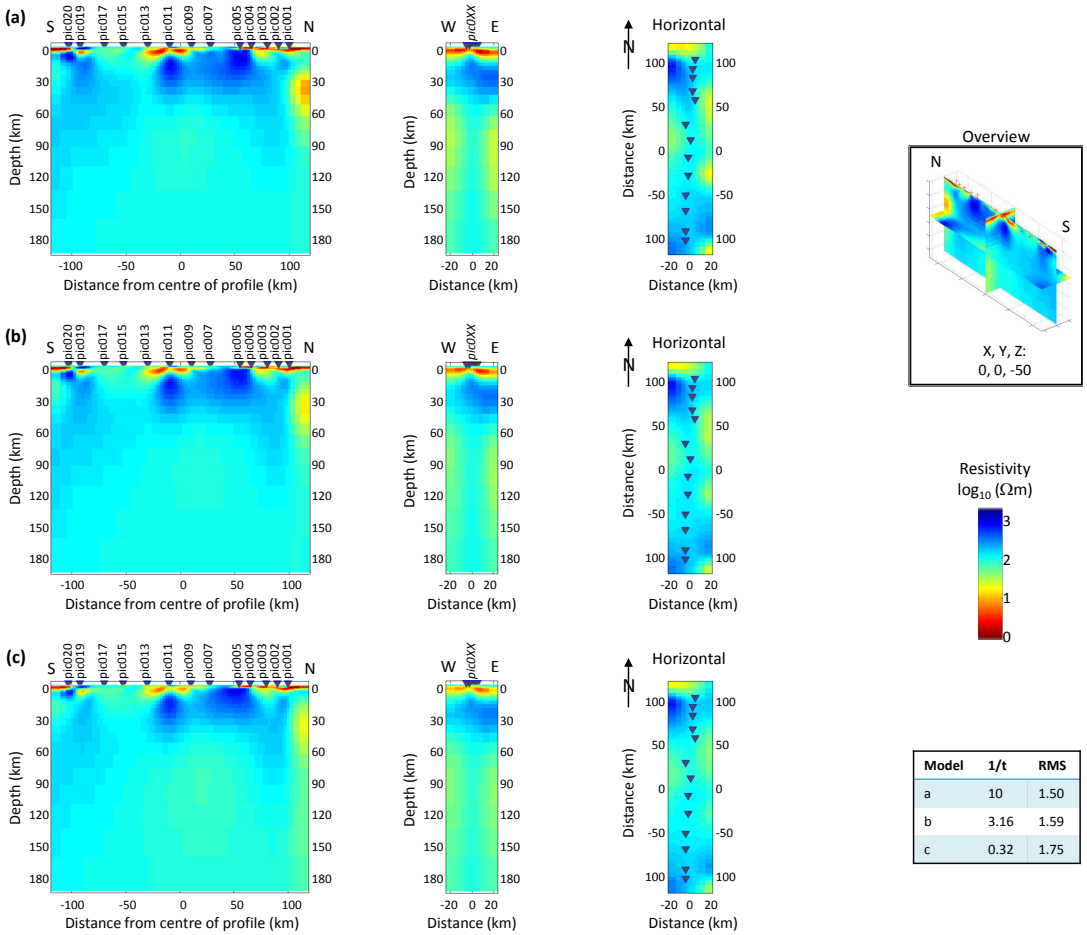

Fig. 10.27.: Results of the second 3D inversion sequence with (a) the lowest misfit model with the highest model roughness, (b) the model with the lowest misfit for a slightly lower roughness, and (c) the lowest roughness model (cf. Fig. 10.25); RMS misfits and model roughness values are shown in the box at the bottom-right of this Figure. Models are displayed, from left to right, by a vertical slice parallel to the N-S axis, i.e. approximately parallel to the PICASSO Phase I profile (left-hand plot); a vertical slice through the central area of the profile, parallel to the E-W axis (middle plot); and a horizontal slice through the model at 50 km depth (right-hand plot); relative positions of the slices are indicated in the overview plot at the top-right of this Figure.

depth, hence the exponential decrease of electric resistivity in the lithospheric-mantle, varies between models (cf. Fig. 10.30) allowing for an assessment of LAB depths beneath the Tajo Basin in terms of RMS misfit for the different forward models. Further, a model is created by assigning electric resistivity values to the lithospheric-mantle region beneath PICASSO Phase I profile that were obtained for the outer regions of the Tajo Basin; i.e. beneath stations pic001 – pic003 and beneath stations pic019 and pic020 (the related model is labelled ‘sidelobe’ in Figure 10.30).

For each LAB depth as well as the ‘sidelobe’ model, two additional models are created in the form of an electrically conductive asthenosphere (20 Ωm for regions below the respective LAB) or in form of an electric uppermost asthenosphere anomaly (two rows of 20 Ωm immediately below the lithosphere and a 100 Ωm halfspace below); indicated by

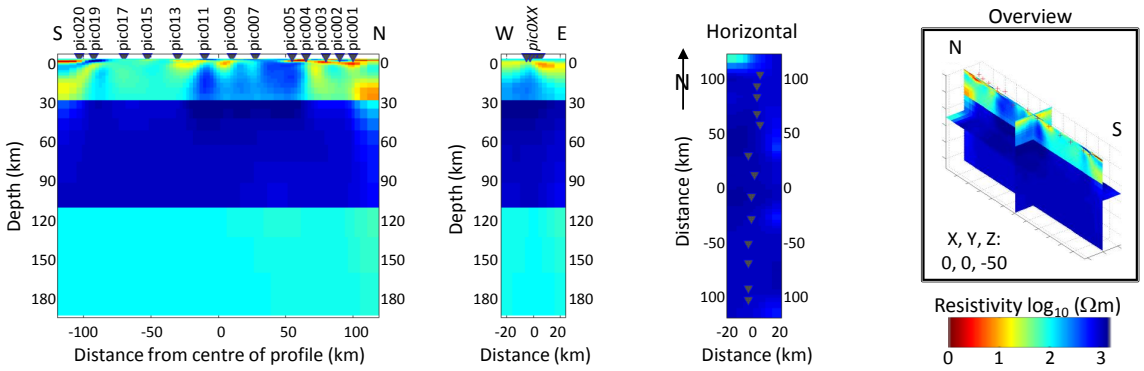

Fig. 10.28.: Lowest misfit model of the third 3D inversion sequence (cf. Fig. 10.25). The model is displayed, from left to right, by a vertical slice parallel to the N-S axis, i.e. approximately parallel to the PICASSO Phase I profile (left-hand plot); a vertical slice through the central area of the profile, parallel to the E-W axis (middle plot); and a horizontal slice through the model at 50 km depth (right-hand plot); relative positions of the slices are indicated in the overview plot at the top-right of this Figure.

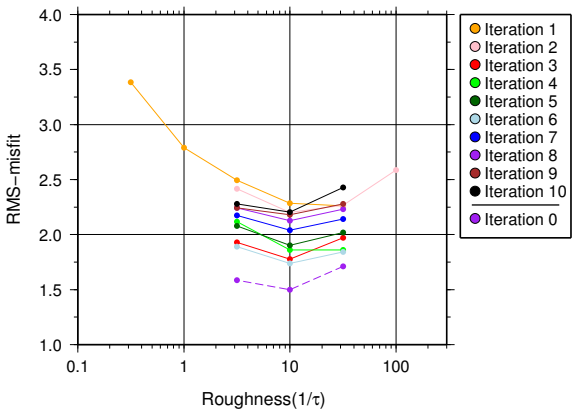

Fig. 10.29.: RMS misfit for isotropic 3D inversion models at different iteration steps of the third inversion sequence using the lowest misfit model of the second inversion sequence as starting model; i.e. the model obtained from the eighth iteration and a model roughness of 10 (cf. Fig. 10.25). The RMS misfits for the eight iteration of the second sequence are indicated by markers connected with the dashed purple line. The `wsinv3d` algorithm [*Siripunvaraporn et al.*, 2005a] determined up to five models at each iteration step and used the lowest misfit model as starting model for the following inversions (cf. Sec. 6.3). Results are plotted in terms of RMS misfit versus roughness[6] for all models at each iteration step.

dotted and dashed lines in Figure 10.30, respectively. These additional forward models are used to investigate the possibility of a more conductive asthenosphere and an uppermost asthenospheric anomaly for the Tajo Basin subsurface, which were derived by long-period EM induction studies for some regions of the Earth (cf. Sec. 5.2.2). Forward modelling is carried out using the `wsinv3d` algorithm [*Siripunvaraporn et al.*, 2005a] with the same mesh, dataset and settings that was used for the previous inversion sequences.

All forward models exhibit a higher RMS misfit than the minimum misfit model of the second inversion sequence (labelled 'a' in Figure 10.23), indicating that the relatively conductive lithospheric-mantle is supported by the PICASSO Phase I data (cf. Fig. 10.31). The increased misfit of forward models with a higher resistivity of the lithospheric-mantle is therein related to longer periods of stations in the centre of the PICASSO Phase I profile (see Figure 10.32 for the misfit distribution among a selection of models). Thus, it

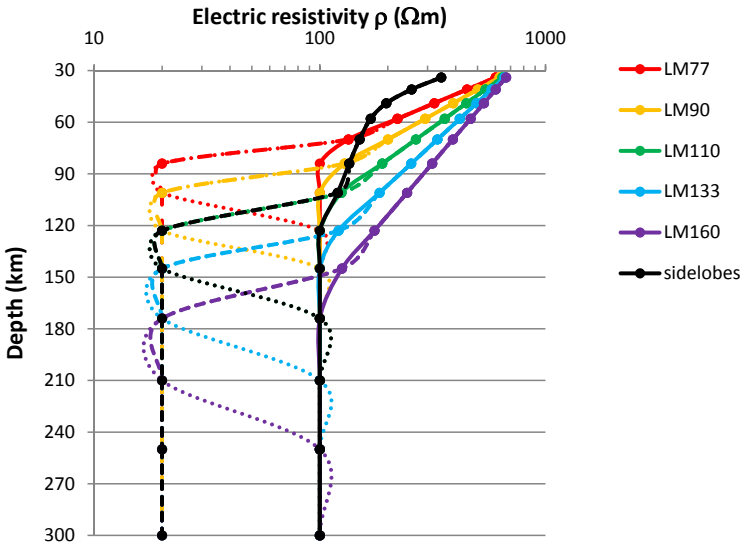

Fig. 10.30.: Smoothed resistivity – depth profiles from models of the Tajo Basin mantle used for forward modelling; at crustal depth all models comprise the resistivity distribution of the model labelled 'a' in Figure 10.27. Profiles for the different models are colour-coded and solid lines denote models with a transition from an exponential decrease of resistivity to a 100 Ωm halfspace at the lithosphere–asthenosphere boundary (LAB), dashed lines are related to models with an entirely electrically more conductive 20 Ωm asthenosphere, and dotted line denote models with an thin, electrically conductive asthenospheric layer (modelled by two rows of 20 Ωm); numbers in model names indicate the LAB depth (for the 'sidelobes' models a 110 km thick lithosphere is used). Markers denote resistivity values in the middle of the related row within a model. Further details about model characteristics and creation are given in the text.

is concluded that the relatively low resistivity of the lithospheric-mantle beneath the Tajo Basin is required by the PICASSO Phase I data. Structures in the asthenosphere are not strongly constrained by the dataset, but a highly conductive asthenosphere anomaly in the order of 20 Ωm (cf. Sec. 5.2.2) is regarded as unlikely for the Tajo Basin subsurface considering the increased misfit of responses for the model comprising a 20 Ωm layer at 110 km (labelled '053081+ea' in Figure 10.31 and 'Minimum misfit model +ea' in Figure 10.32).

The area of relatively low electric resistivity in the lithospheric-mantle beneath the Tajo Basin (Fig. 10.33) coincides with a region of low velocity derived by *Hoernle et al.* [1995], *Bijwaard et al.* [1998], *Villaseñor et al.* [2003], and *Amaru* [2007] (cf. Sec. 7.3.2). Potential sources of correlated seismic velocity decrease and electric conductivity increase in the mantle are increased temperature, or the presence of partial melt or water. Alternative sources of increased conductivity, such as interconnected sulphide or graphite phases, are unlikely to exhibit a low velocity response. Temperature variations have a significant effect on electric conductivity given the exponential ρ-T relationship (cf. Sec. 5.1.1) as well as on seismic velocity (i.e. a decrease of 0.5 -– 2% in V_p for an increase of 100°C [*Goes et al.*, 2000]). Corresponding surface expressions of an increased mantle temperature in terms of an increased surface heat flow are not observed; surface heat flow values of the Tajo Basin (65 – 70 mW/m^2, cf. Sec. 7.3.2) are equal or above the global continental average (65 mW/m^2) but lower than surface heat flow of regions with a thin lithosphere (≈80 mW/m^2) [*Pollack et al.*, 1993]. However, characteristics of the overlying

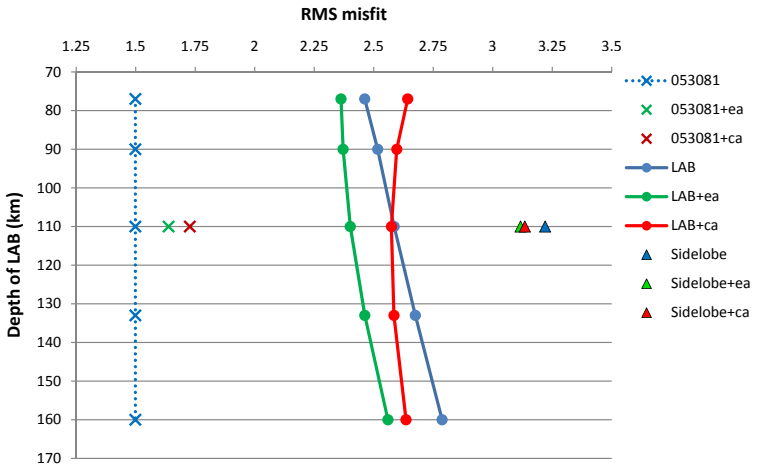

Fig. 10.31.: RMS misfit for different Tajo Basin subsurface models used to investigate the electric resistivity of the lithospheric-mantle and depth of the lithosphere–asthenosphere boundary (LAB). Models are created using crustal values of the minimum misfit model from the second 3D inversion sequence (RMS misfit = 1.50, indicate by the dotted grey line) and an exponential decrease of electric resistivity in the lithospheric-mantle with a variable LAB depth; see text for details about model construction and Figure 10.30 for a sketch of the resistivity – depth profile of the models. Symbols indicate the LAB depth of the model; the original model '053081' has no pre-defined LAB depth, thus is indicated by a dashed line. Models with the suffix 'ca' comprise an entirely electrically conductive (20 Ωm) asthenosphere, whereas models with the suffix 'ea' comprise a thin, electrically conductive asthenospheric layer in form of two rows of 20 Ωm immediately below the lithosphere; in the case of model '053081' the asthenospheric anomaly is introduced below a depth of 110 km.

crust (e.g. thermal conductance, radiogenic heat production) significantly affect surface heat flow values, rendering respective findings less conclusive.

The hypothesis of partial melt as the cause of the low velocity – high conductivity region is supported by the previously suggested extensive HIMU-like[7] reservoir beneath central and western Europe [e.g. *Cebriá and Wilson*, 1995; *Hoernle et al.*, 1995; *Goes et al.*, 1999]. Respective low velocity structures have been observed for a range of regions along the Trans-Morocean, western-Mediterranean, European fault zone (Fig. 7.17) and related to volcanic provinces in, among others, the Massif Central in France and the Eifel region in Germany [e.g. *Spakman et al.*, 1993; *Zielhuis and Nolet*, 1994; *Granet et al.*, 1995; *Bijwaard et al.*, 1998; *Goes et al.*, 2000; *Piromallo et al.*, 2001; *Ritter et al.*, 2001; *Wilson and Downes*, 2006; *Koulakov et al.*, 2009; *Tesauro et al.*, 2009b]. A lower mantle source for the European volcanism has been proposed by different authors, however, as discussed by *Goes et al.* [1999] with the current resolution of seismic tomography it is not possible to verify this hypothesis.

For the southern Tajo Basin region, partial melting may further be promoted by dehydration processes in relation with the subducting slab beneath Alboran Domain and Betic Cordillera (cf. Sec. 7.2). Hydrous phases can significantly lower the solidus of mantle materials, thereby facilitating melting at lower temperatures which results in a respectively lower surface temperature expression [e.g. *Gaillard*, 2004; *Nover*, 2005]. In addition, the presence of a hydrous phase by itself can yield a reduction of seismic veloc-

[7]HIMU: "high μ" with $\mu = {}^{238}\mathrm{U}/{}^{204}\mathrm{Pb}$

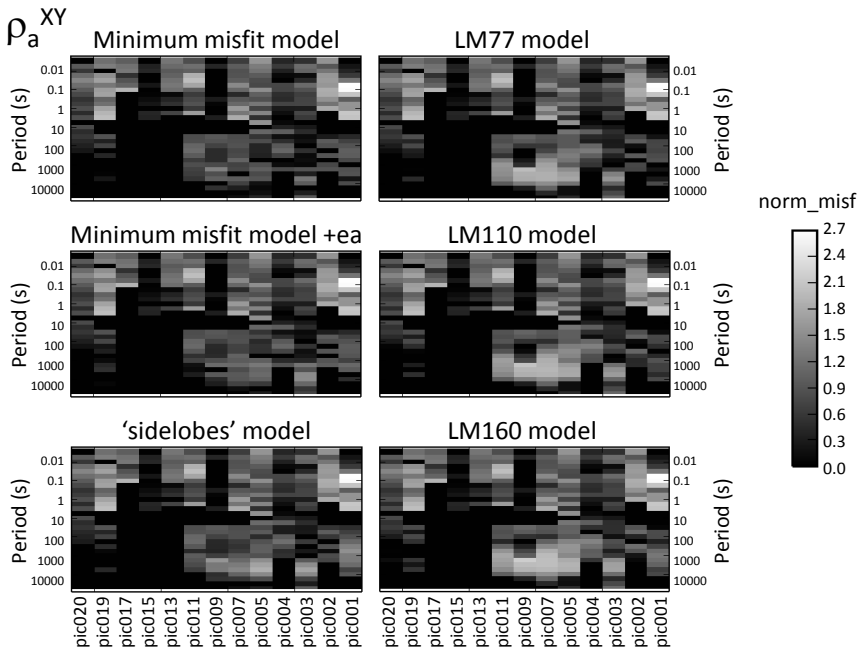

Fig. 10.32.: Misfit distribution for XY apparent resistivity data (ρ_a^{XY}) of the PICASSO Phase I stations and periods for a selection of Tajo Basin subsurface models; therein, the x-axis is positive towards North and y-axis positive towards East. Station responses are derived through forward modelling with the `wsinv3d` [*Siripunvaraporn et al.*, 2005a] and the normalised misfit is calculated via misfit $= \log_{10}\left(\frac{|\rho_a^O - \rho_a^C|}{\mathrm{Err}(\rho_a^O)}\right)$; with ρ_a^O and ρ_a^C observed and calculated apparent resistivity, respectively. The particularly low misfit for longer periods of stations pic013 – pic017 originates from rejection of data due to their low signal-to-noise ratio (cf. Sec. 9). The variation in misfit between models is most significant for longer period data (>10 s) of stations in the centre of the profile (pic007 – pic011) related to the lithospheric-mantle beneath the central region of the Tajo Basin.

ity and an increase of electric conductivity (cf. Secs. 5.1 and 5.2.2), and may be the cause of the lithospheric-mantle anomaly beneath the Tajo Basin.

Answering the question regarding the origin of the low velocity – high conductivity anomaly in the Tajo Basin mantle is impeded by limitations of MT and seismic tomography approaches: whereas MT investigation is challenging due to the limited penetration of EM waves for regions of increased conductivity and the resulting lower sensitivity to deeper regions (cf. Sec. 3.3) as well as the increased uncertainty levels of long periods in the PICASSO Phase I dataset; seismic tomography suffers from, particularly vertically, smearing of features [e.g. *Nolet*, 2008, Section 15.3]. Thus, the extent of subsurface features is not particularly well defined. In addition, the resolution of MT and seismic models is limited by the, downward increasing, cell height of the underlying meshes, resulting in a vertical extent of approximately 20 km and 13 km for cells at a depth of 100 km in the MT and seismic tomography mesh, respectively. In case of the MT model, increasing cell size is required to yield a model with a manageable number of cells that can be handled by the 3D inversion algorithm (cf. Sec. 6.3). A model with a non-linear variation of cell size, which would facilitate smaller cells in an area of interest, is not feasible as it introduces inversion artefacts to the model owing to insufficient resolution at this depth range.

In addition to information about the Tajo Basin mantle, the 3D inversion model pro-

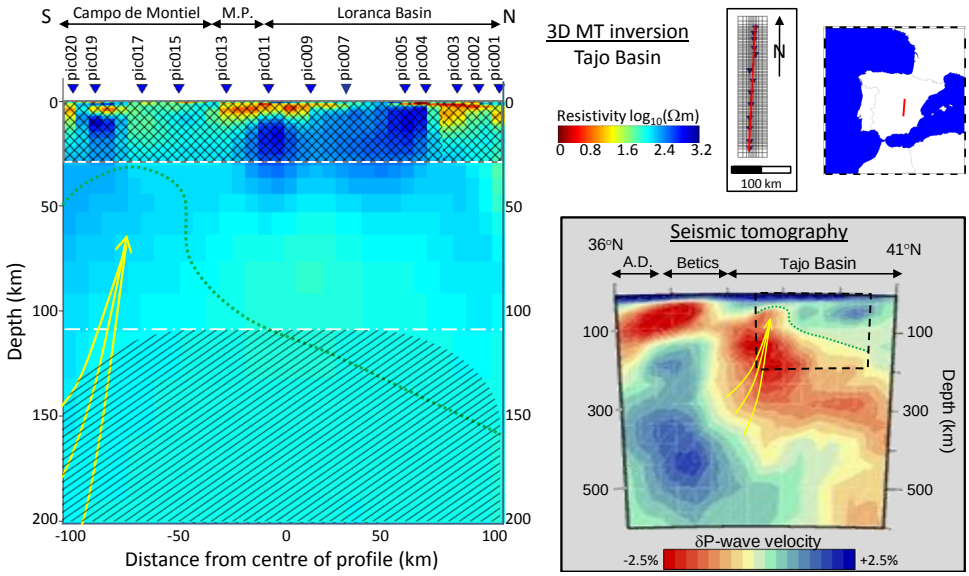

Fig. 10.33.: Comparison of the isotropic 3D inversion result of PICASSO Phase I station responses in the Tajo Basin (left) and a seismic tomography transect extracted from the global P-wave velocity model of *Amaru* [2007] (bottom-right); similar seismic results are obtained by *Hoernle et al.* [1995], *Bijwaard et al.* [1998], and *Villaseñor et al.* [2007] for the same region (cf. Chap. 7). Location of the PICASSO Phase I stations and course of the profile on top of the inversion mesh are shown on the top-right of this figure, next to a map of the Iberian Peninsula in which the PICASSO Phase I profile in the Tajo Basin is indicated by a red line. Geological regions, based on the USGS EnVision map for Europe (Figure 9.1), are shown on the top of the MT inversion model (M.P: Manchega Plain). The location of the MT inversion model in respect to the seismic transect is indicated by the dashed black lines on top of the seismic model. The dotted green line indicates the upper range of the low velocity region beneath the Tajo Basin (plotted on top of the seismic as well as on the MT model). Yellow lines represent potential fluid migration paths that may originate from dehydration of the subducting slab beneath Alboran Domain (A.D.) and Betics (indicated by high velocity feature in the seismic inset) and intrude into the lithosphere beneath the Tajo Basin; see text for details. White dashed and dotted-dashed lines on top of the MT inversion model indicate inferred approximate location of the crust-mantle and the lithosphere–asthenosphere boundary (LAB), respectively (cf. Chapter 7 and Section 8.3.3). Structure at crustal depth are not strongly constrained because the focus of this isotropic 3D inversion was on investigating mantle structures, whereas characteristics of sublithospheric regions are not strongly constrained by the inversion due to the low signal-to-noise ratio of related impedance estimates (the location of these weakly constrained regions are indicated by shaded areas); see text for further details.

vides useful insights about the source of the high conductivity – low velocity anomaly in the middle and lower crust beneath the Campo de Montiel region (feature ‘f’ in Figure 10.6). In the 3D inversion result, the crustal anomaly is modelled to the west of stations pic015 – pic019 at a depth of approximately 10 – 25 km (cf. Fig. 10.34), which is in excellent agreement with induction arrow directions (Figure 10.12) and results of the ambient noise tomography study by *Villaseñor et al.* [2007] (Figs. 7.21 and 10.11). Hence, 3D inversion is supporting previous conclusions that this high conductivity anomaly is a relatively small-scale feature and correlated with the low seismic velocity anomaly; see Section 10.1.5 for a discussion of this feature.

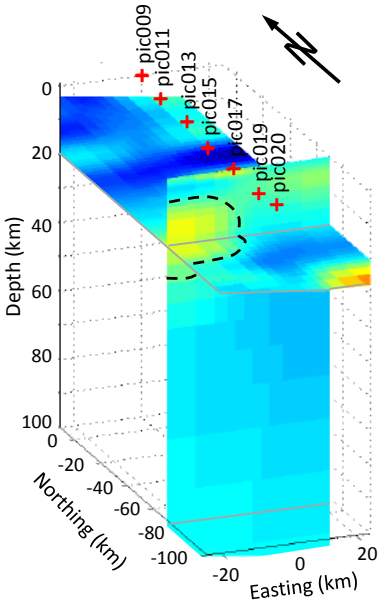

Fig. 10.34.: Location of the southern Tajo Basin mid-crustal high conductivity anomaly in the isotropic 3D inversion model. The anomaly is located to the west of stations pic015 – pic019 at a depth of approximately 10 – 25 km; cf. feature in 'f' Figures 10.6 and the comparison between the crustal inversion model and collocated seismic tomography results in Figure 10.11 as well as the induction vectors in the related region shown in Figure 10.12.

10.3. Summary and conclusions

This Section comprises a summary of the PICASSO Phase I inversion results for crustal and mantle structures of the Tajo Basin that were conducted as part of this thesis work (in Sections 10.1 and 10.2, respectively), as well as a discussion of model features. Findings of previous investigations in the Tajo Basin (presented in Chapter 7) are used to contrast and compare the PICASSO Phase I results. Models of electric resistivity distribution in the Tajo Basin subsurface, derived by the different inversion approaches employed in the PICASSO Phase I investigation, are displayed in Figures 10.6 (crust), 10.14 (mantle, isotropic 2D smooth inversion), 10.16 (mantle, isotropic 2D sharp-boundary inversion), 10.17 (mantle, anisotropic 1D inversion), 10.21 (mantle, anisotropic 2D inversion), 10.22 (average resistivity–depth profile from anisotropic 2D inversion), 10.33 (mantle, isotropic 3D inversion), and 10.34 (location of the conductive crustal anomaly in the Iberian Massif in the 3D inversion model), with thorough descriptions of the models and parameters used for their derivation given in the respective sections.

For the Tajo Basin a sedimentary thickness of approximately 3 km was determined with fluid accumulation concluded as source of the electric conductor at the bottom of the sedimentary layer. The thickness of the sedimentary layer matches previous seismic reflection results by, among others, *Banda et al.* [1981], the *ILIHA DSS Group* [1993], and *Díaz and Gallart* [2009] (cf. Fig. 7.20 and Tab. 7.2). The geoelectric strike direction determined for the Tajo Basin crust, i.e. N40.9W, is in good agreement with the NNW-SSE direction of faults intersecting the PICASSO Phase I profile in this area (cf. Sec. 9.6.1 and Fig. 7.15); vertical extents of the faults, however, could not be determined in this study.

Below the sedimentary layer, a distinct separation between Mesozoic – Cenozoic basement rocks of the "Alpine Spain" and the Precambrian and Paleozoic rocks of the Iberian Massif ("Variscan Spain", cf. Sec. 7.1) is evident in terms of electric resistivity. The Mesozoic – Cenozoic rocks, situated in the north of the PICASSO Phase I profile, exhibit generally a less resistive nature and some indication of layering that is similar to structures proposed by seismic studies for regions in the proximity of the PICASSO Phase I profile (cf. Sec. 7.3.2). The interface between the "Alpine Spain" and "Variscan Spain" regions below the PICASSO Phase I profile is located between stations pic009 and pic011, near the city of Belmonte (Cuenca Province). Therefore, this study suggests an eastward extension of the Iberian Massif beneath large parts of the southern Tajo Basin, much farther to the east as what may be inferred from surface geology maps (cf. Figs. 7.1 and 9.1), confirming results of the surface wave tomography study by *Villaseñor et al.* [2007] (cf. Fig. 7.21).

Within the electrically resistive Iberian Massif, beneath the Campo de Montiel region to the west of the PICASSO Phase I profile, a mid- to lower crustal conductor was derived that coincides with a low velocity anomaly deduced by surface wave tomography studies (cf. Fig. 7.21). Based on observed Miocene and Pliocone volcanic events in the Calatrava Volcanic Province (CVP, located to the west of the PICASSO Phase I profile)

and the proposed source region located to the east of the PICASSO Phase I profile, remnants of asthenospheric partial melt intrusion were identified as most likely cause of the high conductivity – low velocity anomaly. Owing to an insignificant increase of surface heat flow in the region, it was further concluded that conductivity and velocity expressions of the anomaly are increased by a hydrous phase. The hydrous phase may originate from dehydration processes of the subducting slab beneath the Alboran Domain and Betic Cordillera; this hypothesis is supported by low electric resistivities and low seismic velocities of mantle regions beneath the anomaly (cf. Fig. 10.33). However, electric resistivity values of mantle regions are not strongly constrained due to low signal-to-noise ratios of related data.

The electric resistivity distribution of the Tajo Basin mantle were investigated in this thesis using a number of different inversion approaches. In addition to commonly applied isotropic 2D inversion, novel 1D and 2D anisotropic inversion approaches were utilised owing to their successful application in a synthetic model study (cf. Chap. 8). The use of these additional approaches were motivated by the intricate structure of the Tajo Basin subsurface comprising oblique geoelectric strike directions at crustal and mantle depths, which caused severe artefacts in isotropic 2D inversion.

Anisotropic 1D inversion proofed inapplicable owing to the relatively complex nature of the Tajo Basin subsurface, with respective inversion models exhibiting implausible distributions of electric resistivity. Anisotropic 2D inversion yielded more realistic models of the mantle region beneath the Tajo Basin, but results suffer from the fact that the geoelectric strike direction between crustal and mantle region is 70° (instead of 90°). The issue of strike angles different from 90° is related to limitations of the `MT2Dinv` algorithm used for the inversion; i.e. in the `MT2Dinv` algorithm, the direction of the anisotropic axes must coincide with the axes of the inversion mesh. Hence, the anisotropy direction used to image the geoelectric strike at mantle depths, is limited to directions parallel and orthogonal (i.e. 0° or 90°, respectively) to the crustal strike adapted profile.

Despite these limitations, anisotropic 2D inversion results provided a depth estimate of approximately 110 km for the electric lithosphere–asthenosphere boundary (LAB) beneath the Tajo Basin, which is in agreement with previous MT investigations to the south of the PICASSO Phase I profile by *Rosell et al.* [2010] and results of integrated modelling studies by *Fullea et al.* [2007] and *Fullea et al.* [2010], as well as with estimates of the thermal LAB from thermal modelling by *Tejero and Ruiz* [2002] and transformation from seismic tomography results by *Tesauro et al.* [2009a] and *Tesauro et al.* [2009b]. Estimates of the thermal LAB that are based on thermal modelling are, however, associated with a higher degree of uncertainty, due to required assumptions about thermal conductivity and heat production of the crust (cf. Sec. 7.3.2). The estimated depth of 110 km for the electric LAB is within the depth range determined by *Jones et al.* [2010] for Phanerozoic Europe, i.e. 98±56 km (excluding the Alps) or 89±49 km (median smoothed, excluding northern Germany); however, no data from the Iberian Peninsula were included in the study by *Jones et al.* [2010].

Due to the limitations of isotropic and anisotropic 1D and 2D inversion approaches and

owing to availability of a state-of-the-art algorithm and high-end computational facilities, an extensive 3D inversion study was conducted to enhance information about the Tajo Basin mantle region. The most striking feature therein is the low resistivity region in the lithospheric-mantle below the centre of the PICASSO Phase I profile, coinciding with a low velocity region determined in seismic tomography studies by *Hoernle et al.* [1995], *Bijwaard et al.* [1998], *Villaseñor et al.* [2003], and *Amaru* [2007]. Low resistivity – low velocity regions at mantle depth are indicative of increased temperatures, interconnected partial melt or hydrous phases [e.g. *Goes et al.*, 2000; *Nover*, 2005; *Yoshino*, 2010, and reference therein]. In consideration of the reported extensive HIMU-like[7] reservoir beneath central and western Europe [*Cebriá and Wilson*, 1995; *Hoernle et al.*, 1995], partial melt was concluded as most likely source for the lithospheric-mantle anomaly beneath the Tajo Basin. An enhancement of the feature's anomalous seismic velocity and electric conductivity properties by a hydrous phase is possible, with dehydration processes of the subducting slab beneath Alboran Domain and Betic Cordillera identified as potential source for the hydrous phase.

Exceptionally low electric resistivity of the region associated with the lithospheric-mantle beneath the Tajo Basin in the 3D inversion, hence the less distinct contrast in resistivity between lithosphere and asthenosphere, aggravates estimation of the LAB depth and its characteristics. Based on forward modelling results it can be concluded that a conductive uppermost asthenosphere anomaly as well as a uniformly conductive asthenosphere in the order of 20 Ωm, observed in long-period EM induction studies of other regions (cf. Sec. 5.2.2), are unlikely for the Tajo Basin subsurface. However, due to the low signal-to-noise ration of, in particular, long-period data, asthenospheric properties are not strongly constrained by PICASSO Phase I results.

Part V

Summary, Appendix, and Bibliography

There are known knowns. These are things we know that we know. There are known unknowns. That is to say, there are things we know now we don't know. But there are things we do not know we don't know.

– Donald Rumsfeld

11 Summary and conclusions

The key results of this thesis are (i) the development of a novel inversion approach for cases of oblique geoelectric strike directions at crustal and mantle depths and (ii) the processing, modelling, and interpretation of a magnetotelluric (MT) dataset acquired during the PICASSO Phase I fieldwork campaign in central and southern Spain. Principles and application of the novel anisotropic inversion approach in a synthetic 3D model study were illustrated in Part III; application of this approach to a real dataset, together with other methods used for the investigation of the Tajo Basin subsurface, were described in Part IV. In this Chapter, results of the novel inversion approach study and the PICASSO Phase I investigation are summarised and suggestions for future work are given. More detailed summaries of results from the inversion approach and the PICASSO Phase I investigation are given at the end of the respective Parts, i.e. in Sections 8.4 and 10.3.

11.1. Novel anisotropic inversion approaches for the case of oblique geoelectric strike directions

11.1.1. Summary and conclusions

The development of the novel inversion approach was motivated by the oblique geoelectric strike directions observed at crustal and lithospheric-mantle depths in the PICASSO Phase I study area and the problems of commonly employed isotropic 2D inversion of MT data in cases of oblique geoelectric strike directions. Whereas recovery of crustal structures can, in most cases, be achieved in a straightforward manner by limiting the modelled period range to crustal penetration depths, deriving mantle structures is more challenging with isotropic 2D inversion in the case of an overlying crust with different geoelectric strike direction. Thus, investigators may resort to computationally expensive 3D inversion in order to derive the electric resistivity distribution at mantle depths.

In the novel approaches presented in this thesis, electric anisotropy is used to image 2D

structures in one depth range, whereas the other region is modelled with an isotropic 1D or 2D approach; as a result significantly reducing computational costs of the inversion. The 1D and 2D versions of the novel approach were tested using a synthetic 3D subsurface model with orthogonal strike directions at crust and mantle depths and later applied to the PICASSO Phase I dataset from central Spain. Performance of the novel approaches were therein compared to results of isotropic 2D and isotropic 3D inversion.

Structures at crustal depths were reasonably well recovered by all inversion approaches in the synthetic model study, whereas recovery of mantle structures varied significantly between the different approaches. Isotropic 2D inversion models, despite decomposition of the electric impedance tensor and using a wide range of inversion parameters, exhibited severe artefacts in the synthetic model case and yielded implausible structures for the real dataset, confirming the requirement of either an enhanced or a higher dimensionality inversion approach.

With the anisotropic 1D inversion approach, mantle structures of the synthetic model were recovered reasonably well with anisotropy values perpendicular to the mantle strike direction (in this study anisotropy was assigned to the mantle region), indicating applicability of the novel approach for basic subsurface cases. For the more complex Tajo Basin subsurface the anisotropic 1D inversion approach did not yield a plausible model of the electric resistivity distribution. Inadequacy of the derived model originates therein most likely from inapplicability of the 1D approximation to the complex structures of the Tajo Basin subsurface, exhibiting multiple indications of 2D and 3D features.

Owing to the higher number of degrees of freedom, the anisotropic 2D inversion approach can cope with more complex subsurface cases and it yielded a reasonable reproduction of the synthetic model as well as a plausible model for the Tajo Basin subsurface using the PICASSO Phase I dataset. However, the anisotropic 2D inversion algorithm used in this study requires coincident directions of structural strike and anisotropy. Thus, the algorithm facilitates only a difference of 90 degrees between the strike directions of crust and mantle, rather than the approximately 70 degrees determined for the Tajo Basin. Hence, subsurface models obtained with the anisotropic 2D inversion approach for cases with oblique strike directions that are significantly different from the orthogonal case must currently be associated with a higher degree of uncertainty.

11.1.2. Suggestion for future work

Further development of the anisotropic inversion approaches are strongly linked to enhancements of the inversion algorithms. Particularly useful enhancements of 2D algorithms that would improve applicability of this novel inversion approach are:

- Incorporation of anisotropy-axes directions that are independent of the inversion mesh orientation. The 1D inversion algorithm `ai1d` by *Pek and Santos* [2006] permits flexible anisotropy-axes directions, and the principle has been adopted for a 2D algorithm with some success *Pek et al.* [2011]. However, the 2D algorithm

is not yet optimised or adapted for parallel processing; thus, computation time of this algorithm is considerable long, limiting the realisation to a very small number of impedance estimates and making its application to datasets of the scale of the PICASSO Phase I project unfeasible.

- Incorporation of "anisotropy zones" in the inversion algorithm; i.e. constraining anisotropy to a different degree for certain parts of the inversion model, similar to "tear zones", which are already incorporated in current algorithms, e.g. by *Rodi and Mackie* [2001].

Respective suggestions regarding enhancements of the anisotropic 2D inversion codes have been made to the authors [R. Mackie, J. Pek, Pers. Comm., 2011], and their implementation will enable future studies to investigate applicability of this novel approach to more complex subsurface cases. In addition, it is suggested to employ the approach in a wide range of synthetic and real model studies in order to further asses its performance.

11.2. PICASSO Phase I investigation

11.2.1. Summary and conclusion

For the PICASSO Phase I investigation, magnetotelluric (MT) data were acquired along an approximately 400 km long and north-south oriented profile in south-central Spain, crossing the Tajo Basin and the eastern Betic Cordillera regions. Deep-probing investigations of Iberia, particularly in its central regions, are currently very sparse with previous investigations mostly focussing on the boundaries of the peninsula, namely the Pyrenees, the Betic Cordillera, and the Cantabrian Mountains as well as the southwestern region of the Iberian Massif. Detailed *a priori* information about subcrustal structures were previously limited to global or European-scale seismic tomography studies. Information about the electric resistivity distribution from the PICASSO Phase I investigation provides enhanced insights into the geological processes that formed the Iberian Peninsula subsurface.

The PICASSO Phase I investigation was complicated by low signal-to-noise ratios in some parts of the dataset, originating from exceptionally low solar activity during data acquisition and the well-developed DC railway line network in Spain. A range of advanced, robust data processing codes were used and deliberate rejection of corrupted impedance tensor estimates had to be carried out to provide a reliable dataset for subsequent analysis and modelling.

Varying geoelectric strike directions were determined, both along the PICASSO Phase I profile and with depth. For the Tajo Basin, constituting the northern region of the profile, a NW-SE oriented strike direction was determined for the crust and a NNE-SSW direction for the mantle. For the Betics region, located to the south of the PICASSO Phase I profile, an approximately E-W oriented geoelectric strike direction was inferred, but the

high misfits associated with impedance tensor decomposition for every direction indicate invalidity of a 2D approximation for this region. Thus, further investigation was focussed on the Tajo Basin subsurface using the novel inversion approaches developed in the course of this thesis to cope with the issue of oblique geoelectric strike directions in the basin's crust and mantle regions. In addition, extensive isotropic 2D and 3D inversions were conducted to further enhance knowledge about the geological setting.

The final Tajo Basin subsurface model is the synthesis of results from the different inversion approaches. Crustal structures in the model were determined through isotropic 2D inversion of a dataset decomposed according to the crustal geoelectric strike direction with the period range limited to crustal penetration depths. Owing to inadequacy of isotropic 2D and anisotropic 1D inversion results, and uncertainties associated with the anisotropic 2D inversion results, mantle structures were mostly deduced from the 3D inversion model. Most striking features of models for the Tajo Basin crust are:

- *A well-defined difference in terms of electric resistivity of the crust between the southern and northern parts of the Tajo Basin*. The interface between the two regions coincides with a significant change in seismic velocity determined in a seismic tomography study. The southern region exhibits high electric resistivities and high seismic velocities, whereas the northern region comprises relatively low electric resistivities and low seismic velocities. Based on the correlation of the seismic velocity model with the border between the so-called 'Variscan Spain' and 'Alpine Spain' regions for most of the Iberian Peninsula, the southern high resistivity – high velocity region was inferred to be associated with Precambrian and Palaeozoic rocks of the Variscan Iberian Massif, whereas the northern region was attributed to the domain that underwent significant Alpine deformation. Alpine deformation of the northern Tajo Basin region is related to collisions of the Iberian Peninsula with the rest of Eurasia and Africa during Late Mesozoic and Cenozoic times that resulted in the orogeny of the Pyrenees and Betic Mountain chains. It is concluded that the difference of the Alpine Spain and Variscan Spain region in terms of electric resistivity values is due to compositional differences with additional temperature effects. The Precambrian and Palaeozoic rocks of the Iberian Massif, constituting the majority of the Variscan Spain region, are significantly older than the Alpine Spain region (Mesozoic and Cenozoic material). Thus, the Variscan Spain region has undergone a respectively longer cooling, a situation similar to cratonic regions when compared with surrounding mobile belts. Compositional differences may therein involve a higher amount of resistive olivine, pyroxene, garnet components for the Variscan Spain region in contrast to the higher amount of metallic elements as well as graphite and sulphide bearing oxides in the Alpine Spain region (cf. Sec. 5.2.1). Further, higher conductivity may be indicative of an enhanced connectivity of the conducting phases in the Alpine Spain region. The enhanced connectivity may originate from deformation events during the more recent Alpine orogeny in contrast to the relatively undeformed Iberian Massif. However, additional studies about the

composition of the Tajo Basin subsurface, in particular regarding conducting phase constituents, are required before instructive assumption can be made about the connectivity of those phases. It should be noted that the PICASSO Phase I investigation and the seismic tomography model revealed an extension of the Iberian Massif beneath large parts of the southern Tajo Basin, further to the east than suggested by surface geology maps. In surface geology maps the Iberian Massif is only mapped to the west of the Tajo Basin, due to the fact that in the basin relevant outcrops are covered by sediments.

- *An electrically conductive – seismically slow anomaly in the middle and lower crust beneath the Campo de Montiel region (southern Tajo Basin).* The anomaly is situated in the region associated with the Iberian Massif, and remnants of asthenosphere-derived melt intruded during Pliocene times are inferred as the origin of the anomaly. The intrusion is associated with the second sequence of volcanic activity in the Calatrava Volcanic Province (CVP), located to the west of the PICASSO Phase I profile. The proposed source region for the asthenospheric melt is situated to the east of the PICASSO Phase I profile, with the assumed connection path between source region and volcanic province intersecting the PICASSO Phase I profile in the Campo de Montiel region. Due to a lack of a significant high surface heat flow expression in the southern Tajo Basin region, contribution of a hydrous phase was concluded, which lowers the solidus, increases electric conductivity, and lowers seismic velocity in the region. Dehydration processes of the slab subducting beneath Alboran Domain and Betic Cordillera were identified as the potential source for the hydrous phase in the Tajo Basin crust, based on reduced electric resistivities and seismic velocities of the mantle in-between the region associated with the slab and the crustal anomaly. However, large-scale fluid circulation as discussed in *Jones* [1992, and references therein] cannot be excluded as the source of the conducting phase.

- *An extensive region of significantly reduced electric resistivity in the lithospheric-mantle beneath the central Tajo Basin area, coinciding with low seismic velocities.* Low resistivity – low velocity features at mantle depths are indicative of significant melt or fluid phases or increased temperatures, and it is concluded that this anomaly is an expression of a HIMU-like[7] reservoir, the source of volcanic events throughout central and western Europe as well as in northern Morocco. A contribution of fluids originating from dehydration of the subducting slab beneath Alboran Domain and Betic Cordillera is possible. More detailed constraints on the deep-seated features in the Tajo Basin mantle are, however, impeded by the low signal-to-noise ratio of long-period impedance estimates in the PICASSO Phase I dataset.

11.2.2. Suggestion for future work

MT investigations are, like most geophysical studies, limited by availability and quality of the acquired data. Additional, target-oriented, recordings that could improve specific aspects are:

- Broad-band recordings along the 'Variscan Spain' – 'Alpine Spain' boundary in the Tajo Basin region, inferred from seismic tomography, appraising seismic findings and confirming the proposed correlation between seismic velocity and electric resistivity interfaces. These measurements could proved the basis for revising the Iberian Massif outline beneath the Tajo Basin, which is currently based mainly on surface geology mapping.

- An array of broad-band recordings in the Campo de Montiel region, to the west of stations pic017 – pic020, that further investigates properties and extent of the electrically conductive and seismically slow anomaly in the middle and lower crust. Particularly assessing the inferred contribution of a hydrous phase to the response of the proposed asthenospheric remnants and providing additional information about whether the hydrous phase originates from percolation or slab dehydration processes.

- Long-period recordings in the centre of the Tajo Basin to enhance knowledge of the low electric resistivity – low seismic velocity anomaly in the lithospheric-mantle. Further, determining electrical properties of the inferred HIMU-like reservoir and its impact on the local geology.

Future fieldwork campaigns should be scheduled for periods of increased solar activity and recording sites installed an adequate distance from DC railway lines in order to increase the signal-to-noise ratio, hence the quality of the impedance estimates. Since the study area is situated sufficiently far away from equatorial as well as the polar regions, recordings are considerably less affected by equatorial and polar electrojets that are amplified during high solar activity periods. Thus, presuming a continuation of the 11 year solar cycle, recordings during the years 2011–2016, 2022–2027, etc. are expected to yield high-quality results[1].

MT results should be supplemented by additional surface heat flow and seismic measurements, particularly in the Campo de Montiel region where the electrically conductive and seismically slow anomaly is determined. Moreover, advances in combining results of different geophysical methods and understanding of relations between corresponding parameters will significantly enhance understanding of the geological settings by ultimately yielding a petrophysical model of the subsurface. Approaches that seek to provide petrological models of the Earth's mantle have been presented by *Afonso et al.* [2008]

[1] It should be noted that the current solar cycle exhibits an elongated minimum, which may result in a shift of subsequent maxima and minima.

and *Fullea et al.* [2009], but related codes are not yet able to cope with MT responses of complex mantle geometries; nor are they currently applicable to the much more complex crustal regions.

Also suggested is a combination of MT responses from the PICASSO Phase I project and the MAGBET project in order to enhance data coverage in the Betic Cordillera region. With the combined dataset and through, potentially 3D, modelling of the subsurface it might be possible to enhance understanding of the highly complex tectonic orogeny. Again, information from complementary investigations, e.g. seismic tomography, heat flow and gravity measurements, should be used to construct a petrological model of the subsurface. Further, integrating results with projects that investigate the Alboran Sea subsurface (AMELIE, TopoMed), could facilitate detailed examination of the proposed subducting slab structure beneath Alboran Domain and Betic Cordillera. Such investigations may also allow for an evaluating of inferred dehydration processes in connection with the subducting slab and their influence on the regions above.

A Appendix

A.1. Geological evolution of the Iberian Peninsula

The Iberian Peninsula underwent numerous, often highly complex, tectonic processes during its evolution, including the collision with the rest of the Eurasian continent in Mesozoic times and the Cenozoic events that shaped the Betics region. The tectonic evolution of the Iberian Peninsula during Cenozoic times, most relevant for the study area of this thesis, was thoroughly described by *Andeweg* [2002]. In this Chapter a selection of figures from the work by *Andeweg* [2002] is used to illustrate key events with brief descriptions of the events given in the respective figure captions; periods of the events are therein given in terms of million years (Ma) before present.

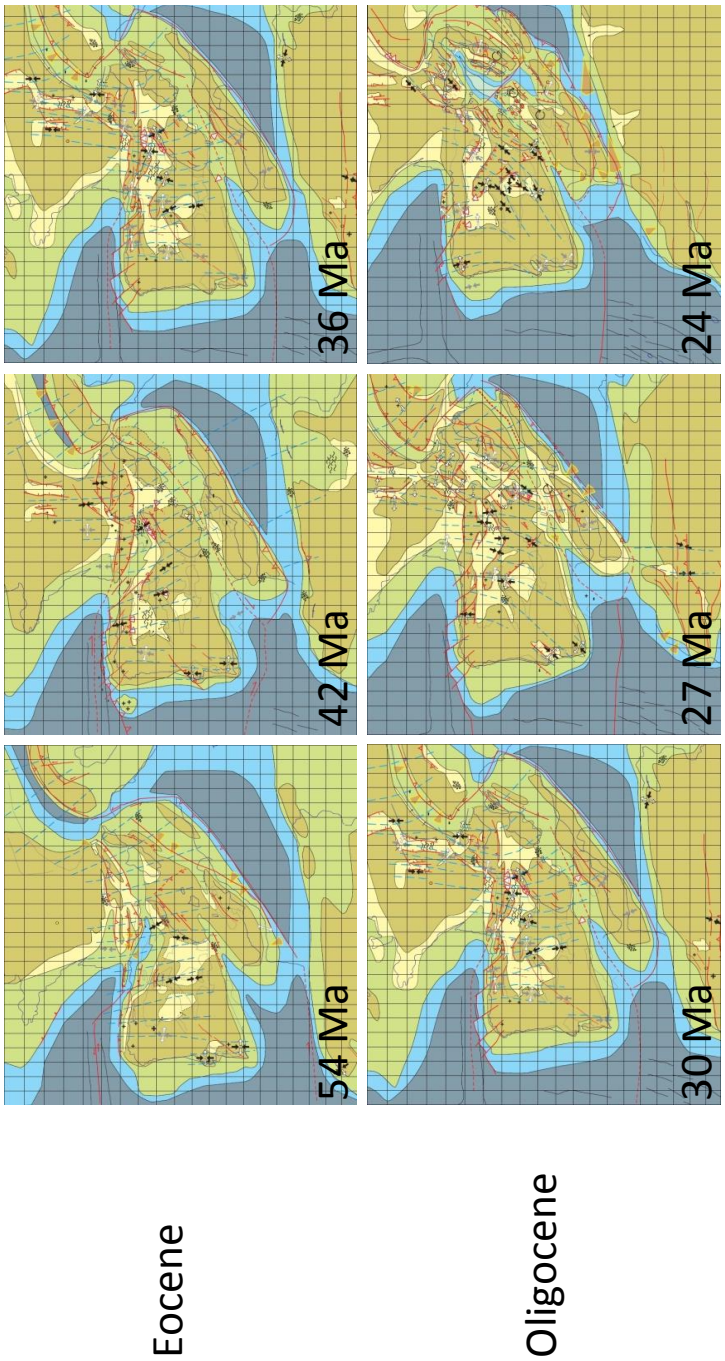

Fig. A.1.: Geological evolution of the Iberian Peninsula in terms of past and present-day stress fields; figures and related description from *Andeweg* [2002] - this Figure is continued on the next page (Fig. A.2). Main tectonic events relevant for the Iberian Peninsula for the period displayed by this figure: uplift of the Hesperic Massif (basement in western and Central Iberia) due to ENE-WSW extension with perpendicular compression, before that only the western part of the present Iberian Peninsula was emerged (54 Ma); the southern margin of the Iberian Peninsula deepens southward, thrust loading of the margin by Internal Betic units is likely (42 Ma); Uplift of the Spanish Central System (SCS) (36 Ma); Internal Betics crustal segments are stacking, resulting in an over-thickening and subsequent extensional deformation of the Internal Betics (36 Ma); inversion of the Iberian Basin starts (30 Ma); first uplift of the Sierra Altomira (24 Ma).

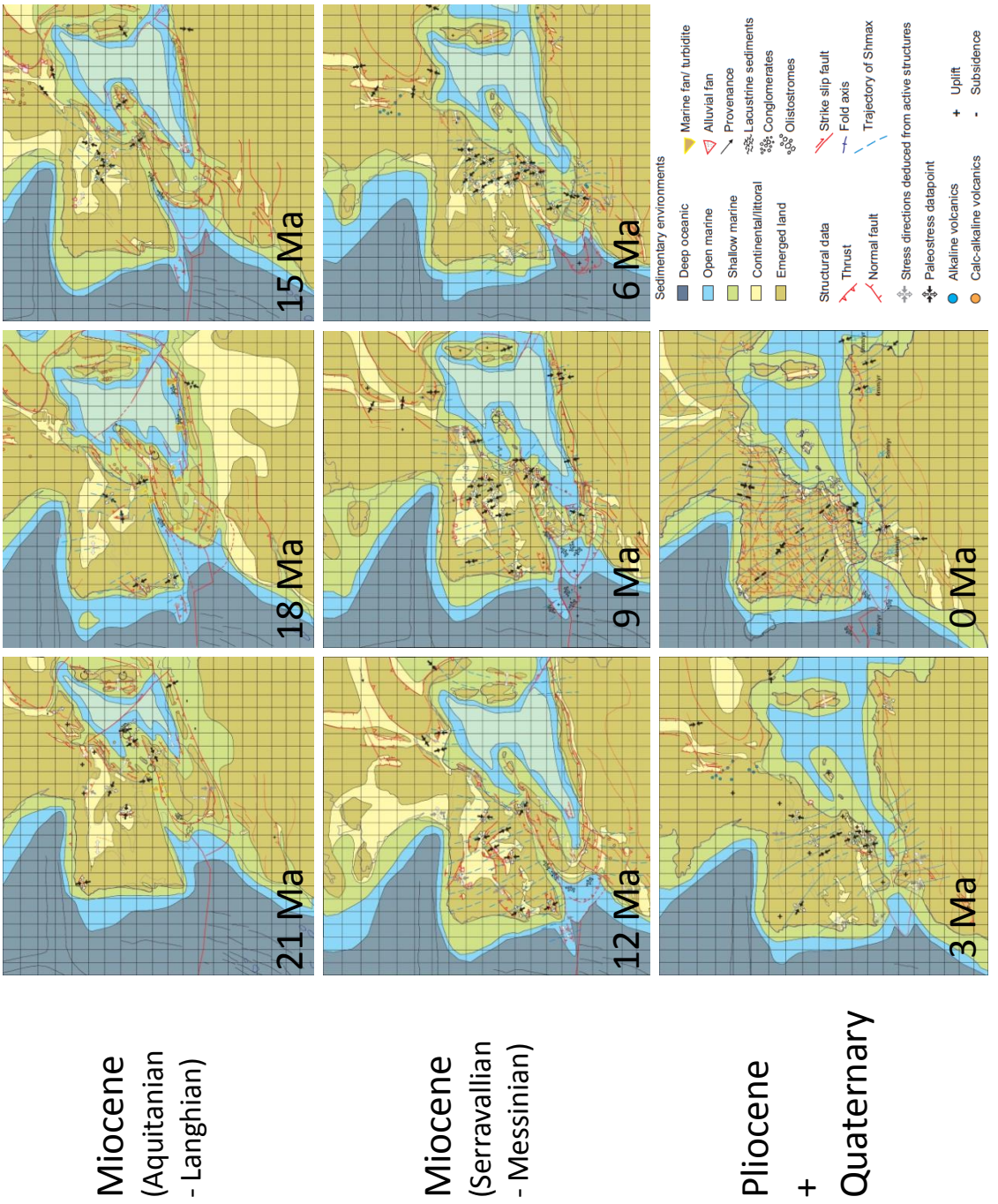

Fig. A.2.: Geological evolution of the Iberian Peninsula in terms of past and present-day stress fields - continued from Figure A.1. Main tectonic events relevant for the Iberian Peninsula for the period displayed by this figures: onset of collision between the Betics and the southern Iberian margin, resulting in compression and folding in the Eastern Prebetics (21 Ma); elevation of the SCS (15 Ma); collision of the Internal Betics with the southern margin of Iberia, resulting in major inversions throughout the entire Iberian Peninsula (12 Ma); SCS thrusts over Duero and Tajo Basins (12 Ma); thrusting of the Subbetics over the eastern Prebetics and submergence of the western External Prebetics (12 Ma); Uplift of the whole Betics, resulting in withdrawal of the sea and disconnection from marine Mediterranean or Atlantic waters (6 Ma).

A.2. Auxiliary information regarding inversion processes

A.2.1. Creating the inversion mesh

This Section explains the general procedure of creating the mesh used for 2D inversion (slight alterations are conducted between inversions). Initially a default mesh without topography is created using the `user defined mesh` tool of the WinGLink inversion software package [*WinGLink*, 2005]; therein the following parameters are applied:

- Mesh resistivity value: 1000 Ωm,
- increase factor for the horizontal block width: 1.2,
- target width for station column: 1.2 of a skin depth,
- increase factor for the vertical block width: 1.1.

Thereafter, additional columns are added along some parts of the profile to facilitate a minimum of two columns between each pair of stations throughout the entire mesh in order to allow compensation of topographic effects not accounted for with the plane model used herein (cf. Section 4 for a discussion of topographic distortion effects). Subsequently mesh values are changed to 100 Ωm (or respective values for the layered model case). In a final step all cells below a depth of approximately ten times the skin depth (see Eq. 3.44) for the longest period are removed to reduce mesh size and, thereby, computationally costs (cf. Sec. 6.3). Moreover, a conductivity of 1 Ωm is assigned to cells in the bottom row to ensure that boundary conditions are met.

A.2.2. Oblique strike intricacy

The problematic in using locally true resistivity values stems from the oblique geoelectric strike direction at crust and mantle depths. For any point on the model, a projection of structures along the mantle strike direction result in a homogeneous halfspace, due to orthogonality of the strike direction in the two depth regions. To illustrate this point a *gedankenexperiment* is conducted here, using Figure A.3 to illustrate the steps within: consider a projection of recording stations (grey) onto a profile orthogonal to the crustal strike direction (black) as shown in plot 'a' of Figure A.3. For that profile an inversion for crustal structures can be carried out using short-period data of the projected stations. The inversion result shown in plot 'b' of Figure A.3 comprises a very simple 2D subsurface model for the crust (more complex models are certainly possible, but this model is chosen to illustrate the issues of oblique strike direction even for a very simple subsurface case). Plot 'c' in Figure A.3 displays the same model together with the locations of recording sites and projected stations in 3D view for clearness. Plot 'd' in Figure A.3 illustrates the projection of the recording stations onto four profiles that are orthogonal to the strike direction at mantle depth (any other profile parallel to the the profiles 1 to 4 is valid as well, but for the sake of simplicity the display is limited to those four profiles). The location of the four profiles orthogonal to the mantle strike are shown on top of the crustal model in plot 'd' in Figure A.3 with dashed-dotted lines indicating the strike direction at mantle depths. Each of the four projected profiles is located on top of a crustal region that is only valid for one of the stations (grey-coloured station in plot 'e' in Figure A.3). Certainly, the true subsurface between each station is defined by the crustal model, but the effects of vertical interfaces on the TE and TM mode are interchanged due to the swapping of transverse and parallel components at crustal and mantle depth.

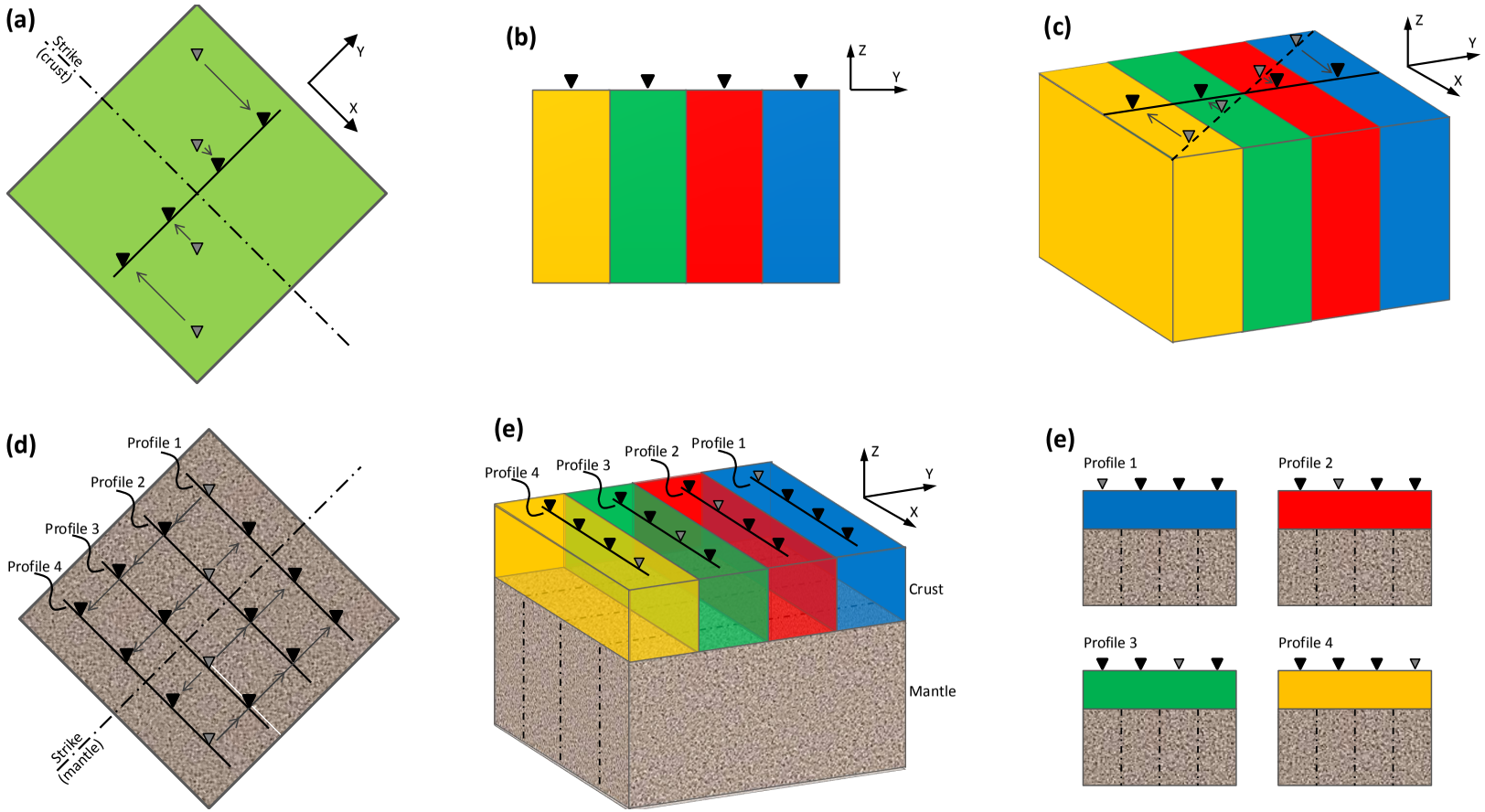

Fig. A.3.: Issues in conjunction with using the true crustal electric resistivity distribution; see text for the description.

A.2.3. Jones Catechism

The term *Jones Catechism*, named after Alan G. Jones, describes a sequence of inversion steps following the approach to "bring in structure slowly". The Catechism pursues the plan to reproduce the observed response by a minimum numbers of features with moderate conductivity values (cf. *Occam's razor*). This approach is motivated by the circumstance that MT inversion models are non-unique and that the MT method is most sensitive to the conductance of the subsurface, rather than to the conductivity of a specific region. This means that localised features with high conductivity can yield, to a certain degree, similar responses than a more extensive feature with lower conductivity (cf. Sec. 5). In MT inversion, the Jones Catechism is implemented by starting the inversion process with the phase of the TM mode, the parameter most sensitive to lateral boundaries and unaffected by static shift, before subsequently introducing the phase of the TE mode and apparent resistivities. The order of the inversion steps is suited to fit the regularisation of nonlinear conjugate gradient (NLCG) inversion (Sec. 6.3), implemented among other in the WinGLink software package [*WinGLink*, 2005].

During inversion of the PICASSO Phase I dataset the Jones Catechism is realised by initially inverting only for the TM mode with a moderate error floor for the phase and for a maximum error floor for the apparent resistivity, making the latter virtually irrelevant. Once the RMS misfit approaches a minimum value, TE mode phase data are added (again by assigning a maximum error floor to the apparent resistivity data). This is followed by further introducing first the apparent resistivity of the TM mode and thereafter of the TE mode by lowering the respective error floors. Once all modes are introduced, error floors for the parameters are subsequently reduced to a minimum, wherein values are a trade-off between error floor and RMS misfit of the model (cf. Sec. 10).

A.2.4. Computation time of inversion approaches

Inversion of the dataset is usually a fundamental but time consuming element of MT investigations; requirements in terms of computational time and equipment are therein highly dependent on the size of the dataset and the mesh as well as on the inversion dimensionality. Whereas 1D inversion can today usually realised with common desktop machines, computational expenses are significantly higher for 2D and particularly 3D inversions.

For 2D inversions of the PICASSO Phase I dataset a 3.33 GHz Intel Xeon X5680 dual core machine with 48 GB RAM was used. 3D inversions were made feasible using a parallel code and 30 nodes of the 2.67 GHz Intel Xeon CPU X5650 six-core cluster of the Irish Centre of High-End Computing (ICHEC). Computation times (in CPU time) of the different inversion approaches utilised in this thesis are summarised in Table A.1 together with respective mesh sizes and number of data points. Note that the number of iterations differs between inversion approaches, as well as between runs of each approach dependent on the inversion parameter choice; thus, computation times are given in terms of average duration required to obtain a final model. Comparison clearly demonstrates advances of 1D and 2D inversion approaches over 3D inversion in terms of associated computation times, which nerves attempts to identify cases in which 3D inversion can be substituted by lower-dimensional approaches as conducted in this work.

Inversion scheme	cpu time[a] (h)	data points[b]	sum of cells	stations	period estimates	impedance elements[c]	cells
aniso-1D	0.5	1,600	640	10	40	4	10×64
aniso-1D	8	33,600	13,440	210	40	4	210×64
iso-2D	5	800	17,064	10	40	2	108×158
aniso-2D	9	2,080	17,064	13	40	4	108×158
iso-3D	400	3,120	233,100	13	30	8	111×35×60

Tab. A.1.: Comparison of computation times for different inversion schemes used in this study, namely the codes `ai1d` (anisotropic 1D inversion) [*Pek and Santos*, 2006], `MT2Dinv` [*Baba et al.*, 2006] (isotropic and anisotropic 2D inversion), and `wsinv3d` [*Siripunvaraporn et al.*, 2005a]. [a]: rounded averages of cpu time (cpu time is the total time of a process running on the nodes of a machine; real world time, "wall time", is approximately cpu time divided by number of nodes used; [b]: product of number of stations, period estimates, and impedance elements [c]: i.e. four elements per period for anisotropic inversion (full tensor), two elements per period for isotropic inversion (off-diagonal elements only).

A.3. Auxiliary inversion results for the synthetic 3D subsurface model

In addition to the results shown in Section 8.3, auxiliary inversion results are derived for multiple profiles over the synthetic 3D model (cf. Fig. 8.5). For the sake of clarity, these additional inversion results are placed in this Appendix, sorted by inversion approach. In general, anisotropic inversion models excel their isotropic counterparts, confirming conclusions presented in Chapter 8 by demonstrating that respective results for the PICASSO Phase I profile can be reproduced for other profiles and stations.

Electric resistivity anomalies of profiles parallel to the strike direction of crust or mantle (Figs. A.5 – A.7 and A.9 – A.10) are due to distortion by off-profile features (as opposed to effects of oblique strike direction of regions below the mantle). Distortion owing to off-profile features is a known issue in 2D MT investigation and has been previously studied by a number of authors, e.g. *Ledo* [2005]; *Siripunvaraporn et al.* [2005b], and is not the topic of this investigation. Respective models are not discussed at great length in this study, but are included in the appendix for completeness and to confirm results of profiles intersecting both regions with oblique geoelectric strike directions.

A.3.1. Isotropic 2D inversion

Inversion for the profiles in this Section is carried with the same choice of parameters that were determined in Section 8.3.1 to yield models closest to the subsurface of the synthetic 3D model. Results of isotropic 2D inversion generally exhibit a low RMS misfit (< 3 with a 5% error floor for phases and 10% error floor for apparent resistivities); increased misfits originate for most models from smoothing constraints of the inversion process contradicting the sudden changes of electric resistivity in the synthetic 3D model. Despite the low misfit, the isotropic 2D inversion model are not an adequate reproduction of the 3D model subsurface. Inversion results for the 3D-mantle profile with stations synE02 – synL09 (Fig. A.4), decomposed according to the strike direction of the mantle (N45E), support the findings of the same profile using stations pic001 – pic020 (cf. Fig. 8.8). Inversion models for the 3D-crust profile with stations synE02 – synL09 (Fig. A.8) decomposed according to the strike direction of the crust (N45W), differ significantly from the synthetic model subsurface. Instead, 3D-crust profile inversion models exhibit values similar to the results of profiles parallel to the mantle strike direction (cf. Figs. A.9 and A.10). Therefore, these models indicate the insensitivity of data decomposed according to the strike direction of the crust to the electric conductivity distribution of the mantle, hence the inadequacy of isotropic 2D inversion for a subsurface with oblique geoelectric strike directions.

3D-mantle profile

Inversion results for the 3D-mantle profile using stations synE02 – synL09 (decomposed for a geoelectric strike direction N45E, see Figure A.4 for inversion results and station names) are similar to the results for the 3D-mantle profile using stations syn001 – syn020 (cf. Sec. 8.3.1). Resemblance of characteristics originates from similar locations of the stations belonging to the two datasets (cf. Fig. 8.4). For stations synE02 – synL09, a model with an overall low RMS misfit (1.51, with a 5% error floor for phases and 10% error floor for apparent resistivities) is obtained. Therein, apparent resistivity responses for TE and TM mode data at stations to the south are generally slightly lower than for the true model, whereas responses for the stations to the north are generally slightly higher. The misfit is likely to originate from smoothing constraints inherent in the inversion process (cf. Sec. 6.3.3). An increased misfit, for both modes, is observable in the impedance phase data at periods 10 – 100 s. For this model, periods in that range are related to a depth of 30 km, i.e. the depth of the crust–mantle boundary (cf. Sec. 3.3). It is therefore reasonable to attribute these misfits to the fact that the synthetic model features an abrupt change from crustal to mantle region values, which is not permitted in the inversion model due to smoothness constraints. The circumstance that the misfit of the TE mode is generally higher than for the TM mode is in agreement with the finding that the TE mode is usually more affected by 3D structures [e.g. *Ledo*, 2005].

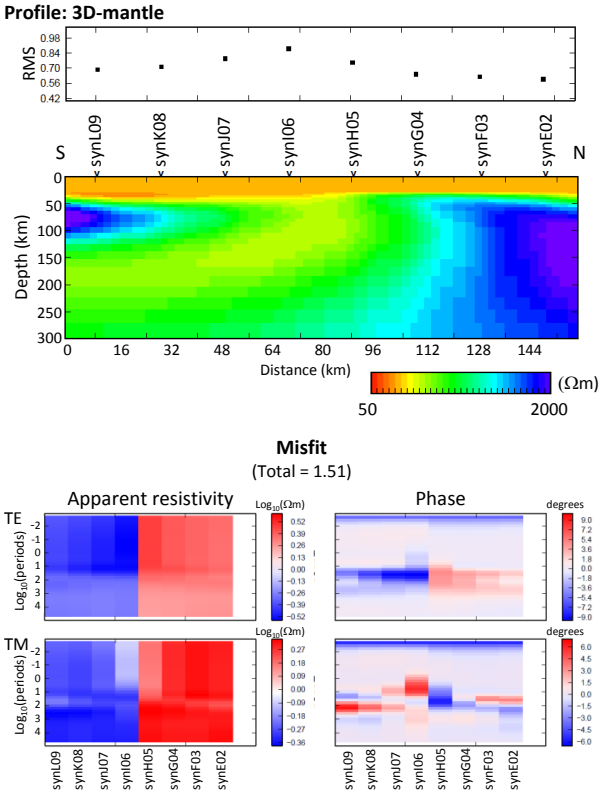

Fig. A.4.: Isotropic 2D inversion results for the '3D-mantle' profile on top of the synthetic 3D model (see Figure 8.5 for profile location). Electric resistivity interfaces at crustal and mantle depths are located between stations synI06 and synH05. Periods between 10 s and 100 s are related to the crust–mantle boundary; see Section 8.2.1 for a description of the model. During the inversion the crust is kept fixed at an electric resistivity value of 100 Ωm. The misfit of the uppermost region originates from the problematic of meeting the cell size requirements for the highest frequencies.

04-centre profile

The profile 04-centre runs parallel to the crustal strike direction and is located on top of the more conductive crustal region (50 Ωm). The profile contains stations synD04 – synM04 (see Fig. 8.4), which are decomposed according to a geoelectric strike direction N45E. The inversion result for the 04-centre profile features two regions of increased electric conductivity located just below the crust mantle boundary (see Fig. A.5). Hence, the erroneous features are likely to originate from the fixing of the crust at 100 Ωm in combination with the effect of different electric strike direction at crust and mantle depth. The inversion model does not exhibit a continuous sharp lateral change in resistivity that can be associated with the interface. Instead, the model contains a highly resistive region in the northwestern to central area at a depth between approximately 50 km and 200 km. Given the relatively low RMS misfit of the model (2.42 with a 5% error floor for phases and 10% error floor for apparent resistivities), an investigator might erroneously infer a feature at one of these depth regions, e.g. an electric asthenosphere at the bottom of the resistor. Like for the 3D-mantle profile (Fig. A.4), the misfit of the impedance phase is mostly constrained to the periods range related to the crust mantle boundary (10 – 100 s), and the misfit for the TE mode, is higher than for the TM mode. The TM mode apparent resistivity misfit exhibits a noticeable striping for periods related to the crust, which is most likely associated with incorrect decomposition of the modes at this depth range. For the case of the 3D model used in this study, with the 90 degree difference between strike directions at crust and mantle depths, the two modes are swapped. TE and TM modes are sensitive to current flow parallel to and charge build up on the face of vertical interfaces with a direction orthogonal to the profile, respectively. Thus, swapping of the modes introduces additional vertical interfaces, which are prohibited here due to the fixing of the crust; however the conductive features at the crust mantle boundary could be indicators of effects due to the mode swapping.

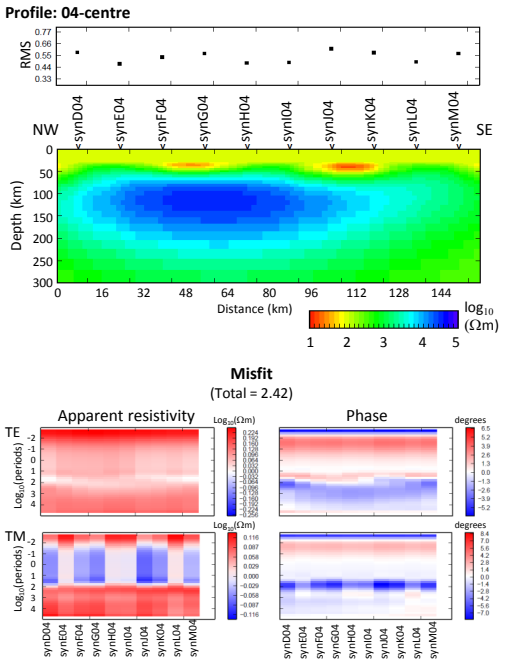

Fig. A.5.: Isotropic 2D inversion results for the '04-centre' profile on top of the synthetic 3D model (see Figure 8.4 for station locations). An electric resistivity interface at mantle depth is located between stations synI04 and synH04. Periods between 10 s and 100 s are related to the crust–mantle boundary; see Section 8.2.1 for a description of the model. During the inversion the crust is kept fixed at an electric resistivity value of 100 Ωm. The misfit of the uppermost region originates from the problematic of meeting the cell size requirements for the highest frequencies.

07-centre profile

The profile 07-centre is parallel to profile 04-centre, with the difference that the 07-centre profile is located on top of the more resistive crustal region (200 Ωm); see Figure 8.4 for the location of the stations. Inversion results for the 07-centre profile (Fig. A.6) are similar to the model for profile 04-centre (note the different colour scale) with the difference that for the 07-centre profile no highly conductive feature is observable at the crust mantle boundary and that the related striping pattern of the TM mode misfit is absent. Instead, the TM mode misfit exhibits a distinct difference between data related to crust and mantle depths, i.e. for periods shorter than 10 s and longer than 100 s. Crustal response data of the inversion model are, however small, generally higher than for the true model, whereas the opposite case occurs for the mantle range. For the TE mode data, on the other hand, the inversion model is slightly lower for all stations and both depth ranges. This occurrence is exactly opposite to the characteristics of the response data for the 04-centre profile, which suggests that the different behaviour is related to the difference in crustal conductivity beneath the two profiles.

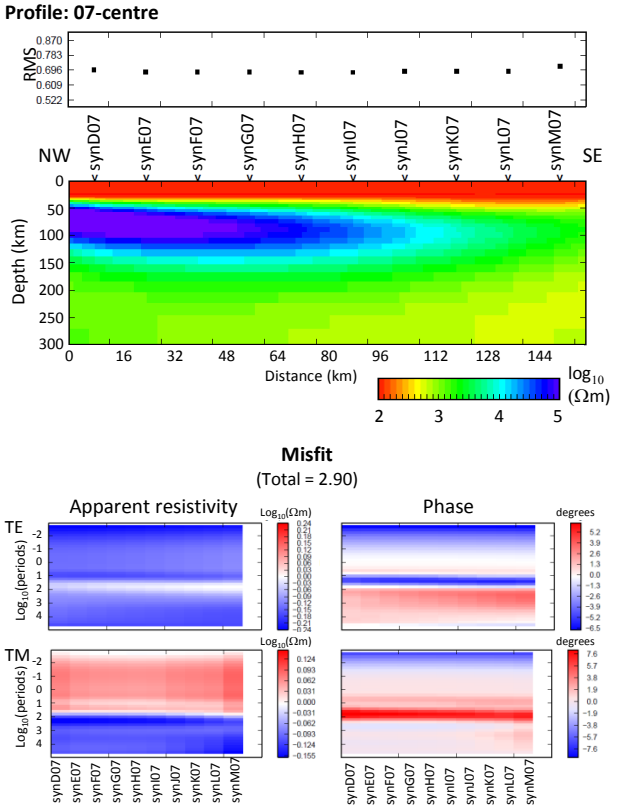

Fig. A.6.: Isotropic 2D inversion results for the '07-centre' profile on top of the synthetic 3D model (see Figure 8.4 for station locations). An electric resistivity interface at mantle depth is located between stations synI07 and synH07. Periods between 10 s and 100 s are related to the crust–mantle boundary; see Section 8.2.1 for a description of the model. During the inversion the crust is kept fixed at an electric resistivity value of 100 Ωm. The misfit of the uppermost region originates from the problematic of meeting the cell size requirements for the highest frequencies.

10-centre profile

The 10-centre profile is parallel to the profiles 04-centre and 07-centre, located on top of the more resistive crustal region, further away from the interface as the 07-centre profile (cf. Fig. 8.4). The inversion model is in general similar to the model for profile 07-centre with the difference of a significantly more conductive region in the SW of the profile (see Fig. A.7). This higher conductivity ($\approx 500\,\Omega$m) is in good agreement with the true model, denoting the decreasing effect of the crustal structures and their oblique strike direction. The RMS misfit of the 10-centre model (2.78 with a 5% error floor for phases and 10% error floor for apparent resistivities) is in the same order as the misfit for the 04-centre and 07-centre models, wherein the misfit distribution is similar to the latter (but with a significantly lower misfit of TM mode crustal data).

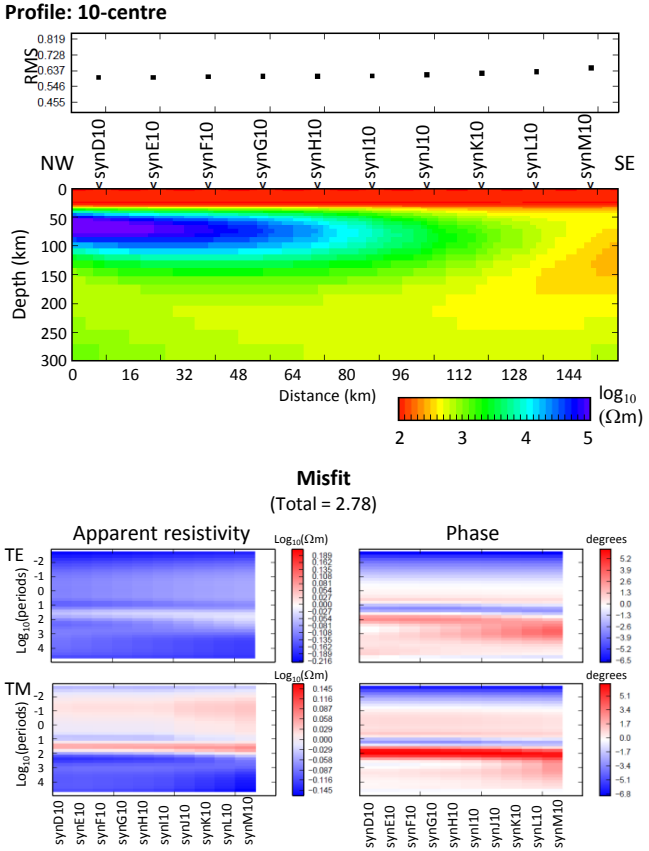

Fig. A.7.: Isotropic 2D inversion results for the '10-centre' profile on top of the synthetic 3D model (see Figure 8.4 for station locations). An electric resistivity interface at mantle depth is located between stations synI10 and synH10. Periods between 10 s and 100 s are related to the crust–mantle boundary; see Section 8.2.1 for a description of the model. During the inversion the crust is kept fixed at an electric resistivity value of 100 Ωm. The misfit of the uppermost region originates from the problematic of meeting the cell size requirements for the highest frequencies.

3D-crust profile

The profile 3D-crust uses data from the same stations as the 3D-mantle profile (see Figures 8.5 and 8.4 for the location of profiles and stations), with the difference being that the data are decomposed for a geoelectric strike direction N45W, thus fitting the crustal strike direction. The inversion adequately reproduces the crustal structures, but fails to recover structures at mantle depth (see Fig. A.8). In particular, the resistivity of the southern model region is too high and the location of the interface cannot be inferred from this inversion model. However, the RMS misfit is very low (0.70 with a 5% error floor for phases and 10% error floor for apparent resistivities), which may result in accepting the inversion model without knowledge of the true subsurface model. The misfits are insignificant (in particular, in the presence of noise) and observable misfits are due to smoothing constraints working against the recovery of the sharp contrast at the horizontal and vertical interfaces, as well as the issue of small grid size on the surface.

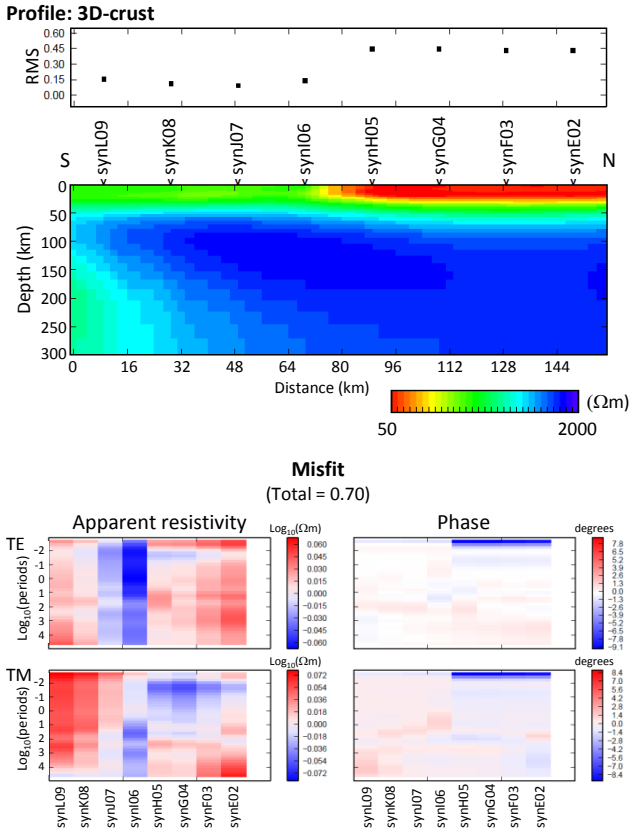

Fig. A.8.: Isotropic 2D inversion results for the '3D-crust' profile on top of the synthetic 3D model (see Figure 8.5 for profile location). Electric resistivity interfaces at crustal and mantle depths are located between stations synH05 and synI06. Periods between 10 s and 100 s are related to the crust–mantle boundary; see Section 8.2.1 for a description of the model. During the inversion the crust is kept fixed at an electric resistivity value of 100 Ωm. The misfit of the uppermost region originates from the problematic of meeting the cell size requirements for the highest frequencies.

G-centre profile

The profile G-centre runs parallel to the mantle strike direction and is located on top of the more resistive part of the mantle (1000 Ωm) containing stations synG01 - synG10 (see Fig. 8.4), which are decomposed for a geoelectric strike direction N45W. The RMS misfit of the inversion model is very low (0.61 with a 5% error floor for phases and 10% error floor for apparent resistivities) and the crustal region is adequately recovered (see Fig. A.9); however, the mantle region is, like for the profile 3D-crust, significantly different from the true model (Fig. 8.3). In particular, the SW region of the inversion model exhibits too high electric resistivity values. This discrepancy between inversion and true model responses is not reflected by the model misfit, which denoted too low apparent resistivities for the SW of the inversion model and too high values for the NE. However, these misfits for the apparent resistivity may be due to smoothing constraints, whereas the misfits of the impedance phase at the surface are due to the problematic in meeting the requirements of the highest frequencies regarding the cell size.

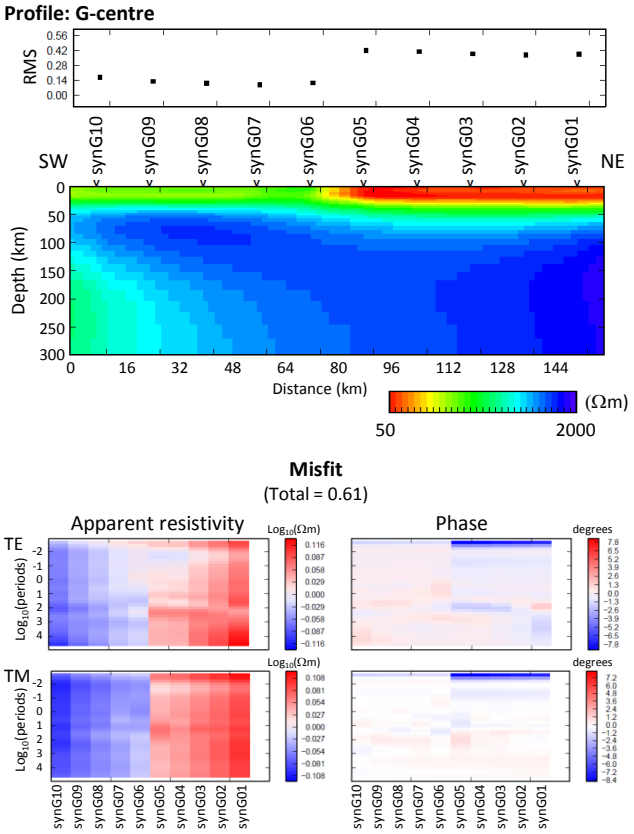

Fig. A.9.: Isotropic 2D inversion results for the 'G-centre' profile on top of the synthetic 3D model (see Figure 8.4 for station locations). An electric resistivity interface at crustal depth is located between stations synG05 and synG06. Periods between 10 s and 100 s are related to the crust–mantle boundary; see Section 8.2.1 for a description of the model. During the inversion the crust is kept fixed at an electric resistivity value of 100 Ωm. The misfit of the uppermost region originates from the problematic of meeting the cell size requirements for the highest frequencies.

J-centre profile

The J-centre profile is parallel to the G-centre profile, with the difference that the J-centre profile is located on top of the more conductive mantle region (500 Ωm); see Figure 8.4 for location of the stations. The inversion results for the J-centre and G-centre profiles are very much alike (cf. Fig. A.10), indicating the impracticality of inversions with data decomposed for the crustal strike direction.

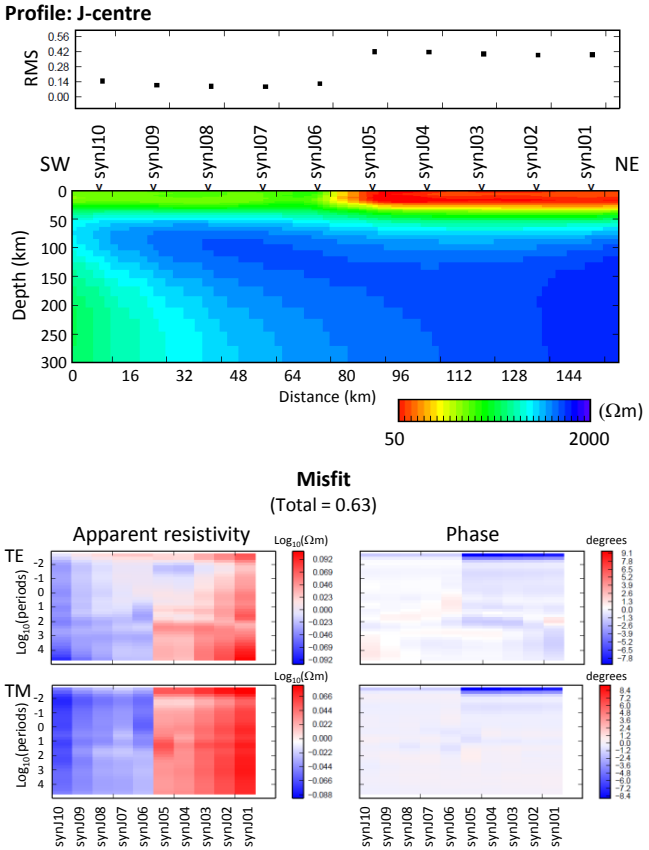

Fig. A.10.: Isotropic 2D inversion results for the 'J-centre' profile on top of the synthetic 3D model (see Figure 8.4 for station locations). An electric resistivity interface at crustal depth is located between stations synJ05 and synJ06. Periods between 10 s and 100 s are related to the crust–mantle boundary; see Section 8.2.1 for a description of the model. During the inversion the crust is kept fixed at an electric resistivity value of 100 Ωm. The misfit of the uppermost region originates from the problematic of meeting the cell size requirements for the highest frequencies.

A.3.2. Anisotropic 2D inversion

This Section contains a collection of figures displaying results of anisotropic 2D inversion for the synthetic 3D model that, for the sake of clarity, are only referred to or partly shown in Section 8.3.3. These models illustrate different aspects of the anisotropic 2D inversion approach which are recapped here in brief.

Figure A.11 demonstrates the current limitation of the second approach for the anisotropic 2D inversion (isotropic inversion of long period data in the first sequence and anisotropic inversion of short period data in the second sequence). Long period data are sensitive not only to mantle but also to crustal structures and their isotropic inversion in the first sequence yields an erroneous mantle region, which is not altered in the subsequent anisotropic inversion of the second sequence. A third sequence, consisting of anisotropic inversion of data from the whole period range can alter previous mantle structures but introduces anisotropy to the mantle region, therefore contradicting the approach and failing to reproduce mantle structures of the synthetic 3D model. As a result, the mantle region of the anisotropic 2D inversion model is significantly different from the synthetic model and any related responses exhibit an increased misfit. On the other hand, crustal structures are recovered to some degree using anisotropy to image effects of the oblique strike direction at crustal depth, with the highest anisotropy magnitude located at the crustal resistivity interface (between stations pic009 and pic011). The recovery of crustal structures indicates the potential of approach 2, which should be further exploited once recommended anisotropy-zones are included in the inversion algorithm (cf. Sec. 8.3.3).

Figures A.12 – A.14 display different results of the anisotropic 2D inversion derived using different sets of smoothness constraints. The best agreement between inversion model and synthetic 3D model is achieved using resistivity gradient regularisation with a lower smoothing parameter (τ=1).

Figures A.15 - A.18 show results of anisotropic 2D inversion for other profiles and stations used to test reproducibility of findings for the 3D-crust profile with the pic-stations (Fig. 8.17), of which only parts are shown in Section 8.3.3 (Fig. 8.19). Profiles 3D-crust-west and 3D-crust-east (Figs. A.17 and A.18) reproduce the resistivity distribution of the 3D model in principle, however, the resistivity interface at mantle depth is less constrained due to large station spacing. Profiles 3D-crust-NS and 3D-crust-EW (Figs. A.15 and A.16), on the other hand, have an equidistant station spacing of 20 km and exhibit an overall good agreement with the resistivity distribution of the synthetic 3D model. Thus, the synthetic subsurface model can principally be recovered using anisotropic 2D inversion given adequate station spacing.

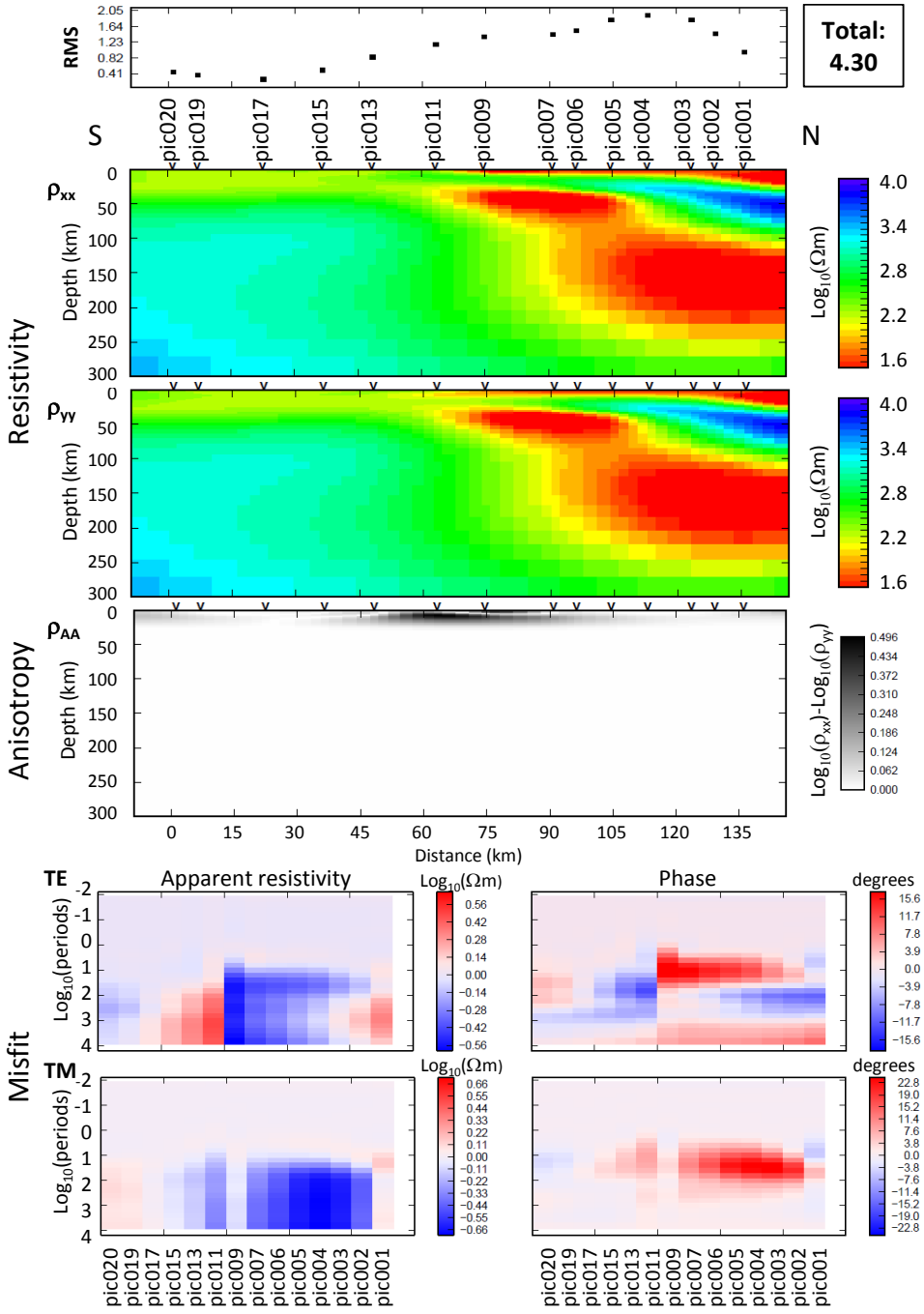

Fig. A.11.: Result of anisotropic 2D inversion for the **3D-mantle profile with stations pic001 - pic020** on top of the synthetic 3D model (cf. Figs. 8.3, 8.4, and 8.5 for synthetic 3D model, station location, and profile location) following the **second anisotropic inversion approach** (cf. 8.3.3). Station data is decomposed according to the strike direction of the mantle (N45E), and laplacian regularisation and an increased smoothing parameter ($\tau = 6$) are used for the inversion. Isotropic inversion of long-period data in the first sequence (hence the similarity of ρ_{xx} and ρ_{yy} at depth > 30 km) is followed by anisotropic inversion of short-period data in the second sequence. See Section 8.3.3 regarding current limitations of the approach.

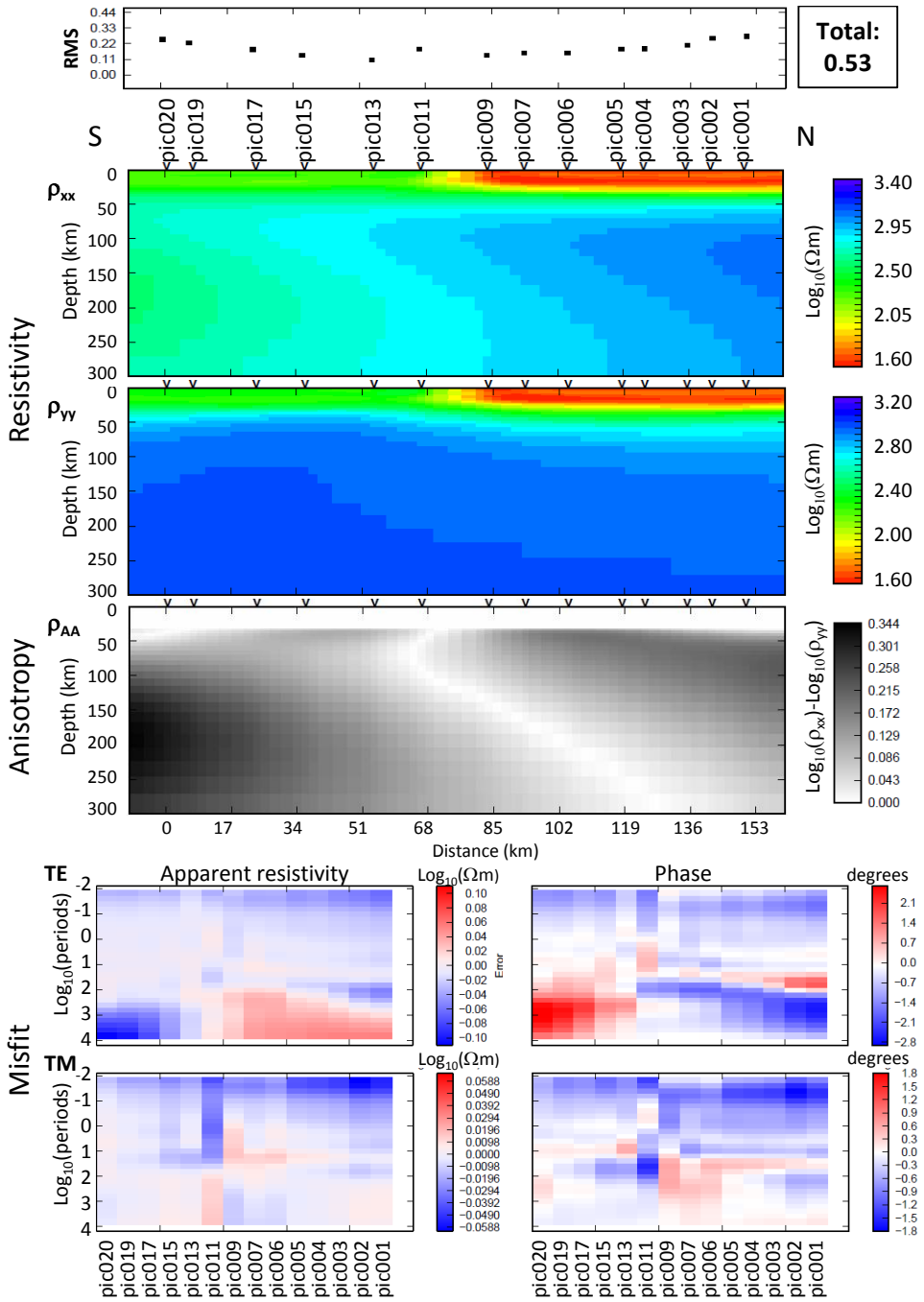

Fig. A.12.: Result of anisotropic 2D inversion for the **3D-crust profile with stations pic001 - pic020** on top of the synthetic 3D model (cf. Figs. 8.3, 8.4, and 8.5 for synthetic 3D model, station location, and profile location). Station data is decomposed according to the strike direction of the crust (N45W), and inversion is carried out with **resistivity gradient regularisation** and an **increased smoothing parameter** ($\tau = 6$), following the first inversion approach: isotropic inversion of short-period data in the first sequence and anisotropic inversion of long-period data in the second sequence.

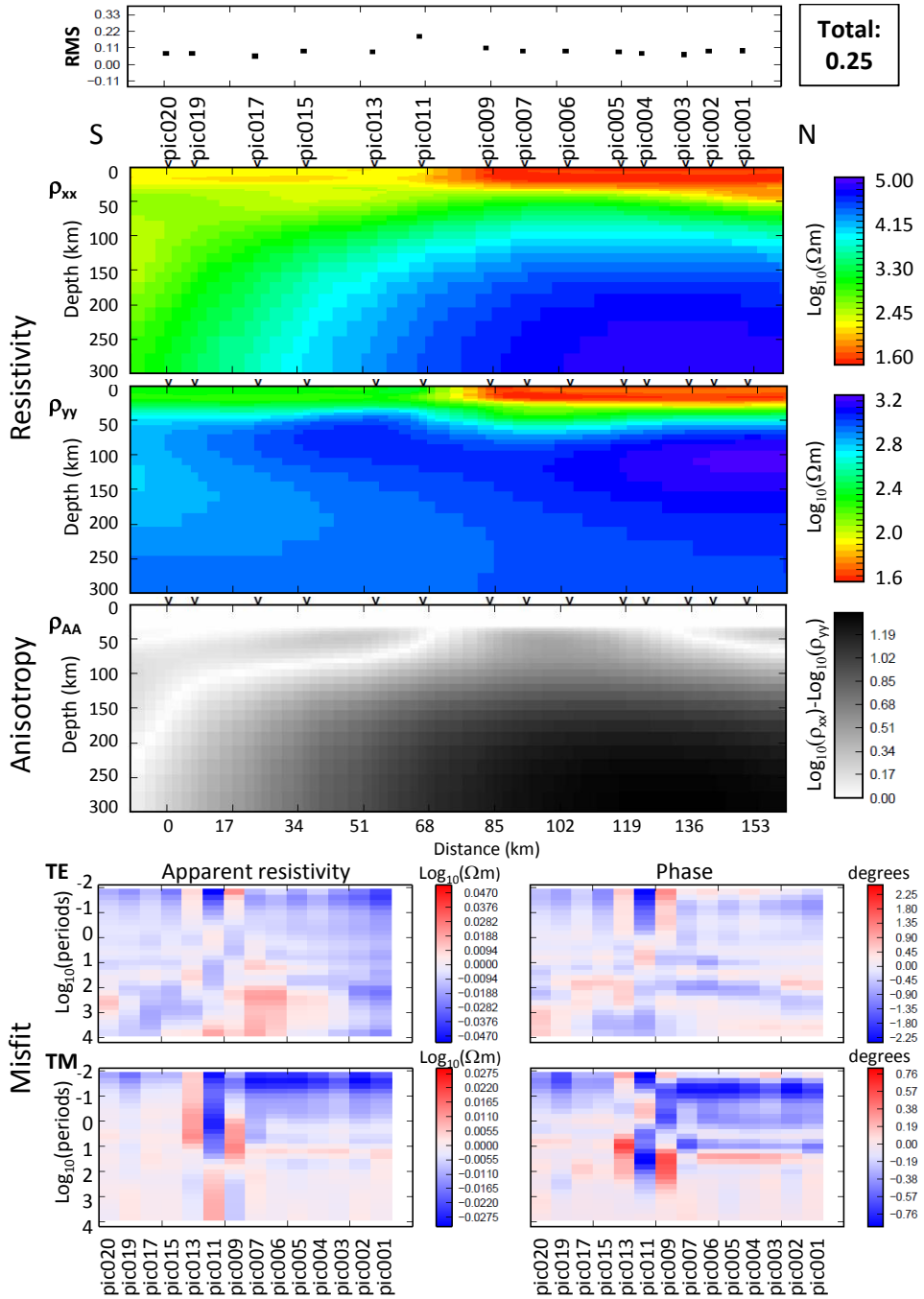

Fig. A.13.: Result of anisotropic 2D inversion for the **3D-crust profile with stations pic001 - pic020** on top of the synthetic 3D model (cf. Figs. 8.3, 8.4, and 8.5 for synthetic 3D model, station location, and profile location). Station data is decomposed according to the strike direction of the crust (N45W), and inversion is carried out with **resistivity laplacian regularisation** and a **lower smoothing parameter** ($\tau = 1$), following the first inversion approach: isotropic inversion of short-period data in the first sequence and anisotropic inversion of long-period data in the second sequence.

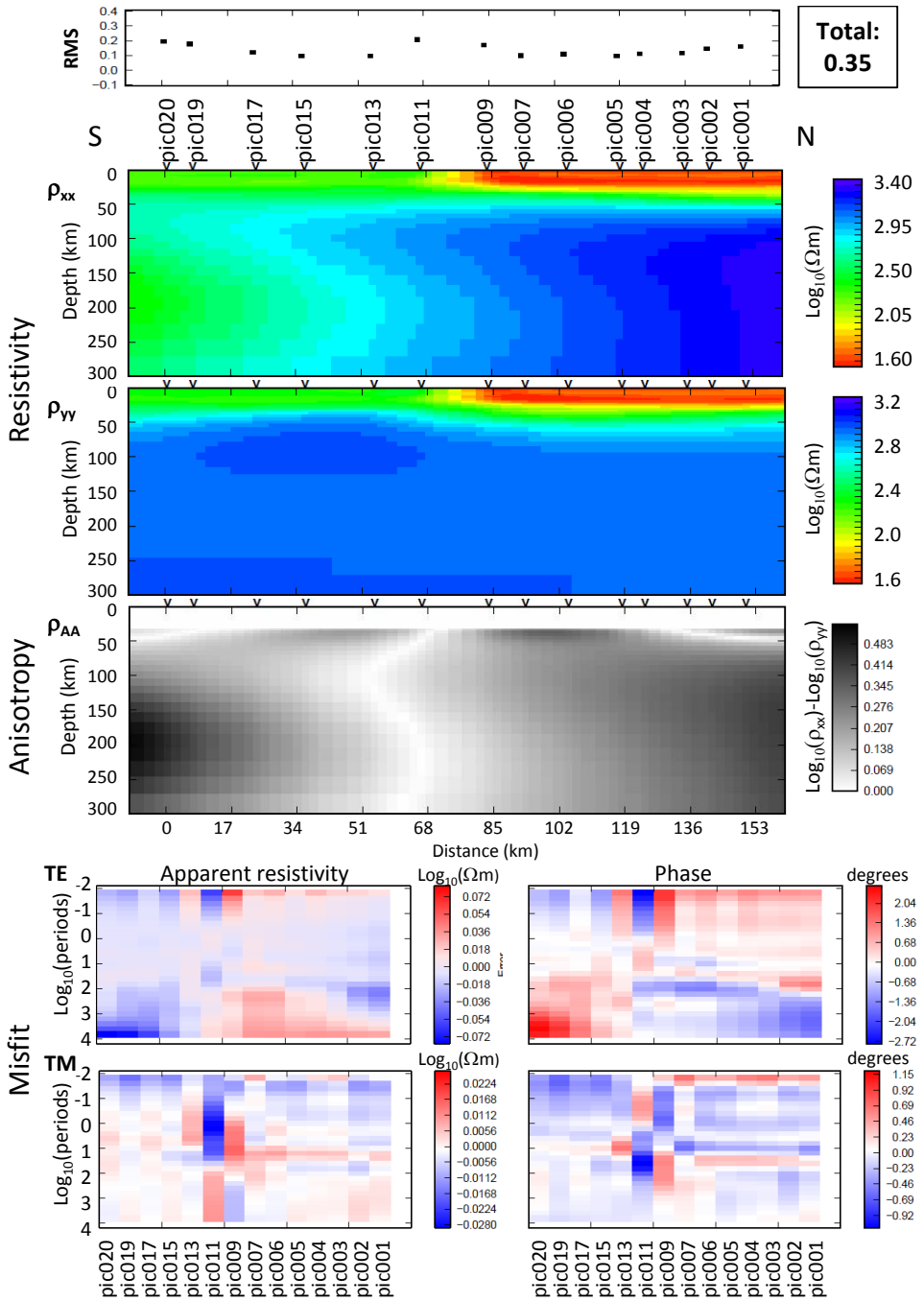

Fig. A.14.: Result of anisotropic 2D inversion for the **3D-crust profile with stations pic001 - pic020** on top of the synthetic 3D model (cf. Figs. 8.3, 8.4, and 8.5 for synthetic 3D model, station location, and profile location). Station data is decomposed according to the strike direction of the crust (N45W), and inversion is carried out with **resistivity gradient regularisation** and a **lower smoothing parameter** ($\tau = 1$), following the first inversion approach: isotropic inversion of short-period data in the first sequence and anisotropic inversion of long-period data in the second sequence.

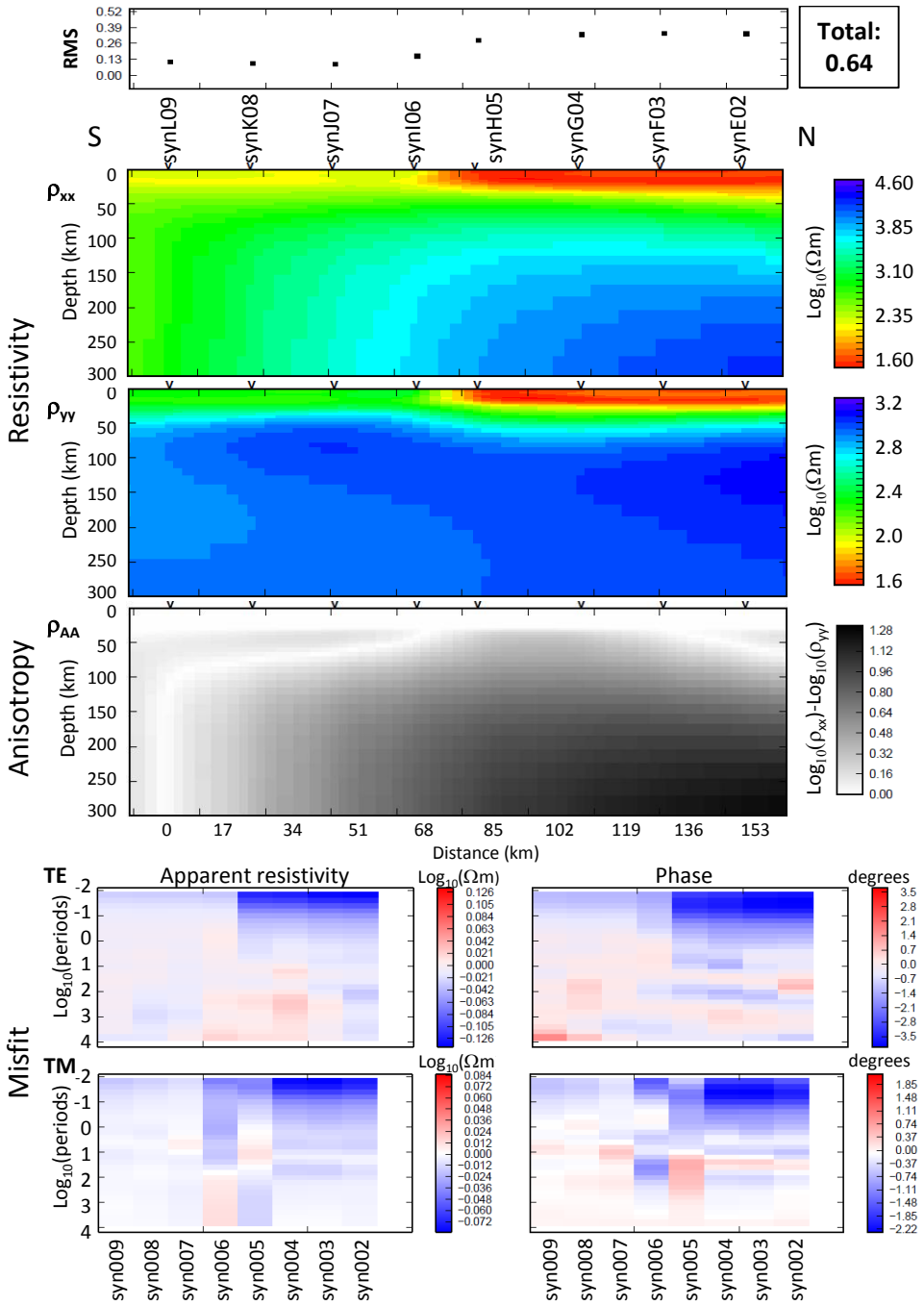

Fig. A.15.: Result of anisotropic 2D inversion for the **3D-crust-NS profile with stations synE02 - synL09** on top of the synthetic 3D model (cf. Figs. 8.3, 8.4, and 8.5 for synthetic 3D model, station location, and profile location). Station data is decomposed according to the strike direction of the crust (N45W), and inversion is carried out with resistivity laplacian regularisation and an increased smoothing parameter ($\tau = 6$), following the first inversion approach: isotropic inversion of short-period data in the first sequence and anisotropic inversion of long-period data in the second sequence.

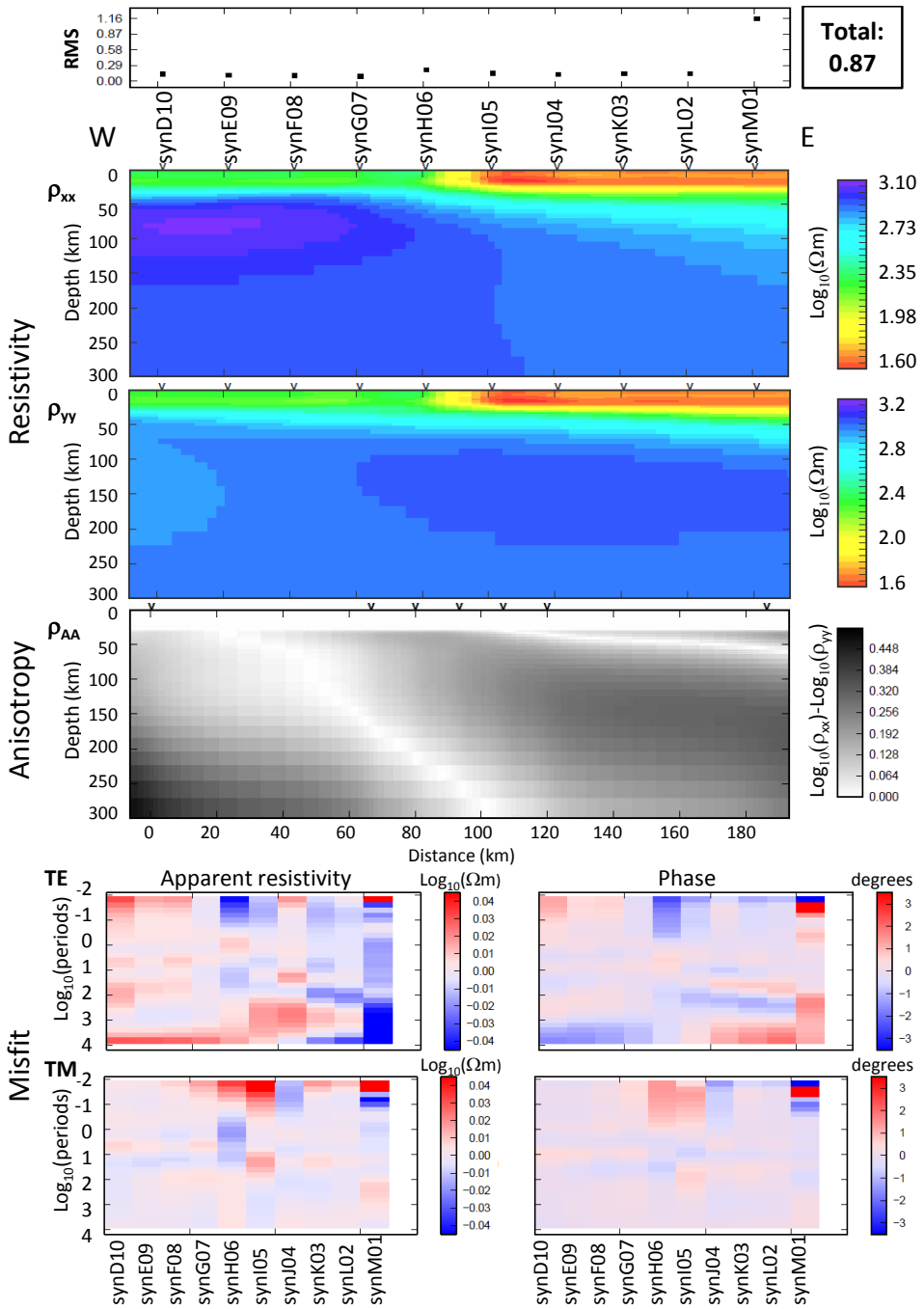

Fig. A.16.: Result of anisotropic 2D inversion for the **3D-crust-EW profile with stations synD10 - synM01** on top of the synthetic 3D model (cf. Figs. 8.3, 8.4, and 8.5 for synthetic 3D model, station location, and profile location). Station data is decomposed according to the strike direction of the crust (N45W), and inversion is carried out with resistivity gradient regularisation and a lower smoothing parameter ($\tau = 1$), following the first inversion approach: isotropic inversion of short-period data in the first sequence and anisotropic inversion of long-period data in the second sequence.

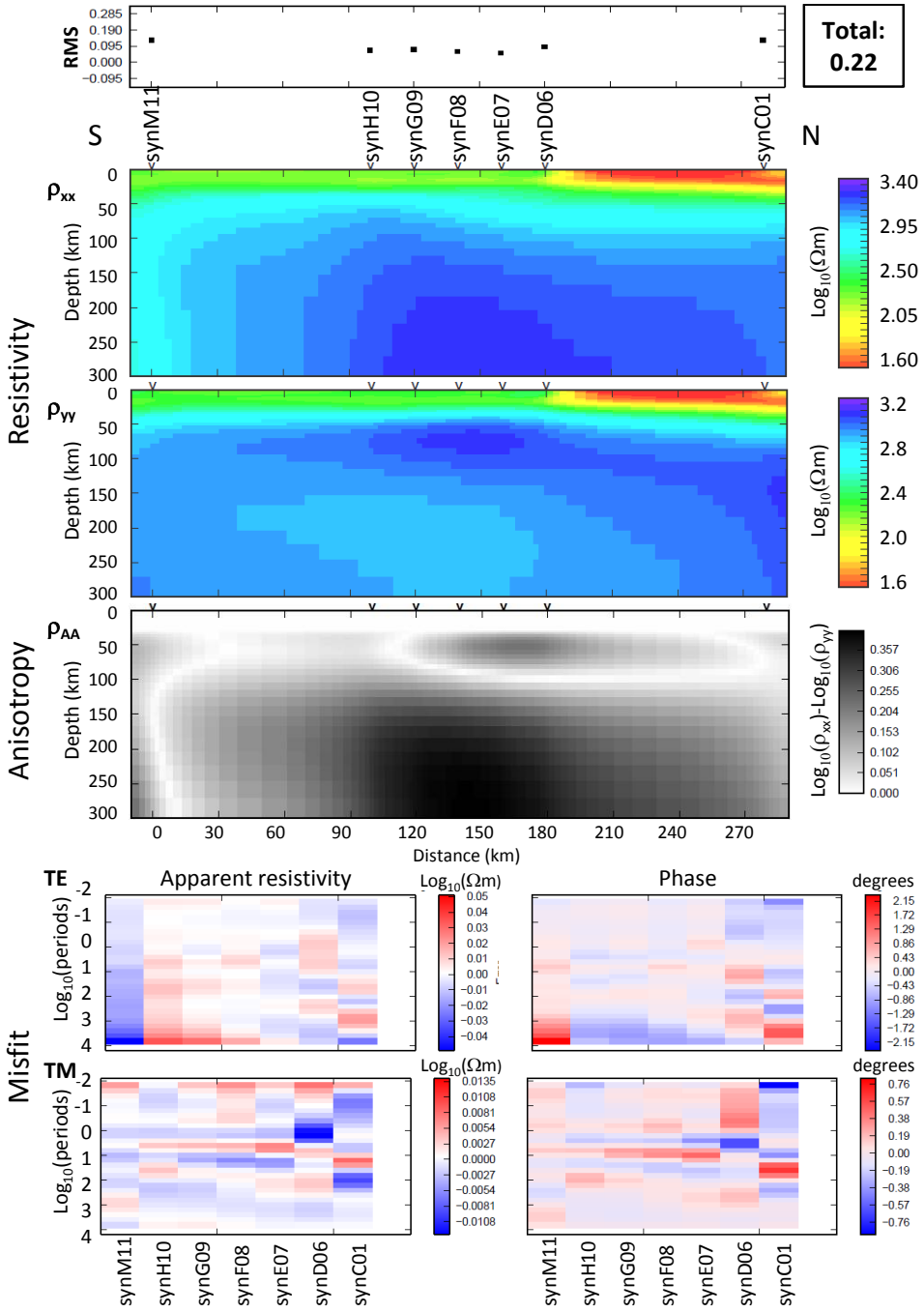

Fig. A.17.: Result of anisotropic 2D inversion for the **3D-crust-west profile with stations synM11 - synC01** on top of the synthetic 3D model (cf. Figs. 8.3, 8.4, and 8.5 for synthetic 3D model, station location, and profile location). Station data is decomposed according to the strike direction of the crust (N45W), and inversion is carried out with resistivity laplacian regularisation and an increased smoothing parameter ($\tau = 6$) following the first inversion approach: isotropic inversion of short-period data in the first sequence and anisotropic inversion of long-period data in the second sequence. The less constrained location of the resistivity interface at upper mantle depth in this model is attributed to smoothing constraints of the inversion and the large station spacing in the area.

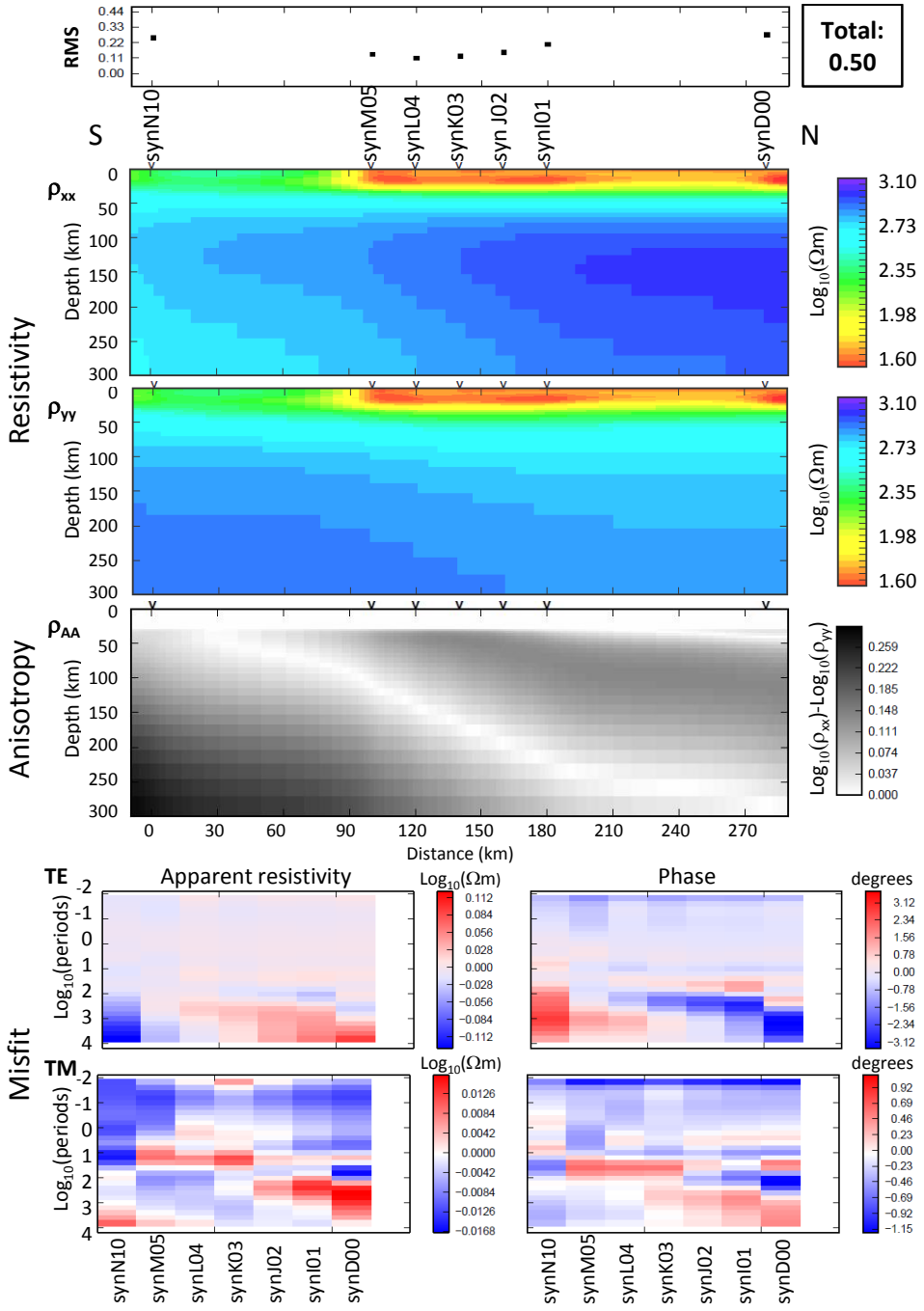

Fig. A.18.: Result of anisotropic 2D inversion for the **3D-crust-east profile with stations synN10 - synD00** on top of the synthetic 3D model (cf. Figs. 8.3, 8.4, and 8.5 for synthetic 3D model, station location, and profile location). Station data is decomposed according to the strike direction of the crust (N45W), and inversion is carried out with resistivity gradient regularisation and an increased smoothing parameter ($\tau = 6$) following the first inversion approach: isotropic inversion of short-period data in the first sequence and anisotropic inversion of long-period data in the second sequence. The less constrained location of the resistivity interface at mantle depth in this model is attributed to smoothing constraints of the inversion and the large station spacing in the area.

A.4. Auxiliary figures of the Tajo Basin subsurface investigation

A.4.1. Responses for crustal inversion model

This Section contains responses for the PICASSO Phase I stations and the isotropic 2D subsurface model for the Tajo Basin crust shown in Figure 10.6. Responses are displayed in terms of apparent resistivity and impedance phase values for periods $\leq 10^3$ s that are related to the crustal depth range (cf. Sec. 10.1). TE mode data are shown on the left-hand side, whereas TM mode data are shown on the right-hand side of each figure. Also shown are the RMS misfit values for both modes at the bottom of each figure as well as the average RMS misfit at the top of each figure.

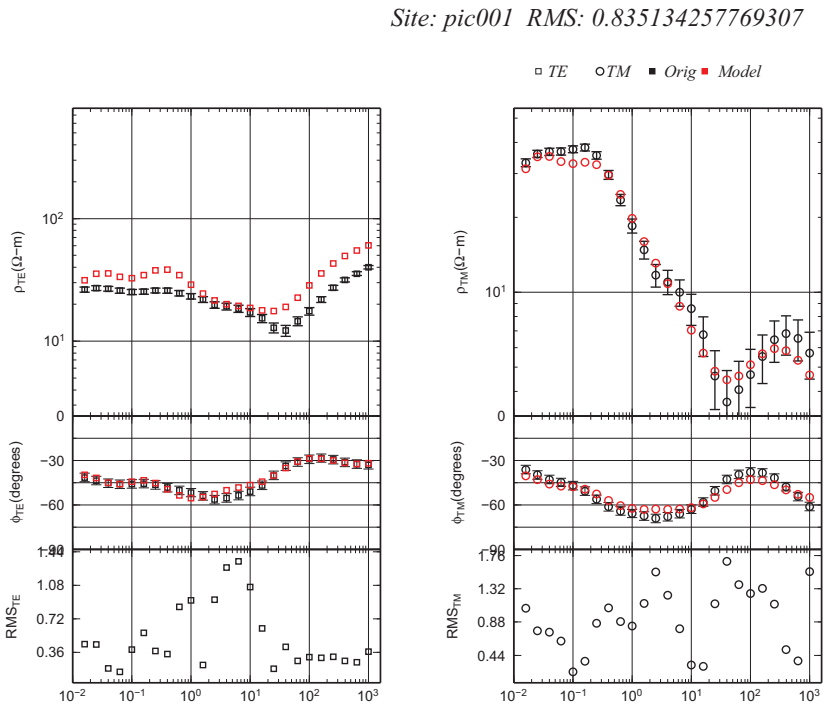

Fig. A.19.: Comparison of observed data for station pic001 and the related model response for the model shown in Figure 10.6.

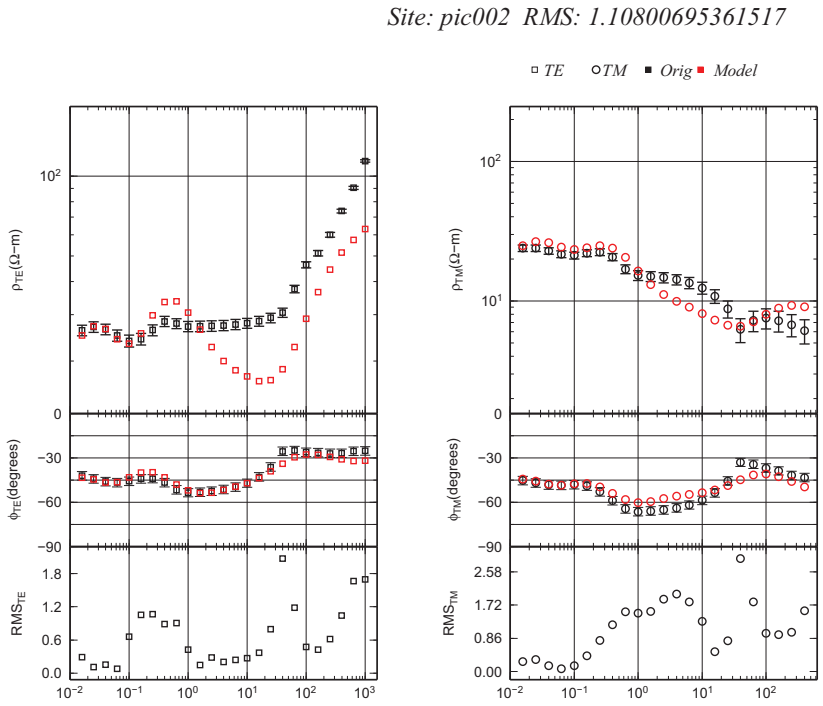

Fig. A.20.: Comparison of observed data for station pic002 and the related model response for the model shown in Figure 10.6.

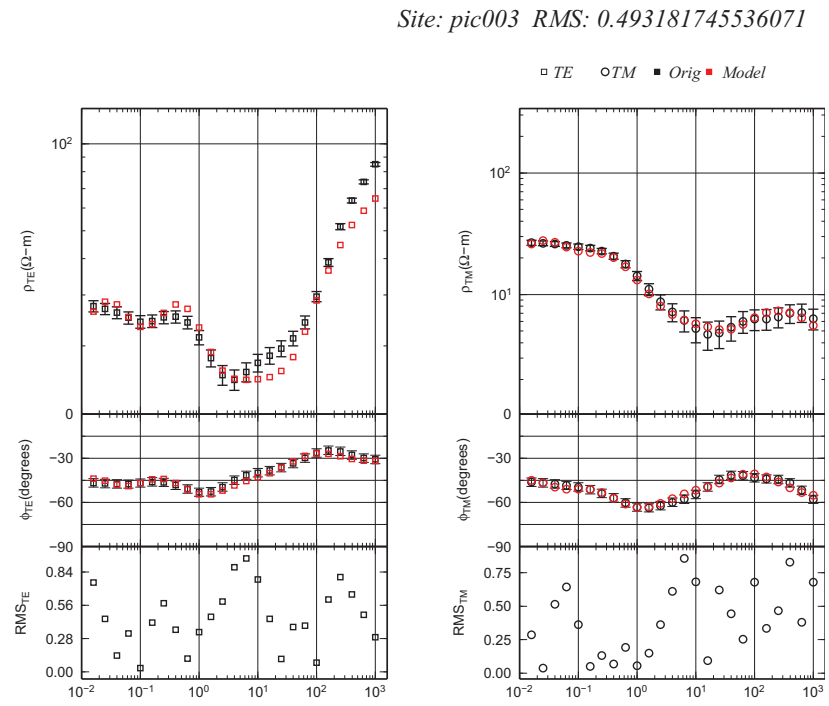

Fig. A.21.: Comparison of observed data for station pic003 and the related model response for the model shown in Figure 10.6.

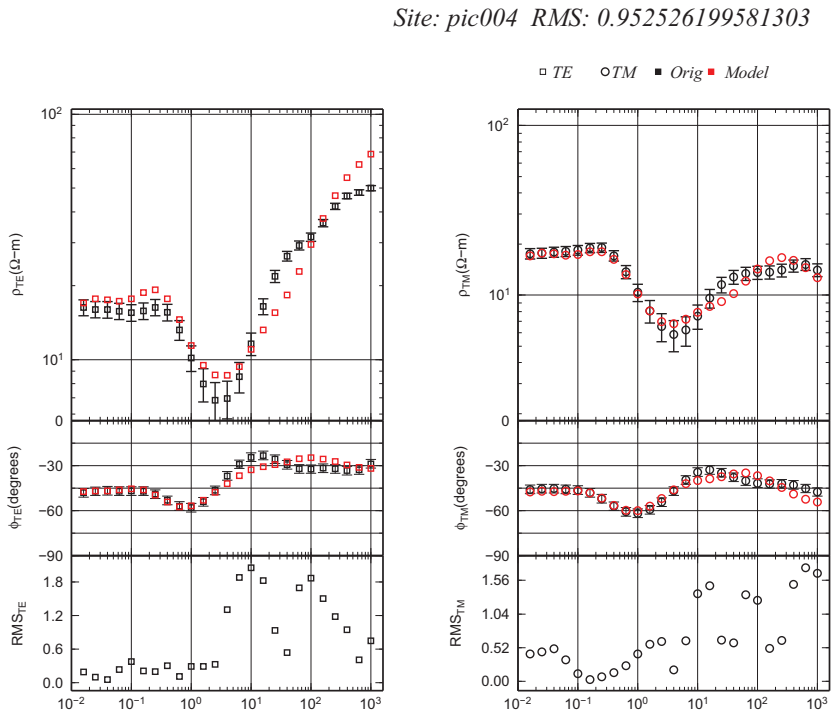

Fig. A.22.: Comparison of observed data for station pic004 and the related model response for the model shown in Figure 10.6.

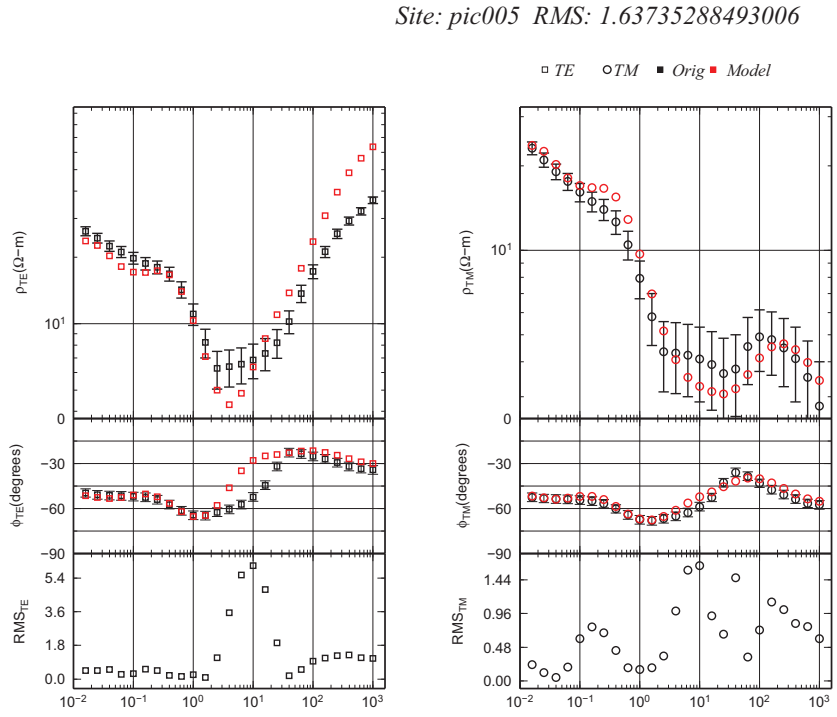

Fig. A.23.: Comparison of observed data for station pic005 and the related model response for the model shown in Figure 10.6.

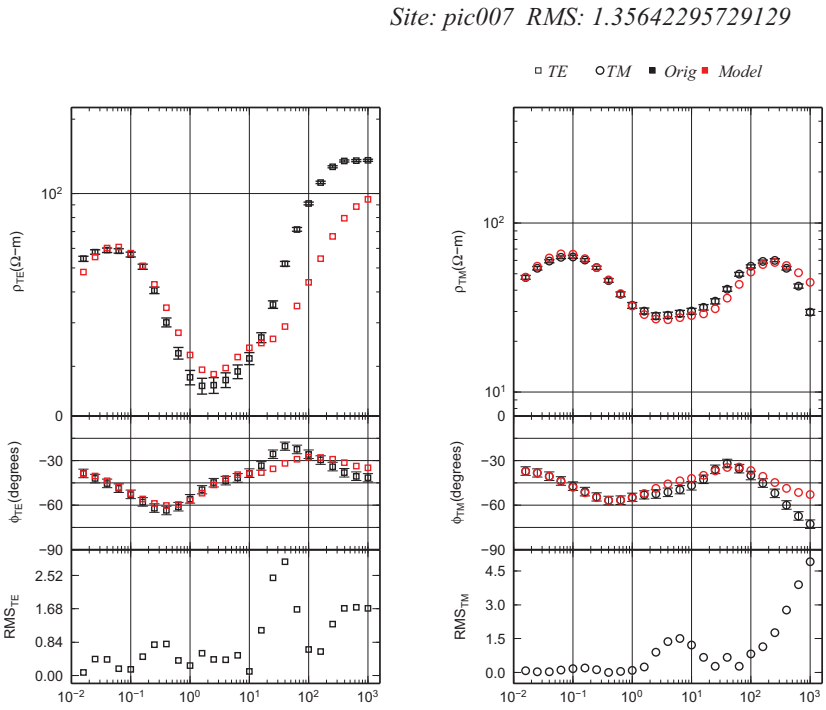

Fig. A.24.: Comparison of observed data for station pic007 and the related model response for the model shown in Figure 10.6.

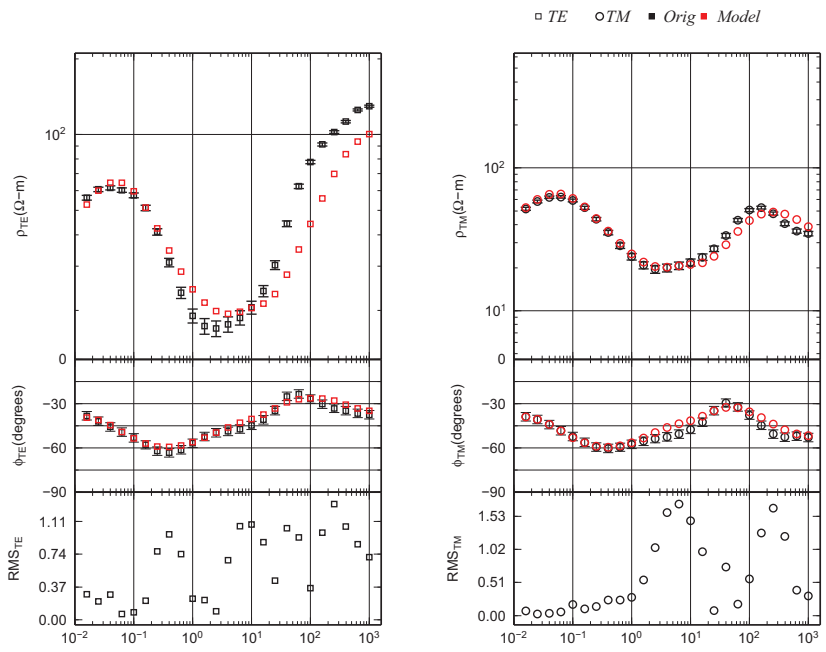

Fig. A.25.: Comparison of observed data for station pic009 and the related model response for the model shown in Figure 10.6.

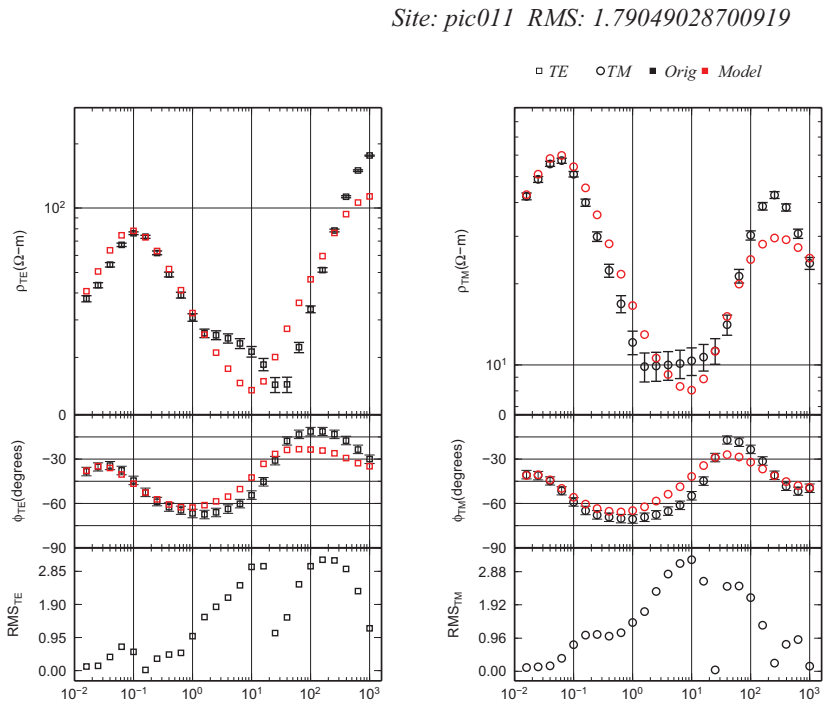

Fig. A.26.: Comparison of observed data for station pic011 and the related model response for the model shown in Figure 10.6.

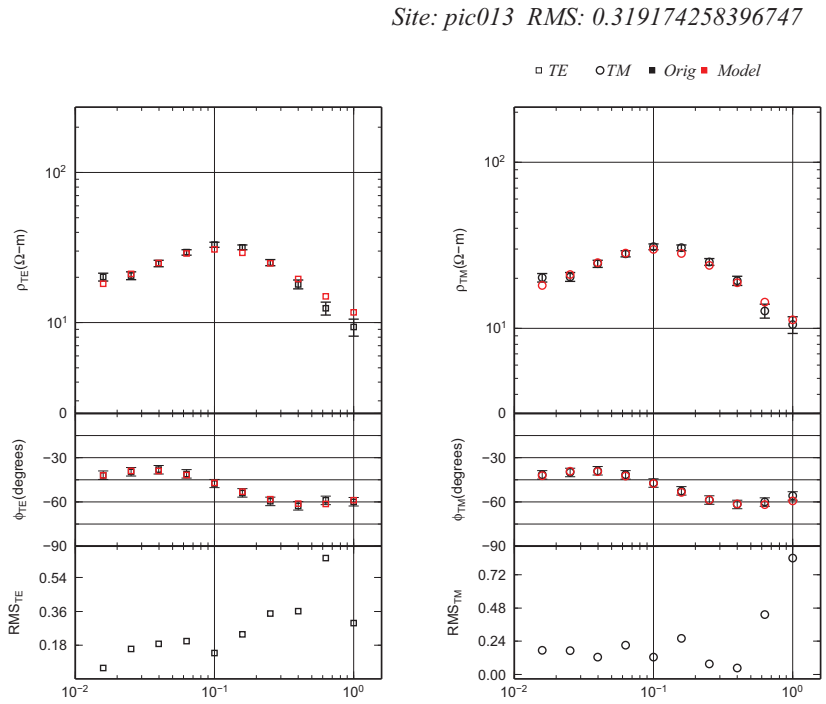

Fig. A.27.: Comparison of observed data for station pic013 and the related model response for the model shown in Figure 10.6.

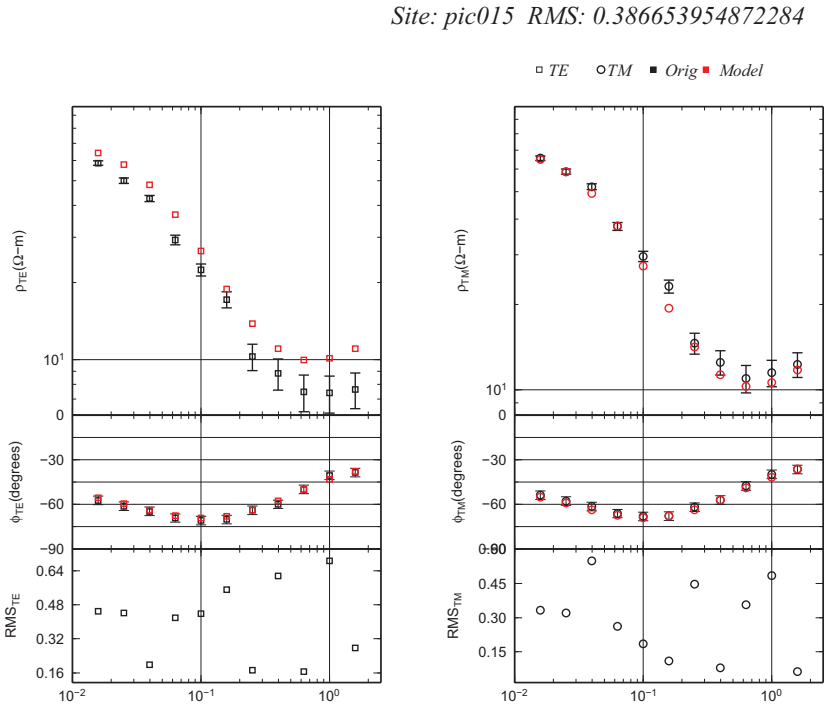

Fig. A.28.: Comparison of observed data for station pic015 and the related model response for the model shown in Figure 10.6.

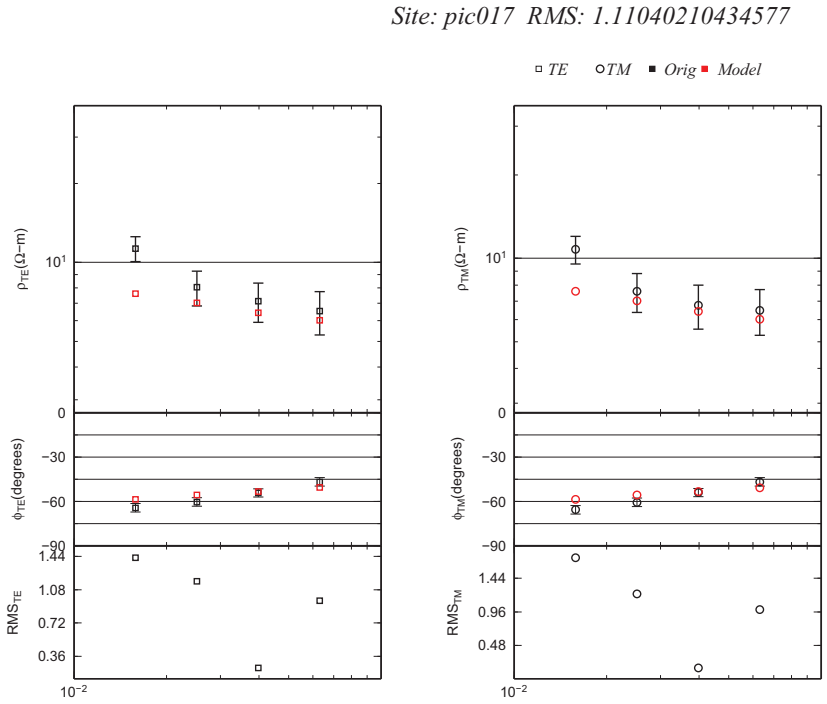

Fig. A.29.: Comparison of observed data for station pic017 and the related model response for the model shown in Figure 10.6.

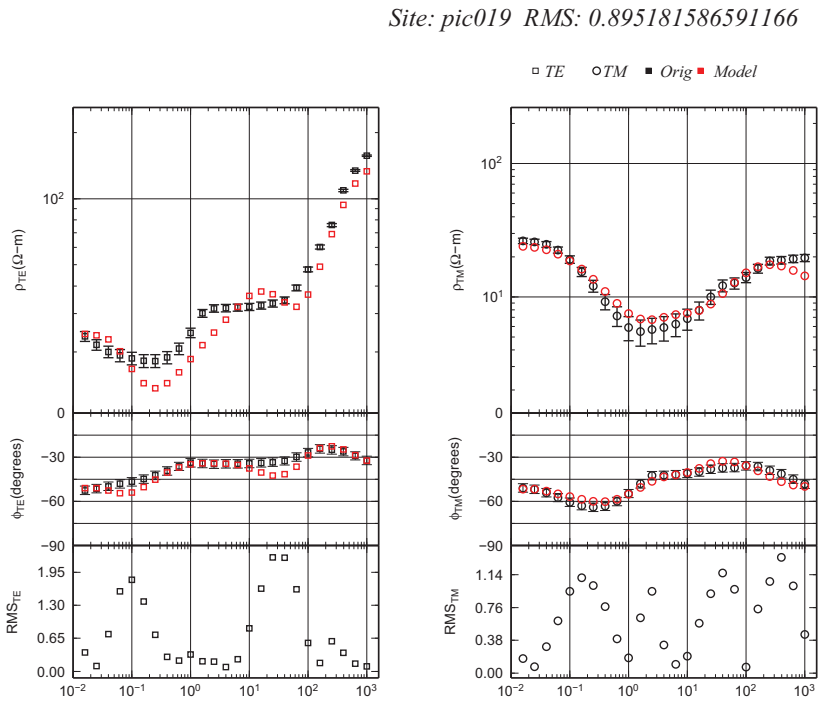

Fig. A.30.: Comparison of observed data for station pic019 and the related model response for the model shown in Figure 10.6.

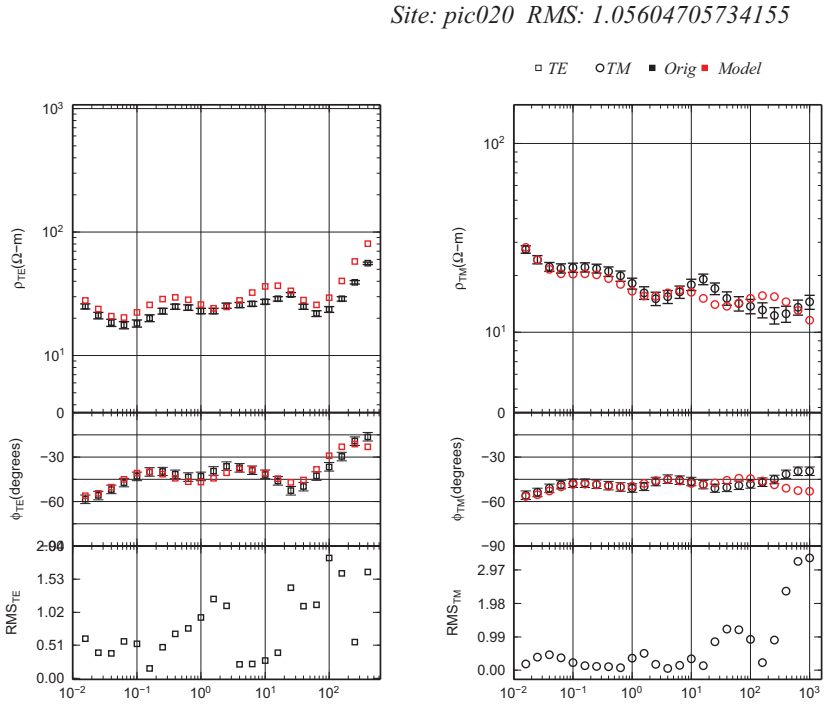

Fig. A.31.: Comparison of observed data for station pic020 and the related model response for the model shown in Figure 10.6.

A.4.2. Responses for 3D inversion model

This Section contains responses for the PICASSO Phase I stations and the isotropic 3D subsurface model of the Tajo Basin labelled 'a' in Figure 10.27. Responses are displayed in terms of apparent resistivity and phase values for impedance vector elements in the period range used for the inversion (10^{-3} – 10^{5} s); details about the 3D inversion are presented in Section 10.2.4). Off-diagonal elements of the impedance vector are shown on the left-hand side and diagonal elements on the right-hand side. Error bars that exceed the display area indicate missing values at the respective periods of a station.

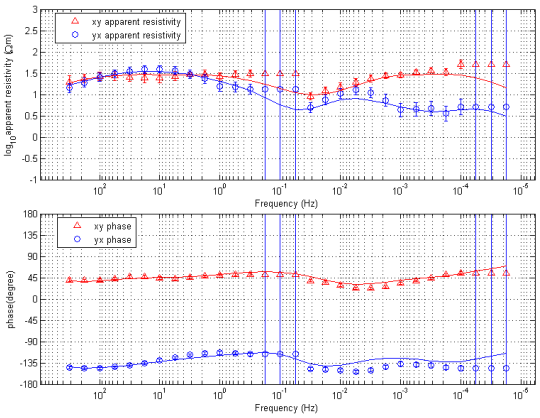

pic001 (off-diagonal elements)

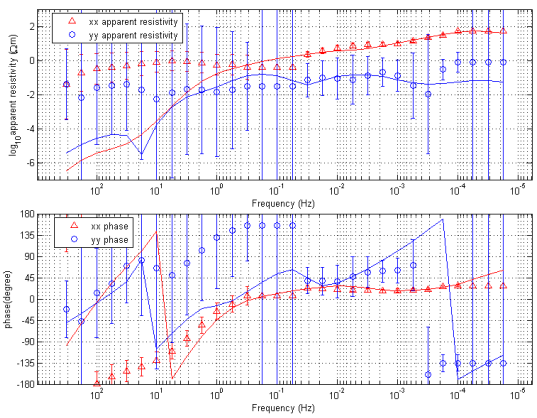

pic001 (diagonal elements)

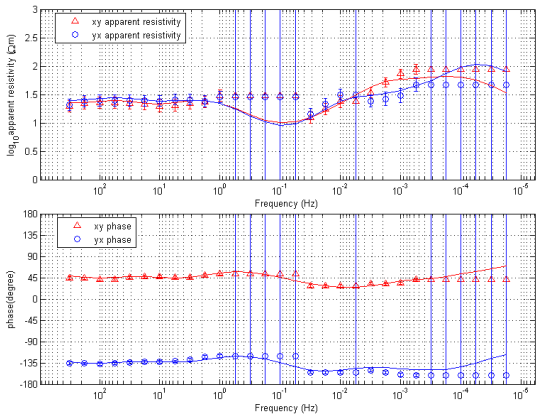

pic002 (off-diagonal elements)

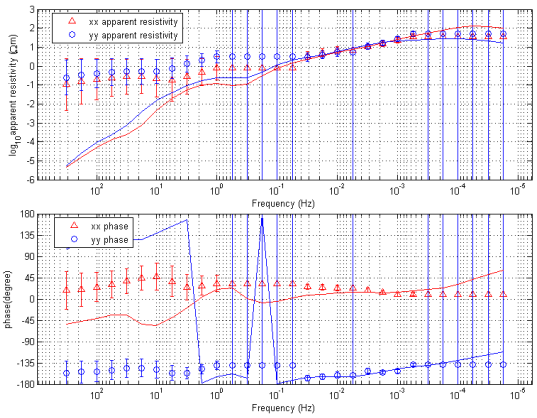

pic002 (diagonal elements)

Fig. A.32.: Comparison of observed and calculated responses for the minimum misfit model of the isotropic 3D inversion

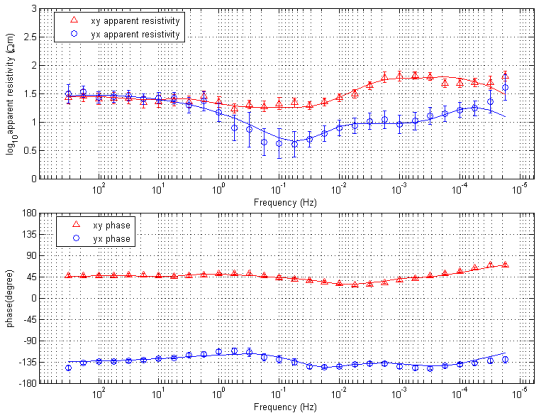

pic003 (off-diagonal elements)

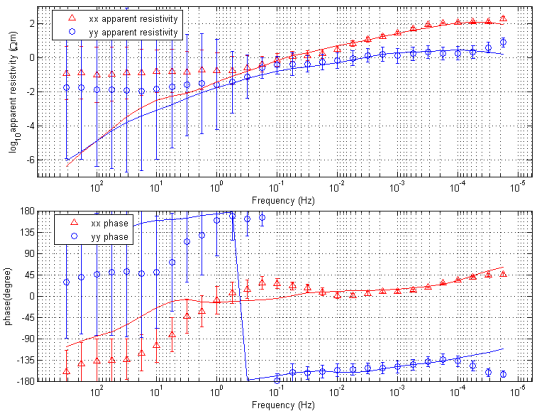

pic003 (diagonal elements)

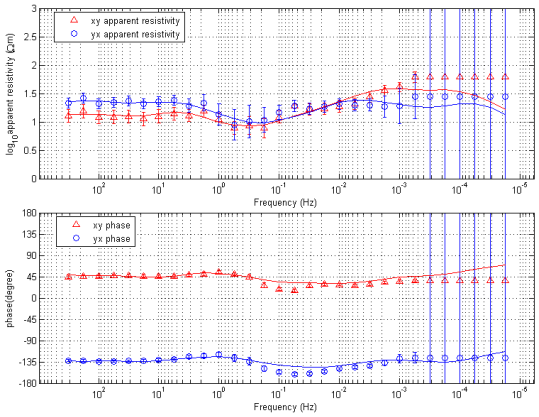

pic004 (off-diagonal elements)

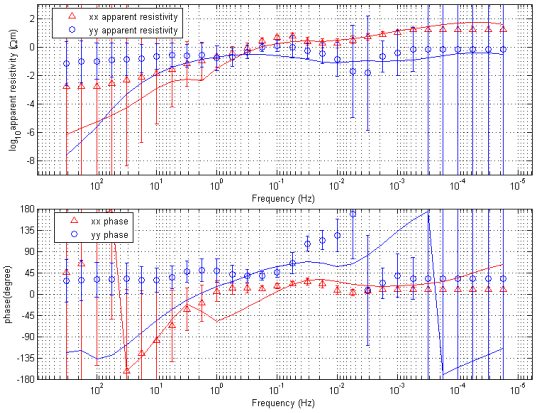

pic004 (diagonal elements)

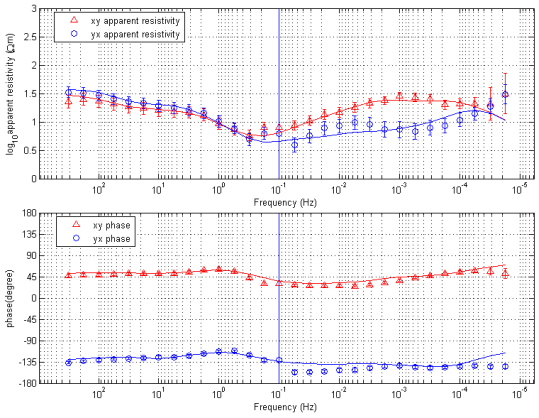

pic005 (off-diagonal elements)

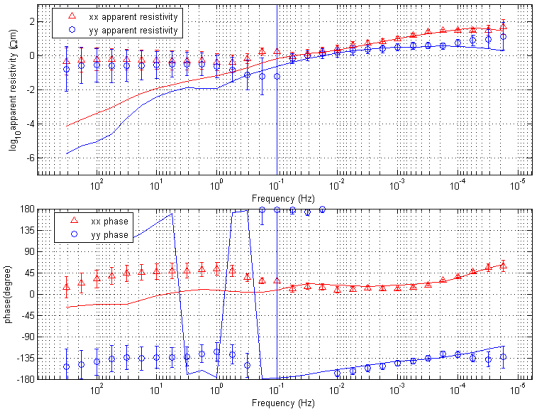

pic005 (diagonal elements)

Fig. A.32 (ctd.) Comparison of observed and calculated responses for the minimum misfit model of the isotropic 3D inversion

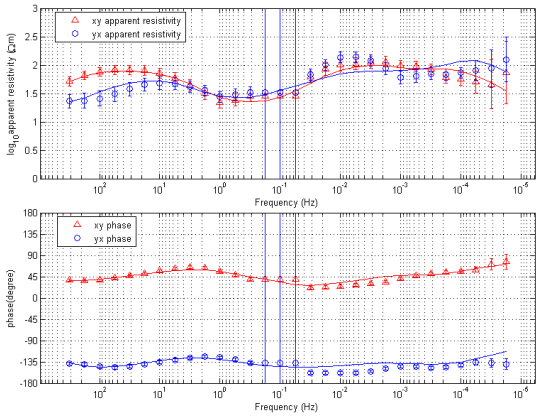

pic007 (off-diagonal elements)

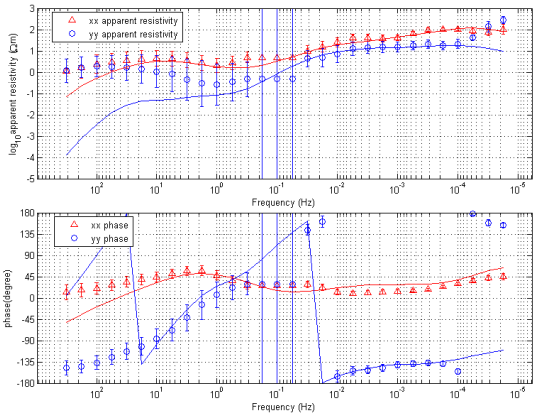

pic007 (diagonal elements)

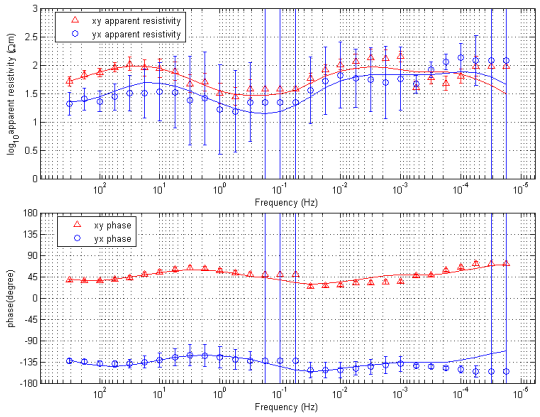

pic009 (off-diagonal elements)

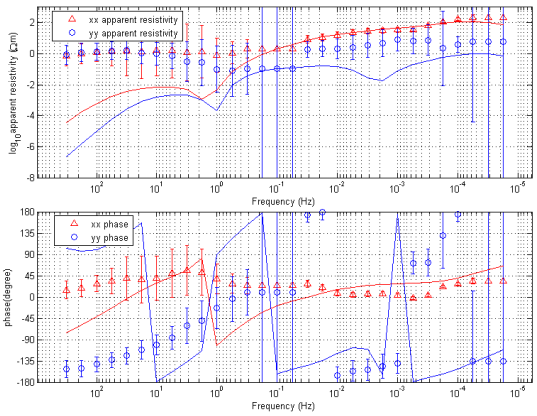

pic009 (diagonal elements)

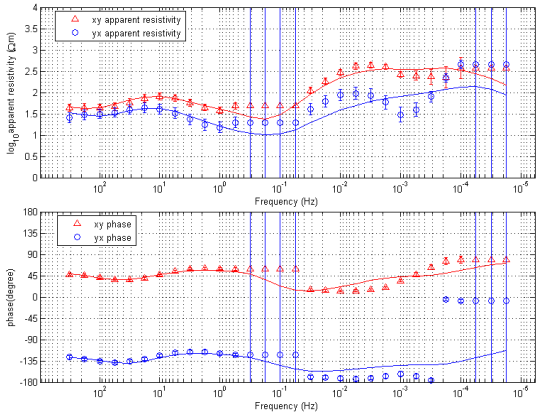

pic011 (off-diagonal elements)

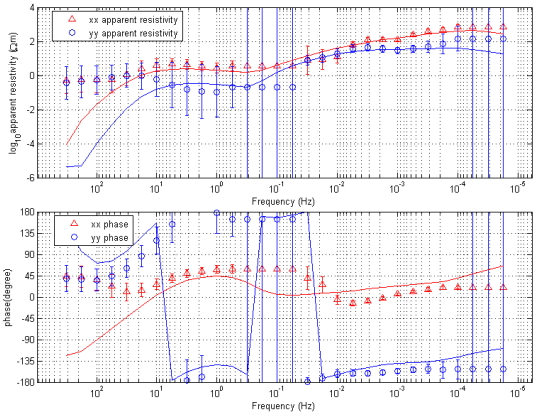

pic011 (diagonal elements)

Fig. A.32 (ctd.) Comparison of observed and calculated responses for the minimum misfit model of the isotropic 3D inversion

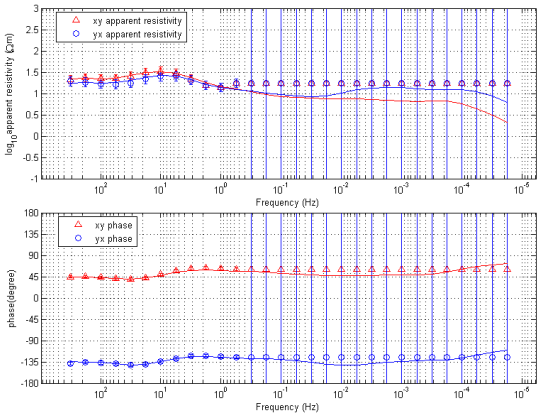

pic013 (off-diagonal elements)

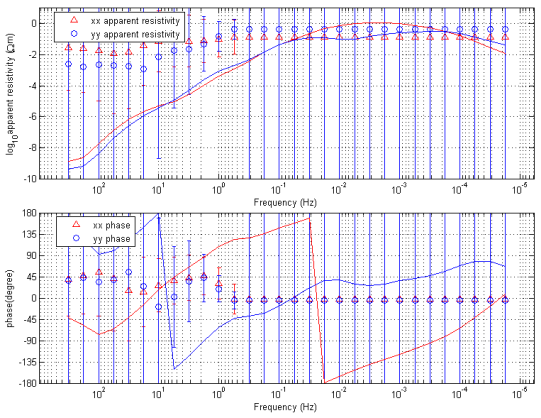

pic013 (diagonal elements)

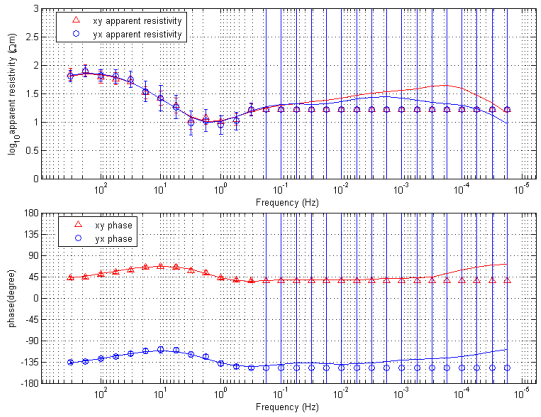

pic015 (off-diagonal elements)

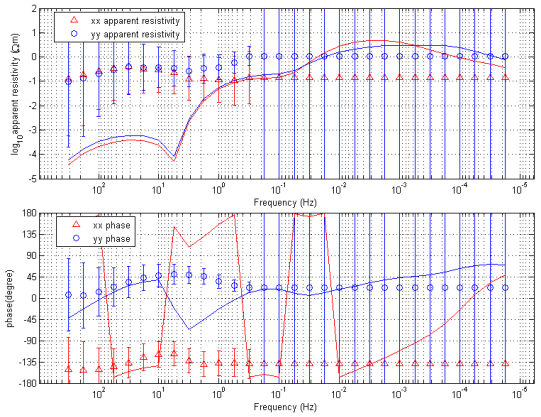

pic015 (diagonal elements)

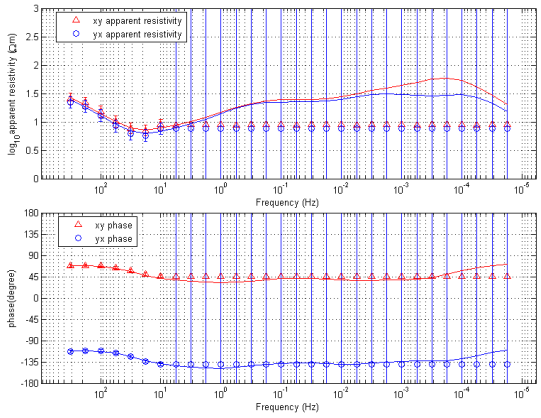

pic017 (off-diagonal elements)

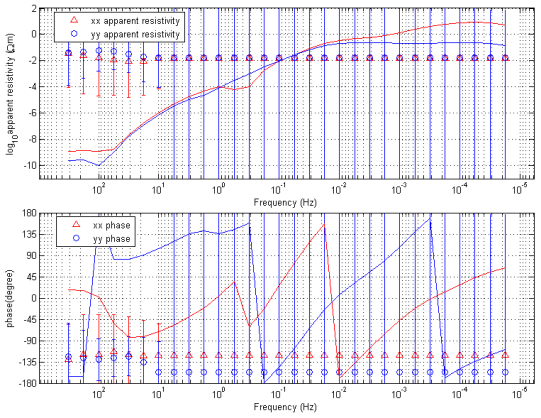

pic017 (diagonal elements)

Fig. A.32 (ctd.) Comparison of observed and calculated responses for the minimum misfit model of the isotropic 3D inversion

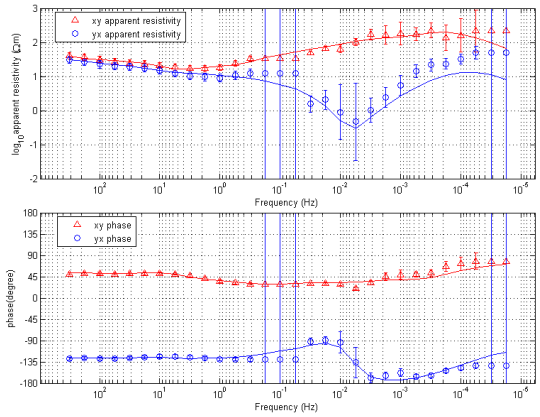

pic019 (off-diagonal elements)

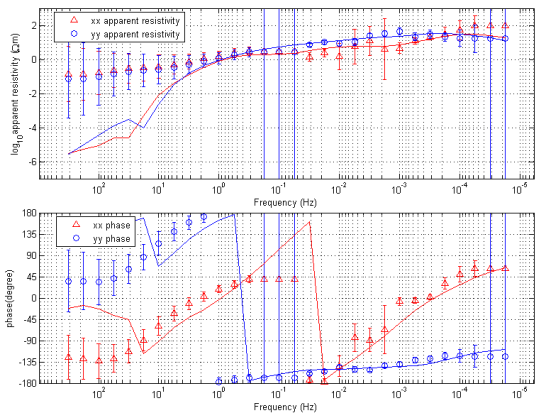

pic019 (diagonal elements)

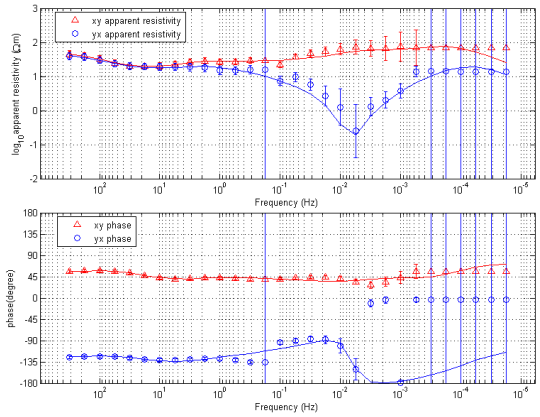

pic020 (off-diagonal elements)

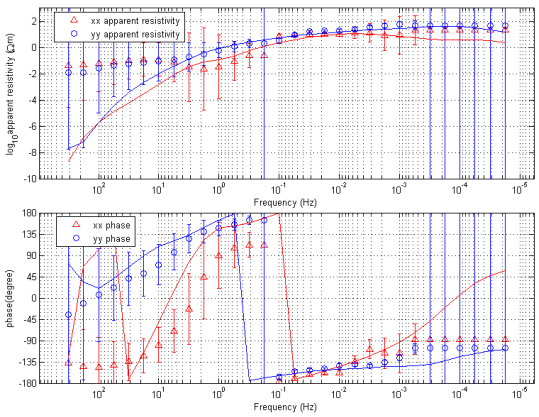

pic020 (diagonal elements)

Fig. A.32 (ctd.) Comparison of observed and calculated responses for the minimum misfit model of the isotropic 3D inversion

Bibliography

Abalos, B., J. Carreras, E. Druguet, J. Viruette, M. Gomez Pugnaire, S. Alvarez, C. Quesada, L. Rodriguez Fernandez, and J. Gil-Ibarguchi (2002), Variscan and Pre-Variscan tectonics, in *Gibbons and Moreno* [2002b], chap. 16, pp. 155–183.

Abt, D. L., K. M. Fischer, S. W. French, H. A. Ford, H. Yuan, and B. Romanowicz (2010), North American lithospheric discontinuity structure imaged by Ps and Sp receiver functions, *Journal of Geophysical Research*, *115*(B9), B09,301, doi: 10.1029/2009JB006914.

Afonso, J., M. Fernàndez, G. Ranalli, W. Griffin, and J. Connolly (2008), Combined geophysical-petrological modelling of the lithospheric-sublithospheric upper mantle: methodology and applications, *Geochemistry, Geophysics, Geosystems*, *9*(5), Q05,008, doi:10.1029/2007GC001834.

Agarwal, A., and J. Weaver (1993), Inversion of the COPROD2 data by a method of modelling, *Journal of Geomagnetism and Geoelectricity*, *45*, 969–983.

Agarwal, A., H. E. Poll, and J. Weaver (1993), One- and two-dimensional inversion of magnetotelluric data in continental regions, *Physics of the Earth and Planetary Interiors*, *81*, 155–176.

Airy, G. B. (1855), On the computation of the effect of the attraction of mountain-masses as disturbing the apparent astronomical latitude of stations of geodetic surveys, *Phil. Trans. R. Soc. Lond.*, *145*, 101–104.

Alonso-Zarza, A., et al. (2002), Tertiary, in *Gibbons and Moreno* [2002b], chap. 13, pp. 293–334.

Amaru, M. L. (2007), Global travel time tomography with 3-D reference models, Ph.D. thesis, Utrecht University, Budapestlaan 4, 3584 CD Utrecht, http://igitur-archive.library.uu.nl/dissertations/2007-0202-201924/index.htm.

Amaru, M. L., W. Spakman, A. Villaseñor, S. Sandoval, and E. Kissling (2008), A new absolute arrival time data set for Europe, *Geophysical Journal International*, *173*(2), 465–472, doi:10.1111/j.1365-246X.2008.03704.x.

Ancochea, E., and J. Brändle (1982), Alineaciones de volcanes en la región volcánica central espaãola, *Revista de Geofisica*, *38*, 133–138.

Ancochea, E., A. Giuliani, and I. Villa (1979), Edades radiométricas K-Ar del vulcanismo de la región central española, *Estudios Geologicos*, *35*, 131–135.

Andersen, D., and T. Fuller-Rowell (1999), The ionosphere, in *Space Environment Topics*, National Oceanic and Atmospheric Administration (NOAA), U.S. department of commence, Space environment center, 325 Broadway, Boulder, CO 80303-3326.

Anderson, D. L. (2004), *Theory of the Earth*, vol. 2, Blackwell Scientific Publications, Oxford, Osney Mead.

Andeweg, B. (2002), Cenozoic tectonic evolution of the Iberian Peninsula: Effects and causes of changing stress fields, Ph.D. thesis, Vrije Universiteit Amsterdam, De Boelelaan 1085, 1081 HV Amsterdam.

Andre, D., and W. Baumjohann (1982), Joint two-dimensional observations of ground magnetic and ionospheric fields associated with auroral currents. 5. current system associated with eastward drifting omega bands, *Journal of Geophysics*, *50*, 194–201.

Andrieux, P., and W. Wightman (1984), The so-called static correction in magnetotelluric measurements, in *54th annual international meeting*, pp. 43–44, Society of Exploration Geophysics, expanded Abstracts.

Arcay, D., E. Tric, and M.-P. Doin (2005), Numerical simulations of subduction zones: Effect of slab dehydration on the mantle wedge dynamics, *Physics of the Earth and Planetary Interiors*, *149*, 133–153.

Archie, G. E. (1942), The electrical resistivity log as an aid in determining some reservoir characteristics, *Transaction of The American Institute of Mining, Metallurgical, and Petroleum Engineers*, *146*.

Argus, D., and R. Gordon (1991), No-net-rotation model of current plate velocities incorporating plate motion model NUVEL-1, *Geophysical Research Letter*, *18*, 2039.

Artemieva, I. M. (2006), Global 1° x 1° thermal model tc1 for the continental lithosphere: Implications for lithosphere secular evolution, *Tectonophysics*, *416*(1-4), 245–277, doi:DOI:10.1016/j.tecto.2005.11.022.

Artemieva, I. M. (2009), The continental lithosphere: Reconciling thermal, seismic, and petrologic data, *Lithos*, *109*(1-2), 23–46, doi:DOI:10.1016/j.lithos.2008.09.015.

Aster, R. C., B. Borchers, and C. H. Thurber (2005), *Parameter Estimation and Inverse Problems*, *International Geophysics*, vol. 90, Elsevier Academic Press, 30 Corporate Drive, Burlington, MA 01803, USA.

Aurell, M., et al. (2002), The geology of spain, in *Gibbons and Moreno* [2002b], chap. 11, pp. 213–253.

Avdeev, D. B. (2005), Three-dimensional electromagnetic modelling and inversion from theory to application, *Surveys of Geophysics*, *26*, 767–799, doi:10.1007/s10712-005-1836-2.

Avdeev, D. B., and A. D. Avdeeva (2009), 3d magnetotelluric inversion using a limited-memory quasi-Newton optimization, *Geophysics*, *74*, F45–F57.

Avdeev, D. B., A. V. Kuvshinov, O. V. Pankratov, and G. A. Newman (2002), Three-dimensional induction logging problems. part i: An integral equation solution and model comparisons, *Geophysics*, *67*, 413–426.

Azanon, J., J. Galindo-Zaldivar, V. Garcia-Duenas, and A. Jabaloy (2002), Alpine tectonics II: Betic Cordillera and Balearic Islands, in *Gibbons and Moreno* [2002b], chap. 16, pp. 401–416.

Baba, K., A. D. Chave, R. L. Evans, G. Hirth, and R. L. Mackie (2006), Mantle dynamics beneath the East Pacific Rise at 17 degrees S: Insights from the Mantle ELectromagnetic and Tomography (melt) experiment, *Journal of Geophysical Research*, *111*, B02,101, doi:10.1029/2004JB003598.

Babuska, V., and J. Plomerová (2006), European mantle lithosphere assembled from rigid microplates with inherited seismic anisotropy, *Physics of The Earth and Planetary Interiors*, *158*(2-4), 264 – 280, doi:DOI:10.1016/j.pepi.2006.01.010.

Badro, J., G. Fiquet, F. Guyot, J. Rueff, V. V. Struzhkin, G. Vanko, and G. Monaco (2003), Iron partitioning in Earth's mantle: Toward a deep lower mantle discontinuity, *Science*, *300*, 789–791, doi:10.1126/science.1081311.

Bahr, K. (1985), Magnetotellurische Messungen des elektrischen Widerstandes der Erdkruste und des oberen Mantels in Gebieten mit lokalen und regionalen Leitfaehigkeitsanomalien, Ph.D. thesis, Univ. Goettingen.

Bahr, K. (1988), Interpretation of the magnetotelluric impedance tensor: regional induction and local telluric distortion, *Journal of Geophysics*, *62*, 119–127.

Bahr, K. (1997), Electrical anisotropy and conductivity distribution functions of fractal random networks and of the crust: the scale effect of connectivity, *Geophysical Journal International*, *130*, 649–660.

Bahr, K., and F. Simpson (2002), Electrical anisotropy below slow- and fast-moving plates: Paleoflow in the upper mantel ?, *Science*, *295*, 1270–1272.

Bahr, K., N. Olsen, and T. J. Shankland (1993), On the combination of the magnetotelluric and the geomagnetic depthsounding method for resolving an electrical conductivity increase at 400 km depth, *Geophysical Research Letters*, *20*(24), 2937–2940.

Bahr, K., M. Bantin, C. Jantos, E. Schneider, and W. Storz (2000), Electrical anisotropy from electromagnetic array data: implications for the conduction mechanism and for distortion at long periods, *Physics of the Earth and Planetary Interiors*, *119*, 237–257.

Bailey, R. (1970), Inversion of the geomagnetic induction problem, *Proceedings of the Royal Society of London. A. Mathematical and Physical Sciences*, *315*(1521), 185–194, doi:10.1098/rspa.1970.0036.

Banda, E., E. Surinach, A. Aparicio, J. Sierra, and E. Ruiz de la Parte (1981), Crust and mantle structure of the central Iberian Meseta (Spain), *Geophysical Journal International*, *67*, 779–789.

Banda, E., J. Gallart, V. García-Dueñas, J. Dañobeitia, and J. Makris (1993), Lateral variation of the crust in the Iberian Peninsula: New evidence from the Betic Cordillera, *Tectonophysics*, *221*(1), 53–66, doi:10.1016/0040-1951(93)90027-H.

Barron, J. (2010), Surface wave tomography of the European upper mantle, part of author's PhD study.

Baumjohann, W. (1983), Ionospheric and field-aligned current systems in the auroral zone: A concise review, *Advances in Space Research*, *2*, 55–62.

Beamish, D. (1979), Source field effects on transfer functions at mid-latitudes, *Geophysical Journal of the Royal Astronomical Society*, *58*(1), 117–134, doi:10.1111/j.1365-246X.1979.tb01013.x.

Berdichevsky, M., and V. Dmitriev (1976a), Basic principles of magnetotelluric sounding curves, in *Geoelectric and geothermal studies*, edited by A. Adam, pp. 165–221, Akademiai Kiado, KAPG Geophysical Monograph.

Berdichevsky, M., I. Bezruk, and C. O.M. (1973), Magnetotelluric sounding with the use of mathematical filters, *Izv. Akad. Nauk. SSSR Fiz. Zeml.*, *3*, 72–92.

Berdichevsky, M., V. Dmitriev, and U. Schmucker (1981), Generalised magnetotelluric and magnetic gradient relations for a layered half-space, in *IAGA general assembly*, Edinburgh.

Berdichevsky, M., L. Vanyan, and V. Dmitriev (1989), Methods used in the U.S.S.R. to reduce near-surface inhomogeneity effects on deep magnetotelluric soundings, *Physics of the Earth and Planetary Interiors*, *53*, 194–206.

Berdichevsky, M., V. Dmitriev, and E. Pozdnjakova (1998), On two-dimensional interpretation of magnetotelluric soundings, *Geophysical Journal International*, *133*(3), 585–606, doi:10.1046/j.1365-246X.1998.01333.x.

Berdichevsky, M. N., and V. I. Dmitriev (1976b), Distortion of magnetic and electrical fields by near-surface lateral inhomogeneities, *Acta Geodaetica, Geophysica et Montanistica, Academy Sciences Hungary*, *11*, 447–483.

Bergamín, J., and A. Carbó (1986), Discusión de modelos para la corteza y manto superior en la zona sur del área centroibérica, basodos en anomalías gravimétricas, *Estidios Geológicos*, *42*, 143–146.

Bibby, H. M., T. G. Caldwell, and C. Brown (2005), Determinable and non-determinable parameters of galvanic distortion in magnetotellurics, *Geophysical Journal International*, *163*(3), 915–930, doi:10.1111/j.1365-246X.2005.02779.x.

Bijwaard, H., and W. Spakman (2000), Non-linear global P-wave tomography by iterated linearized inversion, *Geophysical Journal International*, *141*(1), 71–82, doi:10.1046/j.1365-246X.2000.00053.x.

Bijwaard, H., W. Spakman, and R. E. Engdahl (1998), Closing the gap between regional and global travel time tomography, *Journal of Geophysical Research*, *103*(B12), 30,055–30,078, doi:10.1029/98JB02467.

Birch, F. (1952), Elasticity and condition of the Earth's interior, *Jornal of Geophysical Research*, *57*, 227–286.

Bonadonna, F., and I. Villa (1986), Estudio geochronológico del volcanismo de Las Higueruelas, *Actas Castilla-La Mancha: Espacio y Sociedad*, *3*, 249–253.

Born, M. (1933), *Optik*, Springer-Verlag, New York.

Börner, R.-U. (2010), Numerical modelling in geo-electromagnetics: Advances and challenges, *Surveys of Geophysics*, *31*, 225–245, doi:10.1007/s10712-009-9087-x.

Bostick, F. X. (1977), A simple almost exact method of MT analysis, in *Workshop on Electrical Methods in Geothermal Exploration*, U.S. Geological Survey.

Brace, W., A. Orange, and T. Madden (1965), Effect of pressure on the electrical resistivity of water-saturated crystalline rocks, *Journal of Geophysical Research*, *70*(22), 5669–5698.

Brasse, H. (2003), Erdmagnetische Variationen.

Brasse, H., P. Lezaeta, V. Rath, K. Schwalenberg, W. Soyer, and V. Haak (2002), The Bolivian Altiplano conductivity anomaly, *Journal of Geophysical Research*, *107*(B5), 2096, doi:10.1029/2001JB000391.

Bullard, E., and R. Parker (1970), Electromagnetic induction in the oceans, in *The Sea*, vol. 4, edited by A. Maxwell, Wiley, New York.

BVP-Project (1981), *Basaltic Volcanism on the Terrestrial Planets*, Pergamon Press, New York, Basaltic Volcanism Study Project.

Cagniard, L. (1953), Basic theory of the magneto-telluric method of geophysical prospecting, *Geophysics*, *18*, 605–635.

Caldwell, T. G., H. M. Bibby, and C. Brown (2004), The magnetotelluric phase tensor, *Geophysical Journal International*, *158*, 457–469.

Calvert, A., E. Sandvol, D. Seber, M. Barazangi, S. Roecker, T. Mourabit, F. Vidal, G. Alguacil, and N. Jabour (2000), Geodynamic evolution of the lithosphere and upper mantle beneath the Alboran region of the western Mediterranean: Constraints from travel time tomography, *Journal of Geophysical Research*, *105*, 10,871–10,898, doi:10.1029/2000JB900024.

Capote, R., J. A. Munoz, J. L. Simon, C. L. Liesa, and L. E. Arlegui (2002), Alpine tectonics I: The Alpine system north of the Betic Cordillera, in *Gibbons and Moreno* [2002b], chap. 15, pp. 367–400.

Carbonell, R., V. Sallares, J. Pous, J. J. Dañobeitia, P. Queralt, J. J. Ledo, and G. V. Dueñas (1998), A multidisciplinary geophysical study in the Betic Chain (southern Iberia Peninsula), *Tectonophysics*, *288*(1-4), 137–152, doi:10.1016/S0040-1951(97)00289-8.

Carrasquilla, A., and L. Rijo (1998), Analysis of electrojet-distorted magnetotelluric sounding curves, *Journal of Applied Geophysics*, *40*(4), 187–204, doi:10.1016/S0926-9851(98)00029-9.

Cavaliere, T., and A. G. Jones (1984), On the identification of a transition zone in electrical conductivity between the lithosphere and asthenosphere: a plea for more precise phase data, *Journal of Geophysics*, *55*, 23–30.

Cebriá, J.-M., and J. López-Ruiz (1995), Alkali basalts and leucitites in an extensional intracontinental plate setting: The late Cenozoic Calatrava Volcanic Province (central Spain), *Lithos*, *35*(1-2), 27–46, doi:10.1016/0024-4937(94)00027-Y.

Cebriá, J.-M., and J. López-Ruiz (1996), A refined method for trace element modelling of nonmodal batch partial melting processes: The Cenozoic continental volcanism of Calatrava, central Spain, *Geochimica et Cosmochimica Acta*, *60*(8), 1355–1366, doi: 10.1016/0016-7037(96)00017-8.

Cebriá, J.-M., and M. Wilson (1995), Cenozoic mafic magmatism in Western/Central Europe: a common european asthenospheric reservoir?, *Terranova Abstracts Supplementary*, *7*, 162.

Chalouan, A., et al. (2006), Tectonic wedge escape in the southwestern front of the Rif Cordillera (Morocco), in *Moratti and Chalouan* [2006], pp. 101–118.

Chave, A., D. J. Thomson, and M. E. Ander (1987), On the robust estimation of power spectra, coherence, and transfer functions, *Journal of Geophysical Research*, *92*, 633–648.

Chave, A. D., and J. T. Smith (1994), On electric and magnetic galvanic distorion tensor decompositions, *Journal of Geophysical Research (Solid Earth)*, *99*(B3), 4669–4682.

Chave, A. D., and D. J. Thomson (1989), Some comments on magnetotelluric response function estimation, *Journal of Geophysical Research (Solid Earth)*, *94*(B10), 14,215–14,225.

Chave, A. D., and D. J. Thomson (2003), A bounded influence regression estimator based on the statistics of the hat matrix, *Applied Statistics*, *52*(3), 307–322.

Chen, G., H. Spetzler, I. Getting, and A. Yoneda (1996), Selected elastic moduli and their temperature derivatives for olivine and garnet with different Mg/(Mg+Fe) contents: results from GHz ultrasonic interferometry, *Geophysical Research Letters*, *23*, 5–8.

Clarke, F. (1889), The relative abundance of the chemical elements, *Bulletin Of The Philosophical Society Of Washington*, *11*, 131–142.

Cloetingh, S., E. Burov, F. Beekman, B. Andeweg, P. A. M. Andriessen, D. Garcia-Castellanos, G. D. Vicente, and R. Vegas (2002), Lithospheric folding in iberia, *Tectonics*, *21*(5), 1041, doi:10.1029/2001TC901031.

Cloetingh, S., H. Thybo, and C. Faccenna (2009), TOPO-EUROPE: Studying continental topography and deep earth–surface processes in 4D, *Tectonophysics*, *474*(1-2), 4–32, doi:10.1016/j.tecto.2009.04.015.

Colmenero, J., L. Fernandez, C. Moreno, J. Bahamonde, P. Barba, N. Heredia, and F. Gonzales (2002), Carboniferous, in *Gibbons and Moreno* [2002b], chap. 6, pp. 93–116.

Condie, K. (1982), *Plate tectonics and crustal evolution*, 2 ed., Pergamon, New York.

Constable, S., T. J. Shankland, and A. Duba (1992), The electrical conductivity of an isotropic olivine mantle, *Journal of Geophysical Research*, *97*, doi:10.1029/91JB02453.

Constable, S. C., R. L. Parker, and C. G. Constable (1987), Occam's inversion: A practical algorithm for generating smooth models from electromagnetic sounding data, *Geophysics*, *52*(3), 289–300.

Crespo, E., F. J. Luque, M. Rodas, H. Wada, and F. Gervilla (2006), Graphite-sulfide deposits in Ronda and Beni Bousera peridotites (Spain and Morocco) and the origin of carbon in mantle-derived rocks, *Gondwana Research*, *9*, 279–290.

Dañobeitia, J. J., V. Sallarès, and J. Gallart (1998), Local earthquakes seismic tomography in the Betic Cordillera (southern Spain), *Earth and Planetary Science Letters*, *160*, 225–239.

Dachnov, V. (1959), *Promyslovaja geofizika*, Izdat. Gostoptechizdat, Moscow.

Dachnov, V. (1962), *Interpretazija resultatov geofiziceskich issledovanij razrezov skavzin*, 2 ed., Izdat. Gostoptechizdat, Moscow, pp. 547.

Dachnov, W. (1975), *Geofiziceskie metody opredelenija kollektorskich svoistv is neftegasonasyscenija gornich porod*, Izdat. Nedra, Moscow.

Darbyshire, F. A., and S. Lebedev (2009), Rayleigh wave phase-velocity heterogeneity and multilayered azimuthal anisotropy of the Superior Craton, Ontario, *Geophysical Journal International*, *176*(1), 215–234, doi:10.1111/j.1365-246X.2008.03982.x.

Davies, G. F. (1995), Penetration of plates and plumes through the mantle transition zone, *Earth and Planetary Science Letters*, *133*(3-4), 507 – 516, doi:10.1016/0012-821X(95)00039-F.

de Groot-Hedlin, C., and S. Constable (1990), Occam's inversion to generate smooth, two-dimensional models from magnetotelluric data, *Geophysics*, *55*(12), 1613–1624.

De Mets, C., R. Gordon, D. Argus, and S. Stein (1994), Effect of recent revision to the geomagnetic reversal time scale on estimate of current plate motion, *Geophysical Research Letter*, *21*(20), 2191.

de Vicente, G., and R. Vegas (2009), Large-scale distributed deformation controlled topography along the western Africa-Eurasia limit: Tectonic constrains, *Tectonophysics*, *474*(1-2), 124–143.

de Vicente, G., J. Giner, A. Munoz-Martin, J. Gonzalez-Casado, and R. Lindo (1996), Determination of present-day stress tensor and neotectonic interval in the Spanish Central System and the Madrid Basin, central Spain, *Tectonophysics*, *266*, 405–424.

Debayle, E., B. Kennett, and K. Priestley (2005), Global azimuthal seismic anisotropy and the unique plate-motion deformation of Australia, *Nature*, *433*(7025), 509–512, doi:10.1038/nature03247.

DeMets, C., R. G. Gordon, D. F. Argus, and S. Stein (2006), Current plate motions, *Geophysical Journal International*, *165*(1), 425–478.

Deschamps, F., S. Lebedev, T. Meier, and J. Trampert (2008), Stratified seismic anisotropy reveals past and present deformation beneath the east-central United States, *Earth and Planetary Science Letters*, *274*(3-4), 489 – 498, doi:10.1016/j.epsl.2008.07.058.

Dewey, J. F., M. L. Helman, S. D. Knott, E. Turco, and D. H. W. Hutton (1989), Kinematics of the western Mediterranean, *Geological Society, London, Special Publications*, *45*(1), 265–283, doi:10.1144/GSL.SP.1989.045.01.15.

Díaz, J., and J. Gallart (2009), Crustal structure beneath the Iberian Peninsula and surrounding waters: A new compilation of deep seismic sounding results, *Physics of the Earth and Planetary Interiors*, *173*(1-2), 181–190, doi:10.1016/j.pepi.2008.11.008.

Dmitriev, V. I., and M. N. Berdichevsky (1979), The fundamental model of magnetotelluric sounding, *Proceedings of the IEEE*, *67*(7), 1034–1044.

Doblas, M., J. López-Ruiz, M. Hoyos, C. Martín, and J. Cebriá (1991), Late cenozoic indentation/escape tectonics in the eastern betic cordilleras and its consequences on the iberian foreland, *Estudios Geológicos*, *47*, 193–205.

Duba, A. G. (1976), Are laboratory electrical conductivity data relevant to the Earth?, *Acta Geodaetica, Geophysica et Montanistica, Academy Sciences Hungary*, *11*, 485–495.

Duba, A. G. (1977), Electrical conductivity of coal and coal char, *Fuel*, *56*(4), 441 – 443, doi:10.1016/0016-2361(77)90074-6.

Duba, A. G. (1983), Electrical conductivity of Colorado oil shale to 900°C, *Fuel*, *62*(8), 966 – 972, doi:10.1016/0016-2361(83)90172-2.

Duba, A. G., and T. J. Shankland (1982), Free carbon & electrical conductivity in the Earth's mantle, *Geophysical Research Letters*, *9*(11), 1271–1274.

Duba, A. G., J. N. Boland, and A. E. Ringwood (1973), Electrical conductivity of pyroxene, *Journal of Geology*, *81*, 727–735.

Duba, A. G., H. C. Heard, and R. N. Schock (1974), Electrical conductivity of olivine at high pressure and under controlled oxygen fugacity, *Journal of Geophysical Research*, *79*, doi:10.1029/JB079i011p01667.

Duba, A. G., H. C. Heard, and R. N. Schock (1976), Electrical conductivity of orthopyroxene to 1400°C and the selenotherm, in *7th Lunar Science Conference*, pp. 3173–3191, NASA and Lunar Science Institute New York, Pergamon Press, New York.

Duba, A. G., E. Huengest, G. Nover, G. Will, and H. Jödicke (1988), Impedance of black shale from Münsterland I Borehole: An anomalously good conductor?, *Geophysical Journal*, *94*(3), 413–419, doi:10.1111/j.1365-246X.1988.tb02264.x.

Duba, A. G., S. Heikamp, W. Meurer, G. Nover, and G. Will (1994), Evidence from samples for the role of accessory minerals in lower-crustal conductivity, *Nature*, *367*, 59–61.

Dubrovinsky, L., and J. F. Lin (2009), Mineral physics quest to the Earth's core, *EOS, Transaction of the American Geophysical Union*, *90*, 21–22.

Dziewonski, A. M., and D. L. Anderson (1981), Preliminary reference Earth model, *Physics of the Earth and Planetary Interiors*, *25*, 297–356, doi:10.1016/0031-9201(81)90046-7.

Dziewonski, A. M., and F. Gilbert (1971), Solidity of the Inner Core of the Earth inferred from normal mode observations, *Nature*, *234*(5330), 465–466, doi:10.1038/234465a0.

Eaton, D. W., A. G. Jones, and I. J. Ferguson (2004), Lithospheric anisotropy structure inferred from collocated teleseismic and magnetotelluric observations: Great Slave Lake shear zone, northern Canada, *Geophysical Research Letters*, *31*(10.1029/2004GL020939), L19,614.

Eaton, D. W., F. Darbyshire, R. L. Evans, H. Grütter, A. G. Jones, and X. Yuan (2009), The elusive lithosphere-asthenosphere boundary (LAB) beneath cratons, *Lithos*, *109*(1–2), 1–22, doi:10.1016/j.lithos.2008.05.009.

Edwards, R. N., and M. N. Nabighian (1981), Extensions of the Magnetometric Resistivity (MMR) method, *Geophysics*, *46*, 459–460.

Egbert, G. (1997), Robust multiple-station magnetotelluric data processing, *Geophysical Journal International*, *130*, 475–496.

Egbert, G. D., and J. R. Booker (1986), Robust estimation of geomagnetic transfer functions, *Geophysical Journal of the Royal Astronomical Society*, *87*(2), 173–194.

Egbert, G. D., and J. R. Booker (1992), Very long period magnetotellurics at tuscon observatory: implications for mantle conductivity, *Journal of Geophysical Research*, *98*, 15,099–15,112.

Elthon, D. (1979), High magnesia liquids as the parental magma for ocean floor basalts, *Nature*, *278*, 514–518.

Evans, R. L., J. Escartín, and M. Cannat (2010), A short electromagnetic profile across the Kane Oceanic Core Complex, *Geophysical Research Letters*, *37*, L15,309, doi: 10.1029/2010GL043813.

Fambitakoye, O., and P. N. Mayaud (1976a), Equatorial electrojet and regular daily variation SR - I: A determination of the equatorial electrojet parameters, *Journal of Atmospheric and Terrestrial Physics*, *38*, 1–17.

Fambitakoye, O., and P. N. Mayaud (1976b), Equatorial electrojet and regular daily variation SR - II: The centre of the equatorial electrojet, *Journal of Atmospheric and Terrestrial Physics*, *38*, 19–26.

Fambitakoye, O., and P. N. Mayaud (1976c), Equatorial electrojet and regular daily variation SR - IV: Special features in particular days, *Journal of Atmospheric and Terrestrial Physics*, *38*, 123–134.

Fernandez, M., I. Marzan, A. Correia, and E. Ramalho (1998), Heat flow, heat production and lithospheric thermal regime in the Iberian Peninsula, *Tectonophysics*, *291*, 29–53.

Fernández-Lozano, J., D. Sokoutis, E. Willingshofer, S. Cloetingh, and G. De Vicente (2011), Cenozoic deformation of iberia: A model for intraplate mountain building and basin development based on analogue modeling, *Tectonics*, *30*(1), TC1001, doi:10.1029/2010TC002719.

Fletcher, R., and M. Powell (1963), A rapidly convergent descent method for minimization, *Computer Journal*, *6*, 163–168.

Fletcher, R., and C. Reeves (1964), Function minimization by conjugate gradients, *Computer Journal*, *7*, 149–154.

Forbes, J. M. (1981), The equatorial electrojet, *Reviews of Geophysics and Space Physics*, *19*, 469–504.

Fournier, H. (1968), Proposition d'une méthode pour déterminer la structure du premier millier de kilometres de la terre d'après la résistivé apparente, *Acta Geophysica Polonica*, *16*(3), 215–248.

Franke, A., R.-U. Börner, and K. Spitzer (2007), Adaptive unstructured grid finite element simulation of two-dimensional magnetotelluric fields for arbitrary surface and seafloor topography, *Geophysical Journal International*, *171*, 71–86, doi:10.1111/j.1365-246x.2007.03481.x.

Fullea, J., M. Fernandez, H. Zeyen, and J. Vergés (2007), A rapid method to map the crustal and lithospheric thickness using elevation, geoid anomaly and thermal analysis. application to the gibraltar arc system, atlas mountains and adjacent zones, *Tectonophysics*, *430*, 97–117.

Fullea, J., J. C. Afonso, J. A. D. Connolly, M. Fernàndez, D. García-Castellanos, and H. Zeyen (2009), Litmod3d: An interactive 3-D software to model the thermal, compositional, density, seismological, and rheological structure of the lithosphere and sublithospheric upper mantle, *Geochemistry, Geophysics, Geosystems*, *10*(8), Q08,019, doi:10.1029/2009GC002391.

Fullea, J., J. C. Afonso, M. Fernàndez, and J. Vergés (2010), The structure and evolution of the lithosphere - asthenosphere boundary beneath the trans-mediterranean region, *Lithos*, *120*(1–2), 74–95.

Fullea, J., M. R. Muller, and A. G. Jones (2011), The electrical conductivity of the continental lithospheric mantle: new insights from integrated geophysical and petrological modelling. application to the kaapvaal craton and rehoboth terrane, southern africa, *Journal of Geophysical Research*, iN PROGRESS.

Gaillard, F. (2004), Laboratory measurements of electrical conductivity of hydrous and dry silicic melts under pressure, *Earth and Planetary Science Letters*, *218*(1-2), 215–228, doi:10.1016/S0012-821X(03)00639-3.

Gaillard, F., M. Malki, G. Iacono-Marziano, M. Pichavant, and B. Scaillet (2008), Carbonatite melts and electrical conductivity in the asthenosphere, *Science*, *322*(5906), doi:10.1126/science.1164446.

Galindo-Zaldívar, J., A. Jabaloy, F. González-Lodeiro, and F. Aldaya (1997), Crustal structure of the central sector of the Betic Cordillera (SE Spain), *Tectonics*, *16*, 18–37.

Gallart, J., G. Fernandez-Viejo, J. Diaz, N. Vidal, and J. Pulgar (1995), Deep structure of the transition between the Cantabrian Mountains and the North Iberian Margin from wide-angle ESCIN data, *Rev. Soc. Geol. Espana*, *8*(4), 365–382.

Gamble, T. D., W. M. Goubau, and J. Clarke (1979), Magnetotellurics with a remote magnetic reference, *Geophyiscs*, *44*(1), 53–68.

Ganapathy, R., and E. Anders (1974), Bulk compositions of the Moon and Earth estimated from meteorites, in *Proceedings of Lunar Science conference, 5*, pp. 1181–1206.

Garcia, X., and A. G. Jones (2001), Decomposition of three-dimensional magnetotelluric data, in *Three-Dimensional Electromagnetics: Methods in Geochemistry and Geophysics*, vol. 35, edited by M. S. Zhdanov and P. E. Wannamaker, pp. 235–250, Elsevier, Amsterdam.

Garcia, X., and A. G. Jones (2002), Atmospheric sources for audio-magnetotelluric (amt) sounding, *Geophysics*, *67*(2), 448–458, doi:10.1190/1.1468604.

Garcia, X., and A. G. Jones (2008), Robust processing of magnetotelluric data in the AMT dead band using the continuous wavelet transform, *Geophysics*, *73*(3), F223–F234.

Garcia, X., and A. G. Jones (2010), Internal structure of the western flank of the cumbre vieja volcano, la palma, canary islands, from land magnetotelluric imaging, *Journal of Geophysical Research*, *115*(B7), B07,104, doi:10.1029/2009JB006445.

Garcia, X., A. D. Chave, and J. A. G. (1997), Robust processing of magnetotelluric data from the auroral zone, *Journal of Geomagnetism and Geoelectricity*, *49*(11-12), 1451–1468.

Garcia, X., J. Ledo, and P. Queralt (1999), 2D inversion of 3D magnetotelluric data: The Kayabe dataset, *Earth Planets Space*, *51*, 1135–1143.

Garcia-Alcalde, J., P. Carls, M. Pardo Alonso, J. Sanz Lopez, F. Soto, M. Truyols-Massoni, and J. Valenzuela-Rios (2002), Devonian, in *Gibbons and Moreno* [2002b], chap. 6, pp. 68–91.

Gibbons, W., and T. Moreno (2002a), Introduction and overview, in *Gibbons and Moreno* [2002b], chap. 1, pp. 1–6.

Gibbons, W., and T. Moreno (Eds.) (2002b), *The Geology of Spain*, Geological Society, London.

Glatzmaier, G. A. (2002), Geodynamo simulations - How realistic are they?, *Annual Review of Earth and Planetary Sciences*, *30*, 237–257.

Glatzmaier, G. A., and P. H. Roberts (1995), A three-dimensional self-consistent computer simulation of a geomagnetic field reversal, *Nature*, *377*, 203–209.

Global Hydrology Resource Center, N. (2010), Annual flash rate of lightnings.

Glover, P. W. J. (2010), A generalized Archie's law for n phases, *Geophysics*, *75*(6), E247–E265, doi:10.1190/1.3509781.

Goes, S., W. Spakman, and H. Bijwaard (1999), A lower mantle source for central European volcanism, *Science*, *286*, 1928–1931.

Goes, S., R. Govers, and P. Vacher (2000), Shallow mantle temperatures under Europe from P and S wave tomography, *Journal of Geophysical Research*, *105*, 11,153–11,169.

Goldberg, D. (1989), *Genetic algorithms in search, optimization and machine learning*, Addison-Wesley, Reading, MA.

Goldstein, M., and D. Strangway (1975), Audio-frequency magnetotellurics with a grounded electric dipole source, *Geophysics*, *40*, 669–683.

Gomez, J., M. Diaz-Molina, and A. Lendinez (1996), Tectono-sedimentary analysis of the Loranca Basin (Upper Oligocene-Miocene, central Spain): A 'non-sequenced' foreland basin, in *Tertiary basins of Spain: The stratigraphic record of crustal kinematics*, edited by P. Friend and C. J. Dabrio, chap. C5, pp. 285–294, Cambridge University Press, Cambridge.

Gough, D. I., and J. D. de Beer (1980), Source-field bias in geomagnetic transfer functions: A case history, *Journal of Geomagnetism and Geoelectricity*, *32*, 471–482.

Granet, M., M. Wilson, and U. Achauer (1995), Imaging a mantle plume beneath the French Massif Central, *Earth and Planetary Science Letters*, *136*(3–4), 281–296, doi: 10.1016/0012-821X(95)00174-B.

Groom, R. W., and K. Bahr (1992), Corrections for near surface effects: Decomposition of the magnetotelluric impedance tensor and scaling corrections for regional resistivities: A tutorial, *Surveys in Geophysics*, *13*(4-5), 341–379.

Groom, R. W., and R. C. Bailey (1989), Decomposition of magnetotelluric impedance tensors in the presence of local three-dimensional galvanic distortion, *Journal of Geophysical Research (Solid Earth)*, *94*(B2), 1913–1925.

Gubbins, D. (2004), *Time series analysis and inverse theory for geophysics*, vol. 1, Cambridge University Press, The Edinburgh Building, Cambridge CB2 2RU, UK.

Gutenberg, B., and C. F. Richter (1938), P' and the Earth's core, *Geophysical Journal International*, *4*(5), 363–372, doi:10.1111/j.1365-246X.1938.tb01761.x.

Gutierrez-Elorza, M., et al. (2002), Quaternary, in *Gibbons and Moreno* [2002b], chap. 14, pp. 335–366.

Gutscher, M.-A., J. Malod, J.-P. Rehault, I. Contrucci, F. Klingelhoefer, L. Mendes-Victor, and W. Spakman (2002), Evidence for active subduction beneath Gibraltar, *Geology*, *30*(12), 1071–1074.

Haak, V., and R. Hutton (1986), Electrical resistivity in continental lower crust, *Geological Society, London, Special Publications*, *24*(1), 35–49, doi:10.1144/GSL.SP.1986.024.01.05.

Habashy, T., R. Groom, and B. Spies (1993), Beyond the born and rytov approximations: A nonlinear approach to electromagnetic scattering, *Journal of Geophysical Research*, *98*, 1759–1776.

Haber, E. (1999), Modeling 3D EM using potentials and mixed finite elements, in *Oristaglio and Spies* [1999], pp. 12–15.

Haber, E. (2005), Quasi-Newton methods for large scale electromagnetic inverse problem, *Inverse Problem*, *21*, 305–317.

Haber, E., U. M. Ascher, D. A. Aruliah, and D. W. Oldenburg (2000), Fast simulation of 3d electromagnetic problems using potentials, *Journal of Computational Physics*, *163*(1), 150–171, doi:10.1006/jcph.2000.6545.

Haber, E., U. Ascher, and D. Oldenburg (2005), Inversion of 3D electromagnetic data in frequency and time domain using an inexact all-at-once approach, *Geophysics*, *69*(5), 1216–1228.

Hamilton, M. P., A. G. Jones, R. L. Evans, S. Evans, C. Fourie, X. Garcia, A. Mountford, and J. E. Spratt (2006), Electrical anisotropy of South African lithosphere compared with seismic anisotropy from shear-wave splitting analyses, *Physics of The Earth and Planetary Interiors*, *158*(2-4), 226 – 239, doi:10.1016/j.pepi.2006.03.027.

Hampel, R., M. Ronchetti, P. Rousseeuw, and W. Stahel (1986), *Robust Statistics. The Approach based on influence functions*, Wiley, New York.

Hansen, P. (1998), *Rank Deficient and Discrete Ill-Posed Problems: Numerical Aspects of Linear Inversion*, Monographs on mathematical modeling and computation, Society for Industrial and Applied Mathematics, Philadelphia, PA, p. 247.

Hashin, Z., and S. Shtrikman (1962), A variational approach to the theory of the effective magnetic permeability of multiphase materials, *Journal of Applied Physics*, *33*, 3125–3131.

Hastings, W. (1970), Monte Carlo sampling methods using Markov Chains and their applications, *Biometrika*, *57*, 97–109.

Heinson, G. (1999), Electromagnetic studies of the lithosphere and asthenosphere, *Surveys in Geophysics*, *20*, 229–255.

Heinson, G., and F. Lilley (1993), An application of thin sheet electromagnetic modelling to the Tasman Sea, *Physics of the Earth and Planetary Interiors*, *81*, 231–251.

Heise, W., and J. Pous (2001), Effects of anisotropy on the two-dimensional inversion procedure, *Geophysical Journal International*, *147*(3), 610–621.

Hermance, J. F., and W. R. Peltier (1970), Magnetotelluric fields of a line current, *Journal of Geophysical Research*, *75*, 3351–3355.

Hesse, D. (1982), An investigation of the equatorial electrojet by means of groundbased magnetic measurements in Brazil, *Annals of Geophysics*, *38*, 315–320.

Hirsch, L., T. Shankland, and A. Duba (1993), Electric conduction and polaron mobility in Fe-bearing olivine, *Geophysical Journal International*, *114*, 36–44.

Hoernle, K., Y. Zhang, and D. Graham (1995), Seismic and geochemical evidence for large-scale mantle upwelling beneath the Eastern Atlantic and Western and Central Europe, *Nature*, *374*, 34–39.

Hohmann, G. (1975), Three-dimensional induced-polarization and electromagnetic modeling, *Geophysics*, *40*, 309–324.

Hohmann, G. W. (1987), Numerical modelling of electromagnetic methods of geophysics, in *Nabighian* [1987], pp. 314–364.

Hördt, A., R. Blaschek, A. Kemna, and N. Zisser (2007), Hydraulic conductivity estimation from induced polarisation data at the field scale – the Krauthausen case history, *Journal of Applied Geophysics*, *62*(1), 33 – 46, doi:10.1016/j.jappgeo.2006.08.001.

Hoyt, D. V., and K. H. Schatten (1998a), Group sunspot numbers: A new solar activity reconstruction. part 1, *Solar Physics*, *181*, 189–219.

Hoyt, D. V., and K. H. Schatten (1998b), Group sunspot numbers: A new solar activity reconstruction. part 1, *Solar Physics*, *181*, 491–512.

Huang, X., Y. Xu, and S.-i. Karato (2005), Water content in the transition zone from electrical conductivity of wadsleyite and ringwoodite, *Nature*, *434*(7034), 746–749, doi:10.1038/nature03426.

Huber, P. (1981), *Robust statistics*, Wiley, New York.

Hughes, W. J., and J. R. Wait (1975), Electromagnetic induction over a two-layer earth with a sinusoidal overburden, *Pure and Applied Geophysics*, *113*(1), 591–599, doi: 10.1007/BF01592944.

Hutton, R. (1969), Electromagnetic induction in the Earth by equatorial electrojets, *Nature*, *222*, 363–364.

Hutton, R. (1972), Some problems of electromagnetic induction in the equatorial electrojet region: I - magneto-telluric relations, *Geophysical Journal of the Royal Astronomical Society*, *28*(3), 267–284, doi:10.1111/j.1365-246X.1972.tb06128.x.

Hutton, R., and A. Leggeat (1972), Some problems of electromagnetic induction in the equatorial electrojet region: I - the analysis of magnetic and telluric variation of Zaria, *Geophysical Journal of the Royal Astronomical Society*, *28*(3), 411–424.

Ichiki, M., M. Uyeshima, H. Utada, Z. Guoze, T. Ji, and M. Mingzhi (2001), Upper mantle conductivity structure of the back-arc region beneath northeastern China, *Geophysical Research Letter*, *28*(19), 3773–3776, doi:10.1029/2001GL012983.

ILIHA DSS Group (1993), A seismic sounding investigation of the lithospheric heterogeneity and anisotropy beneath the iberian peninsula, *Tectonophysics*, *221*, 35–51.

Ingham, M. R., H. M. Bibby, W. Heise, K. A. Jones, P. Cairns, S. Dravitzki, S. L. Bennie, T. G. Caldwell, and Y. Ogawa (2009), A magnetotelluric study of Mount Ruapehu volcano, New Zealand, *Geophysical Journal International*, *179*(2), 887–904, doi:10.1111/j.1365-246X.2009.04317.x.

Inhester, B., U. Wedeken, A. Korth, S. Perraut, and M. Stokholm (1985), Generation of pc2 pulsations by energetic O(+) ions, in *Results of the Arcad 3 project and of the recent programmes in magnetospheric and ionospheric physics; Proceedings of the International Conference, Toulouse, France, May 22-25, 1984 (A86-16601 05-46). Toulouse, Cepadues-Editions, 1985, p. 937-942.*, pp. 937–942.

Instituto Geografico Nacional, S. I. S. (2010), Earthquake catalogue, http://www.ign.es/ign/en/IGN/SisCatalogo.jsp.

Irifune, T., and A. Ringwood (1987), Phase transformations in primitive MORB and pyrolite compositions to 25 GPa and geophysical implications, in *High Pressure Research in Mineral Physics*, *Geophysical Monograph*, vol. 39, edited by M. H. Manghnini, pp. 231–242, American Geophysical Union, Washington D.C.

Jacobs, J. A. (1953), The Earth's inner core, *Nature*, *172*(4372), 297–298, doi:10.1038/172297a0.

James, D., F. Boyd, D. Schutt, D. Bell, and R. Carlson (2004), Xenolith constraints on seismic velocities in the upper mantle beneath southern Africa, *Geochemistry, Geophysics, and Geosystems*, *5*, Q01,002, doi:10.1029/2003GC000551.

Jeffreys, H. (1939), The time of the core waves, *Geophysical Journal International*, *4*(7), 548–561, doi:10.1111/j.1365-246X.1939.tb02915.x.

Ji, S., S. Rondenay, M. Mareschal, and G. Senechal (1996), Obliquity between seismic and electrical anisotropies as a potential indicator of movement sense for ductile shear zones in the upper mantle, *Geology*, *24*(11), 1033–1036.

Jin, Z.-M., J. Zhang, H. Green, and S. Jin (August, 2001), Eclogite rheology: Implications for subducted lithosphere, *Geology*, *29*(8), 667–670, doi:10.1130/0091-7613(2001)029⟨0667:ERIFSL⟩2.0.CO;2.

Jiracek, G. R. (1990), Near-surface and topographic distortions in electromagnetic induction, *Surveys in Geophysics*, *11*, 163–203.

Jones, A. (1983a), The problem of current channelling: A critical review, *Geophysical Surveys*, *6*, 79–122.

Jones, A. (1992), Electrical properties of the lower continental crust, in *Continental Lower Crust*, edited by D. Fountain, pp. 81–131, Elsevier, Amsterdam.

Jones, A. (2009), The eLAB, in *DefLAB workshop*, Dublin Institute for Advanced Studies.

Jones, A., and R. Hutton (1979), A multi-station magnetotelluric study in southern scotland - ii: Monte-carlo inversion of the data and its geophysical and tectonic implications, *Geophysical Journal of the Royal Astronomical Society*, *56*, 351–368.

Jones, A., T. Katsube, and P. Schwann (1997), The longest conductivity anomaly in the world explained: Sulphides in fold hinges causing very high electrical anisotropy, *Journal of Geomagnetism and Geoelectricity*, *49*(12), 1619–1629.

Jones, A. G. (1980), Geomagnetic induction studies in scandinavia: I. determination of the inductive response function from the magnetometer array data, *Journal of Geophysics*, *48*, 181–194.

Jones, A. G. (1983b), On the equivalence of the Niblett and Bostick transformations in the magnetotelluric method, *Journal of Geophysics*, *53*, 72–73.

Jones, A. G. (1988), Static shift of magnetotelluric data and its removal in a sedimentary basin environment, *Geophysics*, *53*(7), 967–978.

Jones, A. G. (1999), Imaging the continental upper mantle using electromagnetic methods, *Lithos*, *48*(1-4), 57 – 80, doi:10.1016/S0024-4937(99)00022-5.

Jones, A. G. (2006), Electromagnetic interrogation of the anisotropic Earth: Looking into the Earth with polarized spectacles, *Physics of the Earth and Planetary Interiors*, *158*, 281–291.

Jones, A. G., and J. A. Craven (1990), The North American Central Plains conductivity anomaly and its correlation with gravity, magnetic, seismic, and heat flow data in Saskatchewan, Canada, *Physics of the Earth and Planetary Interiors*, *60*, 169–194.

Jones, A. G., and R. W. Groom (1993), Strike angle determination from the magnetotelluric tensor in the presence of noise and local distortion: rotate at your peril!, *Geophysical Journal International*, *113*, 524–534.

Jones, A. G., and H. Jödicke (1984), Magnetotelluric transfer function estimation improvement by a coherence-based rejection technique, in *54th Annual International Meeting, Expanded Abstracts*, Soc. of Expl. Geophys.

Jones, A. G., A. D. Chave, G. Egbert, D. Auld, and K. Bahr (1989), A comparison of techniques for magnetotelluric response function estimation, *Journal of Geophysical Research (Solid Earth)*, *94*(10), 14,201–14,213.

Jones, A. G., R. L. Evans, and D. W. Eaton (2009), Velocity-conductivity relationships for mantle mineral assemblages in archean cratonic lithosphere based on a review of laboratory data and Hashin-Shtrikman extremal bounds, *Lithos*, *109*(1-2), 131–143, doi:10.1016/j.lithos.2008.10.014.

Jones, A. G., J. Plomerova, T. Korja, F. Sodoudi, and W. Spakman (2010), Europe from the bottom up: A statistical examination of the central and northern European lithosphere–asthenosphere boundary from comparing seismological and electromagnetic observations, *Lithos*, *120*, 14–29.

Jones, C. (1987), Is extension in Death Valley accommodated by thinning of the mantle lithosphere beneath the Sierra Nevada, California?, *Tectonics*, *6*(4), 449–473.

Jones, F., and L. Pascoe (1972), The perturbation of alternating geomagnetic fields by three-dimensional conductivity inhomogeneities, *Geophysical Journal of the Royal Astronomical Society*, *27*, 479–484.

Julià, J., and J. Mejía (2004), Thickness and Vp/Vs ratio variation in the Iberian Crust, *Geophysical Journal International*, *156*(1), 59–72, doi:10.1111/j.1365-246X.2004.02127.x.

Julià, J., J. Vila, and R. Macià (1998), The receiver structure beneath the Ebro Basin, Iberian Peninsula, *Bulletin of the Seismological Society of America*, *88*(6), 1538–1547.

Kalscheuer, T., L. B. Pedersen, and W. Siripunvaraporn (2008), Radiomagnetotelluric two-dimensional forward and inverse modelling accounting for displacement currents, *Geophysical Journal International*, *175*(2), 486–514, doi:10.1111/j.1365-246X.2008.03902.x.

Kao, D. (1984), Geoelectromagnetic induction by a line current in the ionosphere, Submitted to Ann. Geophys.

Karato, S. (1990), The role of hydrogen in the electrical conductivity of the upper mantle, *Nature*, *347*, 272–273.

Karato, S., Z. Wang, B. Liu, and K. Fujino (1995), Plastic deformation of garnets: systematics and implications for the rheology of the mantle transition zone, *Earth and Planetary Science Letters*, *130*(1-4), 13 – 30, doi:10.1016/0012-821X(94)00255-W.

Karato, S., M. R. Riedel, and D. A. Yuen (2001), Rheological structure and deformation of subducted slabs in the mantle transition zone: implications for mantle circulation and deep earthquakes, *Physics of The Earth and Planetary Interiors*, *127*(1-4), 83 – 108, doi:10.1016/S0031-9201(01)00223-0.

Kaufman, A. (1985), Tutorial: Distributing of alternating electrical charges in a conducting medium, *Geophysical Prospecting*, *33*, 171–184.

Kellett, R. L., M. Mareschal, and R. D. Kurtz (1992), A model of lower crustal electrical anisotropy for the Pontiac Subprovince of the Canadian Shield, *Geophysical Journal International*, *111*(1), 141–150, doi:10.1111/j.1365-246X.1992.tb00560.x.

Kelley, M. C. (1989), *The Earth's ionosphere: Plasma physics and electrodynamics*, *International Geophysics Series*, vol. 43, 1 ed., Academic Press, Elsevier, 525 B, Street Suite 1900, San Diego, California 92101-4495, USA, reprint: Dec.2009, 2nd edition, vol. 96, ISBN 978-0-12-088425-4.

Kennett, B. L. N., E. R. Engdahl, and R. Buland (1995), Constraints on seismic velocities in the Earth from travel times, *Geophysical Journal International*, *122*, 108–125.

Kisabeth, J., and G. Rostoker (1977), Modeling of three-dimensional current systems associated with magnetospheric substorms, *Geophysical Journal of the Royal Astronomical Society*, *49*, 655–683.

Kopylova, M., J. Lo, and N. Christensen (2004), Petrological constraints on seismic properties of the Slave upper mantle (northern Canada), *Lithos*, *77*, 493–510, doi: 10.1016/j.lithos.2004.03.012.

Korja, T. (2007), How is the European lithosphere imaged by magnetotellurics?, *Surveys in Geophysics*, *28*, 239–272, doi:10.1007/s10712-007-9024-9.

Korja, T., P. Tuisku, T. Pernu, and J. Karhu (1996), Lapland Granulite Belt: Implications for properties and evolution of deep continental crust, *Terra Nova*, *8*, 48–58.

Koulakov, I., M. K. Kaban, M. Tesauro, and S. Cloetingh (2009), P- and S-velocity anomalies in the upper mantle beneath europe from tomographic inversion of ISC data, *Geophysical Journal International*, *179*(1), 345–366, doi:10.1111/j.1365-246X.2009.04279.x.

Kreutzmann, A., A. Neska, H. Brasse, and the EMTESZ Working Group (2005), The EMTESZ project: Induction vectors, strikes and 2-D modelling, in *21. Kolloquium der Elektromagnetischen Tiefenforschung*, edited by O. Ritter and H. Brasse, pp. 288–291.

Kurtz, R. D., J. A. Craven, E. R. Niblett, and R. A. Stevens (1993), The conductivity of the crust and mantle beneath the Kapuskasing Uplift: Electrical anisotropy in the upper mantle, *Geophysical Journal International*, *113*, 483–498.

Kuvshinov, A., and N. Olsen (2006), A global model of mantle conductivity derived from 5 years of CHAMP, Oersted, and SAC-C magnetic data, *Geophysical Research Letter*, *33*, doi:10.1029/2006GL027083.

Kuvshinov, A., and N. Olsen (2008), A global model of mantle conductivity derived from 7 years of CHAMP, Oersted, and SAC-C magnetic data, Poster on 19th EMIW China.

Kuvshinov, A., H. Utada, A. Avdeev, and T. Koyama (2005), 3-D modelling and analysis of Dst C-responses in the North Pacific Ocean region, revisited, *Geophysical Journal International*, *160*, 505–526.

Kuvshinov, A. V., N. Olsen, D. B. Avdeev, and O. V. Pankratov (2002), Electromagnetic induction in the oceans and the anomalous behaviour of coastal C-responses for periods up to 20 days, *Geophysical Research Letter*, *29*(12), 1595–1599, doi: 10.1029/2001GL014409.

Lahiri, B. N., and A. T. Price (1939), Electromagnetic induction in non-uniform conductors, and the determination of the conductivity of the Earth from terrestrial magnetic variations, *Philosophical Transactions of the Royal Society of London. Series A, Mathematical and Physical Sciences*, *237*(784), 509–540.

Langer, R. (1933), An inverse problem in differential equations, *Bulletin of the American Mathematical Society*, *39*, 814–820.

Larsen, J. (1989), Transfer functions: Smooth estimates by least-square and remote reference methods, *Geophysical Journal International*, *99*(3), 645–663, doi:10.1111/j. 1365-246X.1989.tb02048.x.

Larsen, J. C., R. L. Mackie, A. Manzella, A. Fiordelisi, and S. Rieven (1996), Robust smooth magnetotelluric transfer functions, *Geophysical Journal International*, *124*(3), 801–819, doi:10.1111/j.1365-246X.1996.tb05639.x.

Ledo, J. (2005), 2-D versus 3-D magnetotelluric data interpretation, *Surveys in Geophysics*, *26*, 511–543.

Ledo, J., and A. G. Jones (2005), Upper mantle temperature determined from combining mineral composition, electrical conductivity laboratory studies and magnetotelluric field observations: Application to the intermontane belt, Northern Canadian Cordillera, *Earth and Planetary Science Letters*, *236*, 258–268.

Ledo, J., C. Ayala, J. Pous, P. Queralt, A. Marcuello, and J. A. Muñoz (2000), New geophysical constraints on the deep structure of the pyrenees, *Geophysical Research Letter*, *27*(7), 1037–1040, doi:10.1029/1999GL011005.

Ledo, J., P. Queralt, A. Martí, and A. Jones (2002), Two-dimensional interpretation of three-dimensional magnetotelluric data: An example of limitations and resolution, *Geophysical Journal International*, *150*, 127–139.

Ledo, J., A. G. Jones, I. J. Ferguson, and L. Wolynec (2004), Lithospheric structure of the Yukon, northern Canadian Cordillera, obtained from magnetotelluric data, *Journal of Geophysical Research (Solid Earth)*, *109*(B18), B04,410.

Levin, V., and J. Park (1997), P-sh conversions in a flat-layered medium with anisotropy of arbitrary orientation, *Geophysical Journal International*, *131*(2), 253–266, doi:10.1111/j.1365-246X.1997.tb01220.x.

Livelybrooks, D. (1993), Program 3Dfeem, a multidimensional electromagnetic finite element model, *Geophysical Journal International*, *114*, 443–458.

Livingston, W., and M. Penn (2009), Are sunspots different during this solar minimum?, *EOS, Transaction of the American Geophysical Union*, *90*(30), 257–264.

Lizarralde, D., A. Chave, G. Hirth, and A. Schultz (1995), Northeastern pacific mantle conductivity profile from long-period magnetotelluric sounding using Hawaii-to-California submarine cable data, *Journal of Geophysical Research*, *100*, 17,837–17,854.

Lopez-Gomez, J., A. Arche, and A. Perez-Lopez (2002), Permian and Triassic, in *Gibbons and Moreno* [2002b], chap. 10, pp. 185–212.

López-Ruiz, J., J. M. Cebriá, M. Doblas, R. Oyarzun, M. Hoyos, and C. Martín (1993), Cenozoic intra-plate volcanism related to extensional tectonics at Calatrava, central Iberia, *Journal of the Geological Society*, *150*(5), 915–922, doi:10.1144/gsjgs.150.5.0915.

López-Ruiz, J., J. M. Cebriá, and M. Doblas (2002), Cenozoic volcanism i: the Iberian peninsula, in *Gibbons and Moreno* [2002b], chap. 17, pp. 417–438.

López Sánchez-Vizcaíno, V., D. Rubatto, M. T. Gómez-Pugnaire, V. Trommsdorff, and O. Müntener (2001), Middle Miocene high-pressure metamorphism and fast exhumation of the Nevado-Filábride Complex, SE Spain, *Terra Nova*, *13*, 327–332.

Luterbacher, J., R. Rickli, E. Xoplaki, C. Tinguely, C. Beck, C. Pfister, and H. Wanner (2001), The Late Maunder Minimum (1675-1715): A key period for studying decadal scale climatic change in Europe, *Climatic Change*, *49*(4), 441–462, doi:10.1023/A:1010667524422.

Lviv Centre of Institute for Space Research (2009), *Long-period magnetotelluric instrument LEMI-417M: User Manual*, Lviv centre of institute for space research, 5-A Naukova St., Lviv, 79000, Ukraine.

Mackie, R. (2002), *User manual and software documentation for two-dimensional inversion of magnetotelluric data*, GSY-USA, Inc., 2261 Market Street, PMB 643, San Francisco, California 94114, anisotropy version 6.7.

Mackie, R. L., and T. R. Madden (1993), Three-dimensional magnetotelluric inversion using conjugate gradients, *Geophysical Journal International*, *115*, 215–229.

Mackie, R. L., J. T. Smith, and T. R. Madden (1994), Three-dimensional electromagnetic modeling using finite difference equations: The magnetotelluric example, *Radio Science*, *29*, 923–935.

Madden, T., and R. Mackie (1989), Three-dimensional magnetotelluric modeling and inversion, *Proceedings of the IEEE*, *77*, 318–333.

Malin, S. R. C. (1973), Worldwide Distribution of Geomagnetic Tides, *Philosophical Transactions of the Royal Society of London. Series A, Mathematical and Physical Sciences*, *274*(1243), 551–594, doi:10.1098/rsta.1973.0076.

Mareschal, M. (1986), Modelling of natural sources of magnetospheric origin in the interpretation of regional induction studies: a review, *Surveys in Geophysics*, *8*, 261–300.

Mareschal, M., R. Kellett, R. Kurtz, J. Ludden, S. Ji, and R. Bailey (1995), Archaean cratonic roots, mantle shear zones and deep electrical anisotropy, *Nature*, *375*(6527), 134–137, doi:10.1038/375134a0.

Marquardt, D. (1963), An algorithm for least-squares estimation of nonlinear parameters, *Society for Industrial and Applied Mathematics*, *11*, 431–441.

Marquis, G., A. G. Jones, and R. D. Hyndman (1995), Coincident conductive and reflective middle and lower crust in southern british columbia, *Geophysical Journal International*, *120*(1), 111–131, doi:10.1111/j.1365-246X.1995.tb05915.x.

Marriott, R. T., A. D. Richmond, and S. V. Venkateswaran (1979), The quiet-time equatorial electrojet and counter-electrojet, *Journal of Geomagnetism and Geoelectricity*, *31*, 311–340.

Martí, A. (2007), A magnetotelluric investigation of geoelectrical dimensionality and study of the central Betic crustal structure, Ph.D. thesis, University of Barcelona.

Martí, A., P. Queralt, A. G. Jones, and J. Ledo (2005), Research note: Improving Bahr's invariant parameters using the WAL approach, *Geophysical Journal International*, *163*(1), 38–41, doi:10.1111/j.1365-246X.2005.02748.x.

Martí, A., P. Queralt, E. Roca, J. Ledo, and J. Galindo-Zaldívar (2009a), Geodynamic implications for the formation of the Betic-Rif orogen from magnetotelluric studies, *Journal of Geophysical Research*, *114*(B1), B01,103, doi:10.1029/2007JB005564.

Martí, A., P. Queralt, and J. Ledo (2009b), WALDIM: A code for the dimensionality analysis of magnetotelluric data using the rotational invariants of the magnetotelluric tensor, *Computers and Geosciences*, doi:10.1016/j.cageo.2009.03.004.

Martin-Chivelet, J., et al. (2002), Cretaceous, in *Gibbons and Moreno* [2002b], chap. 12, pp. 255–292.

Matas, J., J. Bass, Y. Ricard, E. Mattern, and M. S. T. Bukowinski (2007), On the bulk composition of the lower mantle: predictions and limitations from generalized inversion of radial seismic profiles, *Geophysical Journal International*, *170*(2), 764–780, doi:10.1111/j.1365-246X.2007.03454.x.

Mathez, E. A., J. J. Roberts, A. G. Duba, A. K. Kronenberg, and S. L. Karner (2008), Carbon deposition during brittle rock deformation: Changes in electrical properties of fault zones and potential geoelectric phenomena during earthquakes, *Journal of Geophysical Research*, *113*(B12), B12,201, doi:10.1029/2008JB005798.

Mavko, G. (1980), Velocity and attenuation in partially molten rocks, *Journal of Geophysical Research*, *85*, 5173–5189.

Mayaud, P. N. (1977), The equatorial counter-electrojet. a review of its geomagnetic aspects, *Journal of Atmospheric and Terrestrial Physics*, *39*(9-10), 1055–1070, doi:10.1016/0021-9169(77)90014-9.

McNeice, G. W., and A. G. Jones (2001), Multisite, multifrequency tensor decomposition of magnetotelluric data, *Geophysics*, *66*(1), 158–173.

McPherron, R. L. (1991), Physical processes producing magnetospheric substorms and magnetic storms, in *Geomagnetism*, vol. 4, edited by J. Jacobs, pp. 593–739, Academic Press, London.

McPherron, R. L. (2005), Magnetic pulsations: Their sources and relation to solar wind and geomagnetic activity, *Surveys in Geophysics*, *26*(5), 545–592, doi:10.1007/s10712-005-1758-7.

Meier, T., S. Bartzsch, and S. Lebedev (2009), Constraints on the LAB depth and sharpness from surface waves, in *DefLAB workshop*, Dublin Institute for Advanced Studies.

Mendelson, K. S., and M. H. Cohen (1982), The effects of grain anisotropy on the electrical properties of sedimentary rocks, *Geophysics*, *47*, 257–263, doi:10.1190/1.1441332.

Merrill, R. T., and M. W. McElhinny (1983), *The Earth's magnetic field*, no. 32 in International Geophysics Series, Academic Press, London-New York.

Metropolis, N., and S. Ulam (1949), The Monte Carlo method, *J. Amer. Stat. Assoc.*, *44*, 335–341.

Miensopust, M. P. (2010), Multidimensional magnetotellurics: A 2D case study and a 3D approach to simultaneously invert for resistivity structure and distortion parameters, Ph.D. thesis, National University of Ireland, Galway, University Road, Galway, Ireland, in collaboration with the School of Cosmic Physics, Dublin Institute for Advanced Studies, Dublin, Ireland.

Miensopust, M. P., A. G. Jones, M. R. Muller, X. Garcia, and R. L. Evans (2011), Lithospheric structures and precambrian terrane boundaries in northeastern botswana revealed through magnetotelluric profiling as part of the southern african magnetotelluric experiment, *Journal of Geophysical Research*, *116*(B2), B02,401, doi:10.1029/2010JB007740.

Mitsuhata, Y., and T. Uchida (2004), 3D magnetotelluric modeling using the T-W document finite-element method, *Geophysics*, *69*, 108–119.

Mohorovičić, A. (1910), Das Beben vom 8. x. 1909, *Jahrbuch des Meteorologischen Observatoriums in Zagreb, für das Jahr 1909*, *9*, 1–63.

Moorkamp, M. (2007a), Comment on 'the magnetotelluric phase tensor' by T. Grant Caldwell, Hugh M. Bibby and Colin Brown, *Geophysical Journal International*, *171*(2), 565–566, doi:10.1111/j.1365-246X.2007.03490.x.

Moorkamp, M. (2007b), Joint inversion of MT and receiver-function data, Ph.D. thesis, National University of Ireland, Galway, University Road, Galway, Ireland, in collaboration with the School of Cosmic Physics, Dublin Institute for Advanced Studies, Dublin, Ireland.

Moorkamp, M., A. G. Jones, and D. W. Eaton (2007), Joint inversion of teleseismic receiver functions and magnetotelluric data using a genetic algorithm: Are seismic velocities and electrical conductivities compatible?, *Geophysical Research Letters*, *34*, L16,311, doi:10.1029/2007GL030519.

Moorkamp, M., A. G. Jones, and S. Fishwick (2010), Joint inversion of receiver functions, surface wave dispersion, and magnetotelluric data, *Journal of geophysical research*, *115*, B04,318, doi:10.1029/2009JB006369.

Moratti, G., and A. Chalouan (Eds.) (2006), *Tectonics of the Western Mediterranean and North Africa*, *Special Publications*, vol. 262, Geological Society, London.

Morgan, J. W., and E. Anders (1980), Chemical composition of Earth, Venus, and Mercury, *Proceedings of the National Academy of Sciences of the United States of America*, *77*(12), 6973–6977.

MTNet (2010), http://mtnet.info/main/source.html.

Mueller, M., R.D. Sdrolias, C. Gaina, and W. Roest (2008), Age, spreading rates and spreading symmetry of the world's ocean crust, *Geochemistry, Geophysics, Geosystems*, *9*(4), Q04,006, doi:10.1029/2007GC001743.

Muller, M., et al. (2009), Lithospheric structure, evolution and diamond prospectivity of the rehoboth terrane and western kaapvaal craton, southern africa: Constraints from broadband magnetotellurics, *Lithos*, *112*, 93 – 105, doi:DOI:10.1016/j.lithos.2009.06.023.

Muñoz, G., W. Heise, A. Paz, E. Almeida, F. Montiero Santos, and J. Pous (2005), New magnetotelluric data through the boundary between the Ossa Morena and CentroIberian zones, *Geologica Acta*, *3*(3), 215–223.

Muñoz, G., A. Mateus, J. Pous, W. Heise, F. Monteiro Santos, and E. Almeida (2008), Unraveling middle-crust conductive layers in Paleozoic Orogens through 3D modeling of magnetotelluric data: The ossa-morena zone case study (SW Iberian Variscides), *Jounal of Geophysical research*, *113*(B6), B06,106, doi:10.1029/2007JB004987.

Muñoz, J. (1992), Evolution of a continental collision belt: Ecors-pyrenees crustal balanced cross-section, in *Thrust Tectonics*, edited by McClay, pp. 235–246, Chapman and Hall, London.

Nabighian, M. N. (1987), *Electromagnetic Methods in Applied Geophysics - Theory*, vol. 1, Society of Exploration Geophysics, Tulsa, OK.

National Oceanic and Atmospheric Administration (NOAA) (2010), Lunar day: Animation of lunar day, last revision: March 25, 2008.

Neal, S. L., R. L. Mackie, J. C. Larsen, and A. Schultz (2000), Variations in the electrical conductivity of the upper mantle beneath North America and the Pacific Ocean, *Journal of Geophysical Research*, *105*, 8229–8242.

Nesbitt, B. (1993), Electrical resistivity of crustal fluids, *Journal of Geophysical Research*, *98*, 4301–4310.

Newman, G., and D. Alumbaugh (1995), Frequency-domain modeling of airborne electromagnetic responses using staggered finite differences, *Geophysical Prospecting*, *43*, 1021–1042.

Newman, G., and G. Hohmann (1988), Transient electromagnetic response of high-contrast prisms in a layered Earth, *Geophysics*, *53*, 691–706.

Newman, G. A., and D. Alumbaugh (1997), Three-dimensional massively parallel electromagnetic - I. theory, *Geophysical Journal International*, *128*, 345–354.

Newman, G. A., and D. Alumbaugh (2000), Three-dimensional magnetotelluric inversion using non-linear conjugate gradients, *Geophysical Journal International*, *140*, 410–424.

Newman, G. A., and D. L. Alumbaugh (2002), Three-dimensional induction logging problems: Part i. an integral equation solution and model comparisons, *Geophysics*, *67*, 484–491.

Newman, G. A., and P. Boggs (2004), Solution accelerators for large-scale three-dimensional electromagnetic inverse problems, *Inverse Problems*, *20*, S151–S170.

Newman, G. A., S. Recher, B. Tezkan, and F. M. Neubauer (2003), Case history: 3D inversion of a scalar radio magnetotelluric field data set, *Geophysics*, *68*(3), 791–802, doi:10.1190/1.1581032.

Niblett, E. R., and C. Sayn-Wittgenstein (1960), Variation of electrical conductivity with depth by the magneto-telluric method, *Geophysics*, *25*, 998–1008.

Nolet, G. (2008), *A breviary of seismic tomography*, Cambridge University Press, Cambridge, UK.

Nover, G. (2005), Electrical properties of crustal and mantle rocks: A review of laboratory measurements and their explanation, *Surveys in Geophysics*, *26*, 593–651.

Nuttall, A. (1981), Some windows with very good sidelobe behavior, *Acoustics, Speech and Signal Processing, IEEE Transactions on*, *29*(1), 84–91.

Olhoeft, G. R. (1985), Low-frequency electrical properties, *Geophysics*, *50*(12), 2492–2503, doi:10.1190/1.1441880.

Olsen, N. (1998), The electrical conductivity of the mantle beneath Europe derived from C-responses from 3 to 720 hr, *Geophysical Journal International*, *133*, 298–308.

Oni, E., and A. O. Alabi (1972), Preliminary results of the upper mantle conductivity structure in Nigeria, *Physics of the Earth and Planetary Interiors*, *5*, 179–183.

Onwumechili, C. A., and C. E. Agu (1982), Regional variations of equatorial electrojet parameters, *Annales de Geophysique*, *38*, 307–313.

Oristaglio, M. J., and B. R. Spies (1999), *Three Dimensional Electromagnetics*, *Geophysical Developments*, vol. 7, Society of Exploration Geophysics.

Osipova, I. L. (1983), Consideration of the influence of ionospheric source field structure on deep electromagnetic sounding results, in *The development of the geoelectric model of the Baltic Shield - Part 1 - Numerical methods*, edited by S. E. Hjelt and L. L. Vanjan, pp. 8–38, Department of Geophysics, University of Oulu, Finland, report Nr. 7.

Padilha, A. L. (1999), Behaviour of magnetotelluric source fields within the equatorial zone, *Earth, Planets, and Space*, *51*, 1119–1125.

Padilha, A. L., I. Vitorello, and L. Rijo (1997), Effects of the equatorial electrojet on magnetotelluric surveys: Field results from northwest Brazil, *Geophysical Research Letters*, *24*(1), 89–92.

Palomeras, I., R. Carbonell, I. Flecha, P. Simancas F. Ayarza, J. Matas, D. Martínez Poyatos, A. Azor, F. González Lodeiro, and A. Pérez-Estaún (2009), Nature of the lithosphere across the Variscan orogen of SW Iberia: Dense wide-angle seismic reflection data, *Journal of Geophysical Research*, *114*, B02,302, doi:10.1029/2007JB005050.

Park, S. K., B. Hirasuna, G. R. Jiracek, and C. Kinn (1996), Magnetotelluric evidence of lithospheric mantle thinning beneath the southern Sierra Nevada, *Journal of Geophysical Research*, *101*(B7), 16,241–16,255, doi:10.1029/96JB01211.

Parker, R. (1982), The existence of a region inaccessible to magnetotelluric sounding, *Geophysical Journal of the Royal Astronomical Society*, *68*, 165–170.

Parker, R., and K. Whaler (1981), Numerical methods for establishing solutions for the inverse problem of electromagnetic induction, *Journal of Geophysical Research*, *86*, 9574–9584.

Parker, R. L. (1980), The inverse problem of electromagnetic induction: Existence and construction of solutions based on incomplete data, *Journal of Geophysical Research*, *85*(B8), 4421–4428, doi:10.1029/JB085iB08p04421.

Parker, R. L. (1983), The magnetotelluric inverse problem, *Geophysical Surveys*, *6*, 5–25.

Parker, R. L. (1994), *Geophysical inverse theory*, Princeton University Press.

Parkinson, W. (1959), Direction of rapid geomagnetic variations, *Journal of the Royal Astronomical Society*, *2*, 1–14.

Parkinson, W. (1983), *Introduction to geomagnetism*, Elsevier, Amsterdam.

Partzsch, G. M., F. R. Schilling, and J. Arndt (2000), The influence of partial melting on the electrical behavior of crustal rocks: laboratory examinations, model calculations and geological interpretations, *Tectonophysics*, *317*(3-4), 189–203, doi: 10.1016/S0040-1951(99)00320-0.

Pádua, M. B., A. L. Padilha, and . Vitorello (2002), Disturbances on magnetotelluric data due to dc electrified railway: A case study from southeastern Brazil, *Earth, Planets and Space*, *54*(5), 591–596.

Peacock, S. M. (1990), Fluid processes in subduction zones, *Science*, *248*(4953), 329–337.

Pedrera, A., C. Marin-Lechado, J. Galindo-Zaldivar, L. R. Rodriguez-Fernandez, and A. Ruiz-Constan (2006), Fault and fold interaction during the development of the Neogene-Quaternary Almeria-Nijar Basin (SE Betic Cordillera), in *Moratti and Chalouan* [2006], pp. 217–230.

Pek, J., and F. A. Santos (2006), Magnetotelluric inversion for anisotropic conductivities in layered media, *Physics of The Earth and Planetary Interiors*, *158*(2-4), 139 – 158, doi:10.1016/j.pepi.2006.03.023.

Pek, J., and F. A. M. Santos (2002), Magnetotelluric impedances and parametric sensitivities for 1-D anisotropic layered media, *Computers & Geosciences*, *28*, 939–950.

Pek, J., F. A. M. Santos, and Y. Li (2011), Magnetotelluric inversion for 2-D anisotropic conductivity, in *Geophysical Research Abstracts of the EGU General Assembly 2011, vol. 13*, European Geophysical Union, poster ID: EGU2011-2953-1.

Pellerin, L., and G. W. Hohmann (1990), Transient electromagnetic inversion: A remedy for magnetotelluric static shifts, *Geophysics*, *55*(9), 1242–1250, doi:10.1190/1.1442940.

Peltier, W. R., and J. F. Hermance (1971), Magnetotelluric fields of a gaussian electrojet, *Canadian Journal of Earth Sciences*, *8*, 338–346.

Phoenix Geophysics (2005), *V5 System 2000 MTU/MTU-A user guide*, Phoenix Geophysics Limited, 3781 Victoria Park Avenue, Unit 3, Toronto, ON Canada M1W 3K5, 1.5 ed.

Pirjola, R. J. (1998), Modelling the electric and magnetic fields at the Earth's surface due to an auroral electrojet, *Journal of Atmospheric and Solar-Terrestrial Physics*, *60*, 1139–1148.

Piromallo, C., A. P. Vincent, D. A. Yuen, and A. Morelli (2001), Dynamics of the transition zone under europe inferred from wavelet cross-spectra of seismic tomography, *Physics of The Earth and Planetary Interiors*, *125*(1–4), 125–139, doi:10.1016/S0031-9201(01)00249-7.

Piwinskii, A. J., and A. Duba (1974), High temperature electrical conductivity of albite, *Geophysical Research Letter*, *1*, doi:10.1029/GL001i005p00209.

Platt, J., and R. Vissers (1989), Extensional collapse of thickened continental lithosphere: a working hypothesis for the Alboran Sea and Gibraltar arc, *Geology*, *17*, 540–543.

Platt, J. P., R. Anczkiewicz, J. I. Soto, S. P. Kelley, and M. Thirlwall (2006), Early miocene continental subduction and rapid exhumation in the western Mediterranean, *Geology*, *34*, 981–984.

Platzman, E. S. (1992), Paleomagnetic rotations and the kinematics of the Gibraltar arc, *Geology*, *20*(4), 311–314, doi:10.1130/0091-7613(1992)020\textless0311:PRATKO\textgreater2.3.CO;2.

Poe, B. T., C. Romano, F. Nestola, and J. R. Smyth (2010), Electrical conductivity anisotropy of dry and hydrous olivine at 8 GPa, *Physics of the Earth and Planetary Interiors*, *181*(3-4), 103–111.

Poirier, J.-P. (2000), *Introduction to the physics of the Earth's interior*, 2 ed., Cambridge University Press.

Pollack, H. N., and D. S. Chapman (1977), On the regional variation of heat flow, geotherms, and lithospheric thickness, *Tectonophysics*, *38*(3-4), 279–296, doi:10.1016/0040-1951(77)90215-3.

Pollack, H. N., S. J. Hurter, and J. R. Johnson (1993), Heat flow from the earth's interior: Analysis of the global data set, *Reviews of Geophysics*, *31*(3), 267–280, doi:10.1029/93RG01249.

Polyak, E., and G. Ribiere (1969), Note sur la convergence des methods conjugees, *Revue francaise d'informatique et de recherche operationnelle*, *16*, 35–43.

Pommier, A., and E. Le-Trong (2011), SIGMELTS: A web portal for electrical conductivity calculations in geosciences, *Computers & Geosciences*, pp. 1–10, doi:10.1016/j.cageo.2011.01.002.

Portero, J., and J. Aznar (1984), Evolucion morfotectonica y sedimentacion terciarias en el Sistema Central y cuencas limitrofes (Duero y Tajo), *Congr. Esp. Geol. Espana*, *3*, 253–263, spanish.

Potemra, T. (1984), Magnetospheric currents, Americal Geophysical Union.

Pous, J., P. Queralt, J. Ledo, and E. Roca (1999), A high electrical conductive zone at lower crustal depth beneath the Betic Chain (Spain), *Earth and Planetary Science Letters*, *167*(1-2), 35–45, doi:10.1016/S0012-821X(99)00011-4.

Pous, J., G. Muñoz, W. Heise, J. C. Melgarejo, and C. Quesada (2004), Electromagnetic imaging of Variscan crustal structures in SW Iberia: the role of interconnected graphite, *Earth and Planetary Science Letters*, *217*(3-4), 435 – 450, doi:10.1016/S0012-821X(03)00612-5.

Prácser, E., and L. Szarka (1999), A correction for Bahr's "phase deviation" method for tensor decomposition, *Earth, Planets and Space*, *51*, 1019–1022.

Pratt, J. H. (1855), On the attraction of the himalaya mountains and of the elevated regions beyond them, upon the plumb line in india, *Phil. Trans. R. Soc. Lond.*, *145*, 53–100.

Praus, O., J. Pecová, V. Petr, V. Babuska, and J. Plomerová (1990), Magnetotelluric and seismological determination of the lithosphere-asthenosphere transition in Central Europe, *Physics of The Earth and Planetary Interiors*, *60*(1-4), 212–228, doi: 10.1016/0031-9201(90)90262-V.

Press, F. (1968), Earth models obtained by Monte-Carlo inversion, *Journal of Geophysical Research*, *73*(16), 5223–5234.

Press, W. H., S. A. Teukolsky, W. T. Vetterling, and B. P. Flannery (2007), *Numerical Recipes: The Art of Scientific Computing*, 3 ed., Cambridge University Press, 32 Avenue of the Americas, New York, iSBN-10: 0521880688, or ISBN-13: 978-0521880688.

Pérez-Flores, M. A., and A. Schultz (2002), Application of 2-d inversion with genetic algorithms to magnetotelluric data from geothermal areas, *Earth Planets Space*, *54*(5), 607–616.

Price, A. T. (1949), The induction of electric currents in non-uniform thin sheets and shells, *The Quarterly Journal of Mechanics and Applied Mathematics*, *2*(3), 283–310, doi:10.1093/qjmam/2.3.283.

Price, A. T. (1973), The theory of geomagnetic induction, *Physics of the Earth and Planetary Interiors*, *7*, 227–233.

Pridmore, D. F., G. W. Hohmann, S. H. Ward, and W. R. Still (1981), An investigation of finite-element modeling for electrical and electromagnetic data in three dimensions, *Geophysics*, *46*, 1009–1024.

Pulgar, J., G. Gallart, J. Fernandez-Viejo, A. Perez-Estaun, and J. Alvarez-Marron (1996), Seismic image of the Cantabrian Mountains in the western extension of the Pyrenees from integrated ESCIN reflection and refraction data, *Tectonophysics*, *264*, 1–19.

Raiche, A. (1974), An Integral Equation approach to three-dimensional modeling, *Geophysical Journal*, *36*, 363–376.

Ranganayaki, R., and T. Madden (1990), Generalized thin sheet analysis in magnetotellurics: An extension of Price's analysis, *Geophysical Journal of the Royal Astronomical Society*, *60*, 445–457.

Rebollal, B. M., and A. Pérez-González (2008), Inland aeolian deposits of the Iberian Peninsula: Sand dunes and clay dunes of the Duero Basin and the Manchega Plain. palaeoclimatic considerations, *Geomorphology*, *102*(2), 207–220, doi:10.1016/j.geomorph.2008.05.009.

Reddy, I. K., D. Rankin, and R. J. Phillips (1977), Three-dimensional modelling in magnetotelluric and magnetic variational sounding, *Geophysical Journal of the Royal Astronomical Society*, *51*, 313–325.

Rein, A., R. Hoffmann, and P. Dietrich (2004), Influence of natural time-dependent variations of electrical conductivity on DC resistivity measurements, *Journal of Hydrology*, *285*(1-4), 215–232, doi:10.1016/j.jhydrol.2003.08.015.

Reuber, I., A. Michard, A. Chalouan, T. Juteau, and B. Jermoumi (1982), Structure and emplacement of the Alpine-type peridotites from Beni Bousera, Rif, Morocco: A polyphase tectonic interpretation, *Tectonophysics*, *82*, 231–251.

Reynard, B., K. Mibe, and B. V. de Moortèle (2011), Electrical conductivity of the serpentinised mantle and fluid flow in subduction zones, *Earth and Planetary Science Letters*, doi:10.1016/j.epsl.2011.05.013.

Richard, G. C., and D. Bercovici (2009), Water-induced convection in the Earth's mantle transition zone, *Journal of Geophysical Research*, *114*, doi:10.1029/2008JB005734.

Richmond, A. D. (1973a), Equatorial electrojet - I - development of a model including winds and instabilities, *Journal of Atmospheric and Terrestrial Physics*, *35*, 1083–1103.

Richmond, A. D. (1973b), Equatorial electrojet - II - use of the model to study the equatorial ionosphere, *Journal of Atmospheric and Terrestrial Physics*, *35*, 1105–1118.

Rikitake, T. (1948), Notes on the Electromagnetic Induction within the Earth, in *Bulletin of the Earthquake Research Institute*, vol. 24, pp. 1–9, Tokyo University's Earthquake Research Institute.

Rikitake, T. (1952), On the electrical conductivity in the Earth's core, in *Bulletin of the Earthquake Research Institute*, chap. 17, pp. 191–205, Tokyo University's Earthquake Research Institute.

Ringwood, A. (1977), Composition and origin of the Earth, in *Publication No. 1229*, Research School of Earth Science, Australian National University, Canberra.

Ringwood, A. E. (1975), *Composition and petrology of the Earth's mantle*, McGraw-Hill, New York.

Ritter, J. R. R., M. Jordan, U. R. Christensen, and U. Achauer (2001), A mantle plume below the Eifel volcanic fields, Germany, *Earth and Planetary Science Letters*, *186*(1), 7–14, doi:10.1016/S0012-821X(01)00226-6.

Ritter, O., A. Junge, and G. Dawes (1998), New equipment and processing for magnetotelluric remote reference observations, *Geophysical Journal International*, *132*(3), 535–548, doi:10.1046/j.1365-246X.1998.00440.x.

Rodi, W., and R. L. Mackie (2001), Nonlinear conjugate gradients algorithm for 2-D magnetotelluric inversion, *Geophysics*, *66*(1), 174–187.

Rosell, O., A. Martí, A. Marcuello, J. Ledo, P. Queralt, E. Roca, and J. Campanyá (2010), Deep electrical resistivity structure of the northern gibraltar arc (western mediterranean): evidence of lithospheric slab break-off, *Terra Nova*, *99*(5), 153–160.

Rostoker, G., M. Mareschal, and J. Samson (1982), Response of dayside net downward field-aligned current to changes in the IMF and to substorm perturbations, *Journal of Geophysical Research*, *87*, 3489–3510.

Roux, E., M. Moorkamp, and A. Jones (2009), Joint inversion of magnetotelluric and surface-wave data in an anisotropic Earth, in *Contributed paper at: EGU 2009, Vienna*, EGU.

Rudnick, R. L., and S. Gao (2003), Composition of the Continental Crust, *Treatise on Geochemistry*, *3*, 1–64, doi:10.1016/B0-08-043751-6/03016-4.

Ruffet, C., M. Darot, and Y. Gueguen (1995), Surface conductivity in rocks: a review, *Surveys in Geophysics*, *16*(1), 83–105, doi:10.1007/BF00682714.

Ruiz-Constán, A., J. Galindo-Zaldivar, A. Pedrera, J. A. Arzate, J. Pous, F. Anahnah, W. Heise, F. A. Monteiro Santos, and C. Marín-Lechado (2010), Deep deformation pattern from electrical anisotropy in an arched orogen (betic cordillera, western mediterranean), *Geology*, *38*(8), 731–734, doi:10.1130/G31144.1.

Sarma, S. V. S., K. R. Ramanujachary, and P. V. S. Narayan (1974), Diurnal and seasonal occurrence patterns of Pc and Pi pulsations at Choutuppal /Hyderabad/, India, *Indian Journal of Radio and Space Physics*, *3*, 221–226.

Sato, H., I. Sacks, and T. Murase (1989), The use of laboratory velocity data for estimating temperature and partial melt fraction in the low velocity zone: Comparison with heatflow and electrical conductivity studies, *Journal of Geophysical Research*, *94*, 5689–5704.

Schlumberger (1989), *Log Interpretation Principles/Applications*, 1 ed., Schlumberger Educational Services, New York.

Schmeling, H. (1986), Numerical models of the influence of partial melt on elastic, anelastic and electric properties of rocks, Part II: electrical conductivity, *Physics of the Earth and Planetary Interiors*, *43*, 123–136.

Schmucker, U. (1970), Anomalies of geomagnetic variations in the southwestern United States, *Bull. Scripps Inst. Oceanography*, *13*.

Schmucker, U. (1973), Regional induction studies: A review of methods and results, *Physics of The Earth and Planetary Interiors*, *7*(3), 365 – 378, doi:DOI:10.1016/0031-9201(73)90061-7.

Schmucker, U. (1980), Induktion in geschichteten Halbraeumen durch inhomogene Felder, in *Protokoll Kolloquium Elektromagnetische Tiefenforschung Berlin-Lichtenrade*, edited by V. Haak and J. Homilius, pp. 197–210, Landesamt fuer Bodenforschung, Stilleweg 2, Niedersachsen, Hannover.

Schmucker, U. (1985), Geophysics of the solid Earth, the Moon and the Planets, in *Numerical Data and Functional Relationships in Science and Technology*, vol. 2, edited by K. Fuchs and H. Soffel, pp. 31–73, Springer-Verlag, Berlin-Heidelberg.

Schmucker, U. (1987), Substitute conductors for electromagnetic response estimates, *Pure and Applied Geophysics*, *125*(2-3), 341–367.

Schoen, J. (1983), *Petrophysik: Physikalische Eigenschaften Von Gesteinen Und Mineralen*, Enke Verlag, Stuttgart.

Schultz, A., R. D. Kurtz, A. D. Chave, and A. G. Jones (1993), Conductivity discontinuities in the upper mantle beneath a stable craton, *Geophysical Research Letters*, *20*, 2941–2944.

Schwalenberg, K., V. Rath, and V. Haak (2002), Sensitivity studies applied to a two-dimensional resistivity model from the Central Andes, *Geophysical Journal International*, *150*(3), 673–686, doi:10.1046/j.1365-246X.2002.01734.x.

Seber, D., M. Barazangi, A. Ibenbrahim, and A. Demnati (1996), Geophysical evidence for lithospheric delamination beneath the Alboran Sea and Rif-Betic mountains, *Nature*, *379*, 785–790.

Sen, P. N., C. Scala, and M. H. Cohen (1981), Self similar model for sedimentary rocks with application to the dielectric constant of fused glass beads, *Geophysics*, *46*, 781–795, doi:10.1190/1.1441215.

Serrano, I., J. Morales, D. Zhao, F. Torcal, and F. Vidal (1998), P-wave tomographic images in the central Betics-Alborán Sea (South Spain) using local earthquakes: Contribution for a continental collision, *Geophysical Research Letters*, *25*(21), 4031–4034, doi:10.1029/1998GL900021.

Serson, P. H. (1973), Instrumentation for induction studies on land, *Physics of the Earth and Planetary Interiors*, *7*, 313–322.

Shankland, T. J. (1975), Electrical conduction in rocks and minerals: parameters for interpretation, *Physics of the Earth and Planetary Interiors*, *10*, 209–219.

Shankland, T. J., and A. Duba (1990), Standard electrical conductivity of isotropic, homogeneous olivine in the temperature range 1200-1500 degree, *Geophysical Journal International*, *103*(1), 25–31, doi:10.1111/j.1365-246X.1990.tb01749.x.

Shankland, T. J., J. Peyronneau, and J.-P. Poirier (1993), Electrical conductivity of the Earth's lower mantle, *Nature*, *366*, 453–455, doi:10.1038/366453a0.

Shankland, T. J., A. G. Duba, E. A. Mathez, and C. L. Peach (1997), Increase of electrical conductivity with pressure as an indicator of conduction through a solid phase in midcrustal rocks, *Journal of Geophysical Research*, *102*(B7), 14,741–14,750, doi: 10.1029/96JB03389.

Shanno, D. (1970), Conditioning of quasi-Newton methods for function minimization, *Mathematics and Computation*, *24*, 647–656.

Sherman, D. M. (1995), Stability of possible Fe-FeS and Fe-FeO alloy phases at high pressure and the composition of the Earth's core, *Earth and Planetary Science Letters*, *132*(1-4), 87 – 98, doi:10.1016/0012-821X(95)00057-J.

Siegel, A. (1982), Robust regression using repeated medians, *Biometrika*, *69*, 801–819.

Silver, P. G., S. S. Gao, K. H. Liu, and the Kaapvaal Seismic Group (2001), Mantle deformation beneath southern Africa, *Geophysical Research Letters*, *28*(13), 2493–2496.

Simpson, F. (2001), Resistance to mantle flow inferred from the electromagnetic strike of the Australian upper mantle, *Nature*, *412*, 632–635.

Simpson, F. (2002a), A comparison of electromagnetic distortion and resolution of upper mantle conductivities beneath continental Europe and the Mediterranean using islands as windows, *Physics of the Earth and Planetary Interiors*, *129*, 117–130.

Simpson, F. (2002b), Intensity and direction of lattice-preferred orientation of olivine: are electrical and seismic anisotropies of the Australian mantle reconcilable ?, *Earth and Planetary Science Letters*, *203*, 535–547.

Simpson, F., and K. Bahr (2005), *Practical Magnetotellurics*, Cambridge University Press.

Siripunvaraporn, W. (2010), Three-dimensional magnetotelluric inversion: An introductory guide for developers and users, in *20th IAGA WG 1.2 Workshop on Electromagnetic Induction in the Earth (EMIW)*, Giza, Egypt.

Siripunvaraporn, W., and G. Egbert (2000), An efficient data-subspace inversion method for 2-D magnetotelluric data, *Geophysics*, *65*(3), 791–803, doi:10.1190/1.1444778.

Siripunvaraporn, W., and G. Egbert (2007), Data space conjugate gradient inversion for 2-D magnetotelluric data, *Geophysical Journal International*, *170*, 986–994.

Siripunvaraporn, W., and W. Sarakorn (2010), An efficient three.dimensional magnetotelluric inversion: A mix of the data space conjugate gradient method and the data space Occam's inversion, submitted.

Siripunvaraporn, W., G. D. Egbert, Y. Lenbury, and M. Uyeshima (2005a), Three-dimensional magnetotelluric inversion: Data-space method, *Physics of the Earth and Planetary Interiors*, *150*(1-3), 3–14, doi:10.1016/j.pepi.2004.08.023.

Siripunvaraporn, W., G. Egbert, and M. Uyeshima (2005b), Interpretation of two-dimensional magnetotelluric profile data with three-dimensional inversion: synthetic examples, *Geophysical Journal International*, *160*, 804–814, doi:10.1111/j.1365-246X.2005.02527.x.

Smirnov, M. Y. (2003), Magnetotelluric data processing with a robust statistical procedure having a high breakdown point, *Geophysical Journal International*, *152*, 1–7, doi:10.1046/j.1365-246X.2003.01733.x.

Smith, J. T., and J. R. Booker (1991), Rapid inversion of Two- and Three-Dimensional magnetotelluric data, *Journal of Geophysical Research*, *96*(B3), 3905–3922, doi:10.1029/90JB02416.

Smith, T. J., and J. R. Booker (1988), Magnetotelluric inversion for minimum structure, *Geophysics*, *53*(12), 1565–1576.

Solar Influence Data Analysis Center (SIDC), Royal Observatory of Belgium (2010), Sunspot index graphics, last revision: March 25, 2008.

Spakman, W., and R. Wortel (2004), A tomographic view on western Mediterranean geodynamics, in *The TRANSMED Atlas - The Mediterranean Region from Crust to Mantle*, edited by W. Canvazza et al., pp. 31–52, Springer, Berlin-Heidelberg.

Spakman, W., S. van der Lee, and R. D. van der Hilst (1993), Travel-time tomography of the European-Mediterranean mantle down to 1400 km, *Physics of the Earth and Planetary Interiors*, *79*, 3–74.

Spitzer, K. (2006), Magnetotelluric static shift and direct current sensitivity, *Geophysical Journal International*, *165*(1), 289–299.

Spratt, J. E., A. G. Jones, V. A. Jackson, L. Collins, and A. Avdeeva (2009), Lithospheric geometry of the Wopmay orogen from a Slave craton to Bear Province magnetotelluric transect, *Journal of Geophysical Research*, *114*(B1), B01,101, doi: 10.1029/2007JB005326.

Stacey, F. D., and P. M. Davis (2008), *Physics of the Earth*, 4 ed., Cambridge University Press, New York.

Stapel, G. (1999), The nature of isostasy in western Iberia, Ph.D. thesis, Vrije Universiteit Amsterdam, Amsterdam.

Sternberg, B. K., J. C. Washburne, and L. Pellerin (1988), Correction for the static shift in magnetotellurics using transient electromagnetic soundings, *Geophysics*, *53*(11), 1459–1468, doi:10.1190/1.1442426.

Stesky, R., and W. Brace (1973), Electrical conductivity of serpentinized rocks to 6 kilobars, *Journal of Geophysical Research*, *78*, 7614–7621.

Stixrude, L., and C. Lithgow-Bertelloni (2005), Mineralogy and elasticity of the oceanic upper mantle: Origin of the low-velocity zone, *Journal of Geophysical Research*, *110*(B3), B03,204, doi:10.1029/2004JB002965.

Surinach, E., and R. Vegas (1998), Lateral inhomogeneities of the Hercynian crust in central Spain, *Physics of the Earth and Planetary Interiors*, *51*, 226–234.

Swift, C. M. (1967), A magnetotelluric investigation of an electrical conductivity anomaly in the southwestern United States, Ph.D. thesis, MIT, Cambridge, MA.

Tarantola, A. (2005), *Inverse problem theory and methods for model parameter estimation*, Society for Industrial and Applied Mathematics.

Tarits, P., S. Hautot, and F. Perrier (2004), Water in the mantle: Results from electrical conductivity beneath the French Alps, *Geophysical Research Letter*, *31*, doi:10.1029/2003GL019277.

Taylor, S., and S. McLennan (1985), *The continental crust: Its composition and evolution*, Blackwell Scientific Publishing, Palo Alto, CA.

Teixell, A., P. Ayarza, H. Zeyen, M. Fernandez, and M. Arboleya (2005), Effects of mantle upwelling in a compressional setting: the atlas mountains of morocco, *Terra Nova*, *17*, 456–461.

Teixell, A., G. Bertotti, D. Frizon de Lamotte, and M. Charroud (2009), The geology of vertical movements of the lithosphere: An overview, *Tectonophysics*, *475*, 1–8, doi: 10.1016/j.tecto.2009.08.018.

Tejero, R., and J. Ruiz (2002), Thermal and mechanical structure of the central Iberian Peninsula lithosphere, *Tectonophysics*, *350*(1), 49–62, doi:10.1016/S0040-1951(02) 00082-3.

Tejero, R., A. Perucha, and J. Rivas, A. Bergamin (1996), Modelos estructural y gravimetrico del Sistema Central, *Geogaceta*, *20*, 947–950, in Spanish.

Telford, W. M., L. P. Geldart, and R. E. Sheriff (1990), *Applied Geophysics*, second ed., Cambridge University Press, New York.

ten Grotenhuis, S. M., M. R. Drury, C. J. Peach, and C. J. Spiers (2004), Electrical properties of fine-grained olivine: Evidence for grain boundary transport, *Journal of Geophysical Research*, *109*(B6), B06,203, doi:10.1029/2003JB002799.

Tesauro, M., M. K. Kaban, and S. A. P. L. Cloetingh (2008), EuCRUST-07: A new reference model for the European crust, *Geophysical Research Letter*, *35*(5), L05,313, doi:10.1029/2007GL032244.

Tesauro, M., M. K. Kaban, and S. A. P. L. Cloetingh (2009a), How rigid is Europe's lithosphere?, *Geophysical Research Letter*, *36*(16), L16,303, doi:10.1029/2009GL039229.

Tesauro, M., M. K. Kaban, and S. A. Cloetingh (2009b), A new thermal and rheological model of the European lithosphere, *Tectonophysics*, *476*(3-4), 478–495, doi:10.1016/j. tecto.2009.07.022.

Thompson, B. A., and J. A. Connolly (1995), Melting of the continental crust: Some thermal and petrological constraints on anatexis in continental collision zones and other tectonic settings, *Journal of Geophysical Research*, *100*(B8), 15,565–15,579, doi:10. 1029/95JB00191.

Thybo, H. (2006), The heterogeneous upper mantle low velocity zone, *Tectonophysics*, *416*(1-4), 53–79, doi:DOI:10.1016/j.tecto.2005.11.021.

Tiab, D., and E. C. Donaldson (2004), *Petrophysics: theory and practice of measuring reservoir rock and fluid transport properties*, Gulf Publishing Company.

Tikhonov, A. N. (1950), The determination of electrical properties of the deep layers of the Earth's crust, *Dokl. Acad. Nauk. SSR*, *73*, 295–297, in russian.

Tikhonov, A. N. (1965), Mathematical basis of the theory of electromagnetic soundings, *USSR Comp. Math. Phys.*, *5*, 201–211.

Tikhonov, A. N., and V. Y. Arsenin (1977), *Solutions of ill-posed problems*, V.H. Winston and Sons, New York.

Torres, T., P. Garcia Alonso, T. Nestares, and J. Ortiz (1997), Terciario entre la Sierra de Altomira y la Serrania de Cuenca: Aspectos basicos de la paleogeografia cenozoica de la Depresion Intermedia, in *Itinerarios geologicos en el Terciario del centro y este de la Peninsula Iberica*, edited by L. Alcala and A. Alonso-Zarza, pp. 57–70, HC Multimedia, Madrid.

Torres-Roldan, R., G. Poli, and A. Peccerillo (1986), An early Miocene arc-tholeitic magmatic dike event from the Alboran Sea: Evidence for precollision subduction and back-arc crustal extension in the westernmost Mediterranean, *Geologische Rundschau*, *75*, 219–234.

Tournerie, B., and M. Chouteau (2005), Three-dimensional magnetotelluric survey to image structure and stratigraphy of a sedimentary basin in hungary, *Physics of the Earth and Planetary Interiors*, *150*, 197–202, doi:10.1016/j.pepi.2004.08.023.

Tubía, J. M., F. Navarro-Vilá, and J. Cuevas (1993), The Maláguide-Los Reales Nappe: An example of crustal thinning related to the emplacement of the Ronda peridotites (Betic Cordillera), *Physics of the Earth and Planetary Interiors*, *78*, 343–354.

Tubía, J. M., J. Cuevas, and J. I. Gil-Ibarguchi (1997), Sequential developments of the metamorphic aureole beneath the Ronda peridotites and its bearing on the tectonic evolution of the Betic Cordillera, *Tectonophysics*, *279*, 227–252.

Turcotte, D. L., and G. Schubert (2002), *Geodynamics*, 2 ed., Press Syndicate of University od Cambridge, The Edinburgh Building, Cambridge, CB2, 2RU, UK.

Untiedt, J. (1967), Model of the equatorial electrojet involving meridional currents, *Journal of Geophysical Research*, *72*, 5799–5810.

USGS Energy Resources Program (2010), Envision, web application, v. 1.1.0.

Utada, H., and H. Munekane (2000), On galvanic distortion of regional three-dimensional magnetotelluric impedances, *Geophysical Journal International*, *140*(2), 385–398, doi: 10.1046/j.1365-246x.2000.00014.x.

Utada, H., T. Koyama, H. Shimizu, and A. D. Chave (2003), A semi-reference model for electrical conductivity in the mid-mantle beneath the North Pacific region, *Geophysical research letter*, *30*(4), 43–1–43–4.

Valladares, M. I., P. Barba, and J. M. Ugidos (2002), Precambrian, in *Gibbons and Moreno* [2002b], chap. 2, pp. 7–16.

van Keken, P. E. (2003), The structure and dynamics of the mantle wedge, *Earth and Planetary Science Letters*, *215*, 323–338.

Varentsov, I. M., E. Y. Sokolova, and the BEAR Working Group (2003a), Diagnostics and suppression of auroral distortions in the transfer operators of the electromagnetic field in the bear experiment, *Izvestiya, Physics of the Solid Earth*, *39*(4), 283—307.

Varentsov, I. M., E. Y. Sokolova, E. R. Martanus, K. V. Nalivaiko, and the BEAR Working Group (2003b), System of electromagnetic field transfer operators for the bear array of simultaneous soundings: Methods and results, *Izvestiya, Physics of the Solid Earth*, *39*(2), 118—148.

Vegas, R., J. Vazquez, E. Surinach, and A. Marcos (1990), Model of distributed deformation, block rotations and crustal thickening for the formation of the Spanish Central System, *Tectonophysics*, *184*, 367–378.

Vilà, M., M. Fernández, and I. Jiménez-Munt (2010), Radiogenic heat production variability of some common lithological groups and its significance to lithospheric thermal modeling, *Tectonophysics*, *490*(3-4), 152–164, doi:10.1016/j.tecto.2010.05.003.

Villaseca, C., H. Downes, C. Pin, and L. Barbero (1999), Nature and composition of the lower continental crust in Central Spain and the granulite-granite linkage: Inferences from granulite xenoliths, *Journal of Petrology*, *40*(10), 1463–1496.

Villaseñor, A., W. Spakman, and E. Engdahl (2003), Influence of regional travel times in global tomographic models, in *EGS-AGU-EUG Joint Assembly*, vol. 5, pp. EAE03–A–08,614, Geophysical Research Abstracts, Nice, France.

Villaseñor, A., Y. Yang, M. H. Ritzwoller, and J. Gallart (2007), Ambient noise surface wave tomography of the Iberian Peninsula: Implications for shallow seismic structure, *Geophysical Research Letters*, *34*, L11,304, doi:10.1029/2007GL030164.

Vinnik, L., R. Green, and L. Nicolaysen (1995), Recent deformations of the deep continental root beneath southern Africa, *Nature*, *375*, 50–52.

Vozoff, K. (1986), *Magnetotelluric methods*, 5, Society of Exploration Geophysics, Tulsa, OK, USA, reprint.

Vozoff, K. (1987), The magnetotelluric method, in *Nabighian* [1987], pp. 641–712.

Wait, J. R. (1954), On the relation between telluric currents and the Earth's magnetic field, *Geophysics*, *19*, 281–289.

Walker, A. D. M., and R. A. Greenwald (1981), Pulsation structure in the ionosphere derived from auroral radar data, in *ULF pulsations in the magnetosphere*, edited by D. Dordrecht, pp. 111–127, Reidel Publishing Co., Center for Academic Publications, Tokyo, Japan.

Wanamaker, B. J., and D. L. Kohlstedt (1991), The effect of melt composition on the wetting angle between silicate melts and olivine, *Physics and Chemistry of Minerals*, *18*(1), 26–36.

Wannamaker, P. (1991), Advances in three-dimensional magnetotelluric modeling using Integral Equations, *Geophysics*, *56*, 1716–1728.

Wannamaker, P. (2005), Anisotropy versus heterogeneity in continental solid Earth electromagnetic studies: Fundamental response characteristics and implications for physicochemical state, *Surveys in Geophysics*, *26*, 733–765, doi:10.1007/s10712-005-1832-1.

Wannamaker, P. E., G. W. Hohmann, and S. W. A. Filipo (1984), Electromagnetic modeling of three-dimensional bodies in layered earths using integral equations, *Geophysics*, *49*, 60–74.

Wannamaker, P. E., G. T. Caldwell, G. R. Jiracek, V. Maris, G. J. Hill, Y. Ogawa, H. M. Bibby, S. L. Bennie, and W. Heise (2009), Fluid and deformation regime of an advancing subduction system at marlborough, new zealand, *Nature*, *460*(7256), 733–736, doi:10.1038/nature08204.

Warburton, J., and C. Alvarez (1989), A thrust tectonic interpretation of the Guadarrama Mountains, Spanish Central System, in *Libro Homenaje a Rafael Soler*, pp. 147–155, Asoc. Geol. Geof. Esp. del Petroleo, Spain.

Ward, S. H. (1967), Electromagnetic theory for geophysical applications, in *Mining Geophysics*, vol. 2, pp. 228–372, The Society of Exploration Geophysicists, Tulsa, Oklahoma,

Ward, S. H., and G. W. Hohmann (1987), Electromagnetic theory for geophysical applications, in *Nabighian* [1987], pp. 131–311.

Weaver, J. T., A. K. Agarwal, and X. H. Pu (1999), Three-dimensional Finite-Difference modeling of the magnetic field in geo-electromagnetic induction, in *Oristaglio and Spies* [1999], pp. 426–443.

Weaver, J. T., A. K. Agarwal, and F. E. M. Lilley (2000), Characterization of the magnetotelluric tensor in terms of its invariants, *Geophysical Journal International*, *141*, 321–336, wALDIM basis paper.

Wedepohl, H. K. (1995), The composition of the continental crust, *Geochimica et Cosmochimica Acta*, *59*(7), 1217–1232, doi:10.1016/0016-7037(95)00038-2.

Weidelt, P. (1972), The inverse problem of geomagnetic induction, *Zeitschrift für Geophysik*, *8*(2), 257–290.

Weidelt, P. (1975), Electromagnetic induction in 3D structures, *Journal of Geophysics*, *41*, 85–109.

Weidelt, P., W. Mueller, W. Losecke, and K. Knoedel (1980), Die Bostick Transformation, in *Protokoll ueber das Kolloquium 'Elektromagnetische Tiefenforschung'*, edited by H. V. and J. Homilius, pp. 227–230, Berlin-Hannover.

Wiese, H. (1962), Geomagnetische Tiefentellurik. II. die Streichrichtung der Untergrundstrukturen des elektrischen Widerstandes, erschlossen aus geomagnetischen Variationen (in Germany), *Geofis. Pura Appl.*, *52*, 83–103.

Wiese, H. (1965), Geomagnetische Tiefentellurik, in *36. Abhandlungen der Deutschen Akademie der Wissenschaften zu Berlin*, Geomagnetisches Institut Potsdam.

Wight, D., and F. Bostick (1980), Cascade decimation: A technique for real time estimation of power spectra, in *Acoustics, Speech, and Signal Processing, IEEE International Conference on ICASSP '80*, pp. 626–629, IEEE, Denver, CO, USA, reprinted in *Vozoff* [1986].

Wilson, M., and H. Downes (1991), Tertiary-quaternary extension-related alkaline magmatism in western and central Europe, *Journal of Petrology*, *32*, 811–849.

Wilson, M., and H. Downes (2006), Tertiary-quaternary intra-plate magmatism in europe and its relationship to mantle dynamics, in *European lithosphere dynamics, Geological Society of London Memoir 32*, edited by D. G. Gee and R. Stephenson, pp. 147–166, Geological Society of London, London.

WinGLink (2005), *WinGLink user's guide*, Geosystems SRL, 17 Viale Abruzzi, 20131, Milan, Italy, 2.07.04 ed., www.geosystems.net.

Wolfgram, P., and J. Scharberth (1986), *Electrical Conductivity Reference Exploration (ECRE)*, Geometra Ltd., 18 pp.

Wright, J. (1988), *VLF interpretation manual*, EDA instruments inc., 87 pp.

Xie, H.-S., W.-G. Zhou, M.-X. Zhu, Y.-G. Liu, Z.-D. Zhao, and J. Guo (2002), Elastic and electrical properties of serpentinite dehydration at high temperature and high pressure, *Journal of Physics: Condensed Matter*, *14*(44), 11,359–11,363.

Xu, Y., and T. J. Shankland (1999), Electrical conductivity of orthopyroxene and its high pressure phases, *Geophysical Research Letter*, *26*(17), 2645–2648, doi:10.1029/1999GL008378.

Xu, Y., B. T. Poe, T. J. Shankland, and D. C. Rubie (1998a), Electrical conductivity of olivine, wadsleyite, and ringwoodite under upper-mantle conditions, *Science*, *280*, 1415–1418, doi:10.1126/science.280.5368.1415.

Xu, Y., C. McCammon, and B. T. Poe (1998b), The Effect of Alumina on the Electrical Conductivity of Silicate Perovskite, *Science*, *282*(5390), 922–924, doi:10.1126/science.282.5390.922.

Xu, Y., T. J. Shankland, and B. T. Poe (2000a), Laboratory-based electrical conductivity in the Earth's mantle, *Journal of Geophysical Research (Solid Earth)*, *105*(B12), 27,865–27,875.

Xu, Y., T. J. Shankland, and A. G. Duba (2000b), Pressure effect on electrical conductivity of mantle olivine, *Physics of The Earth and Planetary Interiors*, *118*(1-2), 149 – 161, doi:10.1016/S0031-9201(99)00135-1.

Yee, K. (1966), Numerical solution of initial boundary value problems involving Maxwell's equations in isotropic media, *IEEE Transactions on Antennas and Propagation*, *14*(3), 302–307, doi:10.1109/TAP.1966.1138693.

Yoshino, T. (2010), Laboratory electrical conductivity measurement of mantle minerals, *Surveys in Geophysics*, *31*, 163–206, doi:10.1007/s10712-009-9084-0.

Yoshino, T., G. Manthilake, T. Matsuzaki, and T. Katsura (2008), Dry mantle transition zone inferred from the conductivity of wadsleyite and ringwoodite, *Nature*, *451*(7176), 326–329, doi:10.1038/nature06427.

Yoshino, T., M. Laumonier, E. McIsaac, and T. Katsura (2010), Electrical conductivity of basaltic and carbonatite melt-bearing peridotites at high pressures: Implications for melt distribution and melt fraction in the upper mantle, *Earth and Planetary Science Letters*, *295*(3-4), 593–602, doi:DOI:10.1016/j.epsl.2010.04.050.

Zandt, G., and C. R. Carrigan (1993), Small-scale convective instability and upper mantle viscosity under California, *Science*, *261*(5120), 460–463.

Zandt, G., H. Gilbert, T. J. Owens, M. Ducea, J. Saleeby, and C. H. Jones (2004), Active foundering of a continental arc root beneath the southern sierra nevada in california, *Nature*, *431*(7004), 41–46, doi:10.1038/nature02847.

Zanetti, L. J., T. A. Potemra, and W. Baumjohann (1983), Ionospheric and Birkeland current distributions inferred from the MAGSAT magnetometer data, *Journal of Geophysical Research*, *88*, 4875–4884, doi:10.1029/JA088iA06p04875.

Zeyen, H., P. Ayarza, M. Fernàndez, and A. Rimi (2005), Lithospheric structure under the western African-European plate boundary: A transect across the Atlas Mountains and the Gulf of Cadiz, doi:10.1029/2004TC001639.

Zhang, P., R. G. Roberts, and L. B. Pedersen (1987), Magnetotelluric strike rules, *Geophysics*, *52*(3), 267–278.

Zielhuis, A., and G. Nolet (1994), Shear-wave velocity variations in the upper mantle beneath central Europe, *Geophysical Journal International*, *117*(3), 695–715, doi:10.1111/j.1365-246X.1994.tb02463.x.

Zonge, K. L., and L. J. Hughes (1991), Controlled source audio-frequency magnetotellurics, in *Electromagnetic Methods in Applied Geophysics - Theory*, vol. 2, pp. 713–784, Society of Exploration Geophysics, Tulsa, OK.

Zyserman, F. I., and J. E. Santos (2000), Parallel finite element algorithm with domain decomposition for three-dimensional magnetotelluric modeling, *Journal of Applied Geophysics*, *44*, 337–351.